

FUNDAMENTAL PARAMETERS OF EXOPLANETS
AND THEIR HOST STARS

BY

JEFFREY LANGER COUGHLIN, B.S., M.S.

A dissertation submitted to the Graduate School

in partial fulfillment of the requirements

for the degree

Doctor of Philosophy

Major Subject: Astronomy

New Mexico State University

Las Cruces New Mexico

September 2012

“Fundamental Parameters of Exoplanets and Their Host Stars” a dissertation prepared by Jeffrey L. Coughlin in partial fulfillment of the requirements for the degree, Doctor of Philosophy, has been approved and accepted by the following:

Linda Lacey
Dean of the Graduate School

Thomas E. Harrison
Chair of the Examining Committee

Date

Committee in charge:

Dr. Thomas E. Harrison, Chair

Dr. Nancy J. Chanover

Dr. Jon Holtzman

Dr. Daniel P. Dugas

DEDICATION

I dedicate this work to my mother, Marcia Langer, the best Mom in the whole universe.

ACKNOWLEDGMENTS

Over the last 5 years I have learned that no person is ever successful completely on their own. Whether it be friends, family, or mentors, we rely on those people for support in our endeavors, and I've been extremely fortunate to have a generous dose of all three in my life.

I would like to thank the National Science Foundation for their generous support through the Graduate Research Fellowship Program. Thanks as well to NASA and the *Kepler* Mission for support through their Guest Observing Program, and to the New Mexico Space Grant Research Consortium.

Tom, thanks for being both a mentor and a friend, for helping to reign in my Astronomy ADD, and enabling me to publish so much and be successful in this field. I apologize to you and Joni for the chocolate handprints, but I regret nothing. Jon, thank you for taking me on as a student early, showing me the ropes on the 1 meter, and for all the encouragement. Nancy, thanks for all the support, award nominations, and planetary group treats. Ofelia and Lorenza, thanks for battling the university bureaucracy on my behalf, and often at your own peril. Dr. Dugas, thanks for showing me how cool geology can be; I've never looked at a mountain, river, or valley the same since taking your class. Mercedes, thank you for taking a chance on working with a first year graduate student five years ago, and for being an amazingly supportive collaborator and friend. And to my undergraduate advisors Rick and Horace back at Emory, thank you for all the time you spent with me in undergrad; I could not have been better prepared for graduate school thanks to you two.

To all the graduate students here, thanks for keeping the department a

friendly and upbeat place to work. Special thanks to Ryan, Maria, Chas, Jillian, Kyle, Leland, Liz, Adam, Cat, Mike, Nick, Roberto, and Glenn for extra support, listening to all my rants, and simply all the fun times. Joni, thanks for letting me know about all the hidden fun in Cruces, and thanks to you and Tom for hosting such awesome parties. Jom, please never haunt my dreams again. Herbert, my dear office plant, I shall miss your massive tentacle-like vines; thanks for making the office greener, and for not eating Sebastian.

Chris, Josie, Jennifer, Vince, Hazel, Ken, Stephanie, and Charlie, i.e., the Krazy Kutacs, thank you so much for letting me become one of those crazy Kutacs over the past few years, and for letting me use your kitchen tables as desks, where much of this thesis was written.

Grampa Ed and Grammy Joan, thank you for remembering every single holiday, birthday, and special occasion; you are always in my thoughts and in my heart. Uncle Marc, Aunt Cathy, Maggie, Marc, Molly, Melissa, and Eva, thank you for your overly generous contributions to “the beer fund”, and especially for your overwhelming love and moral support. Aunt Judy, thank you for being a spirit of confidence and self-worth that I will carry with me always.

Julie, thank you for always making time to hang out during my last-minute Tucson visits and for all the support. To Jon, thanks for all the fun times hanging out and saving my squishy scout. To Ryan, thank you for all the nerdy midnight talks over a six pack and for being a great roommate and friend; I don’t think I’ll ever find a better one. To Maria, thanks for being crazy...I mean, a crazy awesome seriously good friend and for all the trips to Cafe W. To Jamie, although I lament at not being able to write this thesis next to you at Java Monkey, it has still felt

like you've been there every step of the way over the past five years.

My brother J.P. and sister-in-law Jenn, thank you for all the love and support, the fun times, and for simply always being there for me. I realized in writing this I've known you Jenn for almost exactly as long as I've been working on this thesis, and what a great $5\frac{1}{2}$ years it's been! One of these days J.P., I'm going to make up those 31.5 seconds.

My partner Nicholas, thanks for all the time you've spent patiently listening to me ramble on about the various problems I was facing, for the unending encouragement and optimism you've shown me, and for simply making every day since we met brighter than the last. Persistence *is* everything.

Finally, my greatest thanks goes to my mother, Marcia, for all her love and dedication to my education. I would not have gotten here today without all your love, support, and encouragement.

VITA

EDUCATION

- 2007-2009 M.S., Astronomy
New Mexico State University, with Honors
Las Cruces, New Mexico, USA
- 2003-2007 B.S., Physics and Astronomy
Emory University, *Summa cum Laude*
Atlanta, Georgia, USA

AWARDS AND GRANTS

- 2012 NMSU Astronomy Murrell Award for Professional Development
- 2009-2012 NSF Graduate Research Fellowship
- 2009 NASA Graduate Student Research Fellowship (Declined)
- 2009 NMSU Astronomy ZIA Award for Outstanding Research
- 2008 & 2009 New Mexico Space Grant Graduate Research Fellowship

PROFESSIONAL ORGANIZATIONS

- American Astronomical Society (& Division for Planetary Sciences)
- Sigma Pi Sigma National Physics Honors Society

PUBLICATIONS

- Coughlin, J.L. and López-Morales, M., 2012, *The Astrophysical Journal*, 750, 100.
Modeling Multi-Wavelength Stellar Astrometry. III. Determination of the Absolute Masses of Exoplanets and Their Host Stars

- Coughlin, J.L. and López-Morales, M., 2012, *The Astronomical Journal*, 143, 39.
A Uniform Search for Secondary Eclipses of Hot Jupiters in Kepler Q2 Lightcurves
- Harrison, T.E., Coughlin, J.L., Ule, N.M., and López-Morales, M., 2012, *The Astronomical Journal*, 143, 4. *Kepler Cycle 1 Observations of Low Mass Stars: New Eclipsing Binaries, Single Star Rotation Rates, and the Nature and Frequency of Starspots*
- Coughlin, J.L., López-Morales, M., Harrison, T.E., Ule, N., and Hoffman, D. 2011, *The Astronomical Journal*, 141, 78. *Low-Mass Eclipsing Binaries in the Initial Kepler Data Release*
- Coughlin, J.L., Harrison, T.E., and Gelino, D. 2010, *The Astrophysical Journal*, 723, 1351. *Modeling Multi-wavelength Stellar Astrometry. II. Determining Absolute Inclinations, Gravity Darkening Coefficients, and Spot Parameters of Single Stars with SIM Lite*
- Coughlin, J.L., Harrison, T.E., Gelino, D., Hoard, D., Ciardi, D., Benedict, F., Howell, S., McArthur, B., and Wachter, S. 2010, *The Astrophysical Journal*, 717, 776. *Modeling Multi-wavelength Stellar Astrometry. I. SIM Lite Observations of Interacting Binaries*
- López-Morales, M., Coughlin, J.L., Sing, D.K., Burrows, A., Apai, D., Rogers, J.C., Spiegel, D.S., and Adams, E.R. 2010, *The Astrophysical Journal*, 716, 36. *Day-side z'-band Emission and Eccentricity of WASP-12b*
- Holtzman, J., Harrison, T.E., & Coughlin, J.L. 2010, *Advances in Astronomy*, 46. *The NMSU 1m Telescope at Apache Point Observatory*
- Tucker, R.S., Sowell, J.R., Williamon, R.M., and Coughlin, J.L. 2009, *The Astronomical Journal*, 137, 2949. *Orbital Solutions and Absolute Elements of the Eclipsing Binary MY Cygni*
- Coughlin, J.L., Stringfellow, G., Becker, A., López-Morales, M., Mezzalana, F., and Krajci, T. 2008, *The Astrophysical Journal*, 689L, 149. *New Observations and a Possible Detection of Parameter Variations in the Transits of Gliese 436b*
- Coughlin, J.L., Dale, H.A., and Williamon, R.M. 2008, *The Astronomical Journal*, 136, 1089. *Long-term Photometric Analysis of the Active W Uma-type System TU Boo*
- Hoffman, D.I., Harrison, T.E., Coughlin, J.L., et al. 2008, *The Astronomical Journal*, 136, 1067. *New Beta Lyrae and Algol Candidates from the Northern Sky Variability Survey*
- Coughlin, J.L. and Shaw, J.S. 2007, *SARA*, 1, 7C. *Seven New Low-Mass Eclipsing Binaries*
- Coughlin, J.L. 2007, *Emory Undergraduate Research Journal*. *A Spotlight on Starlight*

Coughlin, J.L. 2007, Undergraduate Thesis, Emory University. *Observations and Models of Eclipsing Binary Stars*

CONFERENCE PROCEEDINGS

Coughlin, J. L., López-Morales, M., Harrison, T. E., Ule, N., Hoffman, D. I. 2011, in ASP Conf. Ser. 448, 16th Cambridge Workshop on Cool Stars, Stellar Systems, and the Sun, ed. C. Johns-Krull (Seattle, WA:ASP), 121. *New Low-Mass Eclipsing Binaries from Kepler*

FIELD OF STUDY

Major Field: Extrasolar Planets & Eclipsing Binary Stars

ABSTRACT

FUNDAMENTAL PARAMETERS OF EXOPLANETS
AND THEIR HOST STARS

BY

JEFFREY LANGER COUGHLIN, B.S., M.S.

Doctor of Philosophy

New Mexico State University

Las Cruces, New Mexico, 2012

Dr. Thomas E. Harrison, Chair

For much of human history we have wondered how our solar system formed, and whether there are any other planets like ours around other stars. Only in the last 20 years have we had direct evidence for the existence of exoplanets, with the number of known exoplanets dramatically increasing in recent years, especially with the success of the *Kepler* mission. Observations of these systems are becoming increasingly more precise and numerous, thus allowing for detailed studies of their masses, radii, densities, temperatures, and atmospheric compositions. However, one cannot accurately study exoplanets without examining their host stars in equal detail, and understanding what assumptions must be made to calculate planetary parameters from the directly derived observational parameters.

In this thesis, I present observations and models of the primary transits and secondary eclipses of transiting exoplanets from both the ground and *Kepler* in order to better study their physical characteristics and search for additional exoplanets. I then identify, observe, and model new eclipsing binaries to better understand the stellar mass-radius relationship and stellar limb-darkening, compare these observations to the predictions of stellar models, and attempt to define to what extent these fundamental stellar characteristics can impact derived planetary parameters. I also present novel techniques for the direct determination of exoplanet masses and stellar inclinations via multi-wavelength astrometry, the ground-based photometric observation of stars at sub-millimagnitude precision, the reduction of *Kepler* photometry from pixel-level data, the extraction of radial velocities from spectroscopic observations, and the automatic identification, period analysis, and modeling of eclipsing binaries and transiting planets in large datasets.

Contents

LIST OF TABLES	xvi
LIST OF FIGURES	xvii
1 INTRODUCTION	1
1.1 The Rise of Exoplanets	1
1.2 Detection and Characterization Methods	3
1.2.1 Radial Velocity	3
1.2.2 Transiting Planets	4
1.2.3 Transit Timing and Parameter Variations	6
1.2.4 Microlensing	6
1.2.5 Astrometry	7
1.2.6 Direct Imaging	7
1.3 Inferred Stellar and Planetary Parameters from Directly Determined Quantities	8
1.4 Thesis Goals and Format	12
2 NEW OBSERVATIONS AND A POSSIBLE DETECTION OF PARAMETER VARIATIONS IN THE TRANSITS OF GLIESE 436b	15
2.1 Introduction	15
2.2 Observations	17
2.3 Modeling and Derivation of Parameters	20
2.4 Transit Timing and Eclipse Variations	22
2.5 Discussion and Conclusion	29
3 DAY-SIDE z'-BAND EMISSION AND ECCENTRICITY OF WASP-12b	31
3.1 Introduction	31
3.2 Observations and Analyses	32
3.2.1 Eclipse detection and error estimation	36
3.2.2 Eccentricity	39

3.3	Comparison with atmospheric models	41
3.4	Discussion and Conclusions	43
4	A UNIFORM SEARCH FOR SECONDARY ECLIPSES OF HOT JUPITERS IN <i>KEPLER</i> Q2 LIGHTCURVES	45
4.1	Introduction	45
4.2	Observational Data	48
4.3	Light Curve Modeling	57
4.4	Derivation of Stellar and Planetary Parameters	72
4.4.1	Stellar Parameters	72
4.4.2	Planetary Parameters	74
4.5	Statistical Properties of the Secondary Eclipse Emissions	79
4.6	Properties of Some Individual Objects	102
4.6.1	KOI 1.01 / TrES-2b	103
4.6.2	KOI 2.01 / HAT-P-7b	105
4.6.3	KOI 10.01 / Kepler-8b	107
4.6.4	KOI 13.01	107
4.6.5	KOI 17.01 / Kepler-6b	108
4.6.6	KOI 18.01 / Kepler-5b	109
4.6.7	KOI 20.01 / Kepler-12b	110
4.6.8	KOI 64.01	110
4.6.9	KOI 97.01 / Kepler-7b	111
4.6.10	KOI 183.01	113
4.6.11	KOI 196.01	114
4.6.12	KOI 202.01	115
4.6.13	KOI 203.01 / Kepler-17b	115
4.6.14	KOI 1541.01	116
4.6.15	KOI 1543.01	116
4.7	Summary and Conclusions	117
5	LOW-MASS ECLIPSING BINARIES IN THE INITIAL <i>KEPLER</i> DATA RELEASE	121

5.1	Introduction	121
5.2	Observational Data	124
5.3	Eclipsing Binary Identification	125
5.4	Light Curve Modeling	130
5.5	New Low-Mass Binary Candidates	134
5.6	New Transiting Planet Candidates	155
5.7	Comparison of the New Low-Mass Binary Candidates to Models	158
5.8	Summary	160
6	MASS AND RADIUS DETERMINATION OF NEW LONG-PERIOD LOW-MASS ECLIPSING BINARIES	163
6.1	Introduction	163
6.2	Observational Data	163
6.2.1	Photometric Observations	163
6.2.2	Spectroscopic Observations	164
6.3	Radial-Velocity Measurement	167
6.4	Modeling	170
6.4.1	Light Curve Modeling	170
6.4.2	Radial Velocity Curve Modeling	173
6.5	Discussion	186
7	OBSERVATIONAL DETERMINATION OF LIMB-DARKENING IN THE <i>KEPLER</i> BANDPASS	194
7.1	Introduction	194
7.2	Observational Data and Modeling	202
7.3	Results and Discussion	203
8	MODELING MULTI-WAVELENGTH STELLAR ASTROMETRY: DETERMINATION OF THE ABSOLUTE MASSES OF EXOPLANETS AND THEIR HOST STARS	208
8.1	Introduction	208
8.2	Analytical Formulae for Computing the Reflex Motion	211
8.3	Numerical Modeling via REFLUX	220

8.4 Discussion and Summary	226
Appendices	
A ECLIPSE PHASE DISPERSION MINIMIZATION (EPDM)	231
B GENETIC ALGORITHMS FOR ECLIPSING BINARIES	237
C MODELING MULTI-WAVELENGTH STELLAR ASTROMETRY: SIM LITE OBSERVATIONS OF INTERACTING BINARIES	243
D MODELING MULTI-WAVELENGTH STELLAR ASTROMETRY: DETERMINING ABSOLUTE INCLINATIONS, GRAVITY DARKENING COEFFICIENTS, AND SPOT PARAMETERS OF SINGLE STARS WITH SIM LITE	275
REFERENCES	295

LIST OF TABLES

2.1	Parameters derived from using the JKTEBOP code with 1σ errors	23
2.2	Trends in derived inclination, width, and depth of transit over time	27
4.1	Modeled Systems and Their Host Star Properties	55
4.2	Modeling Results: Median Values and Associated 1σ Uncertainties	64
4.3	Derived System Parameters and Associated 1σ Uncertainties . . .	80
5.1	Period, Effective Temperature, Surface Gravity, and Eclipse Depth Estimates for the Seven New Extremely Shallow Eclipsing Systems	131
5.2	Model System Parameters via JKTEBOP for the 231 DDEBs with $T_{\text{eff}} < 5500$ K	141
5.3	Temperature, Mass, and Radius Estimates for the 95 New LMMS DDEB Candidates with Amplitudes ≥ 0.1 Magnitudes and Both Masses $< 1.0 M_{\odot}$	153
5.4	Model Parameters for the Eight Transiting Exoplanet Candidates	158
6.1	Modeling Results of the Long-Period Low-Mass Binary Light Curves	172
6.2	Physical Masses, Radii, and Temperatures for the Low-Mass Binaries	188
7.1	Effective Temperatures and Linear Limb-Darkening Coefficients of the Stars in the Modeled Eclipsing Binaries	205
7.2	Weighted Mean and Standard Deviation of the Observed and Model Linear Limb-Darkening Coefficients in Three Temperature Bins .	205
8.1	Currently Known Exoplanets with the Most Negative α Values . .	219
C.1	Parameters for the QZ Vul System	254
C.2	Parameters for the Cyg X-1 System	254
C.3	Parameters for the SS Cyg System	257
C.4	Parameters for the V592 Cas System	262
C.5	Parameters for the Sco X-1 System	267
C.6	Parameters for the AR UMa System	270
D.1	Parameters for Capella Aa	283
D.2	Parameters for Capella Ab	283
D.3	Parameters for Vega	283
D.4	Parameters for the K Dwarf System	291

LIST OF FIGURES

1.1	Histogram of the number of exoplanet discoveries per year	2
1.2	Illustration of the primary and secondary eclipses of an exoplanet	5
1.3	Illustration of a planetary transit and the resultant light curve for both a stellar disk of uniform brightness and one that includes limb-darkening	11
2.1	APO 3.5m and 1m light curves of Gliese 436b	18
2.2	O-C diagram for all professional times of minima	27
2.3	Measured inclination, width, and depth of transit over time for all data, with the star and planet radii fixed.	28
3.1	Secondary eclipse light curve for WASP-12b	37
3.2	Histograms of the in and out-of-eclipse flux distributions	40
3.3	Values of A_B and f that reproduce the observed z' -band eclipse depth of WASP-12b	41
3.4	Comparison of the eclipse depth (planet-to-star flux ratio) to models	42
4.1	Plots of the light curves, centroid positions, pixel-level images, and photometric apertures used in the <i>Kepler</i> PA and PDC reduction, for all initial 76 candidate systems	54
4.2	Plots of the phased light curves of the 40 systems produced from the <i>Kepler</i> PDC photometric pipeline	62
4.3	Plots of the phased light curves of the 50 systems produced using our CLM photometric pipeline	63
4.4	Comparison of the values for the planetary radius as given by Borucki et al. (2011) to those we derived	75
4.5	Plots of the effective day side temperature ratio versus the maximum effective day side temperature when fixing eccentricity to zero	93
4.6	Similar to Figure 4.5, but with eccentricity allowed to vary	94
4.7	Plots of the effective day side temperature ratio versus the maximum effective day side temperature for albedos of 0.1, 0.5, and 1.0	98
4.8	Plots of the effective day side temperature ratio versus planetary radii, semi-major axis, stellar effective temperature, and out-of-eclipse luminosity variation	101
4.9	Plots of the 1σ and 3σ upper limits on the maximum possible albedo	103
5.1	Plot of standard deviation versus mean flux for the 150,265 stars in Q1	127

5.2	Kepler 010614012: An apparent red giant, with an unusual, shallow, eclipse-like feature	131
5.3	The effect that the 29.43 minute integration time has on the derivation on the sum of the fractional radii at a given period	140
5.4	Plots of the light curves of the 231 systems modeled with the JKTEBOP code	149
5.5	Kepler 004247791. An example of a system which was determined not to be main-sequence	156
5.6	Plots of the light curves of the eight transiting planet candidates modeled with the JKTEBOP code	157
5.7	Mass-radius diagrams for each binary with both components $< 1.0 M_{\odot}$ and photometric amplitudes greater than 0.1 mag	161
6.1	Light and radial-velocity curves of Kepler 003102024	175
6.2	Light and radial-velocity curves of Kepler 004352168	176
6.3	Light and radial-velocity curves of Kepler 004773155	177
6.4	Light and radial-velocity curves of Kepler 006029130	178
6.5	Light and radial-velocity curves of Kepler 006131659	179
6.6	Light and radial-velocity curves of Kepler 006431670	180
6.7	Light and radial-velocity curves of Kepler 007846730	181
6.8	Light and radial-velocity curves of Kepler 008296467	182
6.9	Light and radial-velocity curves of Kepler 009284741	183
6.10	Light and radial-velocity curves of Kepler 010753734	184
6.11	Light and radial-velocity curves of Kepler 010992733	185
6.12	Mass-Radius diagram for low-mass stars	188
7.1	An illustration of the effect of limb-darkening	196
7.2	Simultaneous multi-wavelength transit observations of HD 209458b, reproduced from Knutson et al. (2007a)	198
7.3	Model atmosphere prediction of intensity variation from stellar center to limb, reproduced from Sing (2010)	201
7.4	Plot of the linear limb-darkening coefficient versus effective temperature	204
8.1	Illustration of a star-planet system	212
8.2	Plots of the reflex motion amplitude versus the wavelength of observations for a Jupiter-like planet	218

8.3	Plots of the reflex motion amplitude versus the wavelength of observations for an Earth-like planet	220
8.4	Plots of the multi-wavelength astrometric orbit for the Wasp-12 system	223
8.5	Plots of the multi-wavelength astrometric orbit for the HD 209458 system	224
8.6	Plots of the multi-wavelength astrometric orbit for the HD 189733 system	225
A.1	Illustration of the EPDM technique	234
B.1	Illustration of how the AGA converges over subsequent generations	241
C.1	Multi-wavelength model of QZ Vul	252
C.2	Multi-wavelength model of Cyg X-1	253
C.3	Multi-wavelength model of SS Cyg	258
C.4	Multi-wavelength model of V592 Cas	263
C.5	Multi-wavelength model of Sco X-1	268
C.6	Multi-wavelength model of AR UMa	272
D.1	Illustration of the astrometric-inclination effect	280
D.2	The astrometric displacement of each bandpass with respect to K -band versus inclination for Capella Aa	284
D.3	The astrometric displacement of each bandpass with respect to K -band versus inclination for Capella Ab	285
D.4	The astrometric displacement of each bandpass with respect to K -band versus inclination for Vega	286
D.5	A simulated cool Spot on CapellaAb	291
D.6	A simulated cool spot on a nearby K dwarf star	292
D.7	A simulated hot spot or flare on a nearby K dwarf star	293

1. INTRODUCTION

1.1. The Rise of Exoplanets

The idea that planets could exist outside our solar system, orbiting stars other than our own sun, has been around for at least hundreds, if not thousands, of years (e.g., Lucretius 58 BCE; Bruno 1584). However, only in the last ~ 20 years have we been able to find and study such planets. The first reported, (and subsequently confirmed), detection of an exoplanet was by Campbell, Walker, & Yang (1988) of a $1.6 M_{\text{Jup}}$, (1.6 times Jupiter's mass), planet in a 2.5 year orbit around the sub-giant γ Cephei A via the observed the velocity variations of the host star. In 1992, Wolszczan & Frail (1992) announced the discovery of two planets only a couple times the mass of Earth around a millisecond pulsar via their perturbations to the pulse arrival times. In 1995 Mayor & Queloz (1995) found the first planetary companion to a main-sequence star, a $0.47 M_{\text{Jup}}$ planet in a 4.2 day orbit around the Sun-like star 51 Pegasi, via radial velocity observations. Since these initial discoveries, the number of exoplanets has increased exponentially due to a combination of increased scientific interest and technological feasibility, as shown in Figure 1.1. At the time of this writing, there are 778 confirmed exoplanets known, in a total of 624 individual stellar systems (Schneider 2012), with thousands of additional exoplanet candidates awaiting confirmation.

In order to perform fundamental science, it is not enough to simply discover exoplanets; we must thoroughly investigate and characterize the fundamental parameters of each one. Only with a large sample of well-studied planets can we start to answer such fundamental questions as:

- How do solar systems and planets form and evolve?

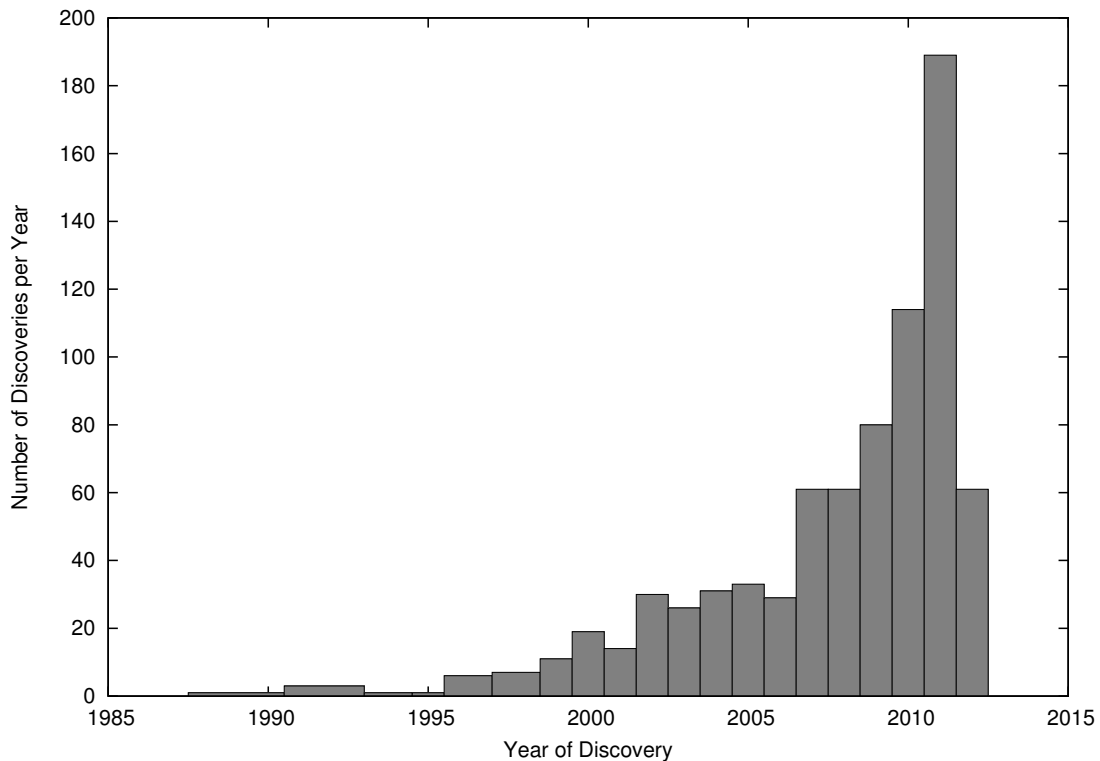


Fig. 1.1.— Histogram of the number of exoplanet discoveries per year, with data obtained from Schneider (2012). The number of discovered exoplanets has been increasing roughly exponentially since the first discoveries ~ 20 years ago. The number of discoveries for the current year, 2012, is incomplete at the time of this writing, but is expected to surpass the number from 2011.

- Are planets common around other stars in our galaxy and are they similar to or different from the planets in our solar system?
- How do planetary atmospheres function under a range of temperatures and compositions?
- Do other planets have conditions capable of supporting life or perhaps even show telltale signs of life?
- Are there any planets like Earth around the nearest stars that we can aspire to one day travel?

Unfortunately, the process of determining the fundamental parameters of exoplanets that we need to answer these questions is not straightforward, and often requires a thorough knowledge of the planet, its host star, and the broader astrophysical processes that govern these objects.

1.2. Detection and Characterization Methods

There are many methods employed to detect and characterize the fundamental parameters of exoplanets. In this section we briefly summarize each one, and what information can be directly determined via each one.

1.2.1. *Radial Velocity*

The amount of light that a star emits varies with the wavelength of light emitted, and is referred to as a stellar spectrum. An extrasolar planet and its host star orbit a common center of mass, such that both the planet and star move and complete an orbit once an orbital period. The star's orbital size and velocity will be many orders of magnitude smaller than that of the planet, precisely by the ratio of the planet and host star's masses. However, the star is many orders of magnitude brighter than the planet, and thus is typically the only visible component of the system. As the star moves, its spectrum is shifted with respect to wavelength via the Doppler Effect, and thus the velocity of the star, in the direction of the observer on Earth, can be directly measured. The directly determined parameters are the period, eccentricity, and longitude of periastron of the planetary orbit, and the velocity amplitude of the star.

1.2.2. *Transiting Planets*

If the inclination of an extrasolar planet's orbit is very close to edge-on as viewed from Earth, then the planet will pass in front of its host star once every orbit. In this case, a measurable drop in flux from the system occurs as the planet blocks out light from the host star, and is called the primary transit. This drop in flux is directly proportional to the square of the ratio of the exoplanet's and host star's radii, i.e., the fractional area of the stellar surface that is obscured by the planet. Also during primary transit, some of the star's light will pass through, but only be partially absorbed by, the very upper reaches of the planetary atmosphere, imparting extra absorption features unto the stellar spectrum that are due to the planetary atmosphere. When the planet passes behind the star half an orbit later, there is a much smaller drop in flux that corresponds to the luminosity ratio between the planet and host star, referred to as the secondary eclipse. An illustration is shown in Figure 1.2. Thus, unlike non-transiting planets, in principle one can determine the mass, radius, density, temperature, and even atmospheric composition of the planet. The detailed study of these characteristics allows the direct testing of various extrasolar planetary atmosphere models, whose predictions as to the existence of key molecular species, general circulation patterns, temperature, and the variation thereof with scale height, can vary widely (e.g., Cooper & Showman 2006; Fortney et al. 2006; Tinetti et al. 2007; Burrows et al. 2008a,b; Showman et al. 2008, 2009; Spiegel et al. 2009). As well, determining atmospheric temperature and composition can provide insights into planetary formation and migration, of which many competing models also exist.

Assuming the star and planet are uniformly illuminated spheres, the directly

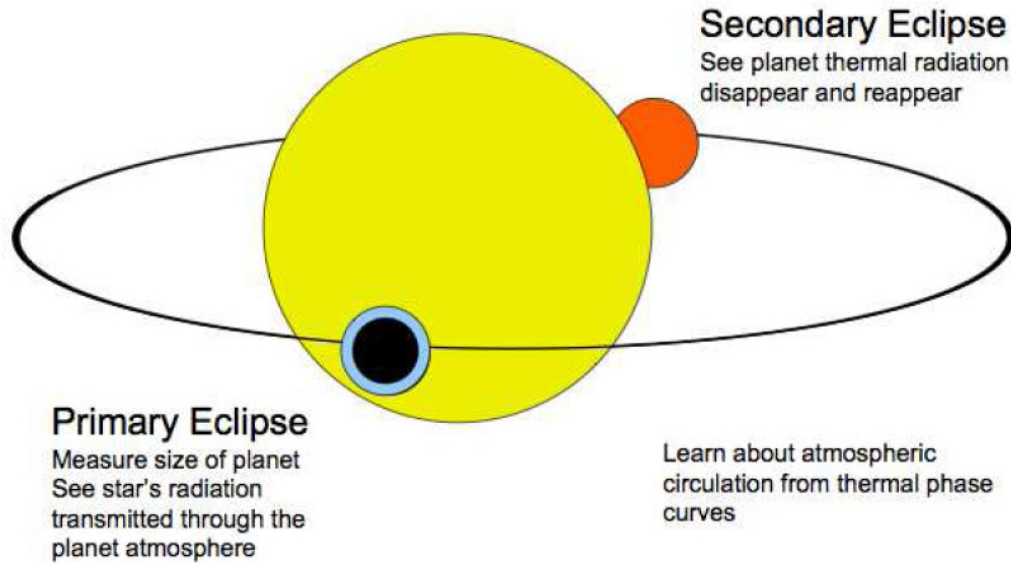


Fig. 1.2.— Illustration of the primary and secondary eclipses of an exoplanet. Figure by S. Seager.

determined parameters from the light curve primary transit are the period of the system, the fractional sum of the radii, (i.e., the sum of the planet and stellar radii divided by the semi-major axis of the orbit), the ratio of the planetary to stellar radii, and the inclination of the orbit. If the secondary eclipse is also observed in the light curve, one may also directly measure the ratio of the planetary to stellar surface brightness, and the eccentricity and longitude of periastron of the orbit. Via mathematical re-arrangements of these directly determined parameters, Seager & Mallén-Ornelas (2003) found that the host star's mean stellar density is directly determined from the primary transit light curve alone, and Southworth et al. (2007) found that the exoplanet's surface gravity is directly determinable with both a primary transit light curve and single-line radial velocity curve.

1.2.3. *Transit Timing and Parameter Variations*

In addition to measuring the depth of a transit, the timing and duration of the transit can also be measured. If there is another planet in the system, or a moon around the transiting planet, it will exert gravitational perturbations on the transiting planet. These perturbations will manifest as changes in the timing, duration, and depth of the observed transits, and can in certain cases directly yield the mass, orbital period, and semi-major axis of the non-transiting planet (Agol et al. 2005; Holman & Murray 2005). Furthermore, if the second planet or the moon also transits, the masses, radii, orbital periods, and semi-major axes of all three components can be directly determined from the light curve alone (Kipping 2010b; Carter et al. 2011).

1.2.4. *Microlensing*

According to General Relativity, any object with mass will warp the space-time surrounding it, and deflect the path that light takes when it travels close to the object. For objects as massive as the Sun and other stars, this effect can be significant, and in fact deflections of stellar positions near the Sun during a solar eclipse were among the first confirmations of the theory of General Relativity. A star, and even a planet, is thus capable of acting like a giant lens, magnifying the light from distant sources. In our galaxy, the amount of deflection provided by a star, and thus its focal length, are of the order such that stars approximately halfway between us and the galactic center are at the right distance to act as a lens, provided that Earth, the intervening system that acts as the lens, and another distant star line up exactly right. Astronomers have monitored a very

large number of stars towards the center of the galaxy, and have detected several microlensing events. In these cases, a primary magnification event is seen that increases the light observed by several orders of magnitude, as the three components slowly drift into alignment, and the intervening lens star focuses the light from the distant star onto the Earth. On top of this primary event, one or more smaller magnification events are often seen, which is due to planetary companions of the lens star also acting as, albeit smaller, lenses. The amplitude of these events directly measures the masses of the host star and its planets, as well as the orbital separation between them.

1.2.5. Astrometry

As discussed with the radial velocity technique, both the planet and host star move over an orbital period around their common center of mass. By precisely measuring the position of a star on the sky, the on-sky projected motion of the star can be measured. This directly yields the projected distance between the star and barycenter of the system, as well as the period, eccentricity, and longitude of periastron of the orbit. Nearly always these measurements also directly determine the distance to the system via geometric parallax, and thus the physical distance between the star and barycenter is also directly determined.

1.2.6. Direct Imaging

In all of the above techniques, the presence and properties of extrasolar planets are deduced via the perturbations they induce upon their host stars. However, it is possible to directly image and detect an extrasolar planet by taking a very

long exposure of the system while using a mask to block light from the host star. Typically, adaptive optics are also employed in order to achieve spatial resolution better than the projected separation of the planet and star. If detected, the relative brightness of the exoplanet compared to the host star can be directly determined, as well as the period, eccentricity, and longitude of periastron of the orbit if multiple images are taken over a significant fraction of the planet's orbit.

1.3. Inferred Stellar and Planetary Parameters from Directly Determined Quantities

Of the techniques discussed above, the radial velocity technique has by far been the most productive technique for finding planets and planet candidates over the past 20 years. However, the amount of information yielded by this technique alone is severely limited. In order to calculate a mass for the planet, one must assume a mass for the host star, as well as an inclination for the planetary orbit. While the former can be estimated based on the stellar spectrum, the latter is impossible to determine from radial velocity observations alone, and thus one can only truly determine lower limits to the planetary mass. Astrometry is a bit more useful, as it directly yields the inclination of the orbit and the star-barycenter distance, and thus with an assumed mass for the star, a mass for the planet and a semi-major axis for its orbit can be calculated.

The transit technique has been the second-most productive to-date, with 240 planets known to transit in 206 individual stellar systems at the time of this writing (Schneider 2012), and is expected to rapidly leap ahead as the most productive technique given the thousands of planet candidates recently announced via the *Kepler* mission (Batalha et al. 2012). Most confirmed transiting planets

have radial velocity observations of the host star taken as well. Although a transiting planet can yield much more information than a non-transiting planet, there are some very important caveats, namely that most of the planetary parameters of interest are inherently dependent on the assumed stellar parameters. Although the inclination is directly determinable from the light curve, since only the radial velocity of the star is known we must assume a mass for the host star in order to calculate a mass for the exoplanet. Since the fractional radii of the star and planet are directly determined from the light curve, if we assume a mass for the star (and either assume a mass for the planet or treat it as negligible compared to the star) we can combine that with the directly determined period to calculate the semi-major axis of the system, and thus a radius for the star and exoplanet. Alternatively, one may assume a radius for the host star, and use the directly determined ratio of radii to calculate a radius for the planet, as is often the case in the absence of radial velocity observations. In practice, since the mean stellar density and the planetary surface gravity are directly determined, one would choose values of mass and radius for the host star that would reproduce the mean stellar density and planetary surface gravity values within the observational errors. The planetary temperature can be calculated from the directly determined ratio of the surface brightness if one knows the wavelength bandpass of observation, assumes a spectral energy distribution over the bandpass for both the planet and star, and assumes a temperature for the star. Generally the stellar spectral energy distribution and temperature of the host star can be directly determined from high-resolution spectroscopic observations. Of course, in order to utilize this technique, the planet has to have the fortuitous alignment that it does transit as seen from Earth, which is quite rare.

An assumption we made in the above statements is that the stellar disk is uniformly bright, which turns out to be a poor assumption. Stellar limb-darkening is the phenomenon that stars are brighter towards the center of their observed disks, and darker towards their edges, or limbs, and can be quite significant when examining exoplanet transit curves (see Section 7.1 for a complete explanation of the effect). Figure 1.3 is an illustration of a primary transit, and the resulting light curve one would observe for both a star with a constant brightness distribution (dashed line) and one that has brightness variation across its surface due to limb-darkening (solid line). The surface brightness distribution of the host star due to limb-darkening will affect the directly determined planetary parameters above, and thus it is important to know if limb-darkening can be directly determined from transit curves, and if not, how well we understand and can characterize it for various stars.

There are a few very recent advances as well that provide more information than we have previously been able to obtain. Snellen et al. (2010), Rodler, Lopez-Morales, & Ribas (2012), and Brogi et al. (2012) were just recently able to directly detect the radial velocity of an exoplanet in the combined spectrum, but only for very special cases. In these cases one is able to determine the velocities of both the planet and star, and if the inclination is known, are thus able to directly determine the absolute masses of both the planet and star. With high-precision light curves, such as those being produced by the *Kepler* mission, one is also able to detect several effects that occur over an entire orbit. First, the star and planet are not point sources, and thus distort each other through gravitational tidal interactions. As the planet raises a tide on the star, it increases the emitting surface area of the star, thus increasing its total observed luminosity in the light

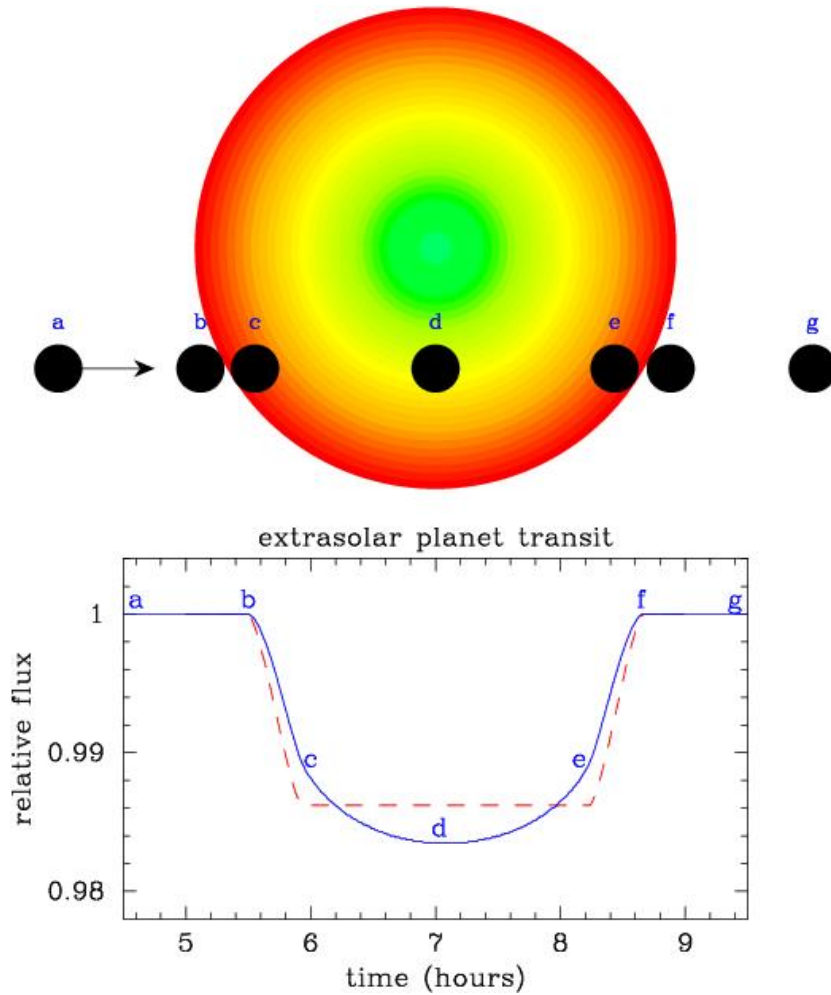


Fig. 1.3.— Illustration of a planetary transit and the resultant light curve for both a stellar disk of uniform brightness (dashed line) and one that includes limb-darkening (solid line).

curve. By measuring this photometric signature, it becomes possible to estimate the mass of the planet by assuming the mass and density profile of the star, or visa versa. Second, light emitted by the star may be reflected off the planet's day side, causing a similar photometric signature over the course of an orbit. If we assume a certain albedo for the planet, this technique can be used to determine the inclination of the orbit, and thus the mass of the planet if combined with

radial velocity observations. Third and finally, it is possible to directly determine the velocity of the star from the light curve alone, without spectroscopic radial velocity measurements at all, via an effect known as photometric beaming. Due to special relativity, the brightness of an object is magnified in the direction of its motion, as seen relative to an observer, as photons emitted from the object are preferentially emitted in the direction of motion. Loeb & Gaudi (2003) first realized this effect could be applied to exoplanets, with the stellar flux change quantified as

$$F = F_0 \left(1 + 4 \frac{v_r}{c}\right) \quad (1.1)$$

where F is the observed flux, F_0 is the flux of the object at rest, v_r is the radial velocity of the object, and c is the speed of light. Thus, if this effect can be measured in a light curve, the velocity of the star is directly determined, and can be applied to determine other quantities of interest just as the radial velocity determined from traditional spectroscopic observations would be used.

1.4. Thesis Goals and Format

Observations of the fundamental parameters of exoplanets and their host stars are critical to performing fundamental science and answering long sought questions regarding planetary formation, evolution, and uniqueness. The accuracy of these observations also depends on critically understanding the interplay between the stellar and planetary parameters, and the assumptions that must be made to extract those parameters. Thus, the questions this thesis aims to answer are:

1. What can be learned from high-precision observations of exoplanet transits?
2. What are the atmospheric properties of exoplanets, how much do they vary planet-to-planet, and how do they change as a function of temperature?
3. How accurately are we able to estimate the fundamental parameters of stars, how much variation exists star-to-star, and what are the implications for the study of planets around them?
4. What new techniques might we employ in the future to better discover and characterize exoplanets?

In Chapter 2 we present high-precision observations of the primary transit of the Neptune-mass exoplanet Gliese 436b in an effort to better characterize its orbit and search for additional low-mass planets in the system, originally published as Coughlin et al. (2008). In Chapter 3 we detect and measure the secondary eclipse of exoplanet Wasp-12b via ground-based observations in the z' -band to probe its atmosphere, originally published as López-Morales et al. (2010). In Chapter 4 we search for and detect the secondary eclipses of numerous hot Jupiters in *Kepler* data, allowing for a statistical study of hot Jupiter atmospheres, originally published as Coughlin & López-Morales (2012a). In Chapters 5 and 6 we identify new low-mass eclipsing binaries in the *Kepler* field, obtain follow-up observations, and model them to accurately measure their masses and radii in an attempt to better understand the long-standing discrepancy between predicted and observed radii of low-mass stars, of which Chapter 5 is published as Coughlin et al. (2011). In Chapter 7 we present observational measurements of the limb-darkening coefficients of main-sequence stars in the *Kepler* bandpass in an effort to test model

predictions and examine star-to-star variation. Finally, in Chapter 8 we present a novel theoretical technique that can directly measure the masses of exoplanets utilizing multi-wavelength astrometry, published as Coughlin & López-Morales (2012b). We also note that Appendices A and B were originally published as appendices to Coughlin et al. (2011), and that Appendices C and D were originally published as Coughlin et al. (2010b) and Coughlin, Harrison, & Gelino (2010a).

2. NEW OBSERVATIONS AND A POSSIBLE DETECTION OF PARAMETER VARIATIONS IN THE TRANSITS OF GLIESE 436b

2.1. Introduction

Gliese 436 is an M-dwarf (M2.5V) with a mass of $0.45 M_{\odot}$ and hosts the extrasolar planet Gliese 436b, which is a Neptune-sized planet with a mass of $23.17 M_{\oplus}$ (Torres 2007). Gliese 436b was first discovered via radial-velocity (RV) variations by Butler et al. (2004), who also searched for a photometric transit, but failed to detect any signal greater than 0.4%. It was thus a surprise when Gillon et al. (2007b) reported the detection of a transit with a depth of 0.7%, implying a planetary radius of $4.22 R_{\oplus}$ (Torres 2007) and thus a composition similar to Uranus and Neptune. In addition, both Deming et al. (2007) and Maness et al. (2007) calculated that the significant eccentricity of the orbit, $e = 0.15$, coupled with its short period of ~ 2.6 days, should result in circularization timescales of $\sim 10^8$ years, which contrasts with the old age of the system at $\gtrsim 6 \times 10^9$ years. The existence of one or more additional planets in the system could be responsible for perturbations to Gliese 436b's orbit, and thus result in the observed peculiarities. We considered this possibility right after the initial publication of Gillon et al. (2007b), and began an intensive campaign to observe the photometric transits of Gliese 436b in order to search for variations indicative of orbital perturbations.

Ribas et al. (2008) reported the possible detection of a $\sim 5 M_{\oplus}$ companion in the Gliese 436 system located near the outer 2:1 resonance of Gliese 436b via analysis of all the RV data compiled to date. Theoretically this planet would be perturbing Gliese 436b so as to increase its orbital inclination at a rate of $\sim 0.1 \text{ deg yr}^{-1}$, and thus its transit depth and length, so that the non-detection

by Butler et al. (2004) and the observed transit of Gillon et al. (2007b) were compatible. Since the RV detection of this second planet had a significant false-alarm probability of $\sim 20\%$, Ribas et al. (2008) proposed that confirmation could be achieved through 2008 observations of Gliese 436b's transits, which would show a lengthening of transit duration by ~ 2 minutes compared to the Gillon et al. (2007b) data. As well, transit-timing variations (TTVs) of several minutes should also be detectable by observing a significant number of transits.

Alonso et al. (2008) reported a lack of observed inclination changes and TTV evidence for the second planet, based on a comparison of a single H -band light curve obtained in March 2008 to $8\mu\text{m}$ data taken with Spitzer 254 days earlier (Gillon et al. 2007a; Deming et al. 2007). This result, combined with additional radial velocity measurements that contradicted the proposed period of the second planet, drove Ribas et al. (2009) to retract their claim of the companion at IAU Symposium 253. However, Shporer et al. (2009) presented multiple light curves obtained in May 2007, and could not rule out TTVs on the order of a minute. While the planet specifically proposed by Ribas et al. (2008) most likely does not exist, Ribas et al. (2009) makes a strong case that a second planet is still needed to explain the peculiarities of Gliese 436b, and most likely exists in a non-resonant configuration where no strong TTVs are induced. Amateur astronomers have been diligent in observing Gliese 436b since its initial transit discovery, and thus along with this data, published data, and our own data, we are able to present a thorough analysis of the TTVs, inclination, duration, and depth of the transit changes in the Gliese 436 system. We present our observations in Section 2.2, our modeling and derivation of parameters in Section 2.3, and explore the observed TTVs and parameters of the system over time in Section 2.4.

2.2. Observations

We observed Gliese 436 (11h 42m 11s, +26° 42' 24" J2000) in the V filter on the nights of April 7, April 28, and May 6 2008 UT with the 3.5-meter telescope at Apache Point Observatory (APO). We used SPIcam, a backside-illuminated SITE 2048×2048 CCD with 2×2 binning, resulting in a plate scale of 0.28"/pixel, and sub-framed to a field of view of 4.8' by 0.56' to decrease readout time. We applied typical overscan, bias, and flat-field calibrations. For photometric reduction we used the standard IRAF task PHOT, with the aperture selected as a constant multiple of the Gaussian-fitted FWHM of each image to account for any variable seeing. We performed differential photometry with respect to the star USNO 1167-0208653 (2MASS ID 175252970) located at 11h 42m 12.08s, +26° 46' 07.45" J2000. This star has $V = 10.82$ and color $V-I = 1.48$, compared to Gliese 436 which has $V = 10.68$, and color $V-I = 1.70$. In the error bar computation, we account for both standard noise from the photometry, as well as due to scintillation following equation 10 of Dravins et al. (1998). Having obtained at least 30 minutes of data on each side of the transit, we subtracted a linear fit for all data outside of transit vs. airmass to account for any differential reddening. Resulting individual data points have errors ranging from 1.5 to 2.8 mmag, which agrees with the rms of the residuals from the model fits, and a typical cadence of about 17 seconds. We have searched for correlated noise on the timescale of ingress and egress, via the technique of Pont et al. (2006), but only find a statistically significant amount for the night of April 7, measured to be 0.11 mmag. The three transits are shown in Figure 2.1.

We also carried out accompanying observations with the New Mexico State

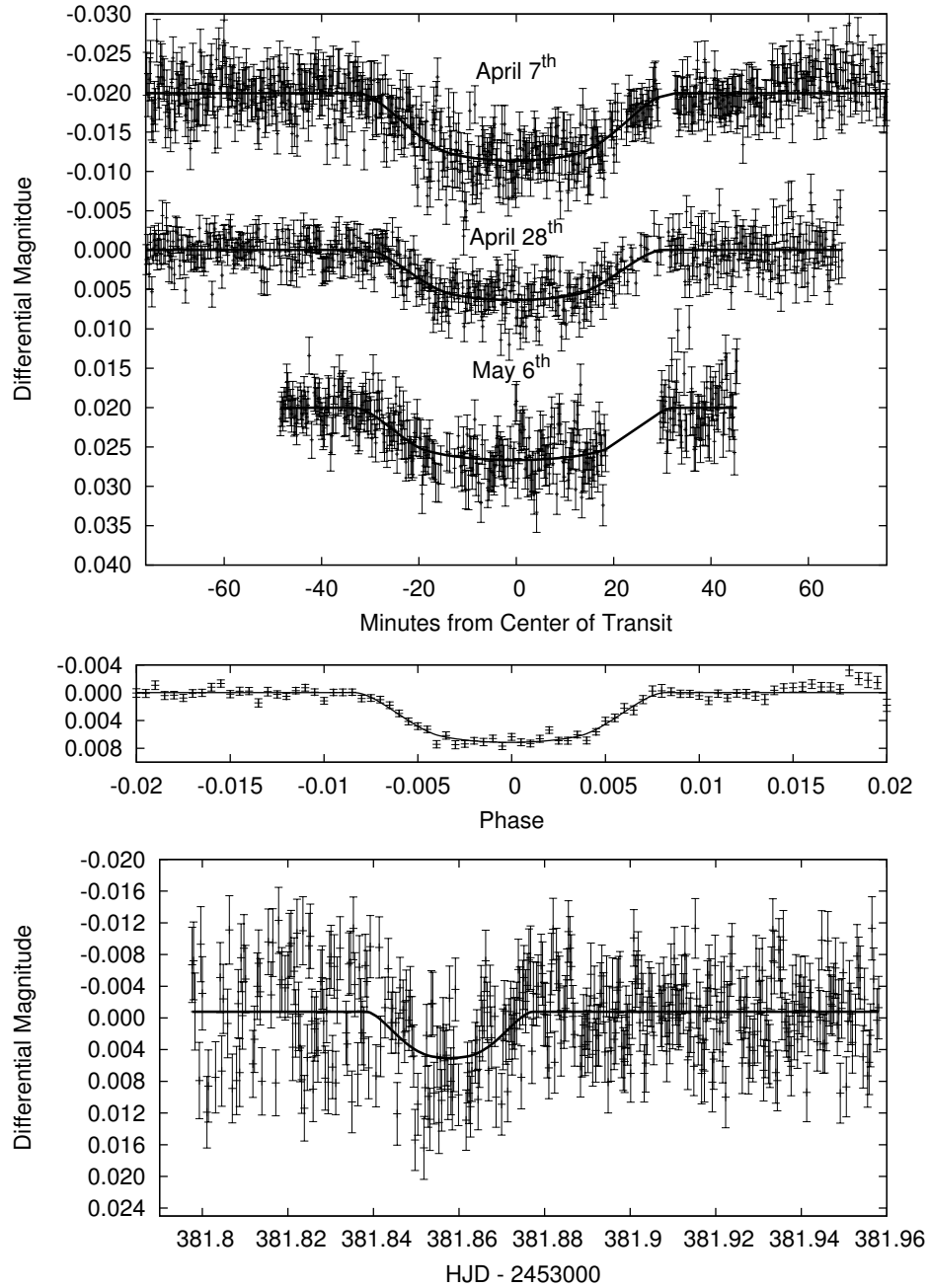


Fig. 2.1.— *Top*: The V-band light curves observed with the APO 3.5-meter in 2008 with model fits. *Middle*: The 2008 3.5-meter data combined, phased, and binned in increments of 0.0005 phase. *Bottom*: The transit observed by the NMSU 1-meter telescope on the night of January 11 2005 UT. A 3-sigma clip has been applied, and is shown with a model fit for which the radii were fixed.

University (NMSU) 1-meter telescope at APO, in the V filter on the night of April 7 2008 UT, and in the I filter on the night of April 28 2008 UT. A 2048×2048 E2V CCD was used with 1×1 binning and sub-framing, resulting in a field of view of $8.0'$ square and a plate scale of $0.47''/\text{pixel}$, and we applied the aforementioned standard calibration and photometric extraction techniques. We performed ensemble photometry with respect to the USNO star that was used as the 3.5m reference, as well as BD+27 2046 ($V = 10.64$, $V-I = 0.44$), and another star at $11\text{h}42\text{m}00\text{s}$, $+26^\circ45'56''$ J2000 ($V = 12.81$, $V-I = 1.46$). Resulting typical errors on individual points range from 3 to 5 mmag with a typical cadence of about 12 seconds.

The NMSU 1-meter telescope can also function as a robotic telescope, and is used intermittently to photometrically monitor stars with known radial-velocity discovered planets to search for transits (Holtzman, Harrison, & Coughlin 2010). A search of the 1-meter archives revealed that it observed Gliese 436 on the night of January 11 2005 UT, during which a transit should have occurred, according to the precise ephemeris for Gliese 436b that is now available by incorporating the many observed transits in 2007 and 2008. At the time, this 1-meter program depended on visual inspection of automatically generated photometry and plots. For this night, the plot had large temporal and brightness ranges, and thus the tiny transit was easily missed visually. However, carefully inspecting the region constrained by the ephemeris, as well as re-performing the photometry to maximize signal-to-noise, we find a transit signature within a minute of that predicted by the ephemeris with reasonable width and depth, as shown in Figure 2.1. Individual data points have an error of about 4 mmag, a cadence of 30 seconds, and we do not detect any correlated noise with any level of significance.

We also conducted observations on the nights of April 28 and May 13 2008 UT using a 24" telescope located at the Sommers-Bosch Observatory (SBO) on the University of Colorado at Boulder campus, using an I filter. These observations also used a windowed chip and an exposure time to maximize signal-to-noise without saturating, and have comparable temporal resolution to the 3.5m and 1m telescopes due to a shorter readout time. As well, we used an unfiltered 11" telescope at Cloudcroft, NM (CC) with a SBIG ST-7E CCD and 2×2 binning on May 6 2008 UT, with a resulting cadence of about 25 seconds. We have also gathered all the amateur data currently available, ~15 light curves, on the system as compiled by Bruce Gary (<http://brucegary.net/AXA/GJ436/gj436.htm>).

2.3. Modeling and Derivation of Parameters

We used the JKTEBOP code (Southworth et al. 2004a,b) to model all the transit light curves, both our own and previously published, in a consistent and uniform manner. Southworth (2008) has performed an exhaustive analysis of fourteen transiting planets using the JKTEBOP code, and shows it compares well with results reported elsewhere. JKTEBOP offers the advantage of incorporating a Levenberg-Marquardt optimization algorithm, improved limb darkening treatments, and extensive error analysis routines, which are critical for confirming any trends in the system.

For each transit curve, we solved for the ratio of radii ($k = R_p/R_s$), the orbital inclination (i), the time of mid-transit (T_0), and a scale factor that defines the normalized value of the out-of-transit flux in the light curves. In order to obtain reasonable results for the scale of the system for all data sets, the sum of

the radii ($R_s + R_p$) was set to that found by Torres (2007). We also fixed the eccentricity to a value of 0.15 and the longitude of periastron to 343° as given by Deming et al. (2007) and Mardling (2008). We used a quadratic limb-darkening law with coefficients taken from Claret (2000a) for $T_{eff} = 3500\text{K}$, $\log(g) = 4.5$, $V_t = 2.0 \text{ km s}^{-1}$, and $[M/H] = 0.0$, for the appropriate filters. In the case of the Spitzer $8\mu\text{m}$ data, we used the coefficients as determined by Gillon et al. (2007a). From each fit, still assuming a constant sum of radii, we were thus also able to calculate the individual star and planet radii, as well as the depth and width of transit. In order to rule out any potential correlations in derived planet size and inclination, we then re-modeled all data with the same procedure, but also fixing k , and thus the star and planet sizes, to that found by Torres (2007). This generally produced similar results, but for the noisier data sets achieved more consistent results. Parameters from both techniques are shown in Table 2.1.

In order to obtain robust errors, we ran 10,000 Monte-Carlo simulations for each data set and performed a residual-permutation analysis (Jenkins et al. 2002) to investigate temporally correlated noise. In both cases, the previously fixed parameters, as well as the limb-darkening coefficients, were allowed to vary so that their individual uncertainties would be taken into account in the derived parameter uncertainties. For each Monte Carlo simulation, random Gaussian noise with amplitude equal to the given error bars, or in the absence thereof the standard deviation of the residual scatter from the best-fit solution, was added to each data point and the curve re-fitted with random perturbations applied to the initial parameter values. This ensured a detailed exploration of the parameter space and parameter correlations. However, this Monte Carlo technique will underestimate errors for certain parameters in the presence of temporally correlated noise, which

can result from trends in seeing, extinction, focus, or other atmospheric or telescope related phenomena (Southworth 2008). The residual-permutation method takes the residuals of the best-fit model, shifts them to the next data point, and finds a new solution. The residuals are shifted again, a new fit is found, and the process repeats as many times as there are datapoints. Thus, there is a distribution of fitted values similar to the Monte Carlo technique, but any temporal trends will have been propagated around the light curve, and thus taken into account. For our final errors we adopt the larger value found between the two methods, although for the majority of parameters and data sets the two methods agree quite well.

In total we modeled 28 light curves, (16 professional and 12 amateur), covering 19 separate transit events over a baseline of nearly 3.3 years.

2.4. Transit Timing and Eclipse Variations

Using the derived time of minima in Table 2.1 for all the data when allowing k to vary, we derive a new linear, error-weighted ephemeris of $T_c(\text{HJD}) = 2454222.6164(1) + 2.643897(2) \cdot E$, where the parentheses indicate the amount of uncertainty in the last digit, and E is the epoch with $E = 0$ the initial transit discovery of Gillon et al. (2007b). Using this ephemeris, we then compute an observed minus calculated (O-C) diagram for the time of transit center, as shown in Figure 2.2. We have currently excluded the amateur data from the plot due to much larger error bars, so that the high-precision data points can be seen clearly. We have examined the TTVs and various subsets thereof using a phase dispersion minimization technique (Stellingwerf 1978), but do not find any periods with

Table 2.1. Parameters derived from using the JKTEBOP code with 1σ errors

Epoch	Source	Filter ^c	T_{\min} (HJD-2450000)	Inclination ($^{\circ}$)	R_{\star} (R_{\odot})	R_p (R_{\oplus})	Depth (mmag)	Width (minutes)
-318	NMSU 1m	V	3381.85584±0.00179	86.02±0.23	0.446±0.046	6.19±4.81	7.05±1.35	47.0±7.1
0	Gillon et al. (2007b) ^b	V	4222.61617±0.00060	86.38±0.18	0.463±0.016	4.32±0.24	6.98±0.43	60.1±1.6
1	Shporer et al. (2009) ^b	None	4225.26052±0.00089	86.43±0.17	0.463±0.015	4.33±0.27	7.16±0.81	61.4±2.5
1	Shporer et al. (2009) ^b	V	4225.26050±0.00072	86.35±0.17	0.462±0.016	4.47±0.25	7.31±0.46	59.2±1.9
9	Shporer et al. (2009) ^b	R	4246.41012±0.00079	86.27±0.18	0.456±0.014	5.10±0.66	9.07±0.87	56.7±2.6
22	Gillon et al. (2007a)	8 μ m	4280.78219±0.00011	86.34±0.16	0.464±0.016	4.23±0.16	7.46±0.10	59.8±1.1
110	Gregor Srdoc ^a	R	4513.43393±0.00174	86.10±0.24	0.457±0.030	5.04±2.91	7.11±1.29	49.8±6.5
110	Tomny Vanmunster ^a	R	4513.44404±0.00247	87.13±0.30	0.461±0.016	4.57±0.45	9.63±1.67	77.8±4.9
112	Bruce Gary ^a	R	4518.72999±0.00278	86.04±0.34	0.443±0.087	6.55±9.38	8.78±2.37	47.0±11.7
113	Gregor Srdoc ^a	R	4521.37338±0.00130	87.27±0.30	0.459±0.015	4.81±0.30	11.06±1.13	80.0±4.2
115	James Roe ^a	V	4526.65995±0.00124	86.03±0.27	0.447±0.036	6.05±3.34	7.47±1.55	48.4±9.0
115	Joao Gregorio ^a	V	4526.65972±0.00130	87.09±0.28	0.468±0.016	3.80±0.25	6.50±0.66	77.1±4.0
117	Richard Schwartz ^a	V	4531.94399±0.00222	86.18±0.20	0.461±0.015	4.51±0.65	6.37±1.67	53.4±6.5
118	Alonso et al. (2008)	H	4534.59611±0.00014	86.39±0.17	0.463±0.016	4.32±0.17	7.74±0.11	61.1±0.9
127	Manuel Mendez ^a	R	4558.38849±0.00173	86.60±0.24	0.466±0.016	3.99±0.33	6.60±0.87	66.6±5.6
129	NMSU 1m	V	4563.67937±0.00257	86.45±0.33	0.467±0.019	3.87±0.61	6.34±1.12	61.5±8.0
129	APO 3.5m	V	4563.67968±0.00051	86.44±0.17	0.459±0.015	4.73±0.28	8.60±0.44	61.8±2.2
132	James Roe ^a	B	4571.61844±0.00107	88.60±0.62	0.455±0.015	5.24±0.24	14.84±0.83	95.5±3.6
137	NMSU 1m	I	4584.83301±0.00117	86.55±0.19	0.449±0.015	5.89±0.51	14.61±1.72	65.2±3.6
137	APO 3.5m	V	4584.83084±0.00035	86.32±0.16	0.464±0.015	4.20±0.20	6.36±0.25	58.3±1.2
137	SBO 24 [?]	I	4584.82868±0.00166	86.63±0.21	0.448±0.015	5.95±0.50	15.23±2.13	67.3±3.8
137	Bruce Gary ^a	R	4587.47754±0.00087	86.51±0.18	0.463±0.015	4.32±0.25	7.41±0.58	64.0±2.4
138	Manuel Mendez ^a	R	4587.47754±0.00170	86.91±0.28	0.462±0.016	4.45±0.35	8.83±1.13	73.9±4.9
140	CC 11 [?]	None	4592.76123±0.00140	86.25±0.17	0.463±0.015	4.38±0.48	6.64±1.03	56.0±3.4
140	APO 3.5m	V	4592.76281±0.00084	86.50±0.17	0.465±0.015	4.12±0.21	6.71±0.36	63.5±3.4
140	SBO 24 [?]	I	4592.76202±0.00177	86.55±0.26	0.453±0.017	5.43±0.84	12.25±1.50	65.3±4.8
143	SBO 24 [?]	I	4600.69795±0.00118	85.88±0.24	0.425±0.067	8.52±6.54	6.75±1.08	42.0±8.5
146	James Roe ^a	V	4608.62470±0.00107	86.32±0.23	0.454±0.015	5.31±0.67	9.86±0.55	58.4±6.3

Ratio of Radii k Allowed to Vary

Table 2.1 (continued)

Epoch	Source	Filter ^c	T_{\min} (HJD-2450000)	Inclination ($^{\circ}$)	R_{\star} (R_{\odot})	R_p (R_{\oplus})	Depth (mmag)	Width (minutes)
...	3.5m Data Combined	V	...	86.39±0.16	0.463±0.015	4.39±0.22	7.25±0.31	60.6±1.3
Star and Planet Radii Fixed by Fixing k								
-318	NMSU Im	V	3381.85596±0.00212	86.15±0.17	0.464±0.016	4.23±0.28	5.61±0.63	52.5±3.2
0	Gillon et al. (2007b) ^b	V	4222.61617±0.00062	86.40±0.16	0.464±0.016	4.23±0.28	6.74±0.69	60.5±2.6
1	Shporer et al. (2009) ^b	None	4225.26049±0.00094	86.45±0.19	0.464±0.016	4.23±0.30	6.86±0.76	61.8±3.7
1	Shporer et al. (2009) ^b	V	4225.26050±0.00076	86.39±0.16	0.464±0.016	4.23±0.30	6.65±0.72	59.9±2.1
9	Shporer et al. (2009) ^b	R	4246.41009±0.00103	86.37±0.17	0.464±0.017	4.23±0.29	6.66±0.70	59.6±3.6
22	Gillon et al. (2007a)	8 μ m	4280.78219±0.00011	86.34±0.16	0.464±0.016	4.23±0.30	7.47±1.00	59.5±1.0
110	Gregor Srdoc ^a	R	4513.43416±0.00191	86.19±0.18	0.464±0.016	4.23±0.28	5.92±0.74	54.0±4.3
110	Tonny Vanmunster ^a	R	4513.44424±0.00386	87.29±0.54	0.464±0.016	4.23±0.28	8.20±1.11	77.5±9.0
112	Bruce Gary ^a	R	4518.73038±0.00358	86.20±0.25	0.464±0.017	4.23±0.31	6.00±1.03	55.7±7.3
113	Gregor Srdoc ^a	R	4521.37312±0.00244	87.34±0.39	0.464±0.016	4.23±0.31	8.32±1.26	80.1±6.3
115	James Roe ^a	V	4526.66055±0.00302	86.14±0.27	0.464±0.015	4.23±0.28	5.56±1.30	51.7±9.1
115	Joao Gregorio ^a	V	4526.65996±0.00101	86.65±0.19	0.464±0.016	4.23±0.29	7.42±0.93	67.3±3.4
117	Richard Schwartz ^a	V	4531.94392±0.00198	86.26±0.26	0.464±0.016	4.23±0.31	5.95±1.08	56.1±7.5
118	Alonso et al. (2008)	H	4534.59610±0.00014	86.40±0.16	0.464±0.016	4.23±0.28	7.42±0.98	61.1±1.0
127	Manuel Mendez ^a	R	4558.38809±0.00164	86.51±0.21	0.464±0.016	4.23±0.23	7.00±0.76	64.2±4.7
129	NMSU Im	V	4563.67966±0.00252	86.38±0.23	0.464±0.016	4.23±0.28	6.63±0.79	60.1±5.3
129	APO 3.5m	V	4563.67971±0.00116	86.53±0.18	0.464±0.016	4.23±0.28	7.06±0.78	64.1±3.2
132	James Roe ^a	B	4571.61831±0.00467	88.62±1.02	0.464±0.016	4.23±0.28	9.25±1.27	93.3±6.5
137	NMSU Im	I	4584.83373±0.00379	86.84±0.78	0.464±0.016	4.23±0.27	7.70±1.19	72.6±14.5
137	APO 3.5m	V	4584.83084±0.00036	86.32±0.16	0.464±0.016	4.23±0.29	6.45±0.62	58.0±1.8
137	SBO 24 ⁿ	I	4584.82787±0.00912	86.64±0.73	0.464±0.016	4.23±0.28	7.05±1.45	67.8±17.1
137	Bruce Gary ^a	R	4584.82874±0.00100	86.53±0.18	0.464±0.016	4.23±0.28	7.07±0.76	64.3±2.8
138	Manuel Mendez ^a	R	4587.47761±0.00204	87.00±0.31	0.464±0.016	4.23±0.29	7.92±0.99	75.0±5.3
140	CC 11 ⁿ	None	4592.76119±0.00142	86.27±0.15	0.464±0.016	4.23±0.29	6.24±0.66	56.5±2.9
140	APO 3.5m	V	4592.76248±0.00093	86.47±0.17	0.464±0.016	4.23±0.29	6.94±0.68	62.6±2.9
140	SBO 24 ⁿ	I	4592.76090±0.00430	86.71±0.32	0.464±0.016	4.23±0.28	7.57±1.06	69.5±7.8
143	SBO 24 ⁿ	I	4600.69668±0.00171	86.08±0.17	0.464±0.016	4.23±0.30	5.54±0.71	50.4±3.6

Table 2.1 (continued)

Epoch	Source	Filter ^c	T_{\min} (HJD-2450000)	Inclination ($^{\circ}$)	R_{\star} (R_{\odot})	R_p (R_{\oplus})	Depth (mmag)	Width (minutes)
146	James Roe ^a	V	4608.62542±0.00508	86.40±0.68	0.464±0.016	4.23±0.28	6.53±2.03	63.8±19.6
...	3.5m Data Combined	V	...	86.43±0.16	0.464±0.016	4.23±0.28	6.82±0.67	61.7±2.7

^aAmateur Observer with data obtained from Bruce Gary. <http://brucegary.net/AXA/GJ436/gj436.htm>

^bData were digitized from published plot

^cJohnson-Cousins System

Note. — All errors are 1σ

statistical significance. Examining the best data, specifically the previously published data and our 3.5-meter observations, there is a standard deviation of 52 seconds. Assuming a sinusoidal TTV trend, we can then rule out any TTVs with amplitude greater than ~ 1 minute.

We have searched for any trends in derived inclination, width, and depth of transit over time via error-weighted least-squares linear regression. In addition, we have also performed 10,000 Monte Carlo simulations for each fit, where Gaussian noise with amplitude equal to each point's error bars was added in each iteration and the data re-fitted, with resulting 1σ parameter distributions giving robust errors. The two methods agree to within 1% for all values. As mentioned in Section 2.3, we modeled all the light curves by both allowing the ratio of radii to vary as well as fixing it, and thus we list the values for each set. Performing fits to all the data, we have a tentative detection of increasing inclination, transit width, and transit depth with time, as shown in Table 2.2. We present these fits with the actual data derived when fixing the radii in Figure 2.3. As a precaution against any bias being introduced by the much larger number of data points at later epochs, we decided to separately bin the 2005, 2007, and 2008 data using an error-weighted mean, and re-fit the three resulting data points for each modeling method. As shown in Table 2.2, the values agree very well with those derived when not binning the data.

The trends are moderately dependent on the single 2005 transit data point, which greatly extends the temporal baseline, and as such we are cautious about any claims. Resulting temporal trends when removing the 2005 data point are also shown in Table 2.2. Although while removing the 2005 data point significantly weakens the claim of a variation of inclination with time, the trend of increasing

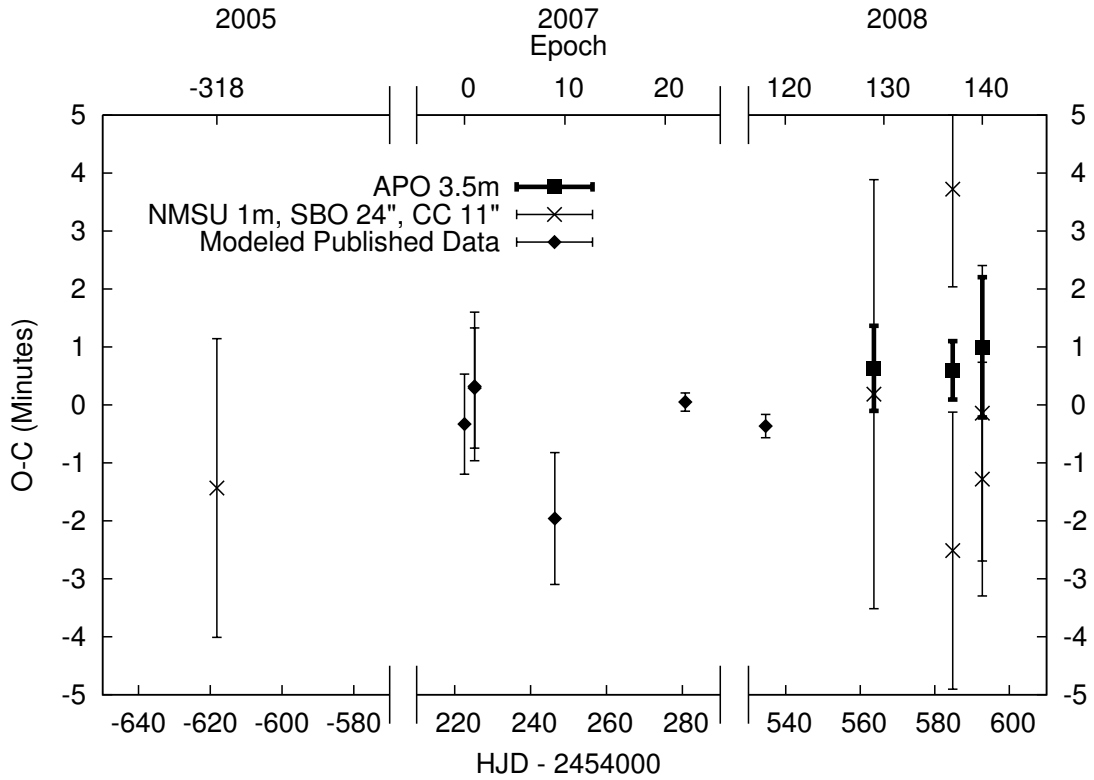


Fig. 2.2.— O-C diagram for all professional times of minima.

Table 2.2. Trends in derived inclination, width, and depth of transit over time

Data Set	deg yr ⁻¹	min yr ⁻¹	mmag yr ⁻¹
Variable Radius			
All	0.120±0.062	3.43±1.01	0.28±0.16
Binned	0.126±0.061	3.53±0.97	0.26±0.14
No 2005	0.092±0.099	3.10±1.10	0.29±0.17
Fixed Radius			
All	0.069±0.051	2.36±0.84	0.32±0.20
Binned	0.071±0.050	2.37±0.81	0.32±0.19
No 2005	0.020±0.099	1.68±1.29	-0.01±0.42

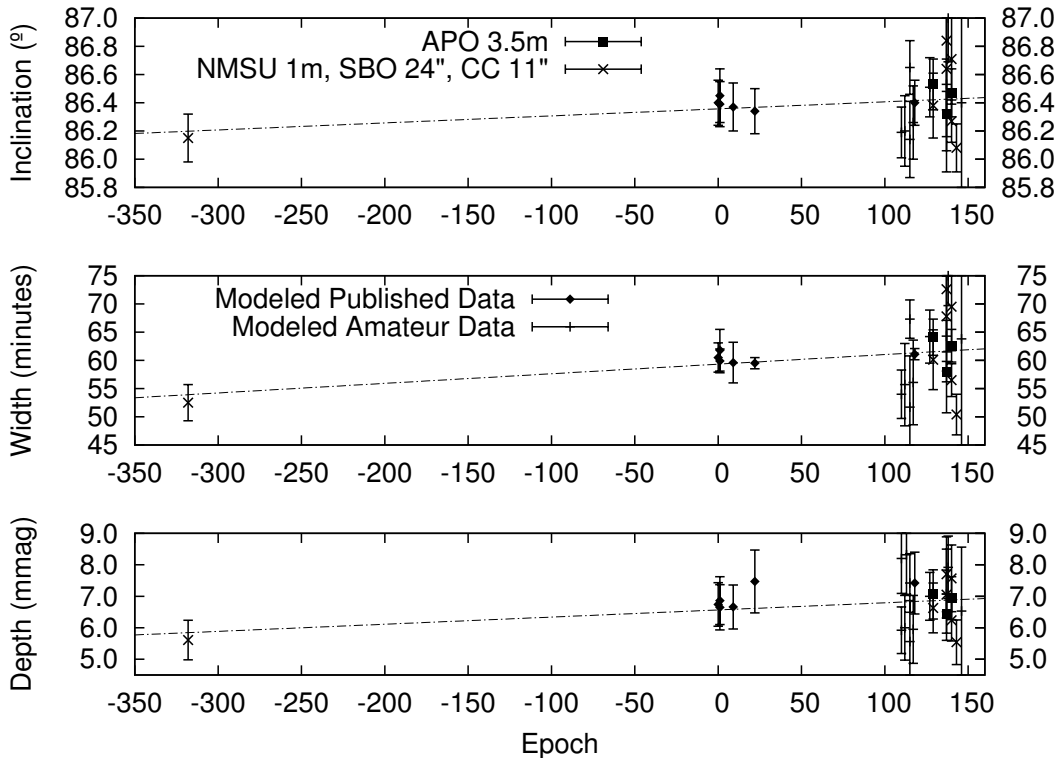


Fig. 2.3.— Measured inclination, width, and depth of transit over time for all data, with the star and planet radii fixed.

width still holds. Also of interest is that at a rate of $0.120 \text{ deg yr}^{-1}$, as derived from our fit to all the data fitted with a variable radius, the JKTEBOP program yields an increase in transit width of 4.36 min yr^{-1} , and depth of $0.544 \text{ mmag yr}^{-1}$, which are in agreement with our observed trends, and thus are self-consistent. As well, the measured rate of inclination change is compatible with the $\sim 0.1 \text{ deg yr}^{-1}$ required to make congruent the non-detection of Butler et al. (2004) and the observed transit of Gillon et al. (2007b). Extending the measurement baseline a couple years into the future will confirm or negate this result.

2.5. Discussion and Conclusion

We have presented a total of ten new primary transit light curves of Gliese 436b, three of which come from the 3.5-meter telescope at APO, and one of which is from the NMSU 1-meter in January 2005. We have collected and uniformly modeled all available professional and amateur light curves, and searched for any trends in transit timing, width of transit, and depth of transit variations. We find statistically significant, self-consistent trends that are compatible with the perturbation of Gliese 436b by a planet with mass $\lesssim 12 M_{\oplus}$ in a non-resonant orbit with semi-major axis $\lesssim 0.08$ AU. This conclusion is based on the numerical simulations of Ribas et al. (2008, see Fig. 1) who constrain the mass and semi-major axis of the theoretical second planet by examining which configurations could produce the observed orbital perturbations while still remaining undetected by the existing radial-velocity data. From our analysis, we infer a non-resonant orbit based on a lack of detected TTVs with amplitude $\gtrsim 1$ minute. We stress that our measured trends are moderately dependent on our 2005 data, and thus subsequent high-precision observations over the next few years need to be carried out to confirm or refute this trend. If confirmed, it would be strong evidence for the first extrasolar planet discovered via orbital perturbations to a transiting planet. Also, we would like to note that although Alonso et al. (2008) had previously limited the rate of inclination change to 0.03 ± 0.05 deg/yr, they did so only by measuring the change in width between the 2007 Spitzer observations and their own 2008 *H*-band data, which they found to be 0.5 ± 1.2 minutes. Via Table 2.1, we find the difference in transit width between the two observations to be 1.5 ± 1.4 minutes, which is in agreement with our derived inclination and width values, and is a more reliable result due to using full model fits with proper limb-darkening coefficients.

With respect to the amateur observations, although they are numerous, the very small depth of the transit makes it a challenge for most small aperture systems, resulting in very large uncertainties in i and T_0 . Also, while amateur observers are aware of the importance of precision timing, we of course cannot examine each of their observing set-ups, and thus one must be aware of the possibility, although small, of systemic time offsets on a given night when interpreting their data.

Very recently, Stevenson et al. (2012) found preliminary evidence for two additional low-mass, sub-Earth-sized transiting planets in both interior and exterior orbits to Gliese 436b via direct observations of their transits in recently obtained *Spitzer* data. Although it is not clear if these planets could be responsible for the parameter variations we observe due to their very low masses, it does provide evidence that the Gliese 436 system is populated by multiple planets, increasing the likelihood that a second planet massive enough to induce the observed variations exists in the system.

3. DAY-SIDE z' -BAND EMISSION AND ECCENTRICITY OF WASP-12b

3.1. Introduction

The transiting hot Jupiter WASP-12b, discovered by Hebb et al. (2009), has many notable characteristics. With a mass of $1.41 \pm 0.10 M_{\text{Jup}}$ and a radius of $1.79 \pm 0.09 R_{\text{Jup}}$, WASP-12b was the planet with the second largest radius reported at discovery, and the sixth largest transiting planet known at the time of this writing (Schneider 2012). It is also one of the most heavily irradiated planets known, with an incident stellar flux at the substellar point of over $9 \times 10^9 \text{ erg cm}^{-2} \text{ s}^{-1}$. In addition, model fits to its observed radial velocity and transit light curves suggest that the orbit of WASP-12b is slightly eccentric. All these attributes make WASP-12b one of the best targets to test current irradiated atmosphere and tidal heating models for exoplanets.

In irradiated atmosphere model studies WASP-12b is an extreme case even in the category of highly irradiated gas giants. Such highly irradiated planets are expected to show thermal inversions in their upper atmospheric layers (Burrows et al. 2008a), although the chemicals responsible for such inversions remain unknown. TiO and VO molecules, which can act as strong optical absorbers, have been proposed (Hubeny et al. 2003; Fortney et al. 2008), but Désert et al. (2008) claim that the concentration of those molecules in planetary atmospheres is too low ($< 10^{-3} - 10^{-2}$ times solar) to cause thermal inversions. Spiegel et al. (2009) argue that TiO needs to be at least half the solar abundance to cause thermal inversions, and very high levels of macroscopic mixing are required to keep enough TiO in the upper atmosphere of planets. S_2 , S_3 and HS compounds have also recently been suggested and then questioned as causes of the observed thermal

inversions (Zahnle et al. 2009).

In the case of tidal heating, detailed models are now being developed (e.g., Bodenheimer et al. 2003; Miller et al. 2009; Ibgui & Burrows 2009; Ibgui et al. 2010, 2011) to explain the inflated radius phenomenon observed in hot Jupiters, of which WASP-12b, with a radius over 40% larger than predicted by standard models, is also an extreme case. All models assume that the planetary orbits are slightly eccentric, and directly measuring those eccentricities is key not only to test the model hypotheses, but also to obtain information about the planets' core mass and energy dissipation mechanisms (see Ibgui et al. 2010).

We present the detection of the eclipse of WASP-12b in the z' -band ($0.9 \mu\text{m}$), which gives the first measurement of the atmospheric emission of this planet, and the first direct estimation of its orbital eccentricity. This is also only the second detection of an exoplanet secondary eclipse at $\lambda < 1 \mu\text{m}$ from ground-based observations, (the first was by Sing & López-Morales (2009) with combined data from 6.5 and 8-meter telescopes), while we employ only a 3.5-meter telescope. Section 3.2 summarizes the observations and analysis of the data. In Section 3.3 we compare the emission of the planet to models. The results are discussed in Section 3.4.

3.2. Observations and Analyses

We monitored WASP-12 [RA = 06:30:32.794, Dec = +29:40:20.29 (J2000), $V = 11.7$] during two eclipses, and under photometric conditions, on February 19 and October 18 2009 UT. An additional attempt on October 30 2009 UT was lost due to weather. The data were collected with the SPICam instrument on the ARC's

3.5-meter telescope at Apache Point Observatory, using a SDSS z' filter with an effective central wavelength of $\sim 0.9 \mu\text{m}$. SPICam is a backside-illuminated SITE TK2048E 2048x2048 pixel CCD with 24 micron pixels, giving an unbinned plate scale of 0.14 arc seconds per pixel and a field of view of 4.78 arc minutes square. The detector, cosmetically excellent and linear through the full A/D converter range, was binned 2x2, which gives a gain of $3.35 \text{ e}^-/\text{ADU}$, a read noise of 1.9 DN/pixel, and a 48 second read time.

On February 19 we monitored WASP-12 from 3:00 to 3:28 UT and from 3:54 to 7:10 UT, losing coverage between 3:28 and 3:54 UT when the star reached a local altitude greater than 85° , the soft limit of the telescope at that time. These observations yielded 1.20 hours of out-of-eclipse and 2.45 hours of in-eclipse coverage, at airmasses between 1.005–1.412. On October 18 we extended the altitude soft limit of the telescope to 87° and covered the entire eclipse from 7:05 to 12:45 UT, yielding 2.73 hours of out-of-eclipse and 2.93 hours of in-eclipse coverage, with airmasses between 1.001–1.801. In both nights we defocused the telescope to a FWHM of $\sim 2''$ to reduce pixel sensitivity variation effects, and also to allow for longer integration times, which minimized scintillation noise and optimized the duty cycle of the observations. Pointing changed by less than $(x,y)=(4,7)$ pixels in the October 18 dataset, and by less than $(x,y)=(3,12)$ pixels on February 19, with the images for this second night suffering a small gradual drift in the y direction throughout the night. Integration times ranged from 10 to 20 seconds. Taking into account Poisson, readout, and scintillation noise, the photometric precision on WASP-12 and other bright stars in the images ranged between 0.07–0.15% per exposure on February 19, and between 0.05–0.09% per exposure on October 18.

The field of view of SPICam was centered at RA = 06:30:25, Dec = +29:42:05 (J2000) and included WASP-12 and two other isolated stars at RA = 06:30:31.8, Dec = +29:42:27 (J2000) and RA = 06:30:22.6, Dec = +29:44:42 (J2000), with apparent brightness and $B-V$ and $J-K$ colors similar to the target. Each night’s dataset was analyzed independently and the results combined in the end. The timing information was extracted from the headers of the images and converted into Heliocentric Julian Days using the IRAF task *setjd*, which has been tested to provide sub-second timing accuracy.

We corrected each image for bias level and flatfield effects using standard IRAF routines. Dark current was negligible. DAOPHOT-type aperture photometry was performed in each frame. We recorded the flux from the target and the comparison stars over a wide range of apertures and sky background annuli around each star. We used apertures between 2 and 35 pixels in one-pixel steps during a first preliminary photometry pass, and 0.05 pixel steps in the final photometric extraction. To compute the sky background around each star we used variable width annuli, with inner radii between 35 and 60 pixels sampled in one-pixel steps. The best aperture and sky annuli combinations were selected by identifying the most stable, (i.e., minimum standard deviation), differential light curves between each comparison and the target at phases out-of-eclipse¹. In the February 19 data, the best photometry results from an aperture radius of 14.7 pixels for both the target and the comparison stars, and sky annuli with a 52-pixel inner radius and 22-pixel wide. For the October 18 data, 17.9 pixel apertures and sky annuli with a 45-pixel inner radius and 22-pixel wide produce the best photometry.

¹We had to iterate on the out-of-eclipse phase limits after finding that the eclipse was centered at $\phi = 0.51$. Out-of-eclipse was finally defined as phases $\phi < 0.45$ and $\phi > 0.57$.

The resultant differential light curves between the target and each comparison contain systematic trends that can be attributed to either atmospheric effects, such as airmass, seeing, or sky brightness variations, or to instrumental effects, such as small changes in the location of the stars on the detector. Systematics can also be introduced by instrumental temperature or pressure changes, but those parameters are not monitored in SPICam. We modeled systematics for each light curve by fitting linear correlations between each parameter (airmass, seeing, sky brightness variations, and target position) and the out-of-eclipse portions of the light curves. All detected trends are linear and there are no apparent residual color difference effects. The full light curves are then de-trended using those correlation fits. In the October 18 dataset, airmass effects are the dominant systematic, introducing a linear baseline trend with an amplitude in flux of 0.07%. The February 19 dataset also shows systematics with seeing and time with a total amplitude of also 0.07%. The systematics on this night were modeled using only the after-eclipse portion of the light curve, and we consider this dataset less reliable than the October 18 one. The 18 pre-ingress images collected between 3:00 and 3:38 UT suffer from a ~ 50 pixel position shift with respect to the rest of the images collected that night, which cannot be modeled using overall out-of-eclipse systematics. We chose not to use those points in the final analysis. Correlations with the other parameters listed above are not significant in any of the two datasets.

Finally, we produce one light curve per night by combining the de-trended light curves of each comparison. The light curves are combined applying a weighted average based on the Poisson noise of the individual light curve points. The result is illustrated in Figure 3.1. The out-of-eclipse scatter of the combined light curves is 0.11% for the February 19 data and 0.09% for the October 18 data. De-trending

significantly improves the systematics, but some unidentified residual noise sources remain, which we have not been able to fully model.

3.2.1. *Eclipse detection and error estimation*

The two-night combined light curve contains 421 points between phases 0.413 and 0.596, based on the Hebb et al. (2009) ephemerides. To establish the presence of the eclipse and its parameters, we fit the data to a grid of models generated using the *JASMINE* code, which combines the Kipping (2008) and Mandel & Agol (2002) algorithms to produce model light curves in the general case of eccentric orbits. The models do not include limb darkening, (which is not important for secondary eclipse observations), and use as input parameters the orbital period, stellar and planetary radii, argument of the periastron, orbital inclination, stellar radial velocity amplitude, and semi-major axis values derived by Hebb et al. (2009). The eccentricity is initially assumed to be $e=0$, which produces models with a total eclipse duration of 2.808 hours. The best fit model is found by χ^2 minimization, with the depth, the central phase of the eclipse, and the out-of-eclipse differential flux as free parameters.

First we fit the individual night light curves to ensure the eclipse signal is present in each dataset. The February 19 data give an eclipse depth of $0.100 \pm 0.023\%$, while the derived eclipse depth for the October 18 data is $0.068 \pm 0.021\%$. The central phases are $\phi=0.510$ for the first eclipse and $\phi = 0.508$ for the second. We assume the difference in depth is due to systematics we have not been able to properly model. The incomplete eclipse from February 19 might seem more prone to systematics, but our inspection of both datasets does not reveal stronger trends

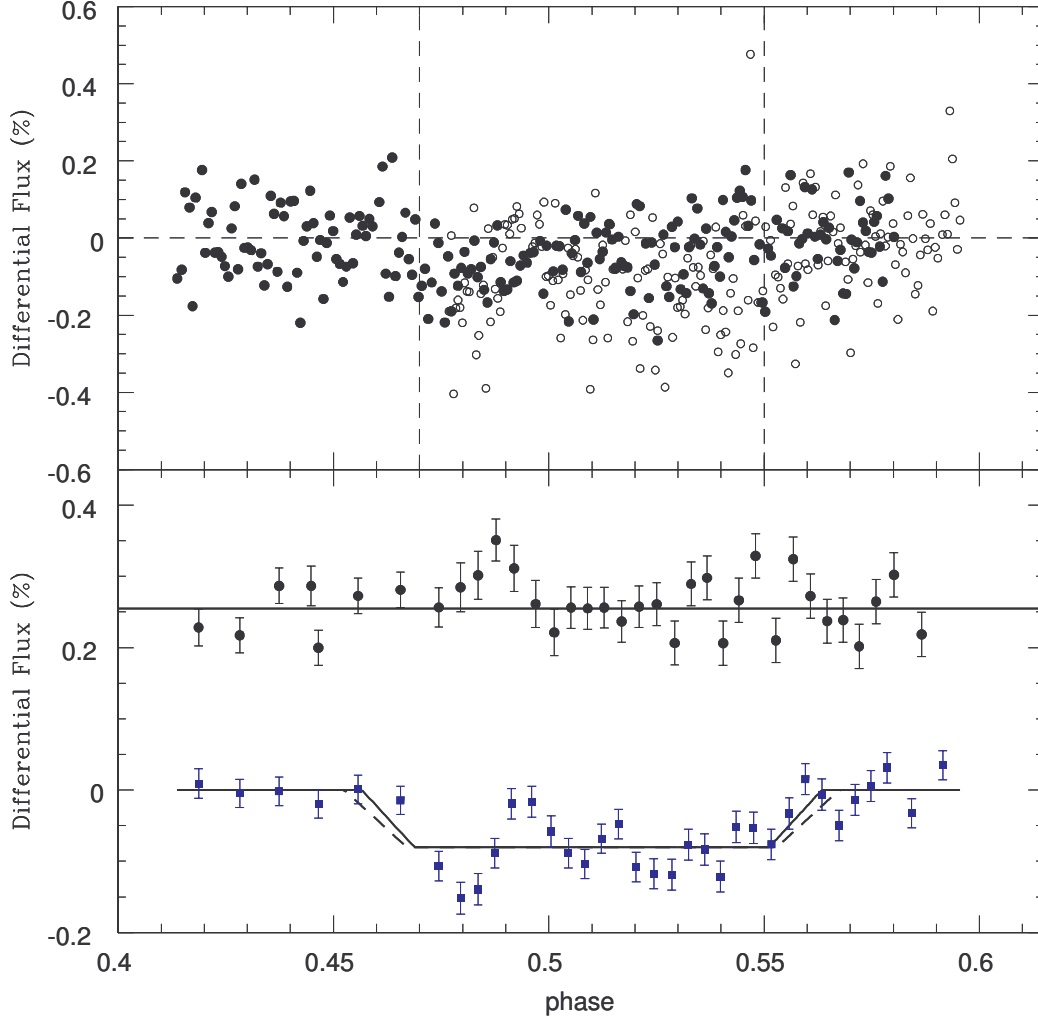


Fig. 3.1.— *Top*: De-trended differential light curves. Open and filled dots show, respectively, the Feb 19 and Oct 18 UT 2009 data. The vertical dashed lines denote the start and end of total eclipse. *Bottom*: Combined light curves binned by a factor of 12. Blue squares correspond to WASP-12 and black dots to the differential light curve of the two comparison stars. The best fit models are shown as solid lines (for $e = 0$) and dashed lines (for $e = 0.057$). Both models produce the same depth and center phase, but the $e = 0.057$ model lasts 11.52 minutes longer. We attribute the flux jumps between phases 0.475 and 0.5 to unremoved systematics. Notice that, although the systematics appear in both curves, the trends in each curve are not correlated in phase.

in that dataset. We therefore combined the data from both nights, weighting each light curve based on its out-of-eclipse scatter.

The result of the combined light curve analysis is the detection of an eclipse with a depth of $0.082 \pm 0.015\%$ and centered at orbital phase $\phi = 0.51$, as shown in Figure 3.1. The reduced χ^2 of the fit is 0.952. The error in the eclipse depth is computed using the equation $\sigma_{depth}^2 = \sigma_w^2/N + \sigma_r^2$, where σ_w is the scatter per out-of-eclipse data point and σ_r^2 describes the red noise. The σ_r is estimated with the binning technique by Pont et al. (2006) to be 1.5×10^{-4} when binning on timescales up to the ingress and egress duration of about 20 minutes.

We investigate to what extent the uncertainties in the system’s parameters affect our eclipse depth and central phase results. Varying the impact parameter, planet-to-star ratio, and scale of the system by 1σ of the reported values in Hebb et al. (2009), the measured eclipse depth changes only by 0.004% or $0.27\sigma_{depth}$, while the central phase remains unchanged. Our result is therefore largely independent of the adopted system parameters.

We perform several more tests to confirm the eclipse detection in a manner similar to previously reported eclipse results (Deming et al. 2005; Sing & López-Morales 2009; Rogers et al. 2009). From the average of the 125 out-of-eclipse light curve data points versus the 228 in-eclipse points (only points where the planet is fully eclipsed, adopting $\phi=0.51$ as the central eclipse phase), we measure an eclipse depth of $0.080 \pm 0.015\%$. We further check the detection by producing histograms of the normalized light curve flux distribution in the in-eclipse and out-of-eclipse portions of the light curve. The result, illustrated in Figure 3.2, shows how the flux distribution of in-eclipse points is shifted by 0.00082 with respect to the out-

of-eclipse flux distribution, centered at zero. We also fit the light curve with the JKTEBOP code (Southworth et al. 2004a,b), and use Monte-Carlo, prayer-bead and bootstrapping analyses to estimate the errors, obtaining errors on the eclipse depth of $\pm 0.011\%$, $\pm 0.008\%$, and $\pm 0.011\%$, and errors on the central phase of ± 0.0021 , ± 0.0026 , and ± 0.0018 , for the three methods, respectively.

Adopting the largest error estimates from all of these analysis techniques, we derive final values of a depth and central phase of $0.082 \pm 0.015\%$ (5.5σ) and 0.5100 ± 0.0026 (3.8σ).

3.2.2. Eccentricity

The eccentricity e of WASP-12b was calculated from the measured central phase shift value using Eq. 6 from Wallenquist (1950),

$$e \cos \omega = \frac{\pi (t_2 - t_1 - P/2)}{P (1 + \csc^2 i)}, \quad (3.1)$$

where P , i and ω are, respectively, the orbital period, inclination, and periastron angle of the system, and $t_2 - t_1$ is the time difference between transit and eclipse. In our case $t_2 - t_1 = 0.51P$. Using the values of P , i and ω from Hebb et al. (2009), we derive an $e = 0.057 \pm 0.015$, which agrees with the non-zero eccentricity result reported by these authors. This eccentricity can be in principle explained if 1) the system is too young to have already circularized, 2) there are additional bodies in the system pumping the eccentricity of WASP-12b, 3) the tidal dissipation factor Q'_P (Goldreich 1963) of WASP-12b is several orders of magnitude larger than Jupiter's, estimated to be between 6×10^4 and 2×10^6 (Yoder & Peale 1981), or 4) the orbit is really circular but there is a wavelength-dependent brightness

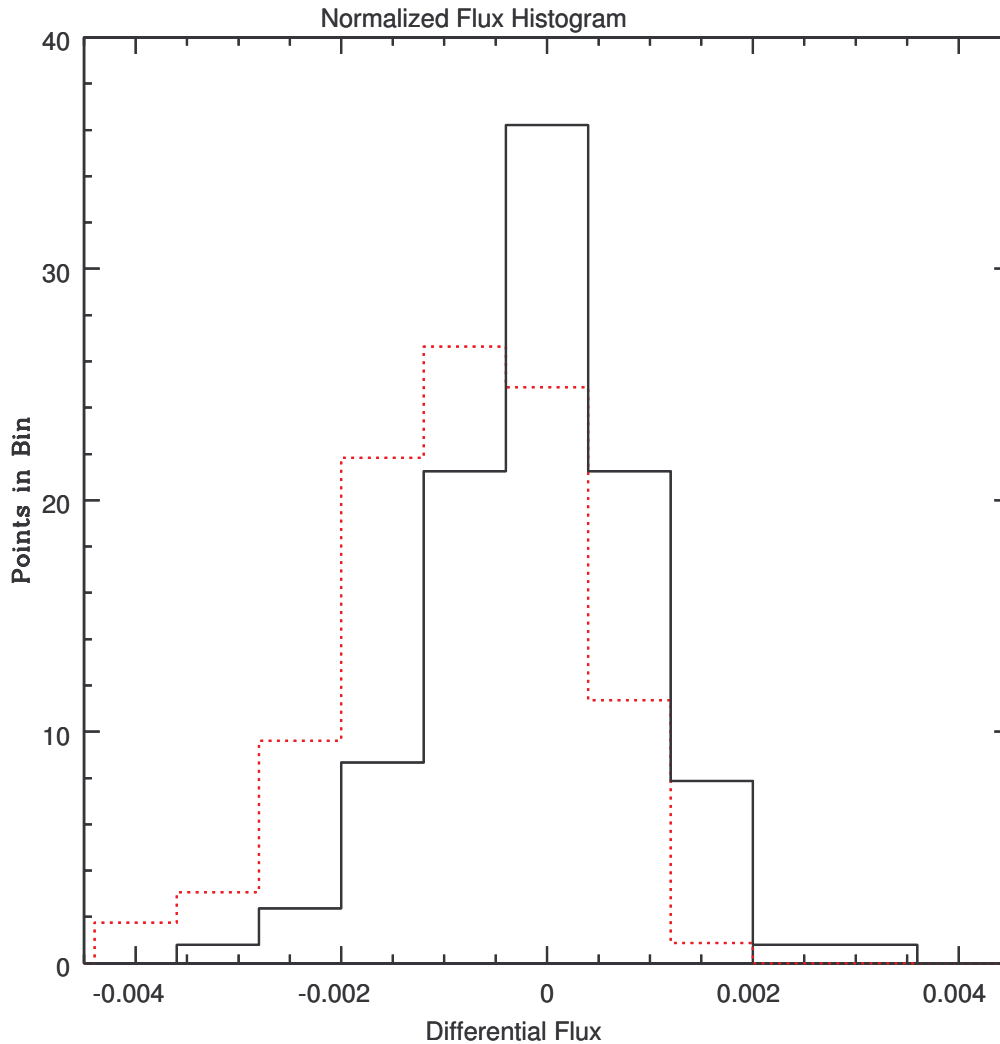


Fig. 3.2.— Normalized flux histograms of the in-eclipse (dotted red line) and out-of-eclipse (solid line) portions of the WASP-12 light curve in Figure 3.1. The bin width is 0.00082 in differential flux, coincident with the detected eclipse depth.

variation across the surface of the planet that would shift the center of the eclipse, as suggested for HD 189733b by Swain et al. (2010).

3.3. Comparison with atmospheric models

We compare the observed z' -band flux of WASP-12b to simple blackbody models and to expectedly more realistic radiative-convective models of irradiated planetary atmospheres in chemical equilibrium, following the same procedure described in Rogers et al. (2009). The results are shown in Figures 3.3 and 3.4.

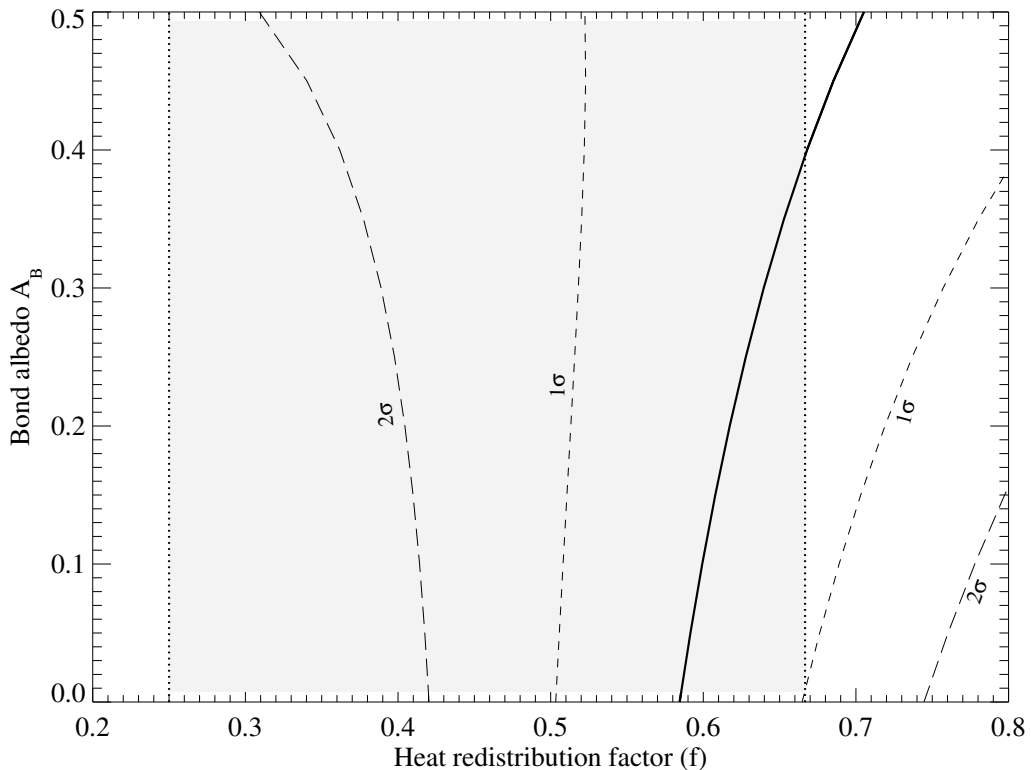


Fig. 3.3.— Values of A_B and f that reproduce the observed z' -band eclipse depth of WASP-12b, assuming the planet emits as a blackbody. The shaded area highlights the region of allowed f values ($1/4 - 2/3$). The short and long dashed lines delimit, respectively, the 1σ and 2σ confidence regions of the result.

In the simplistic blackbody approximation, a $0.082 \pm 0.015\%$ deep eclipse corresponds to a z' -band brightness temperature of $T_{z'} = 3028 \pm 105$ K, slightly

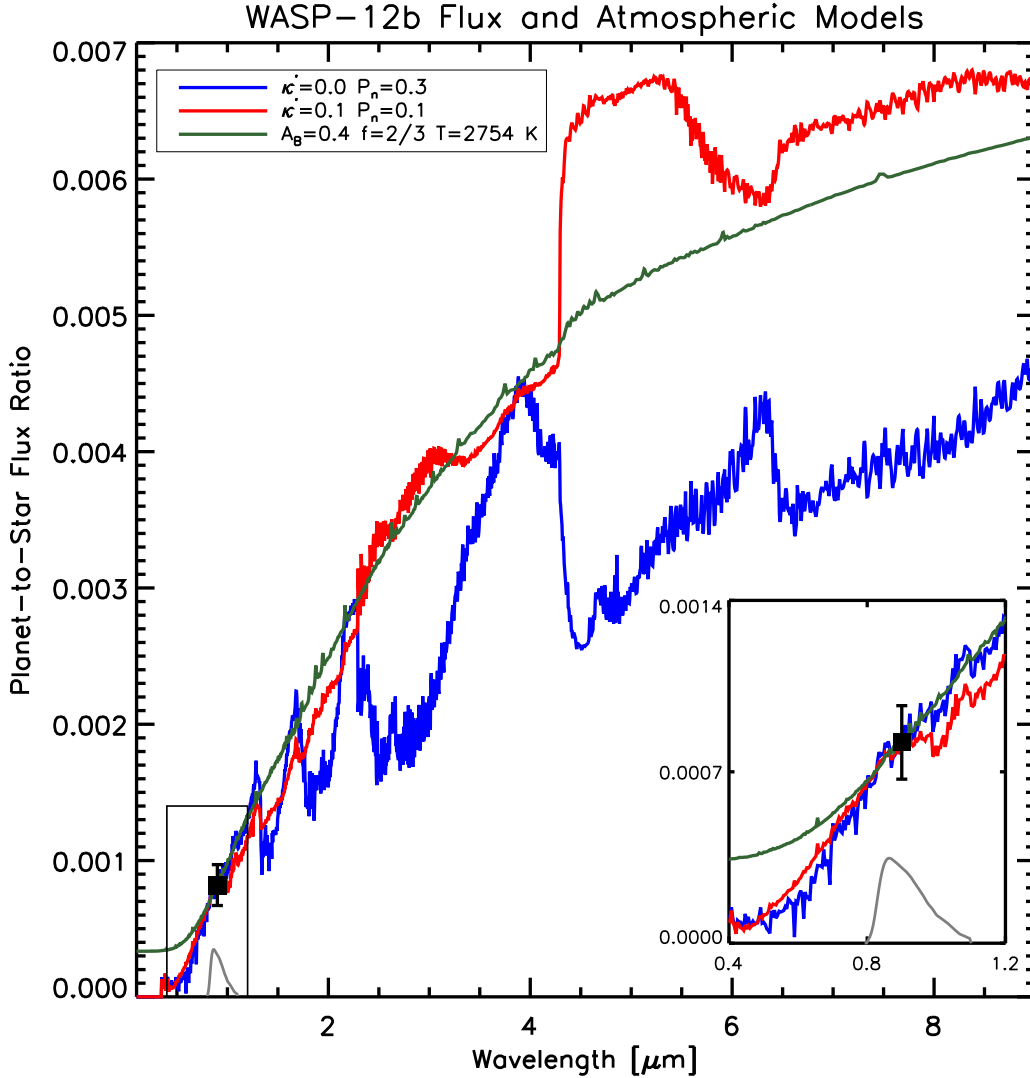


Fig. 3.4.— Comparison of the eclipse depth, (planet-to-star flux ratio), shown as the black square with errorbars, to models. The green line shows the $A_B = 0.4$, $f = 2/3$ blackbody model from Figure 3.3. The blue and red lines show, respectively, the best fit model for an atmosphere with no extra absorber, and with an extra absorber of opacity κ' between 0.43 and $1.0 \mu\text{m}$. The black thin line at the bottom indicates the SPICam plus SDSS z' -band filter response. See Section 3.3 for more details.

lower than the planet's equilibrium temperature of $T_p = 3129 \text{ K}$ assuming zero Bond albedo ($A_B = 0$) and no energy re-radiation ($f = \frac{2}{3}$) (see López-Morales & Seager 2007). However, when the thermal and reflected flux of the planet are

included, different combinations of A_B and f can yield the same eclipse depth, as illustrated in Figure 3.3. From that figure we can constrain the energy redistribution factor to $f \geq 0.585 \pm 0.080$, but the albedo is not well constrained. Assuming a maximum $A_B \leq 0.4$, the temperature of the day-side of WASP-12b is $T_p > 2707 K$.

The more realistic atmospheric models are derived from self-consistent coupled radiative transfer and chemical equilibrium calculations, based on the models described in Sudarsky et al. (2000, 2003), Hubeny et al. (2003) and Burrows et al. (2005, 2006, 2008a) (see Rogers et al. 2009, for details). We generate models with and without thermal inversion layers, by adding an unidentified optical absorber between 0.43 and 1.0 μm , with different level of opacity κ' . The opacity of the absorber varies parabolically with frequency, with a peak value of $\kappa' = 0.25 \text{ cm}^2 \text{ gr}^{-1}$. As Figure 3.4 shows, models with and without extra absorbers produce similar fits to the observed z' -band flux. The best model without absorber has a $P_n = 0.3$.² The best model with an extra absorber has a $P_n = 0.1$ and $\kappa_e = 0.1 \text{ cm}^2 \text{ gr}^{-1}$. Observations at other wavelengths are necessary to further constrain the models.

3.4. Discussion and Conclusions

This first detection of the eclipse of WASP-12b agrees with the slight eccentricity of the planet's orbit found by Hebb et al. (2009), and places initial constraints to its atmospheric characteristics. We note though that detections of

² $P_n = 0$ and $P_n = 0.5$ correspond, respectively, to $f = 2/3$ and $f = 1/4$, however there is not a well-defined $P_n - f$ relation for intermediate values since the physical models account for atmospheric parameters (e.g. pressure, opacity) in a way different than blackbody models.

the secondary eclipse in the near-infrared J , H , and K -bands (Croll et al. 2011), and in the mid-infrared with *Spitzer* (Campo et al. 2011), published after our detection, did not find any significant eccentricity. The most likely explanation is that a bright spot exists on the surface of the planet that is prominent in the z' -band, but not at longer wavelengths.

The presence of other bodies in the system can be tested via radial velocity or transit timing variation observations, although the current RV curve by Hebb et al. (2009) shows no evidence of additional planets, unless they are in very long orbits.

One would expect that if extra absorbers are present in the upper atmosphere of the planet in gaseous form, they might give rise to thermal inversion layers. However, as Figure 3.4 illustrates, the observed $0.9 \mu\text{m}$ eclipse depth can be fit equally well by a model without extra absorbers. Additional observations at longer wavelengths, specially longer than $\sim 4.0 \mu\text{m}$, will break that model degeneracy. Observations at wavelengths below $\sim 0.6 \mu\text{m}$ will also better constrain A_B . Indeed, after our detection was published, Madhusudhan et al. (2011) combined our measurement with those at 1.2, 1.6, 2.1, 3.6, 4.5, 5.8, and $8 \mu\text{m}$ to determine the planet is extremely rich in methane.

4. A UNIFORM SEARCH FOR SECONDARY ECLIPSES OF HOT JUPITERS IN *KEPLER* Q2 LIGHTCURVES

4.1. Introduction

Measuring the secondary eclipses of transiting exoplanets at optical wavelengths is a powerful tool for probing their atmospheres, in particular their albedos, brightness temperatures, and energy redistribution factors. The *Kepler* mission has recently uncovered over a thousand new transiting planet candidates (Borucki et al. 2011), which provide an unprecedented and uniform sample of high photometric precision light curves among which secondary eclipse signals can be detected.

In the past decade, many surprising discoveries regarding the atmospheric properties of hot Jupiters have been made. For example, many hot Jupiters appear to have temperature inversions, with numerous proposed explanations, but no definitive evidence for exactly which physical processes are involved (Hubeny et al. 2003; Fortney et al. 2006; Burrows et al. 2007; Fortney et al. 2008; Spiegel et al. 2009; Zahnle et al. 2009; Knutson et al. 2010; Madhusudhan & Seager 2010). Other results have found that the atmospheric composition of different planets vary significantly, or that they present a wide range of heat circulation efficiencies between their day and night sides (see Baraffe et al. 2010, and references therein).

Most of the observations yielding to those discoveries have been done in the mid-infrared (3.6 - 24 μm) with *Spitzer*. Observations at shorter wavelengths are more scarce, especially in the visible, but most of them point towards the predominance of very low geometric albedo, ($A_g < 0.3$ at the 3σ level upper limits), atmospheres in hot Jupiters (Charbonneau et al. 1999; Leigh et al. 2003a,b;

Rodler et al. 2008, 2010; Rowe et al. 2008; Alonso et al. 2009a,b, 2010; Snellen et al. 2009; Christiansen et al. 2010; Welsh et al. 2010; Kipping & Bakos 2011a; Kipping & Spiegel 2011; Désert et al. 2011a,b; Langford et al. 2011), in contrast to the $A_g \approx 0.5$ albedos observed in the colder gas giants in our Solar System (Karkoschka 1994). Those results are in fair agreement with early theoretical models (e.g., Marley et al. 1999; Sudarsky et al. 2000; Seager et al. 2000), which predict significant absorption of the incident stellar radiation in the visible by sodium and potassium, followed by re-emission in the infrared. Other molecules, such as TiO, VO, and HS, have also been suggested as possible strong optical absorbers (e.g., Hubeny et al. 2003; Fortney et al. 2008; Zahnle et al. 2009).

However, three recent studies suggest higher geometric albedos for two planets. Berdyugina et al. (2011) have published a value of $A_g = 0.28 \pm 0.16$ for HD 189733b via polarized reflected light¹, while Kipping & Bakos (2011a) and Demory et al. (2011) respectively suggest albedos of $A_g = 0.38 \pm 0.12$ and $A_g = 0.32 \pm 0.03$ for Kepler-7b based on measurements of the emission of the planet with *Kepler* during secondary eclipse. Some plausible explanations for such high albedos include Rayleigh scattering and the presence of clouds or hazes in the atmospheres of those planets (Demory et al. 2011). Also, in the case of the hottest planets, some amount of thermal emission could be contributing to the measured emission levels in the reddest edge of the observed visible wavelength windows (e.g., at $\lambda \sim 0.8 \mu\text{m}$).

Although new theoretical work is necessary to determine the cause of appar-

¹We note that (Wiktorowicz 2009) reported a non-detection of polarized light from this planet, and placed an upper limit to the polarimetric modulation of the exoplanet at $\Delta P < 7.9 \times 10^{-5}$.

ently high albedos in some hot Jupiters, the key answer to whether these results are typical or not relies on more observations, since the current discussions are based on a statistically insufficient sample of only three planets. The purpose of this work is to significantly increase that sample by searching for the emission of hot Jupiters among the publicly available *Kepler* light curves of planet candidates reported by Borucki et al. (2011). Given the photometric precision of the *Kepler* data and the wavelength coverage of the *Kepler* passband (0.4 - 0.9 μm), these datasets provide unprecedented quality data to detect the secondary eclipses of those planets in the visible and statistically determine the albedos of hot Jupiters. Furthermore, as Borucki et al. (2011) do not explicitly state how they modeled their light curves or obtained their parameters, a re-modeling of the data will perform an independent test on the methods they employed.

In addition to providing estimations of the planetary albedo, measuring the timing and duration of the secondary eclipse, when coupled with the primary eclipse, can directly measure the orbital eccentricity of a system (e.g., Knutson et al. 2007b). Also, if there is a significant flux contrast between the day and night side of the planet, one may be able to measure the varying amount of emitted light by the planet in the light curve, and directly measure the day-to-night contrast ratio (Harrington et al. 2006; Knutson et al. 2007b). Even a robust upper limit on the eclipse depth can narrow the range of possible planetary albedos and yield useful information on the statistics of exoplanetary albedos.

In Section 4.2 we present our target selection criteria and describe how we reprocess the *Kepler* light curves from the pixel-level data. In Section 4.3 we describe how we model the data using the JKTEBOP code, and obtain robust errors on all parameters while accounting for potential systematic noise. We

present our derived physical parameters of both the planet candidates and their host stars in Section 4.4, and in Section 4.5 we examine possible trends in our results. In Section 4.6 we discuss individual candidates of interest, and finally in Section 4.7 we summarize our findings and examine possible future directions for the study of this sample.

4.2. Observational Data

The first step of our analysis consisted of selecting a set of planet candidates suitable for secondary eclipse detection among the 1,235 planet candidates published by Borucki et al. (2011). We made a pre-selection of potentially detectable objects using the planetary and stellar parameters listed in Table 2 of Borucki et al. (2011), choosing only those systems with $P < 5$ days and $R_p > 0.5 R_J$, after estimating that planets with longer orbital periods and smaller radii are too cool, too small, or too far away from their host star to produce deep enough secondary eclipse signals to be detectable by *Kepler*, even in the most extreme albedo conditions (i.e., $A_g = 1.0$). Our secondary eclipse depth estimations also account for the amount of stellar irradiation, given the effective temperature of the stars reported by Borucki et al. (2011). The result is a list of 76 candidates.

The next step consisted of an inspection of the *Kepler* light curves of those 76 targets. The analysis of Borucki et al. (2011) uses the first four months of *Kepler* observations, which include quarters Q0, Q1, and Q2. However, significantly discrepant systematic noise patterns exist between the light curves from different quarters, which result in additional noise when all the data are combined. Therefore, we decided to use only the data from Q2, which alone contains

continuous 90-day observation coverage and is well suited for our search.

We modeled two different light curves for each target: the Presearch Data Conditioned (PDC) light curve, and our own generated light curves that we produced using the pixel-level data and our own photometric pipeline. In the remainder of the paper we refer to this second analysis as the CLM pipeline, (for Coughlin & López-Morales (2012a)). As detailed in Jenkins et al. (2010b), the first step in creating the PDC light curves was correcting the pixel level data for bias pattern noise, dark current, gain, non-linearity, cosmic rays, shutter smearing, pixel-to-pixel sensitivity, and other pixel-level effects. The calibrated pixels were then run through a Photometric Analysis (PA) that measures and subtracts background flux, and sums up pixels within a photometric aperture for each star, creating the PA light curve. The size of those apertures are defined such that it is supposed to maximize the mean signal-to-noise for each star. The PA light curves were then subjected to Pre-Search Data Conditioning which attempts to remove systematic effects due to temperature, focus, pointing, and other effects by correlating with ancillary engineering data. The PDC module also corrects for any sudden jumps in the data, for example due to sudden pointing changes or pixel sensitivities due to cosmic ray hits, as well as removes excess flux in the photometric aperture due to crowding.

During our inspection of the PDC data we noted that, despite the thorough analysis detailed by Jenkins et al. (2010b), many of the PDC light curves produced by the *Kepler* PDC pipeline still contain significant systematic trends at a level of couple percent variation, an effect that can significantly hinder the detection of secondary eclipses and phase brightness variations. Upon thorough examination of the pixel-level data, PA, and PDC light curves, we concluded that the majority

of the trends correlate with and are due to the 0.1-0.5 pixel centroid position drift experienced by the majority of the target stars each quarter. This drift is principally due to Differential Velocity Aberration (DVA), where the amount of stellar aberration introduced by the spacecraft’s velocity varies over the large field of view, resulting in the shifting of stellar positions on the detector as large as 0.6 pixels over a 90 day period (Jenkins et al. 2010c). Spacecraft pointing error only accounts for 0.05 pixels of the total movement (Jenkins et al. 2010c). This drift in the stellar position causes light from the wings of each star’s point spread function to enter and leave the optimal photometric aperture at different rates, resulting in a flux variance of several percent over each quarter. To remove those effects we re-analyzed the *Kepler* pixel-level data using the CLM pipeline.

The CLM photometric pipeline starts with the calibrated pixel-level data, with background flux removed from each pixel. As the majority of target stars are well-isolated, we simply summed up the flux for every pixel that was downloaded from the spacecraft for each star. We find that this removes the majority of long-term systematic variations due to DVA, usually producing light curves with significantly less systematic noise than the similarly produced PA light curves. Usually the only time summing up all the pixels produced more systematic noise is when there was significant crowding in the field by comparably bright stars, but we find this only affects a small fraction of the selected transiting planet candidates, and note that crowding can still significantly affect PA photometry as well.

Even after minimizing the amount of light variation within the aperture, pixel-to-pixel sensitivity, both in spectral response as well as quantum efficiency, and intra-pixel variations, still produced significant systematics. We cut out areas

of significant systematic variation, which principally occur around BJD 2455015 and BJD 2455065, due to a safe mode event and a pointing tweak. Then, we performed a correlation-based Principal Component Analysis (PCA) (Murtagh & Heck 1987) on the pixel level data, and subtract out the first three PCA components, thus removing the majority of major systematic noise, which is still principally correlated with the large position drift. We have checked and verified that this does not remove or significantly modify the transit signal for any system. We then fit a Bézier curve (Kahaner et al. 1989) to the data, performed a 3-sigma rejection, re-fit a Bézier curve, and then divided by the fit. This iterative procedure does an excellent job of removing any possible remaining low-frequency systematic features in the data without removing or affecting the transits or real high-frequency stellar variations. We then, for only a few systems, removed one or two points that were extremely significant outliers. For one system, KOI 433.01, we removed a single transit that was clearly from another long-period companion in the system. For both the *Kepler* PDC and CLM light curves, we finally subtracted a linear trend to ensure the light curves were completely flat before modeling (see Section 4.3).

We would like to note that, as a possible technique of removing systematic noise, we also attempted to directly solve for a pixel mask that would account for pixel-to-pixel variation in quantum efficiency and spectral response. Every image in the time series was multiplied by this pixel mask, whose values ranged from 0 to 1, and then the pixel fluxes summed to produce a corrected light curve. We used an asexual genetic algorithm, similar to that presented in Coughlin et al. (2011), to solve for the values of each pixel in the pixel mask that produced corrected light curves with a minimum amount of systematic noise, defined via

various methods. We found that the technique was very successful at removing nearly all systematic noise from the light curves. However, depending on the minimization criteria selected, we found that the algorithm was prone to over-correct the light curve, and remove features due to real astrophysical phenomena. As well, even when it did appear to remove the systematic trends and not the real astrophysical signatures, it was difficult to tell, unlike with the PCA analysis, whether or not the solution had a real physical basis. Thus, we decided not to employ this technique in our analysis. However, with more work or a better understanding of the systematic noise sources, it might become a viable means for removing systematic noise from *Kepler*, and possibly other, light curves.

In Figure 4.1 we plot the *Kepler* PA and PDC light curves, our CLM light curves, (including those from simply summing up all the pixels in each frame, applying the PCA correction, and then applying the Bezier correction), the centroid positions, averaged pixel-level image, and the aperture used in the *Kepler* PA and PDC photometry, for each of the 76 candidate systems. Of the original 76 candidates, 36 were deemed unmodelable based on their PDC light curves, due to either strong systematics or intrinsic stellar variability with amplitudes on the order of, or greater than, the depth of the transits. The 36 discarded systems were KOI 1.01, 17.01, 20.01, 127.01, 128.01, 135.01, 183.01, 194.01, 203.01, 208.01, 214.01, 217.01, 254.01, 256.01, 552.01, 554.01, 609.01, 667.01, 767.01, 823.01, 882.01, 883.01, 895.01, 981.01, 1152.01, 1176.01, 1177.01, 1227.01, 1285.01, 1382.01, 1448.01, 1452.01, 1540.01, 1541.01, 1543.01, and 1546.01. In the case of our newly generated CLM pipeline light curves, 26 candidates turned out to be unmodelable, most of them due to stellar variability, as in the case of the PDC light curves above, or due to blends in the images resulting in significant light

contamination of the target light curves. The 26 systems discarded in this case were KOI 102.01, 135.01, 194.01, 199.01, 208.01, 256.01, 552.01, 554.01, 609.01, 823.01, 882.01, 883.01, 895.01, 931.01, 961.02, 961.03, 981.01, 1152.01, 1177.01, 1227.01, 1285.01, 1382.01, 1448.01, 1452.01, 1540.01, and 1546.01. Thus, in total, there are 21 targets that have no modelable light curve from either analysis, (nearly all due to intrinsic stellar variability), 35 systems that have modelable light curves from both the *Kepler* PDC data and our CLM reduction, and 55 systems that have at least one modelable light curve from either the *Kepler* PDC data or our CLM analysis. In Table 4.1 we present the *Kepler* Object of Interest (KOI) number, *Kepler* ID number, and host stars' *Kepler* magnitude, effective temperature, surface gravity, and metallicity from the *Kepler* Input Catalog of each of the 55 modelable candidates.

We now highlight a few systems to illustrate the different types of systematic and stellar noise in the *Kepler* data, and differences between the PDC and CLM light curves. For KOI 17.01, (see Figure 4.1.6), the PA and PDC light curves both show a $\sim 1.7\%$ systematic variation over the quarter, as the PA/PDC aperture does not encompass many pixels in the wing of the PSF that contain significant signal, and the star experiences a ~ 0.4 pixel drift over the quarter. In contrast, the raw pixel-summed CLM light curve shows only a $\sim 0.54\%$ systematic variation, and the PCA-corrected and Bezier-corrected CLM light curves show virtually no remaining systematic noise. For KOI 102.01 and 199.01, (see Figures 4.1.11 and 4.1.22), there is a close companion star that causes the CLM photometry to produce much worse light curves than the PDC data. In the case of KOI 102.01, significant systematics are introduced in the CLM light curve from the movement of the companion in and out of the frame, given the ~ 0.3 pixel drift over the

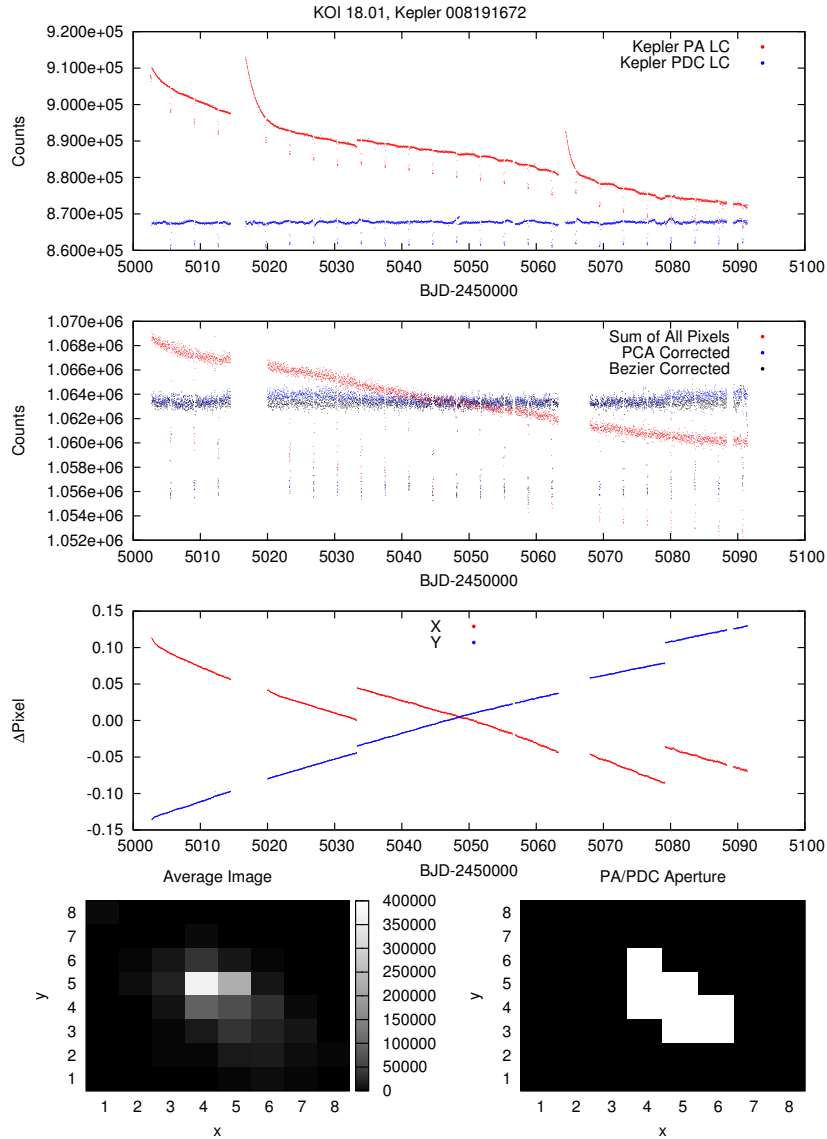


Fig. 4.1.— Plots of the light curves, centroid positions, pixel-level images, and photometric apertures used in the *Kepler* PA and PDC reduction, for all initial 76 candidate systems. The top panel for each system shows the Q2 *Kepler* PA and PDC light curves. The next panel shows our CLM pipeline reduced light curves, including those from simply summing all the pixels in each frame, applying PCA correction, and then applying a Bezier correction, with the most severe systematic noise regions cut out. The next panel shows the flux-weighted relative centroid movement in both X and Y over Q2, using all pixels in the frame, again with the most severe systematic noise regions cut out. The bottom left panel is the average image of all the frames over the quarter. The bottom right panel shows the photometric aperture used in the *Kepler* PA and PDC light curve reduction, where only white pixels were counted and summed. Only a single plot, Figure 4.1.7, is shown in the text for guidance. Figures 4.1.1-4.1.76 are available in the online version of the *Astronomical Journal* under Coughlin & López-Morales (2012a).

Table 4.1. Modeled Systems and Their Host Star Properties

KOI	Kepler ID	m _{kep}	T _* (K)	log g (cgs)	[Fe/H]	M _* ,KIC (M _⊙)	R _* ,KIC (R _⊙)	M _* ,ISO (M _⊙)	R _* ,ISO (R _⊙)
1.01	011446443	11.338	5713	4.14	-0.139	1.133 ^{+1.726} _{-0.681}	1.496 ^{+1.400} _{-0.727}	1.019 ^{+0.060} _{-0.053}	0.943 ^{+0.074} _{-0.060}
2.01	010666592	10.463	6577	4.32	0.000	1.351 ^{+2.059} _{-0.812}	1.336 ^{+1.251} _{-0.649}	1.316 ^{+0.078} _{-0.075}	1.363 ^{+0.115} _{-0.113}
5.01	008554498	11.665	5766	4.04	0.116	1.176 ^{+1.720} _{-0.706}	1.748 ^{+1.574} _{-0.846}	1.035 ^{+0.060} _{-0.055}	0.962 ^{+0.077} _{-0.065}
10.01	006922244	13.563	6164	4.44	-0.128	1.110 ^{+1.718} _{-0.920}	1.056 ^{+1.002} _{-0.520}	1.162 ^{+0.074} _{-0.066}	1.133 ^{+0.109} _{-0.093}
13.01	009941662	9.958	8848	3.93	-0.141	1.813 ^{+1.988} _{-1.087}	2.454 ^{+1.186} _{-0.623}	1.989 ^{+0.053} _{-0.053}	1.616 ^{+0.022} _{-0.022}
17.01	010874614	13.000	5724	4.47	0.000	0.908 ^{+0.538} _{-0.538}	0.911 ^{+0.443} _{-0.443}	1.022 ^{+0.060} _{-0.054}	0.947 ^{+0.075} _{-0.061}
18.01	008191672	13.369	5816	4.46	0.000	0.922 ^{+1.447} _{-0.551}	0.942 ^{+0.862} _{-0.454}	1.050 ^{+0.062} _{-0.059}	0.981 ^{+0.081} _{-0.071}
20.01	011804465	13.438	6012	4.47	-0.161	1.069 ^{+1.637} _{-0.639}	0.999 ^{+0.933} _{-0.483}	1.110 ^{+0.071} _{-0.061}	1.059 ^{+0.100} _{-0.080}
64.01	007051180	13.143	5128	3.94	-0.341	1.180 ^{+1.694} _{-0.694}	1.956 ^{+1.036} _{-0.546}	0.868 ^{+0.046} _{-0.046}	0.786 ^{+0.046} _{-0.046}
97.01	005780885	12.885	5944	4.27	0.052	1.086 ^{+1.705} _{-0.649}	1.279 ^{+1.170} _{-0.616}	1.089 ^{+0.067} _{-0.067}	1.031 ^{+0.094} _{-0.094}
102.01	008456679	12.566	5919	3.90	-0.358	1.216 ^{+1.862} _{-0.727}	2.058 ^{+1.922} _{-0.994}	1.081 ^{+0.060} _{-0.061}	1.020 ^{+0.092} _{-0.075}
127.01	008359498	13.938	5570	4.53	0.174	1.043 ^{+1.581} _{-0.634}	0.921 ^{+0.850} _{-0.436}	0.980 ^{+0.056} _{-0.053}	0.897 ^{+0.066} _{-0.055}
128.01	011359879	13.758	5718	4.18	0.362	1.139 ^{+1.700} _{-0.680}	1.443 ^{+1.284} _{-0.668}	1.020 ^{+0.061} _{-0.053}	0.945 ^{+0.076} _{-0.076}
144.01	004180280	13.698	4724	4.00	0.241	1.098 ^{+0.662} _{-0.662}	1.744 ^{+0.838} _{-0.838}	0.767 ^{+0.053} _{-0.053}	0.694 ^{+0.052} _{-0.049}
183.01	009651668	14.290	5722	4.71	-0.141	1.012 ^{+1.536} _{-0.608}	0.734 ^{+0.678} _{-0.353}	1.022 ^{+0.062} _{-0.054}	0.947 ^{+0.077} _{-0.062}
186.01	012019440	14.952	5826	4.56	0.021	1.059 ^{+1.660} _{-0.632}	0.877 ^{+0.819} _{-0.414}	1.052 ^{+0.063} _{-0.058}	0.984 ^{+0.083} _{-0.070}
188.01	005357901	14.741	5087	4.73	0.255	0.893 ^{+1.353} _{-0.542}	0.671 ^{+0.619} _{-0.348}	0.859 ^{+0.046} _{-0.048}	0.778 ^{+0.043} _{-0.042}
195.01	011502867	14.835	5604	4.50	-0.188	1.058 ^{+0.640} _{-0.640}	0.968 ^{+0.469} _{-0.469}	0.988 ^{+0.051} _{-0.051}	0.907 ^{+0.053} _{-0.053}
196.01	009410930	14.465	5585	4.51	0.096	1.029 ^{+1.574} _{-0.620}	0.937 ^{+0.842} _{-0.450}	0.984 ^{+0.053} _{-0.053}	0.901 ^{+0.067} _{-0.054}
199.01	010019708	14.879	6214	4.60	0.104	1.081 ^{+1.641} _{-0.650}	0.863 ^{+0.797} _{-0.415}	1.182 ^{+0.076} _{-0.070}	1.161 ^{+0.113} _{-0.100}
201.01	006849046	14.014	5491	4.45	0.187	1.039 ^{+1.628} _{-0.620}	0.985 ^{+0.920} _{-0.465}	0.959 ^{+0.053} _{-0.052}	0.875 ^{+0.059} _{-0.052}
202.01	007877496	14.309	5912	4.44	0.120	1.093 ^{+1.677} _{-0.654}	1.052 ^{+0.912} _{-0.515}	1.080 ^{+0.064} _{-0.064}	1.019 ^{+0.078} _{-0.072}
203.01	010619192	14.141	5634	4.49	0.041	1.056 ^{+1.592} _{-0.636}	0.980 ^{+0.915} _{-0.473}	0.996 ^{+0.060} _{-0.051}	0.915 ^{+0.072} _{-0.054}
204.01	009305831	14.678	5287	4.48	-0.104	0.966 ^{+1.447} _{-0.577}	0.950 ^{+0.854} _{-0.460}	0.905 ^{+0.054} _{-0.045}	0.821 ^{+0.054} _{-0.042}
214.01	011046458	14.256	5322	4.44	0.018	1.022 ^{+1.510} _{-0.612}	1.015 ^{+0.890} _{-0.488}	0.916 ^{+0.052} _{-0.048}	0.832 ^{+0.054} _{-0.046}
217.01	009595827	15.127	5504	4.72	0.220	0.975 ^{+1.448} _{-0.649}	0.706 ^{+0.649} _{-0.341}	0.963 ^{+0.054} _{-0.054}	0.879 ^{+0.060} _{-0.060}
229.01	003847907	14.720	5608	4.37	0.219	1.069 ^{+1.616} _{-0.645}	1.124 ^{+1.041} _{-0.645}	0.990 ^{+0.052} _{-0.052}	0.909 ^{+0.067} _{-0.054}
254.01	005794240	15.979	3948	4.54	0.234	0.950 ^{+0.810} _{-0.322}	0.650 ^{+0.602} _{-0.307}	0.347 ^{+0.168} _{-0.118}	0.319 ^{+0.124} _{-0.090}
356.01	011624249	13.807	5124	4.07	-0.503	1.111 ^{+1.623} _{-0.665}	1.593 ^{+1.466} _{-0.750}	0.869 ^{+0.048} _{-0.049}	0.787 ^{+0.045} _{-0.043}
412.01	005683743	14.288	5584	4.28	-0.011	1.093 ^{+1.667} _{-0.654}	1.275 ^{+1.153} _{-0.625}	0.983 ^{+0.058} _{-0.053}	0.901 ^{+0.068} _{-0.054}
421.01	009115800	14.995	5181	4.32	-0.075	1.016 ^{+0.610} _{-0.610}	1.155 ^{+0.547} _{-0.547}	0.880 ^{+0.047} _{-0.047}	0.797 ^{+0.042} _{-0.042}

Table 4.1 (continued)

KOI	<i>Kepler</i> ID	m _{kep}	T_\star (K)	$\log g$ (cgs)	[Fe/H]	M_\star ,KIC (M_\odot)	R_\star ,KIC (R_\odot)	M_\star ,ISO (M_\odot)	R_\star ,ISO (R_\odot)
433.01	010937029	14.924	5237	4.37	0.375	0.986 ^{+1.476} _{-0.559}	1.080 ^{+0.071} _{-0.553}	0.894 ^{+0.052} _{-0.069}	0.810 ^{+0.052} _{-0.102}
611.01	006309763	14.022	6122	4.55	-0.132	1.085 ^{+1.599} _{-0.645}	0.914 ^{+0.852} _{-0.429}	1.149 ^{+0.066} _{-0.066}	1.115 ^{+0.092} _{-0.114}
667.01	006752502	13.826	4135	4.57	0.000	0.607 ^{+0.917} _{-0.364}	0.681 ^{+0.597} _{-0.326}	0.501 ^{+0.126} _{-0.165}	0.431 ^{+0.121} _{-0.054}
684.01	007730747	13.831	5331	3.96	0.113	1.174 ^{+1.743} _{-0.704}	1.870 ^{+1.718} _{-0.873}	0.917 ^{+0.053} _{-0.048}	0.833 ^{+0.054} _{-0.045}
760.01	011138155	15.263	5887	4.62	0.010	1.060 ^{+1.611} _{-0.614}	0.840 ^{+0.801} _{-0.463}	1.072 ^{+0.063} _{-0.050}	1.008 ^{+0.057} _{-0.053}
767.01	011414511	15.052	5431	4.44	0.023	1.026 ^{+0.615} _{-0.625}	1.007 ^{+0.943} _{-0.485}	0.946 ^{+0.050} _{-0.052}	0.862 ^{+0.052} _{-0.054}
801.01	003351888	15.001	5472	4.39	0.182	1.041 ^{+1.590} _{-0.632}	1.080 ^{+1.000} _{-0.510}	0.955 ^{+0.054} _{-0.054}	0.871 ^{+0.059} _{-0.054}
809.01	003935914	15.530	5690	4.48	-0.385	1.047 ^{+1.518} _{-0.630}	0.967 ^{+0.877} _{-0.454}	1.012 ^{+0.061} _{-0.053}	0.934 ^{+0.075} _{-0.059}
813.01	004275191	15.725	5357	4.73	-0.285	0.955 ^{+1.428} _{-0.576}	0.695 ^{+0.641} _{-0.328}	0.924 ^{+0.052} _{-0.050}	0.839 ^{+0.054} _{-0.047}
830.01	005358624	15.224	4915	4.90	0.155	0.797 ^{+0.478} _{-0.478}	0.528 ^{+0.250} _{-0.250}	0.819 ^{+0.052} _{-0.052}	0.742 ^{+0.049} _{-0.049}
838.01	005534814	15.311	5794	4.48	-0.095	1.049 ^{+1.596} _{-0.619}	0.987 ^{+0.913} _{-0.471}	1.043 ^{+0.059} _{-0.057}	0.972 ^{+0.078} _{-0.068}
840.01	005651104	15.028	4916	4.39	-0.091	0.936 ^{+1.379} _{-0.556}	1.023 ^{+0.953} _{-0.481}	0.818 ^{+0.048} _{-0.052}	0.742 ^{+0.042} _{-0.049}
843.01	005881688	15.270	5784	4.40	0.203	1.093 ^{+1.650} _{-0.655}	1.109 ^{+0.972} _{-0.531}	1.041 ^{+0.060} _{-0.057}	0.969 ^{+0.079} _{-0.068}
897.01	007849854	15.257	5734	4.46	0.270	1.066 ^{+1.397} _{-0.594}	1.024 ^{+0.394} _{-0.394}	1.025 ^{+0.060} _{-0.060}	0.951 ^{+0.075} _{-0.064}
908.01	008255887	15.113	5391	4.25	0.128	1.050 ^{+1.591} _{-0.636}	1.279 ^{+1.197} _{-0.618}	0.933 ^{+0.052} _{-0.051}	0.849 ^{+0.050} _{-0.053}
913.01	008544996	15.198	5463	4.75	-0.281	0.967 ^{+1.521} _{-0.589}	0.685 ^{+0.644} _{-0.332}	0.953 ^{+0.052} _{-0.053}	0.869 ^{+0.057} _{-0.053}
931.01	009166862	15.272	5714	4.78	0.319	1.016 ^{+1.547} _{-0.617}	0.685 ^{+0.624} _{-0.330}	1.020 ^{+0.061} _{-0.053}	0.944 ^{+0.075} _{-0.061}
961.02	008561063	15.920	4188	4.56	0.000	0.612 ^{+0.888} _{-0.368}	0.671 ^{+0.609} _{-0.331}	0.536 ^{+0.117} _{-0.115}	0.461 ^{+0.114} _{-0.113}
961.03	008561063	15.920	4188	4.56	0.000	0.626 ^{+0.927} _{-0.377}	0.679 ^{+0.621} _{-0.325}	0.539 ^{+0.115} _{-0.115}	0.463 ^{+0.123} _{-0.123}
1176.01	003749365	15.715	4601	4.69	0.376	0.746 ^{+1.115} _{-0.453}	0.648 ^{+0.614} _{-0.309}	0.736 ^{+0.053} _{-0.078}	0.663 ^{+0.053} _{-0.083}
1419.01	011125936	15.507	5848	4.46	-0.292	1.075 ^{+1.614} _{-0.645}	0.999 ^{+0.920} _{-0.474}	1.059 ^{+0.065} _{-0.059}	0.992 ^{+0.087} _{-0.072}
1459.01	009761199	15.692	4060	4.40	0.098	0.646 ^{+1.001} _{-0.389}	0.830 ^{+0.781} _{-0.393}	0.444 ^{+0.138} _{-0.139}	0.384 ^{+0.115} _{-0.113}
1541.01	004840513	15.189	6164	4.53	0.068	1.100 ^{+0.657} _{-0.657}	0.954 ^{+0.465} _{-0.465}	1.163 ^{+0.068} _{-0.068}	1.134 ^{+0.095} _{-0.095}
1543.01	005270698	14.985	5821	4.54	-0.240	1.044 ^{+1.587} _{-0.618}	0.912 ^{+0.870} _{-0.433}	1.052 ^{+0.061} _{-0.059}	0.983 ^{+0.080} _{-0.071}

quarter, and as well the extra third light causes the transits of the primary to be damped out. In the case of KOI 199.01, the companion is an eclipsing binary, and its light curve is imposed on top of that of the transiting system. Significant systematics are still present in the PA data in these two cases, but much less so than the CLM data, and they appear to be removed in the PDC data. In the cases of KOI 256.01 and KOI 1452.01, (see Figures 4.1.32 and 4.1.71), the stars exhibit clear high-frequency variations at the same level as the transits, possibly due to stellar pulsation or rapid rotation and star spots. Note that the CLM pipeline does not remove the stellar signal because it is high-frequency and intrinsic to the system, and also that for KOI 256.01 additional long-term systematic noise is present in the *Kepler* PA and PDC data due to the small aperture they employ and the ~ 0.35 pixel drift, but does not exist in the CLM data.

4.3. Light Curve Modeling

We used the JKTEBOP eclipsing binary modeling code (Southworth et al. 2004a,b), which is based on the EBOP code (Etzel 1981; Popper & Etzel 1981), to model both the *Kepler* PDC light curves and our own CLM pipeline light curves for the 55 modelable systems. In short, JKTEBOP² models the projection of each star as a biaxial ellipsoid and calculates light curves by numerical integration of concentric ellipses over each star, and is well-suited to modeling detached eclipsing binaries or transiting extrasolar planets. We modeled each light curve first fixing the eccentricity to $e = 0$, and then leaving it as a free parameter. The reason for leaving e as a free parameter is that, even though systems with $P < 5$ days

²For more information on JKTEBOP, see <http://www.astro.keele.ac.uk/jkt/codes/jktebop.html>

are generally expected to be circularized, additional bodies in the system or other evolutionary effects can perturb their orbits. Indeed, at the time of this writing, $\sim 36\%$ of currently known transiting planets with $P < 5$ days have a measured non-zero eccentricity (Schneider 2012). Therefore, since we are performing a blind search for secondary eclipses, restricting the search to only circular orbits might result in detection biases. The results between fixing $e = 0$ and letting it vary can sometimes vary significantly, as shown at the end of this section.

For both cases of either fixing $e = 0$ or letting it vary, we also simultaneously solved for the orbital period of the system, P , time of primary transit minimum, T_0 , the inclination of the orbit, i , $e \cdot \cos(\omega)$ and $e \cdot \sin(\omega)$, where ω is the longitude of periastron, the planet-to-star surface brightness ratio, J , the sum of the fractional radii, r_{sum} , the planet-to-star radii ratio, k , and the out-of-eclipse (baseline) flux. We note for clarity that the relation between J , k , and the planet-to-star luminosity ratio, L_r , is $L_r = k^2 J$. To account for any potential brightness variations with phase, we also multiply the planet's luminosity, L_p , by a factor of one plus a sinusoidal curve, so that

$$L_p(T) = L_p + A_{L_p} \cdot \sin\left(\frac{2\pi(T - T_0)}{P} - \frac{\pi}{2}\right) \quad (4.1)$$

where $L_p(T)$ is the planet's luminosity at a given observed time, T , and A_{L_p} , for which we solve, is the amplitude of the sinusoidal curve. Note that we have fixed the period of this sine wave to the orbital period of each system, and fixed the reference zero phase so that the maximum amplitude peak coincides with the center of the secondary eclipse. Although there has been at least one case of a measured planetary brightness phase curve having its maximum offset from

secondary eclipse in the infrared (Knutson et al. 2007b), many optical observations indicate planetary brightness phase curve maxima coincident with the secondary eclipse (Borucki et al. 2009; Snellen et al. 2009; Welsh et al. 2010; Bonomo et al. 2011). We note that a value of $A_{L_p} = 0.0$ implies no brightness variations with phase. A value of $A_{L_p} = 0.2$ implies the planet is 20% brighter at phase 0.5, when the day-side is visible, and 20% fainter at phase 1.0, when the night-side is visible, compared to phases 0.25 and 0.75. A value of $A_{L_p} = 1.0$ implies a perfectly dark night-side. Negative values of A_{L_p} would imply a brighter night-side than day-side, which is not physically expected, but allowed for in the code so as not to introduce any bias towards positive values of A_{L_p} . Note also that J is allowed to be both positive and negative so as not to introduce any bias towards positive values of J , and thus false detections.

In both cases we assumed a quadratic limb-darkening law for the stars, and fixed coefficients to the values found by Sing (2010) for the *Kepler* bandpass, using the estimated stellar effective temperatures, surface gravities, and metallicities. We also set the values of the gravity darkening coefficients to those derived by Claret (2000b), based on the effective temperature of the stars. Even though we fix the limb and gravity darkening coefficients, they are computed from stellar models and have an associated uncertainty when compared to reality. As the choice of these coefficients can affect the determination of other system parameters, their uncertainty must be taken into account in the error analysis. Claret (2008) determined this uncertainty to be $\sim 10\%$, and thus we allowed the values of the limb and gravity darkening coefficients to vary over a range of $\pm 10\%$ during the error estimation analysis, described below.

Finally, as pointed out by Kipping (2010a), sparse sampling times, such as the

29.4244 minute sampling of the *Kepler* long-cadence data, can significantly alter the morphological shape of a transit light curve and result in erroneous planetary parameter estimations if the effect is not taken into account. Thus, we instructed JKTEBOP to integrate the models over 29.4244 minutes, composed of 10 separate sub-intervals centered on each observed data point, to account for this effect.

We derived error estimates using three error analysis techniques implemented in JKTEBOP: Monte Carlo, Bootstrapping, and Residual Permutation, but chose to adopt the parameter errors estimated by this last technique as it has been shown to best account for the effect of systematic noise in transit light curves (Jenkins et al. 2002). While Monte Carlo and Bootstrapping tend to underestimate errors in the presence of systematic noise, those two techniques have traditionally been chosen over Residual Permutation because in the latter one can only refit the data as many times as available data points. This poses a problem for most ground based transit light curves, which typically have only a couple hundred points, but for *Kepler* Q2 data, which contains almost 5000 data points over a 90-day interval for the long-cadence data, and nearly 30 times more for the short-cadence data, the method is not statistically limited and therefore best suited to derive robust errors.

In Figure 4.2 we plot the resulting phased light curves, with the corresponding best-fit model light curve when allowing eccentricity to vary, along with histograms of the parameter distributions from the error analysis, for the 40 modelable systems with *Kepler* PDC light curves. In Figure 4.3 we do the same, but for the 50 modelable systems with CLM light curves. In Table 4.2 we list the median values for all the modeling parameters, for both sets of light curves, and for both fixing $e = 0$ and allowing it to vary, along with their determined asymmetric, Gaussian,

1σ errors.

As a result of our light curve modeling we find, when fixing $e = 0$, nine secondary eclipse detections at the $1-2\sigma$ level, three detections at the $2-3\sigma$ level and four detections at the $>3\sigma$ level in the PDC light curves. In the CLM light curves, we find 11 secondary eclipse detections at the $1-2\sigma$ level, four detections at the $2-3\sigma$ level and four detections at the $>3\sigma$ level. In the case of allowing eccentricity to vary we find 18 detections at $1-2\sigma$ level, three detections at $2-3\sigma$ level, and four detections at $>3\sigma$ level in the PDC light curves. In the CLM light curves we find 10 detections at $1-2\sigma$ level, 10 detections at $2-3\sigma$ level, and five detections at $>3\sigma$ level. Each set of results has been used independently in the statistical study of candidate emission parameters described in Sections 4.4 and 4.5. Examining both sets of light curves, and both $e = 0$ and e allowed to vary, we find 16 systems with $1-2\sigma$, 14 systems with $2-3\sigma$, and six systems with $>3\sigma$ confidence level secondary eclipse detections in at least one light curve. It is more difficult to quantify the number of systems that have certain level detections among multiple light curves and eccentricity constraints, given that not all systems had both PDC and CLM light curves and that eccentric systems may not be detected in the non-eccentric model, and is best left to the discussion of individual systems in Section 4.6. Additionally, examining the 35 systems that had both modelable PDC and CLM light curves, we find that for the PDC light curves the average reduced χ^2 value is 4.86, while for the CLM light curves it is 2.48, and that on average, each system's CLM light curve has a 27% lower reduced χ^2 value compared to the PDC light curve.

We also note that there were significant detections of negative J values for some systems. When fixing eccentricity to zero, for the PDC light curves, we find

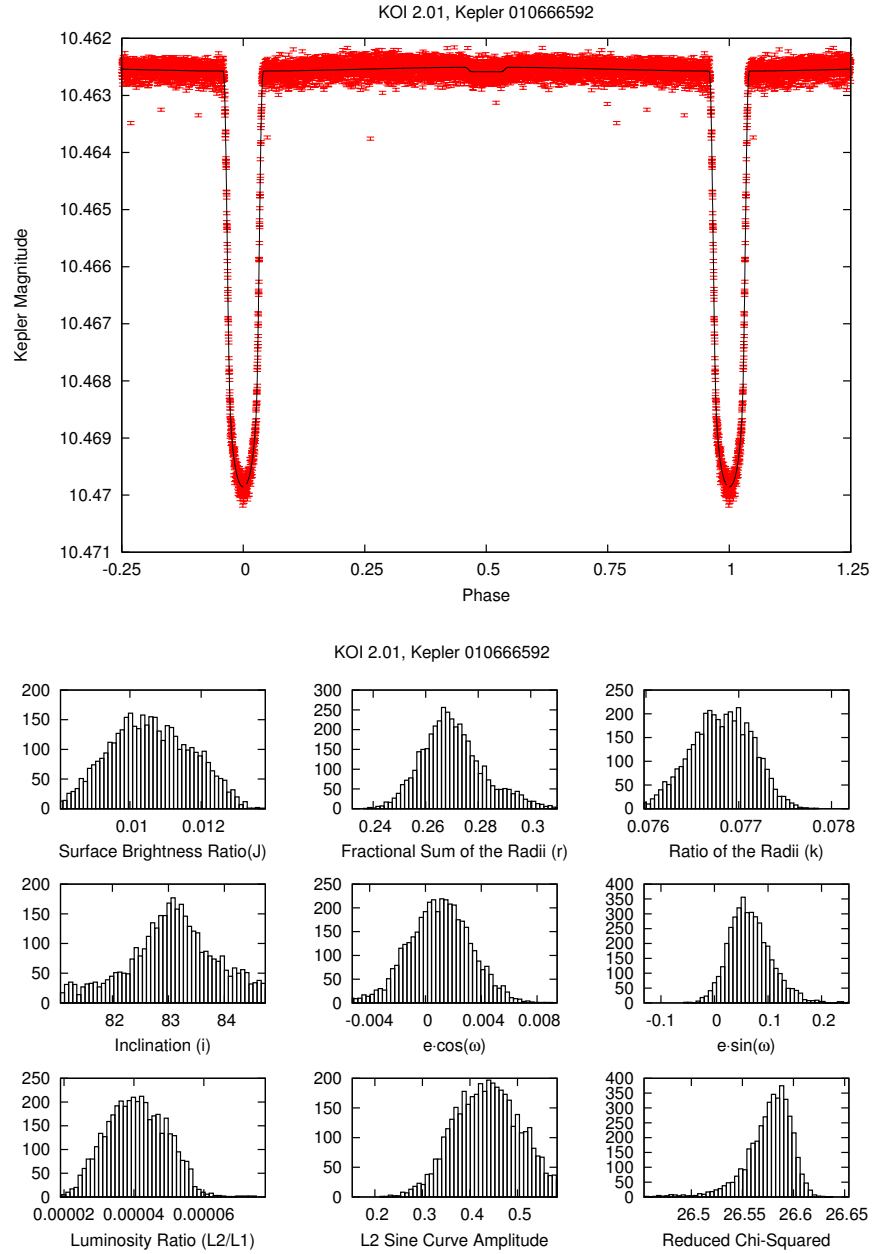


Fig. 4.2.— Plots of the phased light curves of the 40 systems produced from the *Kepler* PDC photometric pipeline, shown with our best model fits, allowing eccentricity to vary, and histograms of the resulting parameter distributions from the error analysis. Only the first plot, Figure 4.2.1, is shown in the text for guidance. Figures 4.2.1-4.2.40 are available in the online version of the *Astronomical Journal* under Coughlin & López-Morales (2012a).

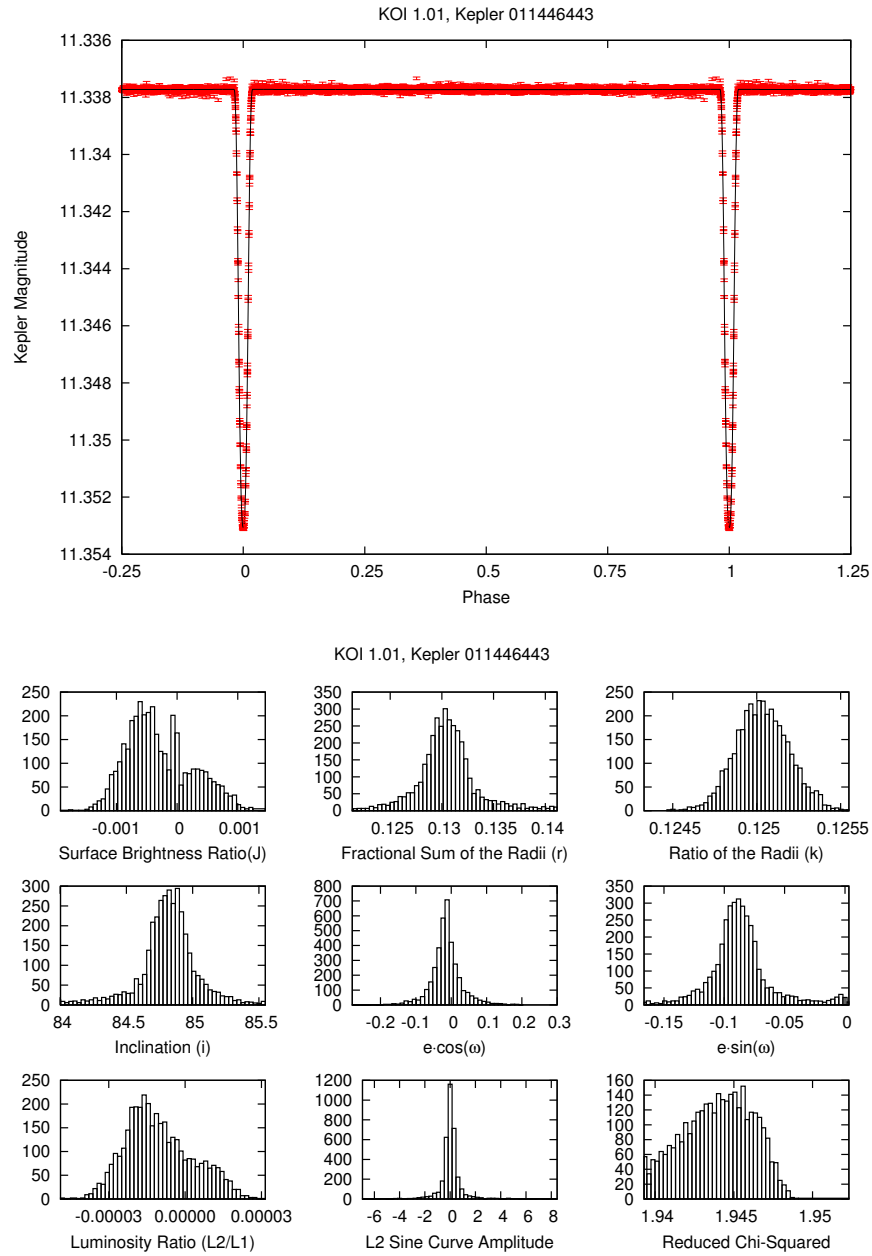


Fig. 4.3.— Plots of the phased light curves of the 50 systems produced using our CLM photometric pipeline, shown with our best model fits, allowing eccentricity to vary, and histograms of the resulting parameter distributions from the error analysis. Only the first plot, Figure 4.3.1, is shown in the text for guidance. Figures 4.3.1-4.3.50 are available in the online version of the *Astronomical Journal* under Coughlin & López-Morales (2012a).

Table 4.2. Modeling Results: Median Values and Associated 1σ Uncertainties

KOI	J	τ_{sum}	k	i ($^{\circ}$)	$e \cos w$	$e \sin w$	P (Days)	T_0 (BJD-2450000)	A_{Lp}	χ^2_{red}
2.01	0.0108 $^{+0.0013}_{-0.0011}$	0.254 $^{+0.005}_{-0.005}$	0.0769 $^{+0.0004}_{-0.0004}$	83.92 $^{+0.7045}_{-0.5848}$	0.000 $^{+0.000}_{-0.000}$	0.000 $^{+0.000}_{-0.000}$	2.204730 $^{+3.16-06}_{-3.06-06}$	4954.35796 $^{+0.00013}_{-0.00013}$	0.421 $^{+0.07}_{-0.07}$	26.5
5.01	-0.0088 $^{+0.0011}_{-0.0097}$	0.123 $^{+0.010}_{-0.013}$	0.0356 $^{+0.0009}_{-0.0011}$	83.60 $^{+0.7978}_{-0.5911}$	0.000 $^{+0.000}_{-0.000}$	0.000 $^{+0.000}_{-0.000}$	4.780381 $^{+6.76-05}_{-6.76-05}$	4965.97227 $^{+0.00119}_{-0.00121}$	0.300 $^{+0.72}_{-0.35}$	2.69
10.01	0.0014 $^{+0.0033}_{-0.0013}$	0.151 $^{+0.004}_{-0.004}$	0.0938 $^{+0.0007}_{-0.0007}$	84.68 $^{+0.3975}_{-0.5070}$	0.000 $^{+0.000}_{-0.000}$	0.000 $^{+0.000}_{-0.000}$	3.522511 $^{+1.36-05}_{-1.36-05}$	4954.11838 $^{+0.00043}_{-0.00043}$	-5.752 $^{+4.04}_{-4.04}$	4.31
13.01	0.0248 $^{+0.0015}_{-0.0011}$	0.294 $^{+0.005}_{-0.006}$	0.0659 $^{+0.0002}_{-0.0002}$	79.79 $^{+0.4079}_{-0.5070}$	0.000 $^{+0.000}_{-0.000}$	0.000 $^{+0.000}_{-0.000}$	1.763589 $^{+2.36-06}_{-2.36-06}$	4953.56510 $^{+0.00014}_{-0.00014}$	0.339 $^{+0.02}_{-0.02}$	15.9
18.01	0.0000 $^{+0.0000}_{-0.0000}$	0.174 $^{+0.027}_{-0.027}$	0.0783 $^{+0.0025}_{-0.0007}$	87.64 $^{+1.7674}_{-3.6176}$	0.000 $^{+0.000}_{-0.000}$	0.000 $^{+0.000}_{-0.000}$	3.548460 $^{+2.46-05}_{-2.46-05}$	4955.90081 $^{+0.00068}_{-0.00068}$	-78.785 $^{+238.}_{-525.}$	9.33
64.01	0.0207 $^{+0.0104}_{-0.0100}$	0.283 $^{+0.018}_{-0.019}$	0.0425 $^{+0.0018}_{-0.0013}$	75.01 $^{+1.1206}_{-1.0527}$	0.000 $^{+0.000}_{-0.000}$	0.000 $^{+0.000}_{-0.000}$	1.951178 $^{+2.86-05}_{-2.86-05}$	4990.53822 $^{+0.00086}_{-0.00086}$	-0.312 $^{+0.62}_{-0.84}$	10.4
97.01	0.0066 $^{+0.0017}_{-0.0016}$	0.156 $^{+0.003}_{-0.004}$	0.0817 $^{+0.0005}_{-0.0005}$	85.93 $^{+0.4176}_{-0.3637}$	0.000 $^{+0.000}_{-0.000}$	0.000 $^{+0.000}_{-0.000}$	4.885495 $^{+1.76-05}_{-1.76-05}$	4967.27590 $^{+0.00030}_{-0.00031}$	0.115 $^{+0.24}_{-0.23}$	2.24
102.01	0.0140 $^{+0.0089}_{-0.0089}$	0.199 $^{+0.026}_{-0.026}$	0.0284 $^{+0.0008}_{-0.0008}$	84.17 $^{+2.8940}_{-2.3598}$	0.000 $^{+0.000}_{-0.000}$	0.000 $^{+0.000}_{-0.000}$	1.735114 $^{+2.16-05}_{-2.16-05}$	4968.06072 $^{+0.00101}_{-0.00101}$	-0.187 $^{+0.34}_{-0.34}$	2.32
144.01	0.0353 $^{+0.0037}_{-0.0029}$	0.127 $^{+0.026}_{-0.026}$	0.0352 $^{+0.0021}_{-0.0021}$	86.86 $^{+2.5586}_{-2.5586}$	0.000 $^{+0.000}_{-0.000}$	0.000 $^{+0.000}_{-0.000}$	4.176149 $^{+1.56-04}_{-1.56-04}$	4966.09112 $^{+0.00322}_{-0.00322}$	2.019 $^{+5.88}_{-5.88}$	6.92
186.01	-0.0014 $^{+0.0026}_{-0.0024}$	0.126 $^{+0.005}_{-0.003}$	0.1218 $^{+0.0011}_{-0.0008}$	88.51 $^{+1.3964}_{-0.8215}$	0.000 $^{+0.000}_{-0.000}$	0.000 $^{+0.000}_{-0.000}$	3.243268 $^{+1.66-04}_{-1.66-04}$	4966.66796 $^{+0.00037}_{-0.00036}$	0.051 $^{+0.93}_{-1.12}$	3.20
188.01	0.0035 $^{+0.0024}_{-0.0022}$	0.092 $^{+0.004}_{-0.004}$	0.1155 $^{+0.0016}_{-0.0018}$	87.37 $^{+0.4475}_{-0.3527}$	0.000 $^{+0.000}_{-0.000}$	0.000 $^{+0.000}_{-0.000}$	3.797023 $^{+1.26-05}_{-1.26-05}$	4966.50793 $^{+0.00029}_{-0.00028}$	-0.309 $^{+0.43}_{-0.68}$	2.14
195.01	0.0047 $^{+0.0027}_{-0.0030}$	0.107 $^{+0.004}_{-0.004}$	0.1165 $^{+0.0011}_{-0.0013}$	86.42 $^{+0.3423}_{-0.2949}$	0.000 $^{+0.000}_{-0.000}$	0.000 $^{+0.000}_{-0.000}$	3.217522 $^{+1.26-05}_{-1.36-05}$	4966.63096 $^{+0.00033}_{-0.00032}$	-0.132 $^{+0.42}_{-0.56}$	2.38
196.01	0.0060 $^{+0.0019}_{-0.0030}$	0.221 $^{+0.005}_{-0.006}$	0.1022 $^{+0.0007}_{-0.0009}$	82.05 $^{+0.4642}_{-0.6684}$	0.000 $^{+0.000}_{-0.000}$	0.000 $^{+0.000}_{-0.000}$	1.855561 $^{+5.06-06}_{-5.06-06}$	4970.18013 $^{+0.00024}_{-0.00024}$	-0.168 $^{+0.19}_{-0.19}$	2.33
199.01	0.0029 $^{+0.0030}_{-0.0032}$	0.151 $^{+0.007}_{-0.007}$	0.0963 $^{+0.0009}_{-0.0009}$	86.81 $^{+0.9287}_{-0.7643}$	0.000 $^{+0.000}_{-0.000}$	0.000 $^{+0.000}_{-0.000}$	3.268695 $^{+1.76-05}_{-1.66-05}$	4970.48096 $^{+0.00044}_{-0.00044}$	0.079 $^{+0.41}_{-0.41}$	1.40
201.01	-0.0059 $^{+0.0051}_{-0.0051}$	0.093 $^{+0.009}_{-0.005}$	0.0800 $^{+0.0021}_{-0.0021}$	88.31 $^{+1.5163}_{-1.1075}$	0.000 $^{+0.000}_{-0.000}$	0.000 $^{+0.000}_{-0.000}$	4.225373 $^{+2.16-05}_{-2.26-05}$	4970.56037 $^{+0.00039}_{-0.00039}$	1.145 $^{+1.92}_{-0.81}$	3.60
202.01	0.0053 $^{+0.0023}_{-0.0023}$	0.225 $^{+0.004}_{-0.004}$	0.1040 $^{+0.0006}_{-0.0006}$	80.75 $^{+0.2992}_{-0.2744}$	0.000 $^{+0.000}_{-0.000}$	0.000 $^{+0.000}_{-0.000}$	1.720867 $^{+4.46-06}_{-4.76-06}$	4966.02007 $^{+0.00023}_{-0.00023}$	-0.333 $^{+0.22}_{-0.38}$	8.81
204.01	-0.0019 $^{+0.0032}_{-0.0041}$	0.151 $^{+0.012}_{-0.014}$	0.0817 $^{+0.0017}_{-0.0022}$	85.16 $^{+1.4103}_{-0.9589}$	0.000 $^{+0.000}_{-0.000}$	0.000 $^{+0.000}_{-0.000}$	3.246708 $^{+2.46-05}_{-2.66-05}$	4966.37897 $^{+0.00067}_{-0.00064}$	1.579 $^{+6.48}_{-3.05}$	2.08
229.01	0.0000 $^{+0.0004}_{-0.0000}$	0.400 $^{+0.005}_{-0.005}$	0.2872 $^{+0.0027}_{-0.0029}$	67.77 $^{+0.3073}_{-0.8507}$	0.000 $^{+0.000}_{-0.000}$	0.000 $^{+0.000}_{-0.000}$	3.573190 $^{+8.56-05}_{-8.76-05}$	4967.93368 $^{+0.00196}_{-0.00196}$	-2.565 $^{+3.04}_{-3.04}$	1.98
356.01	0.0007 $^{+0.0115}_{-0.0115}$	0.169 $^{+0.025}_{-0.026}$	0.0334 $^{+0.0030}_{-0.0030}$	84.64 $^{+4.5146}_{-4.5146}$	0.000 $^{+0.000}_{-0.000}$	0.000 $^{+0.000}_{-0.000}$	1.827099 $^{+3.26-05}_{-3.26-05}$	5003.52457 $^{+0.00093}_{-0.00093}$	-0.007 $^{+1.10}_{-1.10}$	1.52
412.01	0.0063 $^{+0.0121}_{-0.0121}$	0.100 $^{+0.008}_{-0.008}$	0.0571 $^{+0.0030}_{-0.0030}$	87.79 $^{+2.3886}_{-2.3886}$	0.000 $^{+0.000}_{-0.000}$	0.000 $^{+0.000}_{-0.000}$	4.146994 $^{+5.66-05}_{-5.66-05}$	5003.32536 $^{+0.00073}_{-0.00073}$	-0.487 $^{+1.49}_{-2.00}$	2.64
421.01	-0.0059 $^{+0.0048}_{-0.0042}$	0.076 $^{+0.005}_{-0.005}$	0.1197 $^{+0.0021}_{-0.0024}$	88.00 $^{+0.5723}_{-0.4216}$	0.000 $^{+0.000}_{-0.000}$	0.000 $^{+0.000}_{-0.000}$	4.454225 $^{+2.26-05}_{-2.26-05}$	5005.81890 $^{+0.00028}_{-0.00026}$	0.137 $^{+0.83}_{-0.72}$	4.01
433.01	0.0001 $^{+0.0162}_{-0.0202}$	0.352 $^{+0.055}_{-0.070}$	0.2406 $^{+0.1861}_{-0.1474}$	70.78 $^{+4.5618}_{-3.4365}$	0.000 $^{+0.000}_{-0.000}$	0.000 $^{+0.000}_{-0.000}$	4.030457 $^{+1.56-04}_{-1.46-04}$	5004.09086 $^{+0.00179}_{-0.00180}$	0.033 $^{+0.56}_{-0.10}$	7.51
611.01	-0.0030 $^{+0.0078}_{-0.0075}$	0.126 $^{+0.009}_{-0.006}$	0.0760 $^{+0.0077}_{-0.0022}$	83.75 $^{+0.3507}_{-0.5380}$	0.000 $^{+0.000}_{-0.000}$	0.000 $^{+0.000}_{-0.000}$	3.251646 $^{+2.86-05}_{-2.66-05}$	5004.05985 $^{+0.00180}_{-0.00038}$	-0.039 $^{+0.73}_{-0.74}$	2.12
684.01	0.0802 $^{+0.0048}_{-0.0439}$	0.066 $^{+0.016}_{-0.016}$	0.0269 $^{+0.0031}_{-0.0031}$	87.36 $^{+2.0032}_{-2.0032}$	0.000 $^{+0.000}_{-0.000}$	0.000 $^{+0.000}_{-0.000}$	4.035328 $^{+1.86-04}_{-1.86-04}$	5005.25386 $^{+0.00223}_{-0.00223}$	-0.183 $^{+0.32}_{-0.32}$	2.11
760.01	0.0023 $^{+0.0054}_{-0.0054}$	0.094 $^{+0.003}_{-0.003}$	0.1055 $^{+0.0013}_{-0.0013}$	85.85 $^{+0.1909}_{-0.1787}$	0.000 $^{+0.000}_{-0.000}$	0.000 $^{+0.000}_{-0.000}$	4.959343 $^{+4.46-05}_{-4.46-05}$	5005.25676 $^{+0.00043}_{-0.00043}$	-0.300 $^{+1.14}_{-1.38}$	1.83
801.01	0.0061 $^{+0.0067}_{-0.0059}$	0.221 $^{+0.021}_{-0.023}$	0.0865 $^{+0.0023}_{-0.0025}$	83.93 $^{+3.0796}_{-1.9812}$	0.000 $^{+0.000}_{-0.000}$	0.000 $^{+0.000}_{-0.000}$	1.625498 $^{+1.16-05}_{-1.16-05}$	5003.82699 $^{+0.00035}_{-0.00037}$	-0.722 $^{+0.87}_{-2.05}$	2.81
809.01	-0.0023 $^{+0.0041}_{-0.0048}$	0.163 $^{+0.017}_{-0.017}$	0.1177 $^{+0.0027}_{-0.0011}$	87.56 $^{+2.2216}_{-2.2216}$	0.000 $^{+0.000}_{-0.000}$	0.000 $^{+0.000}_{-0.000}$	1.594742 $^{+7.16-06}_{-7.16-06}$	5003.64754 $^{+0.00024}_{-0.00023}$	0.779 $^{+2.22}_{-2.24}$	3.47
813.01	-0.0166 $^{+0.0094}_{-0.0091}$	0.089 $^{+0.017}_{-0.012}$	0.0897 $^{+0.0042}_{-0.0031}$	87.62 $^{+2.2020}_{-1.5063}$	0.000 $^{+0.000}_{-0.000}$	0.000 $^{+0.000}_{-0.000}$	3.895887 $^{+5.26-05}_{-5.46-05}$	5003.52771 $^{+0.00069}_{-0.00066}$	-0.070 $^{+0.34}_{-0.42}$	1.72

PDC Light Curve With Eccentricity Fixed to Zero

Table 4.2 (continued)

KOI	J	r_{sum}	k	i ($^{\circ}$)	$e \cos w$	$e \sin w$	P (Days)	T_0 (BJD-2450000)	A_{L_p}	χ^2_{red}
830.01	$0.0024^{+0.0031}_{-0.0042}$	$0.099^{+0.006}_{-0.009}$	$0.1370^{+0.0026}_{-0.0035}$	$89.03^{+0.8555}_{-0.6292}$	$0.000^{+0.000}_{-0.000}$	$0.000^{+0.000}_{-0.000}$	$3.525638^{+1.16-05}_{-0.000}$	$5003.04715^{+0.00015}_{-0.00015}$	$-0.775^{+1.88}_{-1.60}$	4.23
838.01	$0.0001^{+0.0028}_{-0.0028}$	$0.1118^{+0.010}_{-0.010}$	$0.1047^{+0.0139}_{-0.0139}$	$84.18^{+0.5842}_{-0.5591}$	$0.000^{+0.000}_{-0.000}$	$0.000^{+0.000}_{-0.000}$	$4.859423^{+8.26-05}_{-0.000}$	$5006.01042^{+0.00082}_{-0.00082}$	$1.279^{+1.00}_{-1.81}$	7.50
840.01	$-0.0045^{+0.0061}_{-0.0061}$	$0.1113^{+0.008}_{-0.008}$	$0.1048^{+0.0024}_{-0.0026}$	$85.44^{+0.5689}_{-0.4960}$	$0.000^{+0.000}_{-0.000}$	$0.000^{+0.000}_{-0.000}$	$3.040348^{+2.26-05}_{-0.000}$	$5002.94813^{+0.00041}_{-0.00041}$	$0.104^{+1.14}_{-1.13}$	4.10
843.01	$-0.0007^{+0.0052}_{-0.0135}$	$0.132^{+0.027}_{-0.032}$	$0.0544^{+0.0028}_{-0.0034}$	$84.60^{+2.7198}_{-1.8763}$	$0.000^{+0.000}_{-0.000}$	$0.000^{+0.000}_{-0.000}$	$4.190630^{+1.16-04}_{-0.000}$	$5004.43891^{+0.00134}_{-0.00137}$	$0.935^{+6.11}_{-2.33}$	1.51
897.01	$0.0032^{+0.0036}_{-0.0032}$	$0.159^{+0.008}_{-0.010}$	$0.1166^{+0.0016}_{-0.0019}$	$85.30^{+0.9264}_{-1.7186}$	$0.000^{+0.000}_{-0.000}$	$0.000^{+0.000}_{-0.000}$	$2.052344^{+8.86-06}_{-0.000}$	$5002.89010^{+0.00022}_{-0.00022}$	$-1.469^{+1.28}_{-4.03}$	2.58
908.01	$0.0050^{+0.0060}_{-0.0052}$	$0.092^{+0.012}_{-0.004}$	$0.0839^{+0.0026}_{-0.0010}$	$88.63^{+1.2397}_{-0.8946}$	$0.000^{+0.000}_{-0.000}$	$0.000^{+0.000}_{-0.000}$	$4.708363^{+4.86-05}_{-0.000}$	$5004.44523^{+0.00048}_{-0.00048}$	$0.200^{+0.78}_{-0.61}$	1.47
913.01	$0.0021^{+0.0027}_{-0.0027}$	$0.105^{+0.002}_{-0.002}$	$0.1240^{+0.0007}_{-0.0007}$	$89.05^{+0.8239}_{-0.8239}$	$0.000^{+0.000}_{-0.000}$	$0.000^{+0.000}_{-0.000}$	$4.082286^{+1.96-05}_{-0.000}$	$5002.63669^{+0.00023}_{-0.00023}$	$0.162^{+1.85}_{-1.85}$	2.82
931.01	$0.0007^{+0.0034}_{-0.0034}$	$0.112^{+0.003}_{-0.003}$	$0.1201^{+0.0024}_{-0.0024}$	$88.67^{+1.0903}_{-1.4164}$	$0.000^{+0.000}_{-0.000}$	$0.000^{+0.000}_{-0.000}$	$3.855646^{+2.26-05}_{-0.000}$	$5003.67760^{+0.00028}_{-0.00028}$	$-2.995^{+6.90}_{-45.3}$	2.63
961.02	$0.0017^{+0.0198}_{-0.0184}$	$0.292^{+0.076}_{-0.072}$	$0.0486^{+0.0108}_{-0.0050}$	$75.39^{+4.6244}_{-4.8234}$	$0.000^{+0.000}_{-0.000}$	$0.000^{+0.000}_{-0.000}$	$0.453296^{+6.36-06}_{-0.000}$	$4966.86709^{+0.00116}_{-0.00116}$	$0.048^{+0.32}_{-0.34}$	1.95
961.03	$0.0159^{+0.0472}_{-0.0397}$	$0.060^{+0.004}_{-0.004}$	$0.4879^{+1.0011}_{-0.4024}$	$86.69^{+0.2489}_{-0.2260}$	$0.000^{+0.000}_{-0.000}$	$0.000^{+0.000}_{-0.000}$	$1.865033^{+5.86-05}_{-0.000}$	$4966.79647^{+0.00259}_{-0.00251}$	$0.000^{+0.000}_{-0.000}$	2.30
1419.01	$0.0131^{+0.0145}_{-0.0130}$	$0.322^{+0.049}_{-0.050}$	$0.0555^{+0.0128}_{-0.0034}$	$73.38^{+3.0786}_{-3.1111}$	$0.000^{+0.000}_{-0.000}$	$0.000^{+0.000}_{-0.000}$	$1.336074^{+2.26-05}_{-0.000}$	$5011.25875^{+0.00087}_{-0.00092}$	$-0.874^{+0.85}_{-2.18}$	1.99
1459.01	$0.0267^{+0.0110}_{-0.0127}$	$0.403^{+0.084}_{-0.061}$	$0.0930^{+0.0366}_{-0.0143}$	$69.77^{+3.0380}_{-3.0380}$	$0.000^{+0.000}_{-0.000}$	$0.000^{+0.000}_{-0.000}$	$0.692024^{+7.26-06}_{-0.000}$	$4966.11024^{+0.00092}_{-0.00092}$	$1.794^{+1.17}_{-0.97}$	9.55

CLM Light Curve With Eccentricity Fixed to Zero

1.01	$-0.0002^{+0.0004}_{-0.0004}$	$0.142^{+0.000}_{-0.000}$	$0.1250^{+0.0002}_{-0.0002}$	$83.90^{+0.0307}_{-0.0291}$	$0.000^{+0.000}_{-0.000}$	$0.000^{+0.000}_{-0.000}$	$2.470614^{+1.36-06}_{-0.000}$	$4955.76254^{+0.00005}_{-0.00005}$	$0.250^{+0.80}_{-0.80}$	1.94
2.01	$0.0113^{+0.0014}_{-0.0014}$	$0.255^{+0.005}_{-0.005}$	$0.0766^{+0.0004}_{-0.0004}$	$83.74^{+0.6427}_{-0.6369}$	$0.000^{+0.000}_{-0.000}$	$0.000^{+0.000}_{-0.000}$	$2.204733^{+3.16-06}_{-0.000}$	$4954.35793^{+0.00013}_{-0.00013}$	$0.240^{+0.06}_{-0.06}$	7.61
5.01	$-0.0021^{+0.0087}_{-0.0087}$	$0.114^{+0.016}_{-0.016}$	$0.0354^{+0.0013}_{-0.0011}$	$84.15^{+0.9388}_{-0.9236}$	$0.000^{+0.000}_{-0.000}$	$0.000^{+0.000}_{-0.000}$	$4.780406^{+7.06-05}_{-0.000}$	$4965.97184^{+0.00120}_{-0.00121}$	$0.238^{+0.94}_{-0.92}$	2.08
10.01	$0.0019^{+0.0032}_{-0.0032}$	$0.159^{+0.005}_{-0.005}$	$0.0929^{+0.0007}_{-0.0007}$	$84.11^{+0.3818}_{-0.3455}$	$0.000^{+0.000}_{-0.000}$	$0.000^{+0.000}_{-0.000}$	$3.522496^{+1.96-05}_{-0.000}$	$4954.11867^{+0.00052}_{-0.00053}$	$-1.296^{+2.76}_{-4.42}$	2.71
13.01	$0.0253^{+0.0012}_{-0.0016}$	$0.287^{+0.005}_{-0.005}$	$0.0656^{+0.0002}_{-0.0003}$	$80.36^{+0.4700}_{-0.4390}$	$0.000^{+0.000}_{-0.000}$	$0.000^{+0.000}_{-0.000}$	$1.763585^{+1.96-06}_{-0.000}$	$4953.56529^{+0.00008}_{-0.00009}$	$0.286^{+0.02}_{-0.01}$	3.89
17.01	$-0.0015^{+0.0015}_{-0.0019}$	$0.165^{+0.005}_{-0.006}$	$0.0955^{+0.0008}_{-0.0009}$	$85.73^{+0.6314}_{-0.5396}$	$0.000^{+0.000}_{-0.000}$	$0.000^{+0.000}_{-0.000}$	$3.234699^{+1.26-05}_{-0.000}$	$4954.48575^{+0.00035}_{-0.00036}$	$1.249^{+3.52}_{-1.93}$	2.65
18.01	$-0.0037^{+0.0040}_{-0.0044}$	$0.173^{+0.016}_{-0.004}$	$0.0771^{+0.0015}_{-0.0005}$	$87.86^{+1.6741}_{-2.5098}$	$0.000^{+0.000}_{-0.000}$	$0.000^{+0.000}_{-0.000}$	$3.548447^{+2.66-05}_{-2.76-05}$	$4955.90128^{+0.00074}_{-0.00072}$	$1.457^{+2.51}_{-3.06}$	3.73
20.01	$0.0003^{+0.0005}_{-0.0005}$	$0.142^{+0.002}_{-0.002}$	$0.1174^{+0.0005}_{-0.0005}$	$88.17^{+0.4041}_{-0.4041}$	$0.000^{+0.000}_{-0.000}$	$0.000^{+0.000}_{-0.000}$	$4.437979^{+1.06-05}_{-0.000}$	$5004.00819^{+0.00011}_{-0.00011}$	$-2.544^{+30.3}_{-30.3}$	1.57
64.01	$0.0312^{+0.0117}_{-0.0112}$	$0.304^{+0.028}_{-0.019}$	$0.0427^{+0.0050}_{-0.0014}$	$73.80^{+1.1307}_{-1.7207}$	$0.000^{+0.000}_{-0.000}$	$0.000^{+0.000}_{-0.000}$	$1.951144^{+3.36-05}_{-3.36-05}$	$4990.53863^{+0.00112}_{-0.00109}$	$-0.120^{+0.39}_{-0.51}$	7.24
97.01	$0.0084^{+0.0022}_{-0.0022}$	$0.154^{+0.004}_{-0.004}$	$0.0808^{+0.0005}_{-0.0006}$	$86.17^{+0.5356}_{-0.4202}$	$0.000^{+0.000}_{-0.000}$	$0.000^{+0.000}_{-0.000}$	$4.885522^{+2.06-05}_{-2.06-05}$	$4967.27550^{+0.00034}_{-0.00034}$	$-0.174^{+0.06}_{-0.09}$	2.06
127.01	$-0.0026^{+0.0031}_{-0.0037}$	$0.117^{+0.008}_{-0.008}$	$0.0982^{+0.0018}_{-0.0018}$	$87.45^{+1.3596}_{-0.9077}$	$0.000^{+0.000}_{-0.000}$	$0.000^{+0.000}_{-0.000}$	$3.578772^{+2.16-05}_{-2.16-05}$	$4967.02976^{+0.00048}_{-0.00048}$	$0.151^{+0.87}_{-0.93}$	3.80
128.01	$-0.0007^{+0.0006}_{-0.0006}$	$0.116^{+0.003}_{-0.003}$	$0.0983^{+0.0007}_{-0.0008}$	$85.73^{+0.2412}_{-0.2261}$	$0.000^{+0.000}_{-0.000}$	$0.000^{+0.000}_{-0.000}$	$4.942764^{+2.26-05}_{-2.26-05}$	$4969.32912^{+0.00043}_{-0.00044}$	$3.129^{+88.2}_{-2.57}$	5.15
144.01	$0.0306^{+0.0303}_{-0.0303}$	$0.127^{+0.011}_{-0.011}$	$0.0290^{+0.0011}_{-0.0011}$	$86.94^{+4.6598}_{-4.6598}$	$0.000^{+0.000}_{-0.000}$	$0.000^{+0.000}_{-0.000}$	$4.176232^{+5.86-04}_{-5.86-04}$	$4966.09100^{+0.00052}_{-0.00052}$	$-0.253^{+0.72}_{-0.72}$	2.32
183.01	$0.0009^{+0.0024}_{-0.0024}$	$0.143^{+0.005}_{-0.005}$	$0.1160^{+0.0011}_{-0.0011}$	$86.89^{+0.7468}_{-0.5931}$	$0.000^{+0.000}_{-0.000}$	$0.000^{+0.000}_{-0.000}$	$2.684312^{+9.36-06}_{-9.36-06}$	$4966.35461^{+0.00030}_{-0.00031}$	$-0.485^{+1.71}_{-2.27}$	3.36
186.01	$-0.0044^{+0.0035}_{-0.0035}$	$0.125^{+0.016}_{-0.016}$	$0.1161^{+0.0032}_{-0.0032}$	$88.53^{+2.1341}_{-2.1877}$	$0.000^{+0.000}_{-0.000}$	$0.000^{+0.000}_{-0.000}$	$3.243284^{+2.06-05}_{-2.06-05}$	$4966.66745^{+0.00052}_{-0.00052}$	$1.022^{+1.42}_{-1.42}$	1.87
188.01	$-0.0034^{+0.0031}_{-0.0032}$	$0.096^{+0.005}_{-0.006}$	$0.1119^{+0.0019}_{-0.0019}$	$87.02^{+0.5816}_{-0.4387}$	$0.000^{+0.000}_{-0.000}$	$0.000^{+0.000}_{-0.000}$	$3.797013^{+1.86-05}_{-1.86-05}$	$4966.50811^{+0.00042}_{-0.00042}$	$0.682^{+1.17}_{-0.34}$	1.69

Table 4.2 (continued)

KOI	J	r_{sum}	k	i ($^{\circ}$)	$e \cos w$	$e \sin w$	P (Days)	T_0 (BJD-2450000)	A_{L_p}	χ^2_{red}
195.01	0.0000 ± 0.0016	0.120 ± 0.004	0.1163 ± 0.0011	85.39 ± 0.2986	0.000 ± 0.000	0.000 ± 0.000	$3.217557 \pm 1.76 \pm 0.05$	4966.63025 ± 0.00043	-2.605 ± 5.29	1.36
196.01	0.0053 ± 0.0026	0.222 ± 0.007	0.0987 ± 0.0021	81.90 ± 0.6662	0.000 ± 0.000	0.000 ± 0.000	$1.855556 \pm 6.76 \pm 0.05$	4970.18029 ± 0.00029	-0.070 ± 0.20	1.21
201.01	-0.0015 ± 0.0030	0.094 ± 0.010	0.0795 ± 0.0022	88.18 ± 1.1858	0.000 ± 0.000	0.000 ± 0.000	$4.225404 \pm 2.86 \pm 0.05$	4970.55976 ± 0.00050	1.572 ± 10.9	1.91
202.01	0.0040 ± 0.0031	0.231 ± 0.006	0.0981 ± 0.0007	80.22 ± 0.3450	0.000 ± 0.000	0.000 ± 0.000	$1.720865 \pm 6.16 \pm 0.06$	4966.02018 ± 0.00032	0.041 ± 0.30	1.47
203.01	-0.0007 ± 0.0029	0.211 ± 0.009	0.1286 ± 0.0014	86.30 ± 1.0981	0.000 ± 0.000	0.000 ± 0.000	$1.485701 \pm 4.46 \pm 0.06$	4965.73927 ± 0.00024	0.648 ± 3.78	19.4
204.01	0.0052 ± 0.0088	0.181 ± 0.019	0.0737 ± 0.0022	82.70 ± 2.0921	0.000 ± 0.000	0.000 ± 0.000	$3.246635 \pm 5.86 \pm 0.05$	4966.38059 ± 0.00156	-0.759 ± 2.15	3.28
214.01	-0.0062 ± 0.0121	0.107 ± 0.016	0.0873 ± 0.0059	84.86 ± 1.5310	0.000 ± 0.000	0.000 ± 0.000	$3.311885 \pm 5.86 \pm 0.05$	4964.74112 ± 0.00138	0.297 ± 0.94	9.26
217.01	-0.0035 ± 0.0048	0.308 ± 0.041	0.9595 ± 0.5014	73.38 ± 1.7996	0.000 ± 0.000	0.000 ± 0.000	$3.905132 \pm 4.76 \pm 0.05$	4966.41317 ± 0.00103	0.001 ± 0.02	14.1
229.01	-0.0001 ± 0.0033	0.118 ± 0.030	0.0481 ± 0.0028	87.30 ± 2.0647	0.000 ± 0.000	0.000 ± 0.000	$3.573283 \pm 9.26 \pm 0.05$	4967.93051 ± 0.00220	0.473 ± 16.3	1.55
254.01	-0.0043 ± 0.0074	0.117 ± 0.008	0.1704 ± 0.0047	86.47 ± 0.8810	0.000 ± 0.000	0.000 ± 0.000	$2.455267 \pm 2.86 \pm 0.05$	5003.82069 ± 0.00067	0.567 ± 1.48	6.44
356.01	0.0492 ± 0.0240	0.144 ± 0.006	0.0306 ± 0.0017	88.06 ± 1.4945	0.000 ± 0.000	0.000 ± 0.000	$1.826966 \pm 5.16 \pm 0.05$	5003.52754 ± 0.00143	-0.024 ± 0.14	2.29
412.01	0.0002 ± 0.0090	0.098 ± 0.008	0.0477 ± 0.0012	87.86 ± 2.8928	0.000 ± 0.000	0.000 ± 0.000	$4.146970 \pm 1.36 \pm 0.04$	5003.32630 ± 0.00176	-8.920 ± 39.9	4.62
421.01	-0.0010 ± 0.0048	0.076 ± 0.006	0.1157 ± 0.0038	87.96 ± 0.5885	0.000 ± 0.000	0.000 ± 0.000	$4.454260 \pm 3.65 \pm 0.05$	5005.81883 ± 0.00041	0.687 ± 3.43	2.07
433.01	0.0001 ± 0.0001	0.094 ± 0.027	0.0471 ± 0.0032	88.25 ± 1.4186	0.000 ± 0.000	0.000 ± 0.000	$4.030278 \pm 1.66 \pm 0.04$	5004.09410 ± 0.00190	-5.396 ± 18.5	1.58
611.01	0.0025 ± 0.0093	0.154 ± 0.024	0.1562 ± 0.1307	81.93 ± 1.8034	0.000 ± 0.000	0.000 ± 0.000	$3.251641 \pm 1.36 \pm 0.05$	5004.06018 ± 0.00191	-0.010 ± 0.13	2.82
667.01	0.0002 ± 0.0247	0.086 ± 0.038	0.0775 ± 0.0089	87.96 ± 1.7162	0.000 ± 0.000	0.000 ± 0.000	$4.305106 \pm 2.46 \pm 0.05$	5003.45531 ± 0.00280	-0.353 ± 6.28	2.33
684.01	0.1004 ± 0.0638	0.049 ± 0.016	0.0250 ± 0.0014	88.99 ± 0.0753	0.000 ± 0.000	0.000 ± 0.000	$4.035349 \pm 2.36 \pm 0.04$	5005.25460 ± 0.00308	0.015 ± 0.04	1.86
760.01	0.0020 ± 0.0069	0.096 ± 0.004	0.1044 ± 0.0017	85.70 ± 0.2168	0.000 ± 0.000	0.000 ± 0.000	$4.959295 \pm 5.66 \pm 0.05$	5005.25690 ± 0.00056	-0.112 ± 0.56	1.41
767.01	0.0052 ± 0.0038	0.141 ± 0.006	0.1224 ± 0.0018	85.95 ± 0.5371	0.000 ± 0.000	0.000 ± 0.000	$2.816536 \pm 1.66 \pm 0.05$	5003.96629 ± 0.00028	-0.163 ± 0.46	1.81
801.01	0.0130 ± 0.0074	0.207 ± 0.038	0.0804 ± 0.0038	85.57 ± 3.9176	0.000 ± 0.000	0.000 ± 0.000	$1.625528 \pm 1.76 \pm 0.05$	5003.82578 ± 0.00053	-0.184 ± 0.47	2.13
809.01	0.0074 ± 0.0052	0.205 ± 0.014	0.1153 ± 0.0024	83.03 ± 1.3933	0.000 ± 0.000	0.000 ± 0.000	$1.594732 \pm 1.16 \pm 0.05$	5003.64783 ± 0.00034	0.028 ± 0.19	1.62
813.01	-0.0113 ± 0.0170	0.081 ± 0.022	0.0810 ± 0.0049	88.56 ± 5.3321	0.000 ± 0.000	0.000 ± 0.000	$3.895873 \pm 9.66 \pm 0.05$	5003.52774 ± 0.00122	0.116 ± 0.23	1.84
830.01	0.0012 ± 0.0023	0.099 ± 0.005	0.1274 ± 0.0021	88.94 ± 0.9826	0.000 ± 0.000	0.000 ± 0.000	$3.525644 \pm 1.36 \pm 0.05$	5003.04701 ± 0.00117	-1.527 ± 8.31	1.37
838.01	-0.0151 ± 0.0116	0.152 ± 0.015	0.1845 ± 0.0840	81.97 ± 1.9229	0.000 ± 0.000	0.000 ± 0.000	$4.859266 \pm 1.26 \pm 0.04$	5006.01125 ± 0.00113	-0.043 ± 0.22	1.78
840.01	-0.0053 ± 0.0074	0.112 ± 0.011	0.0952 ± 0.0031	85.44 ± 1.1176	0.000 ± 0.000	0.000 ± 0.000	$3.040330 \pm 3.16 \pm 0.05$	5002.94851 ± 0.00051	0.179 ± 0.99	2.33
843.01	0.0269 ± 0.0223	0.140 ± 0.045	0.0507 ± 0.0039	84.08 ± 4.3353	0.000 ± 0.000	0.000 ± 0.000	$4.190464 \pm 1.86 \pm 0.05$	5004.44160 ± 0.00207	-0.188 ± 0.18	1.74
897.01	0.0065 ± 0.0054	0.172 ± 0.011	0.1163 ± 0.0021	84.24 ± 0.7194	0.000 ± 0.000	0.000 ± 0.000	$2.052357 \pm 1.96 \pm 0.05$	5002.88992 ± 0.00036	-0.020 ± 0.34	2.27
908.01	0.0176 ± 0.0095	0.093 ± 0.020	0.0794 ± 0.0013	88.35 ± 2.1367	0.000 ± 0.000	0.000 ± 0.000	$4.708360 \pm 8.26 \pm 0.05$	5004.44498 ± 0.00087	-0.167 ± 0.24	1.78
913.01	0.0016 ± 0.0041	0.105 ± 0.007	0.1098 ± 0.0017	88.83 ± 1.1304	0.000 ± 0.000	0.000 ± 0.000	$4.082304 \pm 3.16 \pm 0.05$	5002.63661 ± 0.00039	-0.702 ± 2.07	1.82
1176.01	-0.0016 ± 0.0039	0.138 ± 0.014	0.1268 ± 0.0034	86.29 ± 1.6953	0.000 ± 0.000	0.000 ± 0.000	$1.973750 \pm 9.46 \pm 0.06$	5011.08870 ± 0.00021	0.338 ± 1.19	1.87
1419.01	0.0146 ± 0.0371	0.221 ± 0.103	0.0475 ± 0.0060	80.02 ± 6.7217	0.000 ± 0.000	0.000 ± 0.000	$1.336124 \pm 4.16 \pm 0.05$	5011.25829 ± 0.00175	-0.439 ± 1.95	1.91

Table 4.2 (continued)

KOI	J	r_{sum}	k	i ($^{\circ}$)	$e \cos w$	$e \sin w$	P (Days)	T_0 (BJD-2450000)	A_{Lp}	χ^2_{red}
1459.01	$0.0327^{+0.0157}_{-0.0081}$	$0.243^{+0.056}_{-0.005}$	$0.0637^{+0.0053}_{-0.0003}$	$79.92^{+2.7393}_{-0.5317}$	$0.000^{+0.000}_{-0.000}$	$0.000^{+0.000}_{-0.000}$	$0.692019^{+9.36-06}_{-1.56-05}$	$4966.11081^{+0.00113}_{-0.00056}$	$2.865^{+2.60}_{-0.11}$	3.50
1541.01	$0.0494^{+0.0091}_{-0.0025}$	$0.192^{+0.005}_{-0.014}$	$0.1726^{+0.0017}_{-0.0042}$	$85.74^{+0.4268}_{-1.8368}$	$0.000^{+0.000}_{-0.000}$	$0.000^{+0.000}_{-0.000}$	$2.379290^{+1.66-05}_{-4.66-05}$	$4966.65042^{+0.00055}_{-0.00091}$	$0.143^{+0.15}_{-1.05}$	29.8
1543.01	$0.0266^{+0.0225}_{-0.0236}$	$0.158^{+0.014}_{-0.006}$	$0.1422^{+0.0024}_{-0.0024}$	$87.93^{+1.6934}_{-1.6934}$	$0.000^{+0.000}_{-0.000}$	$0.000^{+0.000}_{-0.000}$	$3.964266^{+4.46-05}_{-4.46-05}$	$4969.02968^{+0.00091}_{-0.00091}$	$-1.080^{+1.05}_{-3.26}$	46.4
PDC Light Curve With Eccentricity Allowed To Vary										
2.01	$0.0106^{+0.0013}_{-0.0011}$	$0.270^{+0.013}_{-0.015}$	$0.0768^{+0.0003}_{-0.0004}$	$83.10^{+0.8755}_{-0.9221}$	$0.001^{+0.002}_{-0.002}$	$0.067^{+0.043}_{-0.034}$	$2.204732^{+3.16-06}_{-3.16-06}$	$4954.35797^{+0.00013}_{-0.00013}$	$0.442^{+0.07}_{-0.07}$	26.5
5.01	$0.0077^{+0.0211}_{-0.0100}$	$0.126^{+0.009}_{-0.009}$	$0.0357^{+0.0008}_{-0.0009}$	$83.38^{+0.7151}_{-0.4133}$	$0.014^{+0.028}_{-0.025}$	$0.009^{+0.040}_{-0.058}$	$4.780380^{+6.76-05}_{-6.76-05}$	$4965.97242^{+0.00127}_{-0.00121}$	$-0.141^{+0.31}_{-0.11}$	2.70
10.01	$0.0032^{+0.0043}_{-0.0027}$	$0.125^{+0.012}_{-0.006}$	$0.0938^{+0.0006}_{-0.0007}$	$86.30^{+0.3346}_{-0.6457}$	$-0.002^{+0.024}_{-0.023}$	$-0.188^{+0.089}_{-0.062}$	$3.522511^{+1.16-05}_{-1.66-05}$	$4954.11837^{+0.00046}_{-0.00046}$	$-2.726^{+1.65}_{-9.39}$	4.31
13.01	$0.0250^{+0.0013}_{-0.0015}$	$0.295^{+0.011}_{-0.015}$	$0.0657^{+0.0002}_{-0.0003}$	$79.74^{+0.8677}_{-1.1544}$	$0.002^{+0.001}_{-0.001}$	$0.020^{+0.049}_{-0.032}$	$1.763589^{+2.36-06}_{-2.36-06}$	$4953.56511^{+0.00013}_{-0.00014}$	$0.341^{+0.02}_{-0.02}$	15.9
18.01	$0.0023^{+0.0022}_{-0.0022}$	$0.171^{+0.041}_{-0.015}$	$0.0782^{+0.0010}_{-0.0006}$	$87.70^{+1.7823}_{-2.5452}$	$-0.018^{+0.121}_{-0.160}$	$-0.055^{+0.197}_{-0.111}$	$3.548460^{+2.46-05}_{-2.46-05}$	$4955.90075^{+0.00088}_{-0.00085}$	$-3.250^{+2.41}_{-30.4}$	9.32
64.01	$0.0134^{+0.0090}_{-0.0017}$	$0.231^{+0.015}_{-0.012}$	$0.0427^{+0.0027}_{-0.0005}$	$80.10^{+0.6878}_{-0.6034}$	$-0.009^{+0.012}_{-0.003}$	$-0.226^{+0.064}_{-0.077}$	$1.951177^{+2.86-05}_{-2.86-05}$	$4990.53809^{+0.00096}_{-0.00090}$	$-0.423^{+0.89}_{-0.23}$	10.4
97.01	$0.0070^{+0.0016}_{-0.0015}$	$0.155^{+0.010}_{-0.018}$	$0.0817^{+0.0005}_{-0.0017}$	$86.02^{+0.7233}_{-0.7794}$	$-0.000^{+0.003}_{-0.009}$	$-0.010^{+0.071}_{-0.071}$	$4.885495^{+1.76-05}_{-1.76-05}$	$4967.27590^{+0.00031}_{-0.00031}$	$0.115^{+0.23}_{-0.22}$	2.24
102.01	$0.0255^{+0.0095}_{-0.0120}$	$0.179^{+0.014}_{-0.014}$	$0.0303^{+0.0014}_{-0.0014}$	$84.56^{+0.9164}_{-1.1387}$	$0.010^{+0.009}_{-0.009}$	$-0.402^{+0.218}_{-0.183}$	$1.735108^{+2.16-05}_{-1.76-04}$	$4968.06104^{+0.00108}_{-0.00105}$	$-0.090^{+0.17}_{-0.21}$	2.32
144.01	$0.0712^{+0.0482}_{-0.0409}$	$0.263^{+0.020}_{-0.037}$	$0.0347^{+0.0006}_{-0.0005}$	$79.28^{+3.8171}_{-1.7668}$	$0.397^{+0.086}_{-0.058}$	$0.652^{+0.084}_{-0.173}$	$4.176174^{+1.76-04}_{-1.76-04}$	$4966.09365^{+0.00376}_{-0.00420}$	$1.016^{+1.47}_{-0.55}$	6.89
186.01	$-0.0031^{+0.0033}_{-0.0030}$	$0.119^{+0.014}_{-0.013}$	$0.1224^{+0.0011}_{-0.0010}$	$88.35^{+0.7668}_{-0.7526}$	$-0.002^{+0.028}_{-0.029}$	$-0.075^{+0.103}_{-0.127}$	$3.243267^{+1.36-05}_{-1.36-05}$	$4966.66801^{+0.00037}_{-0.00036}$	$0.027^{+0.46}_{-0.71}$	3.20
188.01	$0.0051^{+0.0030}_{-0.0033}$	$0.077^{+0.009}_{-0.011}$	$0.1153^{+0.0016}_{-0.0012}$	$88.16^{+0.4271}_{-0.5872}$	$-0.006^{+0.008}_{-0.008}$	$-0.174^{+0.120}_{-0.114}$	$3.797023^{+1.36-05}_{-1.36-05}$	$4966.50793^{+0.00028}_{-0.00028}$	$-0.212^{+0.26}_{-0.26}$	2.14
195.01	$0.0071^{+0.0033}_{-0.0021}$	$0.094^{+0.011}_{-0.015}$	$0.1160^{+0.0013}_{-0.0013}$	$87.22^{+0.6459}_{-0.3374}$	$0.006^{+0.007}_{-0.007}$	$-0.113^{+0.121}_{-0.121}$	$3.217521^{+1.36-05}_{-1.36-05}$	$4966.63098^{+0.00033}_{-0.00033}$	$-0.083^{+0.35}_{-0.35}$	2.38
196.01	$0.0073^{+0.0021}_{-0.0019}$	$0.202^{+0.015}_{-0.023}$	$0.1023^{+0.0007}_{-0.0008}$	$83.35^{+1.3374}_{-1.0172}$	$-0.008^{+0.007}_{-0.007}$	$-0.096^{+0.116}_{-0.116}$	$1.855561^{+5.16-06}_{-5.16-06}$	$4970.18009^{+0.00024}_{-0.00024}$	$-0.129^{+0.16}_{-0.16}$	2.33
199.01	$0.0051^{+0.0032}_{-0.0051}$	$0.141^{+0.017}_{-0.017}$	$0.0963^{+0.0009}_{-0.0009}$	$87.34^{+0.9351}_{-0.9736}$	$0.026^{+0.024}_{-0.023}$	$-0.069^{+0.135}_{-0.135}$	$3.268695^{+1.76-05}_{-1.76-05}$	$4970.48100^{+0.00044}_{-0.00044}$	$0.068^{+0.22}_{-0.23}$	1.40
201.01	$-0.0076^{+0.0061}_{-0.0053}$	$0.090^{+0.015}_{-0.008}$	$0.0796^{+0.0018}_{-0.0018}$	$88.72^{+1.1788}_{-1.2048}$	$-0.007^{+0.009}_{-0.009}$	$-0.010^{+0.131}_{-0.131}$	$4.225373^{+2.16-05}_{-2.16-05}$	$4970.56037^{+0.00040}_{-0.00039}$	$0.966^{+1.47}_{-0.62}$	3.60
202.01	$0.0069^{+0.0023}_{-0.0023}$	$0.198^{+0.009}_{-0.012}$	$0.1038^{+0.0006}_{-0.0006}$	$82.79^{+0.7640}_{-0.6781}$	$-0.017^{+0.006}_{-0.007}$	$-0.125^{+0.051}_{-0.051}$	$1.720867^{+4.46-06}_{-4.46-06}$	$4966.01997^{+0.00024}_{-0.00024}$	$-0.238^{+0.16}_{-0.23}$	8.81
204.01	$-0.0053^{+0.0056}_{-0.0056}$	$0.141^{+0.015}_{-0.015}$	$0.0817^{+0.0021}_{-0.0021}$	$85.87^{+0.7645}_{-2.2049}$	$-0.016^{+0.027}_{-0.027}$	$-0.073^{+0.129}_{-0.129}$	$3.246707^{+2.16-05}_{-2.16-05}$	$4966.37895^{+0.00069}_{-0.00069}$	$1.055^{+0.64}_{-0.64}$	2.08
229.01	$0.0264^{+0.0155}_{-0.0168}$	$0.148^{+0.022}_{-0.018}$	$0.0500^{+0.0014}_{-0.0008}$	$85.95^{+2.5816}_{-2.9385}$	$-0.043^{+0.014}_{-0.013}$	$0.236^{+0.134}_{-0.134}$	$3.573177^{+6.76-05}_{-6.76-05}$	$4967.93350^{+0.00156}_{-0.00154}$	$-0.332^{+0.37}_{-0.80}$	1.93
356.01	$0.0262^{+0.0151}_{-0.0201}$	$0.166^{+0.042}_{-0.014}$	$0.0347^{+0.0003}_{-0.0029}$	$84.62^{+0.9385}_{-1.1961}$	$-0.050^{+0.021}_{-0.026}$	$-0.215^{+0.365}_{-0.310}$	$1.827096^{+3.36-05}_{-3.36-05}$	$5003.52430^{+0.00116}_{-0.00116}$	$-0.029^{+0.18}_{-0.21}$	1.52
412.01	$0.0152^{+0.0151}_{-0.0155}$	$0.082^{+0.018}_{-0.011}$	$0.0566^{+0.0029}_{-0.0008}$	$88.87^{+1.0283}_{-1.2331}$	$0.002^{+0.021}_{-0.019}$	$-0.202^{+0.192}_{-0.203}$	$4.146994^{+5.56-05}_{-5.56-05}$	$5003.32538^{+0.00073}_{-0.00076}$	$-0.373^{+1.70}_{-1.70}$	2.64
421.01	$-0.0087^{+0.0055}_{-0.0044}$	$0.086^{+0.009}_{-0.012}$	$0.1188^{+0.0025}_{-0.0026}$	$87.62^{+0.9498}_{-0.5578}$	$0.005^{+0.016}_{-0.007}$	$0.127^{+0.141}_{-0.141}$	$4.454225^{+2.26-05}_{-2.26-05}$	$5005.81889^{+0.00027}_{-0.00027}$	$0.113^{+0.54}_{-0.45}$	4.01
433.01	$0.0437^{+0.0335}_{-0.0335}$	$0.161^{+0.028}_{-0.028}$	$0.0529^{+0.0015}_{-0.0015}$	$84.46^{+2.2758}_{-2.2758}$	$0.269^{+0.006}_{-0.006}$	$0.412^{+0.170}_{-0.170}$	$4.030406^{+1.16-04}_{-1.16-04}$	$5004.09261^{+0.00148}_{-0.00148}$	$0.287^{+0.43}_{-0.43}$	7.50
611.01	$0.0133^{+0.0068}_{-0.0067}$	$0.108^{+0.007}_{-0.005}$	$0.0758^{+0.0077}_{-0.0021}$	$85.39^{+0.3427}_{-0.4494}$	$-0.021^{+0.005}_{-0.005}$	$-0.157^{+0.066}_{-0.066}$	$3.251646^{+2.46-05}_{-2.46-05}$	$5004.05972^{+0.00041}_{-0.00041}$	$0.081^{+0.25}_{-0.25}$	2.12
684.01	$0.0453^{+0.0314}_{-0.0314}$	$0.131^{+0.013}_{-0.013}$	$0.0351^{+0.0207}_{-0.0207}$	$84.59^{+0.7313}_{-1.0427}$	$0.002^{+0.005}_{-0.006}$	$-0.274^{+0.164}_{-0.164}$	$4.035281^{+2.16-04}_{-2.16-04}$	$5005.25327^{+0.00252}_{-0.00252}$	$-0.157^{+0.24}_{-0.24}$	2.11
760.01	$0.0018^{+0.0085}_{-0.0065}$	$0.090^{+0.006}_{-0.006}$	$0.1055^{+0.0013}_{-0.0013}$	$86.16^{+0.4756}_{-0.4756}$	$0.085^{+0.033}_{-0.033}$	$-0.051^{+0.074}_{-0.074}$	$4.959343^{+4.46-05}_{-4.46-05}$	$5005.25710^{+0.00048}_{-0.00048}$	$-0.183^{+0.69}_{-2.58}$	1.83

Table 4.2 (continued)

KOI	J	r_{sum}	k	i ($^{\circ}$)	ecosw	esinw	P (Days)	T_0 (BJD-2450000)	A_{Lp}	χ^2_{red}
801.01	$0.0121^{+0.0064}_{-0.0062}$	$0.215^{+0.030}_{-0.024}$	$0.0837^{+0.0024}_{-0.0016}$	$87.23^{+2.5490}_{-1.9241}$	$-0.012^{+0.024}_{-0.026}$	$0.079^{+0.123}_{-0.160}$	$1.625498^{+1.1e-05}_{-7.1e-06}$	$5003.82697^{+0.00035}_{-0.00038}$	$-0.474^{+0.37}_{-0.32}$	2.81
809.01	$-0.0142^{+0.0058}_{-0.0058}$	$0.151^{+0.022}_{-0.026}$	$0.1230^{+0.0019}_{-0.0019}$	$86.26^{+1.708}_{-1.4899}$	$-0.113^{+0.010}_{-0.016}$	$-0.269^{+0.140}_{-0.171}$	$1.594742^{+7.5e-06}_{-5.3e-06}$	$5003.64725^{+0.00026}_{-0.00026}$	$0.387^{+0.17}_{-0.17}$	3.46
813.01	$-0.0205^{+0.0106}_{-0.0106}$	$0.101^{+0.026}_{-0.018}$	$0.0876^{+0.0031}_{-0.0011}$	$88.09^{+1.4899}_{-2.8157}$	$-0.006^{+0.016}_{-0.045}$	$0.176^{+0.171}_{-0.201}$	$3.895881^{+5.3e-05}_{-5.3e-05}$	$5003.52771^{+0.00078}_{-0.00082}$	$-0.034^{+0.28}_{-0.36}$	1.72
830.01	$0.0070^{+0.0036}_{-0.0036}$	$0.089^{+0.023}_{-0.012}$	$0.1370^{+0.0016}_{-0.0010}$	$89.20^{+0.6777}_{-0.9649}$	$-0.028^{+0.007}_{-0.013}$	$-0.126^{+0.201}_{-0.138}$	$3.525638^{+1.0e-05}_{-1.1e-05}$	$5003.04714^{+0.00015}_{-0.00017}$	$-0.524^{+0.53}_{-0.93}$	4.22
838.01	$0.0001^{+0.0007}_{-0.0007}$	$0.054^{+0.003}_{-0.004}$	$0.1080^{+0.0433}_{-0.0191}$	$88.37^{+0.1654}_{-0.1793}$	$-0.079^{+0.105}_{-0.096}$	$-0.678^{+0.087}_{-0.069}$	$4.859425^{+8.4e-05}_{-8.7e-05}$	$5006.00988^{+0.00111}_{-0.00115}$	$9.589^{+85.4}_{-54.7}$	7.51
840.01	$-0.0074^{+0.0079}_{-0.0078}$	$0.085^{+0.009}_{-0.009}$	$0.1049^{+0.0023}_{-0.0027}$	$87.34^{+0.4691}_{-0.5066}$	$-0.003^{+0.018}_{-0.018}$	$-0.285^{+0.138}_{-0.174}$	$3.040347^{+2.2e-05}_{-2.3e-05}$	$5002.94812^{+0.00042}_{-0.00043}$	$0.085^{+0.82}_{-0.77}$	4.10
843.01	$-0.0005^{+0.0088}_{-0.0088}$	$0.112^{+0.008}_{-0.008}$	$0.0550^{+0.0036}_{-0.0036}$	$86.21^{+0.5054}_{-0.5054}$	$0.024^{+0.164}_{-0.164}$	$-0.240^{+0.185}_{-0.185}$	$4.190622^{+1.1e-04}_{-1.1e-04}$	$5004.43916^{+0.00170}_{-0.00170}$	$0.970^{+0.83}_{-0.83}$	1.51
897.01	$0.0054^{+0.0037}_{-0.0037}$	$0.126^{+0.017}_{-0.017}$	$0.1154^{+0.0018}_{-0.0020}$	$87.18^{+0.8279}_{-0.7868}$	$0.011^{+0.023}_{-0.023}$	$-0.196^{+0.150}_{-0.150}$	$2.052344^{+8.6e-06}_{-8.6e-06}$	$5002.89012^{+0.00024}_{-0.00024}$	$-0.986^{+0.73}_{-0.73}$	2.58
908.01	$0.0093^{+0.0068}_{-0.0068}$	$0.094^{+0.025}_{-0.025}$	$0.0844^{+0.0021}_{-0.0013}$	$88.28^{+1.2959}_{-1.7425}$	$-0.031^{+0.020}_{-0.051}$	$-0.017^{+0.202}_{-0.172}$	$4.708363^{+4.9e-05}_{-4.9e-05}$	$5004.44518^{+0.00051}_{-0.00056}$	$0.155^{+0.52}_{-0.31}$	1.47
913.01	$0.0047^{+0.0031}_{-0.0031}$	$0.095^{+0.012}_{-0.012}$	$0.1241^{+0.0013}_{-0.0008}$	$89.18^{+0.7440}_{-0.7886}$	$-0.013^{+0.014}_{-0.013}$	$-0.103^{+0.103}_{-0.107}$	$4.082286^{+2.0e-05}_{-1.9e-05}$	$5002.63669^{+0.00023}_{-0.00022}$	$0.131^{+0.92}_{-0.92}$	2.82
931.01	$0.0027^{+0.0049}_{-0.0049}$	$0.111^{+0.020}_{-0.020}$	$0.1200^{+0.0013}_{-0.0008}$	$88.76^{+1.3306}_{-1.3306}$	$-0.027^{+0.035}_{-0.076}$	$-0.025^{+0.138}_{-0.097}$	$3.855646^{+2.3e-05}_{-2.3e-05}$	$5003.67756^{+0.00031}_{-0.00035}$	$-1.988^{+1.40}_{-8.15}$	2.63
961.02	$0.0026^{+0.0024}_{-0.0024}$	$0.298^{+0.028}_{-0.028}$	$0.0487^{+0.0046}_{-0.0046}$	$74.29^{+1.1549}_{-1.1549}$	$-0.034^{+0.157}_{-0.157}$	$0.036^{+0.139}_{-0.139}$	$0.453296^{+6.2e-06}_{-6.2e-06}$	$4966.86703^{+0.00144}_{-0.00144}$	$0.007^{+0.21}_{-0.21}$	1.95
961.03	$0.0000^{+0.0015}_{-0.0015}$	$0.061^{+0.005}_{-0.005}$	$0.1002^{+0.2972}_{-0.0580}$	$86.58^{+0.2826}_{-1.6218}$	$-0.085^{+0.583}_{-0.384}$	$-0.017^{+0.039}_{-0.217}$	$1.865069^{+6.2e-05}_{-6.2e-05}$	$4966.79490^{+0.00309}_{-0.00294}$	$-0.010^{+2.92}_{-5.75}$	2.30
1419.01	$0.0249^{+0.0172}_{-0.0150}$	$0.279^{+0.024}_{-0.024}$	$0.0558^{+0.0032}_{-0.0032}$	$77.67^{+1.2237}_{-1.0487}$	$-0.059^{+0.014}_{-0.015}$	$-0.169^{+0.089}_{-0.125}$	$1.336077^{+2.6e-05}_{-2.7e-05}$	$5011.25756^{+0.00102}_{-0.00101}$	$-0.556^{+0.24}_{-0.50}$	1.99
1459.01	$0.0181^{+0.0167}_{-0.0163}$	$0.368^{+0.021}_{-0.026}$	$0.1166^{+0.0424}_{-0.0340}$	$74.20^{+1.9911}_{-1.3131}$	$0.082^{+0.012}_{-0.013}$	$-0.177^{+0.071}_{-0.082}$	$0.692025^{+7.9e-06}_{-7.4e-06}$	$4966.11150^{+0.00100}_{-0.00105}$	$1.872^{+1.08}_{-0.77}$	9.54

CLM Light Curve With Eccentricity Allowed To Vary

1.01	$-0.0004^{+0.0007}_{-0.0004}$	$0.131^{+0.002}_{-0.002}$	$0.1250^{+0.0002}_{-0.0002}$	$84.83^{+0.1677}_{-0.1817}$	$-0.010^{+0.033}_{-0.031}$	$-0.087^{+0.019}_{-0.018}$	$2.470614^{+1.3e-06}_{-1.3e-06}$	$4955.76250^{+0.00015}_{-0.00015}$	$0.210^{+0.46}_{-0.46}$	1.94
2.01	$0.0112^{+0.0014}_{-0.0013}$	$0.264^{+0.009}_{-0.008}$	$0.0765^{+0.0003}_{-0.0003}$	$83.35^{+0.7450}_{-0.7427}$	$-0.001^{+0.002}_{-0.002}$	$0.038^{+0.026}_{-0.026}$	$2.204733^{+3.1e-06}_{-3.0e-06}$	$4954.35792^{+0.00013}_{-0.00014}$	$0.249^{+0.06}_{-0.04}$	7.61
5.01	$-0.0000^{+0.0080}_{-0.0111}$	$0.136^{+0.007}_{-0.007}$	$0.0371^{+0.0009}_{-0.0009}$	$82.79^{+0.5165}_{-0.5651}$	$-0.015^{+0.099}_{-0.100}$	$-0.003^{+0.045}_{-0.046}$	$4.780376^{+7.1e-05}_{-7.1e-05}$	$4965.97212^{+0.00183}_{-0.00180}$	$0.021^{+3.54}_{-2.02}$	2.08
10.01	$0.0043^{+0.0042}_{-0.0039}$	$0.126^{+0.010}_{-0.008}$	$0.0929^{+0.0007}_{-0.0007}$	$86.21^{+0.4192}_{-0.5845}$	$0.012^{+0.021}_{-0.019}$	$-0.231^{+0.083}_{-0.071}$	$3.522496^{+1.9e-05}_{-1.9e-05}$	$4954.11873^{+0.00056}_{-0.00054}$	$-0.844^{+0.51}_{-2.55}$	2.71
13.01	$0.0255^{+0.0015}_{-0.0015}$	$0.309^{+0.010}_{-0.010}$	$0.0653^{+0.0003}_{-0.0003}$	$78.85^{+0.6362}_{-0.6362}$	$0.002^{+0.001}_{-0.001}$	$0.098^{+0.042}_{-0.042}$	$1.763585^{+1.2e-06}_{-1.2e-06}$	$4953.56529^{+0.00009}_{-0.00009}$	$0.292^{+0.01}_{-0.01}$	3.88
17.01	$-0.0038^{+0.0029}_{-0.0025}$	$0.147^{+0.015}_{-0.015}$	$0.0941^{+0.0009}_{-0.0009}$	$87.29^{+2.4895}_{-0.8624}$	$0.020^{+0.019}_{-0.019}$	$-0.058^{+0.102}_{-0.107}$	$3.234699^{+1.3e-05}_{-1.3e-05}$	$4954.48579^{+0.00034}_{-0.00037}$	$0.772^{+1.30}_{-1.30}$	2.65
18.01	$-0.0037^{+0.0046}_{-0.0046}$	$0.177^{+0.042}_{-0.023}$	$0.0771^{+0.0011}_{-0.0006}$	$87.71^{+1.7534}_{-2.8686}$	$0.014^{+0.096}_{-0.153}$	$-0.032^{+0.209}_{-0.153}$	$3.548447^{+2.7e-05}_{-2.8e-05}$	$4955.90133^{+0.00094}_{-0.00086}$	$1.118^{+4.16}_{-2.53}$	3.73
20.01	$0.0007^{+0.0016}_{-0.0016}$	$0.132^{+0.007}_{-0.007}$	$0.1172^{+0.0005}_{-0.0005}$	$88.63^{+0.5590}_{-0.4472}$	$0.007^{+0.039}_{-0.037}$	$-0.068^{+0.054}_{-0.050}$	$4.437979^{+1.1e-05}_{-1.0e-05}$	$5004.00820^{+0.00011}_{-0.00012}$	$-1.722^{+2.52}_{-6.72}$	1.57
64.01	$0.0196^{+0.0104}_{-0.0110}$	$0.268^{+0.020}_{-0.015}$	$0.0428^{+0.0067}_{-0.0016}$	$77.66^{+0.8119}_{-1.1367}$	$0.007^{+0.009}_{-0.010}$	$-0.151^{+0.060}_{-0.064}$	$1.951148^{+3.3e-05}_{-3.6e-05}$	$4990.53869^{+0.00018}_{-0.00012}$	$-0.188^{+0.63}_{-0.78}$	7.25
97.01	$0.0088^{+0.0021}_{-0.0021}$	$0.167^{+0.012}_{-0.012}$	$0.0807^{+0.0006}_{-0.0006}$	$85.55^{+1.0233}_{-1.0233}$	$-0.005^{+0.004}_{-0.004}$	$0.084^{+0.073}_{-0.073}$	$4.885521^{+2.0e-05}_{-2.0e-05}$	$4967.27548^{+0.00034}_{-0.00034}$	$-0.156^{+0.08}_{-0.08}$	2.05
127.01	$-0.0092^{+0.0033}_{-0.0033}$	$0.156^{+0.015}_{-0.012}$	$0.0966^{+0.0008}_{-0.0008}$	$87.18^{+1.7298}_{-0.9968}$	$0.041^{+0.007}_{-0.007}$	$0.341^{+0.073}_{-0.073}$	$3.578773^{+2.1e-05}_{-2.1e-05}$	$4967.02976^{+0.00047}_{-0.00047}$	$0.154^{+0.20}_{-0.28}$	3.79
128.01	$-0.0001^{+0.0000}_{-0.0000}$	$0.086^{+0.002}_{-0.002}$	$0.0984^{+0.0008}_{-0.0008}$	$87.50^{+0.1243}_{-0.1243}$	$0.071^{+0.152}_{-0.187}$	$-0.311^{+0.042}_{-0.042}$	$4.942765^{+2.7e-05}_{-2.6e-05}$	$4969.32936^{+0.00078}_{-0.00082}$	$49.513^{+86.1}_{-49.6}$	5.15
144.01	$0.0880^{+0.0351}_{-0.0314}$	$0.133^{+0.022}_{-0.016}$	$0.0305^{+0.0033}_{-0.0017}$	$85.83^{+1.3423}_{-1.2473}$	$0.035^{+0.006}_{-0.006}$	$-0.155^{+0.209}_{-0.265}$	$4.176281^{+2.5e-04}_{-2.4e-04}$	$4966.09046^{+0.00506}_{-0.00535}$	$-0.090^{+0.11}_{-0.11}$	2.31

Table 4.2 (continued)

KOI	J	r_{sum}	k	i ($^{\circ}$)	$e \cos \omega$	$e \sin \omega$	P (Days)	T_0 (BJD-2450000)	A_{Lp}	χ^2_{red}
183.01	0.0069 ^{+0.0026} _{-0.0023}	0.148 ^{+0.020} _{-0.021}	0.1159 ^{+0.0011} _{-0.0012}	86.78 ^{+1.0868} _{-1.1552}	-0.152 ^{+0.009} _{-0.017}	0.030 ^{+0.124} _{-0.184}	2.684313 ^{+9.76-06} _{-2.76-05}	4966.35439 ^{+0.00031} _{-0.00052}	-0.203 ^{+0.10} _{-0.16}	3.35
186.01	-0.0066 ^{+0.0043} _{-0.0043}	0.122 ^{+0.021} _{-0.021}	0.1161 ^{+0.0007} _{-0.0007}	88.66 ^{+1.4415} _{-1.4415}	-0.005 ^{+0.019} _{-0.019}	-0.035 ^{+0.123} _{-0.123}	3.243285 ^{+2.08-05} _{-2.08-05}	4966.66741 ^{+0.00055} _{-0.00042}	0.780 ^{+0.32} _{-0.32}	1.86
188.01	-0.0003 ^{+0.0009} _{-0.0009}	0.075 ^{+0.005} _{-0.004}	0.1080 ^{+0.0024} _{-0.0022}	88.52 ^{+0.3824} _{-0.3824}	0.103 ^{+0.094} _{-0.093}	-0.147 ^{+0.092} _{-0.098}	3.797011 ^{+1.86-05} _{-1.86-05}	4966.50823 ^{+0.00043} _{-0.00044}	0.957 ^{+9.93} _{-5.83}	1.69
195.01	0.0081 ^{+0.0047} _{-0.0047}	0.081 ^{+0.010} _{-0.010}	0.1163 ^{+0.0012} _{-0.0012}	87.75 ^{+0.4441} _{-0.4550}	0.018 ^{+0.007} _{-0.007}	-0.379 ^{+0.108} _{-0.114}	3.217557 ^{+1.76-05} _{-1.76-05}	4966.63031 ^{+0.00044} _{-0.00045}	-0.242 ^{+0.12} _{-0.29}	1.36
196.01	0.0066 ^{+0.0032} _{-0.0029}	0.180 ^{+0.019} _{-0.019}	0.0988 ^{+0.0011} _{-0.0011}	84.60 ^{+0.9580} _{-1.0762}	0.002 ^{+0.011} _{-0.011}	-0.217 ^{+0.109} _{-0.103}	1.855556 ^{+6.66-06} _{-6.66-06}	4970.18030 ^{+0.00030} _{-0.00030}	-0.055 ^{+0.10} _{-0.15}	1.21
201.01	-0.0034 ^{+0.0034} _{-0.0039}	0.098 ^{+0.013} _{-0.008}	0.0789 ^{+0.0022} _{-0.0025}	88.49 ^{+1.2420} _{-1.4310}	0.031 ^{+0.043} _{-0.033}	0.056 ^{+0.099} _{-0.137}	4.225405 ^{+2.86-05} _{-2.76-05}	4970.55978 ^{+0.00052} _{-0.00035}	1.104 ^{+5.04} _{-5.04}	1.91
202.01	0.0053 ^{+0.0028} _{-0.0028}	0.209 ^{+0.010} _{-0.010}	0.0981 ^{+0.0007} _{-0.0007}	82.02 ^{+0.4738} _{-0.4738}	-0.011 ^{+0.015} _{-0.015}	-0.105 ^{+0.054} _{-0.054}	1.720865 ^{+6.36-06} _{-6.36-06}	4966.02012 ^{+0.00035} _{-0.00035}	0.043 ^{+0.16} _{-0.16}	1.47
203.01	0.0046 ^{+0.0046} _{-0.0046}	0.180 ^{+0.022} _{-0.022}	0.1287 ^{+0.0013} _{-0.0013}	87.23 ^{+1.1967} _{-1.2664}	0.093 ^{+0.031} _{-0.030}	-0.169 ^{+0.138} _{-0.138}	1.485701 ^{+4.426-06} _{-4.426-06}	4965.79338 ^{+0.00025} _{-0.00027}	-0.301 ^{+0.67} _{-1.14}	19.4
204.01	0.0182 ^{+0.0132} _{-0.0157}	0.118 ^{+0.018} _{-0.018}	0.0693 ^{+0.0036} _{-0.0026}	87.19 ^{+1.4075} _{-1.0848}	-0.031 ^{+0.016} _{-0.018}	-0.224 ^{+0.186} _{-0.197}	3.246636 ^{+5.46-05} _{-5.46-05}	4966.38047 ^{+0.00153} _{-0.00150}	-0.428 ^{+0.25} _{-1.01}	3.28
214.01	-0.0233 ^{+0.0192} _{-0.01543}	0.109 ^{+0.008} _{-0.008}	0.0884 ^{+0.0325} _{-0.0057}	84.68 ^{+0.6625} _{-0.6625}	-0.019 ^{+0.008} _{-0.009}	0.015 ^{+0.063} _{-0.113}	3.311884 ^{+5.16-05} _{-5.36-05}	4964.74106 ^{+0.00139} _{-0.00141}	0.183 ^{+0.65} _{-0.18}	9.26
217.01	0.0190 ^{+0.0072} _{-0.0072}	0.102 ^{+0.016} _{-0.012}	0.1081 ^{+0.0031} _{-0.0031}	88.63 ^{+1.2886} _{-1.6538}	0.082 ^{+0.006} _{-0.007}	0.032 ^{+0.121} _{-0.140}	3.905094 ^{+3.76-05} _{-3.76-05}	4966.41399 ^{+0.00079} _{-0.00082}	0.114 ^{+0.35} _{-0.31}	13.8
229.01	0.0030 ^{+0.0168} _{-0.0168}	0.133 ^{+0.023} _{-0.023}	0.0479 ^{+0.0009} _{-0.0009}	86.91 ^{+2.0021} _{-0.9887}	0.020 ^{+0.087} _{-0.087}	0.090 ^{+0.292} _{-0.292}	3.573280 ^{+9.56-05} _{-9.56-05}	4967.93062 ^{+0.00228} _{-0.00228}	-0.248 ^{+3.54} _{-3.54}	1.55
254.01	0.0349 ^{+0.0146} _{-0.0146}	0.069 ^{+0.017} _{-0.013}	0.1713 ^{+0.0045} _{-0.0052}	88.62 ^{+0.3976} _{-2.3117}	0.052 ^{+0.006} _{-0.006}	-0.496 ^{+0.135} _{-0.135}	2.455264 ^{+2.96-05} _{-2.96-05}	5003.82083 ^{+0.00065} _{-0.00069}	-0.126 ^{+0.06} _{-0.06}	6.42
356.01	0.0701 ^{+0.0349} _{-0.0312}	0.139 ^{+0.041} _{-0.026}	0.0310 ^{+0.0030} _{-0.0009}	86.93 ^{+2.7558} _{-2.7558}	-0.003 ^{+0.011} _{-0.010}	-0.174 ^{+0.247} _{-0.247}	1.826970 ^{+5.36-05} _{-5.36-05}	5003.52752 ^{+0.00150} _{-0.00159}	-0.005 ^{+0.11} _{-0.11}	2.29
412.01	-0.0002 ^{+0.0005} _{-0.0005}	0.119 ^{+0.038} _{-0.014}	0.0477 ^{+0.0036} _{-0.0011}	86.47 ^{+2.7070} _{-2.7070}	0.013 ^{+0.512} _{-0.512}	0.026 ^{+0.242} _{-0.321}	4.146984 ^{+1.46-04} _{-1.46-04}	5003.32622 ^{+0.00295} _{-0.00288}	8.721 ^{+51.4} _{-33.8}	4.62
421.01	0.0003 ^{+0.0009} _{-0.0009}	0.063 ^{+0.006} _{-0.004}	0.1134 ^{+0.0031} _{-0.0023}	88.83 ^{+0.6649} _{-0.4695}	0.011 ^{+0.117} _{-0.119}	-0.118 ^{+0.098} _{-0.125}	4.454248 ^{+3.56-05} _{-3.46-05}	5005.81896 ^{+0.00042} _{-0.00042}	-1.164 ^{+7.39} _{-11.3}	2.07
433.01	-0.0002 ^{+0.0028} _{-0.0028}	0.086 ^{+0.013} _{-0.013}	0.0541 ^{+0.0058} _{-0.0058}	87.30 ^{+0.6881} _{-0.6881}	-0.231 ^{+0.110} _{-0.110}	-0.610 ^{+0.372} _{-0.372}	4.030290 ^{+1.96-04} _{-1.96-04}	5004.09156 ^{+0.00284} _{-0.00284}	0.135 ^{+8.29} _{-8.29}	1.58
611.01	-0.0018 ^{+0.0015} _{-0.0015}	0.109 ^{+0.005} _{-0.005}	0.1796 ^{+0.0130} _{-0.0130}	85.78 ^{+0.3952} _{-0.3952}	0.059 ^{+0.011} _{-0.011}	-0.371 ^{+0.107} _{-0.107}	3.251642 ^{+3.96-05} _{-3.96-05}	5004.06072 ^{+0.00061} _{-0.00063}	0.124 ^{+0.23} _{-0.23}	2.82
667.01	0.0003 ^{+0.0146} _{-0.0049}	0.099 ^{+0.020} _{-0.020}	0.0766 ^{+0.0081} _{-0.0026}	87.68 ^{+1.7035} _{-2.8017}	-0.256 ^{+0.282} _{-0.236}	0.029 ^{+0.360} _{-0.412}	4.305101 ^{+2.66-04} _{-2.66-04}	5003.45495 ^{+0.00322} _{-0.00353}	-0.137 ^{+7.53} _{-10.0}	2.33
684.01	0.0388 ^{+0.0504} _{-0.0729}	0.080 ^{+0.013} _{-0.011}	0.0307 ^{+0.0057} _{-0.0042}	87.08 ^{+0.5216} _{-0.7949}	0.040 ^{+0.029} _{-0.026}	-0.378 ^{+0.385} _{-0.236}	4.035404 ^{+2.66-04} _{-2.66-04}	5005.25403 ^{+0.00337} _{-0.00337}	0.017 ^{+0.06} _{-0.06}	1.87
760.01	0.0001 ^{+0.0092} _{-0.0079}	0.091 ^{+0.005} _{-0.005}	0.1048 ^{+0.0018} _{-0.0017}	86.18 ^{+0.3778} _{-0.4901}	0.002 ^{+0.137} _{-0.136}	-0.085 ^{+0.074} _{-0.062}	4.959296 ^{+5.76-05} _{-5.76-05}	5005.25691 ^{+0.00084} _{-0.00084}	-0.044 ^{+1.51} _{-3.02}	1.41
767.01	0.0111 ^{+0.0044} _{-0.0044}	0.122 ^{+0.019} _{-0.021}	0.1224 ^{+0.0016} _{-0.0016}	86.95 ^{+0.7804} _{-1.7431}	0.012 ^{+0.006} _{-0.006}	-0.146 ^{+0.145} _{-0.145}	2.816536 ^{+1.56-05} _{-1.56-05}	5003.96631 ^{+0.00028} _{-0.00028}	-0.075 ^{+0.10} _{-0.14}	1.81
801.01	0.0221 ^{+0.0117} _{-0.0117}	0.153 ^{+0.022} _{-0.022}	0.0798 ^{+0.0039} _{-0.0039}	88.08 ^{+1.7431} _{-2.0569}	-0.004 ^{+0.012} _{-0.012}	-0.289 ^{+0.179} _{-0.179}	1.625529 ^{+1.76-05} _{-1.76-05}	5003.82575 ^{+0.00053} _{-0.00053}	-0.114 ^{+0.21} _{-0.21}	2.13
809.01	0.0168 ^{+0.0064} _{-0.0057}	0.177 ^{+0.028} _{-0.029}	0.1150 ^{+0.0021} _{-0.0026}	84.88 ^{+1.5312} _{-1.6161}	-0.022 ^{+0.009} _{-0.009}	-0.138 ^{+0.152} _{-0.168}	1.594732 ^{+1.06-05} _{-1.06-05}	5003.64776 ^{+0.00034} _{-0.00035}	0.046 ^{+0.08} _{-0.09}	1.62
813.01	-0.0612 ^{+0.0264} _{-0.0308}	0.060 ^{+0.014} _{-0.012}	0.0813 ^{+0.0063} _{-0.0018}	89.17 ^{+0.7397} _{-0.9617}	-0.090 ^{+0.011} _{-0.008}	-0.381 ^{+0.201} _{-0.202}	3.895869 ^{+9.56-05} _{-9.46-05}	5003.52768 ^{+0.00125} _{-0.00123}	0.050 ^{+0.04} _{-0.03}	1.84
830.01	-0.0000 ^{+0.0000} _{-0.0000}	0.095 ^{+0.005} _{-0.002}	0.1288 ^{+0.0019} _{-0.0019}	88.41 ^{+0.7408} _{-0.4725}	0.007 ^{+0.314} _{-0.340}	-0.106 ^{+0.038} _{-0.070}	3.525646 ^{+1.46-05} _{-1.46-05}	5003.04760 ^{+0.00026} _{-0.00028}	50.838 ^{+101.} _{-123.}	1.38
838.01	0.0003 ^{+0.0053} _{-0.0053}	0.087 ^{+0.004} _{-0.004}	0.1254 ^{+0.0055} _{-0.0055}	86.89 ^{+0.2659} _{-0.2659}	-0.022 ^{+0.053} _{-0.053}	-0.449 ^{+0.124} _{-0.124}	4.859269 ^{+1.26-04} _{-1.26-04}	5006.01102 ^{+0.00127} _{-0.00127}	0.199 ^{+5.84} _{-5.84}	1.78
840.01	0.0044 ^{+0.0112} _{-0.0112}	0.089 ^{+0.009} _{-0.009}	0.0959 ^{+0.0039} _{-0.0039}	87.10 ^{+0.4985} _{-0.4985}	0.084 ^{+0.037} _{-0.037}	-0.262 ^{+0.119} _{-0.119}	3.040329 ^{+3.76-05} _{-3.76-05}	5002.94877 ^{+0.00054} _{-0.00054}	-0.069 ^{+1.31} _{-1.31}	2.33
843.01	0.0686 ^{+0.0495} _{-0.0253}	0.148 ^{+0.025} _{-0.025}	0.0507 ^{+0.0037} _{-0.0037}	83.64 ^{+1.0836} _{-1.7704}	0.060 ^{+0.006} _{-0.006}	0.065 ^{+0.157} _{-0.157}	4.190477 ^{+1.76-04} _{-1.76-04}	5004.44189 ^{+0.00209} _{-0.00221}	-0.056 ^{+0.05} _{-0.09}	1.74
897.01	0.0132 ^{+0.0076} _{-0.0076}	0.122 ^{+0.017} _{-0.017}	0.1162 ^{+0.0021} _{-0.0025}	86.96 ^{+0.7474} _{-0.7906}	-0.001 ^{+0.011} _{-0.010}	-0.326 ^{+0.155} _{-0.136}	2.052357 ^{+1.56-05} _{-1.46-05}	5002.88992 ^{+0.00036} _{-0.00039}	-0.006 ^{+0.18} _{-0.18}	2.27
908.01	0.0214 ^{+0.0115} _{-0.0115}	0.098 ^{+0.028} _{-0.017}	0.0794 ^{+0.0031} _{-0.0014}	88.24 ^{+1.3406} _{-2.2814}	-0.000 ^{+0.016} _{-0.014}	0.011 ^{+0.198} _{-0.228}	4.708359 ^{+8.26-05} _{-8.26-05}	5004.44499 ^{+0.00092} _{-0.00092}	-0.114 ^{+0.09} _{-0.18}	1.78

Table 4.2 (continued)

KOI	J	r_{sum}	k	i ($^{\circ}$)	$e \cos w$	$e \sin w$	P (Days)	T_0 (BJD-2450000)	A_{Lp}	χ^2_{red}
913.01	$0.0021^{+0.0058}_{-0.0025}$	$0.103^{+0.013}_{-0.011}$	$0.1112^{+0.0016}_{-0.0028}$	$88.15^{+0.9795}_{-0.5149}$	$-0.017^{+0.040}_{-0.121}$	$-0.069^{+0.124}_{-0.136}$	$4.082302^{+3.16E-05}_{-3.76E-06}$	$5002.63659^{+0.00041}_{-0.00039}$	$-0.604^{+1.27}_{-1.93}$	1.82
1176.01	$0.0002^{+0.0047}_{-0.0047}$	$0.1119^{+0.009}_{-0.009}$	$0.1300^{+0.0033}_{-0.0020}$	$86.97^{+0.5087}_{-0.5639}$	$0.056^{+0.126}_{-0.826}$	$-0.234^{+0.102}_{-0.214}$	$1.973750^{+9.8E-06}_{-9.8E-06}$	$5011.68879^{+0.00030}_{-0.00030}$	$-0.088^{+3.98}_{-1.81}$	1.87
1419.01	$0.0225^{+0.0451}_{-0.0184}$	$0.256^{+0.146}_{-0.037}$	$0.0434^{+0.0020}_{-0.0015}$	$76.88^{+7.5639}_{-27.934}$	$-0.285^{+0.468}_{-0.014}$	$0.390^{+0.214}_{-0.299}$	$1.336130^{+5.8E-05}_{-5.8E-05}$	$5011.25785^{+0.00480}_{-0.00363}$	$-1.040^{+0.97}_{-1.13}$	1.91
1459.01	$0.0498^{+0.0771}_{-0.0366}$	$0.400^{+0.021}_{-0.025}$	$0.0917^{+0.0365}_{-0.0152}$	$69.02^{+2.2429}_{-0.8466}$	$0.004^{+0.014}_{-0.014}$	$0.027^{+0.023}_{-0.096}$	$0.692022^{+9.3E-06}_{-9.4E-06}$	$4966.11051^{+0.00117}_{-0.00119}$	$0.972^{+1.13}_{-0.58}$	3.50
1541.01	$0.0595^{+0.0121}_{-0.0113}$	$0.390^{+0.004}_{-0.005}$	$0.1693^{+0.0008}_{-0.0021}$	$82.85^{+0.6984}_{-0.6713}$	$-0.012^{+0.012}_{-0.008}$	$0.775^{+0.018}_{-0.017}$	$2.379293^{+1.6E-05}_{-1.6E-05}$	$4966.65019^{+0.00052}_{-0.00058}$	$0.485^{+0.13}_{-0.14}$	28.7
1543.01	$0.1226^{+0.0745}_{-0.0324}$	$0.369^{+0.008}_{-0.004}$	$0.1426^{+0.0021}_{-0.0014}$	$86.08^{+3.0058}_{-22.298}$	$0.114^{+0.010}_{-0.011}$	$0.797^{+0.010}_{-0.007}$	$3.964230^{+8.16E-05}_{-7.46E-05}$	$4969.03213^{+0.00187}_{-0.00315}$	$-0.065^{+0.19}_{-0.20}$	38.4

three detections of negative J at the $1-2\sigma$ level, but none at higher significance. In the CLM light curves, we find four detections of negative J at the $1-2\sigma$ level, but none at higher significance. In the case of allowing eccentricity to vary, for the PDC light curves, we find four detections of negative J at the $1-2\sigma$ level, and one detection at the $2-3\sigma$ level, but none at higher significance. In the CLM light curves we find four detections of negative J at the $1-2\sigma$ level, one detection at the $2-3\sigma$ level, and one detection at the $>3\sigma$ level. Since there is no known physical mechanism to increase the flux of the system when the planet passes behind the host star, these detections are obviously spurious. Since there is no bias towards or preference for positive or negative J values in the modeling code, and assuming that the *Kepler* data does not suffer from systematics that preferentially result in either decrements or increments in flux that span expected secondary eclipse durations, statistically speaking we must have as many false detections of positive J values, or secondary eclipses, for as many detections of negative J values we have, per each confidence interval. Thus, when fixing eccentricity to zero, for PDC light curves, we estimate our false alarm probabilities as 33% for $1-2\sigma$ detections, and 0% for $>2\sigma$ detections. For CLM light curves, we estimate a 36% false alarm probability for $1-2\sigma$ detections, and 0% for $>2\sigma$ detections. When allowing eccentricity to vary, for PDC light curves we estimate false alarm probabilities of 22% for $1-2\sigma$ detections, 33% for $2-3\sigma$ detections, and 0% for $>3\sigma$ detections. For the CLM light curves, we estimate a 40% false alarm probability for $1-2\sigma$ detections, 10% for $2-3\sigma$ detections, and 20% for $>3\sigma$ detections. Although we are dealing with small number statistics and the uncertainties on the determined false alarm probabilities are large, we note that these roughly agree with what we would statistically expect for each confidence interval quoted, i.e., a 1σ detection has a

formal 31.73% false alarm probability by definition, though allowing eccentricity to vary does appear to induce false detections at ~ 1.5 times greater frequency. Combining all the results from each light curve type and eccentricity parameter, we can generalize our false alarm probabilities to 31%, 10%, and 6% for the $1-2\sigma$, $2-3\sigma$, and $>3\sigma$ confidence intervals respectively.

4.4. Derivation of Stellar and Planetary Parameters

The secondary eclipse detections presented in the previous section allow, for the first time, to make a statistically significant analysis of the emission properties of exoplanet candidates at visible wavelengths, specifically in the $\sim 0.4 - 0.9 \mu m$ *Kepler* passband.

In this section we first revise the parameters of the host stars necessary to derive the physical properties of the planets and then compute physical and atmospheric parameters for each planet candidate, i.e., the brightness, equilibrium, and maximum effective temperatures, radii, and albedos, using both the originally reported and revised stellar parameter values. A detailed statistical study of the properties for the planets based on those parameters is presented in Section 4.5.

4.4.1. Stellar Parameters

The *Kepler* Input Catalog (KIC) provides estimates of the effective temperature, surface gravity, and radius for all the host stars in our sample. Those parameters have been derived from a combination of broad and narrow-band photometry (Brown et al. 2011), although it has been also recognized that some of the parameter values in the KIC might contain significant errors. As explained

in detail by Brown et al. (2011), the majority of approximately Sun-like stars in the KIC have effective temperatures that only disagree by 200 K or less from the temperature values of a control sample derived by other methods. However, for stars significantly more massive or less massive than the Sun, i.e., with $T_\star \gtrsim 9000$ K and $T_\star \lesssim 4000$ K, where T_\star is the effective temperature of the star, the temperatures in the KIC can suffer from large systematics and are not reliable. As well, in the case of the derived stellar radii, R_\star , the values reported in the KIC are derived from statistical relations between the values obtained for T_\star , the surface gravity of the stars, $\log g$, and the luminosity, L_\star (see sections 7 and 8 of Brown et al. (2011), for more details). Therefore, if any of those parameters are systematically off, (such as $\log g$, which has an associated error of ± 0.4 dex), the values derived for R_\star will be erroneous.

All the host stars in our sample have KIC effective temperature estimates between 4000 and 9000 K, so we have assumed that those values are accurate within the errors. From those temperatures we recomputed the radius and mass of the stars via interpolation of up-to-date stellar evolutionary models by Bertelli et al. (2008) for $M_\star \leq 1.4 M_\odot$ and Siess et al. (2000) for $M_\star > 1.4 M_\odot$. In the models we have assumed that all the stars are nearly coeval, with an age of ~ 1 Gyr and therefore on the main sequence, have abundances similar to the Sun, i.e., $Z = 0.017$, $Y = 0.26$, and have a mixing length of $\alpha = 1.68$.

The errors in those parameters have been estimated by recomputing the mass and radius of each star 10,000 times, each time adding random Gaussian noise to the underlying variables and examining the 1σ spread of the resulting distribution. In the error estimations using the KIC values, we assumed an error of ± 0.4 dex for $\log g$, as reported by Brown et al. (2011). In the error estimations using the

model isochrones we assume an error of ± 200 K for T_{\star} , as reported by Brown et al. (2011). The values for the mass and radius of each star as computed from the KIC, labeled “KIC”, and via interpolation of the stellar isochrones, labeled “ISO”, along with their estimated errors, are listed in Table 4.1.

4.4.2. Planetary Parameters

Given the stellar parameters and their associated errors, we proceeded with calculating physical parameters for each planet. From the orbital period of the system and the mass of the star, we calculated the semi-major axis of the planets via Newton’s version of Kepler’s Third Law. The radius of each planet, R_p , was calculated from the stellar radius and the value of the radius ratio derived in Section 4.3. The obtained R_p values are compared with those reported by Borucki et al. (2011) in Figure 4.4 by multiplying the derived value of the ratio of the radii from each study, including results from both the PDC and CLM data for ours, by the radius of the host star derived via both the KIC and stellar isochrones. Except for a handful of outliers, most values of the planetary radii derived via different parameter estimations seem to agree with the Borucki et al. (2011) results within $\sim 5\%$. We note though that the radii of individual planet candidates can be significantly affected depending on whether their stellar radii are derived from the KIC or stellar isochrones, on average $\sim 20\%$.

We also calculated the sub-stellar equilibrium temperature, maximum effective temperature, and brightness temperature of each planet following the same equations as in Cowan & Agol (2011), who themselves draw upon Hansen (2008) and Burrows et al. (2008a). We calculated the equilibrium temperature of each

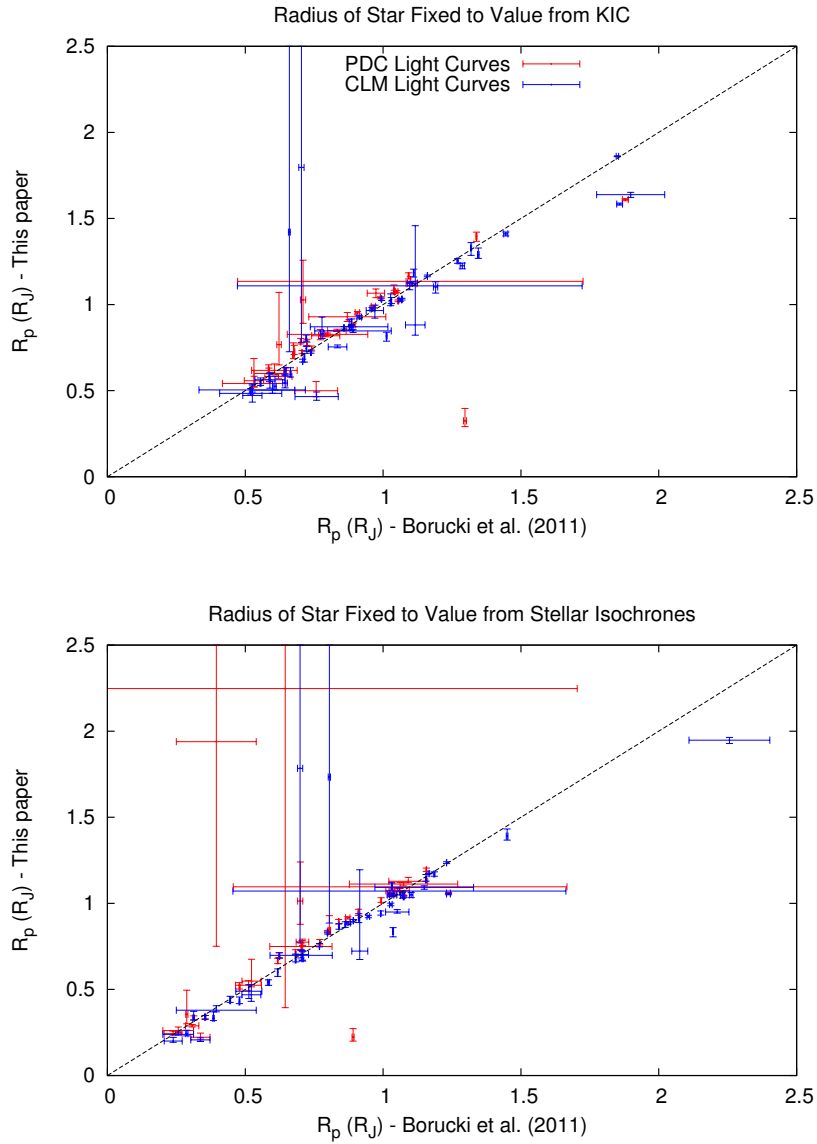


Fig. 4.4.— Comparison of the values for the planetary radius as given by Borucki et al. (2011) and derived in this paper. Red and blue symbols correspond, respectively, to the results from the PDC and CLM light curves. The errorbars are computed assuming a fixed stellar radius, but taking into account the errors on the value of the ratio of the radii. In the top panel the stellar radius has been set to its value in the KIC, while in the bottom panel the stellar radius is computed via stellar isochrones from its given T_{\star} value in the KIC. The dashed line delineates an expected 1:1 correlation.

planet at its sub-stellar point, T_0 , using T_\star and the semi-major axis of the system, a , via,

$$T_0 = T_\star \cdot (R_\star/a)^{0.5} \quad (4.2)$$

We note that this expression assumes non-significant eccentricity effects on the heating of the planet by the star.

We calculated the maximum effective temperature of the planet, $T_{\epsilon=0}$, using the equation

$$T_{\epsilon=0} = (2/3)^{\frac{1}{4}} \cdot T_0 \quad (4.3)$$

assuming no albedo or heat recirculation.

Finally, to calculate the measured brightness temperature of each planet, T_b , we assume both the planet and star emit like blackbodies and compute T_b by integrating their fluxes over the *Kepler* passband from the equation

$$J = \frac{\int t_\lambda \cdot \lambda^{-5} \cdot (\exp(\frac{hc}{\lambda k T_b}) - 1)^{-1} \cdot d\lambda}{\int t_\lambda \cdot \lambda^{-5} \cdot (\exp(\frac{hc}{\lambda k T_\star}) - 1)^{-1} \cdot d\lambda} \quad (4.4)$$

where λ is a given wavelength, t_λ is the net transmission of the telescope and detector at a given wavelength, h is Planck's constant, c is the speed of light, and k is Boltzmann's constant.

In the cases where significant sinusoidal variations were detected in the light curves, i.e., cases where we found a positive value for A_{L_p} with a detection level of at least 2σ , we treated the effect as real and accounted for it in the determination of

the day-side flux of the planet by multiplying the values of J in Eq. 4.4 by $(1+A_{L_p})$. The only systems where significant sinusoidal variations were detected are KOI 2.01 and KOI 13.01, for both the PDC and CLM data, and both fixing eccentricity to zero and letting it vary. For KOI 1541.01 a significant sinusoidal variation was also found, but only for the CLM data and when allowing eccentricity to vary. Notice that, if real, the observed amplitude of sinusoidal variations can be either due to a significant albedo, and thus a varying amount of reflected light with phase, a significant temperature difference between the day and night sides of the planets, i.e., very little heat redistribution, and therefore varying amounts of emitted light with phase, or photometric beaming. It is possible that sinusoidal systematic signals could mask as significant phase variations, but in order to be detected as such by the residual-permutation error analysis we employed, the systematic feature would have to have a stable amplitude and period over the course of the 90-day observations, and have the period and phase of maximum amplitude coincide with the orbital period and secondary eclipse phase of the planet, which we deem unlikely.

In the above temperature calculations we have assumed no albedo and therefore all the observed planetary fluxes are due to thermal emission. However, the atmosphere of the planets can contain clouds or hazes which would reflect at least part of the incident stellar light. To account for those effects, we can estimate the different contribution amounts of reflected light to the measured planet-to-star surface brightness ratio, as

$$F_a = \frac{A \cdot R_\star^2}{a^2} \quad (4.5)$$

where A is the geometric albedo of the planet in the integrated *Kepler* passband. Assuming different values of A between 0.0 (no albedo) and 1.0 (purely reflective atmosphere), we can subtract the resultant value of F_a from J in order to remove the reflected light contribution from the measurements of the eclipse depths before computing the T_b of the planet that accounts for the remaining, thermally emitted, light. Furthermore, given the measured surface brightness ratio and Equation 4.5, we can determine the maximum possible geometric albedo of the planet in the *Kepler* wavelength range, A_{max} , by assuming that all of the detected emission is solely due to reflected light. Setting $F_a = J$ and solving for A , we obtain the expression

$$A_{max} = \frac{a^2 J}{R_\star^2} \quad (4.6)$$

Finally, we have computed robust errors for all the derived quantities, i.e., T_0 , $T_{\epsilon=0}$, T_b , a , R_p , A_{max} , and also T_b/T_0 (see next section) by re-calculating all their values 10,000 times, each time adding random Gaussian noise with amplitudes equal to the errors of the underlying quantities J , P , k , T_\star , M_\star , and R_\star . The resulting median values of each parameter and their asymmetric Gaussian 1σ errors are listed in Table 4.3 along with the detection significance of the secondary eclipse, σ_{sec} , and the luminosity ratio of the system, $L_r = L_p/L_\star$, for both the PDC and CLM light curves, both letting eccentricity vary and fixing it to zero, and both using the stellar parameters derived from the KIC and via stellar isochrones. Negative values of σ_{sec} mean that a negative value of J was found, i.e., an increase of light at secondary eclipse, instead of the expected decrease. We deem those results unphysical, but note we can still use them to establish upper limits for the

depth of the eclipse, and estimate the fraction of spurious eclipse detections in our analysis, as already described at the end of Section 4.3.

4.5. Statistical Properties of the Secondary Eclipse Emissions

Following Cowan & Agol (2011), we plot in Figure 4.5 the dimensionless *Kepler* passband day-side brightness temperature ratio of each planet candidate in our sample, T_b/T_0 , versus their maximum expected day-side temperature, $T_{\epsilon=0}$, for the case of eccentricity fixed to zero. The different panels in the figure correspond to the results from the PDC and the CLM light curves, and both using the stellar parameters derived from the KIC and via stellar isochrones. In all the panels we have assumed zero albedo, which is equivalent to assuming that all the emission from the planet is thermal. (The case of non-zero albedos is considered below.) The $1-2\sigma$, $2-3\sigma$, and $>3\sigma$ detections, and 1σ upper limits of the $<1\sigma$ detections, are represented by solid circles of different colors and sizes. In addition, the open squares correspond to planets with previously published secondary eclipse detections in the optical, i.e., CoRoT-1b (Alonso et al. 2009b), CoRoT-2b (Alonso et al. 2009a), Hat-P-7b (Welsh et al. 2010), Kepler-5b (Kipping & Bakos 2011a), Kepler-7b (Kipping & Bakos 2011a; Demory et al. 2011), and OGLE-TR-56b (Sing et al. 2009; Adams et al. 2011), as well as previously published secondary eclipse upper limits, i.e., HD209458 (Rowe et al. 2008), TrES-2b (Kipping & Bakos 2011b), and Kepler-4b, Kepler-6b, and Kepler-8b (Kipping & Bakos 2011a). Each point is shown with its 1σ x and y-axis errorbars, except for the $<1\sigma$ detection upper limits, where the x-axis errorbars are omitted for clarity. Finally, the three horizontal lines in each plot indicate the expected values of T_b/T_0 for no energy redistribution, i.e., $f = 2/3$, a uniform day-side temperature, i.e., $f = 1/2$, and

Table 4.3. Derived System Parameters and Associated 1σ Uncertainties

KOI	L_r (ppm)	σ_{sec}	T_0 (K)	$T_{e=0}$ (K)	T_b^a (K)	T_b/T_0	R_p (R_{Jup})	a (AU)	A_{max}
2.01	75.0 ^{+9.48} _{-8.13}	9.11	2702 ⁺⁰⁷⁵⁹ ₋₀₅₉₇	2441 ⁺⁰⁶⁸⁶ ₋₀₅₄₀	2851 ⁺⁰⁰⁶² ₋₀₀₆₄	1.055 ^{+0.294} _{-0.232}	1.022 ^{+0.955} _{-0.497}	0.0367 ^{+0.0132} _{-0.0097}	0.38 ^{+0.65} _{-0.24}
5.01	-13.4 ^{+13.4} _{-34.7}	-0.99	2139 ⁺⁰⁵⁹⁷ ₋₀₅₄₆	1932 ⁺⁰⁵³⁹ ₋₀₄₉₃	-2607 ⁺⁰⁸²⁷ ₋₀₂₀₅	-1.159 ^{+0.539} _{-0.351}	0.617 ^{+0.552} _{-0.905}	0.0586 ^{+0.0205} _{-0.0174}	-0.40 ^{+0.39} _{-0.55}
10.01	14.9 ^{+34.7} _{-13.9}	1.07	1993 ⁺⁰⁵⁴⁶ ₋₀₄₂₀	1801 ⁺⁰⁴⁸⁰ ₋₀₃₈₀	2319 ⁺⁰²⁰⁵ ₋₀₃₅₈	1.121 ^{+0.351} _{-0.321}	0.990 ^{+0.470} _{-1.524}	0.0471 ^{+0.0124} _{-0.0348}	0.21 ^{+0.17} _{-0.40}
13.01	124.3 ^{+6.93} _{-7.81}	16.15	5069 ⁺¹⁴¹⁴ ₋₁₁₃₅	4580 ⁺¹²⁷⁸ ₋₁₀₂₅	3744 ⁺⁰⁰⁵⁵ ₋₀₀₅₆	0.738 ^{+0.213} _{-0.161}	1.610 ^{+0.524} _{-0.779}	0.0348 ^{+0.0127} _{-0.0092}	0.23 ^{+0.40} _{-0.14}
18.01	0.2 ^{+1.42} _{-0.27}	0.33	1827 ⁺⁰⁵¹⁴ ₋₀₃₉₈	1651 ⁺⁰⁴⁶⁴ ₋₀₃₆₀	1648 ⁺⁰¹³² ₋₀₂₅₂	0.866 ^{+0.278} _{-0.267}	0.749 ^{+0.703} _{-0.357}	0.0446 ^{+0.0158} _{-0.0118}	0.01 ^{+0.03} _{-0.01}
64.01	47.7 ^{+25.0} _{-23.3}	2.05	2711 ⁺⁰⁷⁴⁸ ₋₀₆₉₅	2449 ⁺⁰⁶⁷⁶ ₋₀₄₇₆	2702 ⁺⁰¹⁶⁵ ₋₀₂₂₇	0.980 ^{+0.294} _{-0.226}	0.829 ^{+0.756} _{-0.403}	0.0324 ^{+0.0115} _{-0.0084}	0.24 ^{+0.49} _{-0.17}
97.01	53.2 ^{+13.0} _{-13.0}	4.08	1899 ⁺⁰⁴⁰⁹ ₋₀₄₀₉	1716 ⁺⁰³⁷⁰ ₋₀₃₇₀	2541 ⁺⁰⁰⁹⁸ ₋₀₀₉₈	1.333 ^{+0.291} _{-0.291}	1.038 ^{+0.506} _{-0.506}	0.0579 ^{+0.0152} _{-0.0152}	0.63 ^{+0.41} _{-0.41}
102.01	13.6 ^{+8.83} _{-9.86}	1.38	3325 ⁺⁰⁹⁵⁷ ₋₀₇₂₆	3005 ⁺⁰⁸⁶⁵ ₋₀₆₅₆	2763 ⁺⁰²¹⁷ ₋₀₄₂₃	0.799 ^{+0.250} _{-0.238}	0.584 ^{+0.546} _{-0.282}	0.0302 ^{+0.0109} _{-0.0079}	0.11 ^{+0.26} _{-0.09}
144.01	59.1 ^{+55.3} _{-48.6}	1.21	1865 ⁺⁰⁵¹⁷ ₋₀₄₀₉	1685 ⁺⁰⁴⁶⁷ ₋₀₃₆₉	2776 ⁺⁰²⁶¹ ₋₀₄₉₇	1.429 ^{+0.455} _{-0.442}	0.629 ^{+0.561} _{-0.300}	0.0524 ^{+0.0185} _{-0.0134}	1.30 ^{+3.27} _{-1.12}
186.01	-25.8 ^{+48.2} _{-49.3}	-0.54	1793 ⁺⁰⁴⁸⁶ ₋₀₃₈₇	1620 ⁺⁰⁴³⁹ ₋₀₃₅₀	-2118 ⁺⁴¹⁸⁸ ₋₀₂₉₈	-1.067 ^{+2.175} _{-0.430}	1.075 ^{+0.992} _{-0.502}	0.0438 ^{+0.0157} _{-0.0116}	-0.12 ^{+0.23} _{-0.51}
188.01	56.2 ^{+38.7} _{-31.4}	1.47	1332 ⁺⁰⁵⁸⁵ ₋₀₄₃₀	1204 ⁺⁰⁴³⁰ ₋₀₃₄₈	2170 ⁺⁰²⁴⁴ ₋₀₂₄₄	1.584 ^{+0.430} _{-0.429}	0.771 ^{+0.362} _{-0.362}	0.0459 ^{+0.0125} _{-0.0125}	0.63 ^{+1.41} _{-0.82}
195.01	76.7 ^{+45.5} _{-24.1}	1.52	1799 ⁺⁰⁵⁰⁴ ₋₀₃₉₉	1626 ⁺⁰⁴⁵⁶ ₋₀₃₆₁	2344 ⁺⁰¹⁶⁰ ₋₀₂₆₅	1.265 ^{+0.390} _{-0.342}	1.121 ^{+0.999} _{-0.543}	0.0435 ^{+0.0155} _{-0.0116}	0.36 ^{+0.82} _{-0.28}
196.01	77.0 ^{+24.1} _{-24.4}	3.13	2132 ⁺⁰⁵⁹⁹ ₋₀₄₆₃	1927 ⁺⁰⁵⁴² ₋₀₄₁₉	2425 ⁺⁰⁰⁹⁸ ₋₀₁₁₆	1.130 ^{+0.319} _{-0.246}	0.950 ^{+0.857} _{-0.455}	0.0298 ^{+0.0108} _{-0.0079}	0.27 ^{+0.48} _{-0.17}
199.01	32.4 ^{+33.9} _{-35.8}	0.91	1871 ⁺⁰⁵²³ ₋₀₄₀₆	1690 ⁺⁰⁴⁷² ₋₀₃₆₇	2339 ⁺⁰²²³ ₋₄₂₆₆	1.167 ^{+0.413} _{-0.061}	0.827 ^{+0.763} _{-0.399}	0.0442 ^{+0.0159} _{-0.0117}	0.26 ^{+0.81} _{-0.30}
201.01	-46.5 ^{+40.3} _{-31.4}	-1.14	1638 ⁺⁰⁴⁵² ₋₀₆₈₈	1480 ⁺⁰⁴⁰⁸ ₋₀₃₂₂	-2398 ⁺⁰⁴⁷⁰ ₋₀₁₃₂	-1.393 ^{+0.474} _{-0.292}	0.790 ^{+0.736} _{-1.019}	0.0518 ^{+0.0191} _{-0.0104}	-0.60 ^{+0.54} _{-0.34}
202.01	68.9 ^{+30.3} _{-27.3}	2.26	2416 ⁺⁰⁵²⁹ ₋₀₄₇₆	2183 ⁺⁰⁶²² ₋₀₄₇₈	2460 ⁺⁰¹³² ₋₀₁₃₂	1.003 ^{+0.210} _{-0.230}	1.073 ^{+0.513} _{-0.373}	0.0290 ^{+0.0078} _{-0.0154}	0.17 ^{+0.12} _{-0.25}
204.01	-15.6 ^{+33.7} _{-33.7}	-0.57	1706 ⁺⁰³⁶⁷ ₋₀₄₀₈	1542 ⁺⁰³³¹ ₋₀₃₆₈	-2130 ⁺⁰²⁴⁸ ₋₀₂₃₀	-1.154 ^{+0.429} _{-0.243}	0.778 ^{+0.725} _{-1.532}	0.0431 ^{+0.0117} _{-0.0168}	-0.17 ^{+0.64} _{-0.02}
229.01	3.0 ^{+42.7} _{-5.58}	0.52	1872 ⁺⁰⁵²⁴ ₋₀₇₁₆	1691 ⁺⁰⁴⁷⁴ ₋₀₃₆₈	1773 ⁺⁰¹⁴⁰ ₋₀₅₂₂	0.915 ^{+0.289} _{-0.243}	3.204 ^{+3.016} _{-1.532}	0.0468 ^{+0.0168} _{-0.0124}	0.02 ^{+0.06} _{-0.02}
356.01	1.1 ^{+19.6} _{-16.6}	0.06	2565 ⁺⁰⁷¹⁶ ₋₀₅₇₃	2318 ⁺⁰⁶⁴⁷ ₋₀₃₇₄	2086 ⁺⁰⁵²² ₋₄₅₄₆	0.682 ^{+0.422} _{-0.186}	0.558 ^{+0.529} _{-0.270}	0.0304 ^{+0.0110} _{-0.0080}	0.02 ^{+0.28} _{-0.19}
412.01	26.3 ^{+50.2} _{-44.4}	0.52	1879 ⁺⁰⁴¹⁴ ₋₀₄₁₄	1698 ⁺⁰³⁷⁴ ₋₀₃₇₄	2426 ⁺⁰⁴⁸³ ₋₀₃₉₈	1.157 ^{+0.424} _{-0.424}	0.744 ^{+0.364} _{-0.364}	0.0520 ^{+0.0136} _{-0.0136}	0.33 ^{+0.76} _{-0.68}
421.01	-104.7 ^{+75.5} _{-75.5}	-1.22	1652 ⁺⁰⁴⁶³ ₋₀₃₆₁	1493 ⁺⁰⁴¹⁹ ₋₀₃₂₆	-2306 ⁺⁰¹⁸⁰ ₋₀₁₈₀	-1.335 ^{+0.444} _{-0.435}	1.391 ^{+1.307} _{-0.672}	0.0534 ^{+0.0192} _{-0.0141}	-0.43 ^{+0.39} _{-1.09}
433.01	8.2 ⁺¹²⁰¹ ₋₂₂₉₇	0.01	1666 ⁺⁰⁴⁵⁹ ₋₀₃₆₉	1505 ⁺⁰⁴¹⁵ ₋₀₃₃₃	-2128 ⁺⁰⁶²² ₋₀₆₂₂	-1.071 ^{+2.722} _{-0.709}	2.616 ^{+3.572} _{-1.778}	0.0493 ^{+0.0176} _{-0.0129}	-0.16 ^{+1.75} _{-2.29}
611.01	-22.6 ^{+59.0} _{-59.0}	-0.39	1912 ⁺⁰⁵²⁴ ₋₀₄₁₂	1728 ⁺⁰⁴⁷⁴ ₋₀₃₇₃	-2327 ⁺⁰³⁹⁷ ₋₀₃₉₇	-1.071 ^{+2.382} _{-0.495}	0.748 ^{+0.663} _{-0.363}	0.0444 ^{+0.0116} _{-0.0116}	-0.19 ^{+0.70} _{-1.17}
684.01	76.3 ^{+41.8} _{-41.8}	1.83	2180 ⁺⁰⁵⁹³ ₋₀₄₃₆	1970 ⁺⁰⁵³⁵ ₋₀₃₉₄	3360 ⁺⁰²⁷⁴ ₋₀₃₃₇	1.516 ^{+0.454} _{-0.585}	0.511 ^{+0.270} _{-0.270}	0.0523 ^{+0.0186} _{-0.0209}	2.68 ^{+5.63} _{-1.92}
760.01	30.6 ^{+70.2} _{-70.2}	0.43	1522 ⁺⁰³²⁹ ₋₀₆₅₄	1375 ⁺⁰²⁹⁷ ₋₀₅₉₁	2339 ⁺⁴⁵²⁹ ₋₀₂₂₅	1.300 ^{+2.787} _{-0.327}	0.883 ^{+0.842} _{-0.424}	0.0580 ^{+0.0152} _{-0.0099}	0.37 ^{+0.96} _{-0.43}
801.01	56.6 ^{+56.2} _{-56.2}	1.01	2343 ⁺⁰⁵⁰⁶ ₋₀₅₁₀	2117 ⁺⁰⁶⁵⁴ ₋₀₄₅₈	2423 ⁺⁰²²⁵ ₋₀₆₉₇	0.978 ^{+0.327} _{-0.440}	0.925 ^{+0.863} _{-0.440}	0.0274 ^{+0.0073} _{-0.0095}	0.15 ^{+0.43} _{-0.15}
809.01	-41.1 ^{+76.2} _{-84.6}	-0.55	2328 ⁺⁰⁶³⁴ ₋₀₅₁₀	2103 ⁺⁰⁵⁷² ₋₀₄₆₁	-2233 ⁺⁴³⁵¹ ₋₀₂₈₂	-0.874 ^{+1.741} _{-0.355}	1.146 ^{+1.058} _{-0.541}	0.0272 ^{+0.0095} _{-0.0071}	-0.07 ^{+0.12} _{-0.30}
813.01	-166.1 ^{+92.3} _{-92.3}	-1.75	1397 ⁺⁰³⁰⁴ ₋₀₃₀₄	1262 ⁺⁰³⁴⁴ ₋₀₂₇₅	-2681 ⁺⁰²⁷³ ₋₀₁₈₂	-1.875 ^{+0.465} _{-0.561}	0.626 ^{+0.571} _{-0.297}	0.0477 ^{+0.0170} _{-0.0126}	-3.07 ^{+2.29} _{-6.51}

PDC Light Curve with Eccentricity Fixed to Zero and Stellar Parameters from the KIC

Table 4.3 (continued)

KOI	L_r (ppm)	σ_{sec}	T_0 (K)	$T_{e=0}$ (K)	T_b^a (K)	T_b/T_0	R_p (R_{Jup})	a (AU)	A_{max}
830.01	$61.8^{+78.4}_{-43.3}$	0.76	1187^{+332}_{-325}	1072^{+3300}_{-3233}	2049^{+3205}_{-3494}	$1.595^{+0.577}_{-0.543}$	$0.725^{+0.560}_{-0.542}$	$0.0420^{+0.0148}_{-0.0206}$	$0.51^{+1.85}_{-0.69}$
838.01	$1.3^{+65.0}_{-36.9}$	0.03	1639^{+3660}_{-3660}	1481^{+3416}_{-3425}	2045^{+3380}_{-4257}	$1.085^{+0.543}_{-2.449}$	$1.084^{+0.042}_{-0.531}$	$0.0571^{+0.0142}_{-0.0147}$	$0.12^{+0.46}_{-0.32}$
840.01	$-61.7^{+85.1}_{-85.3}$	-0.73	1699^{+3472}_{-3364}	1535^{+3426}_{-3329}	-2187^{+4175}_{-3238}	$-1.187^{+2.263}_{-0.436}$	$1.067^{+0.596}_{-0.502}$	$0.0402^{+0.0142}_{-0.0104}$	$-0.23^{+0.32}_{-0.80}$
843.01	$-2.2^{+18.6}_{-48.8}$	-0.13	1811^{+3997}_{-3397}	1637^{+3444}_{-3359}	-2471^{+4686}_{-3364}	$-1.264^{+2.412}_{-0.498}$	$0.593^{+0.532}_{-0.282}$	$0.0524^{+0.0188}_{-0.0138}$	$-0.48^{+0.68}_{-1.95}$
897.01	$52.9^{+62.2}_{-53.9}$	1.00	2181^{+3609}_{-3540}	1970^{+3551}_{-3452}	2307^{+3210}_{-3215}	$1.000^{+0.342}_{-0.427}$	$1.165^{+1.084}_{-0.935}$	$0.0323^{+0.0117}_{-0.0204}$	$0.13^{+0.39}_{-0.13}$
908.01	$45.0^{+47.8}_{-51.1}$	0.95	1762^{+3880}_{-3389}	1592^{+3452}_{-3443}	2362^{+3205}_{-3210}	$1.269^{+0.638}_{-0.638}$	$1.096^{+0.524}_{-0.524}$	$0.0565^{+0.0150}_{-0.0150}$	$0.39^{+0.38}_{-0.38}$
913.01	$39.8^{+51.1}_{-52.2}$	0.76	1388^{+3389}_{-3299}	1254^{+3521}_{-3271}	2128^{+3216}_{-4025}	$1.423^{+0.521}_{-2.662}$	$0.852^{+0.796}_{-0.411}$	$0.0494^{+0.0133}_{-0.0133}$	$0.38^{+0.31}_{-0.50}$
931.01	$12.8^{+62.5}_{-20.0}$	0.67	1460^{+3414}_{-3314}	1320^{+3366}_{-3283}	2198^{+3217}_{-3217}	$1.440^{+0.480}_{-0.473}$	$0.827^{+0.752}_{-0.400}$	$0.0484^{+0.0175}_{-0.0130}$	$0.44^{+1.32}_{-0.40}$
961.02	$6.1^{+68.1}_{-63.7}$	0.09	2358^{+3674}_{-3507}	2131^{+3609}_{-3459}	1922^{+3479}_{-4231}	$0.676^{+0.424}_{-1.691}$	$0.354^{+0.336}_{-0.169}$	$0.0098^{+0.0034}_{-0.0026}$	$0.02^{+0.24}_{-0.18}$
961.03	828.9^{+3971}_{-3971}	0.40	1478^{+3327}_{-3327}	1336^{+3295}_{-3295}	2371^{+3233}_{-3233}	$1.449^{+3.040}_{-0.065}$	$5.349^{+4.065}_{-0.067}$	$0.0254^{+0.0067}_{-0.0067}$	$0.94^{+2.19}_{-0.067}$
1419.01	$54.0^{+73.0}_{-238.8}$	1.00	2572^{+3706}_{-3564}	2324^{+3638}_{-3510}	2755^{+3289}_{-3289}	$1.017^{+0.345}_{-0.466}$	$0.631^{+0.577}_{-0.305}$	$0.0244^{+0.0087}_{-0.0065}$	$0.29^{+0.85}_{-0.28}$
1459.01	$314.2^{+151.1}_{-151.1}$	2.10	2189^{+3622}_{-3470}	1978^{+3562}_{-3424}	2383^{+3146}_{-3185}	$1.076^{+0.303}_{-0.259}$	$0.889^{+0.902}_{-0.432}$	$0.0132^{+0.0048}_{-0.0035}$	$0.27^{+0.52}_{-0.19}$
PDC Light Curve with Eccentricity Fixed to Zero and Stellar Parameters from Isochrones									
2.01	$75.0^{+9.48}_{-8.13}$	9.11	2747^{+3171}_{-3171}	2482^{+3155}_{-3154}	2850^{+3062}_{-3062}	$1.036^{+0.055}_{-0.046}$	$1.042^{+0.088}_{-0.086}$	$0.0363^{+0.0007}_{-0.0007}$	$0.36^{+0.07}_{-0.05}$
5.01	$-13.4^{+13.4}_{-14.8}$	-0.99	1627^{+3106}_{-3095}	1470^{+3096}_{-3086}	-2608^{+30784}_{-3253}	$-1.594^{+0.477}_{-0.175}$	$0.339^{+0.029}_{-0.025}$	$0.0562^{+0.0011}_{-0.0010}$	$-1.49^{+1.43}_{-1.50}$
10.01	$14.9^{+34.7}_{-13.9}$	1.07	2050^{+3144}_{-3129}	1852^{+3130}_{-3117}	2318^{+3204}_{-3344}	$1.124^{+0.121}_{-0.174}$	$1.057^{+0.102}_{-0.087}$	$0.0476^{+0.0010}_{-0.0009}$	$0.21^{+0.23}_{-0.17}$
13.01	$124.3^{+3.93}_{-1.18}$	16.15	4047^{+3100}_{-3118}	3657^{+3090}_{-3066}	3744^{+3056}_{-3026}	$0.925^{+0.015}_{-0.089}$	$1.059^{+0.014}_{-0.067}$	$0.0359^{+0.0003}_{-0.0009}$	$0.56^{+0.03}_{-0.01}$
18.01	$0.2^{+2.27}_{-0.27}$	0.33	1829^{+3112}_{-3106}	1652^{+3101}_{-3066}	1649^{+3026}_{-3026}	$0.896^{+0.148}_{-0.148}$	$0.779^{+0.058}_{-0.058}$	$0.0463^{+0.0009}_{-0.0009}$	$0.01^{+0.01}_{-0.01}$
64.01	$47.7^{+25.0}_{-23.3}$	2.05	1817^{+3106}_{-3101}	1642^{+3096}_{-3092}	2699^{+3170}_{-3228}	$1.484^{+0.099}_{-0.128}$	$0.336^{+0.024}_{-0.021}$	$0.0292^{+0.0005}_{-0.0005}$	$1.32^{+0.67}_{-0.65}$
97.01	$53.2^{+14.1}_{-13.0}$	4.08	1710^{+3118}_{-3105}	1545^{+3107}_{-3095}	2541^{+3089}_{-3096}	$1.485^{+0.085}_{-0.088}$	$0.837^{+0.077}_{-0.063}$	$0.0580^{+0.0012}_{-0.0011}$	$0.97^{+0.29}_{-0.26}$
102.01	$13.6^{+8.83}_{-8.66}$	1.38	2394^{+3165}_{-3149}	2163^{+3149}_{-3132}	2769^{+3215}_{-3215}	$1.148^{+0.107}_{-0.107}$	$0.290^{+0.027}_{-0.023}$	$0.0290^{+0.0006}_{-0.0006}$	$0.49^{+0.35}_{-0.36}$
144.01	$59.1^{+48.6}_{-48.6}$	1.21	1244^{+3083}_{-3083}	1124^{+3075}_{-3075}	2768^{+3058}_{-3058}	$2.236^{+0.430}_{-0.430}$	$0.248^{+0.023}_{-0.023}$	$0.0465^{+0.0011}_{-0.0011}$	$7.98^{+6.49}_{-6.49}$
186.01	$-25.8^{+48.2}_{-49.3}$	-0.54	1888^{+3125}_{-3125}	1706^{+3113}_{-3113}	-2106^{+3272}_{-3272}	$-1.110^{+2.205}_{-0.160}$	$1.196^{+0.099}_{-0.088}$	$0.0436^{+0.0008}_{-0.0008}$	$-0.13^{+0.24}_{-0.25}$
188.01	$56.2^{+41.7}_{-38.5}$	1.47	1438^{+3084}_{-3082}	1299^{+3076}_{-3074}	2169^{+3144}_{-3144}	$1.506^{+0.116}_{-0.177}$	$0.893^{+0.051}_{-0.051}$	$0.0453^{+0.0008}_{-0.0009}$	$0.54^{+0.39}_{-0.37}$
195.01	$76.7^{+45.5}_{-50.2}$	1.52	1766^{+3115}_{-3100}	1596^{+3104}_{-3090}	2348^{+3152}_{-3267}	$1.322^{+0.107}_{-0.159}$	$1.050^{+0.081}_{-0.064}$	$0.0425^{+0.0008}_{-0.0008}$	$0.45^{+0.30}_{-0.29}$
196.01	$77.0^{+24.1}_{-24.1}$	3.13	2109^{+3133}_{-3133}	1906^{+3105}_{-3105}	2425^{+3016}_{-3016}	$1.147^{+0.065}_{-0.126}$	$0.916^{+0.068}_{-0.108}$	$0.0294^{+0.0005}_{-0.0005}$	$0.29^{+0.09}_{-0.09}$
199.01	$32.4^{+33.9}_{-35.8}$	0.91	2140^{+3140}_{-3140}	1933^{+3137}_{-3126}	2345^{+3220}_{-3220}	$1.087^{+0.126}_{-0.126}$	$1.112^{+0.108}_{-0.108}$	$0.0456^{+0.0010}_{-0.0010}$	$0.20^{+0.23}_{-0.23}$
201.01	$-46.5^{+40.3}_{-40.7}$	-1.14	1559^{+3096}_{-3087}	1409^{+3087}_{-3079}	-2397^{+3499}_{-3201}	$-1.532^{+0.326}_{-0.146}$	$0.703^{+0.050}_{-0.044}$	$0.0504^{+0.0009}_{-0.0009}$	$-0.90^{+0.80}_{-0.80}$
202.01	$68.9^{+31.4}_{-30.3}$	2.26	2398^{+3159}_{-3146}	2167^{+3144}_{-3132}	2461^{+3124}_{-3170}	$1.023^{+0.072}_{-0.083}$	$1.053^{+0.092}_{-0.078}$	$0.0288^{+0.0006}_{-0.0006}$	$0.19^{+0.09}_{-0.09}$

Table 4.3 (continued)

KOI	L_r (ppm)	σ_{sec}	T_0 (K)	$T_{\epsilon=0}$ (K)	T_b^a (K)	T_b/T_0	R_p (R_{Jup})	a (AU)	A_{max}
204.01	-15.6 ^{+27.3} _{-32.7}	-0.57	1603 ⁺⁰⁰⁹⁰ ₋₀₀₈₇	1449 ⁺⁰⁰⁹⁰ ₋₀₀₇₆	-2129 ⁺⁴¹¹⁰ ₋₀₂₄₉	-1.323 ^{+2.555} _{-0.039}	0.665 ^{+0.045} _{-0.350}	0.0415 ^{+0.0008} _{-0.0007}	-0.29 ^{+0.48} _{-0.04}
229.01	3.0 ^{+5.58} _{-5.58}	0.52	1708 ⁺⁰¹⁰⁶ ₋₀₀₉₇	1544 ⁺⁰⁰⁹⁶ ₋₀₀₈₈	1771 ⁺⁰¹⁴³ ₋₀₂₃₆	1.031 ^{-0.143} _{-0.143}	2.627 ^{-0.317} _{-0.0008}	0.0456 ^{-0.0008} _{-0.0005}	0.03 ^{-0.03} _{-0.03}
356.01	1.1 ^{+20.2} _{-16.6}	0.06	1856 ⁺⁰¹¹⁰ ₋₀₁₀₆	1677 ⁺⁰⁰⁹⁹ ₋₀₀₉₆	2092 ⁺⁰⁵¹⁷ ₋₄₅₅₅	1.122 ^{-2.287} _{-2.452}	0.268 ^{+0.023} _{-0.020}	0.0279 ^{+0.0005} _{-0.0005}	0.14 ^{+0.79} _{-0.72}
412.01	26.3 ^{+47.4} _{-50.2}	0.52	1614 ⁺⁰¹⁰³ ₋₀₀₉₀	1458 ⁺⁰⁰⁹³ ₋₀₀₈₁	2424 ⁺⁰³⁶¹ ₋₄₈₃₆	1.495 ^{+6.236} _{-2.977}	0.526 ^{+0.045} _{-0.036}	0.0503 ^{+0.0009} _{-0.0009}	0.85 ^{+1.67} _{-1.65}
421.01	-104.7 ^{+85.3} _{-85.5}	-1.22	1400 ⁺⁰⁰⁸⁵ ₋₀₀₈₈	1265 ⁺⁰⁰⁷⁷ ₋₀₀₇₁	-2306 ⁺⁰³⁹⁵ ₋₀₇₄₃	-1.641 ^{+0.285} _{-0.314}	0.949 ^{+0.061} _{-0.053}	0.0508 ^{+0.0010} _{-0.0009}	-1.01 ^{+0.84} _{-0.81}
433.01	8.2 ^{+120.1} _{-229.7}	0.01	1471 ⁺⁰⁰⁸⁰ ₋₀₀₈₀	1329 ⁺⁰⁰⁸¹ ₋₀₀₇₂	-2121 ⁺⁰⁶³⁰ ₋₀₇₆₃	-1.431 ^{-0.439} _{-0.439}	2.128 ^{-1.315} _{-0.0009}	0.0477 ^{-0.0008} _{-0.0009}	-0.40 ^{-3.04} _{-3.04}
611.01	-22.6 ^{+59.0} _{-56.5}	-0.39	2080 ⁺⁰¹⁴⁵ ₋₀₁₃₅	1879 ⁺⁰¹³¹ ₋₀₁₂₂	-2350 ⁺⁴⁸²⁵ ₋₀₃₉₄	-1.118 ^{+2.312} _{-0.207}	0.890 ^{+0.107} _{-0.090}	0.0450 ^{+0.0009} _{-0.0009}	-0.23 ^{+0.60} _{-0.57}
684.01	76.3 ^{+41.8} _{-42.1}	1.83	1511 ⁺⁰⁰⁹³ ₋₀₀₈₄	1365 ⁺⁰⁰⁸⁴ ₋₀₀₇₆	3365 ⁺⁰²⁷¹ ₋₀₃₇₀	2.225 ^{+0.187} _{-0.249}	0.229 ^{+0.026} _{-0.023}	0.0482 ^{+0.0009} _{-0.0008}	12.79 ^{+7.49} _{-6.92}
760.01	30.6 ^{+72.8} _{-70.2}	0.43	1671 ⁺⁰¹¹⁵ ₋₀₁₀₅	1510 ⁺⁰¹⁰⁴ ₋₀₀₉₅	2233 ⁺⁰³⁴⁷ ₋₄₅₃₂	1.326 ^{+0.223} _{-2.698}	1.058 ^{+0.095} _{-0.081}	0.0583 ^{+0.0011} _{-0.0011}	0.36 ^{+0.84} _{-0.81}
801.01	56.6 ^{+56.2} _{-56.2}	1.01	2135 ⁺⁰¹²¹ ₋₀₁₁₃	1929 ⁺⁰¹¹³ ₋₀₁₀₅	2428 ⁺⁰⁶³⁷ ₋₀₆₃₇	1.132 ^{+0.305} _{-0.305}	0.748 ^{+0.056} _{-0.0005}	0.0267 ^{+0.0005} _{-0.0005}	0.28 ^{-0.27} _{-0.27}
809.01	-41.1 ^{+76.2} _{-85.8}	-0.55	2293 ⁺⁰¹⁴⁹ ₋₀₁₃₅	2072 ⁺⁰¹³⁵ ₋₀₁₂₂	-2232 ⁺⁴³⁴⁷ ₋₀₂₈₂	-0.967 ^{+0.136} _{-0.136}	1.109 ^{+0.090} _{-0.073}	0.0268 ^{+0.0005} _{-0.0005}	-0.10 ^{+0.16} _{-0.16}
813.01	-166.1 ^{+94.6} _{-92.3}	-1.75	1540 ⁺⁰⁰⁹⁴ ₋₀₀₈₇	1391 ⁺⁰⁰⁸⁵ ₋₀₀₇₈	-2684 ⁺⁰²⁷⁴ ₋₀₁₈₀	-1.741 ^{+0.187} _{-0.130}	0.756 ^{+0.059} _{-0.051}	0.0472 ^{+0.0009} _{-0.0009}	-2.38 ^{+1.38} _{-1.39}
830.01	61.8 ^{+78.4} _{-83.3}	0.76	1403 ⁺⁰⁰⁸⁶ ₋₀₀₈₇	1268 ⁺⁰⁰⁷⁸ ₋₀₀₇₉	2053 ⁺⁰²⁰² ₋₃₉₁₄	1.459 ^{+0.163} _{-2.785}	1.022 ^{+0.061} _{-0.068}	0.0424 ^{+0.0008} _{-0.0009}	0.37 ^{+0.48} _{-0.50}
838.01	1.3 ^{+85.0} _{-85.0}	0.03	1633 ⁺⁰¹⁰⁶ ₋₀₀₉₆	1475 ⁺⁰⁰⁹⁶ ₋₀₀₈₂	2032 ⁺⁰³⁹⁴ ₋₄₁₅₅	1.231 ^{+0.257} _{-2.816}	1.071 ^{+0.228} _{-0.047}	0.0570 ^{+0.0011} _{-0.0007}	0.16 ^{+0.54} _{-0.54}
840.01	-61.7 ^{+85.3} _{-85.3}	-0.73	1475 ⁺⁰⁰⁸⁶ ₋₀₀₉₀	1332 ⁺⁰⁰⁷⁷ ₋₀₀₈₃	-2194 ⁺⁰²³⁶ ₋₄₁₅₅	-1.486 ^{-0.176} _{-0.176}	0.772 ^{+0.047} _{-0.053}	0.0384 ^{+0.0007} _{-0.0007}	-0.56 ^{+0.75} _{-0.75}
843.01	-2.2 ^{+18.6} _{-48.8}	-0.13	1710 ⁺⁰¹¹³ ₋₀₁₀₃	1545 ⁺⁰¹⁰³ ₋₀₀₉₃	-2482 ⁺⁴⁶⁸⁸ ₋₀₃₅₂	-1.446 ^{+2.733} _{-0.219}	0.520 ^{+0.052} _{-0.046}	0.0516 ^{+0.0010} _{-0.0010}	-0.82 ^{+1.11} _{-1.46}
897.01	52.9 ^{+62.2} _{-52.7}	1.00	2136 ⁺⁰¹³⁸ ₋₀₁₂₈	1930 ⁺⁰¹²⁵ ₋₀₁₁₆	2312 ⁺⁰²⁰⁴ ₋₀₆₃₀	1.076 ^{+0.112} _{-0.303}	1.101 ^{+0.090} _{-0.076}	0.0319 ^{+0.0006} _{-0.0006}	0.18 ^{+0.19} _{-0.17}
908.01	45.0 ^{+53.9} _{-52.7}	0.95	1462 ⁺⁰⁰⁸⁶ ₋₀₀₈₄	1321 ⁺⁰⁰⁷⁸ ₋₀₀₇₈	2365 ⁺⁰²¹⁸ ₋₀₂₁₄	1.614 ^{+0.164} _{-0.164}	0.720 ^{+0.049} _{-0.064}	0.0537 ^{+0.0010} _{-0.0008}	1.05 ^{+1.09} _{-0.41}
913.01	39.8 ^{+51.8} _{-52.2}	0.76	1568 ⁺⁰⁰⁹⁰ ₋₀₀₉₀	1417 ⁺⁰⁰⁸² ₋₀₀₈₂	2131 ⁺⁰⁴³⁹ ₋₀₂₁₄	1.351 ^{-0.445} _{-2.566}	1.077 ^{-0.066} _{-0.066}	0.0492 ^{+0.0009} _{-0.0008}	0.30 ^{+0.41} _{-0.41}
931.01	12.8 ^{+62.5} _{-20.0}	0.67	1721 ⁺⁰¹¹² ₋₀₁₀₀	1555 ⁺⁰¹⁰² ₋₀₀₉₀	2198 ⁺⁰²¹⁹ ₋₀₄₂₈	1.271 ^{+0.144} _{-0.255}	1.139 ^{+0.093} _{-0.075}	0.0484 ^{+0.0009} _{-0.0009}	0.27 ^{+0.35} _{-0.24}
961.02	6.1 ^{+68.1} _{-63.7}	0.09	2001 ⁺⁰²⁶⁵ ₋₀₂₇₄	1808 ⁺⁰²³⁹ ₋₀₂₄₇	1895 ⁺⁰⁵⁰⁰ ₋₄₂₀₇	0.915 ^{+6.314} _{-2.090}	0.239 ^{+0.073} _{-0.068}	0.0094 ^{+0.0006} _{-0.0010}	0.05 ^{+0.40} _{-0.36}
961.03	828.9 ⁺⁴⁸⁵⁰ ₋₃₉₇₁	0.40	1252 ⁺⁰¹⁶³ ₋₀₁₇₁	1132 ⁺⁰¹⁴⁷ ₋₀₁₅₅	2360 ⁺⁰³⁹⁸ ₋₄₇₆₃	1.859 ^{+6.404} _{-3.781}	3.715 ^{+3.999} _{-2.699}	0.0241 ^{+0.0016} _{-0.0026}	2.53 ^{+6.19} _{-5.41}
1419.01	54.0 ^{+53.8} _{-238.8}	1.00	2555 ⁺⁰¹⁵⁵ ₋₀₁₄₀	2309 ⁺⁰¹⁴⁰ ₋₀₁₄₀	2763 ⁺⁰⁶³⁴ ₋₀₃₆₈	1.078 ^{+0.368} _{-0.368}	0.614 ^{+0.083} _{-0.083}	0.0242 ^{+0.0005} _{-0.0005}	0.38 ^{+0.37} _{-0.37}
1459.01	314.2 ^{+238.8} _{-151.1}	2.10	1587 ⁺⁰²²⁸ ₋₀₂₂₂	1434 ⁺⁰²⁰⁶ ₋₀₂₀₁	2381 ⁺⁰¹⁴⁵ ₋₀₁₈₄	1.493 ^{+0.204} _{-0.180}	0.402 ^{+0.181} _{-0.134}	0.0117 ^{+0.0011} _{-0.0016}	1.05 ^{+0.78} _{-0.54}
1.01	-3.9 ^{+8.07} _{-8.07}	-0.48	2461 ⁺⁰⁶⁹⁶ ₋₀₅₄₃	2223 ⁺⁰⁶²⁰ ₋₀₄₉₀	-1727 ⁺³⁴⁶⁵ ₋₀₁₉₅	-0.618 ^{+1.324} _{-0.255}	1.861 ^{+1.740} _{-0.900}	0.0373 ^{+0.0135} _{-0.0098}	-0.00 ^{+0.01} _{-0.02}
2.01	77.7 ^{+10.3} _{-9.51}	8.28	2714 ⁺⁰⁷⁵⁷ ₋₀₅₇₇	2452 ⁺⁰⁶⁸⁴ ₋₀₅₂₁	2865 ⁺⁰⁰⁶⁵ ₋₀₂₈₅	1.055 ^{+0.228} _{-0.228}	1.032 ^{+0.926} _{-0.501}	0.0367 ^{+0.0129} _{-0.0097}	0.39 ^{+0.63} _{-0.24}
5.01	-3.1 ^{+11.8} _{-13.0}	-0.26	2144 ⁺⁰⁵⁸⁶ ₋₀₄₅₄	1937 ⁺⁰⁵³⁰ ₋₀₄₁₀	-2256 ⁺⁴⁷⁰³ ₋₀₄₁₈	-0.915 ^{+2.065} _{-0.462}	0.612 ^{+0.556} _{-0.292}	0.0587 ^{+0.0215} _{-0.0155}	-0.10 ^{+0.37} _{-0.66}
10.01	19.6 ^{+31.6} _{-33.7}	0.58	1997 ⁺⁰⁵⁶¹ ₋₀₄₄₉	1804 ⁺⁰⁵⁰⁷ ₋₀₄₀₆	2200 ⁺⁰²⁹³ ₋₄₃₇₃	0.992 ^{+0.425} _{-2.040}	0.976 ^{+0.425} _{-0.472}	0.0469 ^{+0.0172} _{-0.0123}	0.11 ^{+0.51} _{-0.23}

CLM Light Curve with Eccentricity Fixed to Zero and Stellar Parameters from the KIC

Table 4.3 (continued)

KOI	L_r (ppm)	σ_{sec}	T_0 (K)	$T_{=0}$ (K)	T_b^a (K)	T_b/T_0	R_p (R_{Jup})	a (AU)	A_{max}
13.01	125.6 ^{+6.31} _{-6.16}	15.64	5039 ⁺¹⁴⁰⁹ ₋₁₀₉₂	4553 ⁺¹²⁷³ ₋₁₀₄₉	3754 ⁺⁰⁰⁵⁷ ₋₀₄₅₂	0.744 ^{+0.310} _{-0.426}	1.582 ^{+1.490} _{-0.797}	0.0348 ^{+0.0124} _{-0.0092}	0.24 ^{+0.40} _{-0.15}
17.01	-17.1 ^{+17.2} _{-22.3}	-0.99	1832 ⁺⁰⁵⁰² ₋₀₄₀₈	1656 ⁺⁰⁴⁵⁴ ₋₀₄₅₄	-2142 ⁺⁰⁴⁶⁴ ₋₀₁₈₅	-1.116 ^{+0.372} _{-0.372}	0.864 ^{+0.420} _{-0.267}	0.0414 ^{+0.0107} _{-0.0147}	-0.14 ^{+0.13} _{-0.40}
18.01	-27.4 ^{+30.1} _{-33.2}	-0.91	1824 ⁺⁰⁵⁰⁵ ₋₀₃₉₃	1648 ⁺⁰⁴⁵⁶ ₋₀₃₅₅	-2360 ⁺⁴⁰⁸⁵ ₋₀₂₃₀	-1.215 ^{+2.003} _{-0.421}	0.729 ^{+0.667} _{-0.350}	0.0443 ^{+0.0164} _{-0.0116}	-0.32 ^{+0.33} _{-1.00}
20.01	4.7 ^{+17.2} _{-9.67}	0.49	1758 ⁺⁰⁵⁰⁵ ₋₀₃₈₄	1589 ⁺⁰⁴⁵⁶ ₋₀₃₄₇	1945 ⁺⁰²⁰⁷ ₋₃₆₆₈	1.023 ^{+0.375} _{-1.908}	1.165 ^{+1.091} _{-0.563}	0.0540 ^{+0.0196} _{-0.0142}	0.06 ^{+0.22} _{-0.08}
64.01	75.1 ^{+35.1} _{-17.4}	2.78	2716 ⁺⁰⁷⁴⁸ ₋₅₃₉₄	2454 ⁺⁰⁶⁷⁶ ₋₀₅₈₇	2853 ⁺⁰¹⁵¹ ₋₀₀₉₂	1.046 ^{+0.290} _{-0.379}	0.883 ^{+0.800} _{-0.345}	0.0323 ^{+0.0114} _{-0.0210}	0.38 ^{+0.68} _{-0.25}
97.01	66.1 ^{+17.5} _{-17.4}	3.79	1903 ⁺⁰⁴¹⁰ ₋₀₅₁₀	1719 ⁺⁰³⁷¹ ₋₀₄₉₂	2611 ⁺⁰¹⁰⁹ ₋₀₀₉₂	1.367 ^{+0.297} _{-0.297}	1.032 ^{+0.445} _{-0.485}	0.0586 ^{+0.0156} _{-0.0210}	0.77 ^{+0.50} _{-0.50}
127.01	-31.4 ^{+37.5} _{-43.9}	-0.83	1699 ⁺⁰⁴⁶⁶ ₋₀₃₆₇	1535 ⁺⁰⁴³² ₋₀₃₃₂	-2236 ⁺³⁹⁹⁶ ₋₀₂₁₉	-1.240 ^{+2.113} _{-0.431}	0.902 ^{+0.831} _{-0.428}	0.0464 ^{+0.0167} _{-0.0124}	-0.27 ^{+0.29} _{-0.86}
128.01	-8.3 ^{+8.16} _{-34.3}	-1.01	1918 ⁺⁰⁵³⁶ ₋₀₄₂₅	1735 ⁺⁰³⁸⁴ ₋₀₃₈₄	-2181 ⁺⁰²⁸⁵ ₋₀₁₉₅	-1.108 ^{+0.297} _{-0.341}	1.410 ^{+1.255} _{-0.684}	0.0593 ^{+0.0211} _{-0.0158}	-0.14 ^{+0.12} _{-0.38}
144.01	34.6 ^{+37.5} _{-34.3}	1.01	1856 ⁺⁰⁵²⁵ ₋₀₄₀₄	1677 ⁺⁰⁴⁷⁴ ₋₀₃₆₅	2702 ⁺⁰²⁸⁸ ₋₀₂₈₈	1.375 ^{+0.475} _{-0.676}	0.528 ^{+0.486} _{-0.254}	0.0524 ^{+0.0190} _{-0.0139}	1.04 ^{+2.94} _{-1.03}
183.01	14.4 ^{+40.1} _{-40.1}	0.36	1715 ⁺⁰³⁷³ ₋₀₃₃₇	1550 ⁺⁰³³⁷ ₋₀₃₃₇	2012 ⁺⁰¹³³ ₋₀₁₂₃	1.028 ^{+0.260} _{-0.260}	0.847 ^{+0.406} _{-0.406}	0.0379 ^{+0.0160} _{-0.0160}	0.08 ^{+0.26} _{-0.26}
186.01	-76.3 ^{+59.2} _{-63.7}	-1.25	1786 ⁺⁰³⁸³ ₋₀₃₈₃	1614 ⁺⁰⁴⁴⁴ ₋₀₃₄₆	-2390 ⁺⁰³⁸⁴ ₋₀₁₈₆	-1.281 ^{+0.395} _{-0.415}	1.031 ^{+0.954} _{-0.488}	0.0437 ^{+0.0161} _{-0.0114}	-0.41 ^{+0.35} _{-1.06}
188.01	-54.2 ^{+49.7} _{-52.2}	-1.09	1327 ⁺⁰³⁷⁸ ₋₀₂₉₃	1199 ⁺⁰³⁴¹ ₋₀₂₆₄	-2173 ⁺⁰⁴³⁹ ₋₀₁₇₆	-1.560 ^{+0.560} _{-0.518}	0.741 ^{+0.708} _{-0.354}	0.0459 ^{+0.0164} _{-0.0123}	-0.60 ^{+0.55} _{-1.69}
195.01	0.7 ^{+27.8} _{-1.60}	0.41	1805 ⁺⁰⁵⁰² ₋₀₃₈₇	1631 ⁺⁰⁴⁵⁴ ₋₀₃₅₀	2015 ⁺⁰¹⁷⁵ ₋₀₂₆₅	1.087 ^{+0.328} _{-0.284}	1.122 ^{+1.046} _{-0.535}	0.0437 ^{+0.0156} _{-0.0119}	0.09 ^{+0.24} _{-0.07}
196.01	63.2 ^{+32.8} _{-32.8}	2.00	2134 ⁺⁰⁵⁹⁸ ₋₀₄₆₂	1929 ⁺⁰⁵⁴¹ ₋₀₄₁₈	2397 ⁺⁰¹³³ ₋₀₁₆₅	1.103 ^{+0.322} _{-0.332}	0.925 ^{+0.853} _{-0.452}	0.0299 ^{+0.0108} _{-0.0187}	0.23 ^{+0.46} _{-0.32}
201.01	-12.0 ^{+33.5} _{-33.5}	-0.50	1658 ⁺⁰⁴⁶² ₋₀₃₆₉	1498 ⁺⁰⁴¹⁸ ₋₀₃₃₄	-2158 ⁺⁰²⁵⁹ ₋₀₁₆₅	-1.191 ^{+0.470} _{-0.495}	0.809 ^{+0.752} _{-0.391}	0.0519 ^{+0.0136} _{-0.0136}	-0.20 ^{+0.84} _{-0.84}
202.01	46.0 ^{+30.8} _{-36.1}	1.26	2424 ⁺⁰⁶⁷⁴ ₋₀₅₃₄	2190 ⁺⁰⁶⁰⁹ ₋₀₄₈₂	2354 ⁺⁰⁴⁰³ ₋₀₄₀₃	0.927 ^{+0.299} _{-0.289}	1.026 ^{+0.932} _{-0.503}	0.0290 ^{+0.0105} _{-0.0076}	0.10 ^{+0.27} _{-0.09}
203.01	-14.7 ^{+58.5} _{-58.3}	-0.25	2357 ⁺⁰⁶⁶¹ ₋₀₅₁₃	2130 ⁺⁰⁵⁹⁷ ₋₀₄₆₄	-1937 ⁺⁴¹⁰⁶ ₋₀₃₆₃	-0.695 ^{+1.647} _{-0.376}	1.251 ^{+1.173} _{-0.604}	0.0260 ^{+0.0093} _{-0.0069}	-0.01 ^{+0.09} _{-0.13}
204.01	34.4 ^{+57.2} _{-57.4}	0.60	1701 ⁺⁰⁴⁶⁹ ₋₀₃₈₇	1537 ⁺⁰⁴²⁴ ₋₀₃₄₅	2321 ⁺⁰³⁰¹ ₋₀₄₇₂	1.246 ^{+0.496} _{-0.535}	0.685 ^{+0.619} _{-0.322}	0.0424 ^{+0.0151} _{-0.0155}	0.36 ^{+1.49} _{-0.78}
214.01	-68.3 ^{+127.4} _{-153.}	-0.54	1744 ⁺⁰³⁷⁷ ₋₀₃₄₁	1576 ⁺⁰³⁴¹ ₋₀₃₄₁	-2391 ⁺⁰³²³ ₋₀₂₈₅	-1.248 ^{+0.495} _{-0.495}	1.242 ^{+0.752} _{-0.431}	0.0438 ^{+0.0115} _{-0.0115}	-0.41 ^{+0.69} _{-0.78}
217.01	-3543.0 ⁺⁴⁶³⁴ ₋₈₂₃₂	-0.72	1442 ⁺⁰³¹⁰ ₋₀₃₁₀	1303 ⁺⁰³⁵⁴ ₋₀₂₈₀	-2273 ⁺⁴²⁸⁵ ₋₀₂₅₀	-1.462 ^{+2.753} _{-0.522}	7.469 ^{+8.323} _{-3.949}	0.0481 ^{+0.0171} _{-0.0126}	-0.59 ^{+0.78} _{-1.96}
229.01	-0.3 ^{+10.2} _{-36.3}	-0.04	1873 ⁺⁰⁴⁰⁵ ₋₀₄₀₅	1693 ⁺⁰⁴⁸⁵ ₋₀₃₆₆	-2433 ⁺⁴⁴¹⁷ ₋₀₃₂₅	-1.205 ^{+2.142} _{-0.453}	0.557 ^{+0.528} _{-0.267}	0.0469 ^{+0.0169} _{-0.0123}	-0.37 ^{+0.42} _{-1.38}
254.01	-157.4 ^{+262.} _{-277.}	-0.61	1279 ⁺⁰³⁵⁶ ₋₀₂₈₁	1155 ⁺⁰³²² ₋₀₂₅₄	-1941 ⁺³⁷⁷⁴ ₋₀₂₂₁	-1.386 ^{+2.767} _{-0.528}	1.096 ^{+1.025} _{-0.520}	0.0288 ^{+0.0104} _{-0.0077}	-0.30 ^{+0.50} _{-1.16}
356.01	59.5 ^{+26.6} _{-26.6}	2.25	2544 ⁺⁰⁵⁶⁶ ₋₀₅₀₇	2299 ⁺⁰⁵⁰⁷ ₋₀₅₀₇	3043 ⁺⁰²⁴² ₋₀₂₄₂	1.186 ^{+0.376} _{-0.376}	0.497 ^{+0.235} _{-0.235}	0.0303 ^{+0.0080} _{-0.0080}	0.78 ^{+0.53} _{-0.53}
412.01	0.4 ^{+17.7} _{-0.40}	1.00	1870 ⁺⁰⁵¹¹ ₋₀₄₀₇	1689 ⁺⁰⁴⁶¹ ₋₀₃₆₈	2325 ⁺⁰²²⁴ ₋₀₂₉₁	1.221 ^{+0.373} _{-0.286}	0.614 ^{+0.560} _{-0.291}	0.0521 ^{+0.0186} _{-0.0138}	0.29 ^{+0.77} _{-0.23}
421.01	-17.1 ^{+76.9} _{-79.5}	-0.22	1644 ⁺⁰⁴⁵⁹ ₋₀₃₅₆	1485 ⁺⁰³²² ₋₀₃₂₂	-1963 ⁺⁴¹⁶⁰ ₋₀₅₃₈	-1.020 ^{+2.407} _{-0.538}	1.317 ^{+1.206} _{-0.623}	0.0533 ^{+0.0188} _{-0.0140}	-0.08 ^{+0.43} _{-0.65}
433.01	0.2 ^{+15.1} _{-0.31}	0.74	1663 ⁺⁰⁴⁶⁸ ₋₀₃₆₇	1503 ⁺⁰⁴²³ ₋₀₃₃₁	2200 ⁺⁰²⁰⁴ ₋₀₂₇₃	1.300 ^{+0.396} _{-0.249}	0.521 ^{+0.482} _{-0.249}	0.0494 ^{+0.0178} _{-0.0127}	0.30 ^{+0.79} _{-0.23}
611.01	48.9 ^{+453.} _{-200.}	0.28	1908 ⁺⁰⁵²³ ₋₀₃₀₄	1724 ⁺⁰⁴⁷³ ₋₀₂₇₅	2322 ⁺⁰⁴⁶¹ ₋₀₄₆₁	1.051 ^{+0.318} _{-0.631}	1.643 ^{+2.178} _{-0.503}	0.0441 ^{+0.0156} _{-0.0156}	0.19 ^{+1.37} _{-0.88}
667.01	1.6 ^{+15.2} _{-15.2}	0.11	1108 ⁺⁰²⁴⁶ ₋₀₂₄₆	1002 ⁺⁰²⁷⁵ ₋₀₂₂₃	2274 ⁺⁰³⁵⁷ ₋₀₃₅₇	1.998 ^{+0.563} _{-0.563}	0.555 ^{+0.266} _{-0.266}	0.0439 ^{+0.0115} _{-0.0115}	2.57 ^{+7.19} _{-2.19}
684.01	79.6 ^{+48.8} _{-48.6}	1.63	2173 ⁺⁰⁶¹⁰ ₋₀₄₇₅	1963 ⁺⁰⁵⁵¹ ₋₀₄₂₉	3461 ⁺⁰³¹⁸ ₋₀₄₅₉	1.549 ^{+0.493} _{-0.406}	0.469 ^{+0.441} _{-0.225}	0.0524 ^{+0.0189} _{-0.0140}	3.14 ^{+7.19} _{-2.38}
760.01	25.9 ^{+90.5} _{-91.0}	0.28	1521 ⁺⁰³²⁸ ₋₀₂₉₆	1375 ⁺⁰³⁹⁰ ₋₀₂₉₆	2204 ⁺⁰⁴¹² ₋₄₆₃₃	1.248 ^{+0.647} _{-2.868}	0.864 ^{+0.817} _{-0.413}	0.0581 ^{+0.0210} _{-0.0154}	0.30 ^{+2.17} _{-1.34}
767.01	95.4 ^{+71.2} _{-70.7}	1.35	1870 ⁺⁰⁴⁰³ ₋₀₄₀₃	1690 ⁺⁰⁴⁷³ ₋₀₃₆₅	2351 ⁺⁰³²² ₋₀₃₂₂	1.211 ^{+0.356} _{-0.356}	1.224 ^{+1.138} _{-0.591}	0.0394 ^{+0.0146} _{-0.0106}	0.31 ^{+0.76} _{-0.26}

Table 4.3 (continued)

KOI	L_r (ppm)	σ_{sec}	T_0 (K)	$T_{e=0}$ (K)	T_b^a (K)	T_b/T_0	R_p (R_{Jup})	a (AU)	A_{max}
801.01	$105.4^{+60.8}$	1.58	2338^{+0640}	2113^{+0586}	2622^{+0185}	$1.085^{+0.331}$	$0.885^{+0.812}$	$0.0275^{+0.0099}$	$0.31^{+0.70}$
809.01	$119.6^{+83.3}$	1.45	2314^{+0657}	2091^{+0594}	2516^{+0305}	$1.053^{+0.314}$	$1.106^{+1.007}$	$0.0271^{+0.0094}$	$0.24^{+0.51}$
813.01	$-97.2^{+144.}$	-0.67	1398^{+0388}	1263^{+0351}	-2531^{+4913}	$-1.657^{+3.273}$	$0.580^{+0.538}$	$0.0478^{+0.0173}$	$-1.60^{+2.67}$
830.01	$24.5^{+56.3}$	0.50	1191^{+0327}	1076^{+0296}	1929^{+0237}	$1.457^{+0.668}$	$0.677^{+0.278}$	$0.0423^{+0.0151}$	$0.28^{+1.25}$
838.01	$-380.4^{+319.}$	-1.30	1629^{+0460}	1472^{+0415}	-2785^{+0449}	$-1.639^{+0.501}$	$1.491^{+2.011}$	$0.0573^{+0.0210}$	$-2.02^{+1.70}$
840.01	$-38.0^{+80.7}$	-0.45	1692^{+0368}	1529^{+0332}	-2104^{+0315}	$-1.104^{+0.484}$	$0.957^{+0.892}$	$0.0403^{+0.0104}$	$-0.15^{+0.80}$
843.01	$83.6^{+67.3}$	1.36	1812^{+0501}	1638^{+0452}	3032^{+0269}	$1.611^{+0.525}$	$0.555^{+0.511}$	$0.0524^{+0.0186}$	$2.49^{+6.05}$
897.01	$106.6^{+88.8}$	1.17	2196^{+0604}	1984^{+0546}	2483^{+0205}	$1.081^{+0.465}$	$1.182^{+1.076}$	$0.0323^{+0.0115}$	$0.25^{+0.67}$
908.01	$145.4^{+85.1}$	1.83	1764^{+0491}	1594^{+0444}	2729^{+0184}	$1.520^{+0.459}$	$1.039^{+0.973}$	$0.0559^{+0.0201}$	$1.38^{+3.03}$
913.01	$23.4^{+61.1}$	0.39	1387^{+0390}	1253^{+0353}	2051^{+0260}	$1.286^{+0.367}$	$0.759^{+0.503}$	$0.0495^{+0.0129}$	$0.23^{+0.84}$
1176.01	$-33.2^{+81.8}$	-0.41	1514^{+0429}	1368^{+0385}	-1897^{+4336}	$-1.109^{+2.422}$	$0.808^{+0.773}$	$0.0279^{+0.0099}$	$-0.09^{+0.28}$
1419.01	$44.1^{+107.}$	0.48	2562^{+0720}	2315^{+0651}	2875^{+0275}	$1.022^{+0.437}$	$0.488^{+0.385}$	$0.0243^{+0.0087}$	$0.36^{+1.61}$
1459.01	$182.6^{+87.9}$	2.16	2212^{+0620}	1999^{+0560}	2461^{+0149}	$1.096^{+0.314}$	$0.556^{+0.234}$	$0.0134^{+0.0064}$	$0.34^{+0.65}$
1541.01	$1755.3^{+320.}$	5.42	2167^{+0478}	1958^{+0327}	3414^{+0187}	$1.576^{+0.252}$	$1.640^{+1.450}$	$0.0360^{+0.0131}$	$3.18^{+5.48}$
1543.01	$646.7^{+604.}$	1.12	1697^{+0485}	1533^{+0438}	3000^{+0297}	$1.676^{+0.566}$	$1.306^{+1.240}$	$0.0497^{+0.0179}$	$2.84^{+7.60}$
			-0367	-0332	-0848	$1.676^{+0.682}$	$1.306^{+0.619}$	$0.0497^{+0.0129}$	$2.84^{+2.69}$

CLM Light Curve with Eccentricity Fixed to Zero and Stellar Parameters from Isochrones

KOI	L_r (ppm)	σ_{sec}	T_0 (K)	$T_{e=0}$ (K)	T_b^a (K)	T_b/T_0	R_p (R_{Jup})	a (AU)	A_{max}
1.01	$-3.9^{+8.07}$	-0.48	1994^{+0128}	1802^{+0116}	-1727^{+3460}	$-0.857^{+1.725}$	$1.173^{+0.093}$	$0.0360^{+0.0007}$	$-0.01^{+0.03}$
2.01	$77.7^{+10.3}$	8.28	2746^{+0173}	2481^{+0156}	2865^{+0066}	$1.042^{+0.054}$	$1.039^{+0.087}$	$0.0363^{+0.0007}$	$0.37^{+0.07}$
5.01	$-3.1^{+11.8}$	-0.26	1627^{+0107}	1470^{+0097}	-2248^{+4688}	$-1.373^{+2.867}$	$0.336^{+0.085}$	$0.0562^{+0.0011}$	$-0.42^{+1.27}$
10.01	$19.6^{+31.6}$	0.58	2051^{+0143}	1854^{+0129}	2214^{+0281}	$1.069^{+0.158}$	$1.048^{+0.099}$	$0.0476^{+0.0010}$	$0.14^{+0.26}$
13.01	$125.6^{+6.31}$	15.64	4049^{+0097}	3658^{+0088}	3753^{+0055}	$0.927^{+0.016}$	$1.054^{+0.015}$	$0.0359^{+0.0009}$	$0.57^{+0.03}$
17.01	$-17.1^{+22.3}$	-0.99	1830^{+0106}	1653^{+0092}	-2146^{+0078}	$-1.165^{+0.045}$	$0.899^{+0.015}$	$0.0431^{+0.0008}$	$-0.17^{+0.18}$
18.01	$-27.4^{+30.1}$	-0.91	1826^{+0121}	1650^{+0109}	-2357^{+4075}	$-1.284^{+2.206}$	$0.760^{+0.063}$	$0.0463^{+0.0009}$	$-0.41^{+0.42}$
20.01	$4.7^{+17.2}$	0.49	1804^{+0126}	1630^{+0114}	1954^{+0199}	$1.075^{+0.129}$	$1.238^{+0.116}$	$0.0547^{+0.0011}$	$0.07^{+0.11}$
64.01	$75.1^{+35.1}$	2.78	1815^{+0108}	1640^{+0098}	2849^{+0150}	$1.571^{+0.089}$	$0.354^{+0.036}$	$0.0291^{+0.0005}$	$2.00^{+0.76}$
97.01	$66.1^{+17.4}$	3.79	1710^{+0107}	1545^{+0096}	2612^{+0095}	$1.527^{+0.092}$	$0.828^{+0.029}$	$0.0580^{+0.0012}$	$1.22^{+0.54}$
127.01	$-31.4^{+37.5}$	-0.83	1687^{+0107}	1524^{+0097}	-2237^{+4047}	$-1.319^{+2.372}$	$0.877^{+0.066}$	$0.0455^{+0.0009}$	$-0.35^{+0.39}$
128.01	$-8.3^{+8.16}$	-1.01	1585^{+0104}	1433^{+0094}	-2184^{+0191}	$-1.374^{+0.145}$	$0.923^{+0.074}$	$0.0572^{+0.0011}$	$-0.37^{+0.28}$
144.01	$34.6^{+37.5}$	1.01	1246^{+0081}	1126^{+0077}	2709^{+0915}	$2.176^{+0.249}$	$0.210^{+0.022}$	$0.0465^{+0.0010}$	$6.66^{+6.89}$
			-0085	-0077	-0915	$2.176^{+0.697}$	$0.210^{+0.021}$	$0.0465^{+0.0011}$	$6.66^{+6.48}$

Table 4.3 (continued)

KOI	L_r (ppm)	σ_{sec}	T_0 (K)	$T_{\epsilon=0}$ (K)	T_b^a (K)	T_b/T_0	R_p ($R_{J,up}$)	a (AU)	A_{max}
183.01	14.4 ^{+42.5}	0.36	1946 ⁺⁰¹³⁰	1759 ⁺⁰¹¹⁷	2018 ⁺⁰³⁰⁰	1.026 ^{+0.171}	1.091 ^{+0.089}	0.0381 ^{+0.0008}	0.08 ^{+0.10}
186.01	-76.3 ^{+59.2}	-1.25	1886 ⁺⁰¹²⁷	1704 ⁺⁰¹¹⁵	-2390 ⁺⁰³⁹⁵	-1.260 ^{+0.221}	1.156 ^{+0.100}	0.0436 ^{+0.0009}	-0.40 ^{+0.33}
188.01	-54.2 ^{+49.7}	-1.09	1439 ⁺⁰⁰⁸²	1301 ⁺⁰⁰⁷⁴	-2177 ⁺⁰⁴⁶²	-1.507 ^{+0.329}	0.864 ^{+0.050}	0.0453 ^{+0.0008}	-0.55 ^{+0.50}
195.01	0.7 ^{+27.8}	0.41	1765 ⁺⁰¹¹⁶	1595 ⁺⁰¹⁰⁵	2024 ⁺⁰¹⁷⁴	1.141 ^{+0.113}	1.048 ^{+0.081}	0.0425 ^{+0.0008}	0.11 ^{+0.13}
196.01	63.2 ^{+32.8}	2.00	2111 ⁺⁰¹³⁰	1907 ⁺⁰¹¹⁸	2394 ⁺⁰¹³⁴	1.131 ^{+0.078}	0.885 ^{+0.065}	0.0294 ^{+0.0005}	0.26 ^{+0.14}
201.01	-12.0 ^{+33.8}	-0.50	1561 ⁺⁰⁰⁹¹	1411 ⁺⁰⁰⁸²	-2153 ⁺⁰²⁶⁴	-1.371 ^{+0.184}	0.699 ^{+0.045}	0.0505 ^{+0.0010}	-0.34 ^{+0.60}
202.01	46.0 ^{+30.8}	1.26	2397 ⁺⁰¹⁶³	2166 ⁺⁰¹⁴⁸	2957 ⁺⁰¹⁶⁹	0.977 ^{+0.088}	0.994 ^{+0.089}	0.0288 ^{+0.0006}	0.13 ^{+0.10}
203.01	-14.7 ^{+58.5}	-0.25	2304 ⁺⁰¹⁵¹	2082 ⁺⁰¹³⁷	-1926 ⁺⁰³⁷⁸	-0.829 ^{+1.768}	1.172 ^{+0.093}	0.0255 ^{+0.0005}	-0.02 ^{+0.10}
204.01	34.4 ^{+57.2}	0.60	1604 ⁺⁰⁰⁹⁸	1449 ⁺⁰⁰⁸⁹	2325 ⁺⁰²⁹⁴	1.442 ^{+0.198}	0.596 ^{+0.043}	0.0415 ^{+0.0008}	0.62 ^{+1.04}
214.01	-68.3 ^{+153.}	-0.54	1612 ⁺⁰⁰⁹¹	1457 ⁺⁰⁰⁸⁵	-2401 ⁺⁰³³¹	-1.484 ^{+0.211}	1.005 ^{+0.040}	0.0422 ^{+0.0008}	-0.81 ^{+1.41}
217.01	-3543.0 ⁺⁴⁶³⁴	-0.72	1607 ⁺⁰¹⁰⁰	1452 ⁺⁰⁰⁹⁰	-2274 ⁺⁰²⁹¹	-1.408 ^{+0.657}	9.656 ^{+3.992}	0.0479 ^{+0.0009}	-0.50 ^{+0.67}
229.01	-0.3 ^{+10.2}	-0.04	1708 ⁺⁰¹¹¹	1543 ⁺⁰¹⁰⁰	-2435 ⁺⁰⁴¹⁹	-1.420 ^{+2.575}	0.447 ^{+0.039}	0.0456 ^{+0.0009}	-0.71 ^{+0.82}
254.01	-157.4 ^{+262.}	-0.61	962 ⁺⁰¹⁵⁵	869 ⁺⁰¹⁴⁰	-1944 ⁺³⁷⁸⁸	-1.959 ^{+0.199}	0.538 ^{+0.211}	0.0250 ^{+0.0035}	-1.22 ^{+2.35}
356.01	59.5 ^{+27.0}	2.25	1857 ⁺⁰¹⁰⁹	1678 ⁺⁰⁰⁹⁹	3044 ⁺⁰¹⁹³	1.641 ^{+0.198}	0.245 ^{+0.018}	0.0279 ^{+0.0005}	2.95 ^{+1.37}
412.01	0.4 ^{+17.7}	1.00	1612 ⁺⁰¹⁰⁴	1456 ⁺⁰⁰⁹⁴	2323 ⁺⁰²⁹¹	1.437 ^{+0.151}	0.441 ^{+0.040}	0.0502 ^{+0.0010}	0.59 ^{+0.66}
421.01	-17.1 ^{+76.9}	-0.22	1401 ⁺⁰⁰⁸⁷	1266 ⁺⁰⁰⁷⁸	-1956 ⁺⁰¹⁵³	-1.388 ^{+2.959}	0.913 ^{+0.060}	0.0508 ^{+0.0010}	-0.22 ^{+0.88}
433.01	0.2 ^{+15.1}	0.74	1471 ⁺⁰⁰⁸⁹	1329 ⁺⁰⁰⁸¹	2202 ⁺⁰²⁰⁴	1.496 ^{+0.145}	0.392 ^{+0.032}	0.0477 ^{+0.0009}	0.55 ^{+0.60}
611.01	48.9 ^{+453.}	0.28	2079 ⁺⁰¹⁴⁰	1878 ⁺⁰¹²⁷	2295 ⁺⁰⁴⁷⁹	1.094 ^{+0.246}	2.128 ^{+1.279}	0.0450 ^{+0.0009}	0.19 ^{+0.69}
667.01	1.6 ^{+15.2}	0.11	912 ⁺⁰¹²⁶	824 ⁺⁰¹¹⁴	2283 ⁺⁰²³⁴	2.488 ^{+0.395}	0.350 ^{+0.099}	0.0411 ^{+0.0031}	6.60 ^{+5.29}
684.01	79.6 ^{+48.8}	1.63	1512 ⁺⁰⁰⁹¹	1366 ⁺⁰⁰⁸²	3472 ⁺⁰³⁰⁸	2.298 ^{+0.206}	0.209 ^{+0.018}	0.0482 ^{+0.0009}	15.70 ^{+9.92}
760.01	25.9 ^{+90.5}	0.28	1670 ⁺⁰¹¹²	1509 ⁺⁰¹⁰¹	2214 ⁺⁰⁴⁶³	1.314 ^{+0.266}	1.047 ^{+0.092}	0.0583 ^{+0.0011}	0.33 ^{+1.07}
767.01	95.4 ^{+71.2}	1.35	1758 ⁺⁰¹⁰³	1589 ⁺⁰⁰⁹³	2353 ⁺⁰¹⁷¹	1.334 ^{+0.276}	1.047 ^{+0.067}	0.0383 ^{+0.0007}	0.47 ^{+0.36}
801.01	105.4 ^{+66.4}	1.58	2135 ⁺⁰¹²⁹	1930 ⁺⁰¹¹⁶	2622 ⁺⁰³¹⁸	1.225 ^{+0.156}	0.711 ^{+0.065}	0.0267 ^{+0.0005}	0.53 ^{+0.35}
809.01	119.6 ^{+82.9}	1.45	2290 ⁺⁰¹³²	2069 ⁺⁰¹³⁵	2514 ⁺⁰¹⁸²	1.093 ^{+0.095}	1.069 ^{+0.087}	0.0268 ^{+0.0005}	0.28 ^{+0.20}
813.01	-97.2 ^{+136.}	-0.67	1543 ⁺⁰⁰⁹²	1394 ⁺⁰⁰⁸³	-2941 ⁺⁰³⁴⁰	-1.647 ^{+3.190}	0.698 ^{+0.055}	0.0472 ^{+0.0008}	-1.56 ^{+2.46}
830.01	24.5 ^{+56.3}	0.50	1403 ⁺⁰⁰⁸²	1268 ⁺⁰⁰⁷⁴	1936 ⁺⁰²³⁵	1.379 ^{+0.182}	0.946 ^{+0.054}	0.0424 ^{+0.0008}	0.21 ^{+0.40}
838.01	-380.4 ^{+319.}	-1.30	1632 ⁺⁰¹⁰⁷	1475 ⁺⁰⁰⁹⁶	-2783 ⁺⁰⁴³⁰	-1.700 ^{+0.276}	1.656 ^{+0.321}	0.0570 ^{+0.0011}	-2.40 ^{+1.77}
840.01	-38.0 ^{+84.0}	-0.45	1473 ⁺⁰⁰⁸⁸	1331 ⁺⁰⁰⁷⁹	-2112 ⁺⁰³⁰⁵	-1.428 ^{+0.227}	0.695 ^{+0.050}	0.0384 ^{+0.0007}	-0.39 ^{+0.93}
843.01	83.6 ^{+67.3}	1.36	1713 ⁺⁰¹⁰⁸	1548 ⁺⁰⁰⁹⁸	3027 ⁺⁰²⁷⁷	1.762 ^{+0.178}	0.487 ^{+0.053}	0.0516 ^{+0.0009}	3.63 ^{+2.97}
897.01	106.6 ^{+88.8}	1.17	2137 ⁺⁰¹⁴¹	1931 ⁺⁰¹²⁸	2474 ⁺⁰²¹³	1.152 ^{+0.114}	1.098 ^{+0.093}	0.0319 ^{+0.0010}	0.32 ^{+0.29}
908.01	145.4 ^{+85.1}	1.83	1463 ⁺⁰⁰⁸⁷	1322 ⁺⁰⁰⁷⁹	2727 ⁺⁰¹⁸¹	1.862 ^{+0.236}	0.689 ^{+0.050}	0.0537 ^{+0.0010}	3.29 ^{+1.90}
					2727 ⁺⁰²⁶³	1.862 ^{+0.189}			-1.80

Table 4.3 (continued)

KOI	L_r (ppm)	σ_{sec}	T_0 (K)	$T_{e=0}$ (K)	T_b^a (K)	T_b/T_0	R_p (R_{Jup})	a (AU)	A_{max}
913.01	23.4 ^{+56.7}	0.39	1566 ⁺⁰⁰⁹⁵	1415 ⁺⁰⁰⁸⁶	2040 ⁺⁰³³¹	1.297 ^{+0.234}	0.955 ^{+0.065}	0.0492 ^{+0.0009}	0.21 ^{+0.59}
1176.01	-33.2 ^{+81.8}	-0.41	1533 ⁺⁰¹¹⁰	1389 ⁺⁰⁰⁹⁹	-1897 ⁺³⁸⁸⁴	-1.235 ^{-0.201}	0.829 ^{+0.071}	0.0278 ^{+0.0006}	-0.13 ^{+0.33}
1419.01	44.1 ^{+90.3}	0.48	2552 ⁺⁰¹⁷⁶	2300 ⁺⁰¹⁵⁹	2882 ⁺⁰²⁷⁵	1.125 ^{-2.205}	0.483 ^{+0.068}	0.0242 ^{+0.0005}	0.52 ^{+0.98}
1459.01	182.6 ^{+87.9}	2.16	1588 ⁺⁰²³¹	1435 ⁺⁰²⁰⁹	2458 ⁺⁰¹⁵²	1.542 ^{+0.209}	0.248 ^{+0.079}	0.0117 ^{+0.0011}	1.37 ^{+1.04}
1541.01	1755.3 ^{+320.}	5.42	2337 ⁺⁰¹⁶²	2112 ⁺⁰¹⁴⁷	3411 ⁺⁰¹¹⁸	1.459 ^{+0.080}	1.945 ^{+0.186}	0.0367 ^{+0.0008}	2.35 ^{+0.96}
1543.01	646.7 ^{-578.}	1.12	1763 ⁻⁰¹¹¹	1593 ⁻⁰¹⁰³	2996 ⁻⁰³⁰⁷	1.696 ^{-0.458}	1.405 ^{-0.105}	0.0499 ^{-0.0009}	3.05 ^{-2.78}
PDC Light Curve with Eccentricity Free and Stellar Parameters from the KIC									
2.01	41.1 ^{+9.23}	9.03	2702 ⁺⁰⁷⁵⁹	2441 ⁺⁰⁶⁸⁶	2842 ⁺⁰⁶⁶²	1.052 ^{+0.294}	1.022 ^{+0.356}	0.0367 ^{+0.0132}	0.37 ^{+0.63}
5.01	16.9 ^{+16.8}	0.76	2139 ⁺⁰⁵⁹⁷	1932 ⁺⁰⁴¹¹	2760 ⁻⁰⁸⁵⁸	1.225 ^{-0.556}	0.622 ^{-0.497}	0.0586 ^{+0.0154}	0.62 ^{+0.80}
10.01	-85.6 ^{+52.1}	1.20	1993 ⁺⁰⁵⁴⁶	1801 ⁺⁰⁴⁹³	2445 ⁺⁰²¹¹	1.181 ^{+0.375}	0.990 ^{+0.306}	0.0471 ^{+0.0172}	0.33 ^{+0.82}
13.01	82.4 ^{+6.86}	16.39	5069 ⁺¹⁴¹⁴	4580 ⁺¹²⁷⁸	3750 ⁺⁰⁰⁵⁴	0.740 ^{+0.212}	1.606 ^{+1.520}	0.0348 ^{+0.0124}	0.23 ^{+0.40}
18.01	-118.8 ^{+75.4}	1.01	1827 ⁺⁰⁵¹⁴	1651 ⁺⁰⁴⁶⁴	2518 ⁺⁰²⁵⁴	1.339 ^{+0.431}	0.738 ^{+0.692}	0.0446 ^{+0.0092}	0.61 ^{+1.59}
64.01	16.6 ^{+39.3}	1.46	2711 ⁺⁰⁶⁹⁸	2449 ⁺⁰⁵¹⁷	2553 ⁺⁰³³⁴	0.909 ^{+0.367}	0.846 ^{+0.515}	0.0324 ^{+0.0083}	0.14 ^{+0.54}
97.01	62.3 ^{+19.7}	4.22	1899 ⁺⁰⁵²⁷	1716 ⁺⁰³⁷⁰	2556 ⁺⁰⁰⁹⁵	1.342 ^{-0.294}	1.038 ^{+0.946}	0.0579 ^{+0.0214}	0.66 ^{+1.10}
102.01	25.2 ^{+12.8}	2.11	3325 ⁺⁰⁹⁵⁷	3005 ⁺⁰⁸⁶⁵	2995 ⁺⁰¹⁷⁴	0.886 ^{+0.254}	0.625 ^{+0.584}	0.0302 ^{+0.0109}	0.21 ^{+0.42}
144.01	-4.9 ^{+82.7}	1.74	1865 ⁺⁰⁵¹⁷	1685 ⁺⁰⁴⁶⁷	3049 ⁺⁰²⁴⁷	1.601 ^{+0.474}	0.608 ^{+0.540}	0.0524 ^{+0.0185}	2.77 ^{+5.82}
186.01	-49.7 ^{+92.0}	-0.80	1793 ⁺⁰⁴⁸⁶	1620 ⁻⁰⁴⁵⁹	-2266 ⁺⁴²⁷⁵	-1.168 ^{+2.187}	1.080 ^{+0.895}	0.0438 ^{+0.0157}	-0.23 ^{+0.31}
188.01	66.5 ^{+61.3}	1.67	1332 ⁺⁰³⁶⁷	1204 ⁺⁰²⁶⁰	2265 ⁻⁰²²¹	1.663 ^{-0.417}	0.771 ^{+0.210}	0.0459 ^{+0.0165}	0.94 ^{+2.00}
195.01	103.0 ^{+66.0}	2.10	1799 ⁺⁰⁵⁰⁴	1620 ⁺⁰⁴⁵⁶	2477 ⁺⁰¹³⁵	1.360 ^{-0.398}	1.117 ^{+0.967}	0.0435 ^{+0.0123}	0.60 ^{+1.24}
196.01	82.1 ^{+33.9}	3.76	2132 ⁺⁰⁵⁹⁹	1927 ⁺⁰⁵⁴²	2490 ⁺⁰⁰⁹⁴	1.162 ^{+0.327}	0.951 ^{+0.857}	0.0298 ^{+0.0108}	0.34 ^{+0.59}
199.01	60.0 ^{+40.2}	1.00	1871 ⁺⁰⁵²³	1690 ⁺⁰⁴⁷²	2432 ⁺⁰²¹⁶	1.209 ^{+0.429}	0.828 ^{+0.763}	0.0442 ^{+0.0159}	0.36 ^{+1.08}
201.01	-123.5 ^{+47.4}	-1.23	1638 ⁺⁰³⁵¹	1480 ⁻⁰³¹⁸	-2451 ⁻⁰¹⁹⁷	-1.427 ^{-0.467}	0.787 ^{+0.372}	0.0518 ^{+0.0135}	-0.72 ^{+1.87}
202.01	67.9 ^{+34.8}	2.88	2416 ⁺⁰⁵²⁹	2183 ⁺⁰⁴⁷⁸	2537 ⁺⁰¹³²	1.042 ^{+0.295}	1.072 ^{+0.512}	0.0290 ^{+0.0104}	0.23 ^{+0.42}
204.01	-100.6 ^{+47.0}	-1.13	1706 ⁺⁰⁴⁷⁶	1542 ⁺⁰⁴³⁰	-2353 ⁻⁰¹⁹⁷	-1.325 ^{+0.442}	0.779 ^{+0.724}	0.0431 ^{+0.0154}	-0.46 ^{+0.40}
229.01	114.2 ^{+54.5}	1.57	1872 ⁺⁰⁵²⁴	1691 ⁺⁰⁴⁷⁴	2930 ⁺⁰²²⁴	1.517 ^{+0.466}	0.563 ^{+0.524}	0.0468 ^{+0.0168}	1.74 ^{+3.95}
356.01	39.1 ^{+23.3}	1.30	2565 ⁺⁰⁵⁷⁶	2318 ⁺⁰²³⁵	2727 ⁺⁰²⁵⁵	1.017 ^{+0.400}	0.580 ^{+0.296}	0.0304 ^{+0.0124}	0.29 ^{+0.44}
412.01	21.5 ^{+72.5}	0.98	1879 ⁺⁰⁵²³	1698 ⁺⁰⁴⁷³	2715 ⁺⁰²⁸³	1.357 ^{+0.485}	0.739 ^{+0.672}	0.0520 ^{+0.0188}	0.90 ^{+2.75}
421.01	-134.5 ^{+119.}	-1.59	1652 ⁺⁰⁴⁶³	1493 ⁻⁰³²⁶	-2412 ⁻⁰¹⁵⁷	-1.422 ^{-0.382}	1.382 ^{+1.297}	0.0534 ^{+0.0136}	-0.67 ^{+0.52}
433.01	92.6 ^{+381.}	1.29	1666 ⁺⁰⁴⁵⁹	1505 ⁺⁰³³³	3343 ⁺⁰³⁹⁴	1.954 ^{+0.648}	0.573 ^{+0.511}	0.0493 ^{+0.0176}	7.25 ^{+19.31}
									-5.69

Table 4.3 (continued)

KOI	L_r (ppm)	σ_{sec}	T_0 (K)	$T_{\epsilon=0}$ (K)	T_b^a (K)	T_b/T_0	R_p ($R_{J,up}$)	a (AU)	A_{max}
611.01	105.7 ^{+52.3} _{-33.3}	1.97	1912 ⁺⁰⁵²⁴ ₋₀₄₁₂	1728 ⁺⁰⁴⁷⁴ ₋₀₃₇₅	2820 ⁺⁰¹⁷⁴ ₋₀₂₁₄	1.450 ^{+0.418} _{-0.332}	0.746 ^{+0.658} _{-0.383}	0.0444 ^{+0.0157} _{-0.0177}	1.26 ^{+2.53} _{-0.88}
684.01	72.1 ^{+38.8} _{-43.5}	1.44	2180 ⁺⁰⁵⁹³ ₋₀₄₆₉	1970 ⁺⁰⁵³⁵ ₋₀₄₂₄	3095 ⁺⁰²⁷⁷ ₋₀₄₃₄	1.382 ^{+0.432} _{-0.384}	0.871 ^{+0.903} _{-0.432}	0.0523 ^{+0.0186} _{-0.0138}	1.48 ^{+1.17} _{-0.49}
760.01	10.6 ^{+11.8} _{-83.6}	0.27	1522 ⁺⁰⁴³⁶ ₋₀₃₂₉	1375 ⁺⁰³⁹⁴ ₋₀₂₉₇	2307 ⁺⁰³⁸⁸ ₋₄₆₈₇	1.339 ^{+0.624} _{-2.895}	0.883 ^{+0.842} _{-0.424}	0.0580 ^{+0.0209} _{-0.0152}	0.48 ^{+2.71} _{-1.30}
801.01	158.2 ^{+66.5} _{-63.4}	1.46	2343 ⁺⁰⁶⁵⁴ ₋₀₅₀₆	2117 ⁺⁰⁵⁹¹ ₋₀₄₅₈	2578 ⁺⁰¹⁸⁶ ₋₀₃₅₆	1.057 ^{+0.895} _{-0.300}	0.913 ^{+0.850} _{-0.431}	0.0274 ^{+0.0099} _{-0.0073}	0.27 ^{+0.61} _{-0.22}
809.01	-338.7 ^{+105.} _{-141.}	-2.62	2328 ⁺⁰⁶³⁴ ₋₀₃₄₁	2103 ⁺⁰⁵⁷² ₋₀₃₄₁	-2734 ⁺⁰¹⁷⁰ ₋₀₁₇₂	-1.166 ^{+0.260} _{-3.057}	1.183 ^{+1.089} _{-0.562}	0.0272 ^{+0.0095} _{-0.0171}	-0.48 ^{+0.32} _{-0.66}
813.01	-201.4 ^{+125.} _{-133.}	-1.08	1397 ⁺⁰³⁰⁴ ₋₀₃₃₂	1262 ⁺⁰²⁷⁵ ₋₀₂₃₀	-2653 ⁺⁰²⁴⁷ ₋₀₂₄₇	-1.782 ^{+0.607} _{-0.584}	0.615 ^{+0.290} _{-0.290}	0.0477 ^{+0.0176} _{-0.0148}	-2.43 ^{+6.93} _{-6.93}
830.01	59.6 ^{+133.} _{-144.}	1.19	1187 ⁺⁰³³² ₋₀₂₅₈	1072 ⁺⁰²³³ ₋₀₂₃₃	2243 ⁺⁰¹⁷⁰ ₋₀₅₄₅	1.791 ^{+0.731} _{-0.731}	0.722 ^{+0.655} _{-0.342}	0.0420 ^{+0.0111} _{-0.0111}	1.26 ^{+3.35} _{-1.20}
838.01	22.4 ^{+221.} _{-220.}	0.13	1639 ⁺⁰⁴⁶⁰ ₋₀₃₆₀	1481 ⁺⁰⁴¹⁶ ₋₀₃₂₅	1804 ⁺⁰²²¹ ₋₃₅₅₆	0.989 ^{+0.407} _{-2.025}	1.219 ^{+1.228} _{-0.615}	0.0571 ^{+0.0206} _{-0.0147}	0.04 ^{+0.17} _{-0.07}
840.01	-115.8 ^{+154.} _{-152.}	-0.93	1699 ⁺⁰⁴⁷² ₋₀₃₆₄	1535 ⁺⁰⁴²⁶ ₋₀₃₂₉	-2317 ⁺⁰¹⁰⁰ ₋₀₂₂₀	-1.281 ^{+2.168} _{-0.439}	1.067 ^{+0.995} _{-0.502}	0.0402 ^{+0.0142} _{-0.0104}	-0.39 ^{+0.42} _{-1.18}
843.01	-47.2 ^{+58.0} _{-58.0}	-0.24	1811 ⁺⁰³⁹⁷ ₋₀₃₇₄	1637 ⁺⁰³⁵¹ ₋₀₃₅₁	-2406 ⁺⁰²⁹³ ₋₀₂₉₃	-1.265 ^{+0.443} _{-0.443}	0.598 ^{+0.284} _{-0.284}	0.0524 ^{+0.0138} _{-0.0138}	-0.42 ^{+0.35} _{-0.35}
897.01	-31.5 ^{+112.} _{-94.2}	1.11	2181 ⁺⁰⁶⁰⁹ ₋₀₄₇₄	1970 ⁺⁰⁵⁵¹ ₋₀₄₅₂	2455 ⁺⁰²²¹ ₋₀₄₈₃	1.073 ^{+0.359} _{-0.366}	1.154 ^{+1.073} _{-0.550}	0.0323 ^{+0.0117} _{-0.0087}	0.23 ^{+0.64} _{-0.21}
908.01	93.8 ^{+62.7} _{-87.9}	1.00	1762 ⁺⁰⁵⁰⁰ ₋₀₃₈₀	1592 ⁺⁰⁴⁵² ₋₀₃₄₃	2462 ⁺⁰²¹⁹ ₋₄₃₂₇	1.312 ^{+0.450} _{-2.188}	1.094 ^{+1.033} _{-0.523}	0.0565 ^{+0.0204} _{-0.0150}	0.53 ^{+1.54} _{-0.57}
913.01	103.9 ^{+88.0} _{-114.}	1.16	1388 ⁺⁰³⁸⁹ ₋₀₂₉₉	1254 ⁺⁰³⁵² ₋₀₂₇₁	2292 ⁺⁰¹⁸² ₋₀₅₁₂	1.572 ^{+0.521} _{-0.621}	0.852 ^{+0.795} _{-0.411}	0.0494 ^{+0.0183} _{-0.0133}	0.78 ^{+2.11} _{-0.74}
931.01	-65.0 ^{+83.4} _{-118.}	1.06	1460 ⁺⁰⁴⁰⁵ ₋₀₆₇₄	1320 ⁺⁰³⁶⁶ ₋₀₂₁₄	2357 ⁺⁰²¹² ₋₀₄₂₄	1.546 ^{+0.505} _{-0.389}	0.822 ^{+0.644} _{-0.320}	0.0484 ^{+0.0135} _{-0.0135}	0.82 ^{+2.22} _{-0.51}
961.02	13.3 ^{+83.6} _{-83.6}	0.10	2358 ⁺⁰⁵⁰⁷ ₋₀₄₁₂	2131 ⁺⁰⁶⁰⁹ ₋₀₄₅₉	2223 ⁺⁰⁴²³ ₋₄₅₆₈	0.837 ^{+0.889} _{-1.838}	0.339 ^{+0.320} _{-0.162}	0.0098 ^{+0.0034} _{-0.0026}	0.08 ^{+0.25} _{-0.25}
961.03	-0.1 ^{+65.9} _{-41.5}	0.00	1478 ⁺⁰⁴¹² ₋₀₃₂₇	1336 ⁺⁰³⁷² ₋₀₂₉₅	1629 ⁺⁰²⁷⁹ ₋₃₄₁₈	0.941 ^{+0.493} _{-2.185}	1.617 ^{+1.093} _{-0.646}	0.0254 ^{+0.0092} _{-0.0067}	0.02 ^{+0.18} _{-0.11}
1419.01	54.9 ^{+52.7} _{-53.4}	1.66	2572 ⁺⁰⁷⁰⁶ ₋₀₅₆₄	2324 ⁺⁰⁶³⁸ ₋₀₅₁₀	3007 ⁺⁰²³⁵ ₋₀₃₅₁	1.143 ^{+0.344} _{-0.291}	0.696 ^{+0.646} _{-0.340}	0.0244 ^{+0.0087} _{-0.0065}	0.61 ^{+1.32} _{-0.46}
1459.01	843.8 ^{+196.} _{-196.}	1.74	2189 ⁺⁰⁶²² ₋₀₄₇₀	1978 ⁺⁰⁵⁶² ₋₀₄₂₄	2345 ⁺⁰¹⁷² ₋₀₂₂₃	1.052 ^{+0.310} _{-0.263}	0.972 ^{+1.042} _{-0.494}	0.0132 ^{+0.0048} _{-0.0035}	0.23 ^{+0.50} _{-0.17}

PDC Light Curve with Eccentricity Free and Stellar Parameters from Isochrones									
2.01	41.1 ^{+9.23} _{-8.67}	9.03	2747 ⁺⁰¹⁷¹ ₋₀₁₇₀	2482 ⁺⁰¹⁵⁵ ₋₀₁₅₄	2841 ⁺⁰⁰⁶¹ ₋₀₀₆₃	1.033 ^{+0.055} _{-0.046}	1.042 ^{+0.088} _{-0.086}	0.0363 ^{+0.0007} _{-0.0007}	0.35 ^{+0.07} _{-0.05}
5.01	16.9 ^{+30.4} _{-16.8}	0.76	1627 ⁺⁰¹⁰⁶ ₋₀₀₉₅	1470 ⁺⁰⁰⁹⁶ ₋₀₀₈₆	2760 ⁺⁰³²⁸ ₋₀₈₂₇	1.686 ^{+0.219} _{-0.594}	0.341 ^{+0.029} _{-0.024}	0.0562 ^{+0.0011} _{-0.0010}	2.27 ^{+2.86} _{-2.7}
10.01	-85.6 ^{+52.1} _{-52.1}	1.20	2050 ⁺⁰¹²⁹ ₋₀₁₀₀	1852 ⁺⁰¹¹⁷ ₋₀₁₁₇	2446 ⁺⁰³⁶¹ ₋₀₃₆₁	1.186 ^{+0.182} _{-0.182}	1.057 ^{+0.087} _{-0.087}	0.0476 ^{+0.0009} _{-0.0009}	0.34 ^{+0.26} _{-0.26}
13.01	82.4 ^{+7.79} _{-75.4}	16.39	4047 ⁺⁰¹⁰⁰ ₋₀₁₀₀	3657 ⁺⁰⁰⁹⁰ ₋₀₀₉₀	3749 ⁺⁰⁰⁵⁷ ₋₀₀₅₇	0.927 ^{+0.015} _{-0.015}	1.057 ^{+0.014} _{-0.014}	0.0359 ^{+0.0003} _{-0.0003}	0.57 ^{+0.03} _{-0.04}
18.01	-118.8 ^{+45.6} _{-45.6}	1.01	1828 ⁺⁰¹¹⁸ ₋₀₁₁₂	1652 ⁺⁰¹⁰⁶ ₋₀₁₀₁	2517 ⁺⁰³⁶⁸ ₋₀₃₆₈	1.375 ^{+0.151} _{-0.215}	0.767 ^{+0.064} _{-0.056}	0.0463 ^{+0.0009} _{-0.0009}	0.70 ^{+0.76} _{-0.53}
64.01	16.6 ^{+37.5} _{-39.1}	1.46	1817 ⁺⁰¹⁰⁶ ₋₀₁₀₁	1642 ⁺⁰⁰⁹⁶ ₋₀₀₉₂	2548 ⁺⁰¹⁸⁶ ₋₀₃₃₈	1.400 ^{+0.112} _{-0.186}	0.342 ^{+0.027} _{-0.023}	0.0292 ^{+0.0005} _{-0.0005}	0.83 ^{+0.58} _{-0.58}
97.01	62.3 ^{+18.7} _{-18.7}	4.22	1710 ⁺⁰¹⁴⁸ ₋₀₁₄₈	1545 ⁺⁰⁰⁹⁷ ₋₀₀₉₇	2555 ⁺⁰⁰⁸⁸ ₋₀₀₈₈	1.493 ^{+0.085} _{-0.085}	0.837 ^{+0.067} _{-0.067}	0.0580 ^{+0.0012} _{-0.0012}	1.02 ^{+0.27} _{-0.27}
102.01	25.2 ^{+12.8} _{-14.1}	2.11	2394 ⁺⁰¹⁶⁵ ₋₀₁₆₅	2163 ⁺⁰¹⁴⁹ ₋₀₁₄₉	2997 ⁺⁰¹⁷⁴ ₋₀₁₇₄	1.247 ^{+0.090} _{-0.118}	0.310 ^{+0.032} _{-0.027}	0.0290 ^{+0.0006} _{-0.0006}	0.88 ^{+0.42} _{-0.41}
144.01	-4.9 ^{+82.7} _{-92.6}	1.74	1244 ⁺⁰⁰⁸⁴ ₋₀₀₈₃	1124 ⁺⁰⁰⁷⁶ ₋₀₀₇₅	3042 ⁺⁰²⁵¹ ₋₀₂₅₁	2.459 ^{+0.206} _{-0.289}	0.240 ^{+0.017} _{-0.019}	0.0465 ^{+0.0010} _{-0.0011}	15.80 ^{+10.17} _{-9.16}
186.01	-49.7 ^{+92.0} _{-79.0}	-0.80	1888 ⁺⁰¹²⁵ ₋₀₁₁₆	1706 ⁺⁰¹¹³ ₋₀₁₀₅	-2257 ⁺⁰²⁷³ ₋₀₂₃₉	-1.190 ^{+0.251} _{-0.143}	1.200 ^{+0.100} _{-0.089}	0.0436 ^{+0.0008} _{-0.0008}	-0.25 ^{+0.33} _{-0.33}

Table 4.3 (continued)

KOI	L_r (ppm)	σ_{sec}	T_0 (K)	$T_{\epsilon=0}$ (K)	T_b^a (K)	T_b/T_0	R_p ($R_{J,up}$)	a (AU)	A_{max}
188.01	66.5 ^{+53.2} _{-3.2}	1.67	1438 ⁺⁰⁰⁸⁴ ₋₀₀₇₄	1299 ⁺⁰⁰⁷⁶ ₋₀₀₇₄	2265 ⁺⁰¹⁴⁰ ₋₀₂₃₀	1.572 ^{+0.114} _{-0.160}	0.891 ^{+0.051} _{-0.081}	0.0453 ^{+0.0008} _{-0.0008}	0.80 ^{+0.48} _{-0.37}
195.01	103.0 ^{+66.0} _{-65.8}	2.10	1766 ⁺⁰¹¹⁵ ₋₀₁₀₀	1596 ⁺⁰¹⁰⁴ ₋₀₀₉₀	2481 ⁺⁰¹³⁶ ₋₀₁₈₅	1.399 ^{+0.098} _{-0.118}	1.047 ^{+0.081} _{-0.063}	0.0425 ^{+0.0008} _{-0.0008}	0.71 ^{+0.34} _{-0.34}
196.01	82.1 ^{+33.9} _{-31.2}	3.76	2109 ⁺⁰¹³³ ₋₀₁₂₀	1906 ⁺⁰¹²⁰ ₋₀₁₀₈	2490 ⁺⁰⁰⁹³ ₋₀₁₀₂	1.179 ^{+0.063} _{-0.065}	0.917 ^{+0.068} _{-0.056}	0.0294 ^{+0.0006} _{-0.0005}	0.36 ^{+0.11} _{-0.10}
199.01	60.0 ^{+40.2} _{-64.9}	1.00	2140 ⁺⁰¹⁵¹ ₋₀₁₄₀	1933 ⁺⁰¹³⁷ ₋₀₁₂₆	2431 ⁺⁰²²⁰ ₋₄₄₄₉	1.126 ^{+0.130} _{-2.056}	1.112 ^{+0.108} _{-0.096}	0.0456 ^{+0.0010} _{-0.0009}	0.28 ^{+0.29} _{-0.32}
201.01	-123.5 ^{+53.4} _{-54.3}	-1.23	1559 ⁺⁰⁰⁹⁶ ₋₀₁₀₇	1409 ⁺⁰⁰⁸⁷ ₋₀₁₀₇	-2452 ⁺⁰⁴⁵⁸ ₋₀₁₀₇	-1.567 ^{+0.299} _{-0.067}	0.700 ^{+0.050} _{-0.065}	0.0504 ^{+0.0009} _{-0.0009}	-1.09 ^{+0.93} _{-0.86}
202.01	67.9 ^{+34.8} _{-34.8}	2.88	2398 ⁺⁰¹⁴⁶ ₋₀₁₅₉	2167 ⁺⁰¹³² ₋₀₁₄₄	2539 ⁺⁰¹³⁵ ₋₀₁₃₅	1.056 ^{+0.071} _{-0.067}	1.052 ^{+0.078} _{-0.082}	0.0288 ^{+0.0006} _{-0.0006}	0.25 ^{+0.09} _{-0.09}
204.01	-100.6 ^{+47.0} _{-49.2}	-1.13	1603 ⁺⁰⁰⁹⁹ ₋₀₀₈₇	1449 ⁺⁰⁰⁹⁰ ₋₀₀₇₉	-2351 ⁺⁰⁴⁵¹ ₋₀₂₀₂	-1.463 ^{+0.288} _{-0.138}	0.666 ^{+0.045} _{-0.039}	0.0415 ^{+0.0008} _{-0.0007}	-0.69 ^{+0.60} _{-0.66}
229.01	114.2 ^{+53.8} _{-54.5}	1.57	1708 ⁺⁰¹⁰⁶ ₋₀₀₉₇	1544 ⁺⁰⁰⁹⁶ ₋₀₀₈₈	2927 ⁺⁰²²⁵ ₋₀₃₅₀	1.709 ^{+0.144} _{-0.231}	0.457 ^{+0.035} _{-0.029}	0.0456 ^{+0.0008} _{-0.0008}	2.94 ^{+1.88} _{-1.92}
356.01	39.1 ^{+26.7} _{-33.3}	1.30	1856 ⁺⁰¹¹⁰ ₋₀₁₀₆	1677 ⁺⁰⁰⁹⁹ ₋₀₀₉₆	2731 ⁺⁰²²⁴ ₋₀₅₁₇	1.469 ^{+0.130} _{-0.279}	0.278 ^{+0.029} _{-0.025}	0.0279 ^{+0.0005} _{-0.0005}	1.33 ^{+0.99} _{-1.10}
412.01	21.5 ^{+78.0} _{-119.0}	0.98	1614 ⁺⁰⁰⁹⁰ ₋₀₀₈₅	1458 ⁺⁰⁰⁸¹ ₋₀₀₇₇	2715 ⁺⁴²⁹⁸ ₋₀₁₅₇	1.675 ^{+2.628} _{-0.124}	0.522 ^{+0.034} _{-0.061}	0.0503 ^{+0.0009} _{-0.0010}	2.12 ^{+2.13} _{-2.13}
421.01	-134.5 ^{+104.} _{-123.}	-1.59	1400 ⁺⁰⁰⁷⁸ ₋₀₀₈₀	1265 ⁺⁰⁰⁷⁷ ₋₀₀₇₂	-2410 ⁺⁰²⁵⁸ ₋₀₅₁₃	-1.717 ^{+0.193} _{-0.356}	0.942 ^{+0.029} _{-0.025}	0.0508 ^{+0.0010} _{-0.0009}	-1.48 ^{+0.93} _{-0.92}
433.01	92.6 ^{+38.1} _{-42.3}	1.29	1471 ⁺⁰⁰⁹⁰ ₋₀₀₈₀	1329 ⁺⁰⁰⁸¹ ₋₀₀₇₂	3333 ⁺⁰³⁹⁶ ₋₀₅₁₃	2.271 ^{+0.269} _{-0.356}	0.430 ^{+0.029} _{-0.025}	0.0477 ^{+0.0009} _{-0.0008}	13.67 ^{+13.38} _{-9.38}
611.01	105.7 ^{+52.3} _{-53.3}	1.97	2080 ⁺⁰¹⁴⁵ ₋₀₁₃₅	1879 ⁺⁰¹³¹ ₋₀₁₂₂	2812 ⁺⁰²⁷⁶ ₋₀₂₅₃	1.346 ^{+0.113} _{-0.135}	0.887 ^{+0.106} _{-0.090}	0.0450 ^{+0.0009} _{-0.0009}	0.98 ^{+0.56} _{-0.51}
684.01	72.1 ^{+38.8} _{-41.8}	1.44	1511 ⁺⁰⁰⁹³ ₋₀₁₁₅	1365 ⁺⁰⁰⁸⁴ ₋₀₀₇₈	3098 ⁺⁰²⁷⁶ ₋₀₃₉₉	2.048 ^{+0.193} _{-0.254}	0.389 ^{+0.138} _{-0.085}	0.0482 ^{+0.0009} _{-0.0008}	7.37 ^{+5.40} _{-5.40}
760.01	10.6 ^{+118.} _{-83.6}	0.27	1671 ⁺⁰¹⁰⁵ ₋₀₁₀₅	1510 ⁺⁰¹⁰⁴ ₋₀₀₉₅	2297 ⁺⁰³⁹⁹ ₋₄₆₉₃	1.364 ^{+0.279} _{-2.794}	1.058 ^{+0.081} _{-0.095}	0.0583 ^{+0.0011} _{-0.0011}	0.46 ^{+1.23} _{-1.11}
801.01	158.2 ^{+66.5} _{-63.4}	1.46	2135 ⁺⁰¹³⁴ ₋₀₁₂₅	1929 ⁺⁰¹²¹ ₋₀₁₁₃	2584 ⁺⁰¹⁷⁸ ₋₀₃₄₆	1.204 ^{+0.101} _{-0.167}	0.737 ^{+0.054} _{-0.048}	0.0267 ^{+0.0005} _{-0.0005}	0.47 ^{+0.32} _{-0.33}
809.01	-338.7 ^{+105.} _{-111.}	-2.62	2293 ⁺⁰¹⁴⁹ ₋₀₁₃₅	2072 ⁺⁰¹³⁵ ₋₀₁₂₂	-2735 ⁺⁰¹⁶⁹ ₋₀₁₃₇	-1.190 ^{+0.086} _{-0.077}	1.143 ^{+0.093} _{-0.074}	0.0268 ^{+0.0005} _{-0.0005}	-0.54 ^{+0.21} _{-0.23}
813.01	-201.4 ^{+146.} _{-133.}	-1.08	1540 ⁺⁰⁰⁹⁴ ₋₀₀₈₇	1391 ⁺⁰⁰⁸⁵ ₋₀₀₇₈	-2657 ⁺⁴⁷¹¹ ₋₀₁₆₉	-1.719 ^{+3.057} _{-0.142}	0.744 ^{+0.053} _{-0.065}	0.0472 ^{+0.0009} _{-0.0010}	-2.19 ^{+2.44} _{-0.69}
830.01	59.6 ^{+133.} _{-144.}	1.19	1403 ⁺⁰⁰⁸⁷ ₋₀₀₇₈	1268 ⁺⁰⁰⁷⁹ ₋₀₀₇₆	2244 ⁺⁰⁶⁴⁸ ₋₀₁₆₉	1.596 ^{+0.472} _{-0.142}	1.016 ^{+0.067} _{-0.142}	0.0424 ^{+0.0009} _{-0.0009}	0.84 ^{+0.81} _{-0.81}
838.01	22.4 ^{+220.} _{-220.}	0.13	1633 ⁺⁰¹⁰⁶ ₋₀₀₉₆	1475 ⁺⁰⁰⁹⁶ ₋₀₀₈₇	1800 ⁺⁰²²⁷ ₋₃₅₅₉	1.092 ^{+0.155} _{-2.167}	1.198 ^{+0.376} _{-0.279}	0.0570 ^{+0.0011} _{-0.0010}	0.05 ^{+0.11} _{-0.09}
840.01	-115.8 ^{+154.} _{-132.}	-0.93	1475 ⁺⁰⁰⁸⁶ ₋₀₀₉₂	1332 ⁺⁰⁰⁷⁷ ₋₀₀₈₃	-2322 ⁺⁴⁰²² ₋₀₂₂₀	-1.575 ^{+2.727} _{-0.164}	0.773 ^{+0.047} _{-0.053}	0.0384 ^{+0.0007} _{-0.0008}	0.92 ^{+0.97} _{-1.01}
843.01	-47.2 ^{+27.8} _{-38.0}	-0.24	1710 ⁺⁰¹¹³ ₋₀₁₀₃	1545 ⁺⁰¹⁰³ ₋₀₀₉₃	-2416 ⁺³⁸⁵² ₋₀₂₇₉	-1.408 ^{+2.206} _{-0.179}	0.526 ^{+0.053} _{-0.047}	0.0516 ^{+0.0010} _{-0.0010}	-0.66 ^{+0.66} _{-0.90}
897.01	-31.5 ^{+94.2} _{-65.9}	1.11	2136 ⁺⁰¹³⁸ ₋₀₁₁₆	1930 ⁺⁰¹¹⁶ ₋₀₁₁₆	2461 ⁺⁰⁴¹⁴ ₋₀₄₈₉	1.146 ^{+0.236} _{-0.236}	1.089 ^{+0.075} _{-0.075}	0.0319 ^{+0.0006} _{-0.0006}	0.31 ^{+0.27} _{-0.27}
908.01	93.8 ^{+62.7} _{-87.9}	1.00	1462 ⁺⁰⁰⁸⁴ ₋₀₀₈₄	1321 ⁺⁰⁰⁷⁶ ₋₀₀₈₃	2455 ⁺⁰²²⁹ ₋₄₃₂₉	1.676 ^{+0.172} _{-2.951}	0.719 ^{+0.048} _{-0.044}	0.0537 ^{+0.0010} _{-0.0010}	1.46 ^{+1.43} _{-1.58}
913.01	103.9 ^{+88.0} _{-114.}	1.16	1568 ⁺⁰⁰⁹² ₋₀₀₉₀	1417 ⁺⁰⁰⁸³ ₋₀₀₈₂	2292 ⁺⁰¹⁸² ₋₀₆₀₀	1.457 ^{+0.130} _{-0.387}	1.077 ^{+0.069} _{-0.066}	0.0492 ^{+0.0008} _{-0.0009}	0.59 ^{+0.52} _{-0.57}
931.01	-65.0 ^{+83.4} _{-65.5}	1.06	1721 ⁺⁰¹¹² ₋₀₁₀₀	1555 ⁺⁰¹⁰² ₋₀₀₉₀	2354 ⁺⁰²¹⁸ ₋₀₃₈₈	1.360 ^{+0.142} _{-0.231}	1.132 ^{+0.090} _{-0.074}	0.0484 ^{+0.0009} _{-0.0009}	0.51 ^{+0.54} _{-0.41}
961.02	13.3 ^{+118.} _{-65.9}	0.10	2001 ⁺⁰²⁶⁵ ₋₀₁₆₃	1808 ⁺⁰²³⁹ ₋₀₁₄₇	2221 ⁺⁰⁴¹⁴ ₋₀₂₅₇	1.088 ^{+0.065} _{-0.315}	0.231 ^{+0.065} _{-0.124}	0.0094 ^{+0.0006} _{-0.0006}	0.21 ^{+0.76} _{-0.28}
961.03	-0.1 ^{+41.5} _{-41.5}	0.00	1252 ⁺⁰¹⁷¹ ₋₀₁₆₇	1132 ⁺⁰¹⁵⁵ ₋₀₁₄₇	1622 ⁺³⁴¹⁷ ₋₀₂₅₇	1.253 ^{+2.702} _{-0.106}	1.108 ^{+0.699} _{-0.164}	0.0241 ^{+0.0016} _{-0.0005}	0.06 ^{+0.28} _{-0.24}
1419.01	54.9 ^{+52.7} _{-53.4}	1.66	2555 ⁺⁰¹⁶⁷ ₋₀₁₅₅	2309 ⁺⁰¹⁵¹ ₋₀₁₄₀	3015 ⁺⁰²⁵⁶ ₋₀₃₆₁	1.176 ^{+0.106} _{-0.146}	0.672 ^{+0.164} _{-0.115}	0.0242 ^{+0.0005} _{-0.0005}	0.71 ^{+0.47} _{-0.43}
1459.01	843.8 ^{+166.} _{-199.}	1.74	1587 ⁺⁰²²⁸ ₋₀₂₂₂	1434 ⁺⁰²⁰⁶ ₋₀₂₀₁	2342 ⁺⁰²¹⁹ ₋₀₂₁₉	1.471 ^{+0.212} _{-0.199}	0.447 ^{+0.231} _{-0.174}	0.0117 ^{+0.0011} _{-0.0016}	0.92 ^{+0.84} _{-0.55}

Table 4.3 (continued)

KOI	L_r (ppm)	σ_{sec}	T_0 (K)	$T_{e=0}$ (K)	T_b^a (K)	T_b/T_0	R_p ($R_{J,up}$)	a (AU)	A_{max}
GLM Light Curve with Eccentricity Free and Stellar Parameters from the KIC									
1.01	$-9.3^{+14.2}_{-8.94}$	0.49	2461^{+0696}_{-0543}	2223^{+0629}_{-0490}	-1686^{+3553}_{-0253}	$-0.577^{+1.364}_{-0.293}$	$1.861^{+1.740}_{-0.904}$	$0.0373^{+0.0135}_{-0.0098}$	$-0.00^{+0.02}_{-0.02}$
2.01	$57.7^{+9.30}_{-9.78}$	8.45	2714^{+0757}_{-0577}	2452^{+0684}_{-0521}	2859^{+0064}_{-0064}	$1.054^{+0.228}_{-0.228}$	$1.032^{+0.926}_{-0.501}$	$0.0367^{+0.0129}_{-0.0097}$	$0.38^{+0.62}_{-0.24}$
5.01	$0.0^{+13.7}_{-18.6}$	0.00	2144^{+0586}_{-0454}	1937^{+0530}_{-0410}	-2181^{+4699}_{-0525}	$-0.873^{+2.078}_{-0.498}$	$0.646^{+0.589}_{-0.307}$	$0.0587^{+0.0215}_{-0.0155}$	$-0.07^{+0.45}_{-0.72}$
10.01	$-5.8^{+45.9}_{-41.2}$	1.09	1997^{+0561}_{-0449}	1804^{+0507}_{-0375}	2454^{+0222}_{-0056}	$1.170^{+0.402}_{-0.263}$	$0.976^{+0.923}_{-0.432}$	$0.0469^{+0.0172}_{-0.0123}$	$0.32^{+0.91}_{-0.30}$
13.01	$88.8^{+8.04}_{-8.04}$	16.03	5039^{+1097}_{-0502}	4553^{+0991}_{-0859}	3759^{+0056}_{-0273}	$0.745^{+0.163}_{-0.163}$	$1.575^{+0.760}_{-0.760}$	$0.0348^{+0.0092}_{-0.0092}$	$0.24^{+0.15}_{-0.15}$
17.01	$-71.7^{+33.6}_{-28.2}$	1.28	1832^{+0408}_{-0505}	1656^{+0369}_{-0454}	-2303^{+0359}_{-0169}	$-1.207^{+0.373}_{-0.383}$	$0.853^{+0.786}_{-0.415}$	$0.0414^{+0.0147}_{-0.0107}$	$-0.27^{+0.23}_{-0.67}$
18.01	$-89.8^{+48.6}_{-44.7}$	0.80	1824^{+0393}_{-0505}	1648^{+0456}_{-0355}	-2399^{+4272}_{-0258}	$-1.233^{+2.108}_{-0.435}$	$0.725^{+0.663}_{-0.349}$	$0.0443^{+0.0164}_{-0.0116}$	$-0.36^{+0.40}_{-1.21}$
20.01	$-26.3^{+28.5}_{-13.8}$	0.98	1758^{+0505}_{-0384}	1589^{+0456}_{-0347}	2111^{+0181}_{-0314}	$1.153^{+0.370}_{-0.348}$	$1.163^{+1.090}_{-0.562}$	$0.0540^{+0.0196}_{-0.0142}$	$0.15^{+0.41}_{-0.13}$
64.01	$39.5^{+40.8}_{-40.8}$	1.78	2716^{+0543}_{-0543}	2454^{+0537}_{-0362}	2672^{+0262}_{-0262}	$0.964^{+0.237}_{-0.237}$	$0.909^{+0.834}_{-0.834}$	$0.0323^{+0.0083}_{-0.0083}$	$0.22^{+0.16}_{-0.16}$
97.01	$79.1^{+15.3}_{-15.3}$	4.11	1903^{+0516}_{-0410}	1719^{+0467}_{-0371}	2625^{+0101}_{-0101}	$1.375^{+0.379}_{-0.297}$	$1.031^{+0.948}_{-0.484}$	$0.0586^{+0.0210}_{-0.0156}$	$0.81^{+1.36}_{-0.51}$
127.01	$-92.6^{+39.1}_{-42.1}$	3.21	1699^{+0466}_{-0367}	1535^{+0421}_{-0332}	-2564^{+0126}_{-0111}	$-1.504^{+0.331}_{-0.427}$	$0.889^{+0.819}_{-0.422}$	$0.0464^{+0.0167}_{-0.0124}$	$-0.05^{+0.68}_{-1.94}$
128.01	$-62.9^{+16.4}_{-15.7}$	1.00	1918^{+0536}_{-0425}	1733^{+0484}_{-0384}	-1606^{+0302}_{-0104}	$-0.792^{+0.302}_{-0.259}$	$1.413^{+1.258}_{-0.685}$	$0.0593^{+0.0211}_{-0.0158}$	$-0.01^{+0.01}_{-0.02}$
144.01	$101.3^{+44.0}_{-42.0}$	2.80	1856^{+0525}_{-0479}	1677^{+0474}_{-0435}	3125^{+0191}_{-0112}	$1.671^{+0.476}_{-0.406}$	$0.547^{+0.500}_{-0.781}$	$0.0524^{+0.0190}_{-0.0137}$	$3.55^{+6.35}_{-1.51}$
183.01	$124.8^{+39.4}_{-39.4}$	2.76	1715^{+0373}_{-0491}	1550^{+0337}_{-0444}	2502^{+0139}_{-0139}	$1.448^{+0.324}_{-0.449}$	$0.846^{+0.409}_{-0.409}$	$0.0379^{+0.0100}_{-0.0100}$	$0.81^{+0.54}_{-0.54}$
186.01	$-200.4^{+93.8}_{-75.4}$	1.21	1786^{+0383}_{-0383}	1614^{+0444}_{-0346}	-2473^{+0483}_{-0198}	$-1.317^{+0.433}_{-0.433}$	$1.016^{+0.945}_{-0.480}$	$0.0437^{+0.0161}_{-0.0114}$	$-0.53^{+0.48}_{-1.41}$
188.01	$-33.1^{+17.0}_{-17.0}$	0.28	1327^{+0378}_{-0293}	1199^{+0341}_{-0264}	-2004^{+3583}_{-0216}	$-1.424^{+2.412}_{-0.503}$	$0.721^{+0.683}_{-0.347}$	$0.0459^{+0.0164}_{-0.0123}$	$-0.28^{+0.29}_{-1.02}$
195.01	$99.4^{+79.1}_{-80.9}$	1.71	1805^{+0502}_{-0587}	1631^{+0454}_{-0350}	2516^{+0160}_{-0160}	$1.364^{+0.401}_{-0.340}$	$1.123^{+1.045}_{-0.536}$	$0.0437^{+0.0156}_{-0.0119}$	$0.65^{+1.38}_{-0.52}$
196.01	$75.4^{+39.0}_{-39.0}$	2.29	2134^{+0468}_{-0468}	1929^{+0420}_{-0328}	2466^{+0169}_{-0169}	$1.139^{+0.257}_{-0.257}$	$0.926^{+0.438}_{-0.438}$	$0.0299^{+0.0080}_{-0.0080}$	$0.29^{+0.20}_{-0.20}$
201.01	$21.7^{+25.4}_{-43.0}$	1.00	1658^{+0462}_{-0369}	1498^{+0418}_{-0334}	-2357^{+0443}_{-0214}	$-1.363^{+0.461}_{-0.449}$	$0.807^{+0.764}_{-0.390}$	$0.0519^{+0.0187}_{-0.0136}$	$-0.50^{+0.45}_{-1.41}$
202.01	$63.6^{+37.7}_{-40.2}$	1.85	2424^{+0674}_{-0534}	2190^{+0609}_{-0482}	2455^{+0143}_{-0216}	$0.989^{+0.298}_{-0.235}$	$1.026^{+0.932}_{-0.503}$	$0.0290^{+0.0105}_{-0.0076}$	$0.16^{+0.35}_{-0.12}$
203.01	$52.0^{+98.0}_{-117.7}$	1.00	2357^{+0661}_{-0513}	2130^{+0597}_{-0464}	2319^{+0202}_{-0106}	$0.918^{+0.323}_{-0.350}$	$1.252^{+1.175}_{-0.604}$	$0.0260^{+0.0093}_{-0.0069}$	$0.10^{+0.29}_{-0.11}$
204.01	$54.8^{+97.6}_{-181.6}$	1.15	1701^{+0377}_{-0377}	1537^{+0324}_{-0324}	2660^{+0646}_{-0646}	$1.492^{+0.569}_{-0.569}$	$0.662^{+0.332}_{-0.332}$	$0.0424^{+0.0131}_{-0.0131}$	$1.22^{+0.19}_{-0.19}$
214.01	-224.9^{+1607}_{-1607}	1.21	1744^{+0377}_{-0377}	1576^{+0341}_{-0341}	-3515^{+0559}_{-0472}	$-1.987^{+0.628}_{-0.542}$	$1.088^{+0.536}_{-0.536}$	$0.0438^{+0.0155}_{-0.0115}$	$-8.73^{+6.82}_{-21.74}$
217.01	$260.3^{+118.}_{-112.}$	2.64	1442^{+0392}_{-0310}	1303^{+0354}_{-0280}	2782^{+0142}_{-0173}	$1.917^{+0.431}_{-0.431}$	$0.770^{+0.712}_{-0.359}$	$0.0481^{+0.0171}_{-0.0126}$	$3.81^{+7.08}_{-2.54}$
229.01	$32.5^{+60.6}_{-23.3}$	0.53	1873^{+0405}_{-0537}	1693^{+0485}_{-0366}	2713^{+0326}_{-0614}	$1.383^{+0.467}_{-0.477}$	$0.562^{+0.531}_{-0.269}$	$0.0469^{+0.0169}_{-0.0123}$	$0.93^{+2.85}_{-0.85}$
254.01	$1143.3^{+48.2}_{-48.2}$	2.82	1279^{+0386}_{-0482}	1155^{+0322}_{-0322}	2454^{+0614}_{-0218}	$1.910^{+0.326}_{-0.355}$	$1.103^{+1.028}_{-0.432}$	$0.0288^{+0.0104}_{-0.0104}$	$3.27^{+5.78}_{-4.11}$
356.01	$86.9^{+41.1}_{-41.1}$	2.25	2544^{+0696}_{-0561}	2299^{+0628}_{-0507}	3206^{+0218}_{-0267}	$1.251^{+0.292}_{-0.292}$	$0.515^{+0.442}_{-0.243}$	$0.0303^{+0.0106}_{-0.0080}$	$1.11^{+0.77}_{-0.77}$
412.01	$34.4^{+11.1}_{-14.3}$	0.38	1870^{+0407}_{-0459}	1689^{+0461}_{-0368}	-1908^{+3576}_{-0206}	$-0.950^{+1.740}_{-0.342}$	$0.616^{+0.569}_{-0.291}$	$0.0521^{+0.0186}_{-0.0138}$	$-0.04^{+0.05}_{-0.15}$
421.01	$-53.9^{+23.2}_{-23.2}$	0.35	1644^{+0459}_{-0356}	1485^{+0414}_{-0322}	2071^{+0219}_{-3481}	$1.184^{+0.421}_{-1.847}$	$1.308^{+0.619}_{-0.619}$	$0.0533^{+0.0188}_{-0.0140}$	$0.16^{+0.55}_{-0.16}$

Table 4.3 (continued)

KOI	L_r (ppm)	σ_{sec}	T_0 (K)	$T_{e=0}$ (K)	T_b^a (K)	T_b/T_0	R_p ($R_{J,up}$)	a (AU)	A_{max}
433.01	-10.5 ^{+40.5} _{-10.2}	-0.03	1663 ⁺⁰⁴⁶⁸ ₋₀₄₆₇	1503 ⁺⁰⁴²³ ₋₀₃₂₃	-2503 ⁺⁴⁶³⁶ ₋₄₀₂₂	-1.396 ^{+2.561} _{-0.329}	0.577 ^{+0.544} _{-0.272}	0.0494 ^{+0.0178} _{-0.0156}	-0.79 ^{+0.97} _{-0.32}
611.01	-112.1 ^{+74.4} _{-67.5}	-1.19	1908 ⁺⁰⁵²³ ₋₀₄₀₆	1724 ⁺⁰⁴⁷³ ₋₀₃₆₇	-2451 ⁺⁰³²⁶ ₋₀₂₂₃	-1.251 ^{+0.329} _{-0.387}	1.869 ^{+2.327} _{-1.095}	0.0441 ^{+0.0115} _{-0.0158}	-0.41 ^{+1.04} _{-0.33}
667.01	55.5 ^{+131.1} _{-64.3}	0.05	1108 ⁺⁰³⁰⁴ ₋₀₂₄₆	1002 ⁺⁰²⁷⁵ ₋₀₂₂₃	2065 ⁺⁰²⁷² ₋₃₉₂₇	1.727 ^{+0.655} _{-3.298}	0.547 ^{+0.495} _{-0.262}	0.0439 ^{+0.0158} _{-0.0115}	0.95 ^{+3.82} _{-1.30}
684.01	54.6 ^{+55.2} _{-103.1}	0.53	2173 ⁺⁰⁶¹⁰ ₋₀₄₇₅	1963 ⁺⁰⁵⁵¹ ₋₀₄₂₉	2795 ⁺⁰⁵⁷³ ₋₅₈₄₃	1.132 ^{+0.580} _{-2.538}	0.587 ^{+0.577} _{-0.288}	0.0524 ^{+0.0189} _{-0.0140}	0.57 ^{+3.31} _{-2.02}
760.01	-18.1 ^{+126.6} _{-80.6}	0.01	1521 ⁺⁰⁴³¹ ₋₀₅₂₄	1375 ⁺⁰³⁹⁰ ₋₀₃₆₆	2051 ⁺⁰⁵⁹⁴ ₋₄₁₄₅	1.097 ^{+0.783} _{-1.391}	0.868 ^{+0.820} _{-0.414}	0.0581 ^{+0.0210} _{-0.0146}	0.14 ^{+2.46} _{-1.15}
767.01	189.7 ^{+87.5} _{-102.2}	2.55	1870 ⁺⁰⁴⁶³ ₋₀₄₆₃	1690 ⁺⁰³⁶⁵ ₋₀₄₇₅	2577 ⁺⁰¹²⁹ ₋₀₁₅₉	1.363 ^{+0.305} _{-0.305}	1.226 ^{+0.592} _{-0.146}	0.0394 ^{+0.0106} _{-0.0106}	0.73 ^{+0.49} _{-0.41}
801.01	155.7 ^{+102.1} _{-91.6}	2.14	2338 ⁺⁰⁶⁴⁹ ₋₀₅₀₃	2113 ⁺⁰⁵⁸⁶ ₋₀₄₅₅	2842 ⁺⁰¹⁷⁸ ₋₀₂₃₂	1.196 ^{+0.350} _{-0.274}	0.884 ^{+0.811} _{-0.427}	0.0275 ^{+0.0099} _{-0.0074}	0.62 ^{+1.25} _{-0.42}
809.01	278.8 ^{+110.1} _{-100.1}	2.91	2314 ⁺⁰⁶⁵⁷ ₋₀₄₈₀	2091 ⁺⁰⁵⁹⁴ ₋₀₄₄₃	2801 ⁺⁰¹³⁶ ₋₀₁₅₈	1.205 ^{+0.324} _{-0.275}	1.104 ^{+1.003} _{-0.517}	0.0271 ^{+0.0094} _{-0.0072}	0.60 ^{+1.04} _{-0.40}
813.01	-540.1 ^{+228.1} _{-253.1}	-2.31	1398 ⁺⁰³⁸⁸ ₋₀₃₀₇	1263 ⁺⁰³⁵¹ ₋₀₂₇₇	-3240 ⁺⁰²⁶⁵ ₋₀₂₂₁	-2.292 ^{+0.524} _{-0.669}	0.588 ^{+0.548} _{-0.282}	0.0478 ^{+0.0173} _{-0.0126}	-12.63 ^{+8.63} _{-24.90}
830.01	-89.1 ^{+11.0} _{-11.0}	-0.87	1191 ⁺⁰²⁶² ₋₀₂₃₇	1076 ⁺⁰²³⁷ ₋₀₂₃₇	-1457 ⁺⁰⁰⁹⁵ ₋₀₃₂₁	-1.160 ^{+0.385} _{-0.385}	0.680 ^{+0.321} _{-0.321}	0.0423 ^{+0.0112} _{-0.0112}	-0.01 ^{+0.04} _{-0.04}
838.01	54.9 ^{+93.4} _{-97.2}	0.13	1629 ⁺⁰⁴⁶⁰ ₋₀₃₄₇	1472 ⁺⁰³¹⁴ ₋₀₃₁₄	2187 ⁺⁰³²³ ₋₀₃₀₃	1.205 ^{+0.512} _{-2.465}	1.223 ^{+1.397} _{-0.654}	0.0573 ^{+0.0210} _{-0.0151}	0.23 ^{+1.14} _{-0.44}
840.01	29.4 ^{+142.1} _{-121.1}	0.44	1692 ⁺⁰⁴⁶⁵ ₋₀₃₆₈	1529 ⁺⁰³³² ₋₀₃₃₂	2223 ⁺⁰³²¹ ₋₄₄₅₈	1.187 ^{+0.490} _{-2.489}	0.967 ^{+0.902} _{-0.458}	0.0403 ^{+0.0141} _{-0.0104}	0.26 ^{+1.20} _{-0.60}
843.01	224.3 ^{+138.1} _{-72.7}	2.71	1812 ⁺⁰⁵⁰¹ ₋₀₃₉₅	1638 ⁺⁰⁴⁵² ₋₀₃₅₇	3569 ⁺⁰²⁶³ ₋₀₂₈₉	1.952 ^{+0.580} _{-0.432}	0.565 ^{+0.518} _{-0.276}	0.0524 ^{+0.0186} _{-0.0140}	8.24 ^{+16.44} _{-5.44}
897.01	216.0 ^{+134.1} _{-91.4}	1.88	2196 ⁺⁰⁶⁰⁴ ₋₀₄₉₁	1984 ⁺⁰⁵⁴⁶ ₋₀₄₄₄	2728 ⁺⁰¹⁷³ ₋₀₂₄₅	1.218 ^{+0.370} _{-0.506}	1.179 ^{+1.076} _{-0.956}	0.0323 ^{+0.0135} _{-0.0201}	0.57 ^{+1.22} _{-0.31}
908.01	193.9 ^{+135.1} _{-97.2}	1.12	1764 ⁺⁰³⁹⁰ ₋₀₃₉₀	1594 ⁺⁰³⁵³ ₋₀₃₅₃	2694 ⁺⁰²⁴⁹ ₋₄₄₉₀	1.435 ^{+0.500} _{-2.239}	1.031 ^{+0.500} _{-0.500}	0.0559 ^{+0.0149} _{-0.0149}	1.09 ^{+3.21} _{-1.11}
913.01	-22.3 ^{+96.5} _{-49.3}	0.82	1387 ⁺⁰³⁸³ ₋₀₃₀₃	1253 ⁺⁰³⁴⁶ ₋₀₂₇₄	2303 ⁺⁰²²³ ₋₀₄₉₇	1.584 ^{+0.528} _{-0.580}	0.763 ^{+0.671} _{-0.365}	0.0495 ^{+0.0176} _{-0.0129}	0.82 ^{+2.48} _{-0.77}
1176.01	-30.9 ^{+148.1} _{-100.1}	0.05	1514 ⁺⁰⁴²⁹ ₋₀₃₃₂	1368 ⁺⁰³⁸⁷ ₋₀₃₀₀	1849 ⁺⁰³⁷⁹ ₋₃₉₅₀	1.025 ^{+0.588} _{-2.461}	0.831 ^{+0.793} _{-0.395}	0.0279 ^{+0.0099} _{-0.0075}	0.07 ^{+0.65} _{-0.42}
1419.01	130.0 ^{+109.1} _{-73.9}	1.22	2562 ⁺⁰⁷²⁰ ₋₀₅₂₈	2315 ⁺⁰⁶⁵¹ ₋₀₅₆₀	3201 ⁺⁰³⁶⁴ ₋₀₂₄₅	1.212 ^{+0.392} _{-0.368}	0.434 ^{+0.401} _{-0.892}	0.0243 ^{+0.0087} _{-0.0094}	0.93 ^{+2.33} _{-0.45}
1459.01	25.2 ^{+298.1} _{-357.1}	1.36	2212 ⁺⁰⁴⁷⁸ ₋₀₄₇₈	1999 ⁺⁰⁴³² ₋₀₅₆₀	2728 ⁺⁰³⁶⁶ ₋₀₃₆₆	1.205 ^{+0.329} _{-0.329}	0.898 ^{+0.449} _{-0.898}	0.0134 ^{+0.0035} _{-0.0035}	0.74 ^{+0.58} _{-0.45}
1541.01	1088.9 ^{+397.1} _{-293.3}	5.22	2167 ⁺⁰⁴⁸² ₋₀₄₈₂	1958 ⁺⁰⁵²⁷ ₋₀₄₃₆	3523 ⁺⁰¹³³ ₋₀₁₃₆	1.628 ^{+0.458} _{-0.348}	1.608 ^{+1.428} _{-0.785}	0.0360 ^{+0.0131} _{-0.0094}	3.89 ^{+6.81} _{-2.42}
1543.01	3080.9 ^{+797.1} _{-797.1}	3.77	1697 ⁺⁰⁴⁸⁵ ₋₀₃₆₇	1533 ⁺⁰⁴³⁸ ₋₀₃₃₂	3957 ⁺⁰²⁷⁷ ₋₀₂₇₃	2.320 ^{+0.675} _{-0.526}	1.299 ^{+1.239} _{-0.615}	0.0497 ^{+0.0179} _{-0.0129}	20.14 ^{+37.73} _{-13.27}

CLM Light Curve with Eccentricity Free and Stellar Parameters from Isochrones

1.01	-9.3 ^{+14.2} _{-8.94}	-0.49	1994 ⁺⁰¹²⁸ ₋₀₁₁₅	1802 ⁺⁰¹¹⁶ ₋₀₁₀₄	-1700 ⁺³⁵⁶³ ₋₀₂₄₃	-0.844 ^{+1.779} _{-1.136}	1.173 ^{+0.093} _{-0.074}	0.0360 ^{+0.0007} _{-0.0006}	-0.01 ^{+0.04} _{-0.04}
2.01	57.7 ^{+9.30} _{-9.78}	8.45	2746 ⁺⁰¹⁷³ ₋₀₁₆₇	2481 ⁺⁰¹⁵⁶ ₋₀₁₅₁	2860 ⁺⁰⁰⁶⁵ ₋₀₀₆₅	1.040 ^{+0.054} _{-0.048}	1.038 ^{+0.087} _{-0.085}	0.0363 ^{+0.0007} _{-0.0007}	0.37 ^{+0.07} _{-0.06}
5.01	0.0 ^{+13.7} _{-18.6}	-0.00	1627 ⁺⁰¹⁰⁷ ₋₀₀₉₅	1470 ⁺⁰⁰⁹⁷ ₋₀₀₈₆	-2179 ⁺⁴⁶⁹⁷ ₋₀₅₁₄	-1.326 ^{+2.871} _{-0.337}	0.355 ^{+0.031} _{-0.025}	0.0562 ^{+0.0011} _{-0.0010}	-0.33 ^{+1.42} _{-1.58}
10.01	-5.8 ^{+43.9} _{-45.2}	1.09	2051 ⁺⁰¹⁴³ ₋₀₁₂₉	1854 ⁺⁰¹²⁹ ₋₀₁₂₉	2463 ⁺⁰⁵⁵⁷ ₋₀₀₅₅	1.192 ^{+0.239} _{-0.239}	1.048 ^{+0.089} _{-0.089}	0.0476 ^{+0.0008} _{-0.0008}	0.36 ^{+0.38} _{-0.38}
13.01	88.8 ^{+8.04} _{-8.04}	16.03	4049 ⁺⁰¹¹⁸ ₋₀₁₁₈	3658 ⁺⁰⁰⁸⁸ ₋₀₀₉₂	3758 ⁺⁰⁰⁵⁷ ₋₀₀₅₇	0.929 ^{+0.015} _{-0.015}	1.050 ^{+0.014} _{-0.014}	0.0359 ^{+0.0003} _{-0.0003}	0.58 ^{+0.03} _{-0.03}
17.01	-71.7 ^{+28.2} _{-28.2}	-1.28	1830 ⁺⁰¹¹⁸ ₋₀₁₁₈	1653 ⁺⁰¹⁰⁷ ₋₀₀₉₆	-2306 ⁺⁰³⁶⁹ ₋₀₁₆₃	-1.252 ^{+0.210} _{-0.114}	0.887 ^{+0.070} _{-0.058}	0.0431 ^{+0.0008} _{-0.0008}	-0.33 ^{+0.27} _{-0.27}
18.01	-89.8 ^{+48.6} _{-44.7}	-0.80	1826 ⁺⁰¹²¹ ₋₀₁₁₂	1650 ⁺⁰¹⁰⁹ ₋₀₁₀₁	-2399 ⁺⁴²⁷⁴ ₋₀₂₅₇	-1.308 ^{+0.155} _{-0.155}	0.757 ^{+0.063} _{-0.056}	0.0463 ^{+0.0009} _{-0.0009}	-0.47 ^{+0.51} _{-0.60}

Table 4.3 (continued)

KOI	L_r (ppm)	σ_{sec}	T_0 (K)	$T_{e=0}$ (K)	T_b^a (K)	T_b/T_0	R_p (R_{Jup})	a (AU)	A_{max}
20.01	$-26.3^{+28.5}_{-11.2}$	0.98	1804^{+0126}_{-0119}	1630^{+0114}_{-0100}	2115^{+0180}_{-0312}	$1.165^{+0.118}_{-0.181}$	$1.236^{+0.115}_{-0.045}$	$0.0547^{+0.0011}_{-0.0010}$	$0.16^{+0.17}_{-0.13}$
64.01	$39.5^{+42.6}_{-40.8}$	1.78	1815^{+0108}_{-0101}	1640^{+0098}_{-0091}	2669^{+0178}_{-0271}	$1.471^{+0.105}_{-0.155}$	$0.363^{+0.034}_{-0.075}$	$0.0291^{+0.0005}_{-0.0005}$	$1.22^{+0.69}_{-0.71}$
97.01	$79.1^{+15.3}_{-15.5}$	4.11	1710^{+0117}_{-0106}	1545^{+0106}_{-0096}	2626^{+0090}_{-0101}	$1.534^{+0.085}_{-0.090}$	$0.827^{+0.075}_{-0.062}$	$0.0580^{+0.0012}_{-0.0011}$	$1.26^{+0.36}_{-0.33}$
127.01	$-92.6^{+39.1}_{-42.1}$	-3.21	1687^{+0107}_{-0097}	1524^{+0097}_{-0088}	-2563^{+0129}_{-0112}	$-1.517^{+0.094}_{-0.086}$	$0.863^{+0.064}_{-0.052}$	$0.0455^{+0.0009}_{-0.0008}$	$-1.11^{+0.36}_{-0.41}$
128.01	$-62.9^{+16.4}_{-15.7}$	-1.00	1585^{+0104}_{-0092}	1433^{+0094}_{-0083}	-1604^{+0400}_{-0306}	$-1.003^{+0.246}_{-0.174}$	$0.925^{+0.074}_{-0.024}$	$0.0572^{+0.0011}_{-0.0010}$	$-0.01^{+0.01}_{-0.01}$
144.01	$101.3^{+43.4}_{-43.4}$	2.80	1246^{+0085}_{-0085}	1126^{+0077}_{-0074}	3124^{+0180}_{-0180}	$2.515^{+0.174}_{-0.174}$	$0.218^{+0.024}_{-0.024}$	$0.0465^{+0.0011}_{-0.0011}$	$18.85^{+7.96}_{-6.83}$
183.01	$124.8^{+42.0}_{-39.4}$	2.76	1946^{+0130}_{-0114}	1759^{+0103}_{-0115}	2505^{+0111}_{-0136}	$1.284^{+0.080}_{-0.088}$	$1.091^{+0.089}_{-0.072}$	$0.0381^{+0.0007}_{-0.0007}$	$0.52^{+0.21}_{-0.19}$
186.01	$-200.4^{+93.8}_{-75.4}$	-1.21	1886^{+0127}_{-0112}	1704^{+0115}_{-0101}	-2474^{+0506}_{-0197}	$-1.303^{+0.276}_{-0.126}$	$1.141^{+0.096}_{-0.081}$	$0.0436^{+0.0009}_{-0.0008}$	$-0.53^{+0.46}_{-0.44}$
188.01	$-33.1^{+17.0}_{-13.9}$	-0.28	1439^{+0082}_{-0081}	1301^{+0074}_{-0073}	-2006^{+3594}_{-3594}	$-1.391^{+2.488}_{-0.164}$	$0.838^{+0.050}_{-0.049}$	$0.0453^{+0.0008}_{-0.0008}$	$-0.26^{+0.27}_{-0.41}$
195.01	$99.4^{+80.9}_{-40.1}$	1.71	1765^{+0098}_{-0098}	1595^{+0088}_{-0088}	2518^{+0263}_{-0263}	$1.420^{+0.157}_{-0.157}$	$1.048^{+0.066}_{-0.062}$	$0.0425^{+0.0007}_{-0.0007}$	$0.81^{+0.16}_{-0.48}$
196.01	$75.4^{+39.0}_{-39.0}$	2.29	2111^{+0120}_{-0120}	1907^{+0108}_{-0108}	2463^{+0130}_{-0168}	$1.164^{+0.077}_{-0.092}$	$0.886^{+0.054}_{-0.049}$	$0.0294^{+0.0005}_{-0.0005}$	$0.33^{+0.15}_{-0.15}$
201.01	$21.7^{+25.4}_{-43.0}$	-1.00	1561^{+0096}_{-0091}	1411^{+0086}_{-0082}	-2353^{+0439}_{-0218}	$-1.503^{+0.294}_{-0.152}$	$0.697^{+0.049}_{-0.044}$	$0.0505^{+0.0009}_{-0.0010}$	$-0.76^{+0.65}_{-0.80}$
202.01	$63.6^{+37.7}_{-40.2}$	1.85	2397^{+0163}_{-0144}	2166^{+0148}_{-0131}	2455^{+0138}_{-0207}	$1.019^{+0.077}_{-0.101}$	$0.994^{+0.089}_{-0.073}$	$0.0288^{+0.0006}_{-0.0005}$	$0.19^{+0.10}_{-0.10}$
203.01	$52.0^{+98.0}_{-47.7}$	1.00	2304^{+0131}_{-0131}	2082^{+0100}_{-0100}	2319^{+0292}_{-0292}	$0.999^{+0.160}_{-0.160}$	$1.173^{+0.093}_{-0.078}$	$0.0255^{+0.0005}_{-0.0005}$	$0.14^{+0.14}_{-0.14}$
204.01	$54.8^{+82.5}_{-97.6}$	1.15	1604^{+0098}_{-0087}	1449^{+0089}_{-0079}	2669^{+0641}_{-0641}	$1.657^{+0.402}_{-0.402}$	$0.573^{+0.045}_{-0.045}$	$0.0415^{+0.0007}_{-0.0007}$	$1.92^{+1.74}_{-1.67}$
214.01	$-224.9^{+181.1}_{-160.7}$	-1.21	1612^{+0098}_{-0091}	1457^{+0088}_{-0082}	-3530^{+0591}_{-0475}	$-2.187^{+0.362}_{-0.289}$	$0.881^{+0.222}_{-0.150}$	$0.0422^{+0.0008}_{-0.0008}$	$-13.30^{+9.35}_{-14.68}$
217.01	$260.3^{+118.1}_{-112.1}$	2.64	1607^{+0100}_{-0092}	1452^{+0090}_{-0083}	2783^{+0143}_{-0173}	$1.729^{+0.108}_{-0.121}$	$0.960^{+0.070}_{-0.060}$	$0.0479^{+0.0009}_{-0.0009}$	$2.60^{+1.05}_{-0.99}$
229.01	$32.5^{+60.6}_{-46.3}$	0.53	1708^{+0111}_{-0106}	1543^{+0100}_{-0100}	2707^{+0331}_{-0331}	$1.581^{+0.203}_{-0.212}$	$0.450^{+0.041}_{-0.041}$	$0.0456^{+0.0009}_{-0.0009}$	$1.65^{+2.12}_{-1.14}$
254.01	$1143.3^{+463.3}_{-463.3}$	2.82	962^{+0133}_{-0133}	869^{+0140}_{-0140}	2457^{+0152}_{-0152}	$2.557^{+0.303}_{-0.303}$	$0.541^{+0.153}_{-0.153}$	$0.0250^{+0.0032}_{-0.0032}$	$10.64^{+7.14}_{-4.75}$
356.01	$86.9^{+48.2}_{-41.1}$	2.25	1857^{+0109}_{-0104}	1678^{+0099}_{-0094}	3209^{+0214}_{-0264}	$1.730^{+0.117}_{-0.142}$	$0.254^{+0.020}_{-0.020}$	$0.0279^{+0.0005}_{-0.0005}$	$4.22^{+1.98}_{-1.85}$
412.01	$34.4^{+11.1}_{-14.3}$	-0.38	1612^{+0104}_{-0092}	1456^{+0094}_{-0083}	-1909^{+3565}_{-0202}	$-1.178^{+2.196}_{-0.142}$	$0.444^{+0.042}_{-0.033}$	$0.0502^{+0.0010}_{-0.0009}$	$-0.10^{+0.12}_{-0.15}$
421.01	$-53.9^{+58.1}_{-23.2}$	0.35	1401^{+0087}_{-0077}	1266^{+0078}_{-0078}	2075^{+0219}_{-0219}	$1.478^{+0.167}_{-0.167}$	$0.906^{+0.061}_{-0.051}$	$0.0508^{+0.0010}_{-0.0009}$	$0.39^{+0.56}_{-0.39}$
433.01	$-10.5^{+102.5}_{-102.5}$	-0.03	1471^{+0078}_{-0078}	1329^{+0071}_{-0071}	-2513^{+0957}_{-0957}	$-1.707^{+0.246}_{-0.246}$	$0.437^{+0.051}_{-0.051}$	$0.0477^{+0.0008}_{-0.0008}$	$-1.73^{+3.01}_{-3.01}$
611.01	$-112.1^{+67.5}_{-67.5}$	-1.19	2079^{+0140}_{-0132}	1878^{+0120}_{-0120}	-2452^{+0322}_{-0322}	$-1.175^{+0.163}_{-0.127}$	$2.395^{+1.287}_{-1.062}$	$0.0450^{+0.0009}_{-0.0009}$	$-0.33^{+0.24}_{-0.34}$
667.01	$55.5^{+131.1}_{-64.3}$	0.05	912^{+0124}_{-0126}	824^{+0112}_{-0114}	2074^{+0264}_{-3935}	$2.292^{+0.433}_{-4.241}$	$0.345^{+0.096}_{-0.097}$	$0.0411^{+0.0032}_{-0.0031}$	$2.74^{+5.59}_{-3.69}$
684.01	$54.6^{+55.2}_{-103.1}$	0.53	1511^{+0091}_{-0086}	1366^{+0082}_{-0078}	2823^{+0547}_{-5863}	$1.860^{+0.376}_{-0.376}$	$0.263^{+0.042}_{-0.042}$	$0.0482^{+0.0009}_{-0.0009}$	$3.76^{+9.06}_{-10.32}$
760.01	$-18.1^{+126.6}_{-126.6}$	0.01	1670^{+0112}_{-0103}	1509^{+0096}_{-0093}	2069^{+0596}_{-0126}	$1.233^{+0.366}_{-0.189}$	$1.051^{+0.092}_{-0.067}$	$0.0583^{+0.0011}_{-0.0007}$	$0.18^{+1.39}_{-0.42}$
767.01	$189.7^{+87.5}_{-87.5}$	2.55	1758^{+0103}_{-0103}	1589^{+0092}_{-0092}	2578^{+0165}_{-0165}	$1.465^{+0.105}_{-0.105}$	$1.048^{+0.067}_{-0.067}$	$0.0383^{+0.0007}_{-0.0007}$	$1.01^{+0.41}_{-0.41}$
801.01	$155.7^{+102.1}_{-91.6}$	2.14	2135^{+0129}_{-0122}	1930^{+0117}_{-0110}	2840^{+0183}_{-0234}	$1.330^{+0.094}_{-0.121}$	$0.711^{+0.053}_{-0.047}$	$0.0267^{+0.0005}_{-0.0005}$	$0.98^{+0.51}_{-0.47}$
809.01	$278.5^{+110.0}_{-100.0}$	2.91	2290^{+0150}_{-0132}	2069^{+0135}_{-0120}	2797^{+0138}_{-0160}	$1.219^{+0.077}_{-0.084}$	$1.066^{+0.088}_{-0.071}$	$0.0268^{+0.0005}_{-0.0005}$	$0.65^{+0.26}_{-0.23}$
813.01	$-540.1^{+228.1}_{-253.1}$	-2.31	1543^{+0092}_{-0087}	1394^{+0083}_{-0079}	-3245^{+0268}_{-0218}	$-2.106^{+0.188}_{-0.149}$	$0.707^{+0.060}_{-0.051}$	$0.0472^{+0.0008}_{-0.0009}$	$-9.36^{+4.21}_{-4.44}$

Table 4.3 (continued)

KOI	L_T (ppm)	σ_{sec}	T_0 (K)	$T_{e=0}$ (K)	T_b^a (K)	T_b/T_0	R_p (R_{Jup})	a (AU)	A_{max}
830.01	$-89.1^{+13.1}_{-13.1}$	0.87	1403^{+0082}_{-0082}	1268^{+0074}_{-0074}	-1455^{+2674}_{-0698}	$-1.032^{+1.897}_{-0.686}$	$0.950^{+0.055}_{-0.535}$	$0.0424^{+0.0008}_{-0.0008}$	$-0.01^{+0.01}_{-0.73}$
838.01	$54.9^{+93.4}_{-97.2}$	0.13	1632^{+0107}_{-0098}	1475^{+0096}_{-0088}	2181^{+0327}_{-4295}	$1.330^{+0.213}_{-2.614}$	$1.277^{+0.478}_{-0.478}$	$0.0570^{+0.0011}_{-0.0011}$	$0.32^{+0.55}_{-0.55}$
840.01	29.4^{+142}_{-121}	0.44	1473^{+0088}_{-0092}	1331^{+0079}_{-0083}	2225^{+0331}_{-4466}	$1.509^{+0.235}_{-3.034}$	$0.702^{+0.049}_{-0.052}$	$0.0384^{+0.0007}_{-0.0008}$	$0.63^{+1.39}_{-1.30}$
843.01	$224.3^{+138}_{-72.7}$	2.71	1713^{+0108}_{-0104}	1548^{+0098}_{-0094}	3567^{+0272}_{-0284}	$2.083^{+0.171}_{-0.183}$	$0.494^{+0.052}_{-0.047}$	$0.0516^{+0.0009}_{-0.0010}$	$10.87^{+5.33}_{-4.43}$
897.01	216.0^{+134}_{-132}	1.88	2137^{+0141}_{-0087}	1931^{+0128}_{-0076}	2721^{+0179}_{-0241}	$1.269^{+0.098}_{-0.182}$	$1.096^{+0.092}_{-0.047}$	$0.0319^{+0.0006}_{-0.0010}$	$0.69^{+0.40}_{-0.63}$
908.01	193.9^{+135}_{-135}	1.12	1463^{+0084}_{-0095}	1322^{+0076}_{-0076}	2697^{+4512}_{-4512}	$1.838^{+0.161}_{-3.077}$	$0.683^{+0.043}_{-0.043}$	$0.0537^{+0.0010}_{-0.0009}$	$3.03^{+3.11}_{-3.11}$
913.01	$-22.3^{+96.5}_{-49.3}$	0.82	1566^{+0090}_{-0110}	1415^{+0086}_{-0082}	2301^{+0229}_{-0470}	$1.467^{+0.311}_{-0.271}$	$0.960^{+0.066}_{-0.059}$	$0.0492^{+0.0009}_{-0.0006}$	$0.62^{+0.74}_{-0.56}$
1176.01	-30.9^{+148}_{-100}	0.05	1535^{+0110}_{-0137}	1385^{+0099}_{-0124}	1845^{+0384}_{-3933}	$1.203^{+0.271}_{-2.575}$	$0.854^{+0.071}_{-0.107}$	$0.0278^{+0.0010}_{-0.0010}$	$0.10^{+0.50}_{-0.42}$
1419.01	$130.0^{+109}_{-72.9}$	1.22	2552^{+0176}_{-0154}	2306^{+0159}_{-0139}	3205^{+0355}_{-0523}	$1.252^{+0.149}_{-0.209}$	$0.432^{+0.042}_{-0.035}$	$0.0242^{+0.0005}_{-0.0005}$	$1.09^{+1.06}_{-0.79}$
1459.01	25.2^{+298}_{-298}	1.36	1588^{+0225}_{-0225}	1435^{+0203}_{-0203}	2731^{+0350}_{-0350}	$1.713^{+0.274}_{-0.274}$	$0.397^{+0.133}_{-0.133}$	$0.0117^{+0.0016}_{-0.0016}$	$3.19^{+3.19}_{-3.19}$
1541.01	1088.9^{+397}_{-397}	5.22	2337^{+0162}_{-0151}	2112^{+0147}_{-0136}	3522^{+0137}_{-0137}	$1.507^{+0.085}_{-0.085}$	$1.909^{+0.182}_{-0.160}$	$0.0367^{+0.0008}_{-0.0007}$	$2.87^{+0.73}_{-0.65}$
1543.01	3080.9^{+2933}_{-797}	3.77	1763^{+0114}_{-0108}	1593^{+0103}_{-0097}	3953^{+0282}_{-0268}	$2.245^{+0.165}_{-0.168}$	$1.400^{+0.117}_{-0.102}$	$0.0498^{+0.0009}_{-0.0009}$	$17.89^{+7.72}_{-6.01}$

^aDerived assuming $A = 0.0$

a uniform planetary temperature, i.e., $f = 1/4$ (see López-Morales & Seager 2007; Cowan & Agol 2011). In Figure 4.6 we reproduce the same plots but with eccentricity allowed to vary.

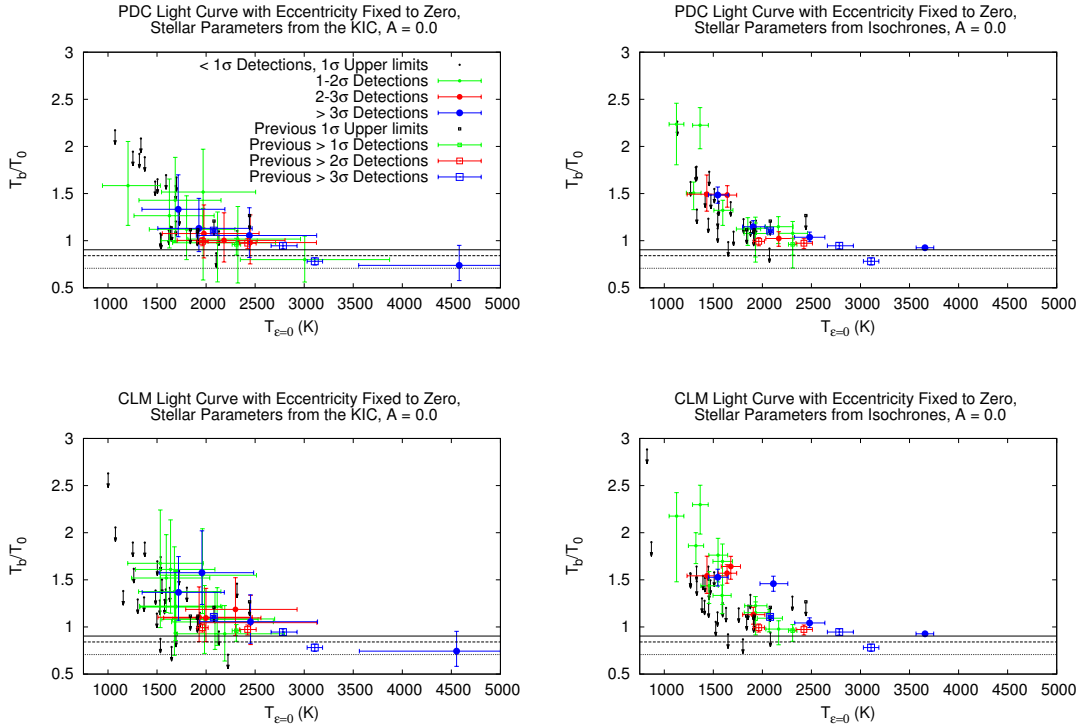


Fig. 4.5.— Plots of the effective day side temperature ratio versus the maximum effective day side temperature when fixing eccentricity to zero. The values obtained when deriving stellar parameters from the KIC are shown in the left column, while values obtained when deriving stellar parameters from stellar isochrones are shown in the right column. Values obtained when using the *Kepler* PDC light curves are shown in the first row, while values obtained when using the CLM pipeline are shown in the second row. Solid circles correspond to *Kepler* systems modeled in this paper, while open squares are previously published detections or upper limits of exoplanet secondary eclipses at optical wavelengths. All errors are 1σ . The x-axis errorbars are not shown for the $<1\sigma$ detections for clarity. The solid, dashed, and dotted black lines in each figure correspond to the expected temperature ratio assuming no heat recirculation, a uniform day-side temperature, and a uniform planetary temperature respectively.

Unless there is some extra emission at optical wavelengths that is not being

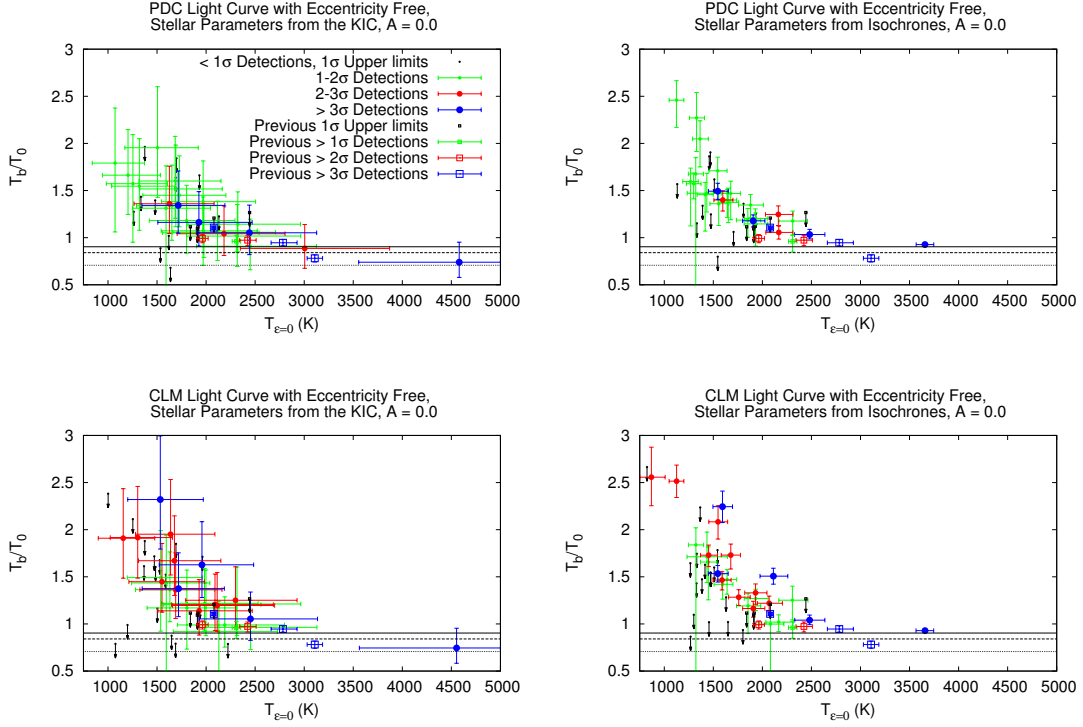


Fig. 4.6.— Similar to Figure 4.5, but with eccentricity allowed to vary.

accounted for, all the planets should lie below the $f = 2/3$ lines in Figures 4.5 and 4.6. However, it is immediately apparent that the vast majority of candidates lie above that line. In addition, there appears to be a trend of increasing T_b/T_0 with decreasing $T_{\epsilon=0}$, with some possible detections approaching 2.5 times the maximum expected brightness temperature, i.e., nearly 40 times more flux than expected. All the planets with previously published secondaries also appear to follow the same trend, although they all have $T_{\epsilon=0} \gtrsim 2000$ K. This trend will be discussed in more detail below.

We have explored several possible explanations for such large observed emissions at visible wavelengths: 1) A bias in the determination of stellar and planetary parameters or the secondary eclipse detection efficiency, 2) high albedos, which

would make reflected light a major contributor to the planetary emission, 3) very large amounts of non-LTE or other thermal emission at optical wavelengths, 4) the presence of a significant source of internal energy generation within the planet, and 5) some of the candidates are in fact very low mass stars or brown dwarf companions, or background eclipsing binary blends.

Potential Biases: The determined stellar parameters of T_\star , M_\star , and R_\star can have significant uncertainties, as noted in Section 4.4, and indeed can vary notably when taken from the KIC or computed from stellar isochrones based on T_\star . The values of those parameters are intimately tied to the derivation of the planetary parameters $T_{\epsilon=0}$, T_0 , T_b , a , R_p , F_a , and A_{max} , and that must be kept in mind when interpreting any possible results. For example, the stellar isochrones assume the stars are main-sequence, and thus if a host star is really a sub-giant or otherwise evolved, the stellar flux at the planet’s surface would be underestimated. This would in turn cause an underestimated value of both $T_{\epsilon=0}$ and T_0 , and thus potentially overestimated values of T_b/T_0 at lower $T_{\epsilon=0}$. However, it is unlikely that a large fraction of the examined systems are significantly evolved, and sub-giants would likely show telltale variations in their light curves. Given this, and that as far as we know there is no other preferential bias in the determination of the stellar parameters, we would not expect this problem to systematically influence the results presented in Figures 4.5 and 4.6.

When examining secondary detection efficiency, we note that the derived upper limits on the secondary eclipse depths are roughly at the same level as the noise of the *Kepler* data. That level of noise is consistent among the set of *Kepler* light curves we have examined. Thus, as we search the data for planets with lower values of $T_{\epsilon=0}$ and T_0 , the corresponding upper limit for T_b/T_0 naturally

increases, as the expected eclipse depth decreases while the noise level remains the same. This introduces an artificial trend of higher T_b/T_0 upper limits as $T_{\epsilon=0}$ decreases, which can be seen in Figures 4.5 and 4.6. Similarly, when examining the $\sim 1\sigma$ detections, about $\sim 32\%$ of the detections will be statistically spurious, as exemplified in the data and already discussed in Section 4.3. We thus expect an artificial trend of higher T_b/T_0 values with decreasing values of $T_{\epsilon=0}$ for $\sim 32\%$ of the $\sim 1\sigma$ detections. However, when we move to the $\gtrsim 2\sigma$ detections, the expected rate of spurious detections drop to $\lesssim 5\text{-}10\%$. The data in Figures 4.5 and 4.6 still reveal a significant trend of increasing T_b/T_0 values with decreasing $T_{\epsilon=0}$ in the $\gtrsim 2\sigma$ detections, (including as well previous secondary eclipse detections from the literature), so we conclude this trend is real and due to either increasing albedos or emission features in the visible as the atmospheric temperature of the planets decrease. The hypothesis of high albedos is further discussed below. As for emission features, a literature search on this topic does not reveal any known physical processes that would produce this effect, so further theoretical work might be necessary.

High Albedos: As mentioned in the introduction, some recent studies suggest high albedos for some known hot giant planets (e.g. Berdyugina et al. 2011; Kipping & Bakos 2011a; Demory et al. 2011). To examine the possibility that the excess flux observed in our list of secondary eclipse candidates is due to albedo, we have recomputed the expected normalized brightness temperature T_b/T_0 of each candidate when assuming increasing values of the albedo. The reflected light contribution is computed using equation 4.5 and subtracted from the total flux measured for each object. T_b is then recomputed using the remaining flux, assuming it is solely due to thermal emission. The results are shown in Figure 4.7 for

three different albedos, $A = 0.1, 0.5,$ and 1.0 , using the secondary eclipse depths measured from the CLM pipeline light curves for $e = 0$, (the eclipse depths measured from the other light curves described in Section 4.2 give similar results).

As expected, T_b/T_0 decreases as the albedo increases, and many of the points in Figure 4.7 go below the $T_b/T_0 = (2/3)^{1/4}$, i.e., $A = 0$ and $f = 2/3$, limit once high enough albedos are assumed. The emission of 53% of the planet candidates can be interpreted as a combination of reflected light and thermal emission when we assume a geometric albedo of $A = 0.5$, set $e = 0$, and derive stellar parameters from the KIC, though only 31% when deriving stellar parameters from stellar isochrones. Those levels of reflectivity might indicate the presence of clouds, haze, or Rayleigh scattering in the atmosphere of those planets, with a general trend of increasing albedo with decreasing planetary temperature responsible for the trend of increasingly excess emission at lower planetary temperatures. We note, however, that a significant number of points, 40% and 63% when deriving stellar parameters from the KIC and stellar isochrones respectively, with $e = 0$, still remain above $T_b/T_0 = (2/3)^{1/4}$, even if we assume perfectly reflecting planets, i.e. $A = 1.0$. Many of these remaining systems are at low values of $T_{\epsilon=0}$, and some of those points are $\gtrsim 2\sigma$ detections, so there is still excess emission and a correlation of T_b/T_0 with decreasing $T_{\epsilon=0}$ that cannot be explained by reflected light, and needs to be explained in some other way.

Non-LTE or Other Thermal Emission: We have used the brightness temperature parameter T_b to represent the amount of thermal emission from each planet, assuming that the planets emit as blackbodies. In that case, if the emission of the planet yields a T_b larger than that predicted by $f = 2/3$ and $A = 0$, that emission is above the so-called equilibrium temperature. However, the atmospheres of

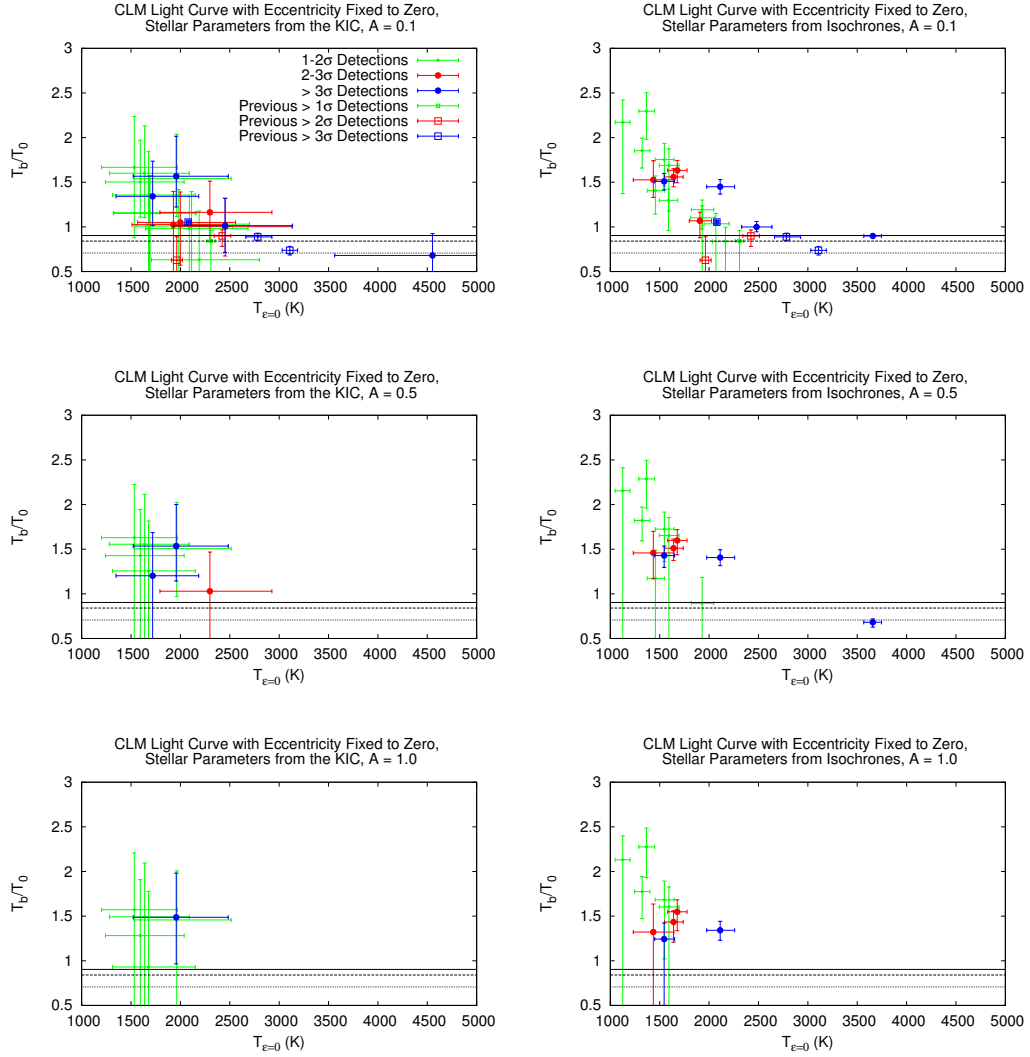


Fig. 4.7.— Plots of the effective day side temperature ratio versus the maximum effective day side temperature for, from top to bottom, albedos of 0.1, 0.5, and 1.0, using the CLM pipeline light curves and assuming no eccentricity. The values obtained when deriving stellar parameters from the KIC are shown in the left column, while values obtained when deriving stellar parameters from stellar isochrones are shown in the right column. Solid circles correspond to *Kepler* systems modeled in this paper, while open squares are previously published detections or upper limits of exoplanet secondary eclipses at optical wavelengths. The solid, dashed, and dotted black lines in each figure correspond to the expected temperature ratio assuming no recirculation, a uniform day-side temperature, and a uniform planetary temperature respectively. Systems that disappear from the plots when moving from low to high albedos can be fully explained by reflected light, while systems that still remain at $A = 1.0$ present excess emission that cannot be explained solely by reflected light.

exoplanets do not necessarily emit as blackbodies, and some spectral models of hot Jupiters (e.g., Fortney et al. 2008) predict significantly higher emission levels in the optical region covered by the *Kepler* bandpass ($\sim 0.4 - 0.9 \mu m$) compared to blackbody approximations. The emission spectrum of a planet will depend strongly on its atmospheric composition and Temperature-Pressure (T-P) profile. Although some models including the presence of strong absorbers, such as TiO and VO, have been proposed (Hubeny et al. 2003; Fortney et al. 2008; Burrows et al. 2008a), uncertainties in the T-P profiles and the lack of previous observational data limit the reliability of those models. In addition, and as already mentioned above, there is currently no model that predicts the increase of T_b/T_0 for decreasing $T_{\epsilon=0}$ observed in Figures 4.5 and 4.6.

Another possibility is that the large amount of stellar irradiation these planets receive induces resonant and non-resonant fluorescent transitions by exciting the chemical species present in their upper atmospheres. Fluorescence has been measured in Solar System objects, i.e., Titan, Saturn and Jupiter, at IR, UV, and X-ray wavelengths (e.g., Yelle & Griffith 2003; López-Valverde et al. 2005; Cravens et al. 2006; Lupu et al. 2011), and possibly in the NIR for the exoplanet HD189733b (Swain et al. 2010), but we could not find any observations of or theoretical work on non-LTE/fluorescence emission in the $0.4 - 0.9 \mu m$ wavelength range covered by *Kepler*. However, it is expected that non-LTE emission lines in exoplanetary atmospheres will not be significantly broadened by collisions, and will appear instead as sharp emission features (Martin-Torres, priv. comm.). Considering the amount of energy required to produce these fluorescent emissions, it is unlikely that, given their narrow emission range, they would be luminous enough to significantly increase the measured emission levels over the very wide *Kepler*

bandpass above the expected LTE emissions observed in Figures 4.5 and 4.6.

Significant Internal Energy Generation: Our own Jupiter radiates about 1.6 times as much energy as it receives from the Sun. The additional heat source is generally attributed to either residual heat left over from the initial Solar System nebula collapse, or ongoing slow contraction of the planet’s core. However, if the planet candidates in our list were undergoing a similar internal energy generation process, T_b/T_0 would only reach up to about $1.6^{1/4} = 1.12$, not high enough to explain the emission of objects in our sample with $T_{e=0} \lesssim 1500$ K.

Low Mass Stars, Brown Dwarfs, or Blends: The last possibility we consider is that some of the objects in the list are in fact brown-dwarfs or low-mass stars, but this assumption also possesses some problems. Exoplanet search results over the years have revealed what appears to be a “brown dwarf desert” within orbital separations from the host star of $a \lesssim 5$ AU, for solar type stars (see e.g., Grether & Lineweaver 2006). However, the discovery of CoRoT-3b, a $21.7 M_{Jup}$ object orbiting at a separation of only 0.057 AU around an F3-type star, has opened some debate about whether this object is really a brown dwarf, or if planets more massive than the defined Deuterium burning limit can form around stars more massive than the Sun. To test this idea we plot in Figure 4.8 the measured T_b/T_0 of each planet candidate versus the effective temperature of the star, T_\star . We see no clear correlation between the temperature of the host star and an excess brightness of the planet candidates, and an error-weighted linear fit does not yield a statistically significant slope. We also plot in Figure 4.8 the values for T_b/T_0 versus R_p , a , and A_{Lp} , but do not see any significant linear correlations either.

We also utilize the upper limits on possible secondary eclipses we derived

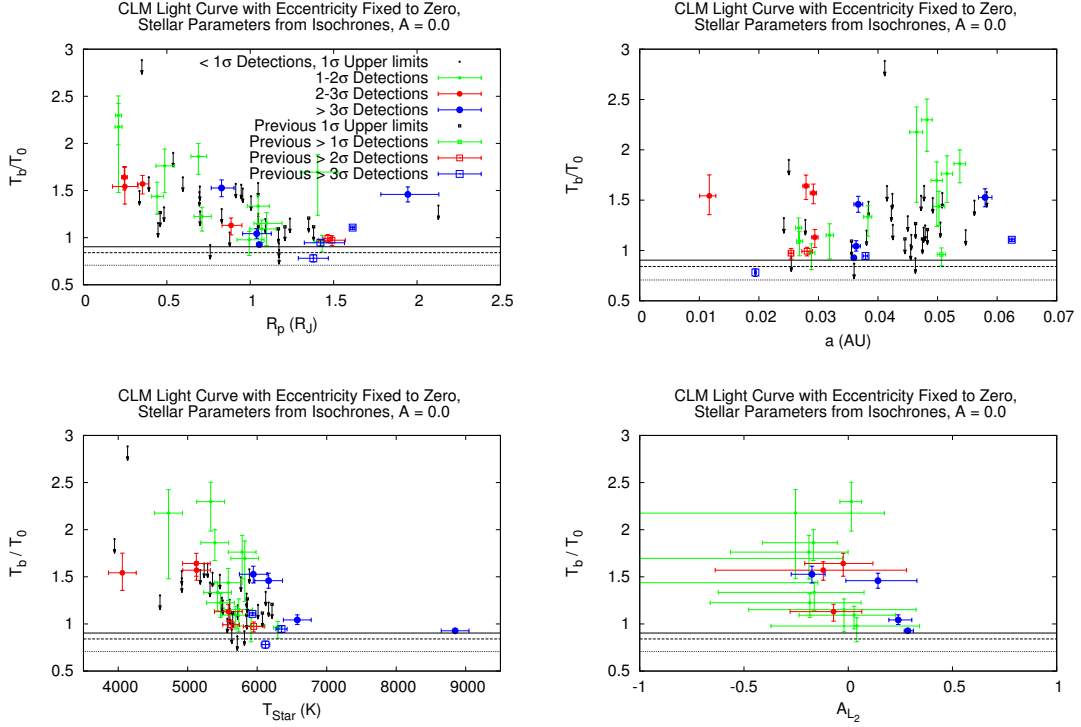


Fig. 4.8.— Plots of the effective day side temperature ratio versus the radius of the planet (top-left), the semi-major axis of the system (top-right), the effective temperature of the star (bottom-left), and the amplitude of the sine curve applied to the planet’s luminosity (bottom-right), using the CLM light curves, assuming no eccentricity, and deriving stellar parameters from stellar isochrones. Results for the PDC light curves are not shown, but produce similar results. Solid circles correspond to *Kepler* systems modeled in this paper, while open squares are previously published detections or upper limits of exoplanet secondary eclipses at optical wavelengths. The x-axis errorbars are not shown for the $<1\sigma$ detections for clarity. The solid, dashed, and dotted black lines in each figure correspond to the expected temperature ratio assuming no recirculation, a uniform day-side temperature, and a uniform planetary temperature respectively.

to examine potential trends in A_{max} as computed using Eq. 4.6. In Figure 4.9 we plot both the 1σ and 3σ upper limits, delineated by solid and dashed lines respectively, on the values of A_{max} versus $T_{\epsilon=0}$ for both fixing eccentricity to zero and allowing it to vary, for the CLM light curves and deriving stellar parameters from isochrones. We also include the values for previously published detections

and upper limits of secondary eclipses in the optical wavelength regime. Also in Figure 4.9 we plot the cumulative number of systems, and total fraction of all systems, that were modeled in this paper and that have their upper limit of A_{max} below a given value of A , for both 1σ and 3σ upper limits. As can be seen, when fixing eccentricity to zero, we can generally obtain constraints on the maximum possible albedo for $\sim 85\%$ of the *Kepler* systems at the 1σ confidence level, and $\sim 45\%$ of systems at the 3σ confidence level. When letting eccentricity vary, we can only constrain A_{max} for $\sim 50\%$ and $\sim 30\%$ of the *Kepler* systems at the 1σ and 3σ confidence levels respectively. However, comparing the $T_{\epsilon=0}$ values of the previously published planets to that of the *Kepler* candidates, we find we have significantly increased the number of systems with constrained albedos in the $T_{\epsilon=0} \lesssim 2000$ K regime. As can be seen, many of the systems in this temperature regime appear to have maximum possible albedos below 0.3 at the 1σ confidence level, thus confirming previous findings of low albedos for hot Jupiters at optical wavelengths, and indicating that such low albedos may be common down to planetary temperatures of 1200 K.

4.6. Properties of Some Individual Objects

In the previous section we analyzed the secondary eclipse detections as a set, in an attempt to find common characteristics of the sample. We have carefully examined each individual system, and in this section present and discuss the most interesting objects in more detail.

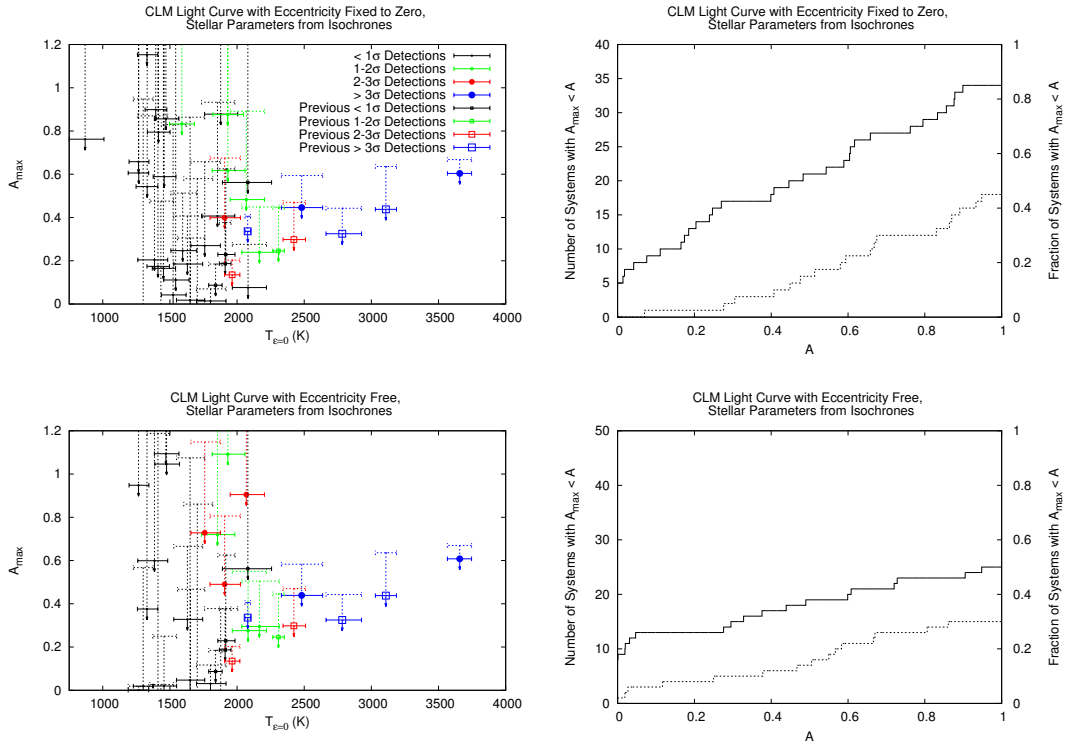


Fig. 4.9.— Left Column: Plots of the 1σ and 3σ upper limits, delineated by solid and dashed lines respectively, on the maximum possible albedo values versus the maximum effective day side temperature when deriving stellar parameters from stellar isochrones, using the CLM pipeline light curves. Right Column: Plots of the cumulative number of systems and total fraction of all systems modeled in this paper that have their upper limit of A_{max} below a given value of A , for both 1σ and 3σ upper limits. Values obtained when fixing eccentricity to zero are shown in first row, while values obtained when allowing eccentricity to vary are shown in the second row. Solid circles correspond to *Kepler* systems modeled in this paper, while open squares are previously published detections or upper limits of exoplanet secondary eclipses at optical wavelengths. The results when using the *Kepler* PDC curves are not plotted, but are very similar to the presented CLM light curves.

4.6.1. KOI 1.01 / TrES-2b

KOI 1.01 is also known as TrES-2b, and was discovered to be a transiting planet by O’Donovan et al. (2006) before the *Kepler* mission was launched. Kipping & Bakos (2011b) determined an upper limit to the eclipse depth of 37ppm

at the 1σ level, and 73 ppm at the 3σ level, based on short-cadence Q0 and Q1 *Kepler* data, thus limiting the geometric albedo to $A_g < 0.146$ at 3σ confidence. Kipping & Spiegel (2011) have recently published the detection of phase curve variations with an amplitude of 6.5 ± 1.9 ppm using Q0-Q2 short cadence data, but do not detect the secondary eclipse itself, calculating that any secondary eclipse measurement must have an uncertainty of ~ 13 ppm. If this variation is due to reflected light, then Kipping & Spiegel (2011) calculate the albedo of the planet as $A_g = 0.0253 \pm 0.0072$.

Using the CLM pipeline light curves, and fixing eccentricity to zero, we determined a secondary eclipse depth of $-3.9_{-8.0}^{+8.1}$ ppm, thus yielding upper limits on the eclipse depth of 4.2 and 20.4 ppm for 1σ and 3σ confidence levels respectively. We determined a value for the maximum possible albedo, A_{max} , using stellar values from the KIC, of $-0.004_{-0.019}^{+0.010}$, yielding upper limits on the albedo of 0.006 and 0.026 for 1σ and 3σ confidence levels respectively. If using values from stellar isochrones, we instead determine $A_{max} = -0.014_{-0.029}^{+0.028}$, and thus 1σ and 3σ upper limits of 0.016 and 0.072, respectively. We did not detect any significant orbital phase variation, although a significant value of the luminosity of the planet must be found in order to produce a significant value of A_{L_p} via our modeling technique. Given a difference in the calculated planet-to-star luminosity ratio between our measurements and those of Kipping & Spiegel (2011) of 10.4 ± 8.3 ppm, our results do not conflict with those of Kipping & Spiegel (2011) at a confidence level greater than 1.25σ .

We also note that the error on individual points in the Q2 long cadence data is 43 ppm, and thus given the predicted 77.1 minute occultation duration, the 29.4244 minute cadence of *Kepler* long cadence data, the 88.7 days of coverage,

and the 2.47 day orbital period of the system, we calculate that one could detect the secondary eclipse of the planet to a 1σ precision of 4.5 ppm. This is in agreement with our 1σ upper limit, although our formal 1σ errors on the eclipse depth are twice as large, likely due to remaining systematics that were accounted for in the residual-permutation error analysis. However, with better systematic noise reduction, and an additional 1-2 quarters of data, the secondary eclipse of this planet could very well be detected to 3σ confidence. Future efforts should be directed towards this goal to confirm the phase signal found by Kipping & Spiegel (2011), and ensure it is not due to remaining systematics in the *Kepler* lightcurves or intrinsic stellar variability.

4.6.2. KOI 2.01 / HAT-P-7b

KOI 2.01 is also known as HAT-P-7 and was discovered by Pál et al. (2008) prior to the launch of the *Kepler* mission. Borucki et al. (2009) detected a secondary eclipse in the Q0 *Kepler* data of 130 ± 11 ppm, and a 122 ppm phase variation. Christiansen et al. (2010) determined an independent 3σ upper limit of 550 ppm on the secondary eclipse depth at optical wavelengths using the EPOXI spacecraft. Using Q1 *Kepler* data, Welsh et al. (2010) determined a secondary eclipse depth of 85.8 ppm, a 63.7 ppm phase variation due to reflection from the planet, a 37.3 ppm phase variation due to ellipsoidal distortions in the star induced by tidal interaction between the planet and star, and determined an albedo in the *Kepler* passband of 0.18, though no errors on the derived quantities were given.

We do not detect any significant orbital eccentricity ($>3\sigma$) in KOI 2.01 /

HAT-P-7 in either the PDC or the CLM light curves when allowing eccentricity to vary. Fixing eccentricity to zero, for the *Kepler* PDC light curve, we determine a planet-to-star luminosity ratio of $75.0_{-8.1}^{+9.5}$ ppm and a value for A_{L_p} of $0.421_{-0.071}^{+0.073}$, and thus a $63.2_{-12.6}^{+13.6}$ ppm phase variation. Similarly, for the CLM light curve, we derive a planet-to-star luminosity ratio of $77.7_{-9.5}^{+10.3}$ ppm and a value for A_{L_p} of $0.240_{-0.045}^{+0.065}$, and thus a $37.3_{-8.3}^{+11.2}$ ppm phase variation. Our determined eclipse depths are very consistent between the CLM and PDC light curves, and within $\sim 1\sigma$ of the value found by Welsh et al. (2010), though are not compatible with the value found by Borucki et al. (2009) at the $\sim 4\sigma$ level. Examining the amplitude of the phase variation of the system, we first point out that there is a $\sim 1.5\sigma$ difference in the values derived between the PDC and CLM light curves, and likely is a result of the different methods employed to remove systematic noise. While the high-frequency signal of the secondary eclipse was not affected, the low-frequency signal of the phase variation, with a period of ~ 2.2 days, was much more easily distorted. It is not clear which measurement on the phase variation is more valid, though the CLM pipeline light curves yields a χ_{red}^2 of 7.6, versus a value of 26.5 for the PDC data. This result should highlight the level of care that needs to be taken when examining and interpreting phase variations and other low-frequency signals in *Kepler* data.

Finally, utilizing stellar isochrones for the mass and radius determination of the host star, we determine 3σ upper limits to the maximum albedo of the planet of 0.556 and 0.594 for the PDC and CLM light curves respectively, in agreement with the values determined by Welsh et al. (2010).

4.6.3. KOI 10.01 / Kepler-8b

KOI 10.01 is also known as Kepler-8b, and was first discovered to be a transiting planet by Jenkins et al. (2010a). Kipping & Bakos (2011a) found that the orbit is consistent with a circular orbit, and placed a 3σ upper limit on a secondary eclipse of 101.1 ppm, thus constraining the albedo to < 0.63 .

We do not detect any significant eccentricity ($>3\sigma$) in either the PDC or CLM light curves when allowing eccentricity to vary. Fixing the eccentricity to zero, we place 3σ upper limits on the secondary eclipse of the planet at 119 ppm, ($14.9^{+34.7}_{-13.9}$ ppm), and 114 ppm, ($19.6^{+31.6}_{-33.7}$ ppm), for the PDC and CLM light curves respectively. Deriving the parameters for the host star from stellar isochrones yields a 3σ limit on the maximum albedo of 0.898 and 0.933 for the PDC and CLM light curves respectively. Thus, we do not provide any additional constraints on the atmosphere of this planet over previous studies.

4.6.4. KOI 13.01

KOI 13 was noted by (Borucki et al. 2011) to be a double star, and unresolved in the *Kepler* images due to the $\sim 4''$ pixel size. Szabó et al. (2011) recently conducted a thorough analysis of the system with careful detail to isolating the transiting planet candidate in the double star system, and concluded that KOI 13.01 is likely a brown dwarf with a radius of $2.2 \pm 0.1 R_J$. They also concluded that the transit showed an asymmetrical profile, due to the rapidly rotating nature of the host of KOI 13.01, detected a secondary eclipse with a depth of 120 ± 10 ppm, and did not find any significant orbital eccentricity. More recently, Shporer et al. (2011) determined a mass of $9.2 \pm 1.1 M_{Jup}$ via photometric beaming, and

Barnes et al. (2011) used the asymmetrical profile of the transit to measure a planetary radius of $1.756 \pm 0.014 R_{\odot}$, thus making it more likely that this object is a massive hot Jupiter. Mazeh et al. (2011) further support this characterization, and additionally measure a secondary eclipse depth of 163.8 ± 3.8 ppm.

We do not detect any significant eccentricity ($>3\sigma$) in either the PDC or CLM light curves when allowing eccentricity to vary, and we can confirm that the asymmetrical transit shape exists in both the PDC and CLM lightcurves. Fixing the eccentricity to zero, we determine a secondary eclipse depth of $124.3^{+6.9}_{-7.8}$ and $125.6^{+6.3}_{-8.6}$ ppm for the PDC and CLM light curves respectively, which are statistically consistent with each other and the values found by Szabó et al. (2011), though is discrepant at the 5σ level with the value measured by Mazeh et al. (2011). We note that KOI 13.01 is the planet with the highest value of $T_{\epsilon=0}$ in our sample, and one of the few that is consistent with a T_b/T_0 value of less than 1.0, although we did not take third light into account in our analysis.

4.6.5. KOI 17.01 / *Kepler-6b*

KOI 17.01 is also known as *Kepler-6b*, and was discovered to be a transiting planet by Dunham et al. (2010). Kipping & Bakos (2011a) did not find any evidence for a non-circular orbit, and constrained any possible secondary eclipses to less than 51.5 ppm, and thus a geometric albedo less than 0.32, both at 3σ confidence. Désert et al. (2011a) was able to use *Kepler* data from Q0-Q5, of which Q3-Q5 were not yet publicly accessible at the time of writing, to measure a secondary eclipse of 22 ± 7 ppm, and did not find any evidence for a non-circular orbit. Combining this eclipse measurement with others obtained via *Spitzer*, they

determined a geometric albedo of 0.11 ± 0.04 .

We do not detect any significant eccentricity ($>3\sigma$), and place a 3σ upper limit on any possible secondary eclipse at 34.5 ppm, $(-17.1^{+17.2}_{-22.3}$ ppm). This constrains the planetary albedo, at the 3σ level, to less than 0.25 and 0.31 when deriving stellar parameters from the KIC and isochrones respectively, consistent with both the values derived by Kipping & Bakos (2011a) and Désert et al. (2011a).

4.6.6. KOI 18.01 / Kepler-5b

KOI 18.01 is also known as Kepler-5b, and was discovered to be a transiting planet by Koch et al. (2010). Kipping & Bakos (2011a) did not find any evidence for a non-circular orbit, though found weak evidence for a secondary eclipse with a depth of 26 ± 17 ppm, implying a geometric albedo of 0.15 ± 0.10 . Désert et al. (2011a) detected the secondary eclipse, again using Q0-Q5 data, to greater precision and determined a depth of 21 ± 6 ppm, which they combined with *Spitzer* observations to determine a geometric albedo of 0.12 ± 0.04 .

We do not detect any significant eccentricity ($>3\sigma$), and do not detect the secondary eclipse in either the PDC or CLM light curves, placing a 3σ upper limit on the eclipse depth of 62.9 ppm $(-27.4^{+30.1}_{-33.2}$ ppm) using the CLM light curve. The derived median value and associated 1σ uncertainties on the secondary eclipse depth for the PDC data is $0.21^{+1.4}_{-0.3}$ ppm, in obvious contradiction to the previously mentioned measured eclipse depths. However, the PDC light curve for KOI 18.01 appears to suffer from a high level of systematic noise, and inspection of the parameter distribution histograms for the surface brightness ratio and luminosity ratio reveal them to significantly deviate from a Gaussian shape, having directly

derived 2σ uncertainties of ${}_{-10.7}^{+36.1}$ ppm, thus providing a more reasonable 3σ upper limit on the eclipse depth of 54.4 ppm for the PDC light curve.

4.6.7. KOI 20.01 / Kepler-12b

KOI 20.01 has recently been announced by Fortney et al. (2011) as Kepler-12b, a $1.7 R_J$, $0.43 M_J$ planet orbiting a slightly evolved G0 star at a period of 4.4 days. Using *Kepler* data from Q0-Q7, of which Q3-Q7 were not publicly accessible at the time of writing, they were able to measure a 31 ± 8 ppm secondary eclipse, which implies a geometric albedo of 0.14 ± 0.04 when combined with additional *Spitzer* observations. They also do not detect any significant orbital eccentricity.

Using our CLM light curves, we derived a 3σ upper limit on the eclipse depth of 56.3 ppm, ($4.7_{-9.7}^{+17.2}$ ppm), when fixing eccentricity to zero, implying a 3σ upper limit on the maximum possible albedo of the planet of 0.40. These results are in agreement with the values recently found by Fortney et al. (2011).

4.6.8. KOI 64.01

Borucki et al. (2011) noted that KOI 64.01 may be a binary system composed of a F-type primary and a M-type secondary. We do not detect any significant eccentricity ($>3\sigma$) in the system, though we do detect marginal evidence for a secondary eclipse in the system. Fixing the eccentricity to zero, we detect a secondary eclipse with a depth of $47.7_{-23.3}^{+25.0}$ and $75.1_{-27.7}^{+35.1}$ ppm, (2.0σ and 2.7σ detections), for the PDC and CLM light curves respectively. Taking the CLM light curve detection as a more reliable measurement, given its χ_{red} value of 7.3 versus a value of 10.4 for the PDC data, we cannot provide any constraints on

the maximum albedo, and in fact even an albedo of 1.0 cannot account for this level of emission. Assuming it has an albedo of 0.0, we calculate a value of $T_b/T_0 = 1.05^{+0.29}_{-0.23}$ if deriving stellar values from the KIC, and $1.57^{+0.09}_{-0.11}$ if using stellar isochrones, which are both above the maximum allowed value of $(2/3)^{\frac{1}{4}}$ for a planet with no heat redistribution. Thus, this object, if the secondary eclipse detection is real, likely has a significant source of internal energy generation, and certainly may be a brown dwarf or low-mass star. We note however that the effective temperature for the star given in the KIC is 5128 K, which would suggest a K0 spectral type, not F-type. Thus if the host star is a K0 dwarf, the companion, if not a planet, would likely be a brown dwarf, unless the system is composed of a foreground K0 dwarf and a background F+M type eclipsing binary.

4.6.9. KOI 97.01 / Kepler-7b

KOI 97.01 is also known as Kepler-7b, and was discovered to be a transiting planet by Latham et al. (2010). Kipping & Bakos (2011a) found a secondary eclipse depth of 47 ± 14 ppm, implying a geometric albedo of 0.38 ± 0.12 , and found a day/night flux difference of 17 ± 9 ppm. Demory et al. (2011) used *Kepler* data from Q0-Q4, of which Q3 and Q4 were not yet publicly available at the time of writing, to detect a secondary eclipse of 44 ± 5 ppm, which implied an albedo of 0.32 ± 0.03 . They also detected an orbital phase curve with an amplitude of 42 ± 4 ppm. Neither study found evidence for significant orbital eccentricity.

We obtain $>3\sigma$ detections of the secondary eclipse in both the PDC and CLM light curves, both fixing eccentricity to zero and allowing it to vary, though we do not detect any significant ($>3\sigma$) eccentricity in the system. Fixing the eccentricity

to zero, we obtain secondary eclipse depths of $53.2_{-13.0}^{+14.1}$ ppm and $66.1_{-17.5}^{+17.4}$ ppm for the PDC and CLM light curves respectively, however we find we cannot place any significant limits on the maximum possible albedo. We determine values for A_{L_p} of 0.12 ± 0.24 and $-0.17_{-0.10}^{+0.06}$ for the PDC and CLM light curves respectively, which translate to phase variations of $12.8_{-25.7}^{+25.8}$ ppm and $-22.5_{-14.5}^{+9.9}$, neither of which is significant at a $>3\sigma$ level.

Both of our values for the eclipse depth are consistent with those obtained by Kipping & Bakos (2011a) at $<1\sigma$ discrepancy, and at $<1.5\sigma$ with those of Demory et al. (2011). Upon inspection of the data, it turns out that we are not able to significantly constrain the albedo, when both Kipping & Bakos (2011a) and Demory et al. (2011) were able to, due to the values we adopt for the stellar mass and radius. We determined median values of $1.09 M_{\odot}$ and $1.28 R_{\odot}$ using the KIC, and $1.09 M_{\odot}$ and $1.03 R_{\odot}$ via stellar isochrones, where the other studies adopted values of $\sim 1.3 M_{\odot}$ and $\sim 1.9 R_{\odot}$, as Latham et al. (2010) found this star to be a G-type sub-giant. Unfortunately the KIC did not hint at this star being non-main-sequence, and the stellar isochrones we employ assume the host star is on the main-sequence. Obviously changing the stellar radius by a factor of ~ 2 greatly impacts the estimate of reflected light, and this should emphasize the connection between the assumed stellar properties and derived planetary properties. Although we do not detect significant phase variations, our obtained values for the PDC light curve are not in conflict with either previously published result at greater than $\sim 1\sigma$ significance. The value for the CLM light curve does conflict at $>3\sigma$ significance, and we attribute it to differences in the light curve processing from the pixel level data. This is another example of how low-frequency signals can change significantly in *Kepler* data depending on the reduction technique employed.

4.6.10. KOI 183.01

We highlight KOI 183.01 due to a possibly significant detection of its secondary eclipse and eccentricity. Using the CLM light curves, we obtain a value for the secondary eclipse depth of 14_{-40}^{+42} ppm when fixing eccentricity to zero, but a value of 125_{-39}^{+42} , (3.2σ), when allowing eccentricity to vary. In the latter case, we measure values of $e \cdot \cos(\omega) = -0.152_{-0.008}^{+0.009}$ and $e \cdot \sin(\omega) = 0.03_{-0.14}^{+0.12}$, yielding values of $e = 0.178_{-0.023}^{+0.075}$ and $\omega = 169_{-34}^{+47}$ degrees.

We employ the Bayesian Information Criterion (BIC) (Schwarz 1978) to determine if allowing the eccentricity to vary, thus adding two more free parameters, provides a statistically significantly better fit to the data than fixing it to zero. Given competing models with different values of χ^2 , and a different number of free parameters, k , the value

$$BIC = \chi^2 + k \cdot \ln(N) \quad (4.7)$$

is computed, where N is the number of data points, and the model with the lowest BIC value is the preferred model. Given the 3,720 data points in the light curve, 8 free parameters with a χ^2 value of 12499 when fixing the eccentricity to zero, and 10 free parameters with a χ^2 value of 12476 when allowing eccentricity to vary, values for the BIC of 12565 and 12558 are obtained for the fixed and free eccentricity models respectively. Given the lower BIC value for the eccentricity free model, and given that the resulting parameter distributions from the residual permutation analysis are well-behaved Gaussian curves and do not show any anomalies (see Figure 4.3.14), we conclude that the eccentricity free model is

preferred and statistically significant.

Adopting values for the host star from stellar isochrones, we compute a maximum possible albedo of $0.52^{+0.21}_{-0.19}$, or a value of $T_b/T_0 = 1.28^{+0.08}_{-0.09}$. These are both reasonable values for a moderately reflective planet, one heated beyond radiative thermal equilibrium via tidal heating due to its significant eccentricity, or likely a combination of the two. Additional *Kepler* data and other follow-up observations should hopefully confirm this detection.

4.6.11. KOI 196.01

KOI 196.01 has recently been confirmed as a $0.49 M_J$, $0.84 R_J$, transiting planet by Santerne et al. (2011) via SOPHIE RV measurements and an analysis of the *Kepler* light curve. They detect a secondary eclipse with a depth of 64^{+10}_{-12} ppm, with corresponding phase variations, and determine a geometric albedo of 0.30 ± 0.08 . They do not find any significant orbital eccentricity.

We also detect the secondary eclipse with a depth of 77 ± 24 ppm and 63^{+33}_{-32} ppm in the PDC and CLM light curves respectively, and also do not find any evidence for significant orbital eccentricity, though we do not find any significant orbital phase variation. Via our eclipse depths, and utilizing stellar isochrones, we determine a maximum possible albedo of $0.29^{+0.10}_{-0.09}$ and $0.26^{+0.14}_{-0.13}$ for the PDC and CLM light curves respectively. Both of our values for the eclipse depth and geometric albedo are consistent and agree with those determined by Santerne et al. (2011).

4.6.12. KOI 202.01

We highlight KOI 202.01 due to a possible detection of its secondary eclipse, and a robust upper limit on its albedo. We measure the secondary eclipse depth of the system as 69_{-30}^{+31} ppm (2.3σ) and 46_{-36}^{+31} ppm (1.3σ), for the PDC and CLM light curves respectively, and do not detect any significant orbital eccentricity nor phase variations. Although these are not significant enough to claim a robust detection, they are certainly interesting enough results to merit further follow-up with additional data, and place robust 3σ upper limits on the maximum albedo of the system at 0.46 and 0.43 for the PDC and CLM light curves respectively, when deriving host star parameters from stellar isochrones.

4.6.13. KOI 203.01 / Kepler-17b

KOI 203.01 is also known as Kepler-17b, and was first confirmed as a transiting planet by Désert et al. (2011b). Using *Kepler* Q0-Q6 observations, of which Q3-Q6 were not yet publicly available at the time of writing, along with follow-up observations from *Spitzer*, they were able to detect a secondary eclipse with a depth of 58 ± 10 ppm, and thus an albedo of 0.10 ± 0.02 , while finding no evidence for any orbital eccentricity. Bonomo et al. (2011) also detect the secondary eclipse at the 2.5σ level using Q1-Q2 observations, after fitting and subtracting 4^{th} order polynomials to 4-day segments of the light curve, with a depth of 52 ± 21 ppm and consistent with a circular orbit.

We were only able to obtain a 3σ upper limit on the secondary eclipse depth of 159 ppm (-15 ± 58 ppm) using the CLM light curve and fixing eccentricity to zero. This corresponds to 3σ upper limits on the albedo of 0.26 and 0.28 when deriving

the host star parameters from the KIC and stellar isochrones respectively. Our results are thus statistically consistent with the detections of Désert et al. (2011b) and Bonomo et al. (2011), although our errorbars are much larger. Examining the data, this star’s lightcurve has large out of eclipse variations, on the order of the depth of the primary transit, due to both intrinsic stellar variability and systematics introduced by the star’s movement, that rendered the PA and PDC data unmodelable. Our CLM pipeline was able to remove a large amount of this variability, (enough to reliably measure the primary transit), but did not fully remove it all, as illustrated by the χ_{red}^2 value of 19.4. Thus, the eclipse signal for this planet is below the noise level for the CLM lightcurve.

4.6.14. KOI 1541.01

We highlight this system due to the unusually deep secondary eclipse and high eccentricity we detect at $>3\sigma$ confidence. However, the value for the eccentricity, ~ 0.78 , along with the unusually deep eclipse depth of ~ 1100 ppm, and a large χ_{red}^2 value of 28.7, lead us to believe this system suffers from severe systematics which happened to phase together in such a way as to create an artificial eclipse. If the signal is real, then this system must be a background eclipsing binary blend or other similar object.

4.6.15. KOI 1543.01

This system is very similar to KOI 1541.01 in that we also obtain a $>3\sigma$ detection of a secondary eclipse, but with an unusually high values for the eclipse depth, eccentricity, and χ_{red}^2 . Inspection of the light curve also reveals this system

to contain significant systematics, or else must be a background eclipsing binary.

4.7. Summary and Conclusions

We have analyzed the *Kepler* Q2 light curves of 76 hot Jupiter transiting planet candidates using both the *Kepler* PDC data and the results from our own photometric pipeline for producing light curves from the pixel-level data. Of the 76 initial candidates only 55 have light curves with high enough photometric stability to search for secondary eclipses. For the remaining targets this search is hindered by either intrinsic variability of the host star or residual systematics in the light curve analyses. We have found that significant systematics in the *Kepler* light curves due to small photometric apertures and large centroid motions hinder analyses if not properly removed or accounted for, and that a re-reduction of the photometry is best done at the pixel-stamp level. We also stress the importance of taking into account how *Kepler* light curves are produced from the pixel level data when considering any detection of low-frequency signals, as they can vary significantly depending on the technique employed.

We have also re-determined the stellar and planetary parameters of each system while deriving robust errors that take into account residual systematic noise in the light curves. We detect what appear to be the secondary eclipse signals of ~ 20 -30 of the targets in our list at $> 1\sigma$ confidence levels, and also derive robust upper limits for the secondary eclipse emission of all the remaining objects in our sample. All of our sample present excess emission compared to what is expected via blackbody thermal emission alone, as well as a trend of increasing excess emission with decreasing expected maximum effective planetary temperature, in

agreement with previously reported secondary eclipse detections of hot Jupiters in the optical, which can be attributed to the 'appearance' of increasing albedos with decreasing planetary temperatures. By performing statistical analyses of those results we arrive to the following main conclusions.

1. Assuming no contribution from reflected light, i.e., $A = 0.0$, the majority of the detected secondary eclipses reveal thermal emission levels higher than the maximum emission levels expected for planets in local thermodynamical equilibrium.
2. While the extra emission from many of the planets can be accounted for by varying the amount of reflected light, the emission from $\sim 50\%$ of the detected objects ($>1\sigma$) can not be accounted for even when assuming perfectly reflective planets (i.e., $A = 1.0$). These planets must either have much higher thermal emission in the optical compared to a blackbody, as predicted by theoretical models, have very large non-LTE optical emission features, have underestimated host star masses, radii, or effective temperatures, or are in fact false-positives and not planets but rather brown dwarfs, very low-mass stars, or stellar blends. Follow-up observations of these systems are necessary to confirm this conclusion. The most outstanding potentially false positive systems are KOI 64.01, 144.01, 684.01, 843.01, 1541.01, and 1543.01. Given that this is 6 of the 55 systems that we modeled, or 11% of the sample, it appears to agree with the expected $\sim 10\%$ false positive rate of the initial 1,235 candidates estimated by Morton & Johnson (2011). We note that Santerne et al. (2012) found a potential false positive rate for *Kepler* hot Jupiters as high as 35% from radial-velocity observations of

KOIs, which could certainly be compatible with our data if we count more of the systems with unusually deep eclipses as false positives.

3. Although we do not identify a sole cause of the observed trend of increasing excess planetary emission with decreasing expected maximum effective planetary temperature, the hypothesis of increasing planetary albedo with decreasing planetary temperature is able to explain many of the systems. This would be physically plausible as the upper atmospheres of Jupiter-like planets transition from very low albedos at high temperatures, as observed for hot Jupiters, to higher albedos at lower temperatures, as observed for cool Jupiters in our own solar system. We note that further observations via *Kepler* and multi-wavelength ground-based facilities of both the planetary candidates and their host stars are still needed to fully explain this trend.
4. From the emission upper limits placed on planet candidates for which we do not detect secondary eclipse signals, we conclude that a significant number, at least 30% at the 1σ level, of those targets must have very low-albedos, ($A_g < 0.3$), which is a result that is consistent with the majority of previous observations and early theoretical hot Jupiter model predictions. All previous observational upper limits had been placed on hot Jupiters with expected atmospheric effective temperatures higher than ~ 1650 K. Our results extend that temperature limit to planets with expected effective temperatures higher than 1200 K and can help further establish what chemicals play a critical role in the atmospheric properties of hot Jupiters.
5. From the inspection of individual targets we conclude that the majority of our secondary eclipse depths for candidates with previously published

eclipse detections are consistent with the results from those other studies. We note that several of those other studies have access to *Kepler* data from quarters after Q2, while our analysis is limited to just the public Q2 data, and therefore our results have larger detection errorbars in some cases.

6. Our results are based on only one quarter of *Kepler* data, but 12-24 quarters should become available in the future. Therefore, we expect that future studies of these targets will be able to improve our secondary eclipse detections and upper limits by factors of 3-5, or much greater if noise systematics in the light curves can be further reduced.

5. LOW-MASS ECLIPSING BINARIES IN THE INITIAL *KEPLER* DATA RELEASE

5.1. Introduction

A double-lined, detached, eclipsing binary (DDEB) is a system that contains two non-interacting, eclipsing stars, in which the spectra of both components can be clearly seen, allowing for the radial-velocity (RV) of each component to be obtained. In these systems, the mass and radius of each star can be determined with errors usually less than 1-2%, thus making DDEBs currently the most accurate method of obtaining masses and radii of stars. Models of main-sequence stars with masses similar to or greater than the Sun have been tested over the years using DDEBs. Popper (1980) compiled available masses and radii of DDEB's with accuracies of $\leq 15\%$, up to that date, and found general agreement with stellar models, though stressed the need for more accurate observations and models. Andersen (1991) provided a compilation of all available DDEB systems up to that date, with accuracies $\leq 2\%$, and showed that the masses and radii of these stars were in general agreement with the current stellar evolution models, with any discrepancies attributable to abundance variations. Torres et al. (2010) recently performed a similar review with nearly double the sample of DDEBs. They were able to show the need to include non-classical effects such as diffusion and convection in stellar models, definitively demonstrate the existence of significant structural differences in magnetically active and fast-rotating stars, test theories of rotational synchronization and orbital circularization, and validate General Relativity via apsidal motion rates. However, while observations of DDEBs have enhanced our understanding of stellar structure and evolution for stars with $M \geq 1.0 M_{\odot}$, low-mass, main-sequence (LMMS) stars, ($M < 1.0 M_{\odot}$ and $T_{\text{eff}} < 5800$ K), have not been

tested to the same extent.

Although a few systems with late G or early K type components had been studied prior to 2000, (c.f. Popper 1980; Andersen 1991; Torres et al. 2006; Clausen et al. 2009, and references therein), only three LMMS DDEBs with late K or M type components were known (Lacy 1977; Leung & Schneider 1978; Delfosse et al. 1999). This number had only increased to nine by the beginning of 2007 (cf. López-Morales 2007, Table 1). Despite the fact that the majority of main-sequence stars are low-mass, these stars are both intrinsically fainter, and physically smaller, than their more massive counterparts. Therefore, they have a lower eclipse probability and are harder to discover and study. As outlined by López-Morales (2007), analysis of these systems showed that the observed radii for these stars are consistently $\sim 10\text{-}20\%$ larger than predicted by stellar models (Baraffe et al. 1998) for $0.3 M_{\odot} \lesssim M \lesssim 0.8 M_{\odot}$. Fernandez et al. (2009) recently showed this was also likely the case for five M dwarfs in short-period eclipsing systems with an F type primary, though since the systems are only single-lined, the masses could not be determined directly. This discrepancy between the radii derived from models and from observations either reveals a flaw in the stellar models for this mass regime, or is due to differences in metallicity, magnetic activity, or interpretation of the light curve data when star spots are present (Morales et al. 2008). As to this last point, Morales et al. (2010) recently noted that improperly taking polar spots into account in the light curve modeling process may possibly cause the derivation of stellar radii a few percent larger than the true values for some of these systems. Of all of these scenarios, enhanced magnetic activity has been proposed as the principal cause of inflated radii (Chabrier et al. 2007; López-Morales 2007; Morales et al. 2008).

If enhanced magnetic activity is the principal cause of the inflated radii, shorter-period binary systems, with the stellar rotation rate enhanced by the revolution of the system, would be expected to show greater activity and thus larger radii than longer-period systems (Chabrier et al. 2007). Binary systems with component masses of $0.5 M_{\odot}$ are expected to synchronize, and therefore be spun-up, in less than 0.1 Gyr for periods less than 4 days, and in less than 1 Gyr for periods less than 8 days (Zahn 1977, 1994). Thus, the discovery of LMMS DDEBs with $P \gtrsim 10$ days, where the binary components should have natural rotation rates, is crucial to probing if enhanced rotation due to binarity is the underlying cause of this phenomenon. This theory might be supported by measurements of isolated field M and K dwarf stars via very long baseline interferometry, which Demory et al. (2009) found to match stellar models. However, recently a much larger sample of nearly two dozen isolated M and K dwarf stars finds, for $\sim 80\%$ of the sample, larger radii than the model predictions for $0.35 < M < 0.65 M_{\odot}$ (Boyajian 2010), indicating that there are likely multiple causes of inflation at work, or a remaining flaw in the stellar models.

Though several more LMMS DDEB systems have been found since 2007, (Coughlin & Shaw 2007; Shaw & López-Morales 2007; Becker et al. 2008; Blake et al. 2008; Devor et al. 2008a,b; Shkolnik et al. 2008; Hoffman et al. 2008; Irwin et al. 2009; Dimitrov & Kjurkchieva 2010; Shkolnik et al. 2010), there are to-date only seven well-studied systems with $1.0 < P < 3.0$ days (López-Morales 2007; Becker et al. 2008; Shkolnik et al. 2008, and references therein), and only one has a larger period, at $P = 8.4$ days (Devor et al. 2008b). This is mostly due to the fact that ground-based photometric surveys, such as NSVS, TrES, and OGLE, are either cadence, precision, magnitude, or number limited, and

thus not sensitive to long periods. The *Kepler Mission*, with 3 years of constant photometric monitoring of over 150,000 stars with $V \lesssim 17$, at 30-minute cadence and sub-millimagnitude precision, is the key to discovering a large number of long-period, LMMS DDEBs.

In this chapter we present the results of our search through all the newly available *Kepler* Q0 and Q1 public data for LMMS DDEBs. Section 5.2 describes the data we use in this chapter. Section 5.3 describes our binary identification technique, and Section 5.4 describes how we model the light curves. Our selection and list of new LMMS DDEBs is presented in Section 5.5, and we present new transiting planet candidates in Section 5.6. In Section 5.7 we compare the new LMMS DDEBs with theoretical models, and conclude with a summary of our results in section 5.8. Once accurate mass and radius values exist for a large range of both mass and period, our understanding of these objects should substantially improve, and we will be one step closer to extending to the lower-mass regime the advanced study of stellar structure and evolution that sun-like and high-mass stars have been a subject of for some time.

5.2. Observational Data

The data used in our analysis consists of the 201,631 light curves made public by the *Kepler Mission*¹ as of June 15, 2010 from *Kepler* Q0 and Q1 observations. All light curves can be accessed through the Multi-mission Archive at STScI (MAST)². The data consist of 51,366 light curves from *Kepler* Q0, (observed from

¹<http://kepler.nasa.gov/>

²<http://archive.stsci.edu/kepler/>

2009-05-02 00:54:56 to 2009-05-11 17:51:31 UT), and 150,265 light curves from *Kepler* Q1, (observed from 2009-05-13 00:15:49 to 2009-06-15 11:32:57 UT), each at 29.43 minute cadence. Individual light curves for Q0 contain ~ 470 data points, and for Q1 contain $\sim 1,600$ data points. Targets range in *Kepler* magnitude from 17.0 at the faintest, to 5.0 at the brightest.

The *Kepler* team has performed pixel level calibrations, (including bias, dark current, flat-field, gain, and non-linearity corrections), identified and cleaned cosmic-ray events, estimated and removed background signal, and then extracted time-series photometry using an optimum photometric aperture. They have also removed systematic trends due to spacecraft pointing, temperature fluctuations, and other sources of systematic error, and corrected for excess flux in the optimal photometric aperture due to crowding (Van Cleve 2010). It is this final, “corrected” photometry that we have downloaded for use in our analysis.

5.3. Eclipsing Binary Identification

Prša et al. (2010) released an initial catalog of eclipsing binary stars they found in the *Kepler* field from the same Q0 and Q1 data we use in this chapter. They first identified EB candidates via *Kepler’s* Transit Planet Search (TPS) algorithm, eliminating those targets already identified as exoplanet candidates. To determine the ephemeris of each candidate, they used Lomb-Scargle, Analysis of Variance, and Box-fitting Least Squares periodogram techniques, combined with manual inspection and modification. They then culled, through manual inspection, non-EB candidates, such as pulsating and heavily spotted stars, as well as duplicates due to contamination from nearby stars, and arrive at their final list

of 1,832 binaries, which are manually classified as detached, semi-detached, over-contact, ellipsoidal, or unknown. Next, they estimate the principal parameters of each system, (temperature ratio, sum of the fractional radii, $e \cdot \cos(\omega)$, $e \cdot \sin(\omega)$, and $\sin(i)$ for detached systems), via a neural network technique called Eclipsing Binaries via Artificial Intelligence (“EBAI” Prša et al. 2008). For our search, which focuses on the detection of LMMS DDEBs, we have devised our own DDEB identification technique, which we apply to the Q1 data. We do not use the Q0 data in this part of the analysis to avoid discrepant systematics between the two quarters, which complicate the analysis.

Our search consisted of two steps. The first was to identify variable stars, and to do so, we placed a light curve standard deviation limit above which the objects are classified as variables. We first subtracted an error-weighted, linear fit of flux versus time from all data, to remove any remaining linear systematic trends, and then plotted the standard deviation of each light curve versus its average flux and fit a power law. These data are shown in Figure 5.1, where the black dots correspond to light curves which deviate by less than 1σ from the standard deviation versus average flux fit, and we thus classify as non-variable. The colored dots indicate the variable candidates that deviate by more than 1σ . Next, we used the flux ratio (FR) measurement criterion, which we adapted from the magnitude ratio given in Kinemuchi et al. (2006), and is defined as

$$\text{FR} = \frac{\text{maximum flux} - \text{median flux}}{\text{maximum flux} - \text{minimum flux}} \quad (5.1)$$

as a measure of whether or not the variable spends most of its time above (low FR value) or below (high FR value) the median flux value. Perfectly sinusoidal variables have $\text{FR} = 0.50$, pulsating variables, such as RR Lyrae’s, have $\text{FR} > 0.5$,

and eclipsing binaries have $FR < 0.5$. As we are principally interested in finding well detached systems with relatively deep, narrow eclipses, which thus have low FR values, we make a further cut of the systems and only examine those variables with $FR < 0.1$, shown by blue dots in Figure 5.1.

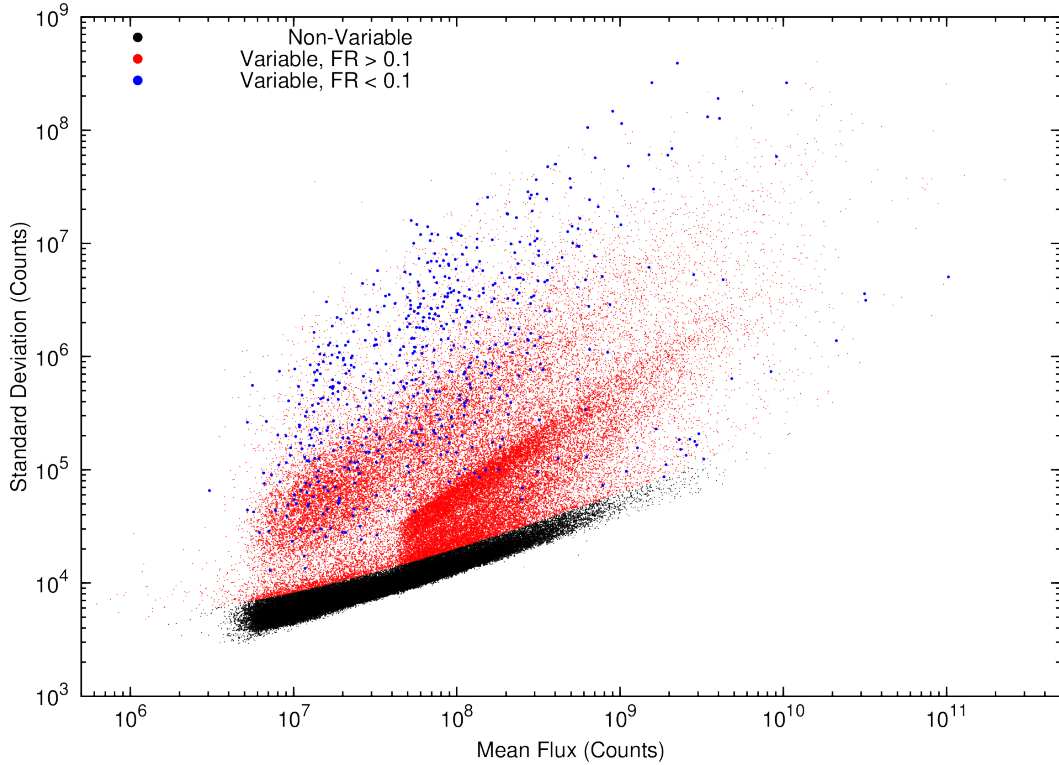


Fig. 5.1.— Plot of standard deviation versus mean flux for the 150,265 stars in Q1. Black dots represent stars that vary by less than 1-sigma from a best-fit power-law to the data, and thus we classify them as non-variables. Red dots represent variables with a flux ratio greater than 0.1. Blue dots represent variables with a flux ratio less than 0.1, and thus are good candidates to be eclipsing binaries.

The second step of the analysis was to determine the orbital period of each candidate. This was done using two independent techniques that are both well-suited for detached eclipsing binary systems. The first is Phase Dispersion Minimization (PDM) (Stellingwerf 1978), which attempts to find the period that best

minimizes the variance in multiple phase bins of the folded light curve. This technique is not sensitive to the shape of the light curve, and thus is ideal for non-sinusoidal variables such as detached eclipsing binaries. The downside of this technique is that if strong periodic features exist in the light curve, which do not correspond to the period of eclipses, such as rapidly varying spots, stellar pulsations, or leftover systematics, they can weaken the signal of the eclipse period. We use the latest implementation given by Stellingwerf (2006), and determine the best three periods via this technique to ensure that the true period is found, and not just an integer multiple, or fraction, thereof.

The second technique we use is one we invented specifically for detached eclipsing binaries, and call Eclipse Phase Dispersion Minimization (EPDM). The idea behind EPDM is that we want to automatically identify and align the primary eclipses in an eclipsing binary, thus finding the period of the system. To accomplish this, EPDM finds the period that best minimizes the dispersion of the actual phase values of the faintest N points in a light curve, i.e. the very bottom of the eclipses. Since EPDM only selects the N faintest points in a light curve, it is not affected by systematics or periodic features that do not correspond to the period of eclipses, assuming the systematics do not extend below the depth of the eclipses. The technique works for all binary systems with equal or unequal eclipse depths, and transiting planets, both with either zero or non-zero eccentricity. Computationally, EPDM is significantly faster than traditional PDM techniques. For a detailed and illustrative explanation of this new technique, please see Appendix A. We use EPDM to find the three best fit periods for each system as well, for the same reasons as we did with PDM.

We identify 577 EB candidates in the Q1 data. Of these, 486 are listed by

Prša et al. (2010) as detached eclipsing binaries, and 20 are identified as semi-detached eclipsing binaries. The 71 remaining candidates were manually inspected by examining both the raw and phased light curves at the 6 best periods found via PDM and EPDM. Of these 71 remaining candidates, 48 turned out to be false positives with significantly large, sharp systematic features, and one is an apparent red giant, (Kepler 010614012, $T_{\text{eff}} = 4859\text{K}$, $\log g = 3.086$, $[M/H] = -0.641$, $R_{\star} = 5.708 R_{\odot}$), with an unusual, asymmetrical, eclipse-like feature that lasts for ~ 3 days with a depth of 1.2%, shown in Figure 5.2. This does not appear to be a systematic feature due to its very flat out of eclipse baseline, contiguous nature, long duration, and the actual time at which the feature occurs, compared to the majority of other objects with strong systematics. The remaining 22 targets are: two transiting exoplanet candidates contained in the recently released list of 306 candidates by Borucki & the Kepler Team (2010), three already published transiting planets, (Kepler-5b, Kepler-6b, and TrES-2b), seven shallow eclipsing systems with primary eclipse depths ranging from 1.4% to 5.7%, visible secondary eclipses ranging from 0.05% to 4.6%, and periods ranging from 4.7 to 45.3 days, the already published transiting hot compact object Kepler 008823868 (Rowe et al. 2010), a 6.4 day eclipsing binary with $T_{\text{eff}} = 5893\text{K}$ and eclipse depths of 38.4% and 12.2% (Kepler 006182849), and eight transiting exoplanet candidates with transit depths ranging from 0.75% to 4.9%, and periods ranging from 2.5 to 24.7 days. For the seven new extremely shallow eclipsing systems, we list their *Kepler* ID numbers, periods, effective temperatures, surface gravities, and primary and secondary eclipse depths in Table 5.1, and note they could be of interest for follow-up due to the potential to contain brown dwarf or extremely low-mass secondaries, or even anomalously hot exoplanet companions. Of the

eight transiting candidates, only one is listed in the *Kepler* false positive catalog³, Kepler 011974540. None of them are in the list of the 306 released candidates by Borucki & the Kepler Team (2010), nor are among the 400 planetary candidates currently reserved for follow-up observations (Borucki & the Kepler Team 2010). These will be further discussed in Section 5.6.

5.4. Light Curve Modeling

Since the system parameters determined by Prša et al. (2010) are only estimates and do not incorporate spots, and since we seek to obtain as accurate physical parameters as possible, we modeled each system using a robust global minimization scheme with a commonly used, physically detailed eclipsing binary modeling code. We took all 314 detached eclipsing binaries with $T_{\text{eff}} < 5500\text{K}$ and that are publicly available, (5 systems are still proprietary), identified from both our search and the Prša et al. (2010) catalog, combined Q0 and Q1 data if available, and via manual inspection classified systems as double-eclipse (i.e. contained two visible eclipses), single-eclipse (i.e. only contained one eclipse), or as spurious results that were not recognizable as eclipsing systems. (Given the errors in the KIC temperature determination, and to ensure the primary is below $1.0 M_{\odot}$, we used 5500K as our cutoff, instead of 5800K. As well, the definition of a “double-lined” system is one in which the lines of both components are visible in an observed spectrum. Although in general if two eclipses are clearly visible in the photometric light curve, it is likely to be “double-lined”, this cannot be determined without an actual spectrum. Thus, we use the term “double-eclipse”

³http://archive.stsci.edu/kepler/false_positives.html

Table 5.1. Period, Effective Temperature, Surface Gravity, and Eclipse Depth Estimates for the Seven New Extremely Shallow Eclipsing Systems

<i>Kepler</i> ID	Period (Days)	T_{eff} (K)	$\log g$	Pri. (%)	Sec. (%)
003098197	38.3840 ^c	5675	4.814	4.9	4.60
004178389 ^a	45.2600 ^c	5645	4.670	3.4	2.80
009016295 ^b	19.9858	5819	4.582	4.1	0.17
009071386 ^a	4.68513	6324	4.267	1.4	0.05
009838975 ^a	18.7000	5018	4.802	5.7	0.21
012017140 ^b	22.8624	6026	4.500	4.7	0.11
012504988 ^a	5.09473	5985	4.464	2.9	0.06

^aSystem is listed in the *Kepler* False Positive Catalog as likely to be an EB.

^bSystem has non-zero eccentricity.

^cPeriod derived assuming zero eccentricity.

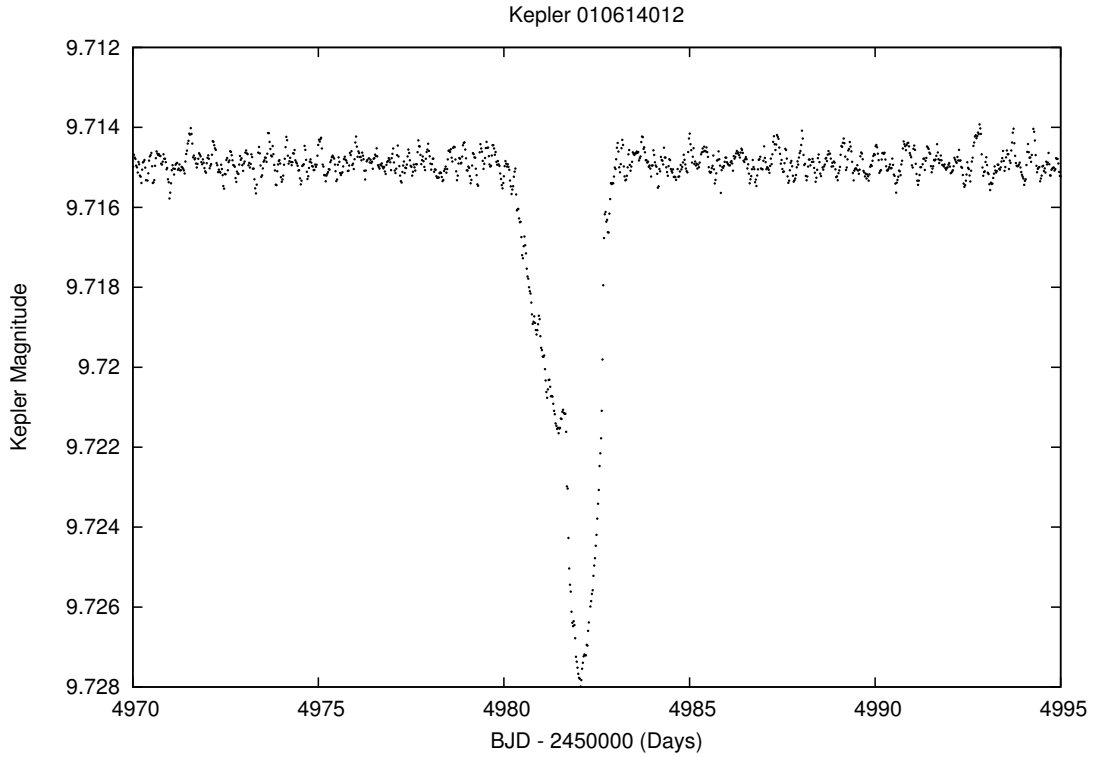


Fig. 5.2.— Kepler 010614012: An apparent red giant, ($T_{\text{eff}} = 4859\text{K}$, $\log g = 3.09$, $[M/H] = -0.64$, $R_{\star} = 5.71 R_{\odot}$), with an unusual, shallow, eclipse-like feature.

throughout the chapter, with the assumption that when observed spectroscopically, the majority of these systems will be observed as “double-lined”.)

We then used the JKTEBOP eclipsing binary modeling program (Southworth et al. 2004a,b) to model every double-eclipse eclipsing binary system, of which there were 231, solving for the period, time of primary minimum, inclination, mass ratio, $e \cdot \cos(\omega)$, $e \cdot \sin(\omega)$, surface brightness ratio, sum of the fractional radii, ratio of the radii, and out of eclipse flux. In addition, we also solved for the amplitude and time of minimum of a sinusoidal term imposed on the luminosity of the primary component, with the period fixed to that of the binary, in order to account for spots. Note that in the JKTEBOP model the mass ratio is only used to determine the amount of tidal deformation of the stars from a pure sphere. Thus, it has no effect on the light curve of long-period systems, which due to their large separations are almost perfectly spherical, but must be included to properly model very short-period systems, where the tidal deformation can have a significant impact on the light curve. We used the quadratic limb darkening law, which works well for late-type stars (e.g. Manduca et al. 1977; Wade & Rucinski 1985; Claret & Gimenez 1990), with coefficients set to those found by Sing (2010) for the *Kepler* bandpass via interpolation given the systems’ effective temperatures, surface gravities, and metallicities as listed in the *Kepler* Input Catalog (KIC)⁴. We also fixed the gravity darkening exponent based on the effective temperature as prescribed by Claret (2000b). As any contaminating flux from nearby stars in the photometric aperture has already been compensated for in the *Kepler* pipeline (Van Cleve 2010), we set the amount of third light to 0.0. Note that third light

⁴http://archive.stsci.edu/kepler/kepler_fov/search.php

might still exist in some systems if there is a background star or tertiary component that is unidentifiable from ground-based surveys, (i.e. less than $\sim 1''$ separation), but since third light is usually unconstrained in a single-color light curve, we do not let it vary. If third light existed in a system and was not accounted for, the solution would result in an inclination determination lower than the true value, and therefore an over-estimation of the stellar radius. However, this should only occur in a minority of systems. For a couple of binaries in our list, the light curves absolutely could not be modeled without the inclusion of third light, (i.e. very sharp eclipses with depths of less than 0.01 mag). For these cases only, we let the third light vary, and thus be a non-zero parameter. Additionally, if the effect of spots in a light curve deviates significantly from the adopted sinusoidal shape, it could affect the derived luminosity ratio to a minor extent, but it should not affect the sum of the radii.

In order to model such a large number of systems over such a large solution space, and to ensure we have found the best global solution, we adapted the JKTEBOP code to use a modified version of the asexual genetic algorithm (AGA) described by Cantó et al. (2009), coupled with its standard Levenberg-Marquardt minimization algorithm. Genetic algorithms (GA) are an extremely efficient method of fitting computationally intensive, multi-parameter models over a large and potentially discontinuous parameter space, and thus ideal for this work. For the details of how genetic algorithms work, and the specific changes we made to the Cantó et al. (2009) AGA, please see Appendix B.

We found that our modified AGA does an excellent job of solving well-behaved light curves, simultaneously varying all 12 aforementioned parameters over the entire range of possible solutions. For some of the systems however, strong systemat-

ics and/or variable star spots introduced a significant amount of noise, especially in systems with shallow eclipses, for which it was more difficult to arrive at a robust solution. For these systems we had to manually correct the systematics, often by either eliminating the Q0 or Q1 data, equalizing the base flux levels of Q0 and Q1 data, or subtracting out a quasi-sinusoidal variation in the base flux level due to remaining *Kepler* systematics. When possible we attempted to minimize the amount of manual interference. Hopefully this will become much less of a problem with subsequent data releases. We then re-ran the AGA using a larger initial population until a good solution was found, i.e., both eclipse depths and widths were fit well by visual inspection. Every light curve in the end was visually inspected to be a good fit compared to the scatter of the data points, i.e., appeared to have $\chi_{\text{red}} = 1.0$ when ignoring systematic errors, and the obtained parameters were confirmed to be reasonable when visually inspecting the light curves.

5.5. New Low-Mass Binary Candidates

In order to identify the main-sequence stars from our list of 231 candidates, and determine the best candidates for follow-up, we employ the following technique to estimate the temperature, mass, and radius of each star using the sum of the fractional radii, r_{sum} , period, P , the luminosity ratio, L_r , (which is derived from the surface brightness ratio, J , and radii ratio, k), obtained from our JKTE-BOP models, and the effective temperature of the system, T_{eff} , obtained from the KIC, with an estimated error of ± 200 K. The value for T_{eff} given in the KIC was determined via interpolation of standard color magnitude relations as determined by ground-based, multi-wavelength photometry (Van Cleve 2010). Although in

principle one might be able to deconvolve two separate spectral energy distributions from this photometry, in reality given the level of photometric error in the KIC and uncertainty at which binary phase the photometry was obtained, this is untenable. Instead, we assume the stars radiate as blackbodies, and that each star contributes to the determined T_{eff} in proportion to its luminosity. Thus, following our assumption, we obtain the following relation,

$$T_{\text{eff}} = \frac{L_1 T_1 + L_2 T_2}{L_1 + L_2} \quad (5.2)$$

where L_1 , L_2 , T_1 and T_2 are the luminosities and effective temperatures of star 1 and 2 respectively. Still assuming the stars radiate as blackbodies, the luminosity of each star is proportional to its radius squared and temperature to the fourth power, with the temperature proportional to its surface brightness to the one-fourth power. Thus, we find that the luminosity ratio can be expressed as,

$$\begin{aligned} L_r &= \frac{L_1}{L_2} = \frac{r_1^2 T_1^4}{r_2^2 T_2^4} = k^2 T_r^4 = k^2 \left[\left(\frac{SB_1}{SB_2} \right)^{1/4} \right]^4 \\ &= k^2 \left(J^{1/4} \right)^4 = k^2 J \end{aligned} \quad (5.3)$$

where SB_1 and SB_2 are the surface brightnesses of star 1 and star 2 respectively, and r_1 and r_2 are the fractional radii of star 1 and 2 respectively, defined as R_1/a and R_2/a , where R_1 and R_2 are the physical radius of each star, and a is the semi-major axis of, or separation between, the components. Combining equations 5.2 and 5.3 yields the expression,

$$T_{\text{eff}} = \frac{L_r T_1 + T_2}{L_r + 1} \quad (5.4)$$

which has two known parameters, T_{eff} and L_r , and two unknown parameters, T_1 and T_2 . To place a further constraint upon the values of T_1 and T_2 , we make the assumption that both stars in the binary are on the main-sequence, and employ the mass, temperature, radius, and average of the V -band and R -band luminosity relations given in Baraffe et al. (1998) for $0.075 \leq M \leq 1.0 M_{\odot}$ and in Chabrier et al. (2000) for $M < 0.075 M_{\odot}$, both assuming an age of 5.0 Gyr and $[M/H] = 0.0$. (We average the V and R -band luminosities to obtain a very close approximation to the *Kepler* bandpass.) From these models, for a given value of T_1 , there is only one value of T_2 which will reproduce the observed value of L_r . Thus, there only exists one set of unique values for T_1 and T_2 that reproduces both the observed T_{eff} and L_r values for the system.

For each T_1 and T_2 then, we obtain the absolute masses and radii, (M_1 , M_2 , R_1 , and R_2), via interpolation from the Baraffe et al. (1998) and Chabrier et al. (2000) models. Then, utilizing Kepler's 3rd law, given the total mass of the system, we calculate the semi-major axis, a , via

$$a = (GM_{\text{tot}})^{\frac{1}{3}} \left(\frac{P}{2\pi} \right)^{\frac{2}{3}} \quad (5.5)$$

where M_{tot} is the total mass of the system, $M_1 + M_2$, and G is the gravitational constant. We then multiply each radius determined above by a constant so that the sum of the fractional radii derived from the JKTEBOP model, r_{sum} , is equal to $(R_1 + R_2)/a$, the sum of the fractional radii when using the physical values of M_1 , M_2 , R_1 , R_2 , and P . This technique is robust because while individual

parameters such as i , J , and k can suffer from degeneracies, especially in systems with shallow eclipses, the values of r_{sum} and $L_r = k^2 J$, which we rely on, are firmly set by the width of the eclipses and the difference in their eclipse depths, respectively.

For clarity, we now illustrate the individual steps of this procedure using the example of an actual system, Kepler 002437452. This system was found to have $T_{\text{eff}} = 5398$ K and $L_r = 3.90$ from the KIC and the JKTEBOP modeling respectively. Now, assuming the stars are main-sequence, one could choose values of $T_1 = 4000$ K and $T_2 = 3620$ K, and looking up their luminosities from the Baraffe et al. (1998) models, find that the luminosity ratio between two main-sequence stars with temperatures of 4000 K and a 3620 K is 3.90. In this case, the luminosity ratio criterion would be satisfied, but T_{eff} would be ~ 3922 K, nowhere near the measured value of 5398 K. Similarly, one could choose values of $T_1 = 5400$ and $T_2 = 5393$, and this would yield $T_{\text{eff}} = 5398$ K, but L_r would be 1.01, nowhere near the needed value of 3.90. The unique solution that satisfies both the effective temperature and luminosity ratio constraints is that $T_1 = 5591$ and $T_2 = 4647$, which yields both $T_{\text{eff}} = 5398$ and $L_r = 3.90$. Now, given these temperatures, interpolating from the Baraffe et al. (1998) models yields values of $M_1 = 0.963 M_{\odot}$, $R_1 = 0.966 R_{\odot}$, $M_2 = 0.792 M_{\odot}$, and $R_2 = 0.783 R_{\odot}$. Taking the masses, and the period of the system of 14.47184 days, and utilizing Eq. 5.5, we find that the semi-major axis, a , would be $30.1 R_{\odot}$. Dividing the sum of the estimated physical radii by the semi-major axis just calculated, we find a value of 0.058 for the sum of fractional radii. Now, from the JKTEBOP model, this system was measured to have a sum of the fractional radii of 0.084, and so it appears that the current values for the radii are underestimated. Thus, we multiply the radii by a factor

of $0.084/0.058 = 1.45$, to obtain our final radii values of $R_1 = 1.40 R_\odot$ and $R_2 = 1.13 R_\odot$, with, as above, $M_1 = 0.96 M_\odot$, $T_1 = 5591$ K, $M_2 = 0.79 M_\odot$, and $T_2 = 4647$ K.

Kipping (2010a) has recently examined the effects of the long, (~ 30 minute), integration time of long-cadence *Kepler* observations on transit light curves, and found that it can significantly alter the morphological shape of a transit curve and result in erroneous parameters if not properly taken into account in the modeling procedure. Certainly, eclipsing binaries are also affected by long integration times, namely by a “smearing” of the eclipses so that they appear to be shallower and have a longer duration. Qualitatively, this would result in a lower inclination and larger sum of the fractional radii, while the luminosity ratio would remain unchanged, since both eclipse depths are equally affected. To quantitatively investigate the extent to which the long integration could affect the derived parameters, we generated model light curves of a typical eclipsing binary, varying its period and the sum of the fractional radii. We then binned these light curves as if they had a 29.43 minute integration time, and the same number of data points as the Q1 *Kepler* light curves. We then re-solved the light curves without accounting for the integration time, and compared the computed parameters to those used to generate the original light curve. We found that for the long-cadence *Kepler* integration time of 29.43 minutes, only systems with very low values of r_{sum} and P are significantly affected, as can be seen in Figure 5.3. These types of systems are less than 2% of our sample. Nevertheless, we modified the JKTEBOP program to perform a numerical integration over a given exposure time, as suggested by Kipping (2010a). We tested our modifications by solving the aforementioned generated light curves, now taking the integration time into account, and successfully

retrieved the inputted parameters.

After estimating the individual mass, radius, and temperature for each component, we re-computed the gravity and limb-darkening coefficients for each individual star, and performed a Levenberg-Marquardt minimization starting from our previously best solutions, taking into account the 29.43 minute integration time. We then repeated the processes of deriving the physical values of the components, interpolating gravity and limb-darkening coefficients, and performing a Levenberg-Marquardt minimization several more times to ensure convergence. The JKTEBOP solutions for all initial 231 candidates are shown in Table 5.2, including the *Kepler* ID number, effective temperature of the system, apparent *Kepler* magnitude, magnitude range of the light curve, period, time of primary minimum, inclination, eccentricity, longitude of periastron, sum of the fractional radii, surface brightness ratio, radii ratio, luminosity ratio, amplitude of the sine curve applied to the luminosity of the primary star to account for spots, and the amount of third light. Although we list the derived surface brightness and radii ratios here, we note again that they are not always reliable on their own, and thus are combined to obtain the luminosity ratio in our analysis via Eq. 5.3. Plots of each of the eclipsing binaries with their model fit are given in Figure 5.4.

As a check on the reliability of our analysis technique we took the well-studied low-mass eclipsing binary GU Boo (López-Morales & Ribas 2005), and modeled only the *R*-band light curve, (not using the radial velocity curves), via the exact same procedure as stated above in Sections 5.4 and 5.5. The only differences were that we used only the *R*-band luminosities from the Baraffe et al. (1998) and Chabrier et al. (2000) models, and an integration time of 2 minutes as stated in López-Morales & Ribas (2005). We used only the period, time of primary

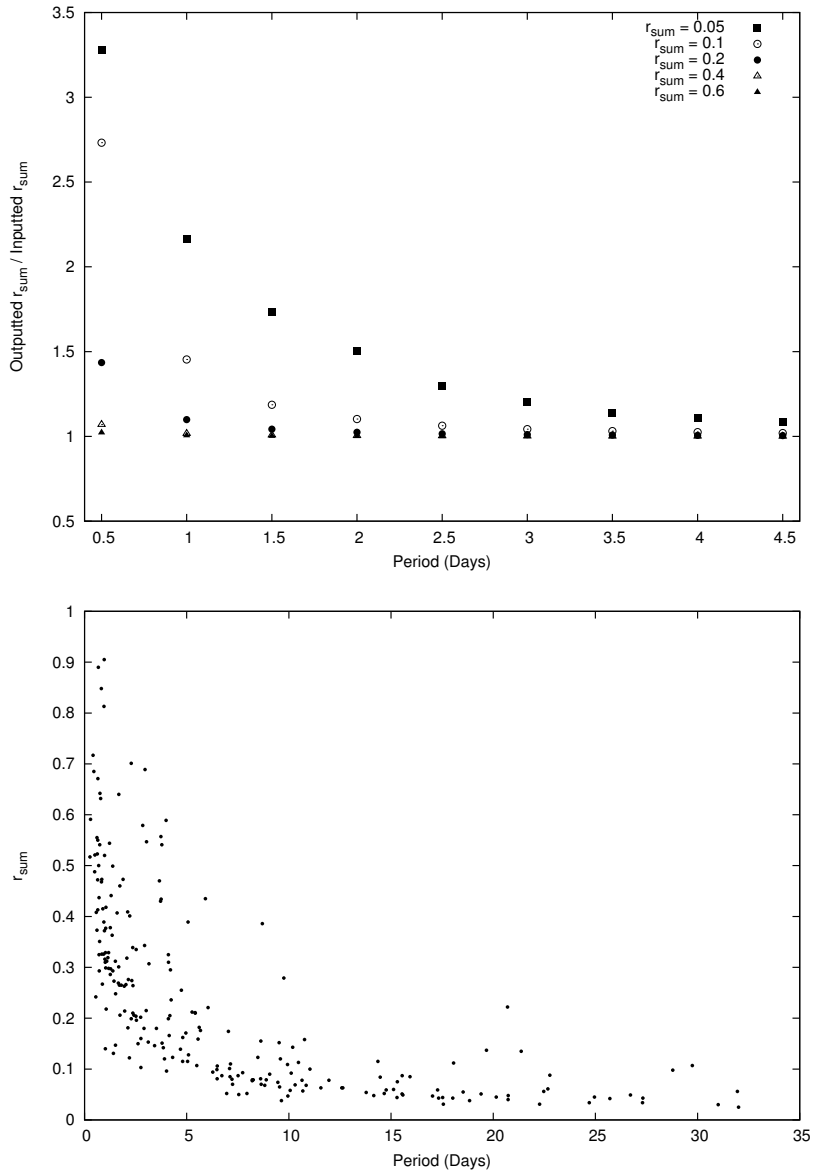


Fig. 5.3.— Top: The effect that the 29.43 minute integration time has on the derivation on the sum of the fractional radii, r_{sum} , at a given period. As can be seen, only very small values of r_{sum} and P yield discrepancies $\gtrsim 10\%$, for example, combinations of $P < 3$ days and $r_{sum} < 0.05$, $P < 1.5$ days and $r_{sum} < 0.1$, $P < 0.75$ days and $r_{sum} < 0.2$, etc. Bottom: The values of r_{sum} versus period for the binaries we have modeled in this chapter, presented in Table 5.2. Very few of the systems, $\lesssim 2\%$, in our sample lie in a region where they would be significantly affected by the 29.43 minute integration time.

Table 5.2. Model System Parameters via JKTEBOP for the 231 DDEBs with $T_{\text{eff}} < 5500$ K

<i>Kepler</i> ID	T_{eff} (K)	m_{kep}	Δm_{kep}	Period (Days)	T_0 (BJD-2450000)	i ($^\circ$)	e^a	ω^a ($^\circ$)	i_{sum}	J	k	L_r	L_1 Sine Amplitude	L_3
002162994	5410	14.162	0.535	4.101544	5002.545861	89.87	0.01	270	0.199	0.991	0.702	0.4888	0.008	0.00
002437452	5398	16.981	0.256	14.47184	5003.759350	87.46	0.08	90	0.084	0.641	2.47	3.905	0.011	0.00
002580872	5293	14.880	0.374	15.92672	4978.550988	87.95	0.26	102	0.084	1.14	1.25	1.774	0.014	0.00
002719873	5086	15.160	0.235	17.27953	4968.273250	87.76	0.31	90	0.059	0.633	2.64	4.425	0.007	0.00
002852560	5381	15.308	0.460	11.96119	4964.912794	88.06	0.44	41	0.079	1.04	0.986	1.008	0.000	0.00
002860788	5319	14.043	0.137	5.259798	4965.066945	82.29	0.00	268	0.212	0.876	0.561	0.2755	0.009	0.00
003003991	5366	13.926	0.115	7.244790	4964.859062	86.88	0.28	270	0.083	0.0438	11.2	5.447	0.000	0.40
003102024	5117	12.809	0.351	13.78248	4958.697309	89.50	0.54	302	0.054	0.605	1.37	1.138	0.000	0.43
003113266	5077	15.577	0.011	0.9958567	5002.193202	72.96	0.01	266	0.325	1.24	9.95	123.3	0.026	0.00
003241344	5422	14.756	0.401	3.912656	4966.427889	90.00	0.02	256	0.121	0.0854	0.509	0.02209	0.012	0.00
003241619	5165	12.524	0.802	1.703368	4965.468231	85.35	0.03	88	0.267	0.303	1.04	0.3286	0.016	0.00
003344419	5348	14.997	0.005	0.6517609	4977.843744	50.18	0.01	269	0.694	1.08	23.4	592.4	0.068	0.00
003458919	5063	13.815	0.121	0.8920383	5002.281060	73.06	0.14	270	0.418	0.362	3.95	5.653	0.056	0.00
003543270	5288	15.220	0.130	4.177213	5003.789822	82.27	0.05	269	0.207	0.254	0.394	0.03937	0.024	0.00
003556742	4921	14.221	0.004	0.8229667	5003.017211	37.02	0.00	247	0.848	2.41	15.5	576.3	0.108	0.00
003656322	5075	13.061	0.150	3.660009	4989.330479	67.54	0.02	125	0.457	0.930	1.66	2.576	0.125	0.00
003730067	4099	14.610	0.594	0.2940818	4964.591764	75.71	0.03	88	0.590	0.420	1.25	0.6522	0.035	0.00
003830820	3902	15.368	0.044	15.58263	4999.277480	87.92	0.47	79	0.057	2.39	2.10	10.57	0.000	0.60
003834364	5449	14.661	0.089	2.908455	4965.315292	82.21	0.10	271	0.182	0.0407	0.874	0.03106	0.006	0.00
003848919	5226	13.901	0.636	1.047253	4964.766251	85.07	0.00	84	0.418	0.903	1.04	0.9684	0.017	0.00
003957477	5395	12.477	0.073	0.9789470	4964.726279	66.89	0.03	91	0.525	1.42	2.97	12.52	0.055	0.00
004049124	5349	14.654	0.175	4.804341	4969.004205	84.04	0.41	89	0.160	1.32	2.24	6.592	0.002	0.00
004077442	4523	13.512	0.153	0.6928736	5002.273033	69.03	0.01	277	0.499	1.94	1.34	3.499	0.183	0.00
004078693	5288	13.485	0.005	2.756407	5001.858784	85.40	0.32	270	0.119	0.0308	0.519	0.008294	0.001	0.79
004247791	4063	11.260	0.152	4.100862	5001.145258	77.90	0.00	87	0.326	0.928	1.48	2.035	0.001	0.00
004281895	5309	12.256	0.078	9.543591	5002.358654	87.52	0.30	4	0.065	1.18	3.41	13.80	0.000	0.00
004346875	5339	15.584	0.284	4.694341	5004.332965	87.08	0.02	267	0.135	0.0866	0.429	0.01592	0.014	0.00
004352168	5115	14.343	0.663	10.64334	4967.942159	89.58	0.18	213	0.072	0.268	1.29	0.4451	0.012	0.35
004484356	5080	14.235	0.177	1.144126	5002.774583	78.62	0.02	271	0.320	0.899	0.652	0.3817	0.025	0.00
004540632	4818	14.991	1.045	31.00996	4983.860841	89.93	0.66	98	0.030	0.315	0.826	0.2150	0.000	0.00
004579313	5363	14.811	0.008	2.112635	5002.947518	68.73	0.00	309	0.390	0.553	13.3	98.34	0.029	0.00

Table 5.2 (continued)

<i>Kepler</i> ID	T_{eff} (K)	m_{kep}	Δm_{kep}	Period (Days)	T_0 (BJD-2450000)	i ($^\circ$)	e^a	ω^a ($^\circ$)	r_{sum}	J	k	L_r	L_1 Sine Amplitude	L_3
004633434	4902	15.362	0.233	22.27067	4967.759577	89.52	0.09	107	0.031	0.0806	1.58	0.2024	0.000	0.77
004672010	4655	14.602	0.049	0.9628780	5002.694396	41.63	0.02	271	0.904	1.97	7.26	103.9	0.038	0.00
004678171	4240	15.993	0.951	15.28859	4965.805465	89.68	0.01	111	0.045	0.474	0.996	0.4702	0.002	0.00
004737267	5156	15.145	0.471	9.523936	5001.185337	89.05	0.01	220	0.154	0.521	1.98	2.032	0.072	0.00
004757331	5092	15.725	0.087	2.362127	5001.736119	81.59	0.11	90	0.210	1.77	2.01	7.157	0.043	0.00
004758368	4594	10.805	0.044	3.750218	5003.200871	67.51	0.02	260	0.489	1.01	3.73	14.11	0.002	0.00
004773155	5447	13.592	0.733	25.70599	4989.643369	89.86	0.43	309	0.042	0.767	1.14	0.9988	0.000	0.03
004908495	4731	13.871	0.359	3.120583	4965.367280	86.08	0.01	265	0.153	0.732	1.01	0.7479	0.076	0.00
004940201	5284	14.984	0.050	8.816203	5002.550394	90.00	0.03	87	0.067	0.455	1.24	0.7023	0.000	0.93
004948863	5490	15.414	0.090	8.643652	4972.829522	87.28	0.26	89	0.070	1.33	3.05	12.37	0.001	0.00
005015913	5487	12.989	0.002	2.359939	4954.580900	72.85	0.00	277	0.312	1.06	22.9	553.2	0.004	0.00
005018787	5215	15.428	0.023	0.6071971	5002.664852	83.52	0.12	89	0.338	0.410	1.98	1.601	0.000	0.96
005036538	4199	13.349	0.758	2.122015	5001.594725	88.69	0.00	285	0.181	0.773	1.02	0.8082	0.033	0.00
005041975	5149	13.981	0.160	2.958502	5003.379626	58.09	0.00	285	0.680	0.427	2.93	3.661	0.054	0.00
005080652	5344	15.080	0.524	4.144388	5001.321781	86.69	0.01	91	0.165	0.556	0.839	0.3915	0.018	0.00
005193386	4797	13.998	0.397	21.37192	4980.205957	88.85	0.01	121	0.134	0.268	3.43	3.148	0.098	0.00
005218014	4752	12.923	0.010	10.84612	4971.331816	88.91	0.24	157	0.068	0.944	1.16	1.266	0.002	0.98
005266937	5483	14.352	0.987	5.916942	5001.400391	88.40	0.05	268	0.429	0.113	0.721	0.05881	0.020	0.00
005286786	4946	15.456	0.006	9.949612	4976.748845	88.88	0.02	230	0.049	0.817	2.81	6.433	0.002	0.98
005294739	5068	13.930	0.994	3.736174	5001.678732	76.49	0.02	278	0.555	0.138	1.85	0.4705	0.068	0.00
005300878	4631	14.767	0.823	1.279424	5002.597321	89.49	0.01	93	0.294	0.817	1.02	0.8576	0.047	0.00
005347784	5392	13.094	0.155	9.584026	5000.621695	85.60	0.01	148	0.121	1.05	1.34	1.885	0.007	0.00
005467126	4683	12.367	0.014	2.845694	5001.431451	77.08	0.15	85	0.575	0.243	1.69	0.6920	0.000	0.98
005597970	5179	12.778	0.218	6.717435	4970.209216	86.01	0.28	270	0.106	0.0127	2.74	0.09511	0.002	0.00
005598639	4847	10.201	0.135	1.297549	5003.022903	83.12	0.00	280	0.441	0.995	0.990	0.9752	0.003	0.69
005696909	5451	14.984	0.006	0.6430210	4964.688376	63.09	0.00	261	0.490	0.965	15.0	218.3	0.035	0.00
005731312	4658	13.811	0.388	7.946392	4968.092030	88.99	0.43	15	0.058	0.113	0.592	0.03952	0.000	0.20
005781192	5372	12.989	0.301	9.459957	4999.722660	88.15	0.07	295	0.077	0.518	0.645	0.2154	0.006	0.00
005802285	4791	15.349	0.017	2.417017	5003.656318	77.87	0.00	89	0.232	0.740	3.74	10.36	0.002	0.00
005802470	5418	13.764	0.337	3.791871	5001.260474	85.11	0.03	90	0.149	0.344	0.985	0.3337	0.013	0.00
005871918	4021	15.701	0.319	12.64175	4972.761250	90.00	0.16	180	0.058	0.246	1.29	0.4091	0.056	0.64

Table 5.2 (continued)

<i>Kepler</i> ID	T_{eff} (K)	m_{kep}	Δm_{kep}	Period (Days)	T_0 (BJD-2450000)	i ($^\circ$)	e^a	ω^a ($^\circ$)	r_{sum}	J	k	L_r	L_1 Sine Amplitude	L_3
006029130	5160	14.832	0.421	12.59140	5005.516830	88.72	0.02	49	0.063	0.851	1.02	0.8859	0.002	0.00
006042116	4771	11.300	0.089	5.407156	5002.038929	80.98	0.11	54	0.211	1.60	1.32	2.789	0.004	0.00
006044064	5095	15.001	1.653	5.063280	5002.149463	83.72	0.03	75	0.389	0.145	1.78	0.4606	0.078	0.00
006060580	5308	13.460	0.019	2.313334	5003.212901	75.37	0.00	27	0.289	0.304	0.298	0.02701	0.001	0.00
006131659	4870	12.534	0.475	17.52783	4960.041441	89.37	0.02	270	0.044	0.316	0.593	0.1111	0.000	0.00
006187893	5103	11.702	0.077	0.7891775	5006.959004	64.02	0.01	274	0.634	0.135	0.349	0.01646	0.008	0.00
006191574	4208	14.353	0.233	0.000000	-5000.000000	0.00	0.00	0	0.000	0.00	0.00	0.000	0.000	0.00
006197038	4937	13.531	0.798	9.752156	5000.794386	80.21	0.19	90	0.277	0.261	2.62	1.790	0.308	0.00
006205460	5242	12.746	0.796	3.722771	5001.134908	85.88	0.01	36	0.419	0.159	2.79	1.238	0.069	0.00
006307537	4253	11.753	0.193	29.74440	4960.659149	87.35	0.04	277	0.108	0.246	4.69	5.396	0.003	0.00
006312534	4897	15.583	0.024	3.015501	5002.128021	81.73	0.36	90	0.213	16.0	2.01	64.38	0.158	0.00
006359798	5452	12.932	0.071	14.15394	4959.543146	89.54	0.41	183	0.048	0.377	1.35	0.6877	0.000	0.90
006367628	5185	13.035	0.548	3.780139	5002.708087	76.36	0.02	267	0.550	0.213	0.840	0.1500	0.016	0.00
006449552	5357	14.904	0.946	20.14888	4968.810574	89.40	0.27	247	0.045	0.188	1.08	0.2176	0.001	0.00
006464285	5061	13.826	0.444	0.8436324	5003.755443	73.04	0.01	286	0.469	0.188	2.74	1.411	0.019	0.00
006466939	4920	14.454	0.733	2.285920	5003.760706	88.72	0.00	95	0.199	0.762	1.14	0.9858	0.021	0.00
006548447	5031	12.880	0.165	10.76541	5009.086049	89.90	0.11	184	0.158	0.617	3.29	6.693	0.004	0.00
006591789	5410	15.353	0.614	5.088435	5002.974423	88.48	0.01	171	0.128	0.318	0.664	0.1399	0.005	0.00
006620003	3955	15.686	0.037	3.428469	4997.172065	82.97	0.01	269	0.146	0.775	1.04	0.8436	0.000	0.00
006629332	5452	13.997	0.073	4.310363	5007.525591	84.14	0.05	90	0.122	2.95	1.46	6.279	0.130	0.00
006694186	5247	12.376	0.189	5.554204	5001.487264	80.66	0.29	271	0.223	0.00832	31.3	8.173	0.000	0.00
006697716	4898	14.424	0.279	1.443221	5008.877209	82.57	0.00	30	0.261	0.505	0.634	0.2030	0.018	0.00
006706287	5182	13.620	0.607	2.535431	5004.418517	87.19	0.00	260	0.196	0.697	0.905	0.5714	0.025	0.00
006778050	5091	14.514	0.420	0.9458108	4964.620719	81.63	0.01	276	0.389	0.822	0.855	0.6013	0.025	0.00
006841577	5478	14.875	0.270	15.53753	4973.272586	89.35	0.19	128	0.059	0.0828	1.72	0.2455	0.000	0.74
006863840	5024	15.138	0.668	3.852650	4964.746207	88.78	0.00	81	0.142	0.830	1.05	0.9234	0.060	0.00
006939670	5436	14.858	0.152	4.238755	4968.201178	79.83	0.05	91	0.235	0.889	2.80	6.980	0.145	0.00
007049486	5498	13.144	0.088	26.71855	4971.051326	88.56	0.29	21	0.052	0.684	0.498	0.1696	0.004	0.64
007097571	5266	11.267	0.153	2.213962	5005.416674	80.18	0.03	91	0.385	0.217	0.314	0.02135	0.001	0.00
007119757	5072	15.608	0.249	0.7429393	4980.909123	71.04	0.02	86	0.541	1.10	1.58	2.750	0.058	0.00
007125636	4358	15.507	0.266	6.490765	4978.048116	87.67	0.02	214	0.081	0.835	0.929	0.7198	0.005	0.00

Table 5.2 (continued)

<i>Kepler</i> ID	T_{eff} (K)	m_{kep}	Δm_{kep}	Period (Days)	T_0 (BJD-2450000)	i ($^\circ$)	e^a	ω^a ($^\circ$)	r_{sum}	J	k	L_r	L_1 Sine Amplitude	L_3
007128918	5386	15.758	0.142	7.118892	4984.394210	88.47	0.01	54	0.085	0.573	0.885	0.4486	0.004	0.70
007129465	5182	15.316	0.427	5.491840	4966.171031	87.83	0.00	271	0.107	0.856	0.941	0.7591	0.004	0.00
007200102	5207	15.213	0.538	14.66695	4972.573070	88.65	0.42	124	0.054	0.564	0.751	0.3181	0.000	0.04
007220322	4887	11.884	0.009	0.7521433	5002.397213	53.82	0.01	85	0.657	1.55	11.1	190.1	0.130	0.00
007257373	5311	13.424	0.745	10.46686	4955.658505	89.72	0.00	89	0.113	1.02	0.922	0.8700	0.001	0.00
007284688	4191	11.234	0.088	0.6461003	5002.783432	64.97	0.00	124	0.552	1.22	2.29	6.374	0.055	0.00
007624297	5135	14.928	0.222	18.01846	4981.666593	88.97	0.05	76	0.042	0.0661	1.73	0.1989	0.000	0.74
007670617	4876	15.517	0.450	24.70190	4969.146845	89.85	0.28	308	0.033	0.201	0.711	0.1018	0.000	0.35
007671594	3717	15.815	0.165	1.410329	4965.398972	84.54	0.00	302	0.138	0.612	1.19	0.8632	0.039	0.00
007691527	5354	15.431	0.463	4.800056	5002.382912	87.47	0.10	130	0.115	1.07	1.21	1.573	0.073	0.00
007749318	5211	14.528	0.341	2.371784	5003.689256	80.47	0.18	270	0.246	0.0569	3.32	0.6277	0.078	0.00
007769072	4858	13.886	0.003	0.6088726	5002.799849	57.25	0.00	72	0.583	1.18	21.8	559.9	0.016	0.00
007798259	4619	15.726	0.411	1.734306	5005.720952	84.29	0.03	270	0.200	0.310	1.22	0.4600	0.070	0.00
007830321	5347	15.476	0.008	2.027248	5003.200747	73.45	0.00	242	0.301	0.672	6.41	27.63	0.010	0.00
007842610	5375	15.289	0.021	1.943760	5001.841852	76.41	0.00	270	0.271	1.32	4.25	23.80	0.027	0.00
007846730	5476	12.956	0.381	11.02825	4969.966521	88.40	0.02	151	0.101	0.599	1.88	2.126	0.000	0.12
007885570	5398	11.679	0.223	1.729021	5001.851398	74.44	0.05	85	0.454	0.747	3.41	8.661	0.237	0.00
007947631	4823	15.179	0.022	2.516590	4987.092316	79.51	0.01	89	0.209	1.13	3.03	10.33	0.008	0.00
007955301	4821	12.672	0.007	15.30817	4960.464666	86.04	0.01	174	0.078	1.42	8.19	95.41	0.001	0.00
007987749	5349	14.461	0.095	17.03109	4978.541107	88.17	0.14	187	0.046	0.398	0.495	0.09742	0.000	0.00
008075618	5288	15.674	0.119	17.56154	4970.923092	88.76	0.02	90	0.031	1.11	0.961	1.027	0.000	0.00
008075755	4075	13.407	0.009	0.4962355	4964.752415	66.36	0.01	94	0.471	0.516	0.0939	0.004556	0.000	0.00
008076905	4214	15.613	0.011	0.4180906	5003.192377	51.07	0.01	279	0.715	1.67	11.8	231.1	0.083	0.00
008094140	4200	15.159	0.606	0.7064196	4973.624150	86.37	0.01	265	0.326	0.274	0.628	0.1079	0.038	0.00
008095110	5370	13.171	0.036	4.206510	4974.280246	76.85	0.02	91	0.300	1.56	4.03	25.26	0.035	0.00
008097825	5329	13.283	0.261	2.937050	4966.633044	78.40	0.00	286	0.343	0.645	1.50	1.449	0.028	0.00
008143170	4957	12.850	0.058	28.78627	4970.110463	85.83	0.20	255	0.103	0.269	6.55	11.55	0.001	0.00
008145789	4829	15.314	0.027	1.670636	5000.039740	75.30	0.01	272	0.311	0.917	5.66	29.34	0.016	0.00
008181016	5179	14.677	0.008	0.7090293	4965.187959	75.06	0.20	270	0.434	0.197	1.37	0.3690	0.000	0.98
008210721	5412	14.274	0.080	22.67256	4971.153407	87.76	0.29	64	0.057	0.234	3.46	2.809	0.000	0.75
008231877	4956	14.932	0.024	2.615519	4975.237630	83.45	0.15	90	0.162	1.87	0.511	0.4880	0.000	0.79

Table 5.2 (continued)

<i>Kepler</i> ID	T_{eff} (K)	m_{kep}	Δm_{kep}	Period (Days)	T_0 (BJD-2450000)	i ($^\circ$)	e^a	ω^a ($^\circ$)	r_{sum}	J	k	L_r	L_1 Sine Amplitude	L_3
008279765	5464	15.235	0.051	2.757746	4965.474866	83.85	0.01	282	0.169	0.0539	0.208	0.002322	0.003	0.00
008288719	5090	13.276	0.043	1.510074	4972.744897	75.00	0.01	95	0.312	1.04	2.58	6.916	0.007	0.00
008296467	5316	15.177	0.987	10.30327	4970.167785	89.99	0.26	320	0.069	0.623	1.06	0.7061	0.006	0.00
008358008	5020	14.674	0.012	10.06506	4968.250048	89.42	0.06	79	0.054	0.533	1.51	1.216	0.000	0.98
008364119	5443	12.408	0.462	7.735857	4970.986699	88.29	0.03	44	0.093	0.897	0.849	0.6471	0.003	0.00
008379547	4861	13.373	0.174	6.041994	4959.163251	81.83	0.35	270	0.222	0.0668	7.25	3.510	0.083	0.00
008397675	5462	13.501	0.002	0.5532564	5001.856348	83.35	0.16	91	0.230	0.933	2.95	8.128	0.092	0.99
008411947	5086	15.300	0.860	1.797734	5003.785574	88.27	0.02	96	0.265	0.607	1.12	0.7612	0.050	0.00
008444552	5388	13.643	0.083	1.178041	4964.597354	77.49	0.11	90	0.323	2.28	1.96	8.734	0.021	0.00
008453324	4733	11.516	0.010	2.524694	5001.646619	72.45	0.00	82	0.341	1.42	5.66	45.59	0.016	0.00
008543278	4950	14.608	0.073	7.549631	4998.208506	88.40	0.12	276	0.052	0.187	0.451	0.03811	0.000	0.57
008559863	5154	12.723	0.055	22.46892	4953.814854	88.21	0.04	217	0.054	0.720	0.437	0.1377	0.002	0.56
008574270	5061	15.166	0.031	15.11963	4972.699012	87.27	0.29	321	0.059	0.0360	0.955	0.03285	0.000	0.00
008580438	5307	14.502	0.152	6.495852	5000.947823	90.00	0.01	80	0.108	0.0314	0.315	0.003107	0.004	0.00
008581232	4314	15.381	0.037	4.012679	5003.764787	87.32	0.33	133	0.086	0.279	0.138	0.005326	0.000	0.00
008616873	5486	15.237	0.015	0.5760785	5002.245893	81.58	0.14	86	0.437	0.140	2.17	0.6544	0.089	0.98
008655458	5210	14.585	0.008	1.594193	5002.299400	88.86	0.03	78	0.397	0.183	0.472	0.04073	0.000	0.98
008718273	4577	10.565	0.006	6.958070	4997.699036	89.55	0.03	269	0.050	0.740	0.0474	0.001664	0.000	0.00
008719897	4905	12.392	0.262	3.151596	4955.232895	80.22	0.02	90	0.315	1.02	1.13	1.291	0.015	0.00
008841616	4550	12.833	0.133	1.679564	4966.238497	61.97	0.02	71	0.650	0.0436	0.639	0.01781	0.022	0.00
008846978	5191	13.371	0.225	1.379281	4970.036969	64.68	0.06	312	0.556	0.0263	3.72	0.3635	0.196	0.58
008848104	5447	12.372	0.041	0.8248496	4972.049484	61.47	0.01	100	0.538	0.307	6.94	14.79	0.029	0.00
008906676	5249	12.121	0.167	8.209521	4967.062429	88.28	0.03	89	0.075	0.118	1.71	0.3441	0.000	0.78
008971432	5057	15.487	0.063	0.6243809	5001.634891	65.63	0.03	89	0.533	0.0555	0.299	0.004965	0.001	0.00
009001468	4949	15.200	0.339	17.32833	4975.727756	89.41	0.52	239	0.043	0.216	1.54	0.5119	0.000	0.57
009029486	5368	13.630	0.342	6.277180	4965.329729	89.54	0.00	279	0.094	0.903	0.981	0.8686	0.007	0.45
009098810	5126	13.448	0.443	8.258238	4972.758295	88.41	0.16	87	0.079	0.957	0.832	0.6620	0.006	0.00
009210828	4893	13.221	0.205	1.656351	4977.002807	80.24	0.02	90	0.269	0.756	1.16	1.016	0.004	0.00
009266285	4184	14.072	0.072	5.613843	4965.571978	82.83	0.27	91	0.182	3.49	1.65	9.496	0.014	0.00
009284741	5085	14.807	0.516	20.72910	4974.226975	89.42	0.37	42	0.041	1.15	1.05	1.265	0.006	0.00
009291629	4629	13.957	0.168	20.69085	4966.893246	84.62	0.13	271	0.214	0.346	4.57	7.243	0.151	0.00

Table 5.2 (continued)

<i>Kepler</i> ID	T_{eff} (K)	m_{kep}	Δm_{kep}	Period (Days)	T_0 (BJD-2450000)	i ($^\circ$)	e^a	ω^a ($^\circ$)	r_{sum}	J	k	L_r	L_1 Sine Amplitude	L_3
009328852	4338	15.330	0.550	0.6458239	5008.159243	84.39	0.04	82	0.410	0.0705	0.519	0.01901	0.047	0.00
009334490	5105	15.695	0.017	18.84520	4982.944981	89.46	0.02	129	0.038	0.797	0.547	0.2389	0.000	0.96
009346655	4183	14.299	0.144	0.8716196	4965.119502	81.56	0.50	90	0.262	6.12	1.50	13.73	0.380	0.00
009412462	5350	14.846	0.518	10.18653	4965.527836	87.39	0.03	230	0.143	0.747	1.19	1.065	0.016	0.00
009418994	5053	13.396	0.021	32.00590	4969.494447	89.65	0.23	54	0.024	0.136	0.668	0.06079	0.000	0.96
009474485	4469	14.884	0.668	1.025164	4965.292428	87.18	0.00	5	0.329	0.864	1.02	0.9024	0.033	0.00
009574614	5276	15.933	0.011	1.964342	5002.018849	78.41	0.01	238	0.220	1.01	4.37	19.23	0.001	0.00
009597095	5331	15.945	0.073	2.745608	5003.145923	81.81	0.02	269	0.203	0.121	0.377	0.01723	0.001	0.00
009632895	5425	13.552	0.097	27.32202	4965.424356	87.89	0.03	257	0.046	0.0428	11.9	6.042	0.000	0.46
009639265	5004	15.575	0.370	0.5063492	4964.814722	75.19	0.02	275	0.520	0.888	0.765	0.5194	0.068	0.00
009658832	4545	13.638	0.029	0.4568510	5002.649683	56.54	0.01	80	0.683	0.335	0.163	0.008909	0.002	0.00
009665503	5141	15.217	0.656	11.56806	4970.339984	89.46	0.28	330	0.063	0.383	0.694	0.1844	0.000	0.00
009714358	4825	14.998	0.283	6.479757	4999.785837	86.63	0.26	272	0.089	0.0295	3.94	0.4572	0.000	0.13
009761199	4060	15.692	0.014	1.383998	4964.727100	74.47	0.00	128	0.289	1.14	3.00	10.29	0.009	0.00
009762519	5435	13.711	0.152	7.515083	4971.079973	86.05	0.18	282	0.095	0.0521	2.31	0.2778	0.007	0.00
009837578	5359	15.726	0.698	20.73369	4965.845828	89.44	0.16	87	0.048	0.681	1.26	1.083	0.000	0.00
009851126	4164	13.183	0.097	8.480306	4968.853813	89.89	0.21	18	0.129	0.137	0.257	0.009052	0.000	0.03
009912977	5158	13.726	0.442	1.887885	5002.578442	79.82	0.01	91	0.473	1.01	1.17	1.380	0.002	0.00
009913798	4659	14.945	0.218	2.143443	5002.935126	83.44	0.01	271	0.269	0.173	0.409	0.02886	0.001	0.00
009934208	4258	15.507	0.166	9.058852	4970.337139	85.96	0.14	51	0.091	0.193	5.49	5.819	0.002	0.00
009944201	4737	15.069	0.032	0.7215318	5002.227862	86.33	0.07	90	0.307	0.215	1.71	0.6296	0.091	0.96
009944421	5304	15.137	0.349	7.095304	4968.370748	86.24	0.26	69	0.100	0.637	1.18	0.8853	0.024	0.00
010014830	4324	14.827	0.897	3.030715	5003.492462	85.95	0.00	185	0.549	0.279	1.80	0.9018	0.058	0.00
010026457	5222	15.390	0.089	9.934463	5005.612121	89.71	0.13	320	0.109	0.990	0.970	0.9321	0.000	0.84
010090246	5442	13.567	0.171	2.285607	5003.110556	56.54	0.03	89	0.695	0.560	2.32	3.022	0.038	0.00
010095484	5486	14.382	0.008	0.6777383	5002.579926	29.31	0.01	97	0.906	0.536	16.2	14.00	0.060	0.00
010129482	4558	15.994	0.268	0.8462873	5002.429877	80.44	0.00	76	0.326	0.190	0.615	0.07199	0.011	0.00
010189523	5002	15.856	0.117	1.013960	5002.929802	74.89	0.05	89	0.325	1.29	0.530	0.3627	0.039	0.00
010215422	5427	14.608	0.444	24.39590	4987.127475	89.06	0.29	9	0.045	0.207	1.43	0.4202	0.000	0.44
010264202	5207	15.777	0.144	1.035161	5002.815429	75.46	0.01	272	0.373	0.672	0.955	0.6130	0.004	0.00
010292465	5258	14.956	0.152	1.353325	5002.832143	73.64	0.00	0	0.348	0.0940	4.64	2.023	0.068	0.34

Table 5.2 (continued)

<i>Kepler</i> ID	T_{eff} (K)	m_{kep}	Δm_{kep}	Period (Days)	T_0 (BJD-2450000)	i ($^\circ$)	e^a	ω^a ($^\circ$)	r_{sum}	J	k	L_r	L_1 Sine Amplitude	L_3
010330495	5132	14.724	0.075	18.06030	4971.608312	85.34	0.14	254	0.117	0.150	10.5	16.46	0.003	0.00
010340522	5286	14.404	1.204	3.988565	5001.472319	85.90	0.01	63	0.585	0.188	0.814	0.1246	0.008	0.00
010491544	4835	13.436	0.031	22.77214	4973.487861	86.42	0.54	56	0.089	15.6	1.34	27.91	0.017	0.00
010592163	5482	15.095	0.098	14.76289	4966.772333	88.98	0.32	329	0.057	0.486	0.628	0.1916	0.000	0.73
010613718	5080	12.735	0.010	1.175802	4966.821353	74.39	0.01	269	0.307	0.966	8.52	70.13	0.006	0.00
010711646	4339	15.787	0.204	0.7376206	4997.149560	78.07	0.08	270	0.343	0.134	1.16	0.1808	0.046	0.42
010753734	5446	13.564	0.725	19.40624	4982.807297	89.74	0.52	18	0.051	0.823	0.849	0.5942	0.005	0.00
010794242	5459	14.170	0.269	7.143779	4970.803174	89.19	0.08	247	0.102	0.0887	0.425	0.01604	0.010	0.00
010794405	5479	14.713	0.005	0.9522659	4979.620590	40.08	0.00	237	0.821	3.37	12.9	557.6	0.192	0.00
010809677	4995	13.942	0.008	7.042849	4970.731749	80.78	0.00	271	0.172	0.968	3.55	12.20	0.000	0.00
010936427	5082	14.419	0.756	14.35935	4971.843223	88.64	0.02	84	0.116	0.401	1.72	1.192	0.042	0.00
010979716	3932	15.774	0.125	10.68394	4967.091349	88.05	0.15	278	0.054	0.307	0.718	0.1586	0.006	0.00
010991989	5021	10.282	0.012	0.9744771	4965.368901	85.97	0.09	268	0.358	0.568	0.597	0.2028	0.000	0.97
010992733	5274	15.124	0.728	18.52628	4977.193722	89.99	0.38	26	0.055	0.704	0.777	0.4255	0.006	0.00
011124509	5417	14.735	0.018	8.893240	4968.729831	85.98	0.01	269	0.080	0.393	1.34	0.7016	0.001	0.74
011134079	5201	14.864	0.232	1.260506	4965.061893	73.28	0.01	265	0.368	0.134	4.48	2.688	0.043	0.00
011147460	4855	13.912	0.009	4.107429	4965.943730	73.69	0.00	71	0.316	0.548	0.139	0.01052	0.000	0.00
011232745	5204	15.973	0.056	9.633799	4970.918869	89.91	0.03	90	0.037	0.574	1.67	1.609	0.058	0.91
011233911	5193	14.742	0.285	4.959761	4969.120822	85.16	0.01	90	0.171	0.789	2.19	3.776	0.103	0.00
011235323	5071	13.486	0.496	19.67035	4965.522562	89.28	0.06	270	0.137	0.458	0.598	0.1636	0.006	0.00
011287726	5167	14.176	0.159	4.736985	4970.064587	78.94	0.07	271	0.258	0.175	1.53	0.4081	0.005	0.00
011350389	5124	15.724	0.037	1.512708	4969.562269	83.00	0.05	270	0.172	0.213	8.74	16.24	0.019	0.59
011391181	5218	15.257	0.276	8.617414	4972.068740	87.23	0.20	30	0.081	0.923	1.15	1.228	0.024	0.00
011391667	5394	12.923	0.011	1.083646	4954.131479	74.63	0.00	292	0.320	0.497	0.116	0.006724	0.000	0.00
011455795	4477	15.414	0.072	1.057351	4964.791193	81.87	0.00	0	0.221	0.0229	7.44	1.271	0.108	0.90
011546211	3682	15.155	0.083	2.194447	4966.712688	85.75	0.67	90	0.133	88.2	0.454	18.17	0.756	0.00
011671660	4867	13.350	0.089	8.702917	4956.587112	72.47	0.03	271	0.368	0.718	5.29	20.08	0.233	0.00
011768970	5038	12.658	0.012	15.54223	4959.412961	87.15	0.87	82	0.089	28.7	1.42	57.58	0.000	0.42
011858541	5375	14.215	0.045	5.674410	4968.755298	81.16	0.06	355	0.180	0.421	4.60	8.922	0.006	0.00
011968514	4940	11.449	0.005	2.073289	5002.408007	73.94	0.01	259	0.304	1.32	16.0	338.4	0.037	0.00
011975363	5482	15.409	0.578	3.518364	4967.411791	88.02	0.01	89	0.180	0.916	1.08	1.061	0.018	0.00

Table 5.2 (continued)

<i>Kepler</i> ID	T_{eff} (K)	m_{kep}	Δm_{kep}	Period (Days)	T_0 (BJD-2450000)	i ($^\circ$)	e^a	ω^a ($^\circ$)	r_{sum}	J	k	L_r	L_1 Sine Amplitude	L_3
012004679	5432	13.231	0.833	5.042429	4955.770424	89.85	0.01	77	0.115	0.803	0.997	0.7988	0.008	0.00
012004834	3576	14.718	0.333	0.2623169	4964.398367	72.47	0.06	269	0.517	1.04	1.56	2.532	0.018	0.00
012105785	5349	13.032	0.021	31.95107	4975.706638	87.34	0.18	114	0.056	2.81	0.507	0.7219	0.000	0.66
012351927	4641	15.520	0.086	10.11594	4972.982326	85.41	0.01	119	0.087	0.0699	7.19	3.613	0.000	0.00
012356914	5368	15.529	0.621	27.30710	4976.502419	89.94	0.44	74	0.035	0.157	0.636	0.06344	0.001	0.00
012365000	5080	13.573	0.028	1.262660	4986.658328	77.85	0.11	269	0.283	0.148	0.912	0.1230	0.025	0.70
012367017	5004	14.730	0.008	1.222133	4970.925867	59.96	0.00	290	0.540	0.806	18.6	277.5	0.026	0.00
012367310	4965	13.835	0.044	8.627137	4972.995164	81.33	0.02	314	0.167	0.147	5.54	4.518	0.017	0.00
012400729	4949	15.227	0.149	0.9317268	4965.479857	72.86	0.13	196	0.366	0.000549	8.92	0.04368	0.219	0.88
012418816	4583	12.402	0.581	1.521896	4965.395396	87.12	0.01	88	0.248	1.00	1.04	1.082	0.038	0.00
012470530	4725	15.300	0.658	8.207057	4968.824442	88.44	0.38	347	0.072	0.302	0.979	0.2889	0.000	0.03
012557713	4594	14.853	0.068	7.214603	4965.498124	87.06	0.43	92	0.077	12.6	0.412	2.134	0.000	0.17
012599700	3887	15.784	0.120	1.017821	4968.317001	87.78	0.03	268	0.136	0.433	1.24	0.6686	0.363	0.87
012645761	4844	13.368	0.018	5.419663	4958.954807	81.82	0.34	90	0.212	23.8	1.91	86.59	0.185	0.00

^aAlthough the values for e and ω are presented in this table for ease of reading, the values of $e \cdot \cos(\omega)$ and $e \cdot \sin(\omega)$ were actually solved for in the analysis.

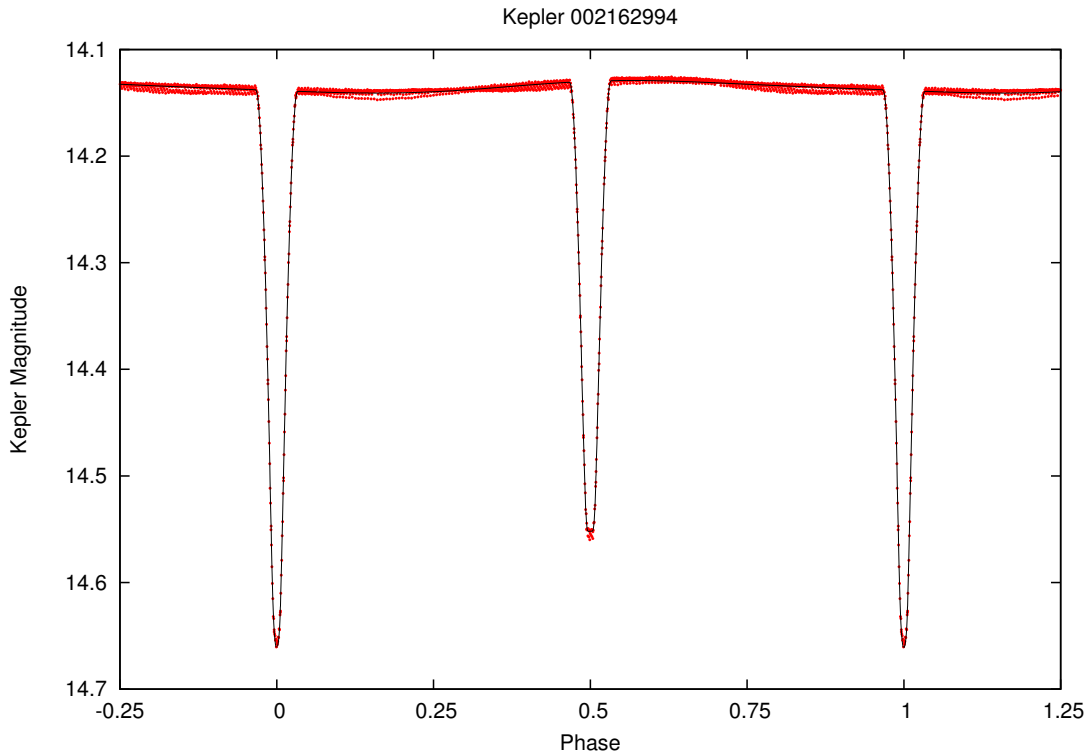


Fig. 5.4.— Plots of the light curves of the 231 systems modeled with the JKTE-BOP code, presented in Table 5.2. Only the first plot, Figure 5.4.1, is shown in the text for guidance. Figures 5.4.1-5.4.231 are available in the online version of the *Astronomical Journal* under Coughlin et al. (2011).

minimum, and estimated effective temperature of the system from broadband photometry provided in López-Morales & Ribas (2005), as we did for the systems in our main study. We find $T_1 = 3912$ K, $M_1 = 0.61 M_\odot$, $R_1 = 0.62 R_\odot$, $T_2 = 3813$ K, $M_2 = 0.57 M_\odot$, and $R_2 = 0.59$ via our technique. In comparison, López-Morales & Ribas (2005) found with multi-color light curves and radial-velocity curves of the system, values of $T_1 = 3920$ K, $M_1 = 0.610 M_\odot$, $R_1 = 0.623 R_\odot$, $T_2 = 3810$ K, $M_2 = 0.599 M_\odot$, and $R_2 = 0.620$. The values derived from our technique using only a single color light curve are accurate to within a few percent of the very precise values derived from a study using multi-color light and radial-velocity

curves, thus validating our technique.

As noted above, Prša et al. (2010) estimated the parameters of temperature ratio, sum of the fractional radii, $e \cdot \cos(\omega)$, $e \cdot \sin(\omega)$, and $\sin(i)$ for detached systems, via the EBAI technique (Prša et al. 2008). Before comparing to the parameters obtained by (Prša et al. 2010), we note that the modeling approach between EBAI and our AGA presented in this chapter have some fundamental differences. EBAI is extremely computationally efficient, but relies on a fitted polynomial to the actual data (Prša et al. 2008), which is then compared to a neural network training set of 33,235 light curves generated by the Wilson-Devinney code (Wilson & Devinney 1971; Wilson 1993). Prša et al. (2008) notes that “...the artificial neural network output is viable for statistical analysis and as input to sophisticated modeling engines for fine-tuning.” In comparison, the use of our AGA coupled with JKTEBOP is computationally slower, but models each actual data point, obtaining an actual best-fit model while varying all physical parameters of interest over the global solution space. As well, our AGA takes into account the 29.43 minute integration time, while EBAI does not. Thus, although the EBAI technique is excellent for mining large databases, identification of light curve morphology, and obtaining estimates of parameters for statistical studies, it is not intended to model individual light curves as precisely and accurately as possible. Keeping this in mind, comparing the parameters obtained by Prša et al. (2010) to our solutions for the same systems, we first note a moderate correlation between the sum of radii given by Prša et al. (2010) and our results, with an average discrepancy of $\sim 20\%$. However some of the Prša et al. (2010) solutions are unphysical, ($r_{sum} < 0.0$), and visual inspection of the polyfit curves given by Prša et al. (2010) appears to reveal a systematic underestimation of the eclipse depths.

With respect to eccentricity, the parameters presented by Prša et al. (2010) reveal an unusually large number of eccentric systems, with only 3% of systems having $e \leq 0.01$, and 11% of systems with $e \leq 0.05$. In contrast, our parameters show 36% of systems with $e \leq 0.01$, and 60% of systems with $e \leq 0.05$, which better matches the large number of systems observed that do not show any offset of secondary eclipse from phase 0.5, and no difference in the eclipse widths, indicative of a circular orbit. There is only a slight correlation between our inclination values and that of Prša et al. (2010), but as we previously noted, the Prša et al. (2010) polyfit curves appear not to fit the eclipse depths well. There is practically no correlation between our values for the surface brightness ratio and EBAI’s temperature ratio provided in Prša et al. (2010), though Prša et al. (2010) notes that for detached systems, the “...eclipse depth ratio is strongly affected by eccentricity and star sizes as well, rendering T_2/T_1 a poor proxy for the surface brightness ratio.”

In Table 5.3 we list the *Kepler* ID number, orbital period, effective temperature of the system, and the estimated effective temperature, mass and radius of each stellar component for the 95 systems that contain two main-sequence stars, which we define as having a radius less than 1.5 times the Baraffe et al. (1998) and Chabrier et al. (2000) model relationships, and a light curve amplitude of at least 0.1 magnitudes, (suitable for ground-based follow-up and less likely to contain any third light). All of these 95 systems have both stars with masses less than $1.0 M_{\odot}$. Note that we have ordered Table 5.3 such that Star 1 is always the more massive star, regardless if L_r was greater or less than 1.0 in Table 5.2. Also note that since we are using $V+R$ -band luminosities, which best correspond to the *Kepler* bandpass, one cannot always use the simple $R^2 \cdot T^4$ relation to derive luminosity ratios from Table 5.3 to compare to Table 5.2, since that would correspond to the

bolometric luminosity. However, if one takes a system from Table 5.3, looks up the $V+R$ -band luminosity for each component, based on their mass and temperature, from the Baraffe et al. (1998) and Chabrier et al. (2000) models, and derives a luminosity ratio, this will exactly match the luminosity ratio in Table 5.2 from the JKTEBOP models, because the technique defines it as such. These results substantially increase the number of LMMS DDEB candidates in general, and provide 29 new LMMS DDEBs with both components below one solar mass, and at least 0.1 magnitude eclipse depths, in the heretofore unexplored period range of $P > 10$ days. We further discuss the impact of these systems and comparison to theoretical models in Section 5.7.

In Figure 5.5 we show an example of a system which did not meet the main-sequence criterion, Kepler 004247791, which has $T_{\text{eff}} = 4063\text{K}$ and a period of 4.100866 days. If this system were main-sequence, via our method, it would have a combined mass of $1.28 M_{\odot}$ and a combined radius of $3.82 R_{\odot}$. This can be seen by the wide, shallow eclipses for a system of this period and effective temperature. Thus, this system contains one or two evolved stars. An additional curiosity of this system is a periodic transit-like feature that is superimposed on the eclipsing binary light curve. The transit feature occurs at just slightly less than half the orbital period of the eclipsing binary, so that it is seen twice per every revolution of the eclipsing binary system, occurring at a slightly earlier phase every revolution. We subtract the model fit from the eclipsing binary, and plot the transit feature at its period of 2.02484 days in the right panel of Figure 5.5. Some possible explanations may include, but are certainly not limited to: 1) a background eclipsing binary with no visible secondary eclipse at 0.49376 times the orbital period of the foreground binary, 2) a background eclipsing binary with

Table 5.3. Temperature, Mass, and Radius Estimates for the 95 New LMMS DDEB Candidates with Amplitudes ≥ 0.1 Magnitudes and Both Masses $< 1.0 M_{\odot}$

<i>Kepler</i> ID	Period (Days)	T_{eff} (K)	T_1 (K)	T_2 (K)	$M_1(M_{\odot})$	$M_2(M_{\odot})$	$R_1(R_{\odot})$	$R_2(R_{\odot})$
002162994	4.102	5410	5593	5038	0.96	0.86	1.39	1.24
002437452	14.47	5398	5591	4647	0.96	0.79	1.40	1.13
002719873	17.28	5086	5246	4382	0.90	0.73	1.08	0.86
002852560	11.96	5381	5385	5378	0.93	0.92	1.06	1.06
003003991	7.245	5366	5554	4598	0.96	0.78	0.83	0.67
003102024	13.78	5117	5160	5069	0.89	0.87	0.79	0.78
003241344	3.913	5422	5461	3688	0.94	0.52	0.94	0.49
003241619	1.703	5165	5344	4622	0.92	0.79	1.04	0.88
003458919	0.8920	5063	5206	4254	0.89	0.70	1.08	0.83
003730067	0.2941	4099	4158	4010	0.68	0.64	0.62	0.58
003848919	1.047	5226	5238	5214	0.90	0.90	1.10	1.10
004049124	4.804	5349	5501	4347	0.95	0.73	1.30	0.97
004077442	0.6929	4523	4643	4094	0.79	0.66	1.03	0.84
004346875	4.694	5339	5367	3599	0.92	0.46	1.21	0.56
004352168	10.64	5115	5281	4744	0.91	0.81	0.93	0.82
004484356	1.144	5080	5250	4636	0.90	0.79	0.94	0.81
004540632	31.01	4818	4953	4190	0.85	0.69	0.80	0.63
004633434	22.27	4902	5041	4219	0.86	0.69	0.67	0.52
004678171	15.29	4240	4331	4048	0.72	0.65	0.68	0.60
004773155	25.71	5447	5448	5447	0.94	0.94	0.96	0.96
004908495	3.121	4731	4791	4655	0.82	0.79	0.82	0.79
005036538	2.122	4199	4236	4155	0.70	0.68	0.71	0.69
005080652	4.144	5344	5536	4858	0.95	0.83	1.17	1.01
005300878	1.279	4631	4667	4590	0.80	0.78	0.87	0.85
005597970	6.717	5179	5284	4060	0.91	0.65	1.08	0.74
005731312	7.946	4658	4701	3583	0.80	0.45	0.68	0.36
005781192	9.460	5372	5546	4482	0.95	0.76	0.97	0.75
005802470	3.792	5418	5620	4859	0.97	0.83	1.00	0.86
005871918	12.64	4021	4052	3983	0.65	0.63	0.79	0.76
006029130	12.59	5160	5201	5114	0.89	0.88	0.88	0.86
006131659	17.53	4870	4970	3972	0.85	0.63	0.84	0.59
006449552	20.15	5357	5537	4532	0.95	0.77	0.93	0.74
006464285	0.8436	5061	5159	4923	0.89	0.84	1.09	1.03
006466939	2.286	4920	4925	4916	0.84	0.84	0.87	0.86
006591789	5.088	5410	5560	4342	0.96	0.73	1.09	0.81
006697716	1.443	4898	5036	4215	0.86	0.69	0.91	0.71
006706287	2.535	5182	5327	4931	0.91	0.85	0.96	0.89
006778050	0.9458	5091	5223	4872	0.90	0.83	0.98	0.91
006841577	15.54	5478	5676	4676	0.98	0.80	1.03	0.83
006863840	3.853	5024	5050	4997	0.87	0.86	0.88	0.87
007119757	0.7429	5072	5242	4607	0.90	0.78	1.20	1.03
007125636	6.491	4358	4417	4277	0.74	0.71	0.69	0.66
007128918	7.119	5386	5574	4968	0.96	0.85	0.86	0.76
007129465	5.492	5182	5269	5069	0.90	0.87	0.87	0.83
007200102	14.67	5207	5390	4643	0.93	0.79	0.88	0.74
007624297	18.02	5135	5291	4352	0.91	0.73	0.81	0.63
007670617	24.70	4876	4971	3945	0.85	0.62	0.80	0.56
007671594	1.410	3717	3773	3597	0.56	0.46	0.40	0.32
007691527	4.800	5354	5492	5138	0.94	0.88	0.87	0.81

Table 5.3 (continued)

<i>Kepler</i> ID	Period (Days)	T _{eff} (K)	T ₁ (K)	T ₂ (K)	M ₁ (M _⊙)	M ₂ (M _⊙)	R ₁ (R _⊙)	R ₂ (R _⊙)
007749318	2.372	5211	5347	4991	0.92	0.86	1.16	1.07
007798259	1.734	4619	4735	4386	0.81	0.74	0.74	0.67
007846730	11.03	5476	5667	5079	0.98	0.87	1.37	1.22
008075618	17.56	5288	5301	5275	0.91	0.91	0.55	0.54
008094140	0.7064	4200	4266	3598	0.71	0.46	0.70	0.44
008296467	10.30	5316	5427	5159	0.93	0.89	0.86	0.82
008364119	7.736	5443	5581	5232	0.96	0.90	0.97	0.91
008411947	1.798	5086	5168	4980	0.89	0.85	1.01	0.97
008580438	6.496	5307	5314	3348	0.91	0.23	1.31	0.35
008906676	8.210	5249	5436	4709	0.93	0.80	0.84	0.71
009001468	17.33	4949	5089	4676	0.87	0.80	0.76	0.69
009029486	6.277	5368	5421	5309	0.93	0.91	0.83	0.81
009098810	8.258	5126	5240	4956	0.90	0.85	0.84	0.79
009210828	1.656	4893	4898	4888	0.84	0.84	0.94	0.94
009284741	20.73	5085	5156	4998	0.88	0.86	0.80	0.78
009328852	0.6458	4338	4357	3375	0.73	0.25	0.94	0.34
009346655	0.8716	4183	4232	3512	0.70	0.39	0.67	0.37
009474485	1.025	4469	4492	4444	0.76	0.75	0.81	0.80
009639265	0.5063	5004	5147	4730	0.88	0.81	0.87	0.79
009665503	11.57	5141	5293	4321	0.91	0.72	0.90	0.69
009714358	6.480	4825	4964	4522	0.85	0.77	0.81	0.72
009762519	7.515	5435	5528	4050	0.95	0.65	0.95	0.62
009837578	20.73	5359	5390	5327	0.93	0.91	0.95	0.94
009934208	9.059	4258	4347	3743	0.73	0.55	1.04	0.76
009944421	7.095	5304	5348	5255	0.92	0.90	0.96	0.94
010129482	0.8463	4558	4622	3669	0.79	0.51	0.83	0.51
010189523	1.014	5002	5143	4239	0.88	0.70	0.91	0.70
010215422	24.40	5427	5625	4944	0.97	0.85	1.04	0.91
010264202	1.035	5207	5347	4971	0.92	0.85	1.01	0.93
010292465	1.353	5258	5417	4965	0.93	0.85	1.15	1.05
010711646	0.7376	4339	4440	3877	0.75	0.59	0.74	0.57
010753734	19.41	5446	5603	5183	0.97	0.89	0.99	0.91
010794242	7.144	5459	5490	3633	0.94	0.49	1.20	0.58
010979716	10.68	3932	3996	3530	0.63	0.41	0.68	0.43
010992733	18.53	5274	5457	4848	0.94	0.83	1.04	0.91
011134079	1.261	5201	5381	4732	0.92	0.81	1.17	1.01
011233911	4.960	5193	5370	4531	0.92	0.77	1.38	1.12
011391181	8.617	5218	5288	5133	0.91	0.88	0.88	0.85
011975363	3.518	5482	5507	5457	0.95	0.94	1.09	1.08
012004679	5.042	5432	5514	5330	0.95	0.92	0.89	0.86
012004834	0.2623	3576	3620	3468	0.48	0.34	0.48	0.35
012356914	27.31	5368	5455	4003	0.94	0.63	0.93	0.60
012400729	0.9317	4949	5005	3715	0.86	0.54	1.03	0.61
012418816	1.522	4583	4603	4563	0.78	0.77	0.81	0.80
012470530	8.207	4725	4863	4245	0.83	0.70	0.78	0.64
012599700	1.018	3887	3936	3816	0.61	0.57	0.32	0.30

nearly identical primary and secondary eclipses at 0.98752 times the orbital period of the foreground binary, 3) a circumbinary transiting object, or 4) a transiting object around one of the stars in an almost 2:1 resonant orbit with the binary. Follow-up multi-color light curves, spectra, and radial velocities will be needed to fully characterize this interesting system.

5.6. New Transiting Planet Candidates

For the eight new transiting planet candidates mentioned in Section 5.3, we combined Q0 and Q1 data, and modeled the transit curves using JKTEBOP, accounting for the 29.43 minute integration time, and using our modified AGA in the same manner described in Section 5.4. We assumed zero eccentricity and negligible flux from each planet, and interpolated the limb-darkening and gravity-darkening coefficients via the effective temperature, surface gravity, and metallicity from the relations of Sing (2010) and Claret (2000b). We then solved for the period, time of primary minimum, inclination, sum of the fractional radii, ratio of the radii, and the out of transit flux level. With this narrowed set of parameters, the AGA proved to be extremely quick and precise, and all fits were confirmed by eye and χ^2 values to accurately fit the data. Plots of the transit light curves with model fits are shown in Figure 5.6.

To estimate the physical radius of each transiting exoplanet candidate, we took the value for the radius of the host star from the KIC, and multiplied by the ratio of the radii, k , found from the model. In Table 5.4 we list the *Kepler* ID number, apparent *Kepler* magnitude, time of primary minimum, period, effective temperature of the star, inclination, radius of the star, and radius of the exoplanet

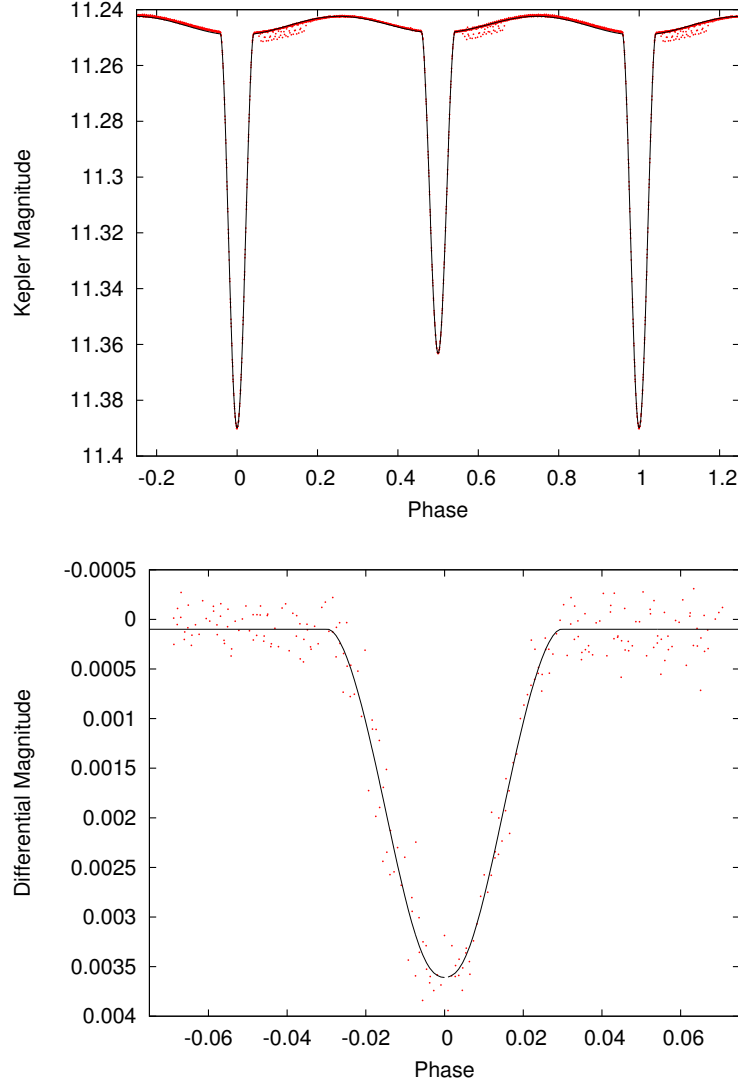


Fig. 5.5.— Kepler 004247791. An example of a system which was determined not to be main-sequence in Section 5.5. Top: The light curve phased at its period of 4.100866 days with our best model fit. Given the shallow, wide eclipses for a ~ 4.1 day period and $T_{\text{eff}} = 4063\text{K}$, if this system were main-sequence, it would have a combined mass of $1.28 M_{\odot}$ and a combined radius of $3.82 R_{\odot}$. Thus, this system contains one or more evolved stars. Bottom: The model-fit subtracted light curve phased at a period of 2.02484 days, showing a transit-like feature imposed on the light curve of the eclipsing binary. Possible explanations may include, but are certainly not limited to a background eclipsing binary with no visible secondary eclipse at 0.49376 times the orbital period of the foreground binary, a background eclipsing binary with nearly identical primary and secondary eclipses at 0.98752 times the orbital period of the foreground binary, a circumbinary transiting object, or a transiting object around one of the stars in an almost 2:1 resonant orbit with the binary.

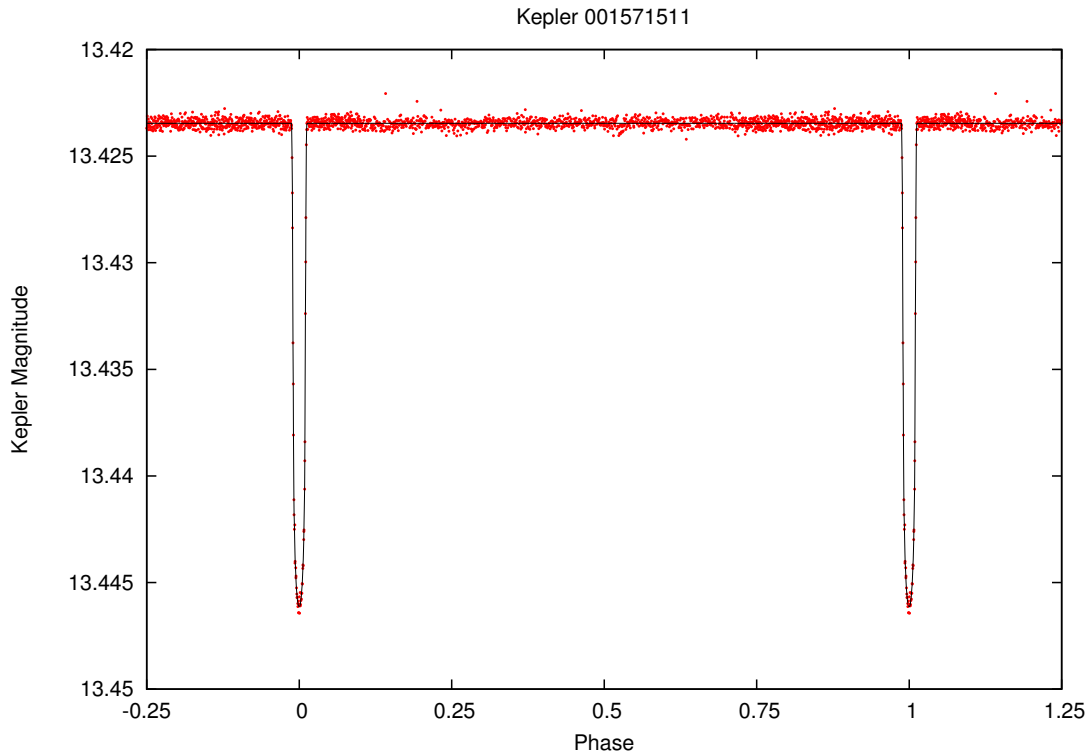


Fig. 5.6.— Plots of the light curves of the eight transiting planet candidates modeled with the JKTEBOP code, presented in Table 5.4. Only the first plot, Figure 5.6.1, is shown in the text for guidance. Figures 5.6.1-5.6.8 are available in the online version of the *Astronomical Journal* under Coughlin et al. (2011).

candidate in both solar radii and Jupiter radii.

As can be seen, the radii for these transiting planet candidates range from 0.56 to 2.1 R_{Jup} , with periods between 4.1 and 24.6 days. Only one of these, Kepler 011974540, has been ruled out as a planet from follow-up RV measurements, which are needed for the rest of the candidates to confirm or refute their planetary nature. However, even if these objects turn out not to be planetary mass, they then must be either brown dwarfs or very low-mass stars, which still are valuable finds. In the case of brown dwarfs, these targets would be located within the so-called “brown dwarf desert” (McCarthy & Zuckerman 2004).

5.7. Comparison of the New Low-Mass Binary Candidates to Models

As described in the introduction, one of the current outstanding questions in the study of low-mass stars is whether the inflated radii observed in binaries is caused by their enhanced stellar rotation, and therefore enhanced magnetic activity. We explore this problem in this section using the list of the 95 new LMMS DDEB candidates with estimated individual masses both below $1.0 M_{\odot}$ and light curve amplitudes greater than 0.1 magnitudes, given in Table 5.3. This sample, for the first time, provides a statistically significant number of systems with orbital periods larger than 10 days.

The left-side panels of Figure 5.7 show mass-radius diagrams using the mass and radius of each binary star component estimated in Section 5.5. The LMMS DDEB candidates have been separated into three categories, with orbital periods $P < 1.0$ day, $1.0 < P < 10$ days, and $P > 10$ days. Each primary and secondary in a binary pair is traced by a connecting line. We also plot in each panel of Figure 5.7 the theoretical mass-radius relation predicted by the Baraffe et al. (1998) models for $M \geq 0.075 M_{\odot}$, and the Chabrier et al. (2000) models for $M < 0.075 M_{\odot}$, both

Table 5.4. Model Parameters for the Eight Transiting Exoplanet Candidates

<i>Kepler</i> ID	M_{kep}	T_0 (BJD-2454900)	P (Days)	$T_{\text{eff},*}$ (K)	i ($^{\circ}$)	R_{*} (R_{\odot})	R_p (R_{\odot})	R_p (R_{Jup})
001571511	13.42	68.529019	14.02065	5804	89.28	1.08	0.14	1.43
003342592	14.92	69.190452	17.17864	5717	89.20	0.93	0.14	1.37
005372966	15.37	67.675070	9.286422	5464	88.91	0.92	0.19	1.87
006756669	15.33	65.860125	5.851827	5353	88.34	0.90	0.16	1.59
006805146	13.21	56.568771	13.77974	6214	89.14	1.41	0.21	2.11
008544996	15.20	65.898818	4.081488	5463	87.61	1.00	0.13	1.27
011974540 ^a	13.22	65.862352	24.67058	6507	89.53	0.69	0.06	0.56
012251650	14.76	71.657743	17.76233	4952	88.97	1.00	0.16	1.64

^aListed in the *Kepler* False Positive Catalog as “velocity measurements indicate eclipsing binary”

for $[M/H] = 0.0$, and an age of 5.0 Gyrs. We have also defined a main-sequence cutoff as 1.5 times the theoretical mass-radius relation, which is illustrated by the solid line in each diagram. In the models we have used an $\alpha = 1.0$ for $M \leq 0.7 M_{\odot}$ and interpolated the radius of the models for $0.7 M_{\odot} < M \leq 1.0 M_{\odot}$ by fixing the radius of the $1.0 M_{\odot}$ model to $1.0 R_{\odot}$, therefore avoiding the dependence of the stellar radius with α between $0.7 M_{\odot}$ and $1.0 M_{\odot}$ (Baraffe et al. 1998). We also include in the mass-radius diagrams estimations of the error in our M and R values at several masses, computed by adding and subtracting 200 K, (the error in the T_{eff} determinations given by the KIC), from a given temperature and interpolating the mass and radius from the theoretical relations. Note that one of the long-period stars, Kepler 008075618, falls well below the main-sequence, with two identical components with $M = 0.91 M_{\odot}$ and $R = 0.53 R_{\odot}$. Inspection of this light curve, coupled with the light curve model, reveals that this system could in fact be a single-lined system at half the listed period.

In the figure, many of the stellar radii of binaries with $P < 1.0$ days appear to fall above the model predictions, but as the orbital period increases, a larger fraction of the systems appear to have radii that are either consistent with or fall below the models. There certainly is a fair amount of scatter in these data introduced by the large error in the mass and radius estimations, but a histogram analysis of the radius distributions confirms these apparent trends. On the right-side panels of Figure 5.7 we show 5% bin-size histograms representing how many stars have a radius that deviates by a given percentage from the models. The average radius discrepancy is 13.0%, 7.5%, and 2.0% for the short ($P < 1.0$ days), medium ($1.0 < P < 10.0$ days), and long-period ($P > 10.0$ days) systems respectively. Although a full analysis of each system with multi-color light and radial-velocity data is still

needed, these preliminary estimates support the hypothesis that binary spin-up is the primary cause of inflated radii in short period LMMS DDEBs.

5.8. Summary

We present 231 new double-eclipse, detached eclipsing binary systems with $T_{\text{eff}} < 5500$ K, found in the Cycle 0 data release of the *Kepler Mission*, and provide their *Kepler* ID, estimated effective temperature, *Kepler* magnitude, magnitude range of the light curve, orbital period, time of primary minimum, inclination, eccentricity, longitude of periastron, sum of the fractional radii, and luminosity ratio. We estimate the masses and radii of the stars in these systems, and find that 95 of them contain two main-sequence stars with both components having $M < 1.0 M_{\odot}$ and eclipse depths of at least 0.1 magnitude, and thus are suitable for ground-based follow-up. Of these 95 systems, 14 have periods less than 1.0 day, 52 have periods between 1.0 and 10.0 days, and 29 have periods greater than 10.0 days. This new sample of low-mass, double-eclipse, detached eclipsing binary candidates more than doubles the number of previously known systems, and extends the sample into the completely heretofore unexplored $P > 10.0$ day period range for LMMS DDEBs.

Comparison to the theoretical mass-radius relation models for stars below $1.0 M_{\odot}$ by Baraffe et al. (1998) show preliminary evidence for better agreement with the models at longer periods, where the rotation rate of the stars is not expected to be spun-up by tidal locking, although, in the absence of radial-velocity measurements, the errors on the estimated mass and radius are still quite large. For systems with $P < 1.0$ days, the average radius discrepancy is 13.0%, whereas

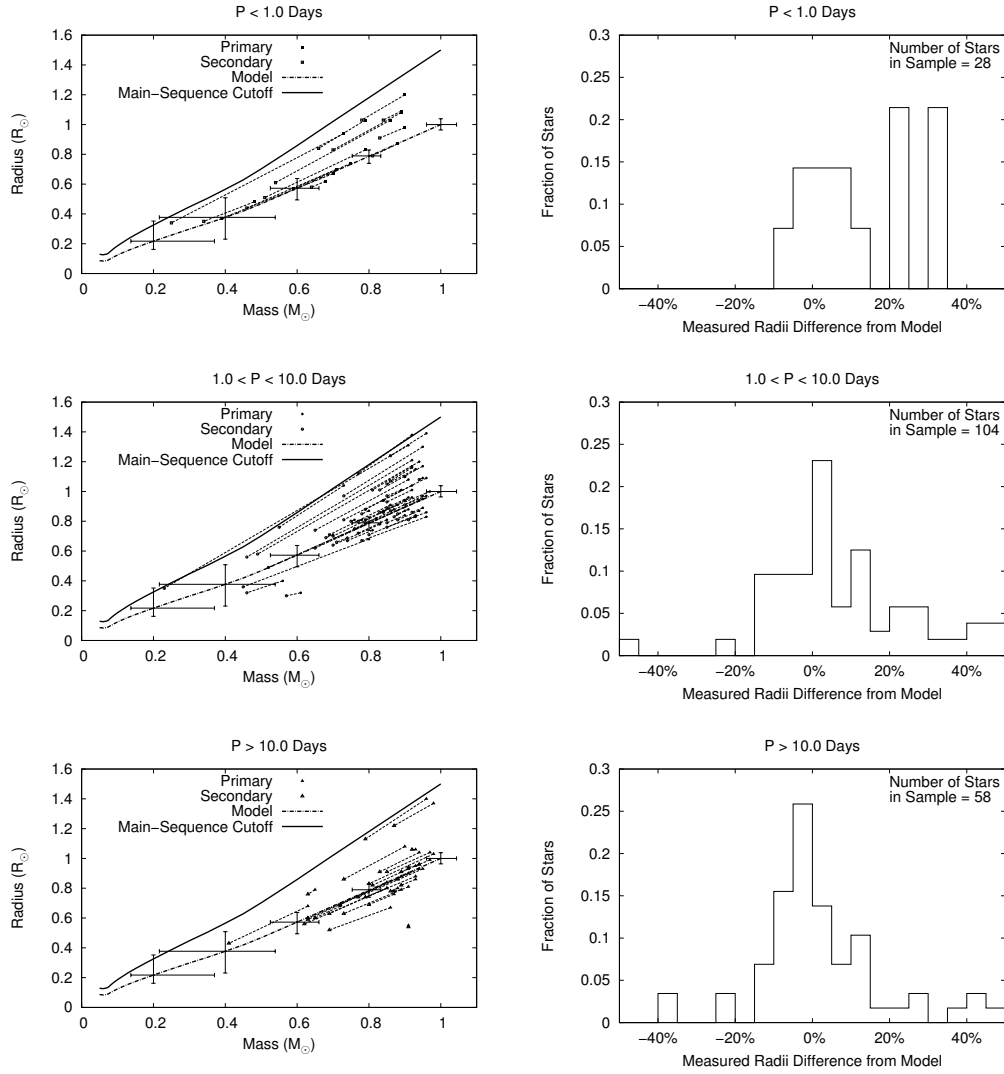


Fig. 5.7.— Left: Mass-radius diagrams for each binary with both components $< 1.0 M_{\odot}$ and photometric amplitudes greater than 0.1 mag, as given in Table 5.3, with systems connected by faint lines. The systems are sorted into short-period ($P < 1.0$ days, top panel), medium-period, ($1.0 < P < 10.0$ days, middle panel), and long-period groupings, ($P > 10.0$ days, bottom panel). The theoretical mass-radius relations of Baraffe et al. (1998) for $0.075 M_{\odot} \leq M \leq 1.0 M_{\odot}$, and of Chabrier et al. (2000) for $M < 0.075 M_{\odot}$, both for $[M/H] = 0.0$ and an age of 5.0 Gyr, are over-plotted. The solid line shows the main-sequence cutoff criterion. The error bars indicate the error in mass and radius obtained when interpolating from the mass-temperature-radius relations with an error of 200K. Right: Histograms of the fraction of stars in the sample versus their deviance from the models for each period grouping. As can be seen by both the mass-radius relation plots and the histograms, shorter period binaries in general appear to exhibit larger radii compared to the models than longer period systems.

for $1.0 < P < 10.0$ days and $P > 10.0$ days, the average radius discrepancy is 7.5% and 2.0%, respectively. Ground-based follow-up, in the form of radial velocity and multi-wavelength light curves, is needed to derive the mass and radius of each star in each system to $\sim 1\text{-}2\%$, which we have already begun to acquire. With accurate masses and radii for multiple long-period systems, we should be able to definitively test the hypothesis that inflated radii in low-mass binaries are principally due to enhanced rotation rates.

We also present eight new transiting planet candidates. Only one of them is currently listed in the *Kepler* False Positive Catalog. The remaining candidates require radial-velocity follow-up to confirm or refute their planetary nature. Even if these systems do not turn out to be planets, they then must be brown dwarf or very low-mass, late-type M dwarfs, which would still be a very valuable find. In fact, all false positive planet candidates determined by the *Kepler* team will be of great interest to stellar astrophysics. We also present seven new extremely shallow eclipsing systems, one well detached binary with deep eclipses, and one apparent red giant with an unusual eclipse-like feature. We also highlight a very unusual eclipsing binary system containing at least one evolved star and an additional transit-like feature in the light curve. Finally, the systems that we determined are not main-sequence, and we therefore did not include in the subsequent analysis, should be further studied for valuable science. Accurate mass, radius, and temperature determinations of those systems could yield valuable insights into stellar and binary evolution.

6. MASS AND RADIUS DETERMINATION OF NEW LONG-PERIOD LOW-MASS ECLIPSING BINARIES

6.1. Introduction

In Chapter 5 we presented the identification of 231 new double-eclipse, detached eclipsing binary systems with $T_{\text{eff}} < 5500$ K, found in the Cycle 0 data release of the *Kepler* Mission, and estimated that 95 of them contained two main-sequence components with eclipses of at least 0.1 magnitudes. Of these, 29 have periods greater than 10 days, and thus provide the opportunity to test whether the large radii, compared to stellar model predictions, historically observed in low-mass eclipsing binaries is principally a result of enhanced rotation rates due to being in short-period systems. Additionally, as part of a *Kepler* Guest Observer program, we found an additional 29.911 day period low-mass eclipsing binary through 90-day monitoring of *Kepler* field stars (Harrison et al. 2012). Although the existing *Kepler* light curves provide excellent constraints on the fractional radii of the components, follow-up spectroscopic observations and radial velocity measurements are needed in order to directly determine the absolute masses and temperatures of each component, as well as the scale of each system.

6.2. Observational Data

6.2.1. Photometric Observations

In sections 4.2 and 5.3 we noted that *Kepler* data can contain discrepant systematics from quarter to quarter, as the spacecraft is rotated 90 degrees and each star lands on a different set of pixels. Consequently, we chose to select only a single quarter of data for each binary system of interest for modeling. For each star, we examined all available public data, which spanned up to Q9 at the time

of analysis, and selected one of the most recently available quarters which showed to have the least amount of systematic noise in the PA and PDC light curves. Given that the PDC pipeline does a comparatively good job compared to our PCA-based analysis (see Section 4.2) for recent quarters of data, we used the PDC data, applying a Bézier curve to the out of eclipse light curve to remove any remaining systematics. We used short-cadence (1 min) when available, but the majority of the systems only had long-cadence (30 minute) data available.

6.2.2. Spectroscopic Observations

For the radial-velocity observations, longslit spectra were obtained at both the Apache Point Observatory 3.5-meter telescope via the Dual Imaging Spectrograph (DIS), and the Kitt Peak National Observatory (KPNO) 4-meter via the R-C Spectrograph. Typically for short-period eclipsing binaries with $P < 1$ day, a single night is sufficient to obtain a good radial-velocity curve, assuming that the system is bright. If the system is fainter, one has to make sure that the individual exposure times are not so long that orbital smearing occurs, where the binary moves a significant fraction of its orbit during the exposure. For long-period systems, orbital smearing is not a concern, but it can take weeks of observing to cover an entire orbit. Thus, we decided to employ the strategy of obtaining single radial velocity observations of as many systems as possible in a given night, spreading the observing nights over several months. From our initial list, we observed the brightest stars first, thus allowing us to maximize the number of systems observed.

The observations were carried out over two observing seasons; the first from

June - December 2010, and the second from May - September 2011. The DIS spectrograph is able to simultaneously obtain spectra in both blue ($\sim 4400 \text{ \AA}$) and red ($\sim 7500 \text{ \AA}$) channels, but since the majority of the flux of low-mass stars is emitted in the red channel, the blue channel was discarded and only the red channel utilized. The R1200 grating was employed resulting in a resolution of 0.58 \AA per pixel, or $R \approx 10,000$. The wavelength range was set to $\sim 5900 - 7100 \text{ \AA}$ for the first observing season, and $\sim 5700 - 6800 \text{ \AA}$ for the second observing season. For the R-C Spectrograph, the KPC-24 grating was used in second order, resulting in a resolution of 0.53 \AA per pixel, or $R \approx 10,000$, with the wavelength range set to $\sim 5700 - 6750 \text{ \AA}$. In total, 615 individual stellar spectra were taken.

All raw frames were bias, dark, and flat-field corrected. For the DIS observations, column 1023 is a dead column, and thus those values were replaced via linear interpolation from the two neighboring columns. Due to the long exposure times ($\gtrsim 5$ minutes) for many systems, there were a significant amount of cosmic rays on the detector for most frames. For all frames, a Laplacian edge algorithm was used to detect and replace cosmic rays via the *lacos_spec* IRAF package, (see van Dokkum (2001)). This routine was thoroughly examined and observed to be robust in only removing cosmic rays, and not altering any real spectral features. We used the *apall* package in IRAF to extract one-dimensional spectra for each image, tracing the apertures to account for curvature on the chip, and subtracting off the night sky background from the science images.

We used lamps containing Helium, Neon, and Argon gas (HeNeAr) in order to produce wavelength calibration frames. For the first observing season of DIS data, one wavelength calibration frame was taken at the start of each night, but for all subsequent DIS observations and all KPNO observations one HeNeAr image

was taken directly before or after each science exposure. After identifying the ~ 20 strong HeNeAr spectral features in each calibration frame, we used a 4th order Legendre polynomial to map the wavelength solution to the pixel values, typically obtaining a dispersion solution with error $\lesssim 0.025 \text{ \AA}$. We then applied that solution to the respective science frames to transform them to wavelength space. As we typically had sufficiently long exposure times so as to measure the position of the 6300.3086 \AA OI(D) terrestrial night glow emission line in the sky spectrum, we used this line to correct for any systematic shifts that might have occurred between the science and wavelength calibration frames. We also note that we disabled rotation when using the DIS instrument to minimize any spurious flexure due to rotation on the 3.5 meter Alt-Az telescope.

After wavelength calibration, all science spectra were flattened, (i.e., we normalized each spectrum by its continuum value at each wavelength), by fitting a 20-piece cubic spline fit over 10 iterations, during which points 3σ above the fit or 1.5σ below the fit were rejected. For each spectrum, the BJD(TT), (the Barycentric Julian Date in Terrestrial Time), was calculated and used for all future time keeping. In order to compensate for the velocity of Earth, the IRAF task *bvcorr* was used to correct all observations to the reference frame of the solar system barycenter.

In the end, sufficient data for a radial-velocity curve analysis was collected for 11 systems: Kepler 003102024, Kepler 004352168, Kepler 004773155, Kepler 006029130, Kepler 006131659, Kepler 006431670, Kepler 007846730, Kepler 008296467, Kepler 009284741, Kepler 010753734, and Kepler 010992733.

6.3. Radial-Velocity Measurement

Traditionally in binary star work, cross-correlation is used to extract the radial velocities of each component from the observed spectrum. In this technique, the observed spectrum and a reference spectrum are each re-binned to the same linear wavelength scale. The correlation value, (i.e., the sum of the products of the spectrum's and reference's flux values at each wavelength), is computed for all possible pixel shifts, and the maximum correlation value corresponds to the most likely value for the pixel shift, or velocity, of the observed spectrum. When two spectra are visible in the observed spectrum, as is typically the case for binary stars, one observes a double-peaked correlation value, with each peak corresponding to a component of each binary. Using only one reference spectrum in this manner has the significant drawbacks of it tends to underestimate the velocity of each component due to line blending, and often does not reveal the velocities of the secondary component if it is significantly fainter than the primary, or the two stars have similar velocities in a given spectrum.

Thus, Zucker & Mazeh (1994) developed TODCOR, a two-dimensional cross-correlation technique for finding the radial velocities of binary stars. TODCOR performs the cross-correlation with two reference spectra simultaneously, finding the values for the velocity of each reference spectrum, and their relative luminosity ratio, α , that results in the highest correlation value. Although this is a significant advantage over one-dimensional cross-correlation, there still exists the drawback that the observed spectrum needs to be re-binned to a linear wavelength scale. This can result in the distortion of spectral lines and thus result in a degradation of accuracy when extracting the component's velocities. Furthermore, it is difficult

to assess the formal error of the observations using the correlation value as a goodness-of-fit parameter, and the need for a constant linear wavelength scale can hamper robust error determination methods such as Monte Carlo or Bootstrapping simulations.

Thus, we present here a new method we invented to extract radial velocity values from double-lined spectra. Instead of using cross-correlation, we directly fit reference spectra to each observed spectrum via a traditional standard deviation minimization, which is equivalent to minimizing χ^2 assuming all observed points have equal errors. Specifically, for each observed spectrum, we fit for the velocity of each reference spectra as well as α , for a total of 3 free parameters. During the fitting, the original observed spectrum is never changed, and thus the original spectrum can have any arbitrary number and distribution of wavelength and flux value pairs. Given a total of M observed spectra, each with N_j points, taken at times t_j , we want to find the values of $V_{1,j}$, $V_{2,j}$, and α , i.e., the velocities of reference spectra 1 and 2 at each t_j and the relative luminosity of the reference spectra, that minimizes the function

$$\sum_{j=0}^M \sum_{i=0}^{N_j} \left(F_{0,i} - \frac{\alpha \cdot F_1 \left(\lambda_{0,i} \cdot \left(1 - \frac{V_{1,j}}{c} \right) \right) + F_2 \left(\lambda_{0,i} \cdot \left(1 - \frac{V_{2,j}}{c} \right) \right)}{\alpha + 1} \right)^2 \quad (6.1)$$

where $F_{0,i}$ is the flux of an observed spectrum at given wavelength, $\lambda_{0,i}$, $F_1(\lambda)$ and $F_2(\lambda)$ are the fluxes of reference stars 1 and 2 at a given wavelength, and c is the speed of light. In order to determine $F_1(\lambda)$ and $F_2(\lambda)$, cubic spline interpolation is used on the original reference spectra.

For reference spectra, we employ the normalized (flattened) synthetic spectra

of Munari et al. (2005), which ensures that no spurious signals are found that correspond to telluric features. The Munari et al. (2005) grid we employ covers models with $3500 \geq T_{\text{eff}} \geq 10,000$ at steps of 250 K, $0.0 \geq \log g \geq 5.0$ at steps of 0.5 dex, $-2.5 \geq [\text{M}/\text{H}] \geq 0.5$ at steps of 0.5 dex, and $0 \geq V_{\text{rot}} \geq 100$ km/s in steps of 10 km/s. We fix the value of α to the value of the luminosity ratio found via the light curve modeling, as the wavelength range of the spectra closely matches the *Kepler* bandpass. Additionally we require that the ratio of blackbodies with temperatures T_1 and T_2 , the temperatures of reference spectra 1 and 2, when integrated over the *Kepler* bandpass, match the observed surface brightness ratio from the light curve. In order to ensure we find the global minimum in both selected reference spectra and their velocities, we perform a global grid search looping over all possible combinations of $V_{1,j}$, $V_{2,j}$, T_1 , (with T_2 set as just mentioned), a common $[\text{M}/\text{H}]$ for both reference spectra, $\log g$ for each reference spectrum, and V_{rot} for each reference star.

To determine robust errors on the derived radial velocities, we employ a Bootstrapping re-sampling method. In Bootstrapping, the original data, which in this case is each observed spectrum, is re-sampled with replacement N times, where N is the number of data points in the original dataset, to create a new dataset. This new dataset is re-fit and new values on the parameters of interest, (in this case the reference velocities), are computed and recorded. The process is repeated a large number of times, which we choose to be 10,000, and thus a median and 1σ confidence interval is able to be computed on the resulting distribution. Bootstrapping is advantageous in this case because it does not require any error estimates on the individual data points, (which are difficult to compute for spectroscopic measurements), and it draws on the inherent distribution of the original dataset without

any assumptions.

To estimate errors on the derived temperature of the components, we utilize the spectroscopic quality-of-fit parameter (López-Morales & Bonanos 2008; Behr 2003), defined as

$$z = \sqrt{N} \left(\frac{rms^2}{rms_{min}^2} - 1 \right) \quad (6.2)$$

where N is the number of data points, rms^2 is the standard deviation of the fit under consideration, and rms_{min}^2 is the best fit found. The z parameter is similar to a reduced χ^2 in the absence of known errors on the individual points. By definition $z = 0$ at the best-fit, and where $z = 1$ represents the 1σ confidence interval. Starting from the best-fit value of T_1 , we compute the rms^2 value for neighboring values of T_1 via Eq. 6.1, which results in a smoothly varying parabolic-like curve of z versus T_1 . Fitting a parabola to these measurements, we find the value of T_1 that minimizes z , i.e., the best fit value, and the confidence interval where $z < 1$, i.e., the resulting 1σ confidence interval. We compute a value of T_2 via the value of the surface brightness ratio from the light curve, as described above, propagating the errors on T_1 and the surface brightness ratio to obtain the error on T_2 .

6.4. Modeling

6.4.1. Light Curve Modeling

We use the JKTEBOP code (Southworth et al. 2004a,b) to model each light curve. As the systems under investigation are well-detached systems, we assume they are perfect spheres and not tidally distorted. As they are all late-type stars,

we assume a linear limb-darkening law, (see Section 7.1), and simultaneously solved for the period, time of primary minimum, inclination, $e \cdot \cos(\omega)$, $e \cdot \sin(\omega)$, surface brightness ratio, sum of the fractional radii, ratio of the radii, out of eclipse flux, and linear limb-darkening coefficient of each star, designated c_p and c_s for the primary and secondary star respectively. We set gravity darkening coefficients for each star based on their estimated T_{eff} via interpolation from stellar models as prescribed by Claret (2000b), although we note that this has extremely minimal impact on the resulting light curves due to the wide separation of the components. For the long cadence data, we instructed the JKTEBOP program to perform 10 sub-integrations over the 29.43 minute integration time to account for photometric smearing (Kipping 2010a). The light curves for each system, along with the best-fit model, are shown in Figures 6.1 - 6.11.

To determine robust errors, we first scaled the error bars so that the best fit had a reduced $\chi^2 = 1$, as sometimes there were remaining systematics in the light curve, and we did not want to consequently underestimate errors by ignoring this source of noise. We then performed 10,000 Monte Carlo simulations where new datasets were created by adding noise to the original light curves via each point's individual error bars. At each iteration the original best-fit parameters were significantly perturbed, and the resulting light curve re-fit via a Levenberg-Marquardt minimization algorithm. The posterior distributions on all the parameters were then used to compute the median and 1σ confidence intervals for all parameters. We list these values for each system in Table 6.1.

Table 6.1. Modeling Results of the Long-Period Low-Mass Binary Light Curves

<i>Kepler</i> ID	<i>P</i> (Days)	r_{sum}	<i>k</i>	<i>J</i>	<i>i</i> ($^{\circ}$)	e^a	ω^a ($^{\circ}$)	c_p	c_s
003102024	13.782617	0.05433±0.00014	0.769±0.007	0.414±0.003	88.876±0.010	0.5709±0.0005	298.74±0.04	0.492±0.014	0.523±0.048
004352168	10.643735	0.06872±0.00007	0.689±0.002	0.328±0.007	89.516±0.006	0.2146±0.0014	224.01±0.41	0.493±0.031	0.741±0.042
004773155	25.706040	0.04272±0.00001	0.902±0.003	0.833±0.008	89.819±0.003	0.4428±0.0009	306.56±0.11	0.674±0.016	0.750±0.020
006029130	12.591616	0.06251±0.00013	1.023±0.018	0.798±0.016	88.731±0.007	0.0156±0.0014	44.92±5.26	0.535±0.036	0.395±0.042
006131659	17.527835	0.04555±0.00009	0.676±0.005	0.281±0.002	89.161±0.011	0.0147±0.0005	270.28±0.01	0.654±0.010	0.314±0.024
006431670	29.911422	0.03628±0.00006	1.091±0.025	1.185±0.052	89.519±0.004	0.3336±0.0008	172.91±1.21	0.675±0.071	1.193±0.057
007846730	11.028234	0.09533±0.00002	0.562±0.000	0.714±0.002	89.482±0.005	0.0462±0.0002	244.38±0.14	0.458±0.003	0.591±0.008
008296467	10.303360	0.06916±0.00003	0.982±0.007	0.774±0.013	89.772±0.010	0.2540±0.0017	320.43±0.48	0.594±0.035	1.160±0.025
009284741	20.729249	0.04113±0.00004	1.027±0.009	1.208±0.018	89.416±0.003	0.3722±0.0011	42.57±0.21	0.498±0.022	0.660±0.030
010753734	19.406540	0.05156±0.00004	0.850±0.002	0.781±0.010	89.784±0.016	0.5200±0.0003	18.00±0.16	0.647±0.029	0.557±0.020
010992733	18.526059	0.05500±0.00008	0.779±0.005	0.696±0.018	89.935±0.060	0.3808±0.0012	25.30±0.47	0.688±0.055	0.726±0.040

6.4.2. Radial Velocity Curve Modeling

In order to model the observed radial velocities of each system, we employ the standard analytical expressions for the radial velocities of two stars in a classic Newtonian orbit (Paddock 1913). The velocities of each star are described by the equations

$$V_1 = V_0 + K_1 \cdot (\cos(\omega + \theta(t)) + e \cos \omega) \quad (6.3)$$

$$V_2 = V_0 - K_2 \cdot (\cos(\omega + \theta(t)) + e \cos \omega) \quad (6.4)$$

where V_1 and V_2 are the velocities of stars 1 and 2 respectively, V_0 is the velocity of the system's center of mass with respect to the solar system barycenter, K_1 and K_2 are the semi-major velocity amplitudes of stars 1 and 2 respectively, e is the eccentricity of the system, ω is the longitude of periastron of the system, and $\theta(t)$ is the true anomaly of the system at a given time, t . The true anomaly is related to the orbital phase of the binary, $\phi(t)$, by the following equations

$$\tan\left(\frac{\theta(t)}{2}\right) = \frac{\sqrt{1+e}}{\sqrt{1-e}} \cdot \tan\left(\frac{E}{2}\right) \quad (6.5)$$

$$2\pi\phi(t) = E - e \sin E \quad (6.6)$$

where E is referred to as the eccentric anomaly. We note that Equation 6.6 is a transcendental equation, and thus $\theta(t)$ must be solved numerically for each $\phi(t)$.

We fit each radial-velocity curve by first fixing the period, time of primary minimum, eccentricity, and longitude of periastron of the system to the values

derived from the light curve analysis, as those quantities are extremely well-defined by the light curve alone. We then solve for K_1 , K_2 , and V_0 via standard χ^2 minimization. Plots of the radial velocity curves and best-fit models are shown in Figures 6.1 - 6.11.

Once the values of K_1 and K_2 are obtained from the radial-velocity curves, we can calculate the mass and radius of each star via the following equations

$$a = \frac{P \cdot (K_1 + K_2) \cdot \sqrt{1 - e^2}}{2\pi \sin i} \quad (6.7)$$

$$M_{tot} = \frac{4\pi^2 a^3}{GP^2} \quad (6.8)$$

$$q = \frac{K_1}{K_2} \quad (6.9)$$

$$M_1 = \frac{M_{tot}}{1 + q} \quad (6.10)$$

$$M_2 = \frac{q \cdot M_{tot}}{1 + q} \quad (6.11)$$

$$R_1 = r_1 \cdot a \quad (6.12)$$

$$R_2 = r_2 \cdot a \quad (6.13)$$

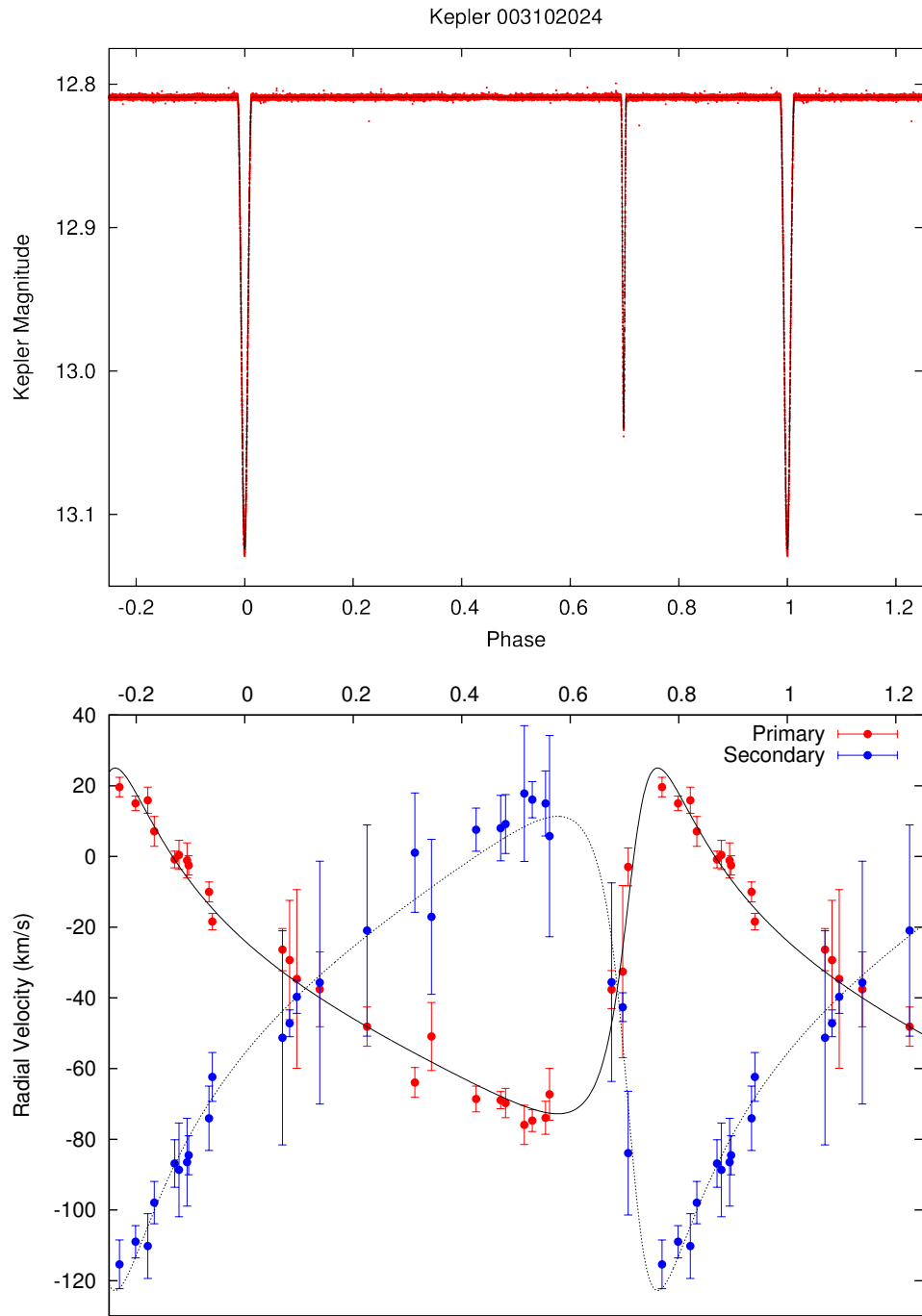


Fig. 6.1.— *Kepler* light curve (top panel) and ground-based radial velocity curves (bottom panel) as a function of orbital phase for Kepler 003102024. The best-fit models are shown via black lines.

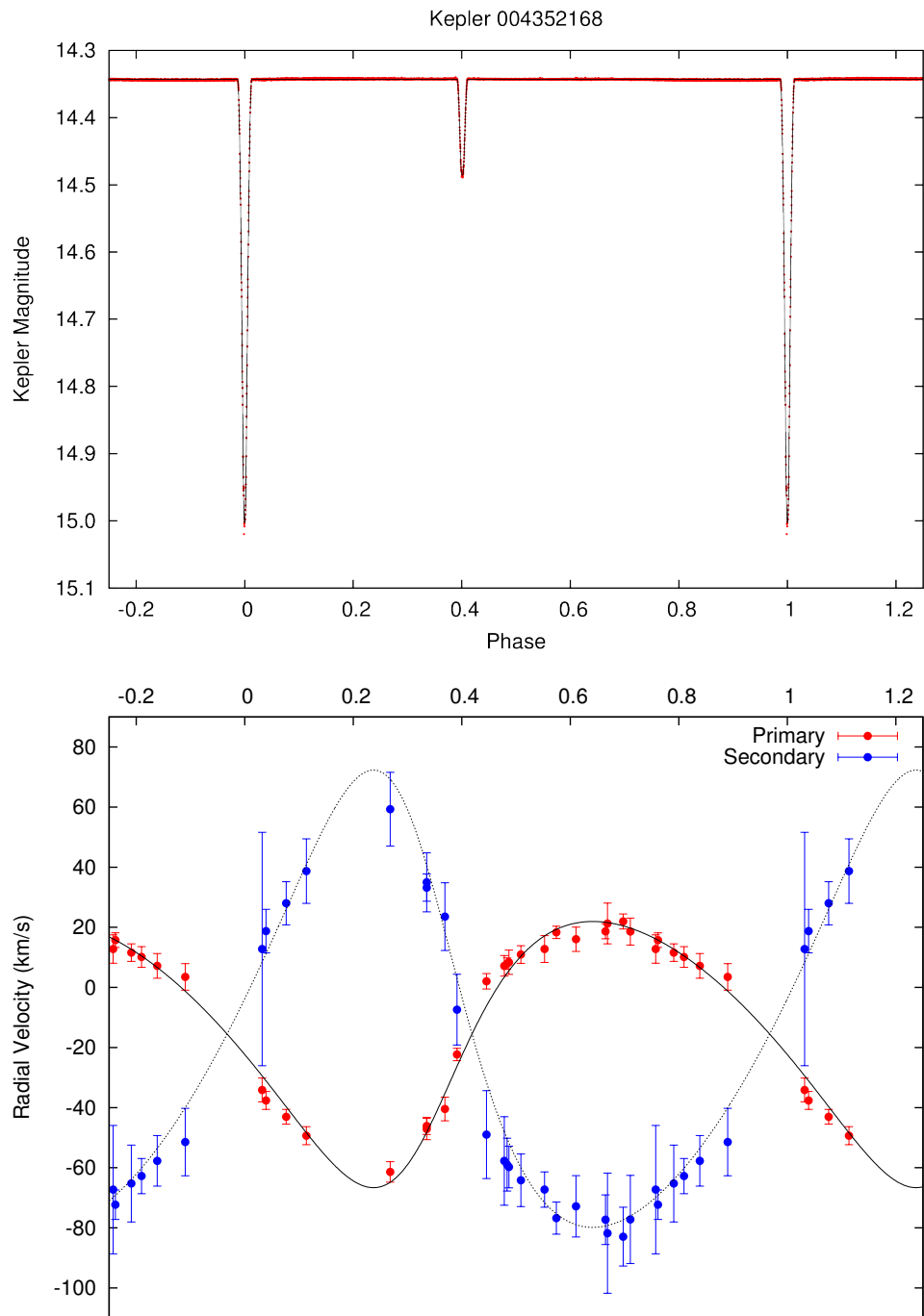


Fig. 6.2.— *Kepler* light curve (top panel) and ground-based radial velocity curves (bottom panel) as a function of orbital phase for Kepler 004352168. The best-fit models are shown via black lines.

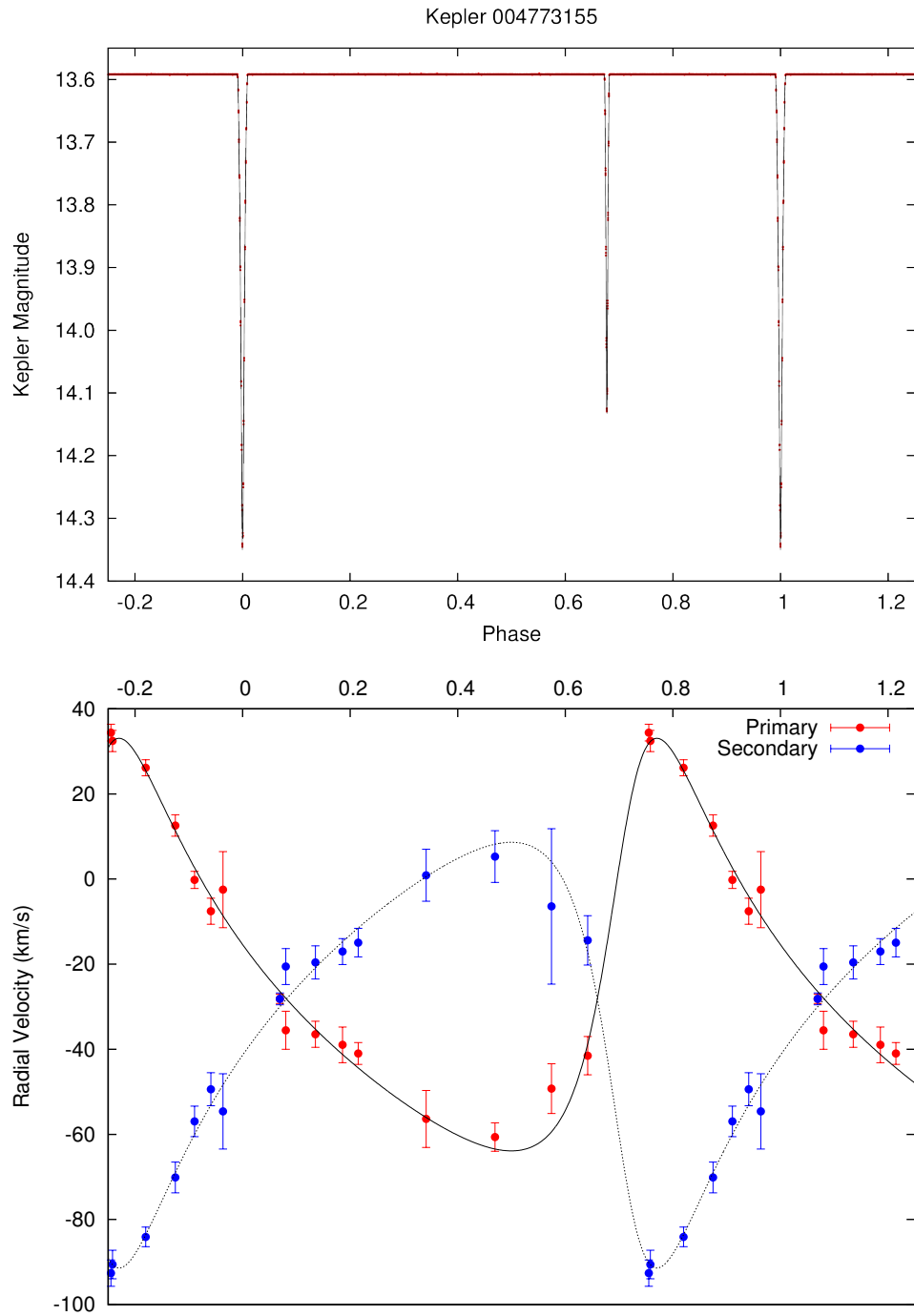


Fig. 6.3.— *Kepler* light curve (top panel) and ground-based radial velocity curves (bottom panel) as a function of orbital phase for Kepler 004773155. The best-fit models are shown via black lines.

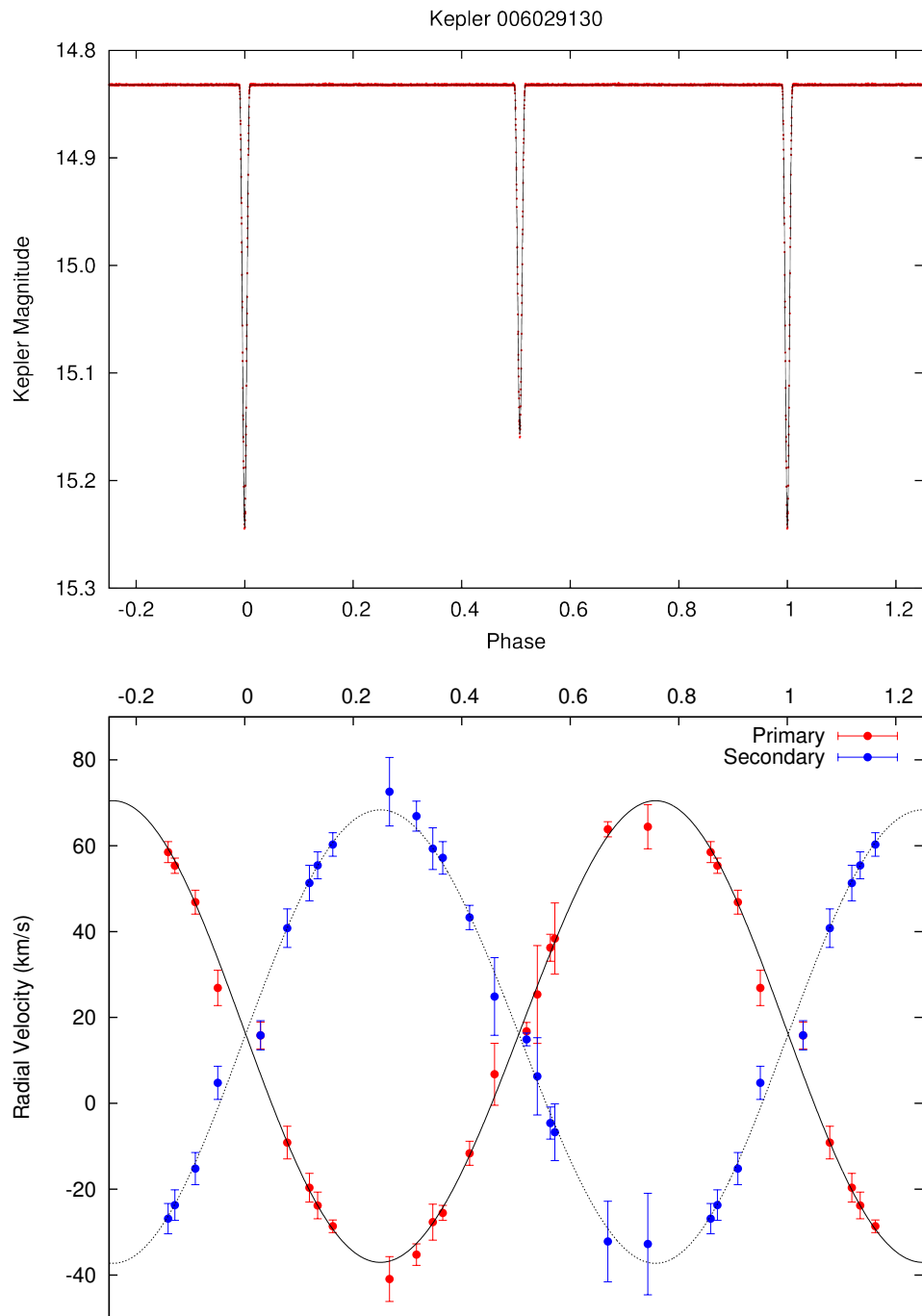


Fig. 6.4.— *Kepler* light curve (top panel) and ground-based radial velocity curves (bottom panel) as a function of orbital phase for Kepler 006029130. The best-fit models are shown via black lines.

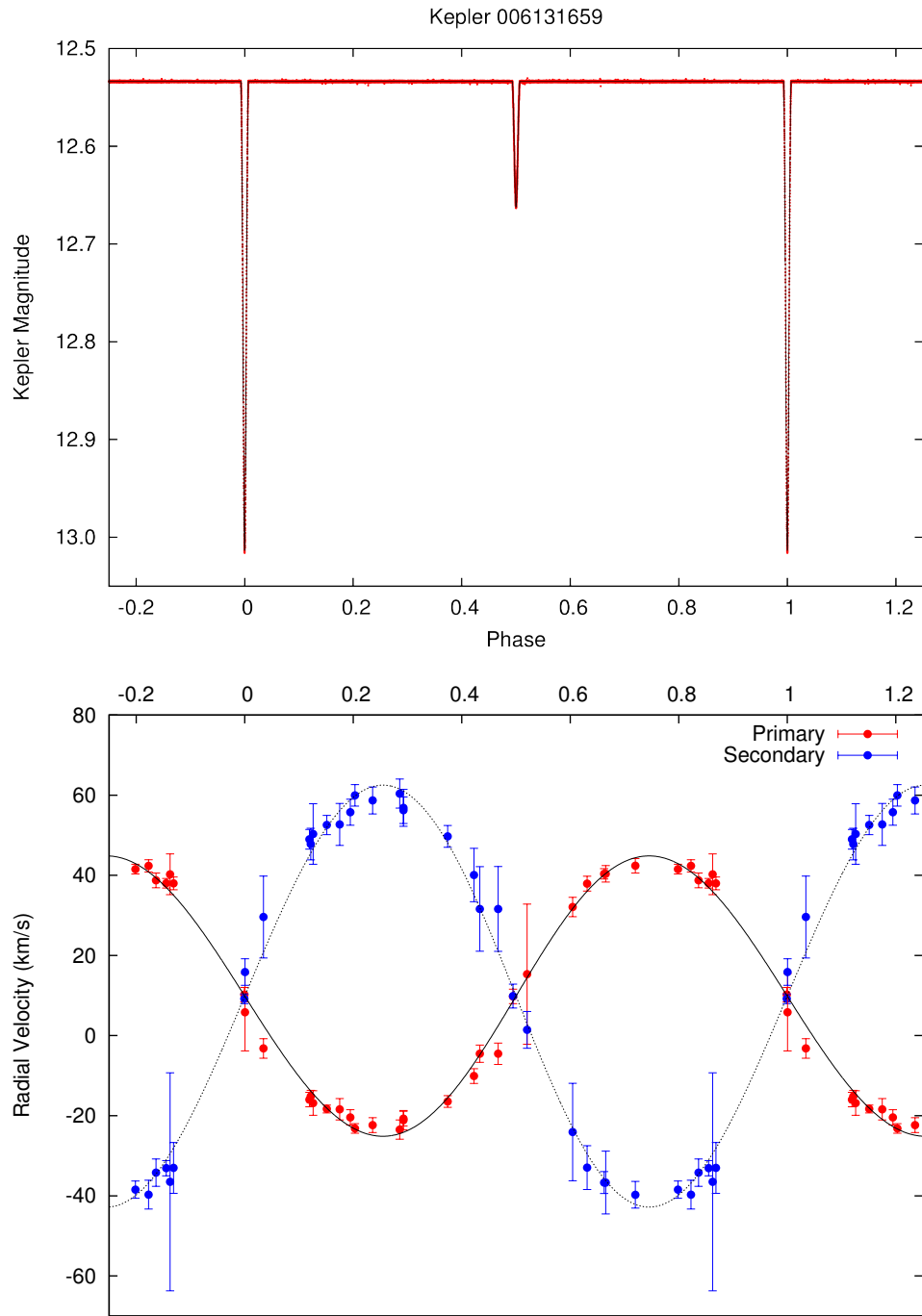


Fig. 6.5.— *Kepler* light curve (top panel) and ground-based radial velocity curves (bottom panel) as a function of orbital phase for Kepler 006131659. The best-fit models are shown via black lines.

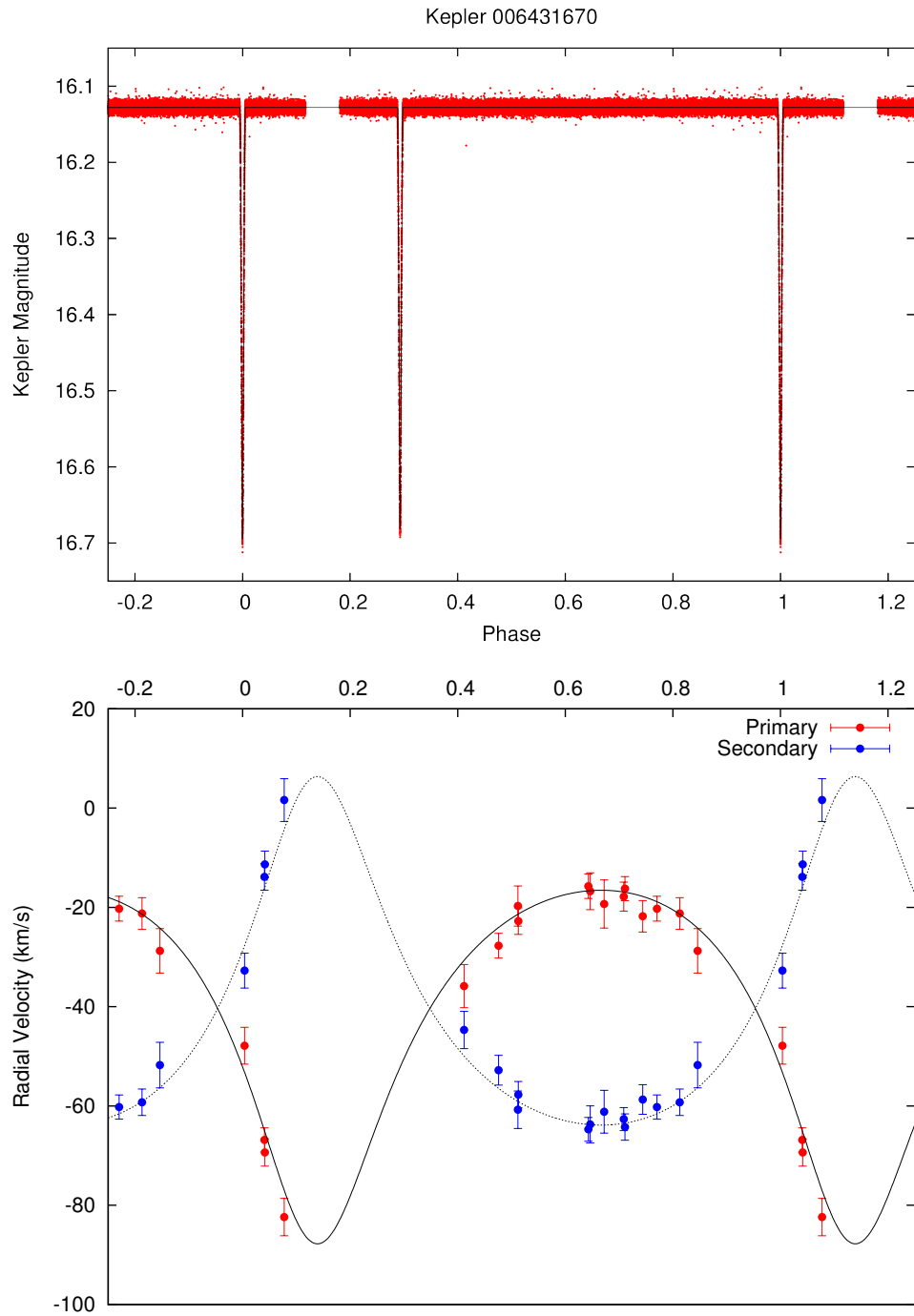


Fig. 6.6.— *Kepler* light curve (top panel) and ground-based radial velocity curves (bottom panel) as a function of orbital phase for Kepler 006431670. The best-fit models are shown via black lines.

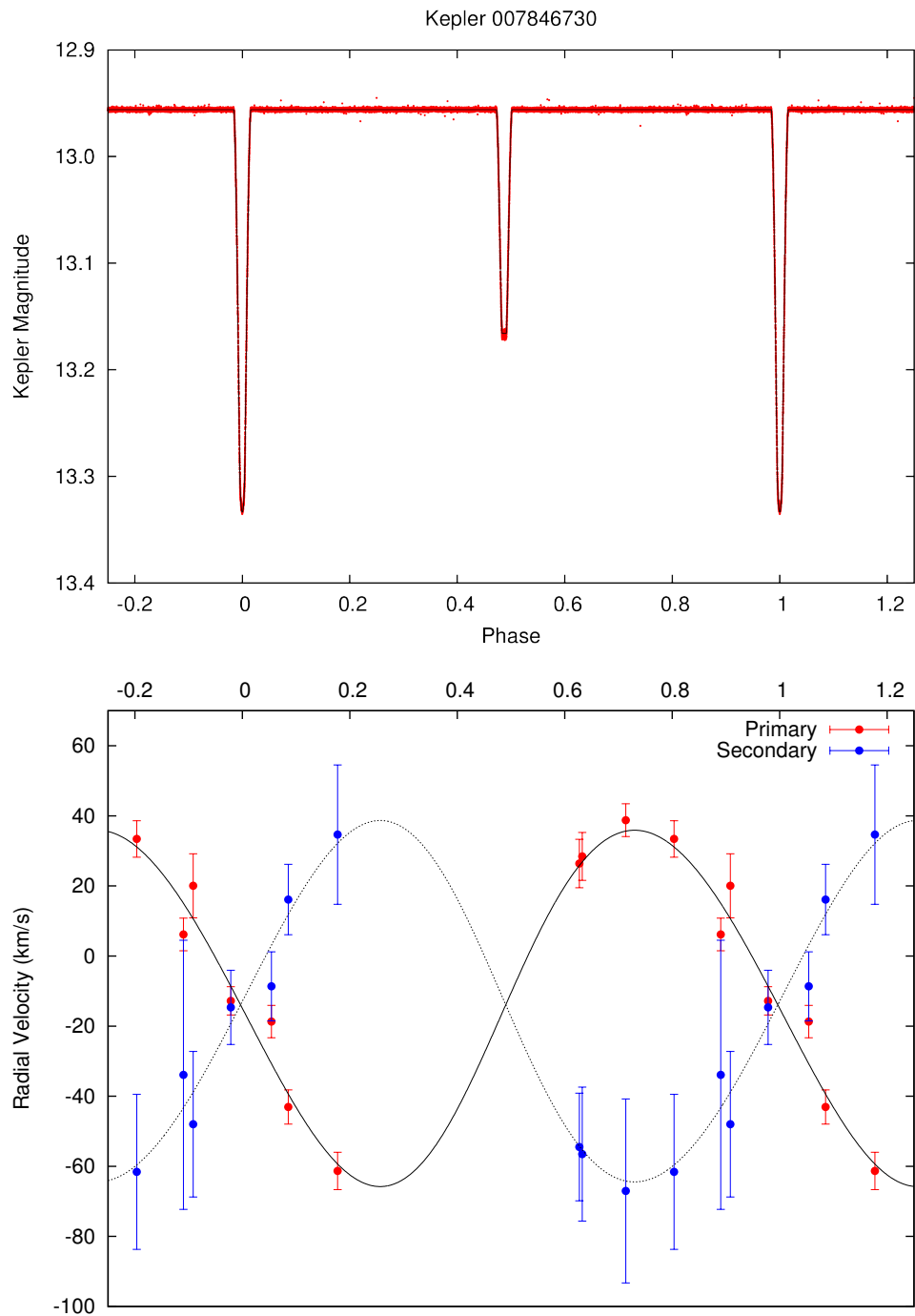


Fig. 6.7.— *Kepler* light curve (top panel) and ground-based radial velocity curves (bottom panel) as a function of orbital phase for Kepler 007846730. The best-fit models are shown via black lines.

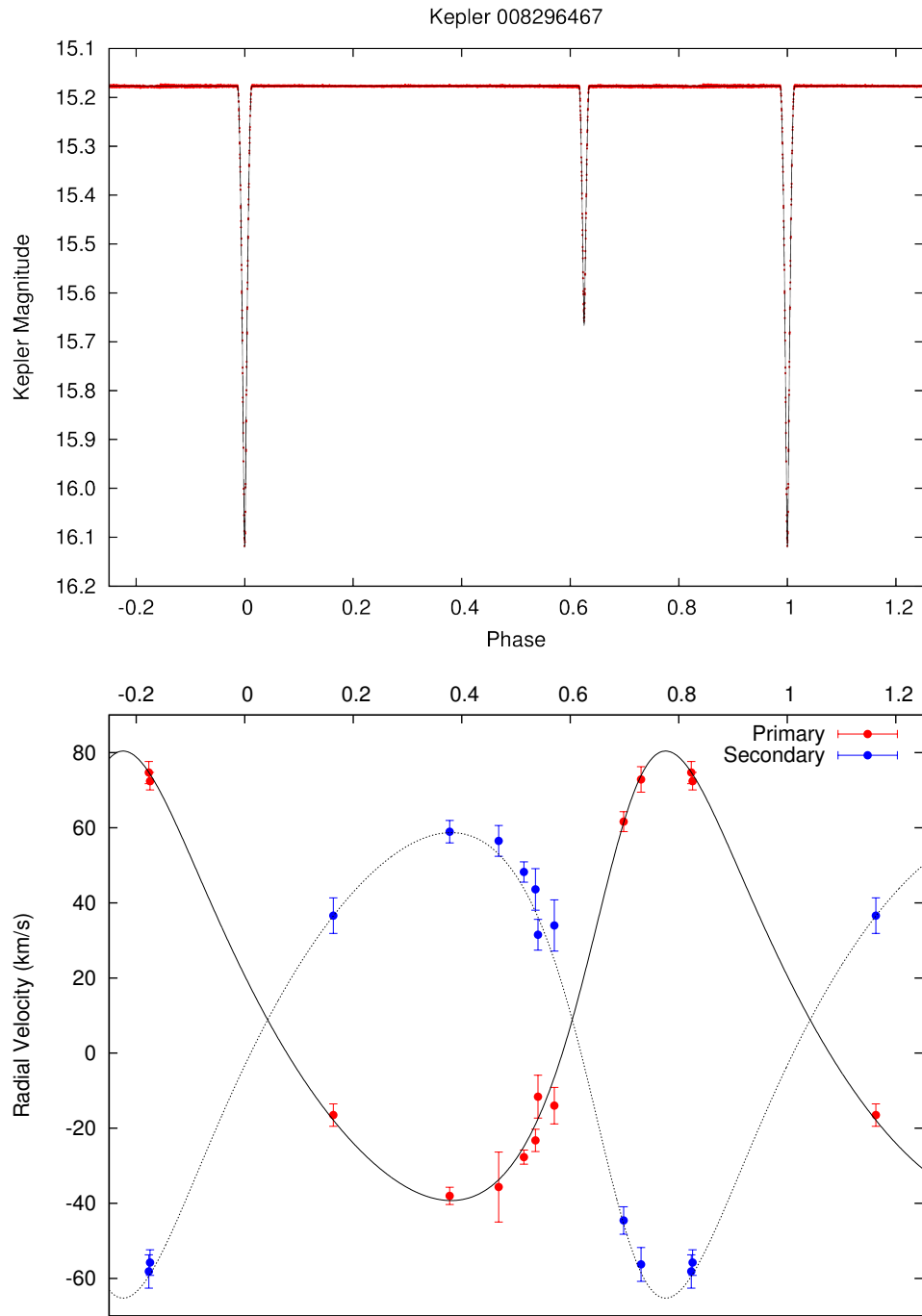


Fig. 6.8.— *Kepler* light curve (top panel) and ground-based radial velocity curves (bottom panel) as a function of orbital phase for Kepler 008296467. The best-fit models are shown via black lines.

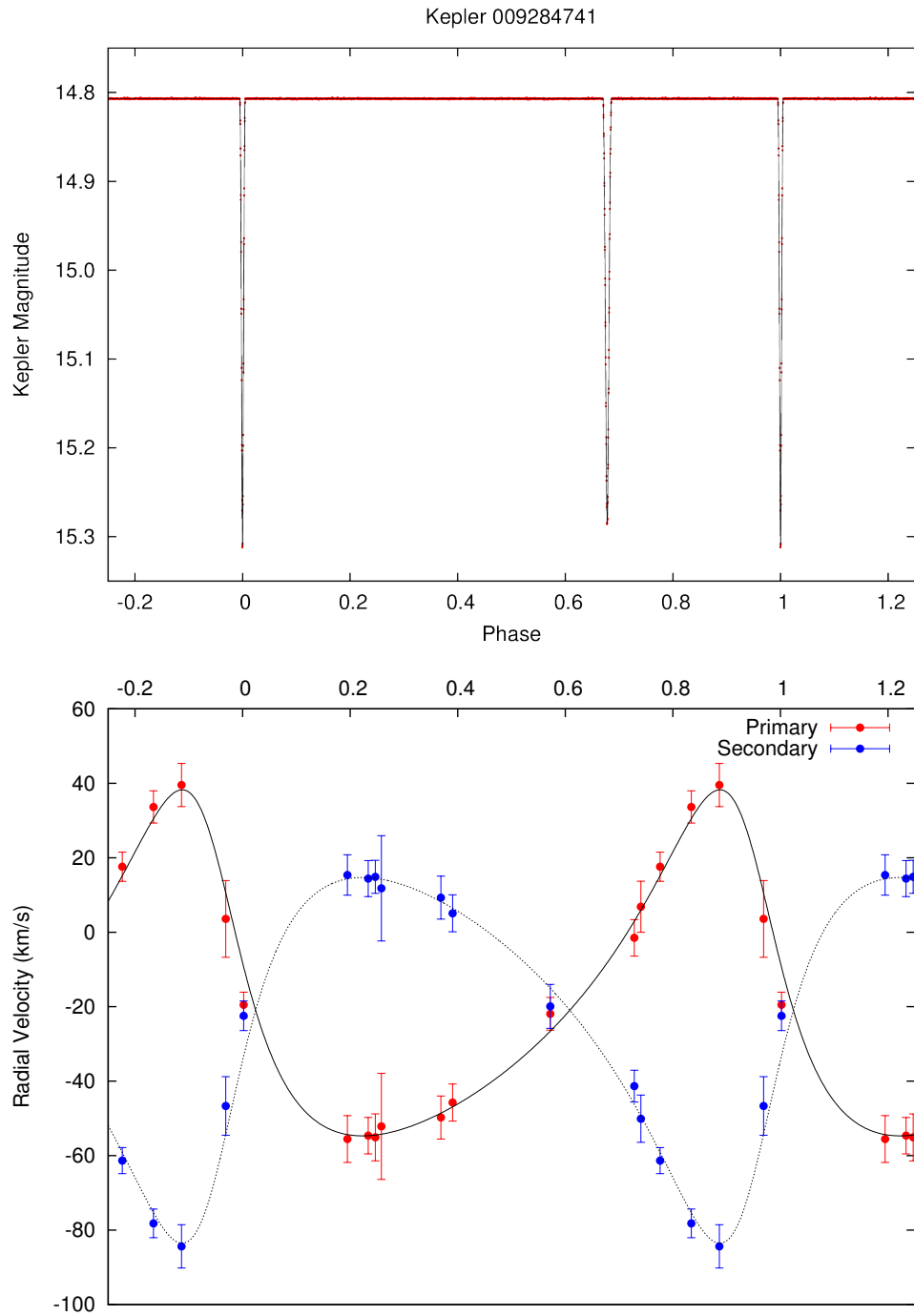


Fig. 6.9.— *Kepler* light curve (top panel) and ground-based radial velocity curves (bottom panel) as a function of orbital phase for Kepler 009284741. The best-fit models are shown via black lines.

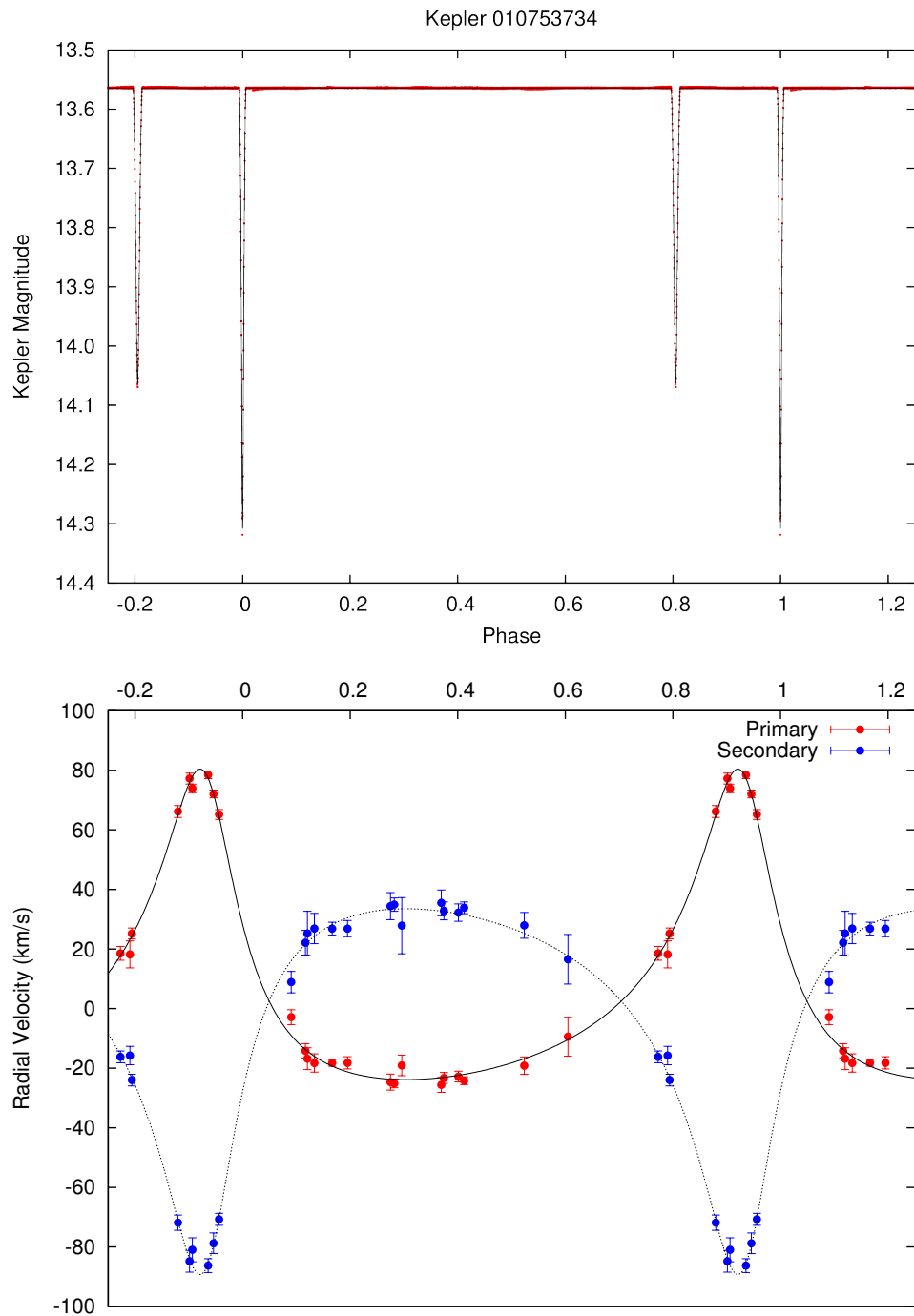


Fig. 6.10.— *Kepler* light curve (top panel) and ground-based radial velocity curves (bottom panel) as a function of orbital phase for Kepler 010753734. The best-fit models are shown via black lines.

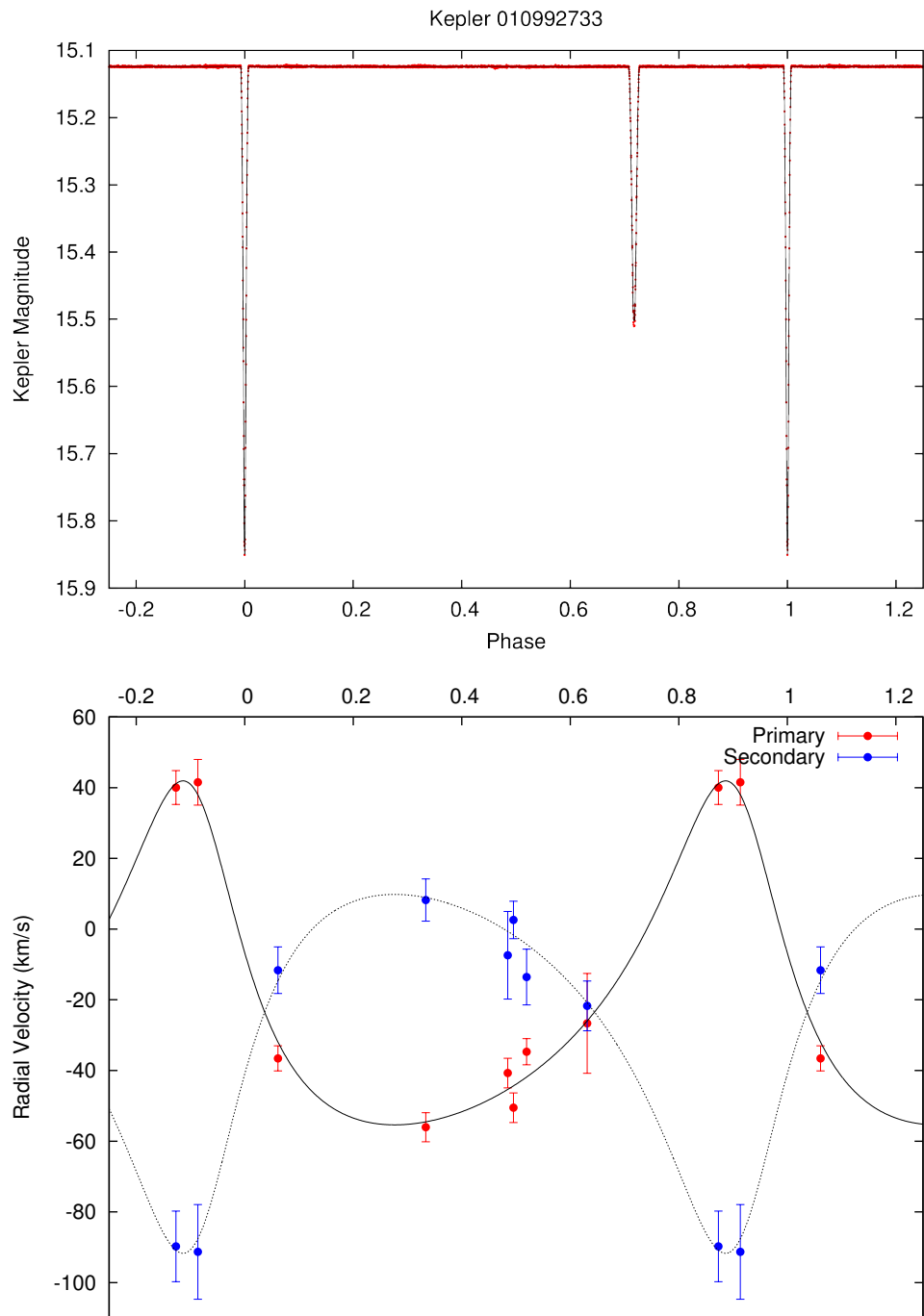


Fig. 6.11.— *Kepler* light curve (top panel) and ground-based radial velocity curves (bottom panel) as a function of orbital phase for Kepler 010992733. The best-fit models are shown via black lines.

where P is the period of the system, i is the inclination of the binary, a is the semi-major axis of the system, G is the gravitational constant, q is the mass ratio of the system, and M_1 , M_2 , R_1 , R_2 , r_1 , and r_2 are the physical masses and radii, and fractional radii, of stars 1 and 2 respectively. We again note that P , i , r_1 , and r_2 are derived from the light-curve analysis.

To determine robust errors, we first scaled the error bars of the radial-velocity measurements so that the best fit had a reduced $\chi^2 = 1$, as sometimes there were remaining systematics in the radial velocity curves, and we did not want to consequently underestimate errors by ignoring this source of noise. We then performed 10,000 Monte Carlo simulations where new datasets were created by adding noise to the original radial-velocity curves via each point's individual error bars. At each iteration the resulting radial velocity curve was re-fit for the values of K_1 , K_2 , and V_0 , while the values of P , T_0 , i , e , ω , r_1 , and r_2 were simultaneously perturbed via the errors determined from the light curve modeling, and the resulting quantities of M_1 , M_2 , R_1 , and R_2 computed. The posterior distributions on all the parameters were then used to compute the median and 1σ confidence intervals for all parameters. We list these values for each system in Table 6.2.

6.5. Discussion

In Figure 6.12 we plot the mass and radius values of each star of the 11 long-period low-mass eclipsing binaries we modeled, for a total of 22 individual stars. We also plot the canonical theoretical mass-radius relation of Baraffe et al. (1998) given $[M/H] = 0.0$ and an age of both 1.0 and 5.0 Gyr, and the more recent theoretical relation of Feiden & Chaboyer (2012) at 5.0 Gyr, which utilizes

the Dartmouth Stellar Evolution Program and tends to predict larger radii at $0.2 \lesssim M \lesssim 0.65 M_{\odot}$ and smaller radii at $0.65 \lesssim M \lesssim 1.0 M_{\odot}$ compared to Baraffe et al. (1998). Furthermore, we plot previously measured low-mass eclipsing binaries from the studies of López-Morales (2007), Blake et al. (2008), Irwin et al. (2009), Carter et al. (2011), and Kraus et al. (2011). Finally, we also plot recent measurements of single low-mass field stars via interferometry by Boyajian et al. (2012), whose direct measurements are physical size and temperature, but where masses have been inferred from mass-luminosity relations with resulting errors in mass of $\sim 10\%$ (not plotted for clarity).

Before delving into the analysis, we note that two systems stand out as particularly peculiar: Kepler 006431670 and 007846730. Kepler 006431670 is composed of two stars with values of $(M, R, T) = (0.455 M_{\odot}, 0.684 R_{\odot}, 5012 \text{ K})$ and $(0.462 M_{\odot}, 0.746 R_{\odot}, 5198 \text{ K})$, which are extremely large and hot for their determined masses. Unless there was some systematic error in the radial-velocity measurements of this system, (which is not immediately obvious from Figure 6.6), the only explanation is that this is a pre-main-sequence binary, as the components would not have had enough time to significantly evolve given the age of the universe. The derived masses and radii are fit well by the Baraffe et al. (1998) models at an age of 20 Myr, however there is no sign of H_{α} emission in the spectra, and the temperature should be cooler than observed. A search for excess X-ray, UV, or infrared emission from this system did not turn up any obvious results, however as the system is very faint with $m_{\text{kep}} = 16.13$ and $m_K = 14.19$ such detections may prove difficult with currently available survey data. The components of Kepler 007846730 are $(M, R, T) = (0.614 M_{\odot}, 1.360 R_{\odot}, 5997 \text{ K})$ and $(0.605 M_{\odot}, 0.764 R_{\odot}, 5537 \text{ K})$, which indicates a highly inflated component for the primary, and

Table 6.2. Physical Masses, Radii, and Temperatures for the Low-Mass Binaries

<i>Kepler</i> ID	M_1 (M_\odot)	M_2 (M_\odot)	R_1 (R_\odot)	R_2 (R_\odot)	T_1 (K)	T_2 (K)
003102024	0.712±0.050	0.520±0.027	0.797±0.016	0.612±0.013	5612±201	4640±150
004352168	1.132±0.082	0.659±0.036	1.006±0.022	0.693±0.015	5547±188	4392±124
004773155	0.931±0.049	0.902±0.040	1.008±0.015	0.909±0.014	5765±318	5523±294
006029130	0.783±0.043	0.797±0.032	0.820±0.014	0.839±0.014	5717±180	5426±167
006131659	0.734±0.026	0.488±0.013	0.825±0.008	0.558±0.007	5493±129	4234± 81
006431670	0.455±0.035	0.462±0.035	0.684±0.018	0.746±0.020	5012±207	5198±226
007846730	0.614±0.208	0.605±0.118	1.360±0.119	0.764±0.067	5997±168	5537±146
008296467	0.887±0.046	0.856±0.038	0.837±0.013	0.822±0.013	5362±178	5069±161
009284741	0.768±0.066	0.728±0.068	0.738±0.021	0.757±0.022	5082±252	5295±271
010753734	0.991±0.027	0.841±0.017	1.036±0.008	0.881±0.007	5818±181	5492±164
010992733	0.763±0.144	0.729±0.097	1.041±0.054	0.811±0.042	5288±129	4892±115

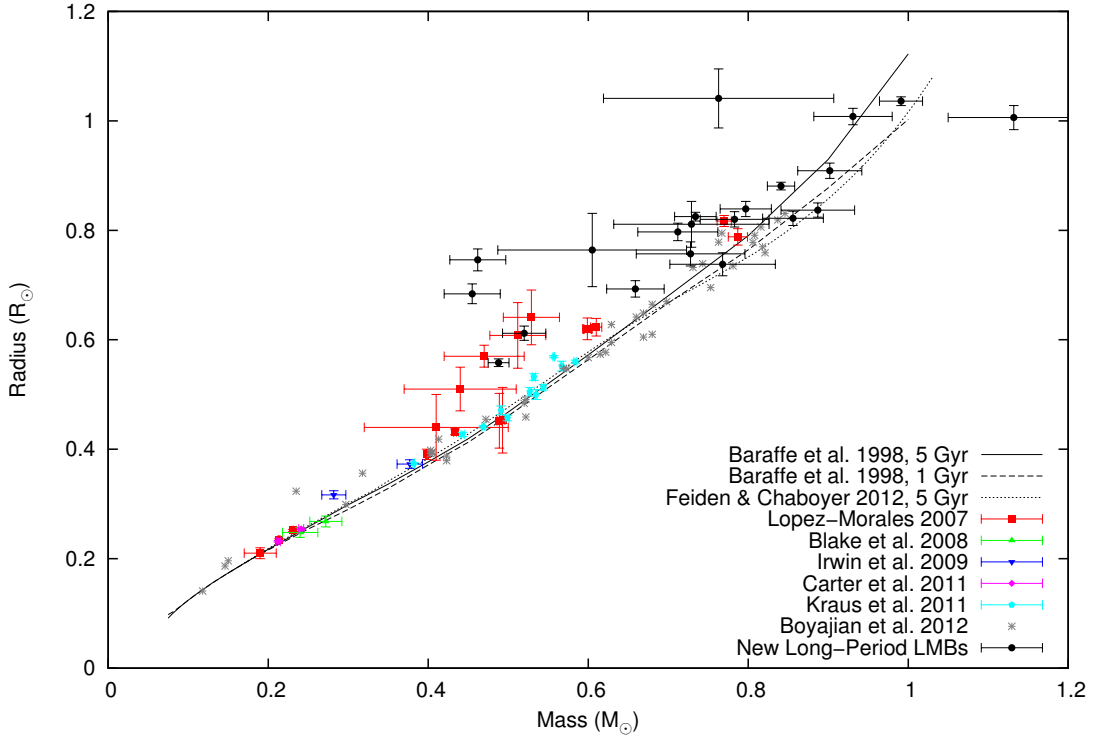


Fig. 6.12.— Mass-Radius diagram for low-mass stars. The measurements of the 22 stars in the 11 new long-period low-mass binaries we measured are shown by solid black circles. Measurements from previous studies are shown by other point types and colors. The theoretical mass-radius relations from the stellar models of Baraffe et al. (1998) are shown for $[M/H] = 0.0$ and ages of both 1 and 5 Gyr via the solid and long-dashed lines, respectively. A more modern mass-radius relationship from the Dartmouth Stellar Evolution Program (Feiden & Chaboyer 2012) is also shown by a short-dashed line.

a moderately inflated component for the secondary. However, the errors on this system are huge, owing in part to the extreme light ratio, (the primary is nearly 5 times more luminous than the secondary), with a $\sim 34\%$ error on the primary mass and a $\sim 20\%$ error on the secondary mass. The interesting aspect is that the radial velocity curve shows a mass ratio close to 1, whereas the light curve reveals a ratio of the radii of nearly 2, with the latter measurement extremely precise as the secondary eclipse is flat-bottomed. If there is not a large systematic error resulting from the extreme light ratio, it is likely that, within the large errors, the primary of this system may be a slightly evolved solar-like sub-giant. More precise spectroscopic observations are required though before anything definitive can be claimed.

Examining the rest of the stars, most of the long-period low-mass binaries are inflated compared to the theoretical stellar models, although there is a wide range of individual errors resulting from each system's brightness, luminosity ratio, and temporal coverage, with an apparent intrinsic scatter of $\sim 5\%$ for the many stars near $0.75 M_{\odot}$. Of particular interest are the three stars located at $(M, R) = (0.488 M_{\odot}, 0.558 R_{\odot})$, $(0.520 M_{\odot}, 0.612 R_{\odot})$, and $(0.659 M_{\odot}, 0.693 R_{\odot})$, which are the secondary stars of Kepler 006131659, 003102024, and 004352168 respectively. These stars have low masses, reasonably small errors, are inflated by $\sim 10\text{-}15\%$ compared to the models, and appear to agree well with the previous measurements of López-Morales (2007) for short-period systems. At face value this argues that low-mass stars in long-period systems, presumed to be at their natural rotation rate, are still in disagreement with theoretical models and thus rotation is not a principal factor in explaining the discrepancy between low-mass stellar models and observations. However, there are a number of factors which

could complicate this assessment and deserve attention.

First, it should be noted that with only 3 stars in the critical mass range, we should be wary about any broad conclusions based on small number statistics. Examining some possible factors though, eccentricity may play a role if it is significant enough to cause tidal interactions at periastron. However, the eccentricities for Kepler 006131659, 003102024, and 004352168 are 0.0147, 0.5709, and 0.2146 respectively, and thus do not present any obvious trend or commonality. The periods for the three systems span a wide range of 17.5, 13.8, and 10.64 days respectively as well. It is possible that even though these binaries are in long-period systems, they still have fast rotation rates. Examining the raw PDC light curve for all three systems reveals a possible, (though very weak and possibly residual spacecraft systematics), spot-induced periodic signature of ~ 15 days for Kepler 006131659 in the out-of-eclipse data, a very clear spot-induced pattern of ~ 5 days with definite signatures of differential rotation for Kepler 003102024, and another very clear spot-induced pattern of ~ 11 days with definite signatures of differential rotation for Kepler 004352168. Thus, from the out-of-eclipse photometric modulations, it is possible that the rotation period of the secondary star in Kepler 003102024 may be at 5 days, and this is fast enough to induce significant inflation, but the fastest rotation periods for Kepler 006131659 and 004352168 are still ~ 11 and ~ 15 days respectively, which theoretically means those stars are at their natural rotation rates. A major complication though is the difficulty in determining whether the multiple periods in the out-of-eclipse modulation, which mimics the signature of differential rotation seen in single stars, is actually from differential rotation on one or both of the stars, the result of each stars' individually different rotation rates, or the result of spot patterns changing over time, coupled with the

near impossibility of knowing which signals arise from the primary star and which from the secondary in each system.

As well, a recent study by Harrison et al. (2012) on the rotation rates of single field low-mass stars from *Kepler* and their spot-induced photometric amplitudes reveal a strong trend of decreasing spot amplitude with rotation period for $P < 40$ days, with a flat trend beyond 40 days. Relative to the spot amplitudes at 40^+ days, low-mass stars with periods of 0-5 days, 5-10 days, 10-20 days, 20-30 days, and 30-40 days exhibit approximately 10, 5, 2.5, 2, and 1.5 larger spot amplitudes respectively, though with a decent amount of intrinsic scatter in each period bin. Thus, if one takes spot-induced photometric levels as a proxy for stellar activity, it is possible that one really needs to find stars in eclipsing binaries that have 40^+ day rotation periods in order to truly be measuring “normal” non-active stars. However, via the derived levels of photometric variation, one would expect a major trend of decreasing radii versus rotation period by $P = 10$ days if rotation was a major factor in contributing to activity and radii inflation.

Metallicity has been previously examined as a potential factor in contributing to the discrepancy (e.g., López-Morales 2007; Boyajian et al. 2012), but it has always been found to be a mostly negligible factor with no observational correlation found, and we are not able to determine metallicity reliably enough from our spectra for our own study. X-ray luminosity has also been examined as a proxy for stellar activity, with (López-Morales 2007) finding a very weak correlation between X-ray flux and the amount of radii inflation for short-period binaries, but Boyajian et al. (2012) finding no correlation for single stars. We were not able to find any X-ray detections for any of our systems. Finally, it is possible that there is unresolved third light in the PDC aperture that will affect the light curve

analysis, but via direct testing we find that adding as much as even 10% third light into the model only affects the radius of the derived stars to <1%, and is often completely ruled out by the very deep eclipses.

Boyajian et al. (2012) recently found that there was no significant statistical difference between low-mass single stars measured via interferometry and low-mass stars in binary systems, with both groups being inflated relative to the stellar models. The new stars that we have measured appear to be more inflated compared to the single stars in Figure 6.12, but it is difficult to perform a rigorous statistical analysis as a result of both our small sample size, and the very large errors on the model-inferred masses of the single stars. If we were able to obtain more accurate temperatures for the eclipsing binaries in the future, then perhaps we could compare more directly to the single stars in the temperature-radius plane.

Although more observations are always needed, for now, we are thus left with the following conclusions:

1. The radii of low-mass main-sequence stars, measured both as components in eclipsing binaries, and interferometrically as single field stars, have radii that are $\sim 5\text{-}10\%$ greater than predicted by both old and new stellar models, with an intrinsic scatter of $\sim 5\%$.
2. Low-mass eclipsing binaries with $P > 10$ days, which should contain components where stars are at their natural rotation rates, analogous to field stars, still present inflated radii relative to stellar models, although more well-studied long-period binaries are still needed to bolster the number of observed stars.

3. No definitive correlation between the amount of radii inflation and a single factor have so far been found.
4. Given the above items, the discrepancy between the observed and predicted radii of low-mass stars appears to be a shortcoming of models of low-mass stars for $0.2 < M < 0.8 M_{\odot}$. This should not be surprising, given that most stellar models are only 1D or 2D models, and thus fail to capture a lot of complicated physics, including magnetic field creation and its resulting effects.
5. When assuming a radius for a single star from photometric or spectroscopic observations, (e.g., deriving the radius of a transiting exoplanet relative to the radius of its host star), one should use the observational mass-radius-temperature relations, and assume an error of $\sim 5\%$ in the interpolated radius due to intrinsic star-to-star scatter.

7. OBSERVATIONAL DETERMINATION OF LIMB-DARKENING IN THE *KEPLER* BANDPASS

7.1. Introduction

Limb-darkening is the observational phenomenon that stars, when observed as projected disks on the sky, appear to be darker towards their edges, or limbs, when compared to their centers. This effect is typically observed in the near infrared, visible, and ultraviolet wavelengths, with the effect becoming more prominent towards ultraviolet and less prominent towards infrared wavelengths. (Limb-brightening, where the limb appears brighter than the center, can also be observed at both very-short wavelengths, such as extreme ultraviolet and X-ray, and very long wavelengths, such as far-infrared and radio.)

The physical cause of limb-darkening results from the fact that a star is a spherical object that contains an extended atmosphere, which has a varying temperature, density, and composition with height, with temperature and density typically decreasing with increasing height. Referring to Figure 7.1, let us assume that one observes a star as shown, and they do so from the right side of the diagram, which is not to scale. If the observer is looking directly towards the center of the star, point O , the photosphere, or visible surface of the star, will lie at point A , where the optical depth of the atmosphere, τ , reaches approximately $\frac{2}{3}$ at a path length, L , from where $\tau \approx 0$. At this layer the stellar atmosphere will have a temperature, T_{HI} , from which most of the observed photons are emitted. However, when one observes towards the limb of the star, away from the center, the layer where $\tau = \frac{2}{3}$ will still lay at a path length $\sim L$ from $\tau \approx 0$, but due to the spherical geometry, this point, B , is physically higher up in the atmosphere. Since point B is higher up, it has a temperature, T_{LO} , which is lower than T_{HI} .

Thus, due to the lower temperature, the amount of flux emitted at point B will be less than point A , as seen by the observer, and thus the limb will appear to be darker. Additionally, photons emitted at point B will travel through a different density and composition of material, thus resulting in different spectral absorption features compared to point A . Since the relative flux between points A and B mostly depend on the relative difference between their temperatures, limb darkening will strongly vary depending on the wavelength of observation. Limb darkening will be more extreme at shorter wavelengths, where the flux difference between two blackbodies with different temperatures is most extreme, and less extreme at longer wavelengths where blackbodies are in the Rayleigh-Jeans tail. Since stars do not radiate as perfect blackbodies, and since the temperature, density, and composition of the atmosphere is not a linear function of scale height, limb-darkening is an inherently non-linear phenomenon.

The accurate determination of limb-darkening is important for any science that requires accurately knowing the flux distribution of the projected stellar disk. Of particular relevance, transiting exoplanets can be greatly affected by stellar limb-darkening. In the absence of limb-darkening, between ingress and egress, the observed flux remains constant throughout the transit, and the transit shape is flat-bottomed with a depth exactly equal to the square of the ratio of the radii. However, with limb-darkening, when the planet is towards the limb of the star it will be blocking less total light than when it is at the center of the star. This will result in a transit shape that is deeper towards the center of the transit, and a round-bottom shape. As limb-darkening becomes more severe at shorter wavelengths, transits will be observed to be more round-bottomed at shorter wavelengths, and more flat-bottomed at longer wavelengths. A classic

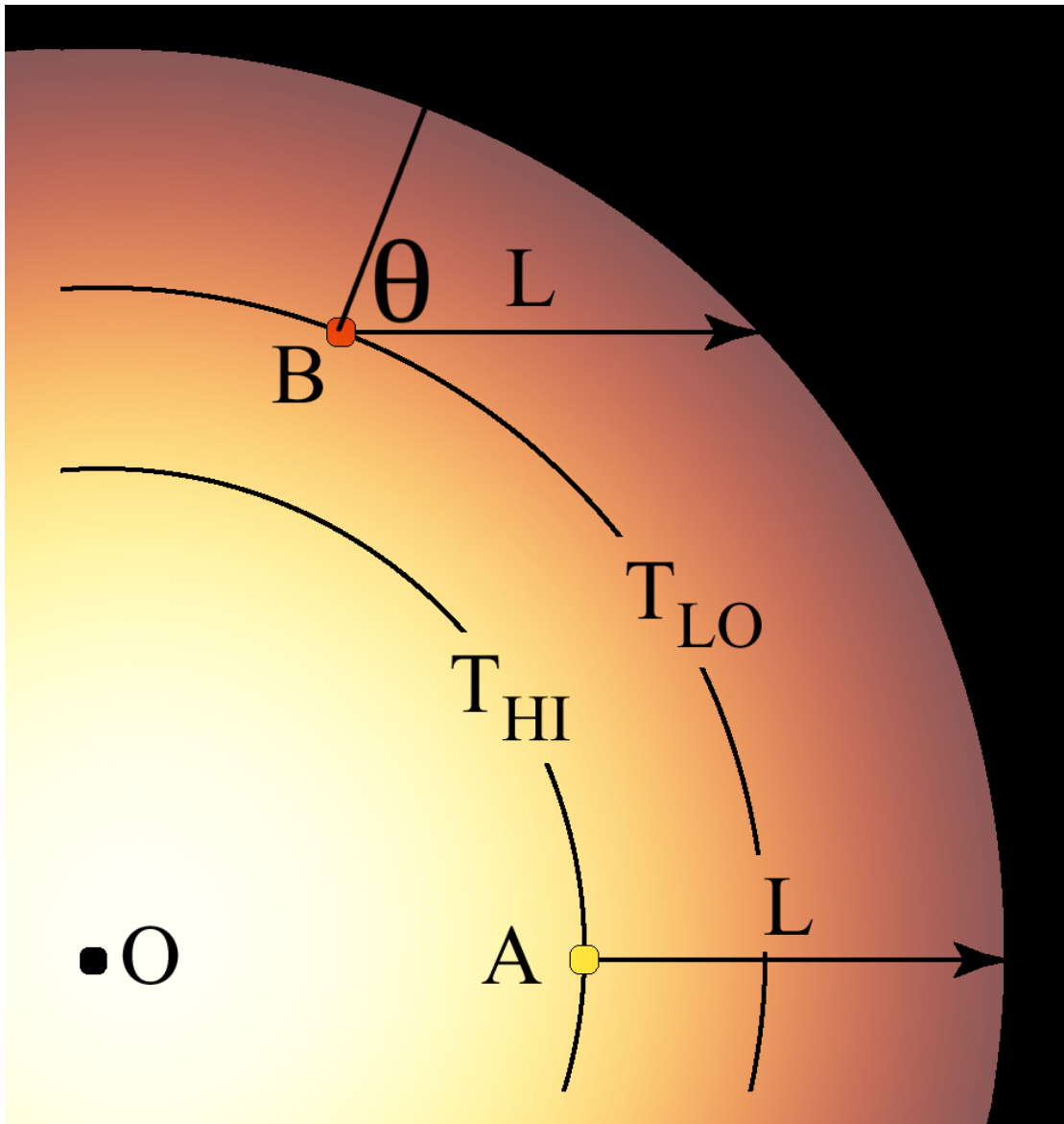


Fig. 7.1.— An illustration of the effect of limb-darkening, not to scale. Light emitted from point A , at a temperature T_{HI} , travels through a path length L to escape into space to reach the observer situated to the right. Light emitted from the limb of the star, at point B , travels a similar path length L , but due to spherical geometry point B is located at a higher physical height, and thus radiates at a lower temperature, T_{LO} . The resulting difference in temperature causes the limb to appear darker to the observer.

illustration of the effect of limb-darkening in extrasolar planet transits is shown in Figure 7.2. This figure is reproduced from Knutson et al. (2007a), who used the STIS spectrometer on the Hubble Space Telescope to obtain simultaneous transit light curves of HD 209458b in 10 passbands ranging from 290-1030 nm. As can be seen, the transit shape transitions from a flat-bottom to a round-bottom shape as wavelength decreases.

Although limb-darkening is inherently non-linear, many attempts have been made to derive simple analytical formulae to represent it to a reasonable accuracy. Typically these laws express the specific intensity of the stellar disk as a function of μ , where $\mu = \cos \theta$, and where θ is the angle between a line perpendicular to the stellar surface and the line of sight of the observer, (see Fig. 7.1), so that $\mu = 1$ at the center of the star, and $\mu = 0$ at the edge. The earliest and simplest expression is known as the linear limb-darkening law, first formulated by Russell (1912) as

$$\frac{I_u}{I_0} = 1 - c \cdot (1 - \mu) \quad (7.1)$$

where I_μ is the intensity at a given μ , I_0 is the intensity at the center of the star, and c is a free coefficient that can be adjusted to best fit the limb-darkening profile for an individual star. In an effort to more accurately represent limb-darkening, the quadratic law was first formulated by Kopal (1950) as

$$\frac{I_u}{I_0} = 1 - c_1 \cdot (1 - \mu) - c_2 \cdot (1 - \mu)^2 \quad (7.2)$$

where now two free coefficients, c_1 and c_2 , can be adjusted for each star. Several

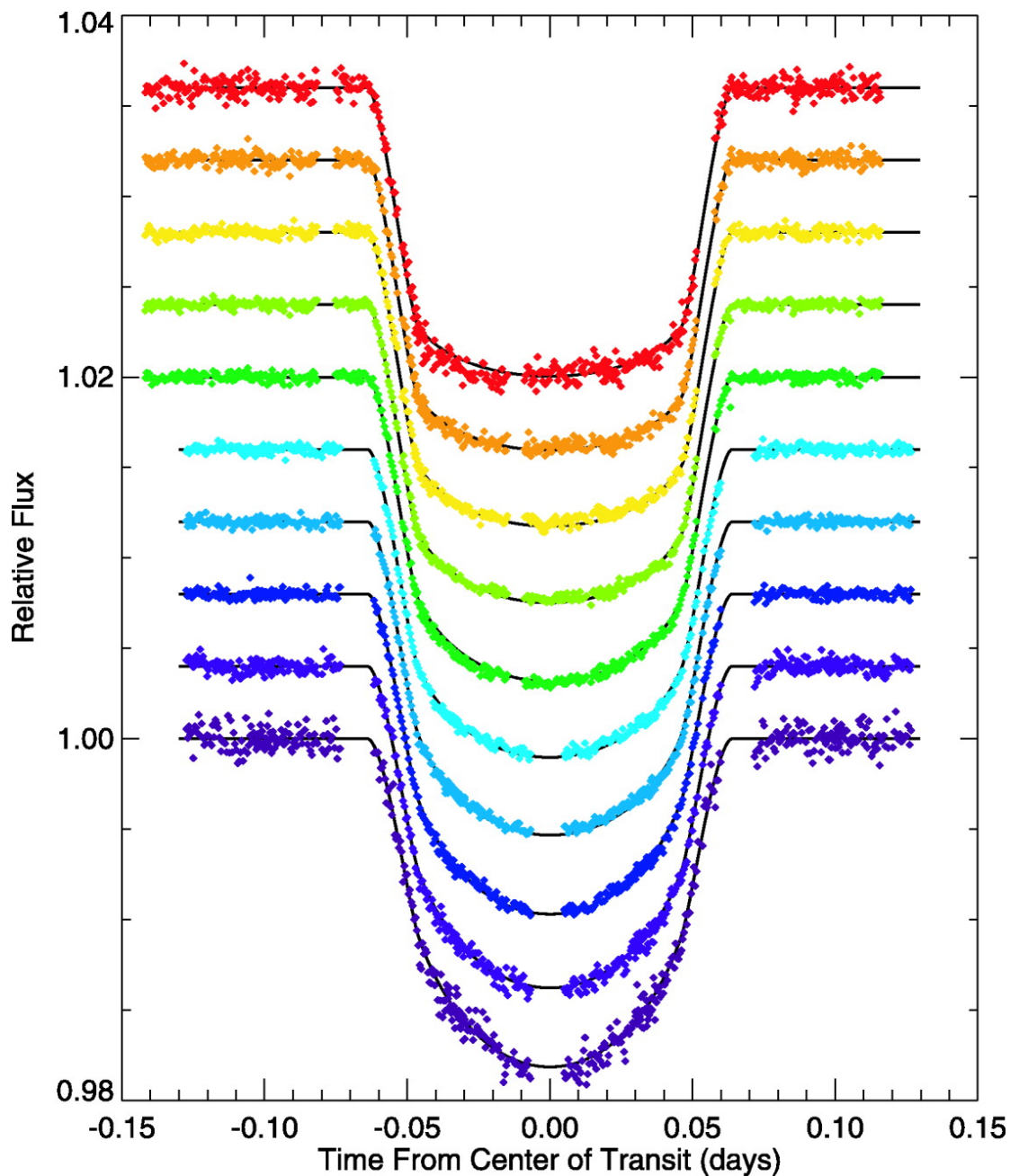


Fig. 7.2.— Simultaneous multi-wavelength transit observations of HD 209458b, reproduced from Knutson et al. (2007a). The observed data is shown with individual points, and the best-fit limb-darkened model with a solid black line. The top light curve is centered on 970.5 nm, the bottom light curve is centered on 320 nm, with wavelength decreasing from top to bottom. Note how the transit shape transitions from a flat-bottom to a round-bottom shape as wavelength decreases.

other 2-parameter have been introduced, notably the logarithmic law (Klingensmith & Sobieski 1970), the square root law (Diaz-Cordoves & Gimenez 1992), and the exponential law (Claret & Hauschildt 2003), expressed as

$$\frac{I_u}{I_0} = 1 - c_1 \cdot (1 - \mu) - c_2 \cdot \mu \cdot \ln \mu \quad (7.3)$$

$$\frac{I_u}{I_0} = 1 - c_1 \cdot (1 - \mu) - c_2 \cdot (1 - \sqrt{\mu}) \quad (7.4)$$

$$\frac{I_u}{I_0} = 1 - c_1 \cdot (1 - \mu) - \frac{c_2}{1 - e^\mu} \quad (7.5)$$

respectively. As a result of more accurate model stellar atmospheres and the desire to better reproduce their resulting limb-darkening profiles, Claret (2000a) introduced a 4 parameter limb-darkening law as

$$\frac{I_u}{I_0} = 1 - c_1 \cdot (1 - \mu^{\frac{1}{2}}) - c_2 \cdot (1 - \mu) - c_3 \cdot (1 - \mu^{\frac{3}{2}}) - c_4 \cdot (1 - \mu^2) \quad (7.6)$$

which could be extended to more terms as needed based on the general power-law

$$\frac{I_u}{I_0} = 1 - \sum_{n=1}^N c_n \cdot (1 - \mu^{\frac{n}{2}}) \quad (7.7)$$

where N is the number of terms desired. Finally, Sing et al. (2009) removed the first term of the Claret (2000a) 4 parameter law to produce a 3 parameter law

$$\frac{I_u}{I_0} = 1 - c_1 \cdot (1 - \mu) - c_2 \cdot (1 - \mu^{\frac{3}{2}}) - c_3 \cdot (1 - \mu^2) \quad (7.8)$$

which Sing et al. (2009) found to produce a smoother and more realistic limb-darkening profile at low values of μ , towards the edge of the star.

More precise, and perhaps more importantly, more accurate characterizations of limb-darkening are especially needed today, as the *Kepler* space telescope is obtaining transit curves of extrasolar planets at unprecedented levels of photometric precision. The physical parameters of extrasolar planets derived from transit light curves are intimately tied to the parameters one assumes for the host star, including its limb-darkening profile. In order to choose appropriate limb-darkening coefficients, typically a limb-darkening law is fit to the stellar disk intensity distribution as predicted via a model stellar atmosphere. Recently, both Sing (2010) and Claret & Bloemen (2011) have derived limb-darkening coefficients for the *Kepler* bandpass for many of the above laws by fitting them to stellar model predictions. Sing (2010) determined coefficients by performing a least-squares fit (LSF) to the ATLAS models, using only values of $\mu > 0.05$, as he noted the model atmospheres seem to over-predict limb-darkening at very low values of μ compared to the Sun. Claret & Bloemen (2011) derived coefficients via both a least-squares fit, as well as a flux conservation method (FSM) that aims to best-fit the model atmospheres while ensuring the overall stellar luminosity from the models is conserved, for both the ATLAS and PHOENIX model atmospheres. Figure 7.3 shows the predicted distribution from the ATLAS stellar models for main-sequence stars at 6500, 5500, and 4500 K effective temperatures in both the *CoRoT* and *Kepler* bandpasses. As can be seen, the limb-darkening profile is mostly linear, with higher-temperature stars being more non-linear. The largest amount of non-linearity occurs near the limb of the stars.

In addition to computing limb-darkening coefficients from model atmospheres,

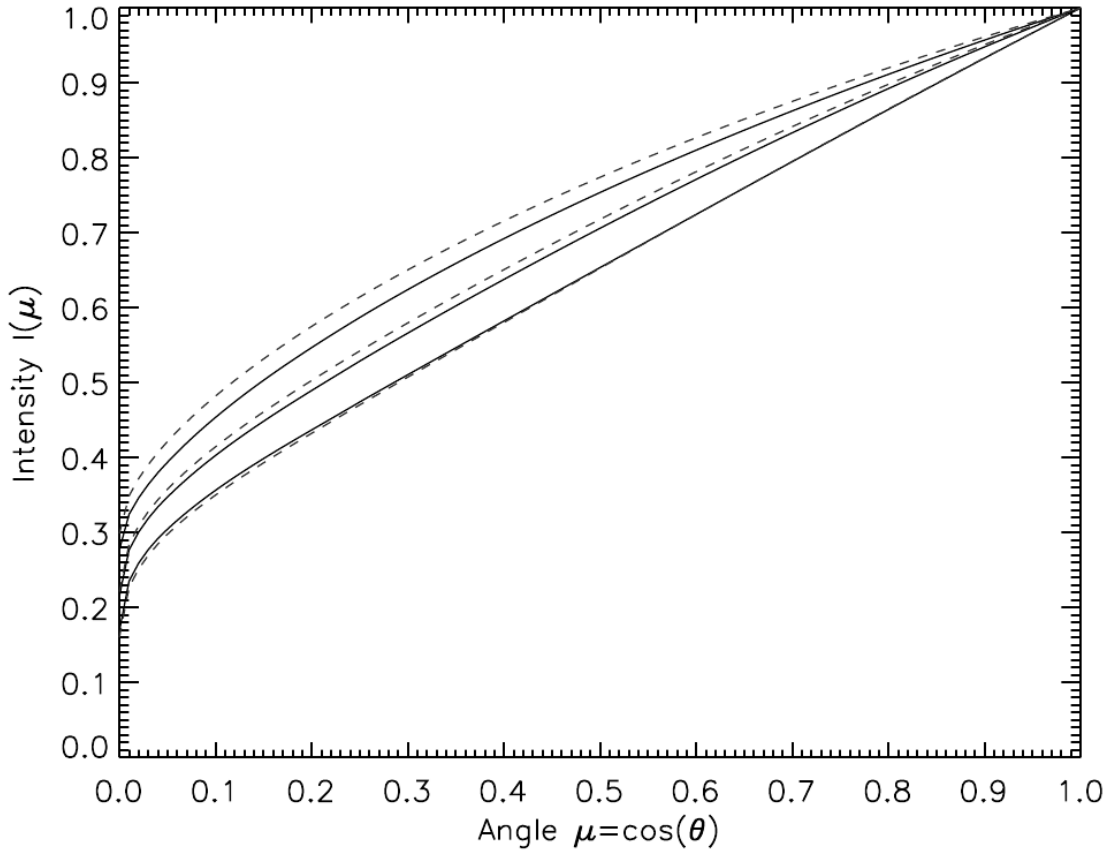


Fig. 7.3.— The predicted variation of intensity from stellar center ($\mu = 1$) to limb ($\mu = 0$) from the ATLAS stellar models, reproduced from Sing (2010). The solid lines are for the *CoRoT* bandpass, while the dashed lines are for the *Kepler* bandpass. From top to bottom, the three sets of lines represent stars with $T_{\text{eff}} = 6500, 5500,$ and 4500 K, each with $\log g = 4.5$ and $[M/H] = 0.0$. Note how the distribution is mostly linear, especially at lower temperatures, with the most non-linearity occurring towards the limb of the star.

the observation of eclipsing binaries can directly yield limb-darkening parameters as each star eclipses the other, yielding uniquely shaped eclipse curves. Although limb-darkening can be partially degenerate with other parameters, such as the radii of the stars or the inclination of the system, it is not completely degenerate and can be accurately measured with sufficiently precise photometric data. Claret (2008) compared linear limb-darkening coefficients derived from very precise *B*, *V*, and *R*-band eclipsing binary light curves to those computed from model atmo-

spheres, and noted a $\sim 15\text{-}20\%$ average discrepancy, with some systems being up to 40% discrepant. Such large errors could certainly result in errors of planetary parameters by $\sim 5\text{-}10\%$ or more, which is quite significant compared to the $\lesssim 1\%$ precision that *Kepler* can obtain. Thus, it is of great importance to both stellar and planetary astrophysics with *Kepler* that limb-darkening be observationally determined, and compared to the various model predictions to see which, if any, of the stellar models and limb-darkening fitting techniques provides an accurate representation of reality.

7.2. Observational Data and Modeling

We have selected known *Kepler* eclipsing binaries for modeling that are well-detached, main-sequence systems with deep eclipses, and thus present good cases for determining accurate and precise limb-darkening coefficients. First, we utilize all the eclipsing binaries we have already modeled in Chapter 5 and for which we already have linear limb-darkening coefficients. Second, we selected additional eclipsing binaries with hotter temperatures in order to extend the temperature range of our study, and targeted them for spectroscopic follow-up during our radial-velocity observations as described in § 6.3. The additional high-temperature systems that we obtained sufficient spectroscopic observations of for temperature determination were Kepler 003327980, Kepler 006610219, Kepler 006766748, and Kepler 009344623. We use the same technique to select and reduce *Kepler* data for these systems as previously discussed in §6.2.1. We then model the light curves for these systems using the same technique as described in §6.4.1 to obtain the linear limb-darkening coefficients, designated c_p and c_s for the primary and secondary star respectively, and model the spectra using the same technique as

described in §6.3. We list the effective temperatures and linear limb-darkening coefficients for both the low-mass binaries discussed in Chapter 6, as well as the new higher-temperature binaries, in Table 7.1.

7.3. Results and Discussion

In Figure 7.4 we plot the observationally determined linear limb-darkening coefficients for the modeled eclipsing binaries versus their spectroscopically determined effective temperatures. We also plot the theoretical linear limb-darkening coefficients of Sing (2010) and Claret & Bloemen (2011), for all combinations of the PHOENIX and ATLAS model atmospheres and the LSM and FCM interpolation techniques they presented, given $[M/H] = 0.0$ and $\log g = 4.5$.

As can be seen from Figure 7.4, the measured linear limb-darkening coefficients have a large amount of scatter compared to the measurement errors. While they tend to cluster around the range of predicted limb-darkening values, no particular theoretical model or interpolation method is clearly favored by the data. As a basic analysis, we divide the data up into three temperature bins that contain enough points for analysis, and as well are common temperatures for exoplanet hosts discovered via *Kepler*: 5250-5500 K, 5500-5750 K, and 5750-6000 K. In each bin we compute the error-weighted mean and error-weighted standard deviation for both the measured points, as well as the mean and standard deviation of all the model predictions. We show these results in Table 7.2. Via these results, we find that the model-predicted linear limb-darkening coefficients have an inherent discrepancy of 4-6% among models, depending on the temperature bin. The observationally determined linear limb-darkening coefficients have an average

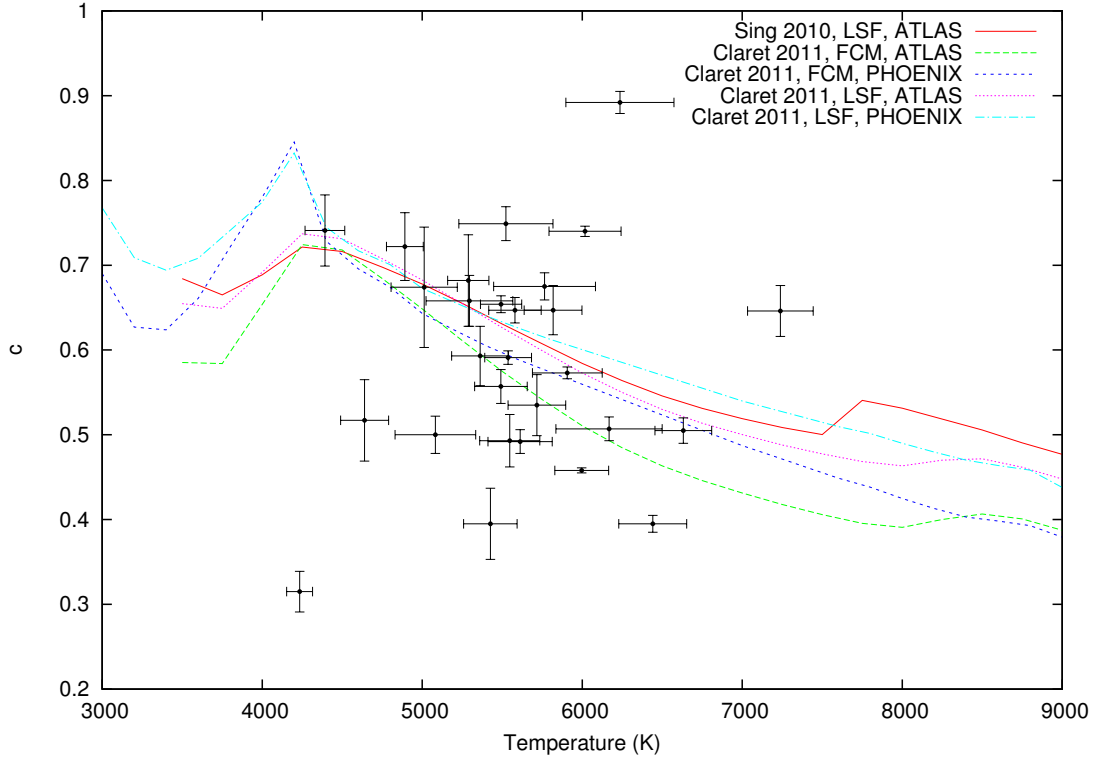


Fig. 7.4. — Plot of the linear limb-darkening coefficient versus effective temperature. Observationally determined coefficients we derived are shown by solid black circles. Theoretical limb-darkening coefficients derived from different model stellar atmospheres and interpolation techniques are shown by lines of varying color and type, all assuming $[M/H] = 0.0$ and $\log g = 4.5$. “Sing 2010” corresponds to the models of Sing (2010), while “Claret 2010” corresponds to the models of Claret & Bloemen (2011). “LSF” corresponds to the least-squares fitting method of interpolation, while “FCM” corresponds to the flux conservation method of interpolation. “ATLAS” and “PHOENIX” correspond to the type of model atmosphere employed. The error-weighted mean and standard deviation for the observed points, as well as the model points, are shown for 3 temperature bins as blue diamonds and red squares respectively.

discrepancy of 13-25%, depending on the temperature bin.

The first caveat when drawing conclusions from this data is that we still suffer from small-number statistics in each temperature bin, and really require observation of additional systems. Examining the data at-hand however, we must attempt to explain how there could be such large star-to-star scatter in the de-

Table 7.1. Effective Temperatures and Linear Limb-Darkening Coefficients of the Stars in the Modeled Eclipsing Binaries

<i>Kepler</i> ID	T_1 (K)	T_2 (K)	c_p	c_s
003102024	5612±201	4640±150	0.492±0.014	0.517±0.048
003327980	7239±205	6632±177	0.646±0.030	0.505±0.015
004352168	5547±188	4392±124	0.493±0.031	0.741±0.042
004773155	5765±318	5523±294	0.675±0.016	0.749±0.020
006029130	5717±180	5426±167	0.535±0.036	0.395±0.042
006131659	5493±129	4234± 81	0.654±0.010	0.315±0.024
006431670	5012±207	5198±226	0.674±0.071	1.194±0.057
006610219	6018±225	5907±218	0.740±0.006	0.573±0.007
006766748	6441±212	5580±164	0.395±0.010	0.647±0.015
007846730	5997±168	5537±146	0.458±0.003	0.591±0.008
008296467	5362±178	5069±161	0.593±0.035	1.160±0.025
009284741	5082±252	5295±271	0.500±0.022	0.658±0.030
009344623	6168±332	6236±338	0.507±0.014	0.892±0.013
010753734	5818±181	5492±164	0.647±0.029	0.557±0.020
010992733	5288±129	4892±115	0.682±0.054	0.722±0.040

Table 7.2. Weighted Mean and Standard Deviation of the Observed and Model Linear Limb-Darkening Coefficients in Three Temperature Bins

T_{eff} Range (K)	Observed Data	Model Data
5250-5500	0.625±0.066	0.624±0.027
5500-5750	0.581±0.078	0.598±0.030
5750-6000	0.519±0.132	0.574±0.034

terminated limb-darkening coefficients. One possibility is that the inclinations of these systems are such that only the very edges of the stars are being probed via the eclipses, and thus we are essentially fitting a line to only a small fraction of the stellar disk and thus a small range of μ , so that the determined coefficients are not the average of the entire disk. However, we have computed the fraction of the stellar disk eclipsed for every star in our sample, and find that every star has at least half of its disk eclipsed, and thus every star has its limb-darkening completely probed from $\mu = 0$ to 1. This is not surprising as we purposely selected systems with very deep eclipses and thus high inclinations. Another possibility is that these stars have a large range of metallicities and surface gravities that result in varying limb-darkening. Examining the models however, for a star with $T_{\text{eff}} = 5500$ K, $\log g = 4.5$, and $[M/H] = 0.0$, varying the surface gravity by 0.5 dex only results in a change of the linear limb-darkening coefficient by $<1\%$, and varying the metallicity by 0.5 dex only results in a change of $\sim 3\%$, which is much less than the observed variation. The last explanation we can think of, and that we deem most likely, is that these stars have a significant amount of star spots and/or plages that result in inhomogeneous stellar disks and affect the derived limb-darkening coefficients. It is well-known that solar-like and low-mass stars can have numerous star spots, sometimes covering a substantial fraction of the star. Although it becomes difficult to model the effect of such spots on the derived limb-darkening coefficients, one telltale sign might be to model the stellar limb-darkening as a function of time. If the limb-darkening coefficients significantly vary for a given system over timescales of months or years, then the most plausible cause would be varying spot patterns, which can change on those time scales. The *Kepler* mission should definitely be capable of examining this possibility after a few years

of data.

Regardless of the cause of the variation, it should be taken as a given that star-to-star linear limb-darkening typically varies by $\sim 15\%$. Thus, the recommended prescription when solving extrasolar planet transit curves, or eclipsing binary light curves, is to directly fit for the limb-darkening coefficients simultaneously with other parameters of interest. In the absence of the ability to directly solve for the limb-darkening coefficients, one should then set them to model predictions, but allow them to vary by $\pm 15\%$ in the error analysis.

8. MODELING MULTI-WAVELENGTH STELLAR ASTROMETRY: DETERMINATION OF THE ABSOLUTE MASSES OF EXOPLANETS AND THEIR HOST STARS

8.1. Introduction

As part of a Space Interferometry Mission (SIM) Science Study, we previously examined the implications that multi-wavelength microarcsecond astrometry has for the detection and characterization of interacting binary systems, (see Appendix C). We found that the astrometric orbits of binary systems can vary greatly with wavelength, as astrometric observations of a point source only measure the motion of the photocenter, or center of light, of the system. For systems that contain stellar components with different spectral energy distributions, the motion of the photocenter can be dominated by the motion of either component, depending on the wavelength of observation. Thus, with multi-wavelength astrometric observations it is possible to measure the individual orbit of each component, and thus derive absolute masses for both objects in the system. Additionally, we have previously found that multi-wavelength astrometry can be used to directly measure the inclination and gravity darkening coefficient of single stars, as well as the temperature, size, and position of star spots, (see Appendix D).

Astrometry has long been used to measure fundamental quantities of binary stars, and more recently has been used to study extrasolar planets. Although no independently confirmed planet has yet been initially discovered via astrometry, many planets discovered via radial-velocity, (which only yields the planetary mass as a function of the system's inclination and host star's mass), have had follow-up astrometric measurements taken in order to determine their inclinations, and thus true planetary mass as a function of only the assumed stellar mass (McArthur

et al. 2004; Benedict et al. 2006; Bean et al. 2007; Martioli et al. 2010; McArthur et al. 2010; Röhl et al. 2010; Reffert & Quirrenbach 2011). There are many ground and space-based microarcsecond precision astrometric projects which are either currently operating or on the horizon. The proposed SIM Lite Astrometric Observatory, a redesign of the earlier proposed SIM PlanetQuest Mission, was to be a space-based 6-meter baseline Michelson interferometer capable of $1 \mu\text{as}$ precision measurements in ~ 80 spectral channels spanning 450 to 900 nm (Davidson et al. 2009), thus allowing multi-wavelength microarcsecond astrometry. Although the SIM Lite mission has been indefinitely postponed at the time of this writing, it has already achieved all of its technological milestones, and it, or another similar mission, could be launched in the future. The PHASES project obtained as good as $34 \mu\text{as}$ astrometric precision of close stellar pairs (Muterspaugh et al. 2010). The CHARA array has multi-wavelength capabilities, and can provide angular resolution to $\sim 200 \mu\text{as}$ (ten Brummelaar et al. 2005). PRIMA/VLTI is working towards achieving $\sim 30\text{-}40 \mu\text{as}$ precision in the K -band (van Belle et al. 2008), with GRAVITY/VLTI expected to obtain $10 \mu\text{as}$ (Kudryavtseva et al. 2010). The ASTRA/KECK project will be able to simultaneously observe and measure the distance between two objects to better than $100 \mu\text{as}$ precision. The GAIA mission will provide astrometry for $\sim 10^9$ objects with 4 - $160 \mu\text{as}$ accuracy, for stars with $V = 10\text{-}20$ mag respectively, and does possess some multi-wavelength capabilities (Cacciari 2009). The MICADO instrument on the proposed E-ELT 40-meter class telescope will be able to obtain better than $50 \mu\text{as}$ accuracy at $0.8\text{-}2.5 \mu\text{m}$ (Trippe et al. 2010). Finally, the NEAT mission proposes to obtain as low as $0.05 \mu\text{as}$ astrometric measurements at visible wavelengths (Malbet et al. 2011). Thus, astrometric measurements of extrasolar planets are going to become significantly

more common in the future.

In this chapter, we examine the multi-wavelength astrometric signature of exoplanets. A star-planet system is a specialized case of a binary system with extreme mass and temperature ratios, and thus the findings in Appendix C apply to exoplanets. Specifically, an extrasolar planet has a combination of reflected and thermally emitted light that cause the photocenter to be displaced from the center of mass of the star. Since the planet’s temperature is very different from that of the host star, the amount of photocenter displacement due to the planet will greatly vary with wavelength. Although the luminosity ratio between a star and planet is extreme, the planet also lies a much farther distance from the barycenter of the system compared to the star, and thus it has a large “moment-arm” with which to influence the photocenter. While conventional single-wavelength astrometric measurements can yield the inclination and spatial orientation of a system’s orbital axis, with multi-wavelength astrometry it should be possible to measure the individual orbits of both the star and planet, and thus determine the absolute masses of both.

In Section 8.2 we derive analytical formulae for estimating the astrometric motion of a star-planet system at a given wavelength. In Section 8.3 we perform numerical simulations of the multi-wavelength astrometric orbits of a few systems of interest using the `REFLUX` code, and examine a few features specific to transiting planets. In both sections we present the most promising systems for future observation and detection of this effect. Finally, in Section 8.4 we discuss our results and what future work is needed to achieve these observations.

8.2. Analytical Formulae for Computing the Reflex Motion

Our objective is to derive an analytical expression for the amplitude of the sky-projected angular astrometric reflex motion of a star-planet system with respect to the wavelength of observation, α . In all of the following equations, we are dealing with sky-projected distances measured along the semi-major axis of the system, and thus they are independent of the inclination of the system. We consider the case of a star and single planet in a circular orbit, with masses M_\star and M_p respectively, separated by an orbital distance, a , as illustrated in Figure 8.1. The system's barycenter, marked via a “+” symbol, lies in-between the star and planet, at a distance of r_\star from the star, and r_p from the planet.

Defining the mass ratio, q , as

$$q = \frac{M_p}{M_\star} \quad (8.1)$$

the values for r_\star and r_p are then

$$r_\star = \frac{a \cdot q}{q + 1} \quad (8.2)$$

$$r_p = \frac{a}{q + 1} \quad (8.3)$$

where by definition $r_\star + r_p = a$.

In the case where all the light from the system is assumed to come from the star, i.e., the system's photocenter is the star's center, the wavelength-independent amplitude of the angular astrometric reflex motion of the system, α_0 , is

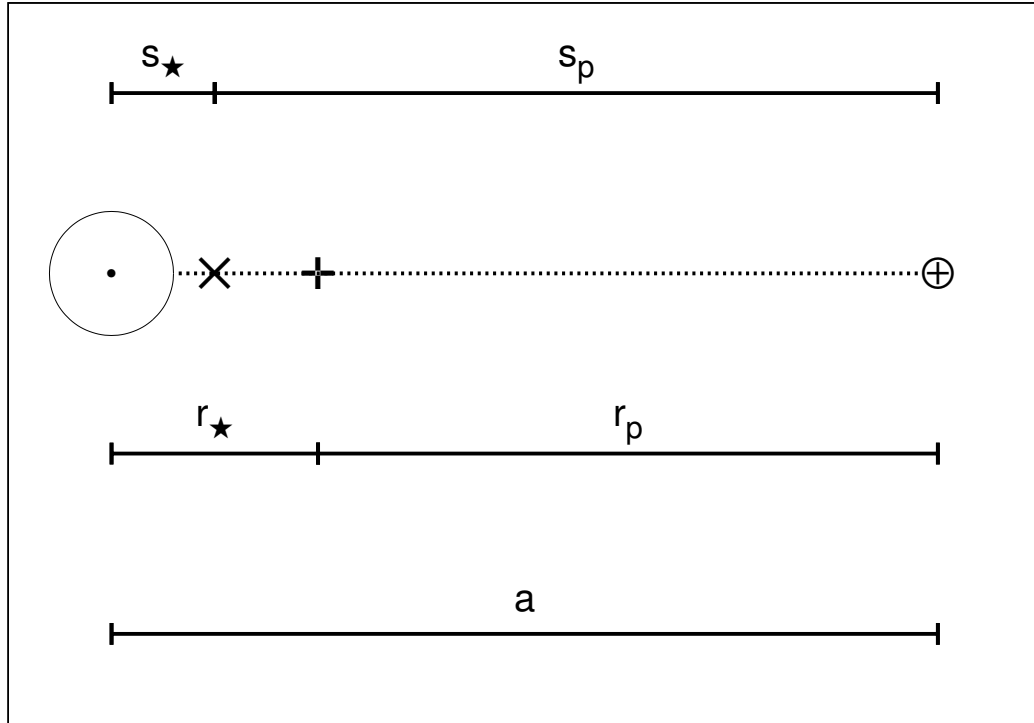


Fig. 8.1.— An illustration of a system containing a star, shown on the left, and a planet, shown on the right, separated by a distance a , not to scale. The star and planet lie at distances of r_\star and r_p , respectively, from the barycenter of the system, which is marked via a “+” symbol. Similarly, the star and planet lie at distances of s_\star and s_p , respectively, from the photocenter of the system, which is marked via a “x” symbol. All distances are sky-projected distances along the semi-major axis of the system, and thus are independent of the system’s inclination. Note that although in this illustration the photocenter is to the left of the barycenter, it can lie anywhere between the star and planet.

$$\alpha_0 = \arctan\left(\frac{r_\star}{D}\right) = \arctan\left(\frac{a \cdot q}{D \cdot (q + 1)}\right) \quad (8.4)$$

where D is the distance to the system from Earth, and a , via Kepler’s third law, is

$$a = (G(M_\star + M_p))^{1/3} \left(\frac{P}{2\pi}\right)^{2/3} \quad (8.5)$$

where G is the gravitational constant, and P is the orbital period of the system.

When the planet's luminosity is not negligible, in order to determine the wavelength-dependent value of α , the location of the system's photocenter, which varies with wavelength, must be determined. We define s_\star and s_p to be the distance to the system's photocenter from the star and planet respectively, as shown in Figure 8.1, where the photocenter is marked with a “ \times ” symbol. We define the luminosity ratio at a given wavelength, L_r , as

$$L_r = \frac{L_p}{L_\star} \quad (8.6)$$

where L_p is the luminosity of the planet, and L_\star is the luminosity of the star. Thus, similar to the previously presented derivations, the values for s_\star and s_p are

$$s_\star = \frac{a \cdot L_r}{L_r + 1} \quad (8.7)$$

$$s_p = \frac{a}{L_r + 1} \quad (8.8)$$

where by definition $s_\star + s_p = a$. The observed astrometric motion results from the movement of the system's photocenter around the system's barycenter. Thus, taking into account light from both the star and planet,

$$\alpha = \arctan\left(\frac{r_\star - s_\star}{D}\right) = \arctan\left(\frac{s_p - r_p}{D}\right) \quad (8.9)$$

and thus

$$\alpha = \arctan \left(\frac{a \cdot (q - L_r)}{D \cdot (q + 1) \cdot (L_r + 1)} \right) \quad (8.10)$$

where we have defined α so that $\alpha > 0$ signifies that the star dominates the observed reflex motion, i.e., $L_r < q$, and $\alpha < 0$ signifies that the planet dominates the observed reflex motion, i.e., $L_r > q$. Note that when the barycenter and photocenter are at the same point, i.e., $L_r = q$, and thus $\alpha = 0$, no reflex motion is observable.

We now estimate the value of L_r based upon the values of readily measurable system parameters. Light emitted from the planet consists of both thermally emitted light, as well as incident stellar light reflected off the planet. Thus,

$$L_r = \frac{L_E + L_A}{L_\star} = \frac{L_E}{L_\star} + \frac{L_A}{L_\star} \quad (8.11)$$

where L_E is the luminosity of the planet from thermal emission, L_\star is the luminosity of the star, and L_A is the luminosity of light reflected off the planet. To estimate the thermal component, we assume that both the star and planet radiate as blackbodies, and thus

$$\frac{L_E}{L_\star} = \frac{R_p^2}{R_\star^2} \cdot \frac{\exp(\frac{hc}{\lambda k T_\star}) - 1}{\exp(\frac{hc}{\lambda k T_p}) - 1} \quad (8.12)$$

where R_p is the radius of the planet, λ is a given wavelength, h is Planck's constant, c is the speed of light, k is Boltzmann's constant, T_\star is the effective temperature of the star, and T_p is the effective temperature of the planet. To derive T_p we first assume that the planet is in radiative equilibrium, and has perfect heat redistribution, i.e. a uniform planetary temperature, and thus

$$T_p = T_\star \cdot \left(\frac{(1 - A_B) \cdot R_\star^2}{4a^2} \right)^{\frac{1}{4}} \quad (8.13)$$

where T_\star is the temperature of the star, A_B is the planetary Bond albedo, and R_\star is the radius of the star.

To estimate the contribution due to reflected light, we first note that the flux received at the planet's surface is L_\star divided by the surface area of a sphere at a distance a , i.e., $4\pi a^2$. The planet intercepts and reflects this light on only one of its hemispheres, which has effective cross sectional area of πR_p^2 , with an efficiency equal to the albedo. Combining these terms and re-arranging to obtain the luminosity ratio due to reflected light yields

$$\frac{L_A}{L_\star} = \frac{A_\lambda R_p^2}{4a^2} \quad (8.14)$$

where A_λ is the planet's albedo at a given wavelength.

Combining the above equations, and assuming values of A_B and A_λ , we can estimate α at a given λ , using only M_\star , R_\star , T_\star , M_p , R_p , P , and D . We note that this assumes that the planet is in radiative equilibrium, but does not account for any additional internal heat sources from the planet, such as gravitational contraction or radioactive decay. While internal heat sources are likely to be negligible for close-in planets, it could significantly contribute to the total luminosity of further out gaseous planets, thus making them even more easily detectable. Our approximation for α also assumes that the planet's luminosity is constant over its orbit as observed from Earth. However, some planets have significant flux differences between their day and night sides due to low day-to-night re-radiation

efficiency and/or significant planetary albedos. In these cases, if the inclination of the system is $\neq 0^\circ$, then the planet’s luminosity will vary with orbital phase as seen by the observer, and the projected astrometric orbit of the photocenter at wavelengths where the planet’s luminosity dominates will deviate from an ellipse, with increasing deviation as the inclination approaches 90° . (This effect is further discussed and illustrated in Section 8.3.) As well, we assumed a circular orbit, and thus eccentric planets with varying levels of stellar insolation and temperature would have unique orbital signatures resulting from time-variant planetary flux. Finally, we assumed in this analytical derivation that the star and planet are effectively point sources, but of course in reality they have a physical size. If the star and/or planet have non-symmetric surface features, such as star spots or planetary hot spots, then the star and planet could each influence the location of the photocenter as these features rotated across their surface. The effect on the photocenter would only be a fraction of their physical radii, and would only cause significant deviations to the observed astrometric orbit if the radii of either object was a significant fraction of the object’s distance from the system’s barycenter. While this would likely be negligible for the planet, it could be significant for the star, e.g., the case of microarcsecond, wavelength-dependent, astrometric perturbations resulting from star spots presented in Appendix D.

In Figure 8.2 we present plots of α versus λ for a Jupiter-like planet, ($M_p = 1.0 M_J$, $R_p = 1.0 R_J$), around F0V, G2V, and M0V stars at 10 parsecs, with periods of 1, 10, 100, and 1000 days. We also show various planetary albedos, assuming $A_B = A_\lambda$, of 0.0, 0.25, 0.5, and 0.75. In Figure 8.3 we do the same for an Earth-like planet, ($M_p = 1.0 M_\oplus$, $R_p = 1.0 R_\oplus$). In general, systems that have large, high-mass stars and large, low-mass planets present the best opportunity to

observe negative values of α , and thus be able to directly determine their masses. (This is a unique parameter space not covered by other exoplanet characterization techniques such as radial-velocity or the transit method.) Short-period, and thus hot, planets around more massive stars transition to negative values of α at shorter wavelengths, but have lower overall amplitudes compared to long-period, and thus cool, planets around low-mass stars. Reflected light is a fairly minor contribution, only having some significant relevance for planets with very short orbital periods, i.e., ~ 1 day. For both hot Jupiters and hot Earths, negative values of α can be observed with wavelengths as short as $\sim 2 \mu\text{m}$, i.e., the *K*-band. Considering $\lambda < 100 \mu\text{m}$, $\alpha < 0$ could only be observed for $P \lesssim 100$ days for a Jupiter-like planet, and for $P \lesssim 500$ days for an Earth-like planet. Earth itself, ($P = 365$ days around a G2V star), would have a value of $\alpha \approx 0.3 \mu\text{as}$ for $\lambda < 10 \mu\text{m}$, and $\alpha \approx -0.05 \mu\text{as}$ at $100 \mu\text{m}$, and thus, theoretically, the absolute mass of an Earth-analogue and its host star could be determined via this technique.

Utilizing exoplanets.org, we have collected the values for all the previously mentioned system parameters for all currently known exoplanets. Selecting those that have well-determined values of all the needed parameters, in Table 8.1 we list the top five exoplanets with the largest negative values of α for each of the K ($2.19 \mu\text{m}$), L ($3.45 \mu\text{m}$), M ($4.75 \mu\text{m}$), and N ($10.0 \mu\text{m}$) infrared bandpasses, with a total of 11 unique exoplanets. We choose these wavelengths as they are the major ground-based infrared observing windows, and no systems examined had negative α values at wavelengths shorter than $\sim 2 \mu\text{m}$. All of the candidate systems ended up being transiting planets both because they have well-determined values for the planetary radii, and transit surveys are most sensitive to close-in planets. As can be seen, the top candidates for detecting $\alpha < 0$, and thus measuring the absolute

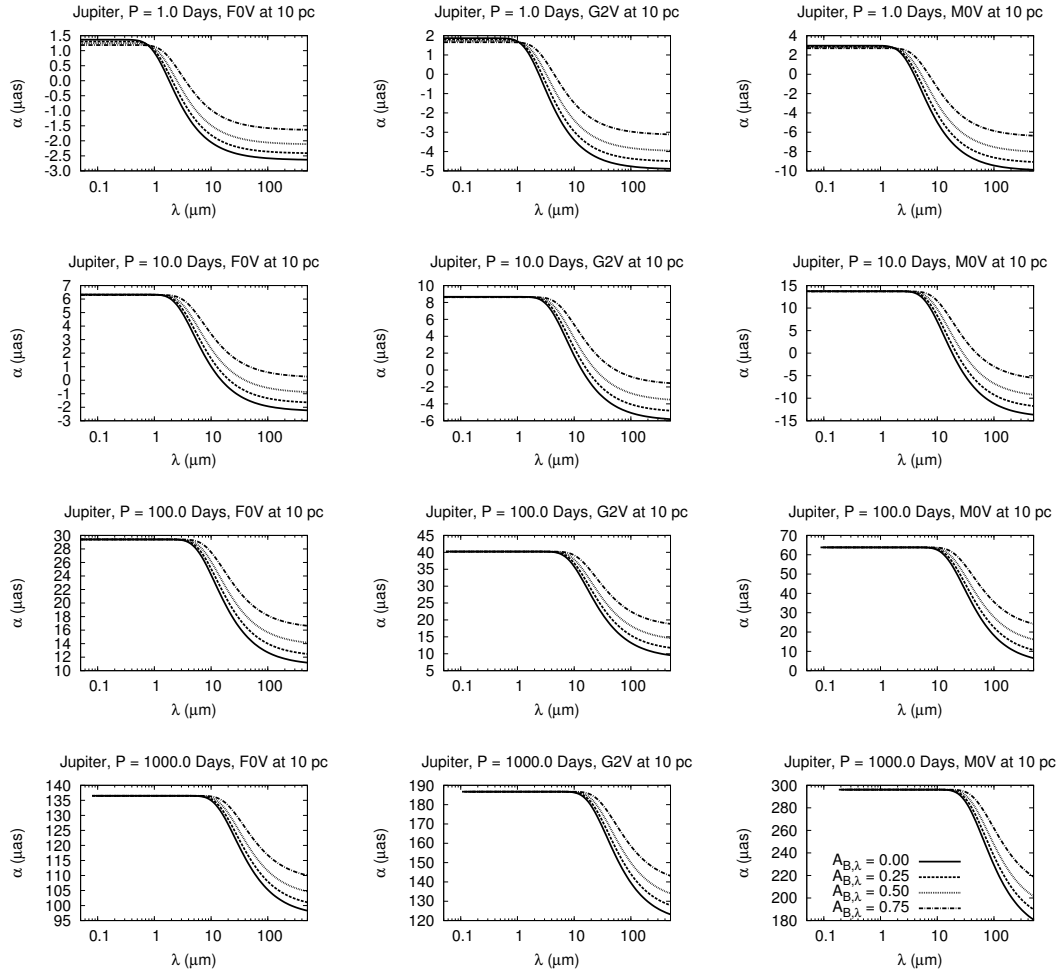


Fig. 8.2.— Plots of the reflex motion amplitude, α , versus the wavelength of observations, λ , for a Jupiter-like planet, ($M_p = 1.0 M_J$, $R_p = 1.0 R_J$) around F0V, G2V, and M0V stars at 10 parsecs, (left, middle, and right columns respectively), at periods of 1, 10, 100, and 1000 days, (top to bottom rows, respectively). The solid, dashed, dotted, and dash-dotted lines represent planetary albedos of 0.0, 0.25, 0.5, and 0.75 respectively.

mass of the planet, are WASP-12 b in the K -band with $\alpha = -0.05 \mu\text{as}$, HD 209458 b in the L and M -bands with $\alpha = -0.23$ and $-0.66 \mu\text{as}$ respectively, and HD 189733 b in the N -band with $\alpha = -3.04 \mu\text{as}$. It is interesting that three Neptune and sub-Neptune mass planets, 55 Cnc e, Gliese 436 b, and GJ 1214 b, also make the list, showing that this technique ‘favors’ the characterization of low-mass planets.

Table 8.1. Currently Known Exoplanets with the Most Negative α Values

Name	D (pc)	M_\star (M_\odot)	R_\star (R_\odot)	T_\star (K)	M_p (M_J)	R_p (R_J)	P (Days)	α (μas)
<i>K</i> -Band (2.19 μm)								
WASP-12 b	427	1.28	1.63	6300	1.35	1.79	1.091	-0.05
WASP-19 b	250	0.93	0.99	5500	1.11	1.39	0.789	-0.05
WASP-33 b	115	1.50	1.44	7430	2.05	1.50	1.220	-0.04
55 Cnc e	12	0.96	0.96	5234	0.03	0.19	0.737	-0.01
CoRoT-1 b	480	0.95	1.11	5950	1.03	1.49	1.509	-0.01
<i>L</i> -Band (3.45 μm)								
HD 209458 b	49	1.13	1.16	6065	0.69	1.36	3.525	-0.23
WASP-33 b	115	1.50	1.44	7430	2.05	1.50	1.220	-0.20
WASP-19 b	250	0.93	0.99	5500	1.11	1.39	0.789	-0.15
WASP-17 b	300	1.19	1.20	6550	0.49	1.51	3.735	-0.11
WASP-12 b	427	1.28	1.63	6300	1.35	1.79	1.091	-0.10
<i>M</i> -Band (4.75 μm)								
HD 209458 b	49	1.13	1.16	6065	0.69	1.36	3.525	-0.66
HD 189733 b	19	0.81	0.76	5040	1.14	1.14	2.219	-0.47
WASP-33 b	115	1.50	1.44	7430	2.05	1.50	1.220	-0.29
WASP-19 b	250	0.93	0.99	5500	1.11	1.39	0.789	-0.21
WASP-17 b	300	1.19	1.20	6550	0.49	1.51	3.735	-0.19
<i>N</i> -Band (10.0 μm)								
HD 189733 b	19	0.81	0.76	5040	1.14	1.14	2.219	-3.04
HD 209458 b	49	1.13	1.16	6065	0.69	1.36	3.525	-1.53
Gliese 436 b	10	0.45	0.46	3684	0.07	0.38	2.644	-0.95
WASP-34 b	120	1.01	0.93	5700	0.58	1.22	4.318	-0.64
GJ 1214 b	12	0.16	0.21	3026	0.02	0.24	1.580	-0.59

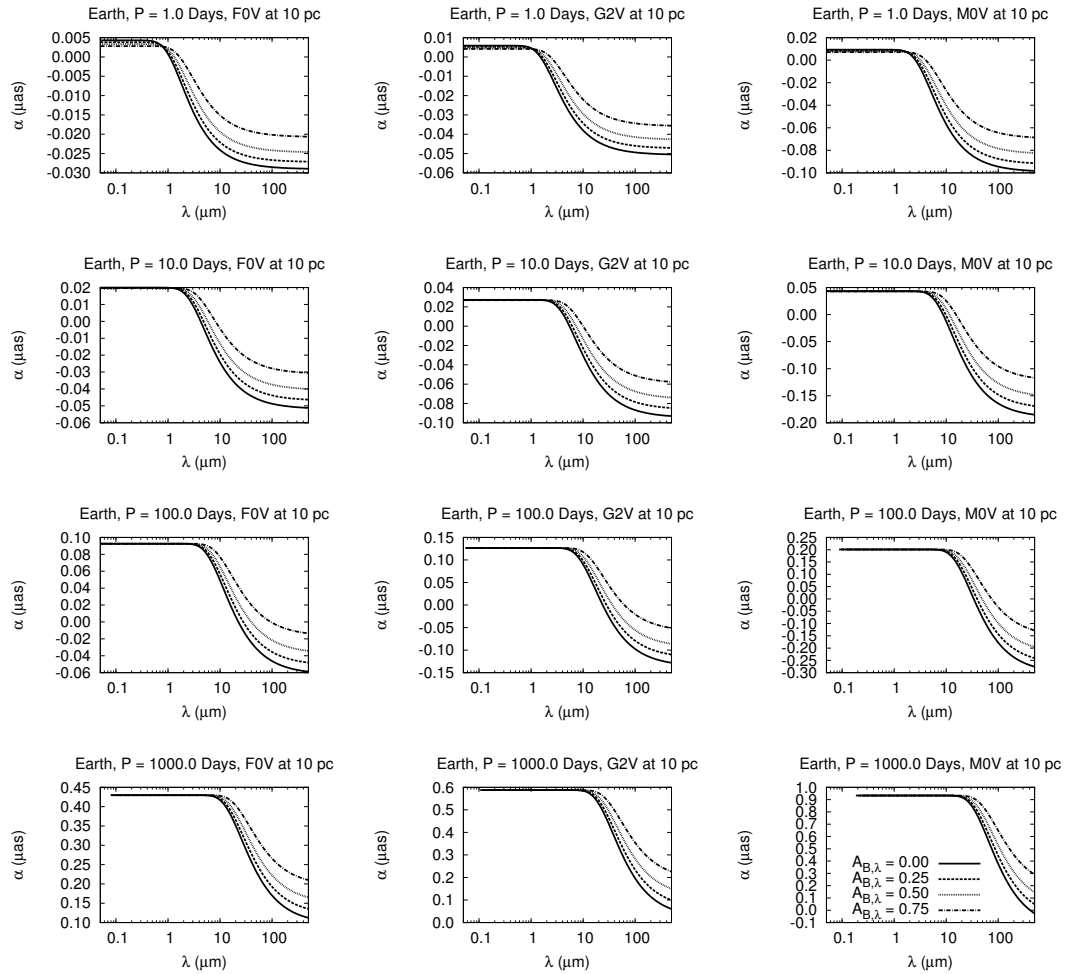


Fig. 8.3.— Plots of the reflex motion amplitude, α , versus the wavelength of observations, λ , for an Earth-like planet, ($M_p = 1.0 M_\oplus$, $R_p = 1.0 R_\oplus$) around F0V, G2V, and M0V stars at 10 parsecs, (left, middle, and right columns respectively), at periods of 1, 10, 100, and 1000 days, (top to bottom rows, respectively). The solid, dashed, dotted, and dash-dotted lines represent planetary albedos of 0.0, 0.25, 0.5, and 0.75 respectively.

8.3. Numerical Modeling via REFLUX

In order to provide a check on our analytical formulae, better illustrate the multi-wavelength astrometric orbits of exoplanet systems, and probe some more

subtle effects, we use the REFLUX¹ code (Coughlin et al. 2010b), which computes the flux-weighted astrometric reflex motion of binary systems at multiple wavelengths, to model a couple known exoplanet systems. We discuss the code in detail in Appendices C and D, but in short, it utilizes the Eclipsing Light Curve (ELC) code, which was written to compute light curves of eclipsing binary systems (Orosz & Hauschildt 2000). ELC includes the dominant physical effects that shape a binary system’s light curve, such as non-spherical geometry due to rotation and tidal forces, gravity darkening, limb darkening, mutual heating, reflection effects, and the inclusion of hot or cool spots on the stellar surface. The ELC code represents the surfaces of two stars, or a star-planet system, as a grid of individual luminosity points, and calculates the resulting light curve given the provided systemic parameters. REFLUX takes the grid of luminosity points at each phase and calculates the flux-weighted astrometric photocenter location at each phase, taking into account the system’s distance from Earth. Although ELC is capable of using model atmospheres, for this chapter we set the code to calculate luminosities assuming both the star and planet radiate as blackbodies.

We choose to model Wasp-12, HD 209458, and HD 189733, as they are all well-studied systems, and have the most negative α values for the K , L , M , and N bandpasses presented in Table 8.1. For each system we set the values for M_\star , R_\star , T_\star , M_p , R_p , P , D , and rotation period of the star to those in the Exoplanets.org database, and set the rotation period of the planet to the orbital period of the system, i.e., assume the planet is tidally locked, and assume a circular orbit. We assume that the spin axes of both the star and planet are perfectly aligned with the

¹REFLUX can be run via a web interface from <http://astronomy.nmsu.edu/jlcough/reflux.html>. Additional details as to how to set-up a model are presented there.

orbital axis. We employ the use of spots in the ELC code to simulate a day/night side temperature difference, by assuming a uniform day-side temperature for the planetary hemisphere facing the star, and a uniform night-side temperature for the planetary hemisphere facing away from the star. We employ the values for the day and night side temperatures derived by Cowan & Agol (2011), which were 2939 K for the day-side of Wasp-12 b, 1486 and 1476 K for the day and night sides respectively of HD 209458 b, and 1605 and 1107 K for the day and night sides respectively of HD 189733 b. We adopted a temperature of 1470 K for the night side of Wasp-12 b, i.e., half that of the day side, assuming very little planetary heat redistribution. For all the systems, we set the star’s gravity darkening coefficients to those determined by Claret (2000b), though do not enable gravity darkening for the planet. For both the planet and star, we assume zero albedo, since we are dealing principally with infrared wavelengths where the effect is negligible, and we have already shown that even in the optical reflected light is a minor contribution to the astrometric motions under investigation. Furthermore, the chosen planets are expected to have very low albedos ($A_B < 0.3$) from model atmospheres (Marley et al. 1999; Seager et al. 2000; Sudarsky et al. 2000), and have even had their albedos constrained to very low values from observations, e.g., López-Morales et al. (2010) for Wasp-12b, Rowe et al. (2008) for HD 209458b, and Wiktorowicz (2009) for HD 189733b. We also do not assume any limb-darkening since we are dealing principally with infrared wavelengths.

In Figures 8.4, 8.5, and 8.6 we present plots of the X and Y components of the photocenter versus phase, as well as the sky-projected X-Y orbit of the photocenter, in the V , J , H , K , L , M , and N passbands, for Wasp-12, HD 209458, and HD 189733 respectively. The point $(X,Y) = (0,0)$ corresponds to the

barycenter of the system, and the projected orbital rotation axis is parallel to the Y-axis. Phase 0.0 corresponds to the primary transit, when the planet passes in front of the star and is closest to the observer, and phase 0.5 corresponds to the secondary eclipse, when the planet passes behind the star and is farthest away from the observer.

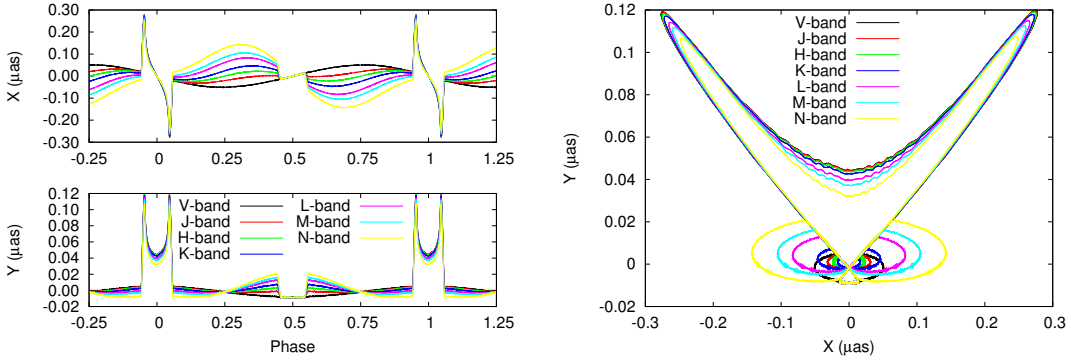


Fig. 8.4.— Plots of the multi-wavelength astrometric orbit for the Wasp-12 system. Left: The X and Y components of motion versus phase. Right: The sky-projected, X-Y, orbit. The point $(X,Y) = (0,0)$ corresponds to the system’s barycenter, and the projected orbital rotation axis is parallel to the Y-axis. Phase 0.0 corresponds to the primary transit, when the planet passes in front of the star and is closest to the observer, and phase 0.5 corresponds to the secondary eclipse, when the planet passes behind the star and is farthest away from the observer.

Examining the modeling results, the values for α determined via the analytical formulae appear to match the numerical modeling results fairly well. For example, via Table 8.1, Wasp-12b was predicted to have α values of -0.05 and $-0.10 \mu\text{as}$ in the *K* and *L*-bands respectively, compared to the maximum, out-of-transit, numerical model results of -0.05 and $-0.08 \mu\text{as}$. For HD 209458b, expected α values were -0.23 , -0.66 , and $-1.53 \mu\text{as}$ for the *L*, *M*, and *N*-bands, compared to -0.30 , -0.74 , and $-1.63 \mu\text{as}$ from the numerical models. For HD 189733b, expected α values were -0.47 and $-3.04 \mu\text{as}$ for the *M* and *N*-bands, compared to -2.10 and -4.68

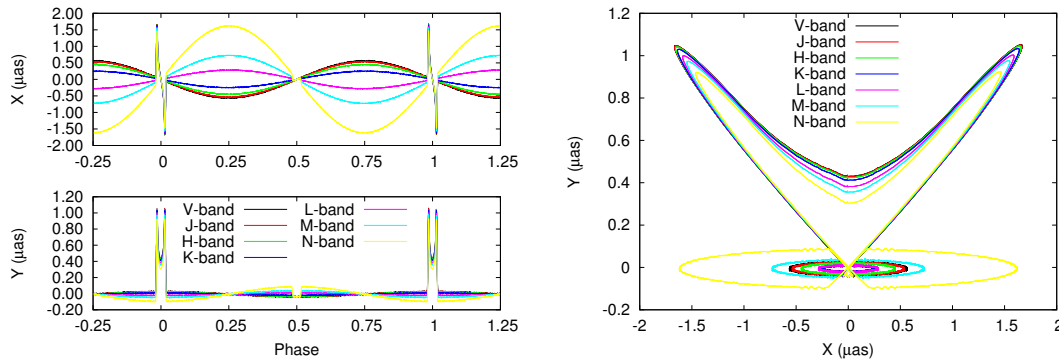


Fig. 8.5.— Plots of the multi-wavelength astrometric orbit for the HD 209458 system. Left: The X and Y components of motion versus phase. Right: The sky-projected, X-Y, orbit. The point $(X,Y) = (0,0)$ corresponds to the system’s barycenter, and the projected orbital rotation axis is parallel to the Y-axis. Phase 0.0 corresponds to the primary transit, when the planet passes in front of the star and is closest to the observer, and phase 0.5 corresponds to the secondary eclipse, when the planet passes behind the star and is farthest away from the observer.

μas from the numerical models. The differences are principally due to the use of observationally determined day and night side temperatures in the numerical models, whereas the analytical formulae assumed perfect radiative equilibrium and a uniform planetary temperature.

Although a transition from positive to negative α appears to occur around the *H*, *K*, and *L*-bands for Wasp-12 b, HD 209458 b, and HD 189733 respectively, a deviation from the visible light signature is clearly visible at shorter wavelengths, and thus it may be possible to disentangle the astrometric motion due to the planet even at shorter wavelengths where it does not dominate the reflex motion of the photocenter. For Wasp-12 b and HD 189733 b the out of transit/eclipse signature deviates from a sinusoid due to the extreme day/night temperature differences on these planets, as discussed in Section 8.2. The different inclinations of the systems are immediately apparent in the X-Y orbit plots, and when actually measured on sky, would directly yield the three-dimensional orbit of the system.

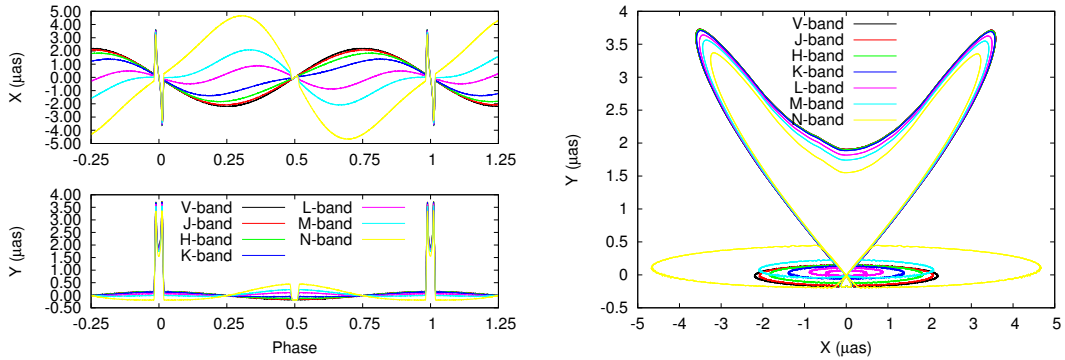


Fig. 8.6.— Plots of the multi-wavelength astrometric orbit for the HD 189733 system. Left: The X and Y components of motion versus phase. Right: The sky-projected, X-Y, orbit. The point $(X,Y) = (0,0)$ corresponds to the system’s barycenter, and the projected orbital rotation axis is parallel to the Y-axis. Phase 0.0 corresponds to the primary transit, when the planet passes in front of the star and is closest to the observer, and phase 0.5 corresponds to the secondary eclipse, when the planet passes behind the star and is farthest away from the observer.

The presence of the primary transit and secondary eclipse is clearly visible in all three cases, with the primary transit dominating the maximum amplitude of the astrometric shift for the visible wavelengths, particularly in the Y-direction. As no limb-darkening was assumed in these models, the variation in the primary and secondary eclipse signatures with wavelength is due to the relative flux of the star and planet in those passbands. As noted by Gaudi (2010), measuring the astrometric shift of the primary transit directly yields the angular radius of the host star, and if the distance to the system is precisely known, one can directly derive the physical radius of the star. Additionally, if the density of the star is directly determined from the photometric light curve (Seager & Mallén-Ornelas 2003), then one can also directly derive the mass of the star. We also note, for the first time, that measuring the astrometric signature of the primary transit and, if observing at longer wavelengths, the secondary eclipse, specifically the duration of ingress and egress, similarly directly yields the angular radius of the planet. Since

one may directly determine the surface gravity of the planet from the photometric light and radial-velocity curves alone (Southworth, Wheatley, & Sams 2007), one may also directly determine the mass of the planet. Thus, for transiting planets, multi-wavelength astrometric measurements yield two independent methods of measuring the physical stellar and planetary masses.

8.4. Discussion and Summary

We have shown that the multi-wavelength astrometric measurements of exoplanetary systems can be used to directly determine the masses of extrasolar planets and their host stars, in addition to the inclination and spatial orientation of their orbital axis. If the planet happens to transit the host star, then the angular radius of both the star and planet can be directly determined, and when combined with the trigonometric parallax of the system, the absolute radii of the planet and host star can directly determined via astrometry alone. We found that this technique is best suited, though is certainly not limited to, large, low-mass planets that orbit large, high-mass stars, and thus covers a unique parameter space not usually covered by other exoplanet characterization techniques.

We have provided analytical formulae and numerical models to estimate the amplitude of the photocenter motion at various wavelengths. We found that, for some systems, the planet can dominate the motion of the system's photocenter at wavelengths as short as $\sim 2 \mu\text{m}$, though the amplitude of the effect is only $\sim 0.05 \mu\text{as}$. If one is able to obtain astrometric measurements at wavelengths up to $10 \mu\text{m}$, then the motion of the photocenter due to the planet could be as high as several microarcseconds, and can often be of a much larger magnitude than

seen at optical wavelengths when the photocenter motion is due solely to stellar motion.

We performed numerical modeling of several exoplanet systems via the REFLUX code, and found it to be consistent with the predictions of our analytical model. The numerical modeling revealed that, even at shorter wavelengths where $\alpha > 0$, the planet has a visible impact on the observed astrometric orbit of the system. As well, deviations from pure sinusoidal motions due to day-night flux differences are clearly visible, and thus multi-wavelength astrometry could probe planetary properties of albedo and heat redistribution efficiency.

One caveat when working to extract the planetary and stellar masses from actual observations is that one will likely need to either precisely know the luminosity ratio of the system, or make assumptions about the luminosity of the planet, e.g., it radiates as a blackbody and is in thermal equilibrium. It may be possible that other observations could yield this information, such as the secondary eclipse depth if the planet happens to transit. The remaining parameters of the system's distance and period should be well determined via other methods such as microarcsecond precision parallax and radial-velocity or photometric light curves.

For the prospects of detection, it is clear that this effect will probably not be detected in the very near-term. Although astrometric measurements are approaching $1 \mu\text{as}$ accuracy, they have not yet been performed. Much of the ground-based work is being focused on the optical and K -bands, where in the latter the effect is just barely detectable. The development of microarcsecond precision astrometric systems in the mid-infrared, or sub-microarcsecond precision in the near-infrared,

are clearly needed, and the methods presented here will serve to preselect the best planetary system candidates to be observed by those systems.

The work presented in this chapter assumed that both the star and planet radiate as blackbodies, however it is known that both can significantly deviate from that assumption, especially in the near infrared (e.g., Gillon et al. 2009; Rogers et al. 2009; Gibson et al. 2010; Croll et al. 2011; de Mooij et al. 2011; Coughlin & López-Morales 2012a). At the extreme end, Swain et al. (2010) and Waldmann et al. (2012) recently found evidence for a very large non-LTE emission feature around $3.25 \mu\text{m}$ in the atmosphere of HD 189733 b². Although via blackbody approximations we calculate that the planet-to-star flux ratio should be 8.3×10^{-4} , Swain et al. (2010) and Waldmann et al. (2012) measure the $3.25 \mu\text{m}$ emission feature to be $\sim 8.5 \times 10^{-3}$ times the stellar flux, or about ten times greater than expected. Assuming blackbody emission, the expected value for α for this system at visible wavelengths is $2.15 \mu\text{as}$, and at $3.25 \mu\text{m}$ is $0.83 \mu\text{as}$. If the emission feature is real however, the expected value for α at $3.25 \mu\text{m}$ is a very large $11.3 \mu\text{as}$, dominated due to the planetary motion. Thus, the key in performing these types of observations may be to select particular wavelengths where the planets are unusually bright.

Finally, although we did not assume any limb-darkening in our models since we were examining near to mid-infrared wavelengths, limb-darkening will be significant when observed at different optical bandpasses. The astrometric signature of transiting planets will vary greatly due to limb-darkening in the optical regime, and thus multi-wavelength astrometry of transiting planets may be used to explore

²We note that Mandell et al. (2011) reported a non-detection of a portion of this feature between the publications of Swain et al. (2010) and Waldmann et al. (2012).

the limb-darkening profiles of stars, or visa versa, stellar limb-darkening may need to be precisely understood in order to extract planetary and stellar parameters of interest.

APPENDICES

APPENDIX A. ECLIPSE PHASE DISPERSION MINIMIZATION (EPDM)

In this appendix we further explain the EPDM technique introduced in Section 5.3. As mentioned in the text, EPDM finds the period of an eclipsing binary system by seeking the value of the period that best minimizes the dispersion in phase of the faintest N points in a light curve. To illustrate how this method works, we show in Figure A.1 the period search analysis of the LMMS DDEB candidate Kepler 006591789, which was found to have a period of 5.088435 days via the JKTEBOP model, (see Table 5.2). The unfolded Q1 light curve is shown in the top-left panel of Figure A.1. EPDM selects the faintest 20 points of the light curve, which are highlighted by the larger points in that same panel. The number of points should be adjusted based on the quality of the data set. Too few points could result in all the points selected belonging to the same eclipse, if that one eclipse is unusually deep due to systematics or another reason, and thus EPDM will be unable to determine a period. Too many points will cause the results of EPDM to be less precise, as more points are included further away from the center of the eclipses. We have found that 20 points is a good number for *Kepler* data, for which many systems do suffer from moderate systematics, as is evidently the case for Kepler 006591789, as seen by the quasi-sinusoidal variation in the baseline flux.

Having selected the faintest points from the light curve, EPDM then loops over a range of period values. In this case we choose a set of 5,000 period values that range from 0.3 to 30 days, evenly distributed in log space, so that shorter periods are as well-sampled as longer periods. At each period, the phase of each of the 20 faintest points are calculated via the following standard equation,

$$p = \frac{T}{P} - \text{int}\left(\frac{T}{P}\right) \quad (\text{A.1})$$

where p is the phase of a given point, with a time value, T , for a given period, P , and $\text{int}()$ returns the argument rounded down to the nearest integer value. The standard deviation of these 20 phase values is then computed, and we are left with a standard deviation for each trial period. In the bottom-left panel of Figure A.1, we plot the standard deviation in phase of the 20 points versus each trial period. The lowest values for the standard deviation indicate the best periods, where the eclipses align in phase-space, while high values indicate bad periods. As can be seen in the bottom-left panel, the standard deviation approaches a value of 0.0 near 10.2 days, 5.1 days, 2.05 days, and decreasing fractions thereof, or period aliases. To determine the three best periods, EPDM first selects the lowest standard deviation, which in this case yields a value of 5.09004 days. It then selects the next lowest value, whose corresponding period value differs from the first by at least 10%, and yields a value of 10.1747 days. The third period selected via the same method yields a value of 2.54402 days.

To further clarify the technique visually, in the top-right panel of Figure A.1, we show the same plot as in the bottom-left panel, but limited in period range to straddle the best period found, 5.09004 days. At the same period range, in the bottom-right panel, we plot the actual values of the phase for each of the 20 points at each period. (For ease of viewing, we use a lower trial period resolution in the bottom-right panel than the top-right panel.) As can be seen in the lower-right panel, when the trial period is far from the true period of the system, the actual phase values have a large dispersion, and range completely from 0.0 to 1.0. As

the given period gets closer to the true period, the phase values begin to clump, with their dispersion decreasing as the trial period approaches the true value. Indeed, as highlighted by the box in the bottom-right panel of Figure A.1, at the best period, all the phase values are tightly grouped together at $P = 5.0904$ days, indicating that all the eclipses are extremely well aligned, and the period of the system has been found.

One complication that can arise is if EPDM encounters an eccentric system with two similarly deep eclipses. In this case, when the algorithm selects the N faintest points, it will be selecting points from both eclipses. Since the system is eccentric, there is a phase offset not equal to 0.5 between primary and secondary eclipse, i.e. the two eclipses occur closer to each other in time compared to the period of the system. In this case, if we were to run EPDM as just described, in a plot like the bottom-right panel of Figure A.1, at the true period of the system there would be two groups of points, each by itself having a very small deviation, but separated from each other in phase by a large amount. Thus, the standard deviation calculation will show a much higher value than it should, and the correct period could not be found. Along similar lines, a problem arises when we consider how to calculate the standard deviation of, for example, the distribution of phase points in the bottom-right panel of Figure A.1 at a period of 4.9 days, which ranges from 0.8 - 1.0, and then jumps to 0.0 - 0.05. It is clear this is a continuous group of points, which simply experiences an abrupt jump from phase 1.0 to 0.0. Although they represent a fairly good period, a calculation of their standard deviation would show a high value, and thus indicate a bad period.

To reconcile both these problems, we insert an additional step into the EPDM technique. At each trial period, EPDM searches for a reflection phase, p_r , whose

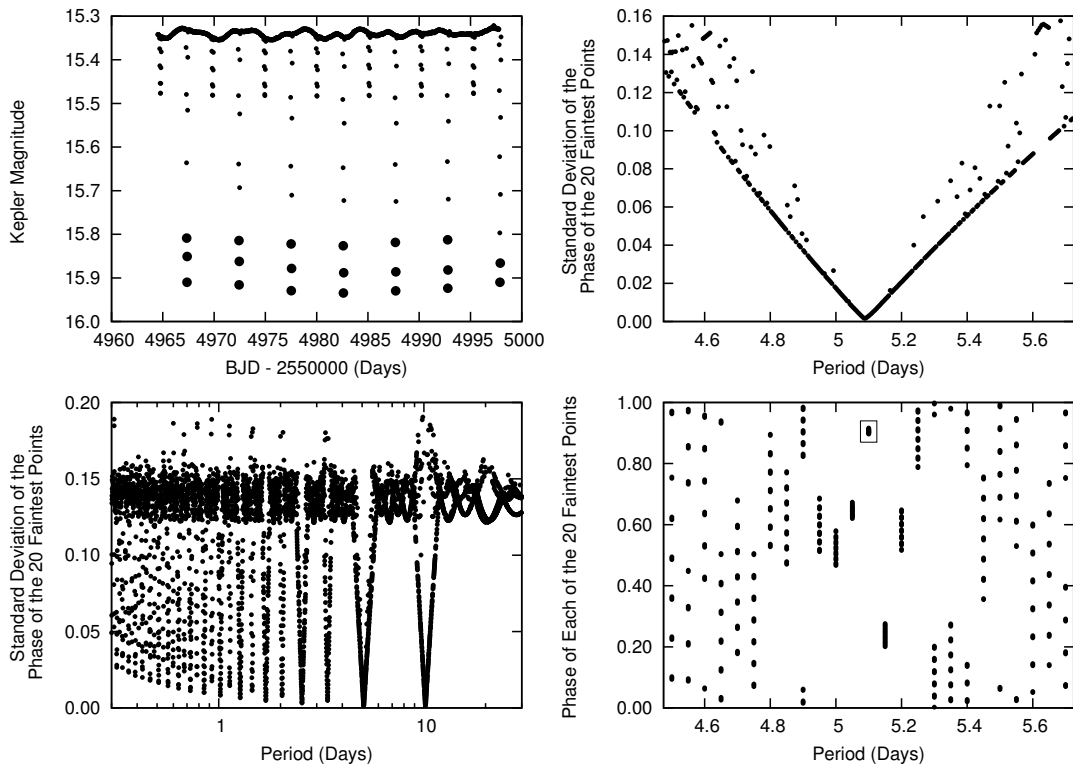


Fig. A.1.— Illustration of the EPDM technique. Top-left: The unphased light curve of Kepler 006591789, with the 20 faintest points highlighted by using larger point sizes. Bottom-left: Standard deviation of the phase values of the 20 faintest points versus period for this system. As can be seen, the standard deviation approaches 0.0 at ~ 5.1 days, and integer multiples and fractions thereof. Top-Right: The same plot as in the bottom-left panel, but with the period range restricted to show only the period with the lowest standard deviation, and true period of the system. Bottom-Right: The actual phase values for each of the 20 faintest points at multiple periods, spanning the same period range, (but with a lower period resolution, for clarity), as the plot in the top-right panel. As can be seen, as the examined period approaches the true period of the system, the phase values of the 20 faintest points strongly clump together, producing a very small standard deviation. The best period is highlighted by a box in the lower-right panel.

value is between 0.0 and 1.0, that will allow the two distinct phase groupings to align. For each value of p_r , if the phase value of a given point is larger than p_r , a new value for the phase of the point, p , is calculated as

$$p = p - 2.0 \cdot (p - p_r) \tag{A.2}$$

The value of p_r which yields the lowest standard deviation for a given trial period is the correct reflection value, and that corresponding lowest standard deviation should be assigned to that trial period. Thus, in the case of an equal depth, eccentric system, where say the N lowest points group around two phases of 0.2 and 0.4, at a value of $p_r = 0.3$, the two distinct groupings would merge into a single group at phase 0.2, with a very small standard deviation at the correct period of the system. As well, in the case where a group of phase points that range from 0.9 to 1.0 and 0.0 to 0.1, p_r allows the points to merge into a single group that only ranges from 0.0 to 0.1. In fact, we have already implemented the use of p_r when generating the bottom-left and top-right plots of Figure A.1.

In conclusion, because EPDM only utilizes the faintest N points of a light curve, the computations are very quick, especially compared to traditional phase dispersion minimization techniques, which utilize every point in a light curve. This also allows for a more precise determination of the period, as one can apply more computing time towards finer period resolution. As well, for the same reason, EPDM is not affected by systematics or varying star spots, as long as their photometric amplitudes are not on the order of or greater than the amplitude of the eclipses. By selecting the faintest point, or the earliest of the N faintest points, one is also given a good value for the time of primary minimum. We have shown EPDM can be applied to both eccentric and non-eccentric binaries, and since a transiting planet's light curve is similar to an eclipsing binary with only one visible eclipse, the technique works equally well for transiting exoplanets. In theory,

EPDM could also be applied to other variables, such as stars with rotating spots, pulsating variables, and contact binaries, although periods for these systems will be less precise than detached eclipsing binaries, due to the broader minima of those systems. In theory though, one may not have to select the faintest points of a light curve, but possibly a very narrow flux range, and achieve the same result.

APPENDIX B. GENETIC ALGORITHMS FOR ECLIPSING BINARIES

As mentioned in the text, in fitting our sample of eclipsing binaries, we have 12 parameters: period, time of primary minimum, inclination, mass ratio, $e \cdot \cos(\omega)$, $e \cdot \sin(\omega)$, surface brightness ratio, sum of the fractional radii, ratio of the radii, out of eclipse flux level, and the amplitude and phase shift of the sinusoid applied to the luminosity of the primary in order to account for spots. We aim to vary these parameters over their entire range of possible solutions, which if left to a grid search for 10^{-3} precision, would require computing on the order of $\sim 10^{36}$ light curves; a computationally prohibitive task. Standard steepest descent minimization schemes such as Levenberg-Marquardt have extreme difficulties in large, multi-parameter solution spaces, especially for eclipsing binaries as the solution space is not at all smooth and has many local minima. Thus, we need a minimization technique that is computationally efficient, not adversely affected by a non-smooth solution space, and able to find the global minimum. These criteria are superbly met by the class of optimization schemes known as Genetic Algorithms (GAs).

In a standard GA, (cf. Charbonneau 1995), light curve parameter sets, called individuals, for an initial population of solutions, are randomly generated within a predefined parameter space, and compared to the observational light curve. Their corresponding χ^2 value is used as a measure of fitness for natural selection, with parameters from fit individuals bred with each other, (subjected to crossover like chromosomes), to create a second generation of new solutions, and parameters from unfit individuals eliminated. After being subject to random mutations, to maintain parameter diversity and ensure discovery of the global minimum, this

second generation is compared to the observational data, and bred into a third generation of solutions. The process continues for a specified number of generations, until a satisfactorily low χ^2 is found. Charbonneau (1995) demonstrated the application of GAs to problems in Astronomy and Astrophysics, specifically fitting galactic rotation curves, finding pulsation periods in δ Scuti stars, and fitting magnetodynamical wind models with multiple critical points, showing how the GA quickly finds the global minimum, regardless of the topography of the solution space. It is this type of GA that has been already been incorporated into the ELC eclipsing binary modeling code, and used with much success (Orosz & Hauschildt 2000; Orosz et al. 2002).

Cantó et al. (2009) recently proposed a new form of GA called an Asexual Genetic Algorithm (AGA). In the AGA, instead of breeding new individuals via crossover, individuals are randomly created within a small predefined parameter space, or breeding box, centered on the fittest members of the previous generation. The size of this breeding box can be shrunk over successive generations to quickly converge to the best-fit solution. As shown by Cantó et al. (2009), the AGA is computationally simpler and more precise since it does not require encoding parameters for crossover, and converges much faster than traditional GAs, without sacrificing any ability to migrate to the global solution, so long as the breeding box size does not decrease too quickly. Cantó et al. (2009) first showed that it far outperformed the standard GA in both computational efficiency and final precision by solving one of the exact same problems presented by Charbonneau (1995). Cantó et al. (2009) additionally demonstrated the application of the AGA to fitting the radial-velocities of extrasolar planets and the spectral energy distributions of young stellar objects.

As eclipsing binary solutions have an even larger parameter space with many local minima than most problems, we make a few modifications to the AGA described by Cantó et al. (2009) to ensure discovery of the global minimum. First, while we do exactly copy the fittest 10% of individuals of one generation to the next generation, to ensure forward progress is always made while maintaining parameter diversity, instead of picking the fittest N members of a generation, each of which breeds M offspring, to create a new generation, we randomly select individuals for breeding by weighting them by a factor of $(1/\chi^2)^2$. This ensures that the fittest individuals breed the most offspring, but still allows for a few less fit individuals to breed, maintaining parameter diversity and exploration of the entire parameter space. Second, instead of randomly creating new members within a breeding box of fit individuals, we randomly select a number for each parameter from a Gaussian probability distribution centered on each parameter of a fit individual. Thus, new individuals are not strictly confined to a breeding box, but merely are very likely to be created near a fit individual, and maintain a very small probability that they will be created at many standard deviations away. This mimics mutation in traditional GAs and ensures that the algorithm will not become trapped in a local minimum. Third, as suggested by Cantó et al. (2009), the standard deviation of this normal distribution is chosen for each parameter to be the standard deviation of that parameter in the entire population, times the function $0.1^{(1/\chi_0^2)}$, where χ_0^2 is the χ^2 value of the fittest member of the population. This allows parameters with the greatest impact on the fit, or the smallest range of possible parameters, such as the out of eclipse flux level, to converge rapidly, while allowing parameters that are less certain to converge more slowly and thoroughly explore their parameter space. Furthermore, via this

method, the standard deviation is shrunk over successive generations, so that the algorithm converges, but only very slowly initially, rapidly increasing as χ_0^2 approaches 1.0, i.e. the global minimum has been found. Finally, we take the fittest 10% of the final generation and perform a standard Levenberg-Marquardt minimization for each member, choosing the member with the resulting lowest χ^2 value as our final solution.

We nominally found, for the eclipsing binaries in our sample, that a population of 100 individuals, bred for 200 generations, does an excellent job of solving the light curves. This only requires the generation of 20,000 light curves, which with the JKTEBOP code only required ~ 3 minutes per light curve to solve on a single 2.0 GHz CPU. Of course, some systems may require a smaller or greater number of individuals and/or generations, but it should not be more than a factor of ~ 2 . One may substantially reduce the number of individuals or generations required, and thus the run time, if one can limit the range of parameter space. For example, if one knows, or wants to assume, the orbit is circular or nearly circular, one could constrain $|e \cdot \cos(\omega)| < 0.1$ and $|e \cdot \sin(\omega)| < 0.1$. Furthermore, the AGA code is extremely parallelizable, and thus with a multi-core computing cluster one could easily use this technique to model thousands of eclipsing binary lightcurves, as is to be expected from Pan-STARRS and other large photometric surveys, in a very reasonable time frame.

To visually demonstrate how the AGA works, we have generated a light curve with the following parameters: $r_{sum} = 0.25$, $k = 1.1$, $i = 89.0^\circ$, $q = 1.2$, $e \cdot \cos(\omega) = 0.1$, $e \cdot \sin(\omega) = -0.1$, $J = 1.1$, $P = 2.20$ days, $T_0 = 312.3$ days, and out of eclipse magnitude = 13.5. We then re-bin this data to match the number of data points in the *Kepler* Q1 data sets, and add typical Gaussian noise for a bright *Kepler*

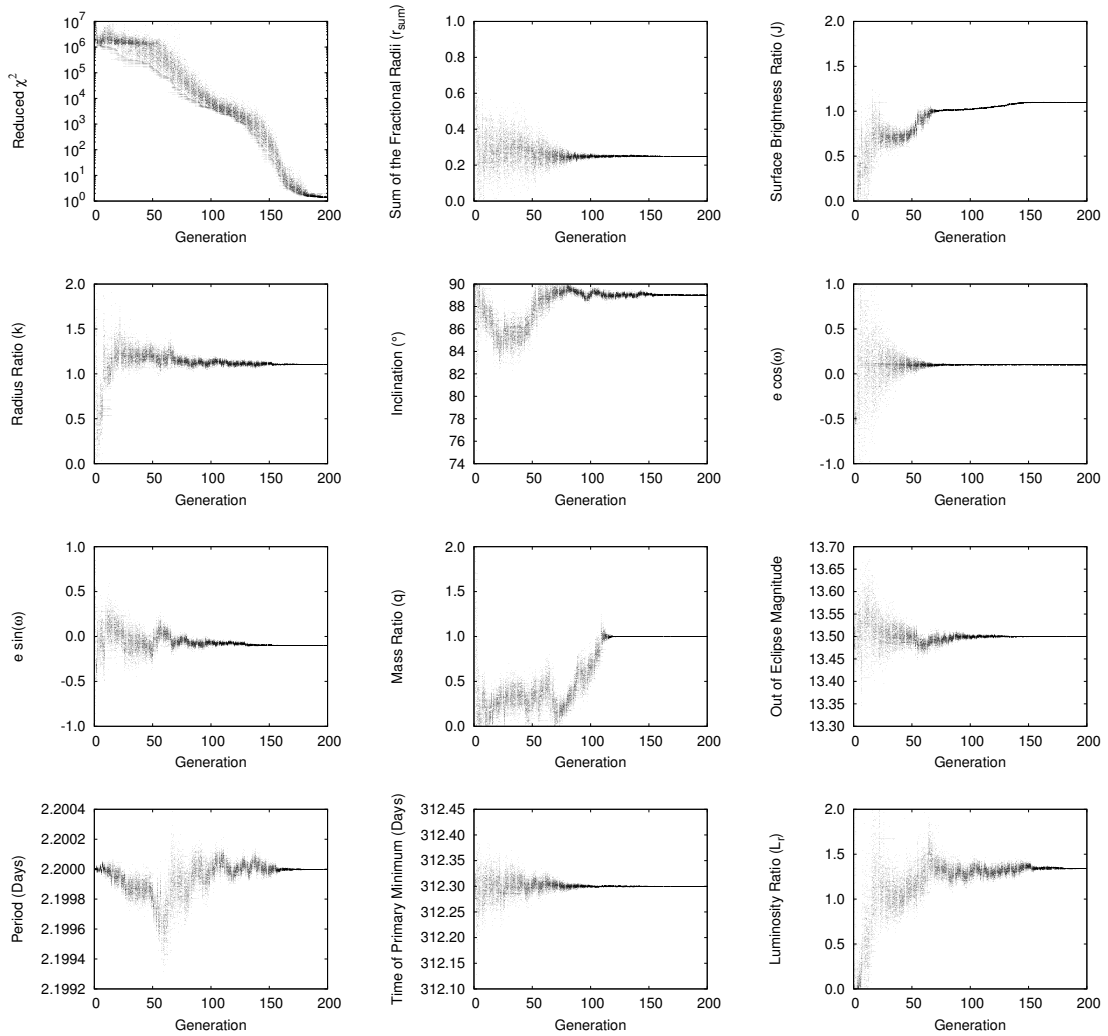


Fig. B.1.— Illustration of how the AGA converges over subsequent generations (x-axis) by solving an artificially generated light curve, re-binned to the number of data points and error typical for a *Kepler* light curve. Each point represents the parameter of each member in each generation. The parameters of the system are $r_{sum} = 0.25$, $k = 1.1$, $i = 89.0^\circ$, $q = 1.2$, $e \cdot \cos(\omega) = 0.1$, $e \cdot \sin(\omega) = -0.1$, $J = 1.1$, $P = 2.20$ days, $T_0 = 312.3$ days, and out of eclipse magnitude = 13.5. The derived reduced χ^2 and luminosity ratio are also plotted. The AGA converges rapidly, decreasing the lowest χ^2 value found by an order of magnitude every ~ 20 generations. It can be seen that the parameters that are most significant to the light curve converge the fastest.

star of 0.1 mmag per data point. We then re-solve this light curve with the AGA, varying all the aforementioned parameters, and show in Figure B.1 the value of

each parameter for every individual in each generation, as well as the values for the derived reduced χ^2 and luminosity ratio. One can see how even while searching over the entire global solution space, the AGA rapidly converges to the solution that was used to generate the light curve, with the χ^2 decreasing by a factor of ~ 10 every ~ 20 generations. Even though the best solution of the 200th generation has $\chi^2 \sim 1.5$, if allowed to continue for more generations, this run would eventually converge to $\chi^2 = 1.0$, and performing a simple Levenberg-Marquardt minimization from the best solution quickly produces a $\chi^2 = 1.0$ fit.

APPENDIX C. MODELING MULTI-WAVELENGTH STELLAR ASTROMETRY: SIM LITE OBSERVATIONS OF INTERACTING BINARIES

C.1. Introduction

The field of stellar evolution has matured to the point that we generally understand the entire evolution of an isolated star if we know its initial mass. While many details remain to be solved, it is unlikely that SIM Lite will provide a revolution in our understanding of the evolutionary processes for single stars of low and intermediate mass. The same cannot be said for binary star systems, where there are at present a number of outstanding issues that remain unsolved. Among the most difficult is how mass transfer proceeds during the common envelope stage that occurs in the post-main sequence lives of close binaries. The formation of nearly every mass transferring binary requires a common envelope phase where the secondary star helps to strip the atmosphere of the primary while driving mass from the system, and shrinking the binary's orbit. Current theory (c.f., Podsiadlowski et al. 2003) has a difficult time explaining the creation of systems with massive black hole primaries ($M_{\text{BH}} \geq 9 M_{\odot}$) and very low mass secondary stars ($M_2 \leq 0.7 M_{\odot}$). Similar problems exist across the mass spectrum of close and interacting binaries (IBs), which for the purposes of the current study include systems with a black hole, neutron star, or white dwarf (WD) primary and a non-degenerate companion. For example, Howell et al. (2001b) explores the well known 2-3 hr period gap observed in cataclysmic variable (CV) systems, which is postulated to be a result of cessation of mass-transfer from the main-sequence, low-mass secondary star to the white dwarf companion for periods between 2-3 hours. Howell et al. (2001b) runs binary population synthesis models that show this theory is only correct if the secondary stars in these systems are up to 50%

oversized, and thus both components are really much less massive than has been typically assumed via standard main-sequence mass-radius-temperature relations. Thus, if accurate masses can be determined for these systems, their formation theories can be directly tested.

Typically in binary star work, radial velocity curves are used to obtain masses for the components. While it can be quite simple to get a radial velocity curve for one component of an IB, (the secondary star if it dominates the luminosity, else typically the disk), it is difficult, or even impossible, to get such data for their black hole, neutron star, or WD primaries. Thus, along with the radial velocity amplitude of the secondary or disk, one must also assume a mass and know the binary orbital inclination in order to solve for the component masses. It is especially difficult to determine the binary inclination. In a large number of IBs the secondary star can be quite prominent at infrared wavelengths, and since the object is distorted, it exhibits ellipsoidal variations as it orbits the primary (c.f. Gelino et al. 2001). The amplitude of these variations are dependent on the orbital inclination, and to a lesser extent, the properties of the secondary star. However, even a small amount of contamination by the accretion disk introduces considerable uncertainty in this method, and nearly all interacting binary systems have some level of contamination from the accretion process. Thus, this technique of using infrared ellipsoidal variations to determine the inclination fails if one cannot ascertain the spectrum and level of the contaminating source.

This paper will show how SIM Lite, with multi-wavelength, microarcsecond astrometry, will be the first mission capable of determining the multi-wavelength astrometric orbits of IBs. The field of optical astrometry has recently been making great progress from both ground-based observations, as well as is posed to

make dramatic leaps with the upcoming space-based missions GAIA and SIM Lite. The limits of ground-based astrometry have been recently pushed by both CHARA and PRIMA/VLTI, but neither are capable of the kind of astrometric measurements needed to probe IBs. CHARA has multi-wavelength capabilities, but can only provide angular resolution to $\sim 200 \mu\text{as}$ (ten Brummelaar et al. 2005), which is far larger than the reflex motions to be discussed in this paper, and requires very bright targets. PRIMA/VLTI will achieve $\sim 30\text{-}40 \mu\text{as}$ precision (van Belle et al. 2008), which may be at the limit of usefulness for these systems, but only in K -band, which does not help distinguish individual component orbits, as will be shown. The GAIA mission will provide astrometry for $\sim 10^9$ objects with 4 - 160 μas accuracy, for stars with $V=10\text{-}20$ respectively, and does possess multi-wavelength capabilities (Cacciari 2009). However, GAIA is a scanning satellite and cannot perform pointed or time-critical observations, and in fact only achieves this accuracy by averaging ~ 80 individual measurements, the individual errors of which range from 36 - 1,431 μas , again for stars with $V=10\text{-}20$ respectively (Mignard 2005). Thus, GAIA cannot provide the high-precision, time-critical pointed observations needed to study IBs. In contrast, SIM Lite will be able to point at any desired object for any length of time, providing single-measurement accuracy of $\sim 1 \mu\text{as}$ (Davidson et al. 2009). As well, SIM Lite will have ~ 80 spectral channels, spanning 450 to 900 nm, thus providing multi-wavelength, microarcsecond astrometry (Davidson et al. 2009).

SIM Lite will offer the first chance at measuring astrometric orbits for a large number of IBs, thus directly yielding inclinations and allowing for the precise measurement of the masses of both components in these systems. Determining the inclination of a zero-eccentricity system from astrometry is as straightforward

as determining the ratio the semi-major and semi-minor axes of the projected ellipse on the sky. Ideally, one can derive accurate values for the masses of both components from the astrometry of a single component (Benedict et al. 2000), but to do so requires that one knows the orbital period, the semi-major axis of the apparent orbit, the parallax of the system, and the mass ratio of the two components. SIM Lite can provide the first three of these four parameters, but the mass ratios must be estimated for many of the main systems of interest. However, for binaries where there is a significant amount of light from more than one component, *SIM Lite can determine absolute masses for both components*. Since SIM Lite only measures the location of the photocenter of the system, the observed reflex motion of the system will be wavelength-dependent. For example, in a binary where one component is hotter than the other, the measured motion in the blue part of the spectrum will be different from that measured in the red, with shorter wavelengths tracing the motion of the hotter component, and vice-versa. Thus, if one has at least two astrometric orbits at different wavelengths, and one knows the ratio of luminosities in each bandpass, (i.e. the spectra of the components), then one could reconstruct the individual orbits of each component and obtain absolute masses for both. Since SIM Lite is currently designed to have ~ 80 spectral channels, and since multi-color photometry and spectroscopy already exists for most IBs of interest, this technique should be quite feasible for most IBs.

In the next section we describe the procedure and code used to model the reflex motions of IBs. In section 3 we examine the results for “proto-typical” systems, including both X-ray binaries and cataclysmic variables, and estimate the required observing time required by SIM Lite to obtain reasonably accurate

parameters for each system. We also briefly investigate how the presence of disk temperature gradients and hotspots in the systems affect the derived orbits. In section 4 we present a full modeling of simulated SIM Lite data for one system, and show the precision and accuracy of recovered astrometric parameters and derived system masses. We summarize our results in section 5.

C.2. The Modeling Procedure: The REFLUX Code

REFLUX¹ is a code that computes the flux-weighted astrometric reflex motions of binary systems. At its core is the Eclipsing Light Curve (ELC) code, which is normally used to compute light curves of eclipsing binary systems (Orosz & Hauschildt 2000). Besides specifying the primary and secondary stars, ELC allows for the inclusion of an accretion disk. As with other light curve modeling programs, an array of physical effects are taken into account, such as non-spherical geometry, gravity brightening, limb darkening, mutual heating, and reflection effects. The program can either use a blackbody formula for local intensities of the stellar components, or interpolate from a large grid of NextGen model atmospheres (Hauschildt et al. 1999). ELC also allows for up to two hot or cool spots to be placed on each star, and on the accretion disk. Thus, ELC can reproduce nearly any binary system, including complicated systems such as cataclysmic variables, RS CVn systems, and Low Mass X-ray Binaries (LMXBs). Additionally, we have modified the ELC code to allow for a mixture of blackbody and model atmosphere intensities for use among different system components, and to allow for the possibility of a free-free, or bremsstrahlung, accretion disk, which follows

¹REFLUX can be run via a web interface from <http://astronomy.nmsu.edu/jlcough/reflux.html>. Additional details as to how to set-up a model are presented there.

the form $F_\lambda \propto T^{-\frac{1}{2}} e^{-\frac{hc}{\lambda kT}} \lambda^{-2}$, where T is the temperature in Kelvin, and F_λ is the flux in power per unit area per unit wavelength, λ .

REFLUX takes input parameters for a specified system and feeds them to the ELC program, which generates an intensity map of the system at a specified phase and wavelength, composed of N points evenly spaced on a grid around each star and the disk, if present. REFLUX then computes the system’s center of light position using the formula

$$(X, Y) = \sum_{i=0}^N F_i \cdot (x, y)_i, \quad (\text{C.1})$$

where (X, Y) is the system’s center of light (“photocenter”), with the center of mass located at $(0,0)$, and F_i is the flux of a grid point i , located at (x, y) . This is done for a complete orbit at 8 different wavelengths, currently chosen to be the standard *UBVRIJHK* bandpasses, with the astrometric reflex motion output in μas using an estimate of the system’s distance. REFLUX also calculates the observed spectral energy distribution (SED) of both the sum and the individual components (as seen at quadrature) for comparison to multi-wavelength photometry to help constrain system parameters. REFLUX will also output a 3D animated gif of the system, the apparent multi-wavelength astrometric orbit, and the x and y components of this motion versus orbital phase. The actual light curves over an orbit are written to a text file for comparison with existing phased-resolved photometric data.

While SIM Lite only operates in the 4500 to 9000 Å bandpass, we include *JHK* photometry into the modeling process to help constrain the SEDs for systems of interest. We do this because it is often possible to detect the secondary star in the near-infrared, allowing one to better quantify its contribution at the

wavelengths accessible to SIM Lite. (For consistency and possible comparison to future work in NIR astrometry, we also include the J and K -band astrometric motions in the output plots.) Thus, before one can model the expected reflex motions for an IB, it is critical to have both reasonable parameters for the system, as well as multi-color photometry. REFLUX requires as inputs estimates of the masses of the two stellar components, their temperatures, their radii, the orbital period, and orbital inclination. The eccentricity of the binary is assumed to be zero since in the majority of these systems the companion star fills its Roche lobe, indicating a close orbit with strong tidal forces. In addition, the V magnitude and distance must be input for model normalization. If the system has an accretion disk, the temperature at its inner edge, the power-law index for the radial dependence of its temperature, and the radius of the inner and outer edges must be inputted. Alternatively, one can choose whether the disk follows a blackbody or free-free emission law. In the latter case, one has to specify and adjust a normalization constant for the luminosity of the disk emission to best match the observed SED. To demonstrate the use of REFLUX, we model several proto-typical IB systems below.

C.3. Modeling the Reflex Motions of Interacting Binaries

It is critical that one uses reasonable system parameters to first match the observed SED before relying on the output reflex motions. There are three main scenarios for the visual SEDs of IBs: 1) systems where one stellar component dominates the optical SED, 2) where more than one component contributes to the optical SED, and 3) disk-dominated systems. Besides the stellar components, and symmetric accretion disks, there are a number of other features that are

present in IB systems such as accretion disk hot spots, accretion streams, magnetic structures, jets, and other outflows that both affect the SED *and* which might have appreciable astrometric signatures. We investigate some of these features below, but to completely cover all of the behavior exhibited by IBs is beyond the scope of the current investigation. In the following we perform case studies for three different IB scenarios, using several well known objects. Additionally, we examine how accretion disk or photospheric “hotspots” can distort the reflex motions of an IB. Finally, for each system we also examine the feasibility of observing the system with SIM Lite, providing rough estimates for the amount of time that will be required of SIM Lite to observe the system at a given precision, using the SIM Differential Astrometry Performance Estimator (DAPE) (Plummer 2010).

C.3.1. IBs with SEDs Dominated by the Primary or Secondary Star

There are quite a number of IBs where the primary or secondary star completely dominates the SED of the system. For these systems, determining an astrometric orbit is straightforward. We examine two cases: 1) QZ Vul, a LMXB with a black hole primary and a cool, main sequence secondary star, and 2) Cyg X-1, a high mass X-ray binary (HMXB) with an O supergiant primary, and a black hole “secondary”.

C.3.1.1. QZ Vul As shown in Gelino et al. (2010), the SED of QZ Vul appears to be that of a reddened K2 dwarf from the optical through the mid-infrared. The system parameters are shown in Table C.1. These parameters were input into REFLUX to model the astrometric motions, with a NEXTGEN model atmosphere used for the secondary star. The model SED, a 3D model of the system, and its

wavelength-dependent reflex motions are shown in Fig. C.1. Since there is only a single visible component, QZ Vul does not exhibit any discernible wavelength dependency to its reflex motions. However, since the black hole is ~ 24 times more massive than the secondary star, the K2 dwarf has a large apparent motion, and thus even at a distance of 2.29 kpc, the system's astrometric reflex motion ($\sim 8 \mu\text{as}$), in theory, would be detectable with microarcsecond astrometry. However, in practice, this particular system is so faint ($V = 21.2$), and has such a short period (0.3342 days), that, according to DAPE, SIM Lite can not reach the needed precision without integrating for longer than the orbital period. Thus, one would need to find a much closer, and thus brighter, LMXB to observe with SIM Lite. The estimated orbital inclination for QZ Vul is 64° (Gelino 2001), and the only effect one would see with a QZ Vul type system with a different inclination is a reduction or amplification of the y-component of the astrometric motion, corresponding to an increase or decrease of the inclination respectively.

C.3.1.2. Cyg X-1 Cyg X-1 is a well-known HMXB dominated by an O-type supergiant orbited by a $10 M_\odot$ black hole with a period of 5.6 d. Cyg X-1 exhibits a wide variety of behavior, such as highly variable X-ray and radio emission, some of which is presumably due to a relativistic jet. The optical light also varies, but much more weakly ($\Delta m \approx 0.05 \text{ mag}$). Thus, in contrast to QZ Vul, the primary star will be the visible source in this system. We model this system using the parameters listed in Table C.2, using a blackbody for the O star. As can be seen in Fig. C.2, there is no wavelength dependence to the astrometric reflex motion, and a single bandpass is sufficient to determine the orbit. Even at a distance of 2.1 kpc, the large separation of the components in Cyg X-1 produces a significant

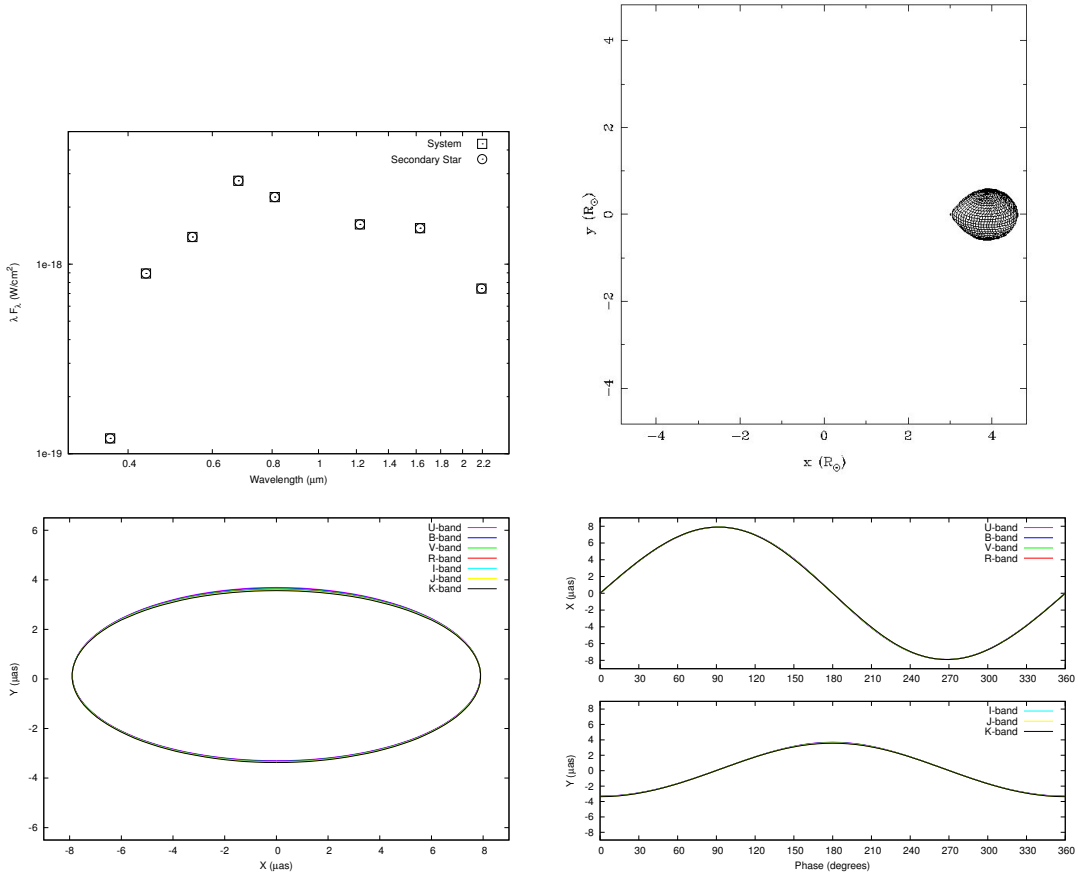


Fig. C.1.— *Top Left*: SED plot for QZ Vul. *Top Right*: 3D model of QZ Vul at Phase=90°. *Bottom Left*: Reflex orbit for QZ Vul. *Bottom Right*: X and Y components of the reflex orbit versus phase for QZ Vul.

astrometric signature ($\sim 25 \mu\text{as}$), even though it is the more massive component that is responsible for the visible astrometric motion in this system. Given the brightness of the system ($V = 8.95$), and the long orbital period, this system is easy to observe with SIM Lite. According to DAPE, 10 individual measurements, each with $2.5 \mu\text{as}$ precision, could be obtained in only a total of 1 hour and 40 minutes of mission time, (given 5 minutes of target integration time per visit, broken into 5, 1-minute chops between the target and reference star.) This would provide

more than sufficient high-precision measurements to obtain a good solution for this system, directly yielding the inclination of the system and the semi-major axis of the primary star's orbit, and thus indirectly the masses of the components. For systems in which one component completely dominates the visual SED, having accurate photometry for the system is unnecessary in interpreting the astrometric data.

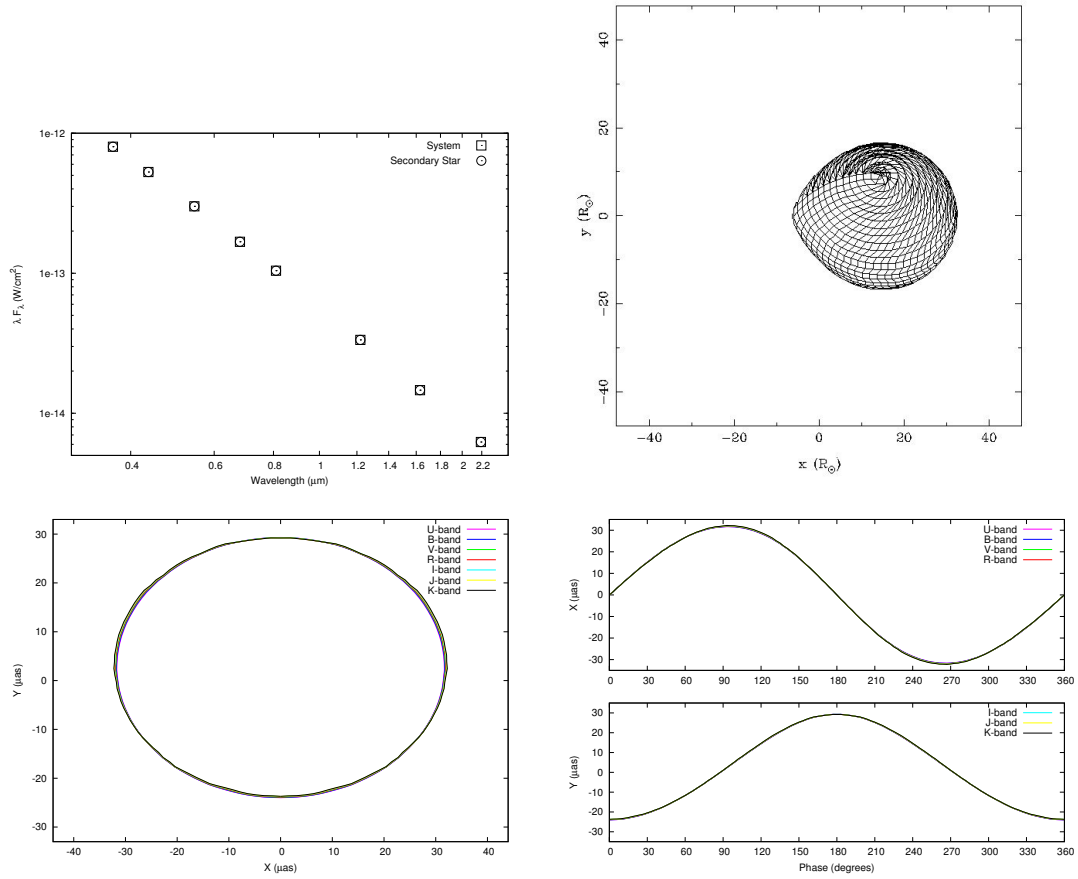


Fig. C.2.— *Top Left:* SED plot for Cyg X-1. *Top Right:* 3D model of Cyg X-1 at Phase=90°. *Bottom Left:* Reflex orbit for Cyg X-1. *Bottom Right:* X and Y components of the reflex orbit versus phase for Cyg X-1.

Table C.1. Parameters for the QZ Vul System

Parameter	Value ^a
Magnitude (V)	21.2
Distance (kpc)	2.29
Inclination (°)	64.0
Period (Days)	0.3342
Eccentricity	0.0
Mass of Star 1 (M_{\odot})	0.32
Mass of Star 2 (M_{\odot})	7.7
Radius of Star 1 (R_{\odot})	0.397 ^b
Radius of Star 2 (R_{\odot})	0.0
T_{eff} of Star 1 (K)	4500
T_{eff} of Star 2 (K)	0

^aValues from Gelino (2001)

^bSecondary star fills Roche lobe

Table C.2. Parameters for the Cyg X-1 System

Parameter	Value ^a
Magnitude (V)	8.95
Distance (kpc)	2.10
Inclination (°)	35
Period (Days)	5.566
Eccentricity	0.0
Mass of Star 1 (M_{\odot})	17.8
Mass of Star 2 (M_{\odot})	10.1
Radius of Star 1 (R_{\odot})	16
Radius of Star 2 (R_{\odot})	0.0
T_{eff} of Star 1 (K)	32000
T_{eff} of Star 2 (K)	0

^aValues from Herrero et al. (1995)

C.3.2. IBs Where the SED is Not Fully Dominated by Either the Primary or Secondary Star

C.3.2.1. SS Cygni SS Cyg is a bright, well-known, cataclysmic variable. In quiescence, SS Cyg has an apparent magnitude of $V = 12.2$. During outbursts, it brightens to $V \sim 8.8$. It has an orbital period of 6.603 hrs, and the secondary star has a spectral type of K5 (Harrison et al. 2004). Dubus et al. (2004) obtained near-simultaneous multi-wavelength photometry of SS Cyg. As shown in Figure 5 of Harrison et al. (2007) the white dwarf and accretion disk dominate the blue end of the SED, while the secondary star becomes prominent in the red and near-infrared. Harrison et al. (2007) modeled the SED of SS Cyg as a combination of the two stellar components plus a free-free accretion disk around the white dwarf. Due to the availability of simultaneous *UBVRIJHK* photometry, and well-constrained stellar parameters, SS Cyg is an ideal system to investigate what happens when more than one component in the binary system is visible. As we demonstrate, SS Cyg has strongly wavelength-dependent astrometric reflex motions. We only consider the reflex motion in quiescence, since during outburst, the luminosity of the system is completely dominated by the hot (10,000 K), optically thick accretion disk.

We have generated a model system with the parameters listed in Table C.3, where the temperatures and radii of the stellar components have been derived from the literature. In the case of SS Cyg, we used a NEXTGEN model atmosphere for the secondary star, and assumed a blackbody for the white dwarf primary. We attempted both blackbody and free-free accretion disk models, and found that the free-free model provides the best match to the photometry. The results are shown in Fig. C.3, where the model SED is compared to the photometry, with the

contributions from each of the three components shown with separate symbols. As can be seen from these plots, the white dwarf dominates the flux contribution in the U -band, and fades thereafter, with the secondary dominating from B through K (though the accretion disk contribution becomes quite important in the infrared). A wire grid representation of the SS Cyg system at phase 0.25 is also shown in Fig. C.3. As shown in the bottom-left panel, the amplitudes of the reflex motions smoothly increase from B (semi-major axis $a = 12 \mu\text{as}$) to R ($a = 28 \mu\text{as}$), and then decline at longer wavelengths due to the contribution of the accretion disk. The reflex motion in the U -band is larger than in B , as it is almost completely dominated by the WD primary. In the B -band, the two stars have similar luminosities, and thus the motions are a mixture of the individual astrometric orbits. If there was no accretion disk, and the white dwarf was invisible, the total amplitude of the reflex motions for the secondary star in this system would be $a = 34.1 \mu\text{as}$. Thus, the true reflex motions are diluted, and one cannot determine the actual astrometric orbit without modeling the system. However, with proper modeling, one can deconvolve the motion of the white dwarf + accretion disk and the secondary star, thus directly yielding the semi-major axis of each component's orbit, which when combined with the well-known period and distance to the system, directly yields absolute masses for each component, (see §4).

Careful examination of the wavelength-dependent astrometric orbits reveals that the actual center about which the motion occurs is wavelength dependent. Note that the U -band reflex motion is centered on $(0,0)$, but at the other wavelengths, the motions are offset from this position. This subtle effect has two causes: 1) the secondary star in SS Cyg fills its Roche lobe, and therefore has

Table C.3. Parameters for the SS Cyg System

Parameter	Value ^a
Magnitude (V)	8.8 (max) 12.20 (min)
Distance (pc)	159.5
Inclination (°)	50.5
Period (Days)	0.275130
Eccentricity	0.0
Mass of Star 1 (M_{\odot})	0.555
Mass of Star 2 (M_{\odot})	0.812
Radius of Star 1 (R_{\odot})	0.684 ^b
Radius of Star 2 (R_{\odot})	0.015
T_{eff} of Star 1 (K)	4400
T_{eff} of Star 2 (K)	35000
Disk Inner Radius (R_{\odot})	0.022
Disk Outer Radius (R_{\odot})	0.407
Disk Inner Temperature (K)	10000 ^c
Disk Temp Power-Law Exponent	0.0

^aValues from Bitner et al. (2007)

^bStar fills its Roche Lobe

^cDisk is free-free

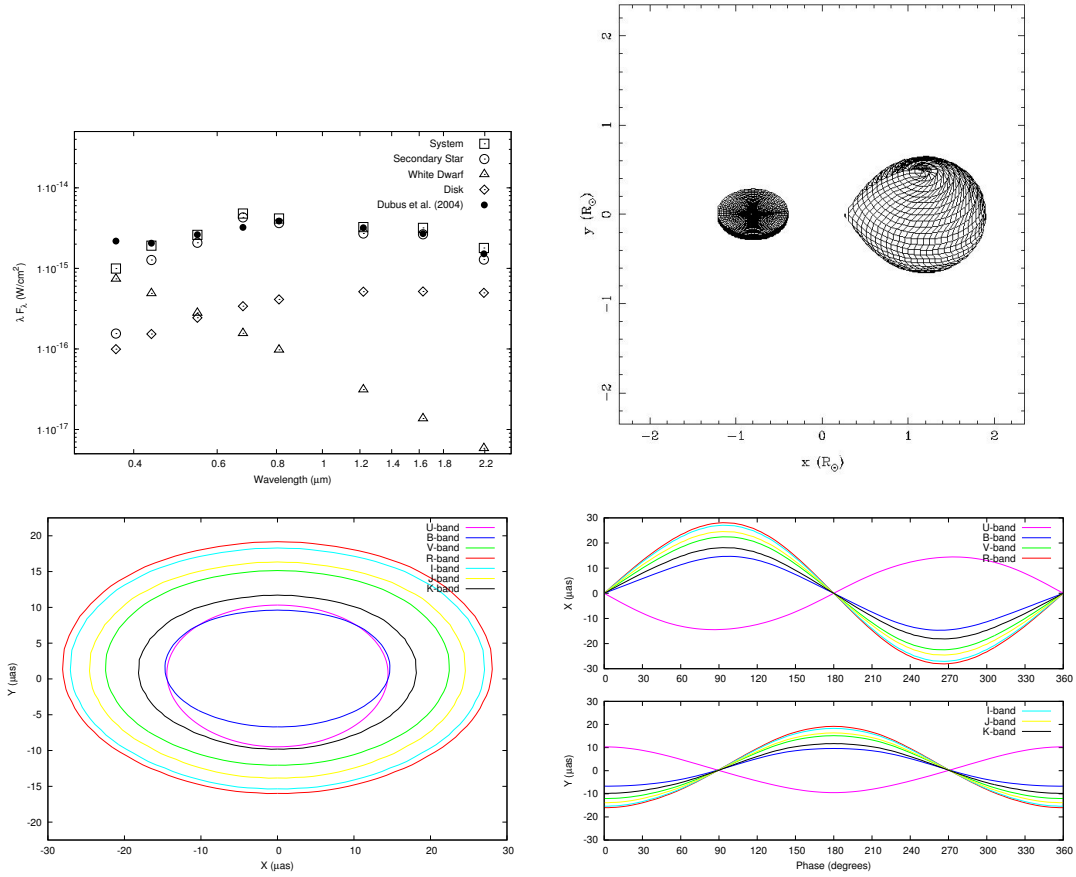


Fig. C.3.— *Top Left*: SED plot for SS Cyg compared to photometry from Dubus et al. (2004). *Top Right*: 3D model of SS Cyg at Phase=90°. *Bottom Left*: Reflex orbit for SS Cyg. *Bottom Right*: X and Y components of the reflex orbit versus phase for SS Cyg.

a teardrop shape, and 2) gravity brightening for non-degenerate stars is significant. These two effects combine to offset the center of light of the secondary star from its center of mass. This creates an offset in the astrometric motions in the bandpasses where the secondary star dominates the systemic luminosity. Since the WD is spherical, and does not have gravity brightening effects, the *U*-band motion remains centered at (0,0). For more detailed modeling on the wavelength dependence of the astrometric center due to gravity brightening, see Coughlin

et al. (2010a).

One of the important consequences of these effects is that the actual orbital inclination is harder to derive. Naively, one would assume that the orbital inclination can be calculated from the ratio of the minor and major axes of the orbital ellipse. If we do this in the R -band [$i = \cos^{-1}(17.5/28.0)$] we derive an orbital inclination of 51.4° , instead of the input value of 50.5° . Depending on the bandpass, the orbital inclinations derived for our simulation of SS Cyg range from a minimum of 47° in the U -band, to a maximum of 51.4° in the R -band! While it is likely that these differences will be lost in the astrometric noise for most IB systems, there will be a small number of IBs (and many non-interacting binary systems) where this difference should be detectable, and proper modeling is required to accurately extract the system's inclination.

With respect to observing this system with SIM Lite, according to DAPE, even in its low state with $V = 12.1$, a total mission time of 6 hours and 40 minutes would provide 10 measurements with respect to an astrometric standard star, each with $1.7 \mu\text{as}$ precision and an individual integration time of 20 minutes per measurement, each composed of 20 chops between the target and reference stars, with 1 minute exposures on the target and 30 second exposures on the reference. As a minimum of 7 points are needed to solve for a full astrometric orbit, (given that 7 parameters describe an orbit), and as the orbital period of SS Cyg is ~ 6.6 hours, this would successfully measure the full astrometric orbit with limited orbital smearing, (see §C.4).

SS Cyg can be used as a template for cases of CVs and LMXBs where the secondary star is clearly visible in the optical. It simply requires changing the

input values of the stellar components, the relative prominence (and nature) of the accretion disk, and altering the orbital inclination. Other changes, such as orbital period, mass ratio, and distance, act to scale the amplitude of the reflex motions. However, it remains critically important to have simultaneous multi-wavelength photometry, and a reasonable handle on the system properties to derive accurate astrometric orbits for these types of objects. As one would expect, the wavelength dependent behavior of the astrometric motions for these types of systems is more complex than for systems with only a single, visible component, but the potential scientific payoff is much higher. When varying the inclination angle for a SS Cyg type system, the y component of the astrometric motion decreases with increasing inclination angle for all wavelengths as expected, but at large inclination angles eclipse effects produce significant deviations from simple sinusoidal reflex motions.

C.3.3. IBs with Accretion Disk Dominated SEDs

The majority of LMXBs, and many CVs, have their optical light dominated by the accretion disk. The accretion disk surrounds the compact object, and thus the observed astrometric motion is that of the compact object, although there are some complications arising from the extended structure of the disk. Here we examine two cases, the short period CV system V592 Cas, and the well-known LMXB Sco X-1.

C.3.3.1. V592 Cas V592 Cas is a short-period ($P_{\text{orb}} = 2.76$ hr) CV system consisting of a Roche lobe-filling M dwarf, a very hot white dwarf, and a disk that dominates the luminosity at optical and near-infrared wavelengths. The majority of short period CVs closely resemble V592 Cas, and thus it can act as a

prototype for disk-dominated CVs. The SED of the system has been investigated by Hoard et al. (2009), who reproduced the observed photometry using a model that included a red dwarf, white dwarf, and a two component blackbody disk around the white dwarf consisting of an inner flat component and an outer flared component. To model the mid-infrared excess, a circumbinary dust disk was also included. This dust disk is only important at mid-infrared wavelengths, and thus can be ignored in this present study. We model the reflex motions of V592 Cas using the parameters from Hoard et al. (2009) shown in Table C.4, while using a single component blackbody disk model with a flare inclination that is the average of the angles in their two component disk model. The SED produced by REFLUX is compared to that of Hoard et al. (2009) in Fig. C.4, where the contributions from each component are also shown. We find a greater contribution of flux from the M dwarf compared to Hoard et al. (2009), by a factor of ~ 1.75 . This is most likely due to the fact that Hoard et al. (2009) used the spectrum of a field M5.0V dwarf, while our model, which incorporates full Roche geometry, produces a star with the same effective temperature, but a larger surface area by the same factor of ~ 1.75 , adopting the radius for an isolated M5.0V as $0.21 R_{sun}$, as shown by recent measurements of low-mass stars (c.f., López-Morales 2007). Either way, the M dwarf is a few percent of the total system flux, and thus does not greatly affect the derived astrometric measurements.

As seen in Figure C.4, due to the domination by the disk, the system shows less wavelength dependent motion than SS Cyg. However, there is still a discernible effect towards longer wavelengths as the secondary becomes a more significant source of flux. Thus, with enough measurements, one could in theory derive the individual component masses. The influence of the orbital inclination

Table C.4. Parameters for the V592 Cas System

Parameter	Value ^a
Magnitude (V)	12.8
Distance (pc)	364.0
Inclination (°)	28.0
Period (Days)	0.115063
Eccentricity	0.0
Mass of Star 1 (M_{\odot})	0.210
Mass of Star 2 (M_{\odot})	0.751
Radius of Star 1 (R_{\odot})	0.270 ^b
Radius of Star 2 (R_{\odot})	0.014
T_{eff} of Star 1 (K)	3030
T_{eff} of Star 2 (K)	45000
Disk Inner Radius (R_{\odot})	0.0106
Disk Outer Radius (R_{\odot})	0.371
Disk Inner Temperature (K)	109,700 ^c
Disk Temp Power-Law Exponent	-0.75

^aValues from Hoard et al. (2009)

^bStar fills its Roche Lobe

^cDisk is blackbody

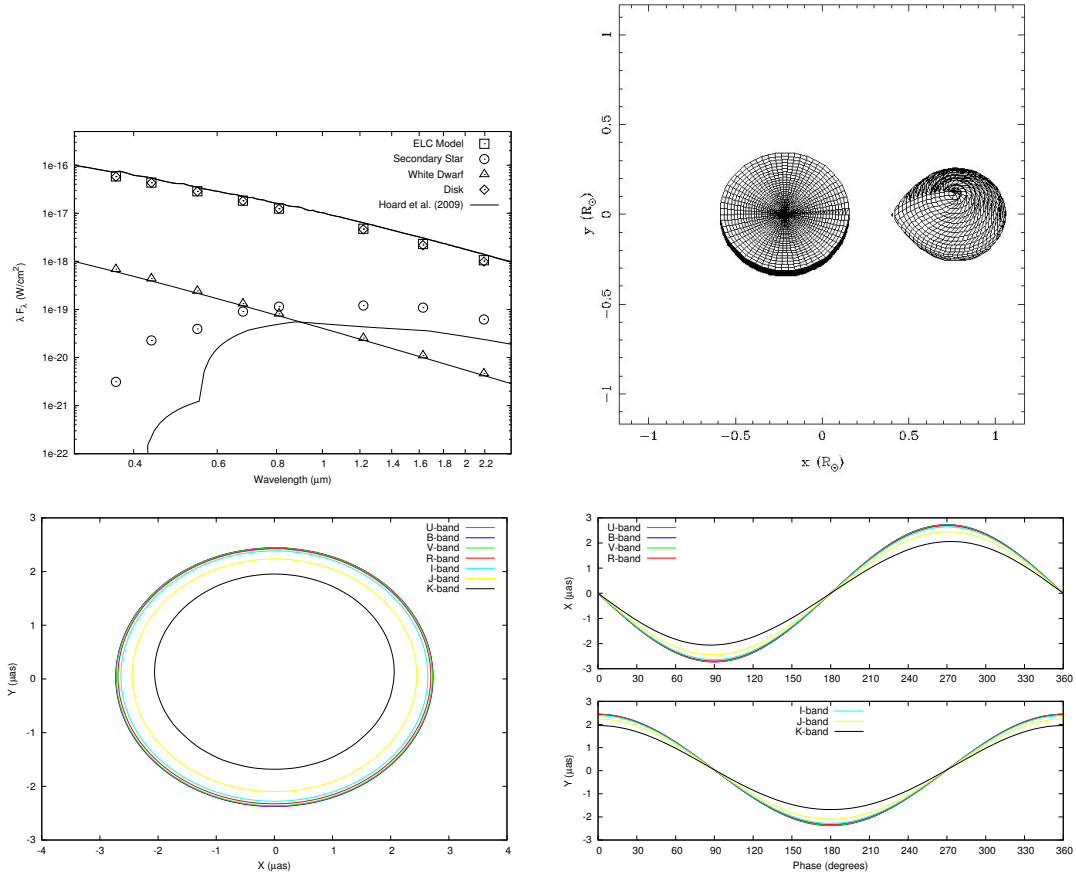


Fig. C.4.— *Top Left:* SED plot for V592 Cas compared to models from Hoard et al. (2009). *Top Right:* 3D model of V592 Cas at phase 0.5. *Bottom Left:* Reflex orbit for V592 Cas. *Bottom Right:* X and Y components of the reflex orbit versus phase for V592 Cas.

is readily apparent, and is uncontaminated by the secondary star gravity effects that were visible in our models for SS Cyg. With respect to SIM Lite observing time, this system would require a moderate amount of SIM Lite mission time, given its small amplitude and short period. According to DAPE, if we constrain individual integration times to 15 minutes, (0.1 of the orbital period), to prevent orbital smearing, one could obtain $2.3 \mu\text{as}$ precision per visit (composed of 20 target-reference chops of 45 second target integration each), which is on par with

the amplitude of the observed reflex motions. Thus, in comparison to SS Cyg and Cyg X-1, discussed above, one might need more than 10 measurements to build up signal-to-noise and really nail down the system parameters. 30 measurements would take a total mission time of 17.5 hours, and thus we can say with reasonable confidence that this system would require less than a day of total mission time to observe so that the astrometric parameters could be obtained with reasonable precision.

We decided to use this system to investigate the possibility of using the multi-wavelength astrometric capability of SIM Lite to discern two more subtle properties of disk-dominated systems: the disk temperature gradient and disk hotspots. The disk model employed in ELC allows for an inner disk temperature to be specified, along with a power law exponent, so that the disk temperature will vary radially according to the formula

$$T(r) = T_{inner} \cdot \left(\frac{r}{R_{inner}}\right)^\chi, \quad (\text{C.2})$$

where T is the temperature at a given distance from the compact object, r , given a temperature T_{inner} at the innermost radius, R_{inner} , and a power law exponent χ (Orosz & Hauschildt 2000). Usually a value of $\chi = -0.75$ is assumed for a steady-state disk (Pringle 1981), but we wanted to test if changing χ to -0.5 or -1.0 , (which physically reflect a centrally irradiated disk (Friedjung 1985; Vrtilik et al. 1990; Bell 1999) and its corresponding extrema), would have a discernible effect on the wavelength dependent astrometric reflex motion. Thus, we produced two models, one with $\chi = -0.5$ and the other with $\chi = -1.0$, while also adjusting the inner disk temperature so that the resulting SED best matched that with $\chi = -0.75$. Neither the SEDs nor the reflex motions differed significantly from the

models that used $\chi = -0.75$. Thus, it will not be possible to constrain the overall temperature gradient in accretion disks using astrometry.

C.3.3.2. Sco X-1 In many CV systems, the optical light is orbitally modulated due to the presence of a hotspot on the outer edge of the accretion disk. This hotspot is where the accretion stream from the secondary impacts the disk. These spots typically have temperatures of 20,000 K, and can produce modulations on order of $\pm 50\%$ in visible bandpasses (Mason et al. 2002). Because this feature is on the outer edge of the disk, it has the potential to distort the reflex motions in systems where it is prominent. In addition, due to its higher temperature than the surrounding disk, the hotspot could be the source of strong line emission, especially in HI or HeI lines (Skidmore et al. 2002). Thus, its detection might be isolated, and the reflex motions amplified, using very narrow bandpasses centered on the strongest emission lines. To investigate the effects of a hotspot, we used the same V592 Cas model as above, but added a hotspot (20,000 K) on the outer edge of the accretion disk that leads the secondary by 30° in phase, and that is 30% of the V -band flux. The differences between a model with a spot, and one without are extremely slight, with a maximum difference in models with and without a spot of $0.15 \mu\text{as}$. Increasing the inclination of the system does not have a significant effect. To be even remotely detectable, V592 Cas would have to be ~ 3 times closer, making the spot signature $\sim 0.5 \mu\text{as}$, although it would still only be $\sim 5\%$ of the reflex amplitude signature. Unless an IB has a hotspot that is much more dominant, such features will remain undetectable.

Sco X-1 is the proto-type LMXB consisting of a neutron star accreting from a low-mass companion. The X-ray luminosity of Sco X-1 is very close to the Edding-

ton limit for a $1.4 M_{\odot}$ neutron star. The secondary star in Sco X-1 has never been directly detected, though an orbital period of 0.787 days was detected through the analysis of 85 years of visual photometry (Gottlieb et al. 1975), and from radial velocity measurements (LaSala & Thorstensen 1985). Steeghs & Casares (2002) detected narrow HI emission lines that they showed are from the irradiated secondary star. From these data they estimate masses for the components in this system of $M_1 = 1.4 M_{\odot}$ and $M_2 = 0.42 M_{\odot}$, thus making the secondary star a significantly evolved subgiant. Since the accretion disk dominates the spectrum, we have simply assumed a Roche lobe-filling M type secondary star corresponding to the observed mass, and an invisible neutron star. The stellar and accretion disk parameters are listed in Table C.5, and the accretion disk model we employ is similar to that for V592 Cas.

As seen in Figure C.5, the accretion disk dominates until the near-infrared when the secondary star begins to contribute. Thus, as also seen in Figure C.5, the reflex motion has a weak wavelength dependence, but SIM Lite cannot observe in the near infrared where the reflex motion reverses, and thus it will be difficult to disentangle the components with such a weak wavelength dependence in the optical. However, it might be possible to recover the contribution to the astrometric reflex motion for systems with slightly more prominent secondary stars (e.g., Cyg X-2). As seen in Figure C.5, Cyg X-1 has a very small reflex motion, only $\sim 1.25 \mu\text{as}$, and can get relatively faint, ($V = 14.1$ at its faintest), and thus this system is just at the limit of SIM Lite’s capabilities. Adopting the faintest magnitude of 14.1 of the system to be conservative, and limiting ourselves to observations of 110 minutes, (0.1 of the orbital period), to prevent orbital smearing, we find via DAPE that we can achieve individual measurements with precisions

Table C.5. Parameters for the Sco X-1 System

Parameter	Value ^a
Magnitude (V)	11.1 (max) 14.1 (min)
Distance (kpc)	2.80
Inclination ($^{\circ}$)	50.0
Period (Days)	0.7875
Eccentricity	0.0
Mass of Star 1 (M_{\odot})	0.42
Mass of Star 2 (M_{\odot})	1.4
Radius of Star 1 (R_{\odot})	1.473 ^b
Radius of Star 2 (R_{\odot})	0.000
T_{eff} of Star 1 (K)	4500
T_{eff} of Star 2 (K)	0
Disk Inner Radius (R_{\odot})	0.026
Disk Outer Radius (R_{\odot})	1.011
Disk Inner Temperature (K)	100 000 ^c
Disk Temp Power-Law Exponent	-0.75

^aValues from Steeghs & Casares (2002), Gottlieb et al. (1975), and LaSala & Thorstensen (1985)

^bStar fills its Roche Lobe

^cDisk is blackbody

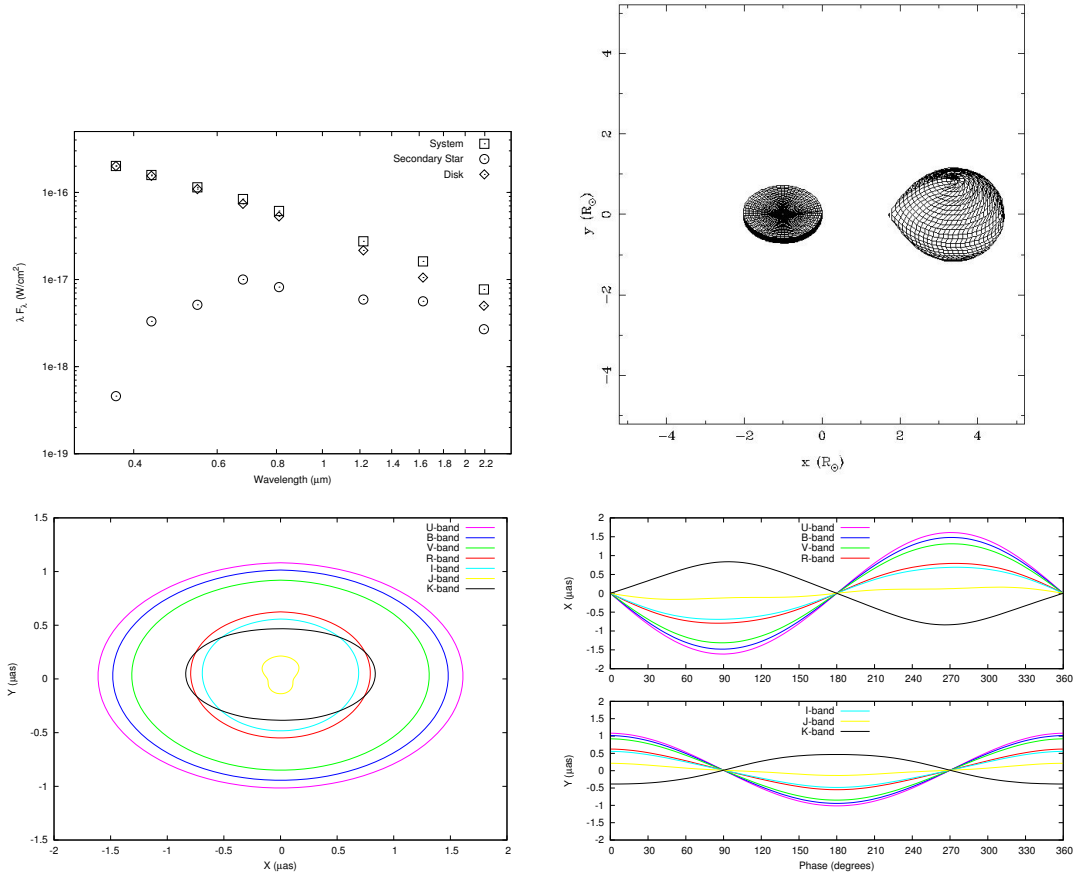


Fig. C.5.— *Top Left*: SED plot for Sco X-1. *Top Right*: 3D model of Sco X-1 at Phase=90°. *Bottom Left*: Reflex orbit for Sco X-1. *Bottom Right*: X and Y components of the reflex orbit versus phase for Sco X-1.

of 2.2 μas , almost twice the semi-major axis of the system. Thus, assuming we would need at least 50 measurements to begin to derive a reasonable orbit for this system, this system would require at least 4 days of SIM Lite mission time, which may prove more expensive than the scientific payoff justifies. If we are able to observe in its high state when $V = 11.1$, we could achieve 30 measurements with 1.5 μas precision in only 20 hours of mission time, which is far more reasonable. When varying the inclination of a Sco X-1 type system, the contribution from the

secondary star becomes more significant as more of the disk becomes self-eclipsed and its total luminosity decreases, and thus alters the individual wavelength reflex motions accordingly.

C.3.4. Polars and the Astrometric Signature of Magnetic Threading Regions

C.3.4.1. AR UMa AR UMa is a “polar”, a CV with a highly magnetic WD primary and a Roche lobe filling M5/6 dwarf (Harrison et al. 2005). As shown in Szkody et al. (1999), the V -band light curve is complex, being dominated by phase-dependent cyclotron emission. The near-IR light curve shows normal ellipsoidal variations, allowing Howell et al. (2001a) to estimate an orbital inclination of 70° . The magnetic field strength in AR UMa has been estimated to be as high as $B = 240$ MG, though Howell et al. (2001a) argue for a lower value of 190 MG. In these systems, at some point after material from the secondary star has passed through the inner Lagrangian point, it is captured by the magnetic field of the white dwarf, producing a “magnetic threading region” that can be a significant source of luminosity in H_α . We investigate the possibility of astrometrically detecting this region via the following modeling process. We model the system as a white dwarf + red dwarf system without an accretion disk, using the parameters shown in Table C.6, but for *only* the H_α bandpass add a narrow “accretion” disk halfway between the inner Lagrangian point and the WD. This disk then has a hot spot leading the inner Lagrangian point by 45° in phase. The actual contribution from the disk has been made to be completely negligible, but the spot itself makes the system 25% brighter in H_α . In effect, it is an isolated emission spot located between the WD and secondary star, mimicking a threading region.

Table C.6. Parameters for the AR UMa System

Parameter	Value ^a
Magnitude (V)	14.50 (max) 18.00 (min)
Distance (pc)	85.0
Inclination (°)	65.0
Period (Days)	0.0805
Eccentricity	0.0
Mass of Star 1 (M_{\odot})	0.70
Mass of Star 2 (M_{\odot})	1.40
Radius of Star 1 (R_{\odot}) ^b	0.322
Radius of Star 2 (R_{\odot})	0.013
T_{eff} of Star 1 (K)	3200
T_{eff} of Star 2 (K)	35000

^aValues from Howell et al. (2001a) and Harrison et al. (2005)

^bStar fills its Roche Lobe

^cDisk is free-free

As can be seen in Figure C.6, there is a large amount of wavelength dependent astrometric reflex motion as expected, ranging from $\sim 10\text{-}20 \mu\text{as}$ in the optical, with the WD dominating at short wavelengths and the secondary star dominating at long wavelengths. This should easily allow the determination of both component masses with orbital coverage at a few passbands. According to DAPE, limiting individual observations to 12 minutes, (0.1 of the orbital period), to prevent orbital smearing, one could obtain individual measurements of $\sim 6 \mu\text{as}$ precision at the system's brightest, ($V = 14.5$), or $\sim 48 \mu\text{as}$ at its faintest, ($V = 18.0$). Thus, in its high state one could obtain 30, $\sim 6 \mu\text{as}$ precision, measurements in as little as 9 hours of total mission time, but in its low state, assuming 100, $\sim 48 \mu\text{as}$ precision, measurements would yield a meaningful solution, a total mission time of 30 hours would be required, which is still a reasonable amount of time for the scientific payoff in our opinion.

Of particular interest is that in H_α the threading region produces a detectable astrometric signature that has a phase offset of $\sim 15^\circ$ from the broadband wavelengths, due to the original 45° offset of the hot spot diluted by the light from the rest of the system. Thus, through use of narrow-band astrometry, one could recover the location of the threading accretion regions in these types of systems. When varying the inclination angle for a AR UMa type system, the y component of the astrometric motion decreases with increasing inclination angle for all wavelengths as expected, but at large inclination angles eclipse effects produce significant deviations from simple sinusoidal reflex motions.

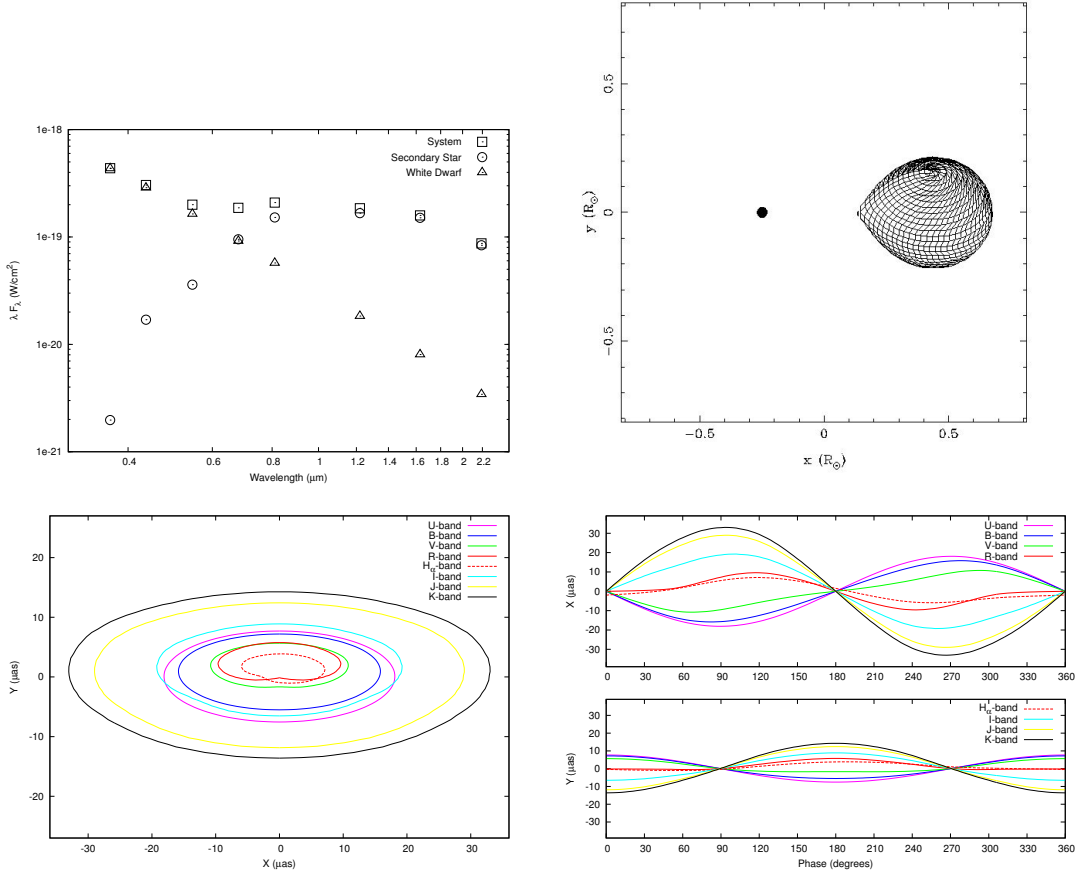


Fig. C.6.— *Top Left:* SED plot for AR UMa. *Top Right:* 3D model of AR UMa at Phase=90°. *Bottom Left:* Reflex orbit for AR UMa. *Bottom Right:* X and Y components of the reflex orbit versus phase for AR UMa.

C.4. Simulated SIM Observations

Although it is beyond the scope of this paper to perform a full simulation of exactly what parameters and to what precision one could extract with a given amount of SIM Lite time at specific wavelengths for each system, we can present a basic analysis for the SS Cyg system. To test the accuracy and precision to which we can recover system parameters, we generated simulated astrometric data for SS Cyg in the U and V -bands, using the parameters listed in Table C.3, but with

an inclination of 54.0° , comprised of 10 measurements at random phases with $1.7 \mu\text{as}$ Gaussian noise added to each measurement. We then simultaneously solved for the astrometric parameters of period, semi-major axis, inclination, the position angle of the line of nodes, and the angle in the plane of the true orbit between the line of nodes and the major axis, while fixing the eccentricity and the epoch of passage through periastron to be zero, using the GAUSSFIT program (Jefferys et al. 1988), with a procedure described in Benedict et al. (2001). We recover inclinations of 55.6 ± 5.1 and 54.0 ± 3.8 degrees, and semi-major axes of 13.58 ± 0.94 and $23.58 \pm 1.28 \mu\text{as}$, each for the U and V -bands respectively. Given the distance to the system of 159.5 parsecs (Dubus et al. 2004), and assuming that 58% of the U -band astrometric motion results from the white dwarf, and 69% of the V -band flux results from the secondary star, as per the modeling, (see §3.2.1), this yields masses of 0.559 ± 0.070 and $0.815 \pm 0.096 M_\odot$ for the secondary star and white dwarf respectively, compared to the input masses of 0.555 and $0.812 M_\odot$. Thus, one will be able to disentangle individual component masses with reasonable uncertainties for this system with only ~ 8 hours of SIM mission time.

C.5. Conclusion

We have presented a modeling code, REFLUX, that is capable of modeling the multi-wavelength astrometric signature of interacting binaries. We have presented models for multiple IB systems, and find that for primary or secondary star dominated systems, the contamination of the photocenter is minimal and SIM Lite will provide good astrometric orbits if the system is bright enough, yielding absolute inclinations and indirect masses. For mixed component systems, SIM Lite will be able to directly determine absolute masses for both components

when multi-wavelength astrometric curves are obtained and combined with existing spectroscopy and multi-color photometry. For disk-dominated systems, SIM Lite will only be able to obtain astrometric orbits for a few systems, due to the small relative motion of the compact object that the disk surrounds, but these should yield accurate inclinations. We find that while multi-wavelength SIM Lite data will be unable to distinguish between various disk temperature gradients and disk hotspots, it should be able to determine the location of magnetic threading regions in polars, and thus similar effects in other systems, via narrow wavelength astrometry. In total, SIM Lite should contribute greatly to our understanding of interacting binary systems, especially if its multi-wavelength capability is maintained in the final design.

APPENDIX D. MODELING MULTI-WAVELENGTH STELLAR ASTROMETRY: DETERMINING ABSOLUTE INCLINATIONS, GRAVITY DARKENING COEFFICIENTS, AND SPOT PARAMETERS OF SINGLE STARS WITH SIM LITE

D.1. Introduction

SIM Lite is currently expected to have ~ 80 spectral channels (Davidson et al. 2009), spanning 450 to 900 nm, thus allowing multi-wavelength microarcsecond astrometry, which no current or planned ground or space-based astrometric project, (GAIA, CHARA, VLT/PRIMA, etc.) is able to match. We showed in Appendix C the implications multi-wavelength microarcsecond astrometry has for interacting binary systems. In this paper, we discuss an interesting effect we encountered while modeling binary systems, namely that gravity darkening in stars produces a wavelength dependent astrometric offset from the center of mass that increases with decreasing wavelength. It is possible to use this effect to derive both the inclination and gravity darkening exponent of a star in certain cases.

Determining the absolute inclination of a given star has many practical applications. There is much interest in the formation of binary stars, where whether or not the spin axis of each star is aligned with the orbital axis provides insight into the formation history of the system (Turner et al. 1995). The mutual inclination between the stellar spin axes and orbital axis can greatly affect the rate of precession, which is used to probe stellar structure and test general relativity (Sterne 1939a,b,c; Kopal 1959; Jeffery 1984). Albrecht et al. (2009) recently reconciled a 30-year-old discrepancy between the observed and predicted precession rate of DI Herculis through observations which showed the stellar spin axes were nearly perpendicular to the orbital axis. Along similar lines, extrasolar planets

discovered via the radial velocity technique only yield the planetary mass as a function of the inclination of the orbit (Mayor & Queloz 1995; Noyes et al. 1997; Marcy & Butler 2000), and thus, if one assumes the planetary orbit and stellar rotation axes are nearly parallel, determining the absolute inclination of the host star yields the absolute mass of the planet. If the stellar spin axis is found not to be parallel to the planetary orbital axis, this provides valuable insights into the planet’s formation, migration, and tidal evolution histories (Winn et al. 2006; Fabrycky & Winn 2009). A final example is the study of whether or not the spin axes of stars in clusters are aligned, which both reveals insight into their formation processes, as well as significantly affects the determination of the distances to those clusters (Jackson & Jeffries 2010).

Our proposed technique can also be used in conjunction with other methods of determining stellar inclination to yield more precise inclination values and other stellar parameters of interest. Gizon & Solanki (2003) and Ballot et al. (2006) have shown that one can derive the inclination of the rotation axis for a given star using the techniques of astroseismology given high-precision photometry with continuous coverage over a long baseline, such as that provided by the *CoRoT* and *Kepler* missions. This technique is sensitive to rotation rates as slow as the Sun’s, but becomes easier with faster rotation rates. Domiciano de Souza et al. (2004) discuss how spectro-interferometry can yield both the inclination angle and amount of differential rotation for a star, parameterized by α . For both eclipsing binaries and transiting planets, the observation of the Rossiter-McLaughlin (RM) effect can yield the relative co-inclination between the two components (Winn et al. 2006; Albrecht et al. 2009; Fabrycky & Winn 2009). The technique we propose in this paper would be complementary to these techniques in several ways. First, it would

provide an independent check on the derived inclination axis from each method, confirming or refuting the astroseismic models and spectro-interferometric and RM techniques. Second, in principle the astroseismic technique is not dependent on the gravity darkening coefficient β_1 , and the spectro-interferometric technique is correlated with the value for α ; combining techniques would yield direct and robust observationally determined values for i , α , and β_1 . Finally, the accurate, observational determination of α and β_1 , (along with stellar limb-darkening), is critical to accurately deriving the co-inclination from the RM effect, as well as other quantities in stellar and exoplanet astrophysics.

In this paper, we also present models for and discuss the determination of spot location, temperature, and size on single stars, which produce a wavelength-dependent astrometric signature as they rotate in and out of view. Star spots are regions on the stellar surface where magnetic flux emerges from bipolar magnetic regions, which blocks convection and thus heat transport, effectively cooling the enclosed gas, and thus are fundamental indicators of stellar magnetic activity and the internal dynamos that drive it. İşik et al. (2007) discuss how the observation of spot location, duration, stability, and temperature can probe the stellar interior and constrain models of magnetic flux transport. Through the observation of the rotation rates of starspots at varying latitudes, one is able to derive the differential rotation rate of the star (Collier Cameron 2002), which may be directly related to the frequency of starspot cycles. Mapping spots in binary star systems provides insight into the interaction between the magnetic fields of the two components, which can cause orbital period changes (Applegate 1992), radii inflation (López-Morales 2007; Morales et al. 2008), and may possibly explain the ~ 2 -3 hour period gap in cataclysmic variable systems (Watson et al. 2007). De-

tecting and characterizing star spots via multi-wavelength astrometry would be complementary to other existing techniques, namely optical interferometry (Witkowski et al. 2002), tomographic imaging (Donati et al. 2006; Aurière et al. 2008), photometric monitoring (Alekseev 2004; Mosser et al. 2009), and in the future, microlensing (Hwang & Han 2010).

We present the details of our modeling code, `REFLUX`, in Section D.2, discuss the inclination effect and present models for multiple stars in Section D.3, discuss the spot effects and present models in Section D.4, and present our conclusions in Section D.5.

D.2. The `REFLUX` Code

`REFLUX`¹ is a code that computes the flux-weighted astrometric reflex motion of binary systems. We discussed the code in detail in Appendix C, but in short, it utilizes the Eclipsing Light Curve (ELC) code, which was written to compute light curves of eclipsing binary systems (Orosz & Hauschildt 2000). The ELC code represents the surfaces of two stars as a grid of individual luminosity points, and calculates the resulting light curve given the provided systemic parameters. ELC includes the dominant physical effects that shape a binary’s light curve, such as non-spherical geometry due to rotation, gravity darkening, limb darkening, mutual heating, reflection effects, and the inclusion of hot or cool spots on the stellar surface. For the work in this paper we have simply turned off one of the stars, thus allowing us to probe the astrometric effects of a single star. To

¹`REFLUX` can be run via a web interface from <http://astronomy.nmsu.edu/jlcough/reflux.html>. Additional details as to how to set-up a model are presented there.

compute intensity, ELC can either use a blackbody formula or interpolate from a large grid of NextGen model atmospheres (Hauschildt et al. 1999). For all the simulations in this paper, we have used the model atmosphere option, and will note now, and discuss more in detail later, that the calculation of limb-darkening is automatically included in NextGen model atmospheres. These artificially derived limb-darkening coefficients have recently been shown to be in error by as much as $\sim 10\text{-}20\%$ in comparison to observationally derived values (Claret 2008), and thus their uncertainties must be included, although for this work, due to symmetry, we find the introduced error is negligible. For all our simulations, we model the U , B , V , R , I , J , H , and K -bands for completeness and comparison to future studies, though we note that SIM Lite will not be able to observe in the U , J , H , or K bandpasses.

D.3. Inclination and Rotation

The astrophysical phenomenon of gravity darkening, also sometimes referred to as gravity brightening, is the driving force behind the ability to determine the inclination of a single star using multi-wavelength astrometry. A rotating star is geometrically distorted into an oblate spheroid, such that its equatorial radius is greater than its polar radius, and thus the poles have a higher surface gravity, and the equator a lower surface gravity, than a non-rotating star with the same mass and average radius. This increased surface gravity, g , at the poles results in a higher effective temperature, T_{eff} , and thus luminosity; decreased g at the equator results in a lower T_{eff} and luminosity. This temperature and luminosity differential causes the star's center of light, or photocenter, to be shifted towards the visible pole, away from the star's gravitational center of mass. Since the in-

clination determines how much of the pole is visible, the amount of displacement between the photocenter and the center of mass is directly related to the inclination. Furthermore, since the luminosity difference effectively results from a ratio of blackbody luminosities of differing temperatures, the effect is wavelength dependent, with shorter wavelengths shifted more than longer wavelengths. Thus, the amount of displacement between the measured photocenter in two or more wavelengths is directly related to the inclination. See Figure D.1 for an illustration of the effect.

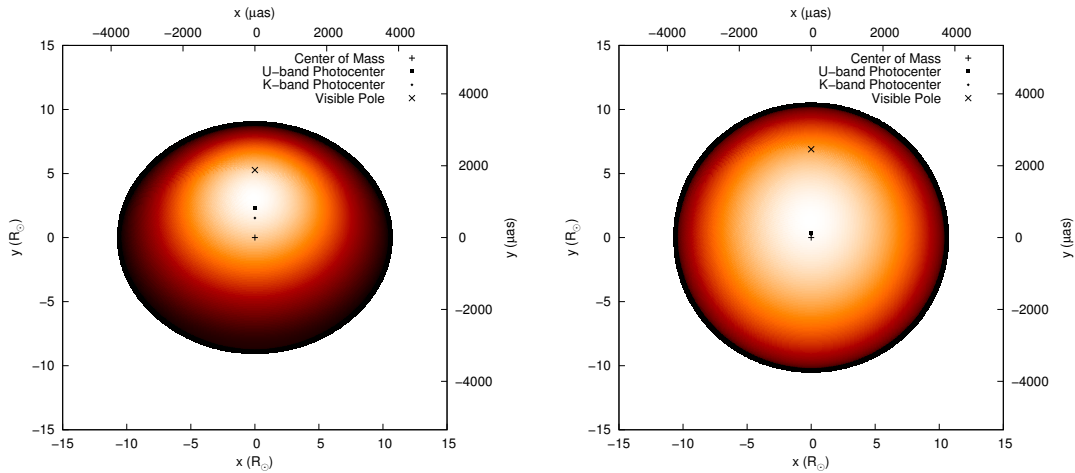


Fig. D.1.— Illustration of the inclination effect using brightness maps of Capella Ab, which has an inclination of 42.788° (Torres et al. 2009). Left: Capella Ab artificially spun-up to near its break-up speed, to accentuate the gravity darkening effect for ease of viewing. As can be seen, the photocenter of the system is dramatically shifted away from the center of mass, towards the visible pole, which is brighter than the rest of the star due to gravity darkening. Furthermore, since the pole is physically hotter, the U -band photocenter is shifted more than the K -band photocenter, and in the direction of the projected rotation axis, or y -axis. Right: Capella Ab at its actual rotation period. As can be seen, the actual effect is small compared to the angular size of the star on the sky, but still large compared to the $1 \mu\text{as}$ benchmark of SIM Lite. The presence of gravity darkening is clearly visible, which causes a decrement in flux towards the limb of the star. Note that the broad wavelength coverage of SIM Lite will only cover the B , V , R , and I bandpasses.

An additional complicating factor is the exact dependence of temperature on local gravity. von Zeipel (1924) was the first to derive the quantitative relationship between them, showing that $T_{\text{eff}}^4 \propto g^{\beta_1}$, where β_1 is referred to as the gravity darkening exponent. The value of β_1 has been a subject of much study and debate; for a complete review, see Claret (2000b), who presents both an excellent discussion of past studies, as well as new, detailed computations of β_1 using modern models of stellar atmospheres and internal structure that encompass stars from 0.08 to 40 M_{\odot} . Since the value of β_1 affects the temperature differential between equator and pole, the multi-wavelength displacement will also be dependent on the value of β_1 . The total amplitude of the effect will be scaled by the angular size of the star, which depends on both its effective radius and distance. Thus, in total, the components of this inclination effect are the effective stellar radius, distance, effective temperature, rotation rate, β_1 , and inclination of the star. In principle, one is able to determine the effective stellar radius, effective temperature, rotation rate, and distance of a target star using ground-based spectroscopy and space-based parallax measurements, including from SIM Lite. Thus, when modeling the multi-wavelength displacement of the stellar photocenter, the only two components that need to be solved for are the inclination and β_1 , with β_1 already having some constraints from theory.

A good trio of stars for modeling and testing this inclination effect are the components of the binary system Capella, (Aa and Ab), and the single star Vega. Torres et al. (2009) has very recently published an extremely detailed analysis of both the binary orbit of Capella and the physical and evolutionary states of the individual components, providing both new observations, as well as drawing from the previous observations and analyses of Hummel et al. (1994) and Strassmeier

et al. (2001). Vega, in addition to being one of the most well-studied stars in the sky, has recently been discovered to be a very rapid rotator seen nearly pole-on (Aufdenberg et al. 2006; Peterson et al. 2006; Hill et al. 2010). In total, these three stars represent both slow and rapid rotators for giant and main-sequence stars at a range of temperatures, as Capella Aa is a slow-rotating K-type giant, Capella Ab is a fast-rotating G-type giant, and Vega is a very fast-rotating A-type main-sequence star. With many ground-based interferometric observations to compare with, and being bright and nearby, these stars also present excellent targets for SIM Lite.

We use the REFLUX code to generate models of the astrometric displacement from U -band to H -band, with respect to the K -band photocenter, for inclinations from 0 to 90° , for each star, as shown in Figures D.2, D.3, and D.4. We use systemic parameters given by Torres et al. (2009) for Capella Aa and Ab, and by Aufdenberg et al. (2006) and Peterson et al. (2006) for Vega, listed in Tables D.1, D.2, and D.3 respectively. We employ the model atmospheres incorporated into the ELC code, as well as automatically chosen values for β_1 based on Figure 1 of Claret (2000b). Additionally, in each figure we show a dashed line to indicate the effect of decreasing the gravity darkening coefficient by 10% to simulate the uncertainty of the models (Claret 2000b) and explore the correlation with other parameters.

As can be seen from these models, we find that the effect is quite large for a Capella Ab-like or Vega-like fast rotator, but only marginally detectable for a slower-rotating system like Capella Aa. This also implies that this effect would not be detectable for a slow-rotating, main-sequence star like our Sun. Our modeling confirms this, showing a total U-K amplitude of $\ll 0.1 \mu\text{as}$ for a $1.0 M_\odot$, $1.0 R_\odot$

Table D.1. Parameters for Capella Aa

Parameter	Value ^a
Distance (pc)	12.9
Rotation Period (Days)	106.0
Mass (M_{\odot})	2.70
Radius (R_{\odot})	12.2
Effective Temperature (K)	4940
β_1	0.43

^aValues from Torres et al. (2009)

Table D.2. Parameters for Capella Ab

Parameter	Value ^a
Distance (pc)	12.9
Rotation Period (Days)	8.64
Mass (M_{\odot})	2.56
Radius (R_{\odot})	9.2
Effective Temperature (K)	5700
β_1	0.39

^aValues from Torres et al. (2009)

Table D.3. Parameters for Vega

Parameter	Value ^a
Distance (pc)	7.76
Rotation Period (Days)	0.521
Mass (M_{\odot})	2.11
Radius (R_{\odot})	2.5
Effective Temperature (K)	9602
β_1	1.02

^aValues from Aufdenberg et al. (2006) and Peterson et al. (2006)

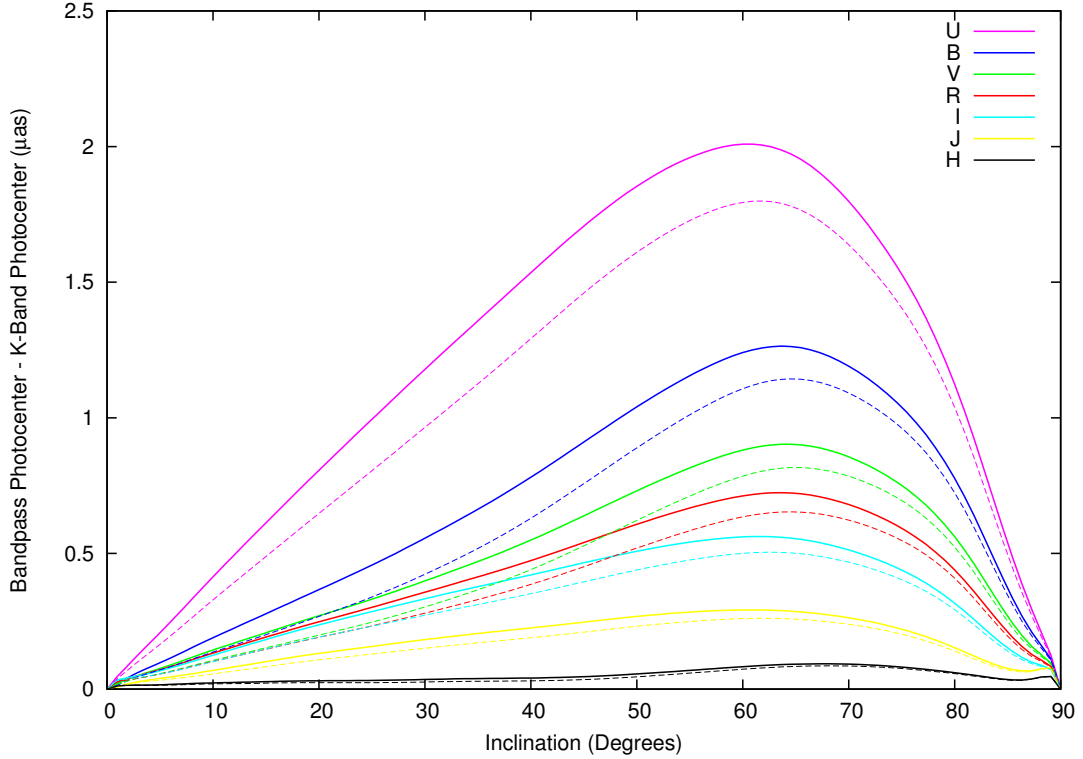


Fig. D.2.— The astrometric displacement of each bandpass with respect to K -band versus inclination for Capella Aa. Dashed lines are a model with β_1 decreased by 10%. Due to the slow rotation rate of Capella Aa, the effect is limited to a maximum of ~ 2.0 microarcseconds between U and K -band, and only a maximum of $\sim 0.7 \mu\text{as}$ between B and I -band, where SIM Lite will operate. This puts the detection of this effect for Capella Aa at the very edge of SIM Lite’s capability.

star with a rotation period of 30.0 days at 10.0 parsecs. These conclusions on detectability are made with the assumption that, for bright stars like these, SIM Lite can achieve its microarcsecond benchmark. We show this is possible in narrow angle (NA) mode by employing the SIM Differential Astrometry Performance Estimator (DAPE) (Plummer 2010). For a target star with magnitude $V=5$, and a single comparison star with $V=10$ located within a degree of it on the sky, by integrating 15 seconds on the target, and 30 seconds on the reference, for 10 visits at 5 chop cycles each, a final precision of $\pm 1.01 \mu\text{as}$ is achieved in only 1.04 hours of

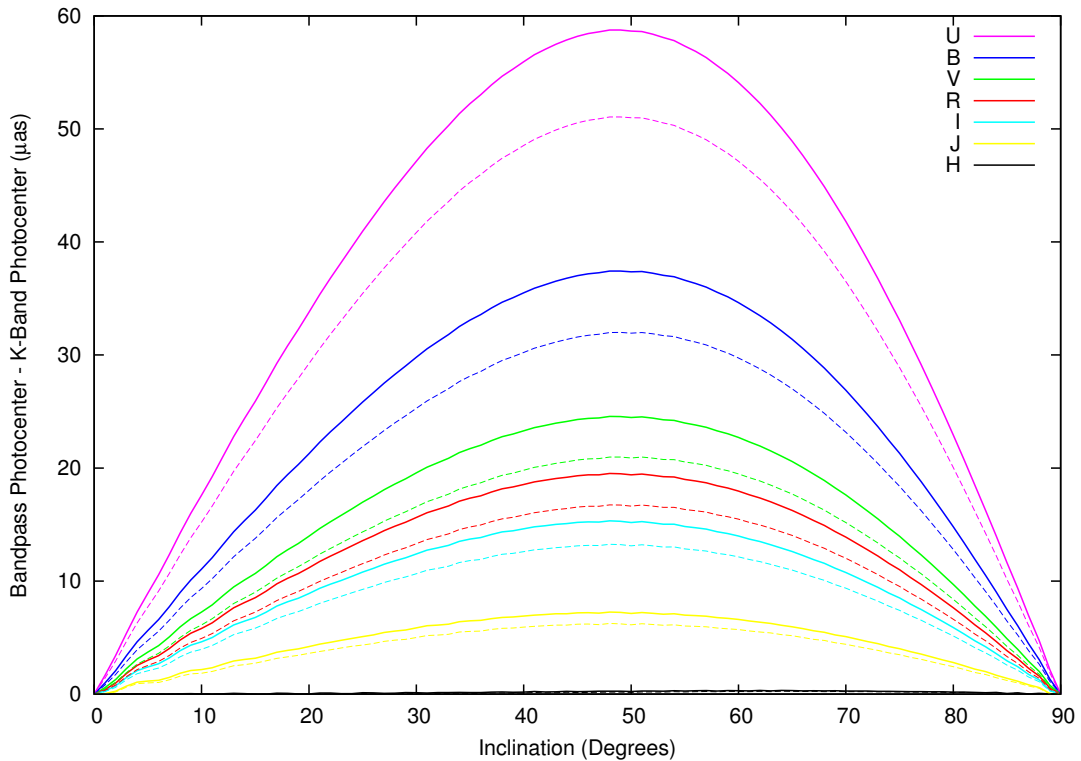


Fig. D.3.— The astrometric displacement of each bandpass with respect to K -band versus inclination for Capella Ab. Dashed lines are a model with β_1 decreased by 10%. Due to the fast rotation rate of a Capella Ab like star, the effect is moderate with tens of microarcseconds of displacement, and thus these types of stars are excellent targets for SIM Lite. The actual inclination of Capella Ab is 42.788° (Torres et al. 2009), and thus Capella Ab itself should show a large shift of the photocenter with wavelength. Note that the broad wavelength coverage of SIM Lite will only cover the B , V , R , and I bandpasses.

total mission time. For a fainter target with $V=10$, this precision is only reduced to $\pm 1.32 \mu\text{as}$ in the same amount of mission time. In utilizing NA mode, one must be careful in choosing the reference star(s), to ensure that they are not stars with a substantial wavelength dependent centroid. Given the only constraints on reference stars are that they need to have $V \gtrsim 10$ and are within one degree on the sky, one could easily choose a slow-rotating, main-sequence star, determined as such via ground-based observations, as a wavelength-independent astrometric

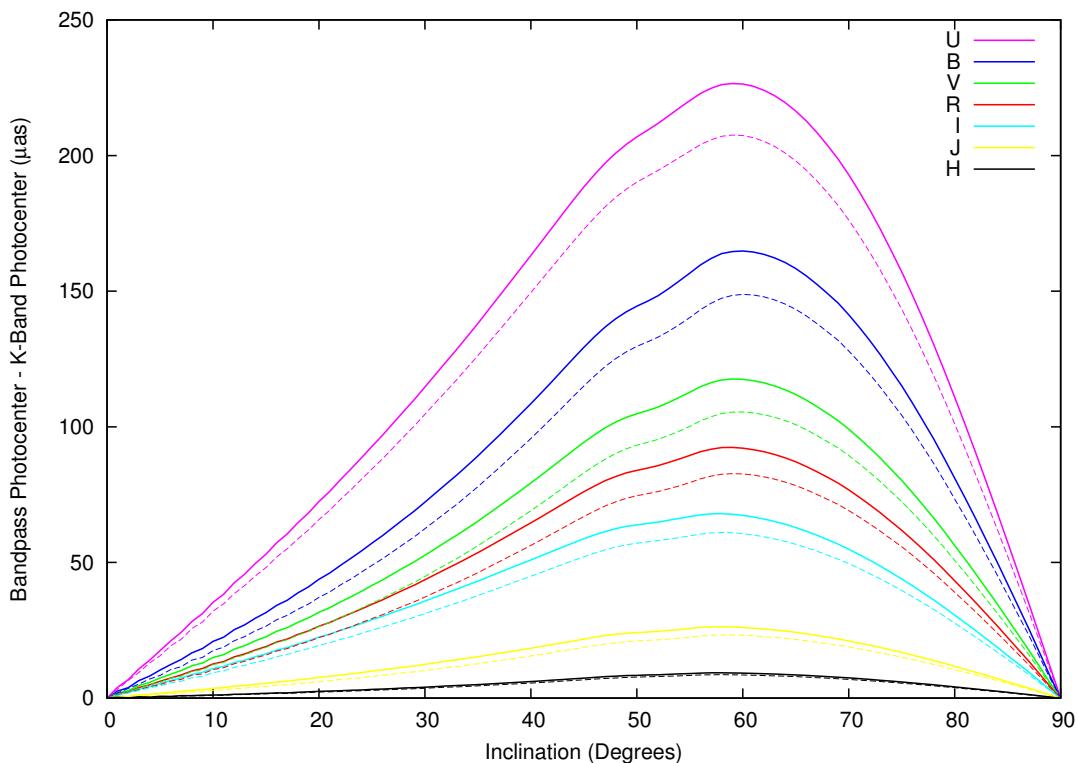


Fig. D.4.— The astrometric displacement of each bandpass with respect to K -band versus inclination for Vega. Dashed lines are a model with β_1 decreased by 10%. Note that due to the very fast rotation of Vega, along with a high value of β_1 , the effect can be quite large, at a couple hundred micro-arcseconds. For a Vega-like star, SIM Lite observations would yield very accurate values for β_1 and the inclination. For Vega itself, which is known to be nearly pole on, with an inclination of 5.7° (Hill et al. 2010), there should be a B -band minus I -band displacement of $6.0 \mu\text{as}$, still detectable by SIM Lite. Note that the broad wavelength coverage of SIM Lite will only cover the B , V , R , and I bandpasses.

reference star. We also note that wide angle SIM Lite measurements, with a precision of $\sim 5 \mu\text{as}$, may not detect the wavelength dependent photocenter of a system like Capella, but will have no difficulty detecting it in stars like Capella Ab or Vega.

The effect of decreasing the gravity darkening exponent is to decrease the total amplitude of the effect in each wavelength, with shorter wavelengths affected more than longer wavelengths. Thus, the choice of gravity darkening exponent

is intimately tied to the derived inclination. If one were to model observed data with a gravity darkening exponent that was $\sim 10\%$ different than the true value, they would derive an inclination that would also be $\sim 10\%$ different from the true inclination. However, the two combinations of inclination and gravity darkening exponent do not produce identical results, and can be distinguished with a sufficient precision at a number of wavelengths. For example, if one were to adopt the nominal value for β_1 and derive an inclination of 40 degrees for a Vega-like star, then adopt a β_1 value that was 10% lower, one would derive an inclination of 43 degrees, a 7.5% change. In this case though, with the lower β_1 value, the measured photocenter in the U , B , V , R , I , J , and H bandpasses, with respect to the K -band photocenter, would differ from the nominal β_1 model by ~ 0.5 , -1.0 , -2.0 , -2.0 , -1.6 , -1.0 , and $0.2 \mu\text{as}$ respectively. Note that for B , V , R , and I , where SIM Lite can observe, these discrepancies, on the order of $\sim 1.0 \mu\text{as}$, should be large enough to be distinguished in NA mode. Thus, a unique solution exists for the values of i and β_1 if the photocenter is measured in three or more wavelengths. (The photocenter of one wavelength is used as a base measurement that the photocenters of other wavelengths are measured with respect to, as we have chosen K -band as the base measurement in our models. With the photocenter measured in three or more wavelengths total, there are two or more photocenter difference measurements, with two unknown variables for which to solve.) Another complication is the possibility of having equally good fitting high and low solutions for i . For example, if one observed and determined a best-fit inclination of 70 degrees for a Vega-like star, one could obtain a reasonably good fit as well at 46 degrees, (see Fig D.4). However, just as in the case of the uncertainty in the value of β_1 , discernible discrepancies would exist. In this case, the discrepancies

in the measured photocenter in the U , B , V , R , I , J , and H bandpasses, with respect to the K -band photocenter, would be ~ 0.1 , -9.0 , -2.0 , 1.5 , 6.0 , 1.0 , and $0.2 \mu\text{as}$ respectively. Just as in the case of the uncertainty in the value of β_1 , this discrepancy between equally good fitting high and low inclination solutions can be resolved if one has three or more wavelengths obtained in NA mode.

As mentioned in Section D.1, we note that the limb-darkening function, which was automatically chosen by the ELC code as incorporated into the model atmospheres, can differ from actual observed values by $\sim 10\%$ (Claret 2008). We have tested how changing the limb-darkening coefficients by 10% affects the resulting astrometric displacements, and find that the result is less than 0.5% for all wavelengths, and thus is negligible in the modeling. The reason is that limb-darkening is symmetric, and thus while increased limb-darkening damps the visible pole, it also damps the rest of the star, and thus the relative brightness between regions is maintained.

Additionally, this inclination technique yields the orientation of the projected stellar rotation axis on the sky, which is parallel to the wavelength dispersion direction. When coupled with the derived inclination, this technique thus yields the full 3-dimensional orientation of the rotation axis. This could be a powerful tool in determining the overall alignment of stellar axes in the local neighborhood and in nearby clusters.

D.4. Star Spots

Another area of astrophysical interest to which multi-wavelength astrometric measurements from SIM Lite can contribute is the study of star spots. As the

cause of star spots are intense magnetic fields at the photosphere, they are typically found in stars with convective envelopes, especially rapidly rotating stars. Thus, both low-mass, main-sequence K and M dwarfs, as well as rapidly rotating giant and sub-giant stars, are known to host large spots on their surface. The study of the distribution, relative temperature, and size of these spots would greatly contribute to the study of magnetic field generation in stellar envelopes. A starspot that rotates in and out of view will cause a shift of the photocenter for a single star, which has been a subject of much recent discussion in the literature (e.g. Hatzes 2002; Unwin 2005; Eriksson & Lindgren 2007; Catanzarite et al. 2008; Makarov et al. 2009; Lanza et al. 2008), especially in light of its potential to mimic, or introduce noise when characterizing, an extrasolar planet. However, there has been no mention in the literature of the multi-wavelength astrometric signature of stellar spots, where, just as in the case of the gravity darkening inclination effect, we are looking at essentially two blackbodies with varying temperatures, and thus shorter wavelengths will be more affected by a spot than longer wavelengths.

To characterize the multi-wavelength astrometric signature of stellar spots, we model two spotty systems, again using the `REFLUX` code. We model Capella Ab, which shows evidence of large spots and is suspected of being a RS CVn variable (Hummel et al. 1994), and a typical main-sequence K dwarf. For Capella Ab, we use the parameters listed in Table D.2, along with the star’s determined inclination of 42.788° (Torres et al. 2009), and add a cool spot that has a temperature that is 60% of the average surface temperature, located at the equator, at a longitude such that it is seen directly at phase 270° , and having an angular size of 10° , (where 90° would cover exactly one half of the star). For the K dwarf system, we use the physical parameters listed in Table D.4, simulating a typical K Dwarf at

10 parsecs, and add a cool spot with the same parameters as we do for Capella Ab. Additionally, to investigate the effects of cool versus hot spots or flares, we also run a model with a hot spot by changing the spot temperature to be 40% greater than the average surface temperature. We present our models in Figures D.5, D.6, and D.7.

As can be seen for CapellaAb, the gravity darkening inclination effect presented in Section D.3 dominates the spread of colors in the y-direction, the direction parallel to the stars' projected rotation axis. However, the amplitude of the spot motion is quite large, with a total amplitude of $\sim 40 \mu\text{as}$ in all band-passes, which would be easily detectable by SIM Lite. For the K dwarf with a cool spot, we see a much smaller, but still detectable shift of amplitude $\sim 5\text{-}8 \mu\text{as}$, depending on the wavelength. In the case of a hot spot or flare, we see a much larger displacement, on the order of $\sim 10\text{-}200 \mu\text{as}$, depending on the wavelength, which would be easily detectable by SIM and provide extremely precise values in deriving the spot parameters.

In general, the temperature of the spot, in relation to the mean stellar surface temperature, is related to the spread in observed wavelengths, with a larger spread indicating a larger temperature difference. The duration of the astrometric displacement in phase, coupled with the overall amplitude of the astrometric displacement, yields the size of the spot, as larger spots will cause larger displacements and be visible for a larger amount of rotational phase. The latitude of the spot can also affect the total duration. Finally, the amplitude of the astrometric displacement in the x versus the y direction is dependent on both the latitude of spot as well as the inclination of the star. Thus, when modeled together, one is able to recover these parameters. This work can also be combined with our work

Table D.4. Parameters for the K Dwarf System

Parameter	Value
Distance (pc)	10.0
Inclination ($^{\circ}$)	60.0
Period (Days)	20
Mass (M_{\odot})	0.6
Radius (R_{\odot})	0.6
Effective Temperature (K)	4500
Latitude of Spot ($^{\circ}$)	90
Longitude of Spot ($^{\circ}$)	270
Angular Size of Spot ($^{\circ}$)	10
Cool Spot Temperature Factor	0.6
Hot Spot Temperature Factor	1.4

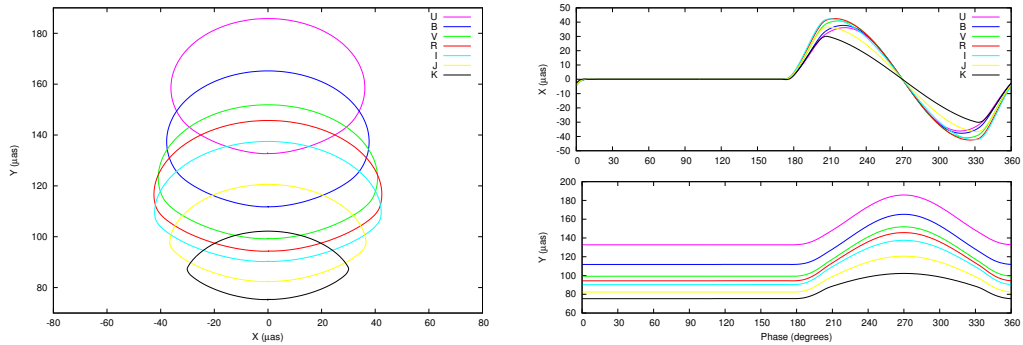


Fig. D.5.— A simulated cool Spot on CapellaAb. The spot is located on the equator, with a longitude such that it is seen directly at phase 270° . The strong presence of the gravity darkening effect, discussed in Section D.3, dominates the wavelength spread in the y direction. Note that the broad wavelength coverage of SIM Lite will only cover the *B*, *V*, *R*, and *I* bandpasses.

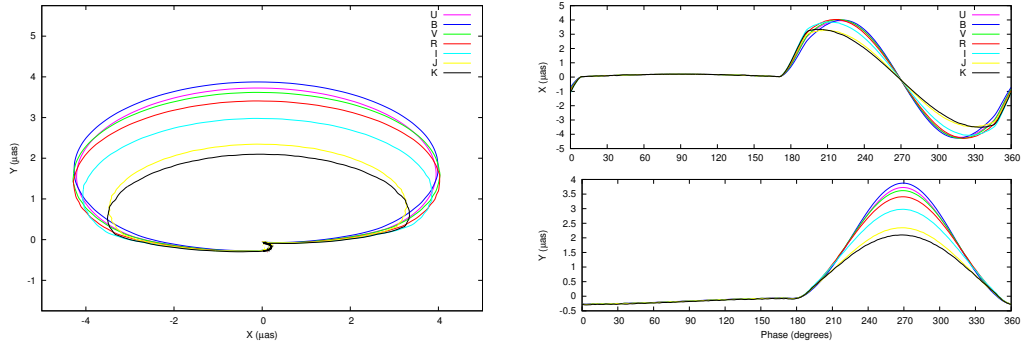


Fig. D.6.— A simulated cool spot on a nearby K dwarf star with an inclination of 60° , whose parameters are given in Table D.4. The spot is located on the equator, with a longitude such that it is seen directly at phase 270° . Note that the broad wavelength coverage of SIM Lite will only cover the B , V , R , and I bandpasses.

in Appendix C to derive the location of spots in binary systems, as the astrometric signature of the spot is simply added to the astrometric signature of the binary system.

The astrometric motion induced upon a parent star by a host planet does not have a wavelength dependence. Spots however, as we have shown via our modeling, have a clear wavelength dependence. Thus, if one has a candidate planetary signal from astrometry, but it shows a wavelength-dependent motion, it must then be a false positive introduced from star spots at the rotation period of the star, (assuming that the planet's emitted flux is negligible compared to the star.) Furthermore, when SIM is launched, there will likely be many cases where a marginally detectable signal due to a planetary companion is found at a very different period than the rotation period of the star. However, starspots will still introduce extra astrometric jitter which will degrade the signal from the planetary companion. Multi-wavelength astrometric data can be used to model and remove the spots, which will have a wavelength dependence, and thus strengthen the

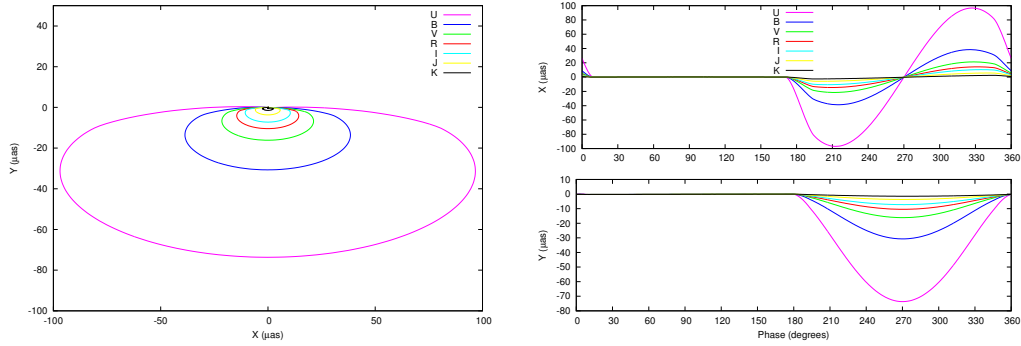


Fig. D.7.— A simulated hot spot or flare on a nearby K dwarf star with an inclination of 60° , whose parameters are given in Table D.4. The spot is located on the equator, with a longitude such that it is seen directly at phase 270° . Note that the broad wavelength coverage of SIM Lite will only cover the *B*, *V*, *R*, and *I* bandpasses.

planetary signal, which will not have a wavelength dependence.

D.5. Discussion and Conclusion

We have presented detailed models of the multi-wavelength astrometric displacement that SIM Lite will observe due to gravity darkening and stellar spots using the REFLUX code. We find that SIM Lite observations, especially when combined with other techniques, will be able to determine the absolute inclination, gravity darkening exponent, and 3-dimensional orientation of the rotational axis for fast and slow rotating giant stars, and fast-rotating main-sequence stars. This technique will be especially useful in probing binary star and exoplanet formation and evolution, as well as the physics of star forming regions. Direct observational determination of the gravity darkening exponent has direct applications in both stellar and exoplanet astrophysics. This technique is also relatively inexpensive in terms of SIM Lite observing time, as one need only to observe a given star once, as opposed to binary stars and planets, which require constant monitoring over an

entire orbit. It should be noted that this effect should be taken into account when constructing the SIM Lite astrometric reference frame, such that fast-rotating giants should be excluded so as not to produce a wavelength-dependent astrometric reference frame.

We also have presented models of star spots on single stars, and find that SIM Lite should be able to discern their location, temperature, and size. Combined with other techniques, this will provide great insight into stellar differential rotation, magnetic cycles and underlying dynamos, and magnetic interaction in close binaries. From this modeling, it should especially be noted that multi-wavelength astrometry is a key tool in the hunt for extrasolar planets, either by ruling out false signals created by spots, or simply removing extra astrometric jitter introduced by spots. Thus, it remains critical that SIM Lite maintains a multi-wavelength astrometric capability in its final design.

REFERENCES

- Adams, E. R., et al. 2011, ArXiv e-prints
- Agol, E., Steffen, J., Sari, R., & Clarkson, W. 2005, MNRAS, 359, 567
- Albrecht, S., Reffert, S., Snellen, I. A. G., & Winn, J. N. 2009, Nature, 461, 373
- Alekseev, I. Y. 2004, Sol. Phys., 224, 187
- Alonso, R., Barbieri, M., Rabus, M., Deeg, H. J., Belmonte, J. A., & Almenara, J. M. 2008, A&A, 487, L5
- Alonso, R., Guillot, T., Mazeh, T., Aigrain, S., Alapini, A., Barge, P., Hatzes, A., & Pont, F. 2009a, A&A, 501, L23
- . 2010, A&A, 512, C1+
- Alonso, R., et al. 2009b, A&A, 506, 353
- Andersen, J. 1991, A&A Rev., 3, 91
- Applegate, J. H. 1992, ApJ, 385, 621
- Aufdenberg, J. P., et al. 2006, ApJ, 645, 664
- Aurière, M., et al. 2008, A&A, 491, 499
- Ballot, J., García, R. A., & Lambert, P. 2006, MNRAS, 369, 1281
- Baraffe, I., Chabrier, G., Allard, F., & Hauschildt, P. H. 1998, A&A, 337, 403
- Baraffe, I., Chabrier, G., & Barman, T. 2010, Reports on Progress in Physics, 73, 016901
- Barnes, J. W., Linscott, E., & Shporer, A. 2011, ApJS, 197, 10
- Batalha, N. M., et al. 2012, ArXiv e-prints
- Bean, J. L., McArthur, B. E., Benedict, G. F., Harrison, T. E., Bizyaev, D., Nelan, E., & Smith, V. V. 2007, AJ, 134, 749
- Becker, A. C., et al. 2008, MNRAS, 386, 416
- Behr, B. B. 2003, ApJS, 149, 67
- Bell, K. R. 1999, ApJ, 526, 411
- Benedict, G. F., McArthur, B. E., Franz, O. G., Wasserman, L. H., & Henry, T. J. 2000, AJ, 120, 1106
- Benedict, G. F., et al. 2001, AJ, 121, 1607
- . 2006, AJ, 132, 2206

- Berdyugina, S. V., Berdyugin, A. V., Fluri, D. M., & Pirola, V. 2011, *ApJ*, 728, L6+
- Bertelli, G., Girardi, L., Marigo, P., & Nasi, E. 2008, *A&A*, 484, 815
- Bitner, M. A., Robinson, E. L., & Behr, B. B. 2007, *ApJ*, 662, 564
- Blake, C. H., Torres, G., Bloom, J. S., & Gaudi, B. S. 2008, *ApJ*, 684, 635
- Bodenheimer, P., Laughlin, G., & Lin, D. N. C. 2003, *ApJ*, 592, 555
- Bonomo, A. S., et al. 2011, ArXiv e-prints, 1110.5462
- Borucki, W. J., & the Kepler Team. 2010, ArXiv e-prints, 1006.2799
- Borucki, W. J., et al. 2009, *Science*, 325, 709
- . 2011, *ApJ*, 736, 19
- Boyajian, T. 2010 (Presentation at Cool Stars 16 in Seattle, WA)
- Boyajian, T. S., et al. 2012, ArXiv e-prints
- Broggi, M., Snellen, I. A. G., de Kok, R. J., Albrecht, S., Birkby, J., & de Mooij, E. J. W. 2012, *Nature*, 486, 502
- Brown, T. M., Latham, D. W., Everett, M. E., & Esquerdo, G. A. 2011, ArXiv e-prints
- Bruno, G. 1584, *De l'infinito universo e mondi* (Venice)
- Burrows, A., Budaj, J., & Hubeny, I. 2008a, *ApJ*, 678, 1436
- Burrows, A., Hubeny, I., Budaj, J., Knutson, H. A., & Charbonneau, D. 2007, *ApJ*, 668, L171
- Burrows, A., Hubeny, I., & Sudarsky, D. 2005, *ApJ*, 625, L135
- Burrows, A., Ibgui, L., & Hubeny, I. 2008b, *ApJ*, 682, 1277
- Burrows, A., Sudarsky, D., & Hubeny, I. 2006, *ApJ*, 650, 1140
- Butler, R. P., Vogt, S. S., Marcy, G. W., Fischer, D. A., Wright, J. T., Henry, G. W., Laughlin, G., & Lissauer, J. J. 2004, *ApJ*, 617, 580
- Cacciari, C. 2009, *Mem. Soc. Astron. Italiana*, 80, 97
- Campbell, B., Walker, G. A. H., & Yang, S. 1988, *ApJ*, 331, 902
- Campo, C. J., et al. 2011, *ApJ*, 727, 125
- Cantó, J., Curiel, S., & Martínez-Gómez, E. 2009, *A&A*, 501, 1259
- Carter, J. A., et al. 2011, *Science*, 331, 562

- Catanzarite, J., Law, N., & Shao, M. 2008, in Society of Photo-Optical Instrumentation Engineers (SPIE) Conference Series, Vol. 7013, Society of Photo-Optical Instrumentation Engineers (SPIE) Conference Series
- Chabrier, G., Baraffe, I., Allard, F., & Hauschildt, P. 2000, *ApJ*, 542, 464
- Chabrier, G., Gallardo, J., & Baraffe, I. 2007, *A&A*, 472, L17
- Charbonneau, D., Noyes, R. W., Korzennik, S. G., Nisenson, P., Jha, S., Vogt, S. S., & Kibrick, R. I. 1999, *ApJ*, 522, L145
- Charbonneau, P. 1995, *ApJS*, 101, 309
- Christiansen, J. L., et al. 2010, *ApJ*, 710, 97
- Claret, A. 2000a, *A&A*, 363, 1081
- . 2000b, *A&A*, 359, 289
- . 2008, *A&A*, 482, 259
- Claret, A., & Bloemen, S. 2011, *A&A*, 529, A75
- Claret, A., & Gimenez, A. 1990, *A&A*, 230, 412
- Claret, A., & Hauschildt, P. H. 2003, *A&A*, 412, 241
- Clausen, J. V., Bruntt, H., Claret, A., Larsen, A., Andersen, J., Nordström, B., & Giménez, A. 2009, *A&A*, 502, 253
- Collier Cameron, A. 2002, *Astronomische Nachrichten*, 323, 336
- Cooper, C. S., & Showman, A. P. 2006, *ApJ*, 649, 1048
- Coughlin, J. L., Harrison, T. E., & Gelino, D. M. 2010a, *ApJ*, 723, 1351
- Coughlin, J. L., & López-Morales, M. 2012a, *AJ*, 143, 39
- . 2012b, *ApJ*, 750, 100
- Coughlin, J. L., López-Morales, M., Harrison, T. E., Ule, N., & Hoffman, D. I. 2011, *AJ*, 141, 78
- Coughlin, J. L., & Shaw, J. S. 2007, *Journal of the Southeastern Association for Research in Astronomy*, 1, 7
- Coughlin, J. L., Stringfellow, G. S., Becker, A. C., López-Morales, M., Mezzalana, F., & Krajci, T. 2008, *ApJ*, 689, L149
- Coughlin, J. L., et al. 2010b, *ApJ*, 717, 776
- Cowan, N. B., & Agol, E. 2011, *ApJ*, 729, 54

- Cravens, T. E., Clark, J., Bhardwaj, A., Elsner, R., Waite, J. H., Maurellis, A. N., Gladstone, G. R., & Branduardi-Raymont, G. 2006, *Journal of Geophysical Research (Space Physics)*, 111, A07308
- Croll, B., Lafreniere, D., Albert, L., Jayawardhana, R., Fortney, J. J., & Murray, N. 2011, *AJ*, 141, 30
- Davidson, J., Edberg, S., Danner, R., Nemati, B., & Unwin, S., eds. 2009, *SIM Lite: Astrometric Observatory (National Aeronautics and Space Administration)*
- de Mooij, E. J. W., de Kok, R. J., Nefs, S. V., & Snellen, I. A. G. 2011, *A&A*, 528, A49
- Delfosse, X., Forveille, T., Mayor, M., Burnet, M., & Perrier, C. 1999, *A&A*, 341, L63
- Deming, D., Harrington, J., Laughlin, G., Seager, S., Navarro, S. B., Bowman, W. C., & Horning, K. 2007, *ApJ*, 667, L199
- Deming, D., Seager, S., Richardson, L. J., & Harrington, J. 2005, *Nature*, 434, 740
- Demory, B., et al. 2009, *A&A*, 505, 205
- Demory, B.-O., et al. 2011, *ApJ*, 735, L12+
- Désert, J.-M., Vidal-Madjar, A., Lecavelier Des Etangs, A., Sing, D., Ehrenreich, D., Hébrard, G., & Ferlet, R. 2008, *A&A*, 492, 585
- Désert, J.-M., et al. 2011a, *ArXiv e-prints*
- . 2011b, *ArXiv e-prints*
- Devor, J., Charbonneau, D., O'Donovan, F. T., Mandushev, G., & Torres, G. 2008a, *AJ*, 135, 850
- Devor, J., et al. 2008b, *ApJ*, 687, 1253
- Diaz-Cordoves, J., & Gimenez, A. 1992, *A&A*, 259, 227
- Dimitrov, D. P., & Kjurkchieva, D. P. 2010, *MNRAS*, 866
- Domiciano de Souza, A., Zorec, J., Jankov, S., Vakili, F., Abe, L., & Janot-Pacheco, E. 2004, *A&A*, 418, 781
- Donati, J., Forveille, T., Cameron, A. C., Barnes, J. R., Delfosse, X., Jardine, M. M., & Valenti, J. A. 2006, *Science*, 311, 633
- Dravins, D., Lindegren, L., Mezey, E., & Young, A. T. 1998, *PASP*, 110, 610
- Dubus, G., Campbell, R., Kern, B., Taam, R. E., & Spruit, H. C. 2004, *MNRAS*, 349, 869

- Dunham, E. W., et al. 2010, *ApJ*, 713, L136
- Eriksson, U., & Lindegren, L. 2007, *A&A*, 476, 1389
- Etzel, P. B. 1981, in *Photometric and Spectroscopic Binary Systems*, ed. E. B. Carling & Z. Kopal, 111–+
- Fabrycky, D. C., & Winn, J. N. 2009, *ApJ*, 696, 1230
- Feiden, G. A., & Chaboyer, B. 2012, *ArXiv e-prints*
- Fernandez, J. M., et al. 2009, *ApJ*, 701, 764
- Fortney, J. J., Cooper, C. S., Showman, A. P., Marley, M. S., & Freedman, R. S. 2006, *ApJ*, 652, 746
- Fortney, J. J., Lodders, K., Marley, M. S., & Freedman, R. S. 2008, *ApJ*, 678, 1419
- Fortney, J. J., et al. 2011, *ArXiv e-prints*
- Friedjung, M. 1985, *A&A*, 146, 366
- Gaudi, B. S. 2010, in *Bulletin of the American Astronomical Society*, Vol. 42, American Astronomical Society Meeting Abstracts 215, 349.05–+
- Gelino, D. M. 2001, PhD thesis, Center for Astrophysics and Space Sciences, University of California, San Diego [EMAIL]dgelino@ucsd.edu[/EMAIL]
- Gelino, D. M., Gelino, C. R., & Harrison, T. E. 2010, *ApJ*, 718, 1
- Gelino, D. M., Harrison, T. E., & McNamara, B. J. 2001, *AJ*, 122, 971
- Gibson, N. P., et al. 2010, *MNRAS*, 404, L114
- Gillon, M., et al. 2007a, *A&A*, 471, L51
- . 2007b, *A&A*, 472, L13
- . 2009, *A&A*, 506, 359
- Gizon, L., & Solanki, S. K. 2003, *ApJ*, 589, 1009
- Goldreich, P. 1963, *MNRAS*, 126, 257
- Gottlieb, E. W., Wright, E. L., & Liller, W. 1975, *ApJ*, 195, L33
- Grether, D., & Lineweaver, C. H. 2006, *ApJ*, 640, 1051
- Hansen, B. M. S. 2008, *ApJS*, 179, 484
- Harrington, J., Hansen, B. M., Luszcz, S. H., Seager, S., Deming, D., Menou, K., Cho, J. Y.-K., & Richardson, L. J. 2006, *Science*, 314, 623

- Harrison, T. E., Coughlin, J. L., Ule, N. M., & López-Morales, M. 2012, *AJ*, 143, 4
- Harrison, T. E., Howell, S. B., Szkody, P., & Cordova, F. A. 2005, *ApJ*, 632, L123
—. 2007, *AJ*, 133, 162
- Harrison, T. E., Osborne, H. L., & Howell, S. B. 2004, *AJ*, 127, 3493
- Hatzes, A. P. 2002, *Astronomische Nachrichten*, 323, 392
- Hauschildt, P. H., Allard, F., & Baron, E. 1999, *ApJ*, 512, 377
- Hebb, L., et al. 2009, *ApJ*, 693, 1920
- Herrero, A., Kudritzki, R. P., Gabler, R., Vilchez, J. M., & Gabler, A. 1995, *A&A*, 297, 556
- Hill, G., Gulliver, A. F., & Adelman, S. J. 2010, *ApJ*, 712, 250
- Hoard, D. W., et al. 2009, *ApJ*, 693, 236
- Hoffman, D. I., Harrison, T. E., Coughlin, J. L., McNamara, B. J., Holtzman, J. A., Taylor, G. E., & Vestrand, W. T. 2008, *AJ*, 136, 1067
- Holman, M. J., & Murray, N. W. 2005, *Science*, 307, 1288
- Holtzman, J. A., Harrison, T. E., & Coughlin, J. L. 2010, *Advances in Astronomy*, 2010
- Howell, S. B., Gelino, D. M., & Harrison, T. E. 2001a, *AJ*, 121, 482
- Howell, S. B., Nelson, L. A., & Rappaport, S. 2001b, *ApJ*, 550, 897
- Hubeny, I., Burrows, A., & Sudarsky, D. 2003, *ApJ*, 594, 1011
- Hummel, C. A., Armstrong, J. T., Quirrenbach, A., Buscher, D. F., Mozurkewich, D., Elias, I. N. M., & Wilson, R. E. 1994, *AJ*, 107, 1859
- Hwang, K., & Han, C. 2010, *ApJ*, 709, 327
- Ibgui, L., & Burrows, A. 2009, *ApJ*, 700, 1921
- Ibgui, L., Burrows, A., & Spiegel, D. S. 2010, *ApJ*, 713, 751
- Ibgui, L., Spiegel, D. S., & Burrows, A. 2011, *ApJ*, 727, 75
- İşık, E., Schüssler, M., & Solanki, S. K. 2007, *A&A*, 464, 1049
- Irwin, J., et al. 2009, *ApJ*, 701, 1436
- Jackson, R. J., & Jeffries, R. D. 2010, *MNRAS*, 402, 1380
- Jeffery, C. S. 1984, *MNRAS*, 207, 323

- Jefferys, W. H., Fitzpatrick, M. J., & McArthur, B. E. 1988, *Celestial Mechanics*, 41, 39
- Jenkins, J. M., Caldwell, D. A., & Borucki, W. J. 2002, *ApJ*, 564, 495
- Jenkins, J. M., et al. 2010a, *ApJ*, 724, 1108
- . 2010b, *ApJ*, 713, L87
- . 2010c, *ApJ*, 713, L120
- Kahaner, D., Moler, C., & Nash, S. 1989, *Numerical methods and software*, ed. Kahaner, D., Moler, C., & Nash, S.
- Karkoschka, E. 1994, *Icarus*, 111, 174
- Kinemuchi, K., Smith, H. A., Woźniak, P. R., & McKay, T. A. 2006, *AJ*, 132, 1202
- Kipping, D., & Bakos, G. 2011a, *ApJ*, 730, 50
- . 2011b, *ApJ*, 733, 36
- Kipping, D. M. 2008, *MNRAS*, 389, 1383
- . 2010a, *MNRAS*, 408, 1758
- . 2010b, *MNRAS*, 409, L119
- Kipping, D. M., & Spiegel, D. S. 2011, *MNRAS*, L317+
- Klingensmith, D. A., & Sobieski, S. 1970, *AJ*, 75, 175
- Knutson, H. A., Charbonneau, D., Noyes, R. W., Brown, T. M., & Gilliland, R. L. 2007a, *ApJ*, 655, 564
- Knutson, H. A., Howard, A. W., & Isaacson, H. 2010, *ApJ*, 720, 1569
- Knutson, H. A., et al. 2007b, *Nature*, 447, 183
- Koch, D. G., et al. 2010, *ApJ*, 713, L131
- Kopal, Z. 1950, *Harvard College Observatory Circular*, 454, 1
- . 1959, *Close binary systems*, ed. Kopal, Z.
- Kraus, A. L., Tucker, R. A., Thompson, M. I., Craine, E. R., & Hillenbrand, L. A. 2011, *ApJ*, 728, 48
- Kudryavtseva, N., et al. 2010, in *In the Spirit of Lyot 2010*
- Lacy, C. H. 1977, *ApJ*, 218, 444
- Langford, S. V., Wyithe, J. S. B., Turner, E. L., Jenkins, E. B., Narita, N., Liu, X., Suto, Y., & Yamada, T. 2011, *MNRAS*, 415, 673

- Lanza, A. F., De Martino, C., & Rodonò, M. 2008, *New Astronomy*, 13, 77
- LaSala, J., & Thorstensen, J. R. 1985, *AJ*, 90, 2077
- Latham, D. W., et al. 2010, *ApJ*, 713, L140
- Leigh, C., Collier Cameron, A., Horne, K., Penny, A., & James, D. 2003a, *MNRAS*, 344, 1271
- Leigh, C., Collier Cameron, A., Udry, S., Donati, J.-F., Horne, K., James, D., & Penny, A. 2003b, *MNRAS*, 346, L16
- Leung, K., & Schneider, D. P. 1978, *AJ*, 83, 618
- Loeb, A., & Gaudi, B. S. 2003, *ApJ*, 588, L117
- López-Morales, M. 2007, *ApJ*, 660, 732
- López-Morales, M., & Bonanos, A. Z. 2008, *ApJ*, 685, L47
- López-Morales, M., Coughlin, J. L., Sing, D. K., Burrows, A., Apai, D., Rogers, J. C., Spiegel, D. S., & Adams, E. R. 2010, *ApJ*, 716, L36
- López-Morales, M., & Ribas, I. 2005, *ApJ*, 631, 1120
- López-Morales, M., & Seager, S. 2007, *ApJ*, 667, L191
- López-Valverde, M. A., Lellouch, E., & Coustenis, A. 2005, *Icarus*, 175, 503
- Lucretius, T. 58 BCE, *De Rerum Natura* (Rome)
- Lupu, R. E., Feldman, P. D., McCandliss, S. R., & Strobel, D. F. 2011, *ApJ*, 732, 37
- Madhusudhan, N., & Seager, S. 2010, *ApJ*, 725, 261
- Madhusudhan, N., et al. 2011, *Nature*, 469, 64
- Makarov, V. V., Beichman, C. A., Catanzarite, J. H., Fischer, D. A., Lebreton, J., Malbet, F., & Shao, M. 2009, *ApJ*, 707, L73
- Malbet, F., et al. 2011, *Experimental Astronomy*, 87
- Mandel, K., & Agol, E. 2002, *ApJ*, 580, L171
- Mandell, A. M., Drake Deming, L., Blake, G. A., Knutson, H. A., Mumma, M. J., Villanueva, G. L., & Salyk, C. 2011, *ApJ*, 728, 18
- Manduca, A., Bell, R. A., & Gustafsson, B. 1977, *A&A*, 61, 809
- Maness, H. L., Marcy, G. W., Ford, E. B., Hauschildt, P. H., Shreve, A. T., Basri, G. B., Butler, R. P., & Vogt, S. S. 2007, *PASP*, 119, 90
- Marcy, G. W., & Butler, R. P. 2000, *PASP*, 112, 137

- Mardling, R. A. 2008, ArXiv e-prints
- Marley, M. S., Gelino, C., Stephens, D., Lunine, J. I., & Freedman, R. 1999, *ApJ*, 513, 879
- Martioli, E., McArthur, B. E., Benedict, G. F., Bean, J. L., Harrison, T. E., & Armstrong, A. 2010, *ApJ*, 708, 625
- Mason, E., Howell, S. B., Szkody, P., Harrison, T. E., Holtzman, J. A., & Hoard, D. W. 2002, *A&A*, 396, 633
- Mayor, M., & Queloz, D. 1995, *Nature*, 378, 355
- Mazeh, T., Nachmani, G., Sokol, G., Faigler, S., & Zucker, S. 2011, ArXiv e-prints, 1110.3512
- McArthur, B. E., Benedict, G. F., Barnes, R., Martioli, E., Korzennik, S., Nelan, E., & Butler, R. P. 2010, *ApJ*, 715, 1203
- McArthur, B. E., et al. 2004, *ApJ*, 614, L81
- McCarthy, C., & Zuckerman, B. 2004, *AJ*, 127, 2871
- Mignard, F. 2005, in *Astronomical Society of the Pacific Conference Series*, Vol. 338, *Astrometry in the Age of the Next Generation of Large Telescopes*, ed. P. K. Seidelmann & A. K. B. Monet, 15–+
- Miller, N., Fortney, J. J., & Jackson, B. 2009, *ApJ*, 702, 1413
- Morales, J. C., Gallardo, J., Ribas, I., Jordi, C., Baraffe, I., & Chabrier, G. 2010, *ApJ*, 718, 502
- Morales, J. C., Ribas, I., & Jordi, C. 2008, *A&A*, 478, 507
- Morton, T. D., & Johnson, J. A. 2011, *ApJ*, 738, 170
- Mosser, B., Baudin, F., Lanza, A. F., Hulot, J. C., Catala, C., Baglin, A., & Auvergne, M. 2009, *A&A*, 506, 245
- Munari, U., Sordo, R., Castelli, F., & Zwitter, T. 2005, *A&A*, 442, 1127
- Murtagh, F., & Heck, A., eds. 1987, *Astrophysics and Space Science Library*, Vol. 131, *Multivariate Data Analysis*
- Muterspaugh, M. W., et al. 2010, *AJ*, 140, 1579
- Noyes, R. W., Jha, S., Korzennik, S. G., Krockenberger, M., Nisenson, P., Brown, T. M., Kennelly, E. J., & Horner, S. D. 1997, *ApJ*, 483, L111+
- O'Donovan, F. T., et al. 2006, *ApJ*, 651, L61
- Orosz, J. A., & Hauschildt, P. H. 2000, *A&A*, 364, 265
- Orosz, J. A., et al. 2002, *ApJ*, 568, 845

- Paddock, G. F. 1913, *PASP*, 25, 208
- Pál, A., et al. 2008, *ApJ*, 680, 1450
- Peterson, D. M., et al. 2006, *Nature*, 440, 896
- Plummer, K. 2010, *TaPE Webtool User Guide* 1.1, http://mscws4.ipac.caltech.edu/simtools_v2
- Podsiadlowski, P., Rappaport, S., & Han, Z. 2003, *MNRAS*, 341, 385
- Pont, F., Zucker, S., & Queloz, D. 2006, *MNRAS*, 373, 231
- Popper, D. M. 1980, *ARA&A*, 18, 115
- Popper, D. M., & Etzel, P. B. 1981, *AJ*, 86, 102
- Pringle, J. E. 1981, *ARA&A*, 19, 137
- Prša, A., Guinan, E. F., Devinney, E. J., DeGeorge, M., Bradstreet, D. H., Giammarco, J. M., Alcock, C. R., & Engle, S. G. 2008, *ApJ*, 687, 542
- Prša, A., et al. 2010, *ArXiv e-prints*, 1006.2815
- Reffert, S., & Quirrenbach, A. 2011, *A&A*, 527, A140+
- Ribas, I., Font-Ribera, A., & Beaulieu, J.-P. 2008, *ApJ*, 677, L59
- Ribas, I., Font-Ribera, A., Beaulieu, J.-P., Morales, J. C., & García-Melendo, E. 2009, in *IAU Symposium*, Vol. 253, *IAU Symposium*, 149–155
- Rodler, F., Kürster, M., & Henning, T. 2008, *A&A*, 485, 859
- . 2010, *A&A*, 514, A23+
- Rodler, F., Lopez-Morales, M., & Ribas, I. 2012, *ApJ*, 753, L25
- Rogers, J. C., Apai, D., López-Morales, M., Sing, D. K., & Burrows, A. 2009, *ApJ*, 707, 1707
- Röll, T., Seifahrt, A., Neuhäuser, R., & Köhler, R. 2010, in *Astronomical Society of the Pacific Conference Series*, Vol. 435, *Binaries - Key to Comprehension of the Universe*, ed. A. Prša & M. Zejda, 419–+
- Rowe, J. F., et al. 2008, *ApJ*, 689, 1345
- . 2010, *ApJ*, 713, L150
- Russell, H. N. 1912, *ApJ*, 36, 54
- Santerne, A., Bonomo, A. S., Hébrard, G., Deleuil, M., Moutou, C., Almenara, J. ., Bouchy, F., & Díaz, R. F. 2011, *ArXiv e-prints*
- Santerne, A., et al. 2012, *ArXiv e-prints*

- Schneider, J. 2012, The Extrasolar Planets Encyclopaedia, <http://exoplanet.eu/catalog/>
- Schwarz, G. 1978, *The Annals of Statistics*, 6, 461
- Seager, S., & Mallén-Ornelas, G. 2003, *ApJ*, 585, 1038
- Seager, S., Whitney, B. A., & Sasselov, D. D. 2000, *ApJ*, 540, 504
- Shaw, J. S., & López-Morales, M. 2007, in *Astronomical Society of the Pacific Conference Series*, Vol. 362, *The Seventh Pacific Rim Conference on Stellar Astrophysics*, ed. Y. W. Kang, H.-W. Lee, K.-C. Leung, & K.-S. Cheng, 15
- Shkolnik, E., Liu, M. C., Reid, I. N., Hebb, L., Cameron, A. C., Torres, C. A., & Wilson, D. M. 2008, *ApJ*, 682, 1248
- Shkolnik, E. L., Hebb, L., Liu, M. C., Reid, I. N., & Cameron, A. C. 2010, *ApJ*, 716, 1522
- Showman, A. P., Cooper, C. S., Fortney, J. J., & Marley, M. S. 2008, *ApJ*, 682, 559
- Showman, A. P., Fortney, J. J., Lian, Y., Marley, M. S., Freedman, R. S., Knutson, H. A., & Charbonneau, D. 2009, *ApJ*, 699, 564
- Shporer, A., Mazeh, T., Pont, F., Winn, J. N., Holman, M. J., Latham, D. W., & Esquerdo, G. A. 2009, *ApJ*, 694, 1559
- Shporer, A., et al. 2011, *AJ*, 142, 195
- Siess, L., Dufour, E., & Forestini, M. 2000, *A&A*, 358, 593
- Sing, D. K. 2010, *A&A*, 510, A21
- Sing, D. K., Désert, J.-M., Lecavelier Des Etangs, A., Ballester, G. E., Vidal-Madjar, A., Parmentier, V., Hebrard, G., & Henry, G. W. 2009, *A&A*, 505, 891
- Sing, D. K., & López-Morales, M. 2009, *A&A*, 493, L31
- Skidmore, W., Wynn, G. A., Leach, R., & Jameson, R. F. 2002, *MNRAS*, 336, 1223
- Snellen, I. A. G., de Kok, R. J., de Mooij, E. J. W., & Albrecht, S. 2010, *Nature*, 465, 1049
- Snellen, I. A. G., de Mooij, E. J. W., & Albrecht, S. 2009, *Nature*, 459, 543
- Southworth, J. 2008, *MNRAS*, 386, 1644
- Southworth, J., Maxted, P. F. L., & Smalley, B. 2004a, *MNRAS*, 351, 1277
- Southworth, J., Wheatley, P. J., & Sams, G. 2007, *MNRAS*, 379, L11

- Southworth, J., Zucker, S., Maxted, P. F. L., & Smalley, B. 2004b, *MNRAS*, 355, 986
- Spiegel, D. S., Silverio, K., & Burrows, A. 2009, *ApJ*, 699, 1487
- Steehls, D., & Casares, J. 2002, *ApJ*, 568, 273
- Stellingwerf, R. F. 1978, *ApJ*, 224, 953
- . 2006, PDM2 Application, Technical Manual, and test data sets
- Sterne, T. E. 1939a, *MNRAS*, 99, 451
- . 1939b, *MNRAS*, 99, 662
- . 1939c, *MNRAS*, 99, 670
- Stevenson, K. B., et al. 2012, *ApJ*, 755, 9
- Strassmeier, K. G., Reegen, P., & Granzer, T. 2001, *Astronomische Nachrichten*, 322, 115
- Sudarsky, D., Burrows, A., & Hubeny, I. 2003, *ApJ*, 588, 1121
- Sudarsky, D., Burrows, A., & Pinto, P. 2000, *ApJ*, 538, 885
- Swain, M. R., et al. 2010, *Nature*, 463, 637
- Szabó, G. M., et al. 2011, *ApJ*, 736, L4+
- Szkody, P., Vennes, S., Schmidt, G. D., Wagner, R. M., Fried, R., Shafter, A. W., & Fierce, E. 1999, *ApJ*, 520, 841
- ten Brummelaar, T. A., et al. 2005, *ApJ*, 628, 453
- Tinetti, G., Liang, M.-C., Vidal-Madjar, A., Ehrenreich, D., Lecavelier des Etangs, A., & Yung, Y. L. 2007, *ApJ*, 654, L99
- Torres, G. 2007, *ApJ*, 671, L65
- Torres, G., Andersen, J., & Giménez, A. 2010, *A&A Rev.*, 18, 67
- Torres, G., Claret, A., & Young, P. A. 2009, *ApJ*, 700, 1349
- Torres, G., Lacy, C. H., Marschall, L. A., Sheets, H. A., & Mader, J. A. 2006, *ApJ*, 640, 1018
- Trippe, S., Davies, R., Eisenhauer, F., Schreiber, N. M. F., Fritz, T. K., & Genzel, R. 2010, *MNRAS*, 402, 1126
- Turner, J. A., Chapman, S. J., Bhattal, A. S., Disney, M. J., Pongracic, H., & Whitworth, A. P. 1995, *MNRAS*, 277, 705

- Unwin, S. C. 2005, in *Astronomical Society of the Pacific Conference Series*, Vol. 338, *Astrometry in the Age of the Next Generation of Large Telescopes*, ed. P. K. Seidelmann & A. K. B. Monet, 37–45
- van Belle, G. T., et al. 2008, *The Messenger*, 134, 6
- Van Cleve, J. 2010, *Kepler Data Release 5 Notes*, NASA Ames Research Center, Moffett Field, CA
- van Dokkum, P. G. 2001, *PASP*, 113, 1420
- von Zeipel, H. 1924, *MNRAS*, 84, 665
- Vrtilek, S. D., Raymond, J. C., Garcia, M. R., Verbunt, F., Hasinger, G., & Kurster, M. 1990, *A&A*, 235, 162
- Wade, R. A., & Rucinski, S. M. 1985, *A&AS*, 60, 471
- Waldmann, I. P., Tinetti, G., Drossart, P., Swain, M. R., Deroo, P., & Griffith, C. A. 2012, *ApJ*, 744, 35
- Wallenquist, Å. 1950, *Arkiv for Astronomi*, 1, 59
- Watson, C. A., Steeghs, D., Shahbaz, T., & Dhillon, V. S. 2007, *MNRAS*, 382, 1105
- Welsh, W. F., Orosz, J. A., Seager, S., Fortney, J. J., Jenkins, J., Rowe, J. F., Koch, D., & Borucki, W. J. 2010, *ApJ*, 713, L145
- Wiktorowicz, S. J. 2009, *ApJ*, 696, 0902.0624
- Wilson, R. E. 1993, in *Astronomical Society of the Pacific Conference Series*, Vol. 38, *New Frontiers in Binary Star Research*, ed. K.-C. Leung & I.-S. Nha, 91–+
- Wilson, R. E., & Devinney, E. J. 1971, *ApJ*, 166, 605
- Winn, J. N., et al. 2006, *ApJ*, 653, L69
- Wittkowski, M., Schöller, M., Hubrig, S., Posselt, B., & von der Lühne, O. 2002, *Astronomische Nachrichten*, 323, 241
- Wolszczan, A., & Frail, D. A. 1992, *Nature*, 355, 145
- Yelle, R. V., & Griffith, C. A. 2003, *Icarus*, 166, 107
- Yoder, C. F., & Peale, S. J. 1981, *Icarus*, 47, 1
- Zahn, J. 1977, *A&A*, 57, 383
- . 1994, *A&A*, 288, 829
- Zahnle, K., Marley, M. S., Freedman, R. S., Lodders, K., & Fortney, J. J. 2009, *ApJ*, 701, L20
- Zucker, S., & Mazeh, T. 1994, *ApJ*, 420, 806